UCRL-11828

University of California

Ernest O. Lawrence Radiation Laboratory

NUCLEAR CHEMISTRY DIVISION ANNUAL REPORT

1964

Berkeley, California

DISCLAIMER

Research and Development

UCRL-11828
UC-4 Chemistry
TID-4500 (37th Ed.)

UNIVERSITY OF CALIFORNIA

Lawrence Radiation Laboratory
Berkeley, California

AEC Contract No. W-7405-eng-48

NUCLEAR CHEMISTRY DIVISION ANNUAL REPORT, 1964

January 1965

I. Perlman, Director, Nuclear Chemistry Division
Editors: J. M. Hollander, F. Reynolds, and B. B. Cunningham

Work done under the auspices of the U. S. Atomic Commission

Printed in USA. Price $6.00. Available from the Clearinghouse for Federal Scientific and Technical Information, National Bureau of Standards, U. S. Department of Commerce, Springfield, Virginia.

NUCLEAR CHEMISTRY DIVISION ANNUAL REPORT, 1964

Contents

UCRL-11828

NUCLEAR CHEMISTRY DIVISION ANNUAL REPORT, 1964

Lawrence Radiation Laboratory
University of California
Berkeley, California

December 1964

A. RADIOACTIVITY AND NUCLEAR STRUCTURE

1. DELAYED ALPHA DECAY OF Na^{20}†

R. D. Macfarlane* and A. Siivola

The delayed alpha emitter, Na^{20}, was first observed by Alvarez[1] and confirmed afterward by Sheline.[2] This nuclide decays by positron emission, with a half-life of 0.385 sec,[3] to α-particle unstable states in Ne^{20} at excitation energies of 8 to 10 MeV.

We have measured the α-particle spectrum associated with Na^{20} decay and have found that each of the groups observed can be correlated with previously measured 2^+ levels of Ne^{20}. Of particular interest is a 2^+, T = 1 state at 10.28 MeV in Ne^{20} which is significantly populated in Na^{20} beta decay and which alpha decays to the ground state of O^{16}, a transition which does not conserve isobaric spin.

Bombardments were made with the heavy-ion beams of the Hilac, with use of a target assembly and detection system designed for studying short-lived alpha emitters.[4] Simple dE/dx experiments were performed in order to identify the particles detected. A thin Al leaf absorber of known thickness was placed between the source and the detector, and the decrease in the energies of the various groups was measured and compared with the expected attenuation for α particles.

Our first observation of Na^{20} delayed alpha activity was in measurements of the alpha spectra of the products of Ru^{96} + Ne^{20} and Pd^{102} + Ne^{20} reactions, using 80- to 200-MeV Ne^{20} ions. Further bombardments using Al, Ni, and Cu targets and Ne^{20} as the projectile also produced the same alpha spectrum (Fig. A. 1-1 and Table A. 1-I). This means that the activity is associated with the Ne^{20} projectile and not with any particular target. The most likely nuclide that could give rise to these α groups appeared to be Na^{20}. Alvarez[1] established that the α particles had an energy greater than 2 MeV, but a detailed spectrum has never been measured.

In order to determine whether the alpha activity was due to Na^{20}, the alpha spectrum of this nuclide was measured when it was produced in simple compound-nucleus reactions. The reactions studied were $C^{12}(B^{10}, 2n)Na^{20}$, $C^{12}(B^{11}, 3n)Na^{20}$, and B^{11} + B^{10}. The products of the first two reactions yielded the same alpha spectrum as was observed in the Ne^{20} bombardments and which decayed with a half-life of 0.39 ± 0.05 sec, a value in agreement with the reported half-life of Na^{20}. The B^{11} + B^{10} reaction did not produce this activity over a broad range of bombarding energies (36 to 112 MeV_{lab}). This established that the activity was due to an isotope of Na. Excitation functions were obtained with use of the intensities of the more prominent 2.14- and 4.44-MeV α groups to determine relative yield. The shapes of the excitation functions, shown in Fig. A. 1-2, are characteristic of compound-nucleus reactions. For both the C^{12} + B^{11} and C^{12} + B^{10} reactions the activity was not detected at low energies, but became measurable at energies near and above threshold energies for the $C^{12}(B^{11}, 3n)Na^{20}$ and $C^{12}(B^{10}, 2n)Na^{20}$ reactions (23.8 and 12.4 MeV respectively).[5] The relative intensities of the α groups were independent of bombarding energy. These results showed that the α groups were associated with the same nuclide, and also established that this nuclide was Na^{20}.

As shown in Table A. 1-II, the major levels of Ne^{20} that are populated by the positron decay of Na^{20} and that alpha decay are all 2^+ levels. The ground-state spin and parity of Na^{20} are not known. However, the most probable assignment based on F^{20} measurements[6] is that

it is 2^+. Positron decay from Na^{20} should then fall into the classification of allowed unfavored transitions. To determine whether this is consistent with our data, we obtained estimates of log ft values for the transitions which involve delayed α-particle emission. The nuclide F^{20} decays 100% to the 2^+ level of Ne^{20} at 1.63 MeV, and the log ft for this transition is 5.1. We assigned this same log ft value to Na^{20} decay to the 1.63-MeV level and to the 7.40-MeV 2^+ level, which is α-particle unstable. No levels are known between these two 2^+ levels which would be populated by an allowed beta transition from Na^{20}. From the intensities of the α groups decaying from the 7.82-, 9.48-, and 10.28-MeV levels relative to the intensity from the 7.40-MeV level, log ft values and beta branching fractions were calculated. These are listed in Table A. 1-III. The log ft values for the transitions to the 7.82-, 9.48-, and 10.28-MeV levels are consistent with the values for allowed unfavored transitions.

The 2^+ level at 10.28 MeV was first reported by Pearson and Spear,[7] who detected it by the reaction $O^{16}(\alpha,\gamma)Ne^{20}$. They assigned a spin and parity of 2^+ to this state on the basis of radiative width measurements.

Our results show that the positron decay of Na^{20} to the 10.28-MeV level is highly favored over transitions to lower-lying states having the same spin and parity and to states just above the 10.28-MeV level. The reason for this enhanced beta transition is undoubtedly that the 10.28-MeV level is the lowest-lying T = 1 state of Ne^{20} and is the $T_z = 0$ state of the mass 20 isobaric triplet.

The presence of a $T = 1, 2^+$ level at 10.28 MeV affects the properties of the 2^+ level at 9.48 MeV, as one would expect. This level elastically scatters α particles, so it must therefore have a large T = 0 component. However, our results show that it is preferentially populated over lower-lying 2^+ states in Na^{20} beta decay, which indicates the presence of a significant T = 1 impurity component from the 10.28 MeV.

The total widths (essentially the alpha widths of the 7.40-, 7.82-, and 9.48-MeV levels) are known from previous work and are listed in Table A. 1-II.[6] From our measurements we conclude that the width of the 10.28-MeV level is <10 keV. The Coulomb barrier is mainly responsible for the low values of Γ for the 7.40- and 7.82-MeV levels. For states above about 8 MeV, the alpha barrier penetrability factor approaches unity and the widths of several levels above this energy approach 1 MeV. The width of the 9.48-MeV 2^+ level (24 keV) is quite low, and must be due to the T = 1 impurity admixture from the 10.28-MeV level. Calculations made following the procedure used by Wilkinson[8] show that the width of the T = 0 level at 9.48 MeV should be reduced to ≈16 keV because of the presence of a 2^+, T = 1 state at 10.28 MeV.

The 10.28-MeV T = 1 level is in a region of excitation where large isobaric spin impurities of levels may be expected because of the high density of states. The origin of the T = 0 impurity of the 10.28 MeV which allows it to alpha decay to the ground state of O^{16} may be the 2^+ level at 9.48 MeV, or higher-lying 2^+ levels which have not been identified.

Footnotes and References

† Shortened version of UCRL-11348, Nucl. Phys. (to be published).

* McMaster University, Hamilton, Ontario, Canada.

1. L. W. Alvarez, Phys. Rev. 80, 519 (1950).
2. R. K. Sheline, Phys. Rev. 82, 954 (1951).
3. C. A. Birge, private communication, quoted by F. Ajzenberg and T. Lauritsen, Rev. Mod. Phys. 24, 321 (1952).
4. R. D. Macfarlane and R. D. Griffioen, Nucl. Instr. Methods 24, 461 (1963).
5. L. A. König, J. H. E. Mattauch, and A. H. Wapstra, Nucl. Phys. 31, 18 (1962).
6. Nuclear Data Sheets, National Academy of Sciences, National Research Council, Washington, D. C., 1961.
7. J. D. Pearson and R. H. Spear, Bull. Am. Phys. Soc. 6, 505 (1961).
8. D. H. Wilkinson, Phil. Mag. 1, 379 (1956).

Table A. 1-I. Summary of results of alpha energy measurements

E_α (lab) (MeV)	Q_α (c.m.) (MeV)	Relative intensity[a]
2.14 ± 0.02	2.67 ± 0.02	100
2.49 ± 0.03	3.09 ± 0.03	5
3.80 ± 0.03	4.75 ± 0.03	1.6
4.44 ± 0.01	5.55 ± 0.01	21

a. Normalized to the intensity of the 2.14-MeV group, which was arbitrarily set equal to 100.

Table A. 1-II. Assignment of alpha groups to known levels of Ne^{20}.

Ne^{20} excitation energy[a] (MeV)	Known levels of Ne^{20} which coincide in energy[b]		
	Energy (MeV)	J^π	Γ(keV)
7.40 ± 0.02	7.43	2^+	8
7.82 ± 0.03	7.84	2^+	2
9.48 ± 0.03	9.50	2^+	24
10.28 ± 0.01	10.27	$2^+(T=1)$	< 10

a. From alpha energy measurements.
b. From reference 6.

Table A. 1-III. Estimated log ft values and beta branching fractions related to the Na^{20} decay scheme, for the transition $Na^{20}(2^+) \rightarrow 2^+$

Level (Ne^{20}) (MeV)	$E_{\beta^+ max}$ (MeV)	Partial $t_{1/2}$ (sec)	Log ft	Beta branching fraction
1.63	12.7	0.41	5.1[a]	0.94
7.40	6.9	≈ 8	5.1[a]	≈0.047
7.82	6.5	≈160	6.3	≈0.002
9.48	4.8	≈500	6.1	≈0.0008
10.28	4.0	≈ 38	4.7	≈0.01

a. Assumed value taken from F^{20} decay.

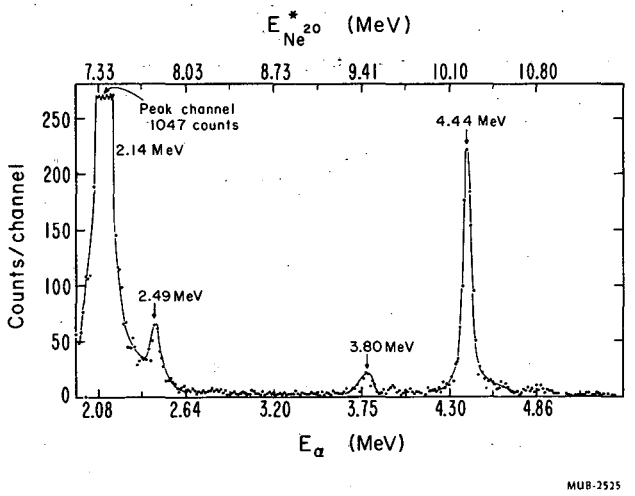

Fig. A. 1-1. The α-particle spectrum associated with the delayed alpha decay of Na^{20}.

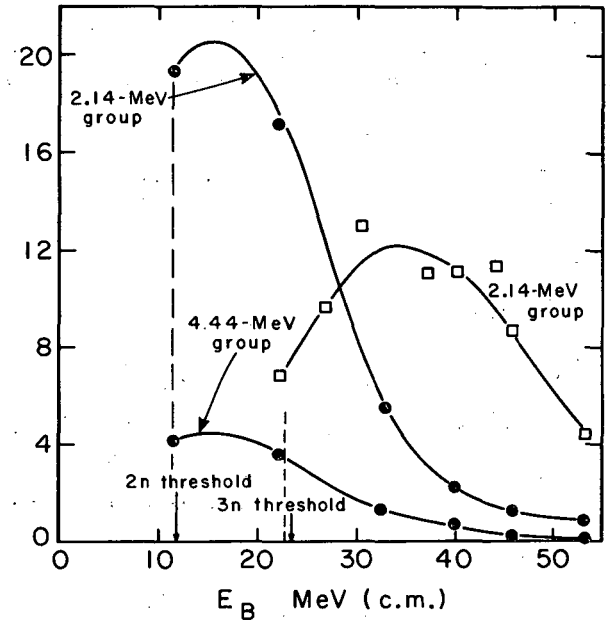

Fig. A. 1-2. Excitation functions for the production of Na^{20} by the reactions
● $C^{12} + B^{10} \rightarrow Na^{22*}$ and
□ $C^{12} + B^{11} \rightarrow Na^{23*}$. E_B refers to the c.m. energy of the B^{10} and B^{11} projectiles.

2. AN INTERNAL CONVERSION COEFFICIENT SPECTROMETER UTILIZING SEMICONDUCTOR DETECTORS†

H. T. Easterday,* A. J. Haverfield, and J. M. Hollander

The measurement of internal conversion coefficients has been a tool of wide use in nuclear spectroscopy. The internal conversion coefficient is very sensitive to several nuclear parameters--e.g., atomic number, transition energy, and transition multipolarity. Thus it is in principle possible to deduce the multipole orders of gamma transitions of particular energy and Z by comparison of experimentally measured conversion coefficients with appropriate values from tables of theoretically calculated coefficients.[1,2]

The recent availability of semiconductor detectors sensitive to both electrons and photons with moderate efficiency and energy resolution provides the possibility of measuring internal conversion coefficients in a direct and convenient manner. This report describes a simple "electron-gamma spectrometer" utilizing silicon and germanium detectors for this purpose. With it, conversion coefficients can be measured routinely with an accuracy of about 15%. The method is generally applicable, but, in particular, conversion coefficients of short-lived activities can be determined readily because the electron and gamma spectra are recorded simultaneously by use of multichannel analyzers.

A picture of the conversion-coefficient spectrometer is shown in Fig. A. 2-1 and a scale drawing is given in Fig. A. 2-2. It is essentially a small vacuum chamber in which are mounted, at 180° fixed geometry, lithium-drifted silicon and germanium detectors, for recording electron and gamma spectra, respectively. A 1/16-in. aluminum absorber placed in front of the Ge(Li) crystal prevents electron lines from being recorded in the gamma channel. No problem is encountered from gamma detection in the electron channel because the efficiency of Si(Li) for absorption of γ rays above about 80 keV is very low, and in any event gamma peaks fall at different energies from conversion-electron peaks. Dimensions of the Si(Li) detector

are 1 cm^2 by 3 mm deep. In order to minimize edge effects in this crystal, a 5/16-in.-diam aluminum collimator was placed in front of it. Dimensions of the Ge(Li) detector are 4 cm^2 by 5 mm deep. Both detectors were produced at this Laboratory.[3]

The active sources are introduced into the vacuum chamber through an air lock of conventional design, evacuated by a separate roughing pump. The source holder is designed so as to assure reproducible positioning of the source between the Si(Li) and Ge(Li) detectors. Sources are usually liquid-deposited, on backings of Au-coated Mylar, over an area of about 0.3 cm^2. The system is maintained at a pressure of 2×10^{-6} mm with the use of a standard oil diffusion pump, separated from the vacuum chamber by two cold traps in series to minimize deposition of pump oil on the detectors.

The Ge(Li) detector is maintained at -196°C with use of 10-liter gravity-feed liquid nitrogen reservoirs of commercial manufacture. The Si(Li) detector is maintained at -65°, at which temperature it was found to have the best energy resolution, by the introduction of a heat leak at the Si-detector mount.

An example of the electron and photon spectra taken with the conversion coefficient apparatus is shown in Fig. A.2-3. Here, the K, L, and M electron lines of the 279-keV transition in Hg^{203} decay are resolved, with line width 4.2 keV. The 279-keV photon line width is 4.6 keV.

The internal conversion coefficient may be expressed as

$$\epsilon_K = \frac{A_e}{\eta_e(E_e)} \cdot \frac{\eta_\gamma(E_\gamma)}{A_\gamma} , \qquad (1)$$

where A_e is the area under the conversion electron peak,
A_γ is the area under the corresponding γ-ray peak,
$\eta_e(E_e)$ is the detection efficiency of the Si(Li) system for electrons in the full-energy peak (including solid-angle factor), and
$\eta_\gamma(E_\gamma)$ is the detection efficiency of the Ge(Li) system for γ rays in the full-energy peak (including solid-angle factor).

Calibration of the instrument was done in the following way: First, a determination was made of the relative photopeak efficiency, $\eta_\gamma(E_\gamma)$, of the Ge(Li) detector as a function of γ-ray energy E_γ, by the use of a number of isotopes with well-measured photon relative intensities. The experimental gamma efficiency function is shown in Fig. A.2-4. A suitably normalized electron efficiency function $\eta_e(E_e)$ was then determined, with the use of Eq. (1), by measuring the areas under the electron and γ-ray lines from transitions with known conversion coefficients. The standard coefficients are listed in Table A.2-I. All solid-angle factors are constant and need not be considered explicitly. The normalized electron efficiency function so obtained is shown in Fig. A.2-5.

As a check on the shape of the electron efficiency function, a source containing Bi^{205} and Bi^{206} was prepared, and the relative electron efficiencies were independently determined. Satisfactory agreement with the curve of Fig. A.2-5 was obtained.

As an example of the application of this method, the internal conversion coefficients of the 191-keV transition from 18-hour Pt^{197} decay and of the 346-keV transition from 90-minute Pt^{197m} were measured. Comparison of the experimental conversion coefficient, 0.69 ± 0.07, with the quoted theoretical values yields the result that the 191-keV transition is an M1-E2 mixture with $33\pm9\%$ E2 admixture. The electron K/L ratio, 5.2 ± 0.6, indicates a $22\pm11\%$ E2 admixture. The experimental values, $\epsilon_K = 3.9\pm0.4$ and $K/L = 1.8\pm0.2$, clearly establish the multipolarity of the 346-keV transition as M4, since the theoretical M4 values[1] are $\beta_K(M4) = 4.2$, $K/L = 1.75$.

Footnotes and References

† Material condensed from H. T. Esterday, A. J. Haverfield, and J. M. Hollander, An Internal Conversion Coefficient Spectrometer Utilizing Semiconductor Detectors, Nucl. Instr. Methods (in press).

* Present address: Oregon State University, Corvallis, Oregon.

1. L. A. Sliv and I. M. Band, Coefficients of Internal Conversion of Gamma Radiation (USSR Academy of Sciences, Moscow-Leningrad, 1956) Part I: K Shell; Part II: L Shell.
2. M. E. Rose, Internal Conversion Coefficients (North-Holland Publishing Co., Amsterdam, 1958).
3. F. S. Goulding and W. L. Hansen, An Automatic Lithium-Drifting Apparatus for Silicon, UCRL-11261, Feb. 1964.

Table A. 2-I. "Standard" internal conversion coefficients used for calibration of e-γ spectrometer.

Isotope	Transition energy (keV)	Electron energy (keV)	ϵ_k
Hg^{203}	279	193	0.162 ± 0.003
Au^{198}	412	329	0.0303 ± 0.0005
Cs^{137}	662	625	0.095 ± 0.004
Bi^{207}	1771	1683	0.0025 ± 0.0005
Cd^{109}	88	62	9.9 ± 0.5

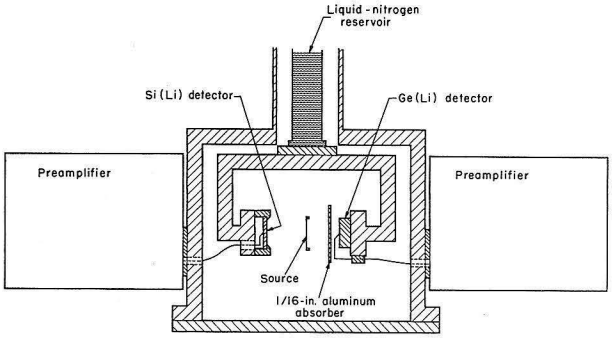

Fig. A. 2-2. Drawing of conversion-coefficient spectrometer.

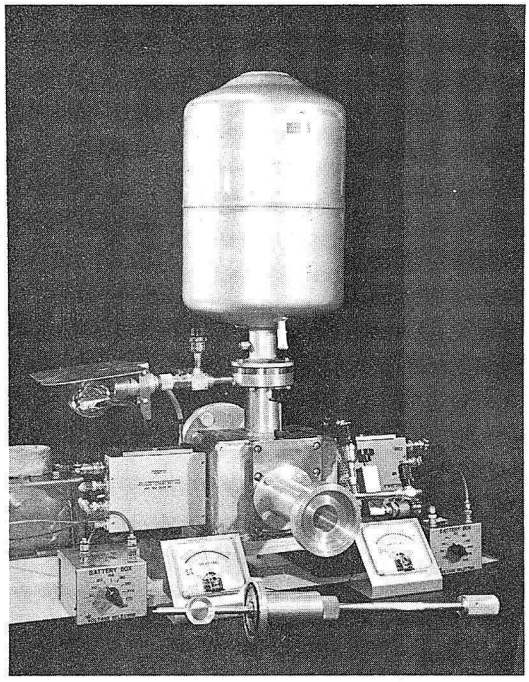

Fig. A. 2-1. Photograph of conversion-coefficient spectrometer utilizing Si(Li) and Ge(Li) detectors.

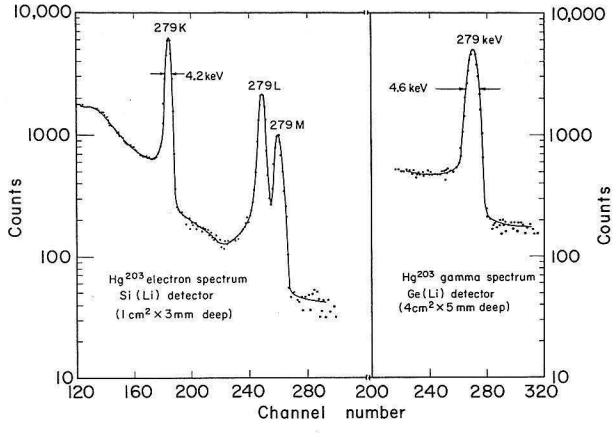

Fig. A. 2-3. Portions of Hg^{203} electron and γ-ray spectra taken with conversion-coefficient spectrometer.

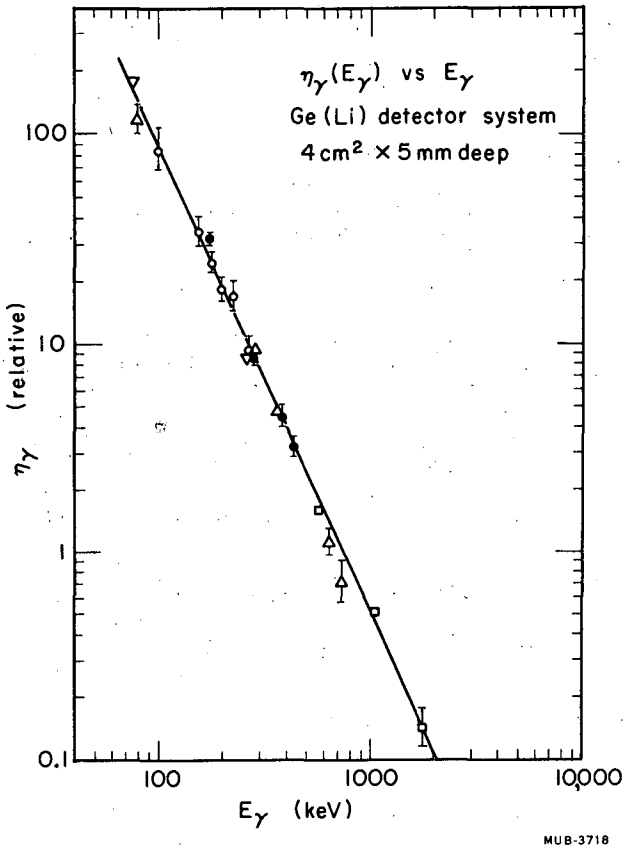

Fig. A. 2-4. Efficiency function for photoelectric absorption of γ rays in the 4 cm^2 × 5 mm Ge(Li) detector of the electron-gamma spectrometer. The following symbols denote isotopes used for the calibration: ○, Ta^{182}; ●, Lu^{177m}; □, Bi^{207}; ▽, Hg^{203}; △, I^{131}.

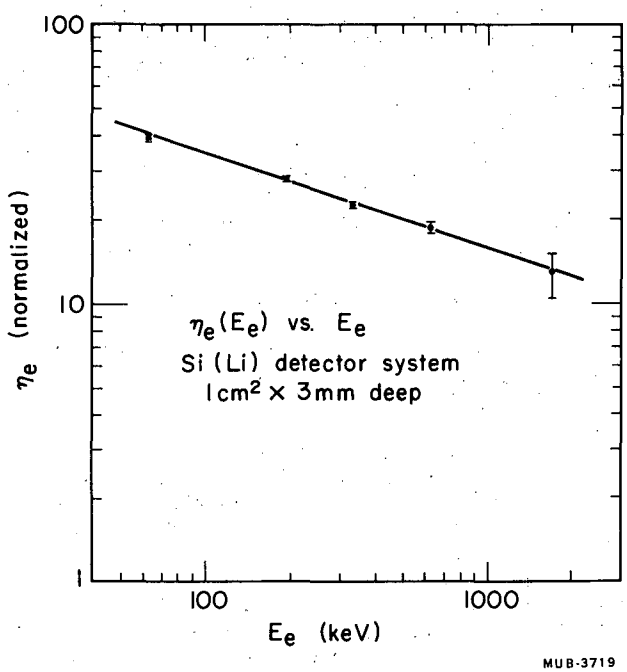

Fig. A. 2-5. Efficiency function for "full energy" electron absorption in the Si(Li) detector of conversion-coefficient spectrometer, normalized to the γ-ray efficiency function for use in determining internal conversion coefficients. Points obtained from the "standard" conversion coefficients, shown with error bars, were used to obtain this normalized function.

3. NOTE ON THE Pt AND Hg MASS-197 ISOMERS*

A. J. Haverfield, H. T. Easterday,† and J. M. Hollander

The low-lying energy levels of $_{79}Au^{197}$ are well known as the result of studies of 18-h $_{78}Pt^{197}$, 65-h $_{80}Hg^{197}$, and 24-h Hg^{197m}, and also from studies of particle inelastic scattering of Au^{197}. The six known levels in Au^{197} below 600 keV have been discussed by Braunstein and de Shalit[1] in terms of two intrinsic single-proton states, $d_{3/2}$ (ground) and $h_{11/2}$ (409 keV), plus a quadruplet (1/2, 3/2, 5/2, 7/2) arising from the coupling of a 2+ core excitation with the $d_{3/2}$ proton. This situation is represented in Fig. A. 3-1.

The present experiments were motivated by the following considerations:

(a) As pointed out by Artna,[2] doubt has been cast on the assignment of spin 3/2 to the 268-keV level as a result of the recent measurements by Joshi et al.[3] of the internal conversion coefficient of the 191-keV transition. The value obtained by these workers, 2.0 ± 0.5, is considerably higher than the theoretical value[4] for a pure M1 transition, 0.79, and suggests that the 191-keV transition has E0 admixture and therefore that the 268-keV state has spin 1/2 rather than 3/2 as previously thought.

(b) A recent paper by Griesacker and Roy,[5] reporting the results of β-γ and γ-γ coincidence experiments on neutron-irradiated Pt^{196} (enriched), has suggested a more complicated decay scheme for Pt^{197} and Pt^{197m} than had previously been accepted; also a new level in Au^{197} at 155 keV was reported.
(c) The multipolarity of the isomeric transition in Pt^{197m} has not been definitely established.

Accordingly, the decays of Pt^{197}, Pt^{197m}, Hg^{197}, and Hg^{197m} have been examined with the use of semiconductor detector spectrometers. Gamma-ray spectra were recorded with lithium-drifted germanium detectors, and internal conversion coefficients were measured with an electron-gamma spectrometer employing both silicon and germanium detectors.

Briefly, we have found the following:

(a) The conversion coefficient of the 191-keV transition in Au^{197} following Pt^{197} decay is $\epsilon_K = 0.69 \pm 0.07$, $K/L = 5.2 \pm 0.6$. This transition is interpreted as having multipolarity M1 + ($\approx$28%)E2, and the 268-keV level is assigned spin and parity of 3/2+, consistent with the "core-excitation" interpretation of these levels by Braunstein and de Shalit.
(b) The reported existence of a level in Au^{197} at 155 keV has not been confirmed.
(c) The conversion coefficient of the 346-keV isomeric transition in Pt^{197m} is $\epsilon_K = 3.9 \pm 0.4$, $K/L = 1.8 \pm 0.2$, and is interpreted as an M4.
(d) From the decay patterns of Pt^{197} and Pt^{197m}, spin assignments 1/2- and 13/2+ are made for these isomers, respectively.
(e) The absolute transition probability of the 202-keV E2 radiation connecting the 279-keV (5/2+) and 77-keV (1/2+) states in Au^{197} was found to be much greater than that predicted from the wave functions given by de Shalit.[1] It seems that this high transition probability could be better accounted for if the wave functions given by Kisslinger and Sorensen,[6] in their generalized theoretical treatment of the energy levels and moments of spherical nuclei, were used.

Our revised decay scheme is shown in Fig. A. 3-2.

Footnotes and References

* Material condensed from A. J. Haverfield, H. T. Easterday, and J. M Hollander, Note on the Pt and Hg Mass-197 Isomers, Nucl. Phys. (in press).
† Present address: Oregon State University, Corvallis, Oregon.
1. A. Braunstein and A. de Shalit, Phys. Letters 1, 264 (1962).
2. A. Artna, private communication, Jan. 1963.
3. M. C. Joshi and B. V. Thosar, in Proceedings of the International Conference on Nuclear Structure, Kingston, Canada, D. A. Bromley and E. V. Vogt, Eds. (University of Toronto Press, 1960), p. 623.
4. L. A. Sliv and I. M. Band, Coefficients of Internal Conversion of Gamma Radiation (USSR Academy of Sciences, Moscow-Leningrad, 1956), Part I: K Shell; Part II: L Shell.
5. P. B. Griesacker and R. R. Roy, Nucl. Phys. 50, 41 (1964).
6. L. S. Kisslinger and R. A. Sorensen, Rev. Mod. Phys. 35, 853 (1963).

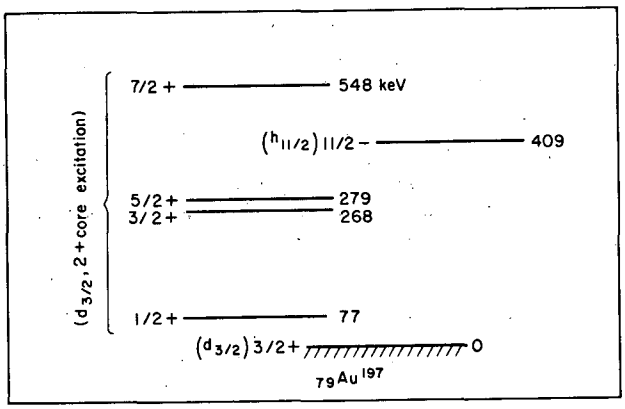

Fig. A. 3-1. Energy levels of Au^{197} arranged according to the "core-excitation" model of Braunstein and de Shalit (reference 1).

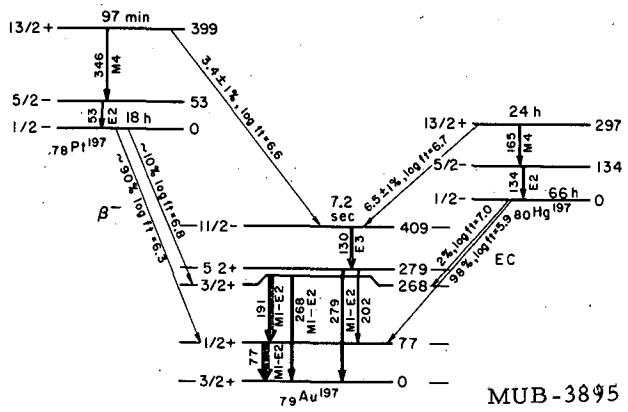

Fig. A. 3-2. Decay scheme of the A=197 isomers of Hg and Pt. The 7/2+ level in Au^{197} at 548 keV is not shown on this figure.

4. DIGITAL-COMPUTER CALCULATION OF MATRIX ELEMENTS OF NUCLEAR INTERACTIONS

Martin G. Redlich and Robert M. Baer*

We consider the interaction

$$V(1,2) = V_{X\kappa}(r)\ P_X\ Q_\kappa \qquad (1)$$

between nucleons 1 and 2, with four operators P_X:

$$P_W = 1 \qquad P_M = \text{Space-coordinate exchange operator}$$
$$P_\sigma = \vec{\sigma}_1 \cdot \vec{\sigma}_2, \quad P_{M\sigma} = P_M\, \vec{\sigma}_1 \cdot \vec{\sigma}_2.$$

The index κ equals 0 or 2, and

$$Q_0 = 1, \qquad Q_2 = S_{12} = \text{Tensor interaction operator.}$$

It has been shown by Horie and Sasaki[1] that the shell-theoretical matrix elements defined by (1) for harmonic-oscillator single-particle wave functions can be expressed as linear combinations of simple radial integrals $K_m^{(\kappa)}$ which depend only upon $V_{X\kappa}(r)$ and the harmonic oscillator parameter ν. The subscript m takes integer values ≤ 14 for states up to and including $1j_{15/2}$. Thus

$$\langle j_1 j_2 J | V_{X\kappa}(r) P_X Q_\kappa | j_1' j_2' J \rangle = \sum_m C_m(j_1 j_2, j_1' j_2', J, X_1 \kappa)\ K_m^{(\kappa)}. \qquad (2)$$

The coefficients C_m can be expressed as

$$\sqrt{d}\ \frac{e}{f}\,, \tag{3}$$

with d, e, and f integers. Multiple-precision fixed-point arithmetic[2] has therefore been used in a digital-computer program to calculate the exact values of the coefficients C_m for given j_1, j_2, j_1', and j_2'. Another program calculates in an entirely independent way the exact values of matrix elements of the zero-range central and (singular) tensor interactions. This serves as a check upon the C_m calculated by the first program, because for the zero-range interactions, the following simple formulas hold:

$$K_m^{(0)} = \sqrt{2\nu^3/\pi}\,, \text{ for all m,} \tag{4}$$

$$K_m^{(2)} = (2m+3)I_1/5.$$

Here I_1 is a Talmi integral.

FORTRAN programs for the $K_m^{(\kappa)}$ for the Gaussian, Yukawa, and Coulomb interactions have been constructed with double-precision floating-point arithmetic. Double-precision arithmetic is also used for the final steps given in Eq. (2).

Execution times are small. Even for heavy nuclei, the average time needed to calculate all sets of the C_m of Eq. (2) for given j_1, j_2, j_1', and j_2' and all total angular momenta J for the four central and two tensor interactions is less than 1 minute.

Footnotes and References

* Computer Center, Campbell Hall, University of California, Berkeley.

1. H. Horie and K. Sasaki, Prog. Theor. Phys. (Kyoto) 25, 475 (1961).
2. R. M. Baer and M. G. Redlich, Commun. Assoc. Computing Machinery 7, 657 (1964).

5. ENERGY LEVELS OF Pb^{210} FROM SHELL THEORY

Martin G. Redlich

Calculations for Pb^{210} have been based upon the double-closed-shell core model with harmonic-oscillator wave functions. Matrix elements for several two-nucleon interactions were calculated on a digital computer.[1] All two-neutron configurations of the $2g_{9/2}$, $1i_{11/2}$, $1j_{15/2}$, $3d_{5/2}$, $4s_{1/2}$, $2g_{7/2}$, and $3d_{3/2}$ main shell were included.

A singlet-even Gaussian effective interaction with parameters determined by low-energy proton-proton scattering and zero triplet odd effective interaction give to within 50 keV both the binding energy of the two outer neutrons determined from experimental data and the energies of the four excited states which have so far been identified. The harmonic-oscillator parameter ν and the interaction are similar to those which gave excellent agreement[2] with experimental energies for Pb^{206}.

Calculations with a Yukawa singlet-even interaction[3] and with additional attractive and repulsive central and central + tensor triplet-odd interactions were also made for Pb^{210}. They all lead to somewhat worse agreement. None of these interactions is, however, definitely excluded by the present data.

Footnotes and References

1. M. G. Redlich and R. M. Baer, preceding report.
2. W. W. True and K. W. Ford, Phys. Rev. 109, 1675 (1958).
3. M. J. Kearsley, Nucl. Phys. 4, 157 (1957).

6. NUCLEAR STRUCTURE AND PAIRING CORRELATIONS FOR THE HEAVY ELEMENTS*

H. J. Mang,† J. K. Poggenburg, and J. O. Rasmussen

The theoretical prediction of alpha decay rates[1] for the heavy elements requires the calculation of wave functions describing the nuclear states. The calculation takes for a starting point the shell-model wave functions of Nilsson[2] and seeks variational solutions of the Bardeen, Cooper, Schrieffer[3] (BCS) type

$$\Psi = \prod_{\nu}(u_\nu + v_\nu b^+_\nu b^+_{\nu-})\,|0\rangle$$

to determine the orbital occupation probabilities v^2_ν. The method seeks stationary values of $H - \lambda N$, where the chemical potential λ is adjusted to give the number operator N the proper expectation value.

The nonlinear simultaneous equations for the method have been given by Belyaev,[4]

$$\Delta_\nu = \frac{1}{2}\sum_{\nu'} \frac{G_{\nu\nu'}\Delta_{\nu'}}{\sqrt{(\tilde{\epsilon}_{\nu'}-\lambda)^2+\Delta^2_{\nu'}}} = \sum_{\nu'} G_{\nu\nu'}u_{\nu'}v_{\nu'}\ , \tag{1}$$

$$N = \sum_{\nu} 2v^2_\nu\ , \tag{2}$$

$$\tilde{\epsilon}_\nu = \epsilon_\nu - \sum_{\nu'} \bar{G}_{\nu\nu'}v^2_{\nu'}\ , \tag{3}$$

$$v^2_\nu = \frac{1}{2}\left(1 - \frac{\tilde{\epsilon}_\nu - \lambda}{\sqrt{(\tilde{\epsilon}_\nu-\lambda)^2+\Delta^2_\nu}}\right). \tag{4}$$

The Δ_ν are the pairing correlation energy parameters of the orbitals with Nilsson-state energies ϵ_ν. The $G_{\nu\nu'}$ are the usual pairing-force matrix elements, and the $\bar{G}_{\nu\nu'}$ are matrix elements which give rise to terms in the self-consistent field in which the orbitals have the "self-energy" $\tilde{\epsilon}_\nu$. The matrix elements are defined by Belyaev,

$$G_{\nu\nu'} = \langle \nu+\ \nu-|G|\nu'+\ \nu'-\rangle \ - \ \langle \nu+\ \nu-|G|\nu'-\ \nu'+\rangle\ ,$$

$$\bar{G}_{\nu\nu'} = \langle \nu+\ \nu'+|G|\nu+\ \nu'+\rangle \ - \ \langle \nu+\ \nu'+|G|\nu'+\ \nu+\rangle$$

$$+ \ \langle \nu+\ \nu'-|G|\nu+\ \nu'-\rangle \ - \ \langle \nu+\ \nu'-|G|\nu'-\ \nu+\rangle\ .$$

The $\bar{G}_{\nu\nu'}$ have usually been neglected with the result that $\tilde{\epsilon}_\nu = \epsilon_\nu$, but we have included them. The matrix elements were calculated from Nilsson wave functions for $\eta = 6$, using a delta force. The choice of a delta force leads to the identity $\bar{G}_{\nu\nu'} = G_{\nu\nu'}$.

The calculations assume an inert core which is completely filled and treats the outer orbitals in the Nilsson scheme. For protons the core is 76, and 25 outer orbitals are

considered, while for neutrons 40 orbitals are considered outside a core of 106 neutrons. The pairing-force strengths were adjusted to constant values over the whole heavy region to give the best fit to the respective experimental odd-even mass differences.

Figure A.6-1 shows a plot of the correlation functions Δ_ν for some important proton orbitals labeled by their Nilsson asymptotic quantum numbers, and Figs. A.6-2 and A.6-3 are corresponding plots for neutrons. It is interesting to note the effect of the "gap" at 152 neutrons. Figure A.6-4 shows the depression of the self-energy terms $\tilde{\epsilon}_\nu$ caused by the $\overline{G}_{\nu\nu'}$ matrix elements as protons are added to the system. Figure A.6-5 is the corresponding plot for neutrons.

It is well known that the BCS wave functions do not conserve exact particle number, but only the average. Figure A.6-6 shows, for example, the probability $\mathcal{P}$ of components with p pairs in the wave function for n average pairs. It is possible to project out only that component of the BCS wave function with proper pair number and renormalize. This procedure gives a lower ground-state energy than ordinary BCS, and we refer to the method as PBCS. Dietrich, Mang, and Pradal[5] have given a formulation whereby the variation is performed on a projected wave function with fixed particle number. This method, which we designate FBCS, gives the lowest ground-state energies. It is clearly the best method within the BCS framework, and preserves pairing correlations where ordinary BCS fails.

As a measure of pairing correlation we define the "diffuseness" parameter D as a sum over all orbitals of the square root of the product of the occupation probability of an orbital times the probability it is empty. For ordinary BCS this gives the equation

$$D = \sum_\nu u_\nu v_\nu ,$$

with analogous equations for PBCS and FBCS. Figure A.6-7 shows the differences among the three methods, in particular, the weakening of pairing in the PBCS method and the smoothing effect of the BCS compared with FBCS method. Figure A.6-8 demonstrates that the occasional abrupt disappearance of pairing as the force strength is decreased is symptomatic of the defect of nonconservation of particle number, and does not occur with the FBCS fixed-particle-number variation.

Figures A.6-9 and A.6-10 compare theoretical with experimental odd-even mass differences for protons and neutrons. Figures A.6-11 and A.6-12 are based on the FBCS method. They show theoretical band-head positions for odd-proton and odd-neutron systems.

The general agreement with experimental odd-even mass differences and the correct ground-state prediction and reasonably correct level ordering in Figs. A.6-11 and A.6-12 are indicative of the reliability of the calculated wave functions. The superiority of the FBCS method is clearly demonstrated with regard to the nuclear diffuseness, which enhances the calculated theoretical alpha-decay rates.

Footnotes and References

* Condensed version of paper (UCRL-10939, June 1964) submitted to Nucl. Phys.
† Present address Technische Hochschule, Munich, Germany.
1. H. J. Mang and J. O. Rasmussen, Kgl. Danske Videnskab. Selskab Mat.-Fys. Skr. 2, No. 3 (1962), H. J. Mang et al., in Chemistry Division Annual Report, 1963, UCRL-11213, Feb. 1964.
2. S. G. Nilsson, Kgl. Danske Videnskab. Selskab Mat.-Fys. Medd. 29, No. 16 (1955).
3. J. Bardeen, L. N. Cooper, and J. R. Schrieffer, Phys. Rev. 108, 1175 (1957).
4. S. T. Balyaev, Kgl. Danske Videnskab. Selskab Mat.-Fys. Medd. 31, No. 11 (1959).
5. K. Dietrich, H. J. Mang, and J. H. Pradal, Phys. Rev. 135, B22 (1964).

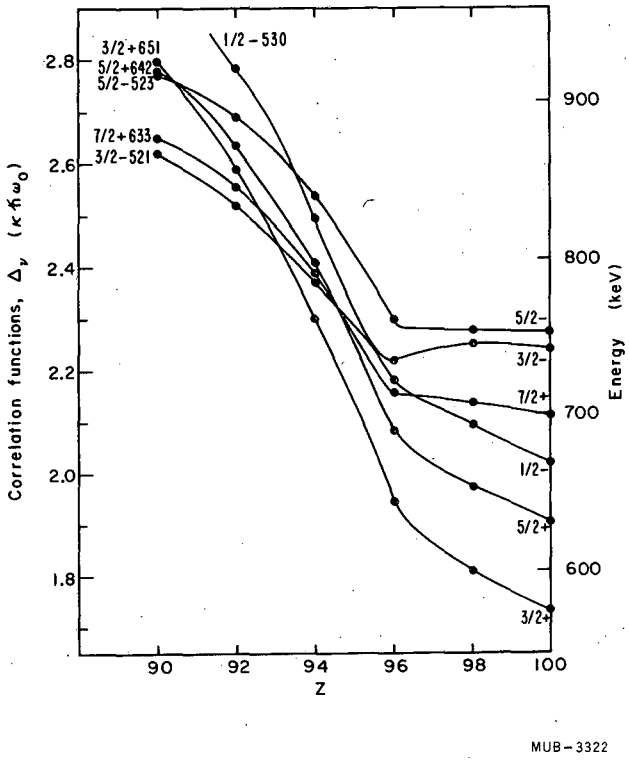

Fig. A. 6-1. Plot of proton correlation functions Δ_ν as a function of proton number. The energy is indicated in units of 0.05 $\hbar\omega_0$ on the left and in keV on the right.

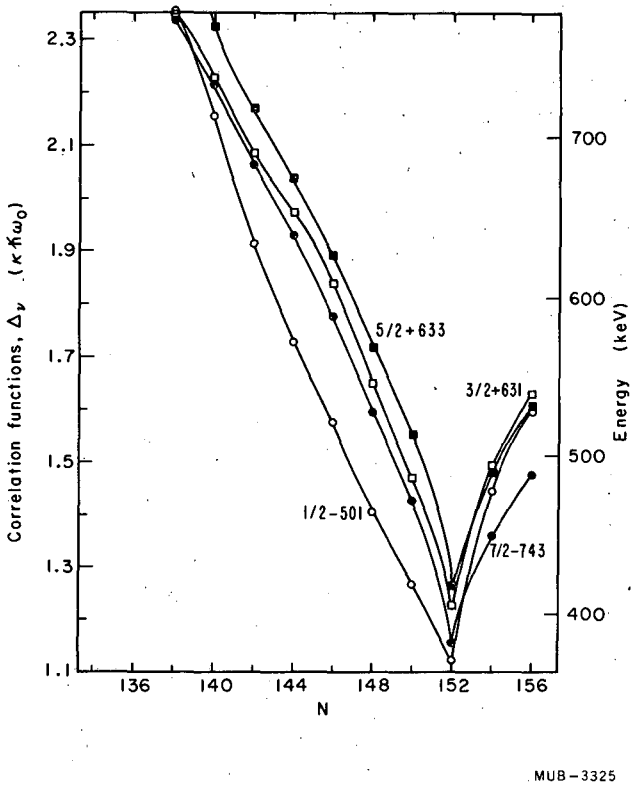

Fig. A. 6-2. Plot of neutron correlation functions Δ_ν as a function of neutron number for some neutron orbitals.

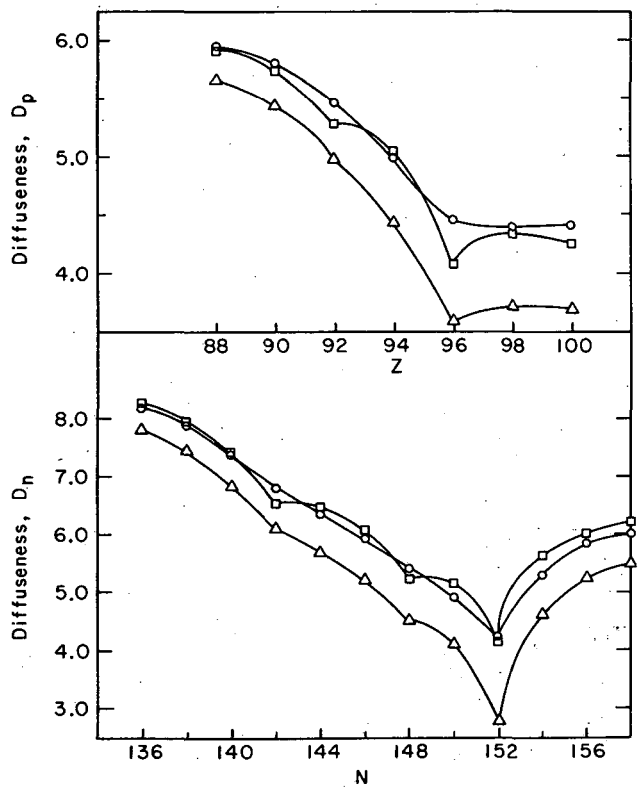

MUB-3328

Fig. A. 6-7. Plots of diffuseness of the Fermi surface for proton and neutron systems. The three variational methods are plotted with the following symbols: O BCS, Δ PBCS, □ FBCS.

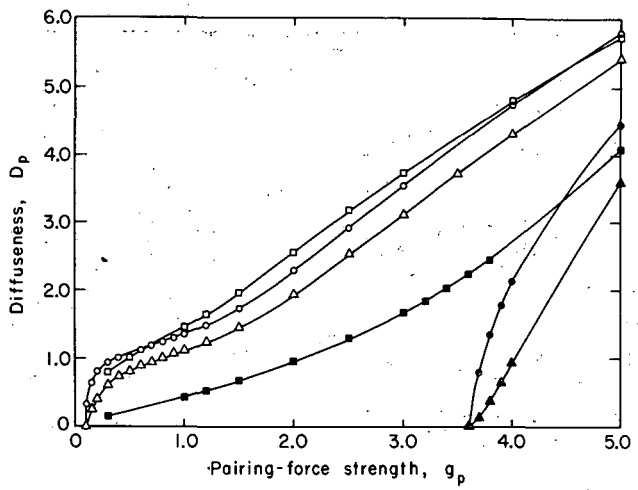

MUB-3329

Fig. A. 6-8. Plots of diffuseness of the Fermi surface for proton systems as a function of decreasing pairing-force strength. Open symbols denote 7 pairs (Z = 90), and closed symbols, 10 pairs (Z = 96). O BCS, Δ PBCS, □ FBCS.

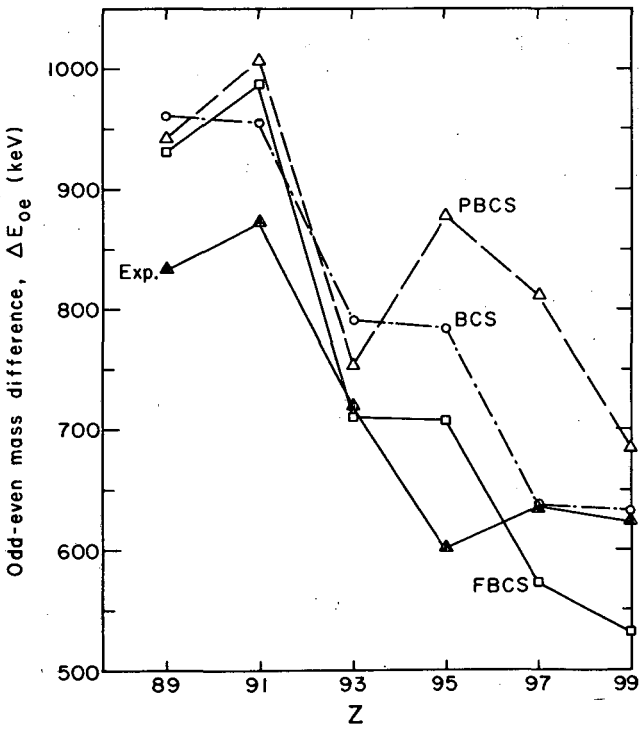

MUB-3330

Fig. A. 6-9. Odd-even mass differences for proton systems (O BCS, Δ PBCS, □ FBCS theoretical, and ▲ experimental).

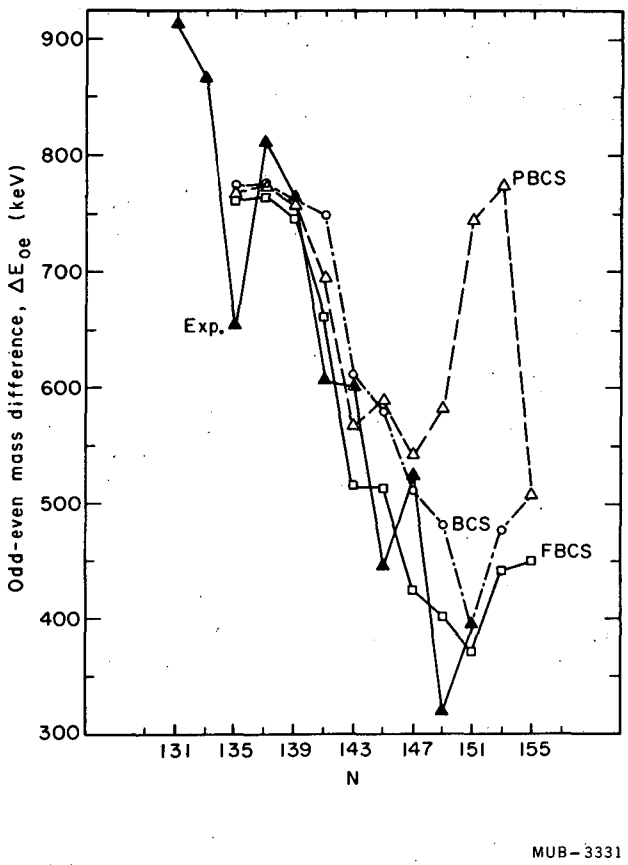

Fig. A. 6-10. Odd-even mass differences for neutron systems (O BCS, Δ PBCS, □ FBCS theoretical, and ▲ experimental.

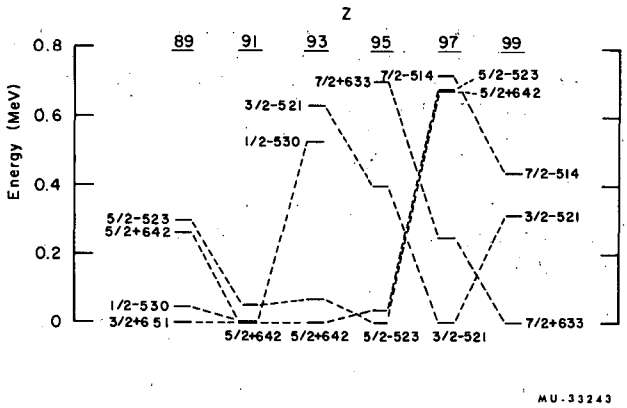

Fig. A. 6-11. Theoretical (FBCS) energies of various bands in odd-proton nuclei.

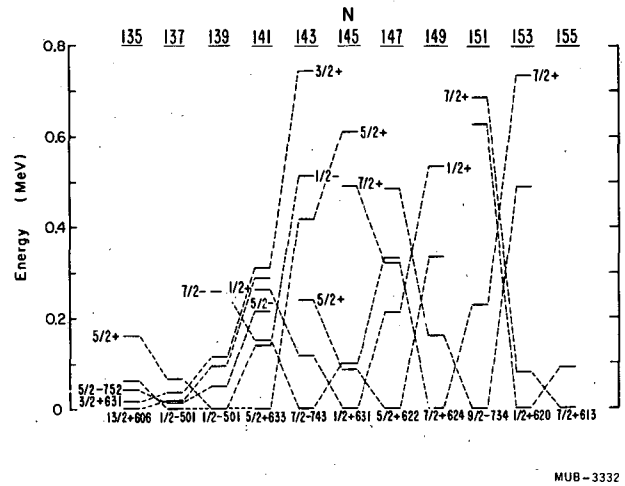

Fig. A. 6-12. Theoretical (FBCS) energies of various bands in odd-neutron nuclei.

7. EFFECT OF AN EXTERNAL ELECTRIC FIELD ON INNER ELECTRON SHELLS IN URANIUM OBSERVED BY MEANS OF INTERNAL CONVERSION*

T. Novakov† and J. M. Hollander

A recent work by Novakov, Hollander, and Graham[1] described a method for the recoil measurement of subnanosecond lifetimes of nuclear levels following alpha decay, that makes use of a high-resolution electron spectrometer in conjunction with an electrostatic double-grid system. During the testing of this method it was shown that internal conversion lines from beta-emitting sources underwent no change either in shape or intensity when electric fields up to 5×10^4 V/cm were used. It seemed interesting to find out if any changes in conversion line shapes could be induced with the use of much higher field strengths.

For the production of the electric field a stainless steel razor blade was used in conjunction with the grid system described in reference 1. The radioactive material was vacuum sublimed onto the blade edge. The blade edge occupied the usual spectrometer source position.

A 5-mm separation was maintained between the blade edge and first grid, as well as between the first and second grid. The blade itself (source) and the second grid were always kept at ground potential, while the first grid was connected to a positive or negative voltage up to about 12 kV. For recording spectra with field off, the first grid was also connected to ground. The whole blade and grid assembly was mounted in the position of the regular source holder of the Berkeley 50-cm iron-free $\pi\sqrt{2}$ double-focusing electron spectrometer.[2]

The strength of the electric field at the blade edge surface can be estimated from the values of the applied voltage V (10 kV) and the radius of curvature r ($\approx 10^{-4}$ cm) of the edge according to the formula

$$E = V/r \ln (R/r),$$

where R is the distance between the blade edge and the first grid. With an applied voltage of 10 kV, mostly used, the value of the field is calculated to be 6×10^6 V/cm.

Because the accelerating and decelerating voltages in the grid system are equal, there is no net change in electron energy in these experiments. However, in principle the focusing properties of the spectrometer can be affected by the applied electric field, so it is important to search for and demonstrate any instrumental focusing effects in order that they not obscure the observation of real line-shape changes, if any. This was done, with sources of Sm^{153}, Lu^{177}, and Pa^{233}. The following focusing effects became evident during the course of the experiments: When the electron energies are of the same order as the applied voltage, the spectrometer transmission is increased and the half-widths of the conversion lines become narrower if the first grid is negative. Reversing the polarity reverses the effect, that is, the transmission decreases and the line widths increase. It was noted that the focusing effects are energy-sensitive, being greater for lower electron energies.

However, not all measured conversion lines showed a behavior consistent with the above instrumental focusing effects.

Figure A.7-1 shows the M_I and L_{III} conversion lines of the 28- and 40-keV transitions, respectively, in U^{233} taken with the Pa^{233} source, with and without negative voltage on the first grid. It is seen that the M_I28 line, apart from the instrumental increase in intensity, shows no obvious change in shape. However, the $L_{III}40$ line with field on shows a definite shoulder on the low-energy side. The separation between the shoulder and the main peak is about 45 eV.

A similar shoulder was found accompanying the $M_{II}28$ line, separated from the main peak by about 50 eV. A scan of the $M_{III}28$ line also revealed a shoulder, but in this case it was separated by about 100 eV from the main peak. In contrast to the $L_{III}40$ line, the $L_{II}40$ line showed only the established instrumental effects, and no shoulder appeared on this line upon application of the field.

The shoulder, or satellite line, is not affected by a reversal of the field. This is illustrated by Fig. A.7-2, which shows the spectrum obtained with positive voltage on the first grid.

K-, L-, M-, and N-conversion lines of the 113-keV transition in Hf^{177} were also studied. The N 113 group, although not resolved completely, showed a change in shape that could not be explained by the instrumental focusing effect of the field. The K-, L-, and probably M-conversion lines showed only the instrumental changes.

The following summarizes the evidence that the shoulders, or satellite lines, are of origin other than instrumental effects:

(a) The energy separation between the M_I28 and $L_{III}40$ lines is very small, $\approx$150 eV. Therefore any instrumental effect on one of these lines should also be seen on the other line. The experiments, however, showed that the M_I28 line behaves regularly while the $L_{III}40$ shows a satellite or shoulder. The $L_{II}40$ line does not produce a satellite.
(b) Reversal of the field direction does not change the result.

Therefore we ascribe the observed effect to changes in the inner electron shells induced by the external electric field. The occurrence of shoulders rather than shifts of the entire line is probably due to the fact that only a small fraction of the radioactive atoms is actually located in the region of the highest electric field at the razor blade edge.

Some regularities in the behavior of the observed line shifts are the following:

(a) The action of the external field is such as to reduce the energy of the conversion electron energy, that is, to increase the electron binding energy of the affected shell.
(b) The magnitude of the energy shift for a given field increases from $s_{1/2}$ to $p_{1/2}$ to $p_{3/2}$ subshells, and from inner to outer shells.
(c) The direction of the shift is independent of the sign of the applied voltage.
(d) The magnitude of the shift has a higher dependence than linear on the magnitude of the field.

The characteristics of the observed effect strongly resemble the Stark effect. However, the energy shifts are relatively so big that the external field would be unable to produce them directly. Moreover, the fact that L and M shells in uranium are well screened makes the direct Stark effect even less probable. An order-of-magnitude estimate of the field at the positions of these levels needed to produce Stark shifts of the observed magnitudes indicates that fields of 10^9 to 10^{10} V/cm would be required. Therefore we must assume that some kind of indirect field action is involved. It may be possible, for instance, that an internal atomic or molecular mechanism amplifies the external field.

Footnotes and References

* This report is a condensation of material in UCRL-11673, Oct. 1964.
† On leave from Faculty of Sciences, University of Belgrade, Yugoslavia.

1. T. Novakov, J. M. Hollander, and R. L. Graham, Nucl. Instr. Methods 26, 189 (1964).
2. K. Siegbahn, C. L. Nordling, and J. M. Hollander, Chemistry Division Annual Report, 1961, UCRL-10023, Jan. 1962, p. 232; J. M. Hollander and R. L. Graham, Chemistry Division Annual Report, 1962, UCRL-10624, Jan. 1963, p. 273.

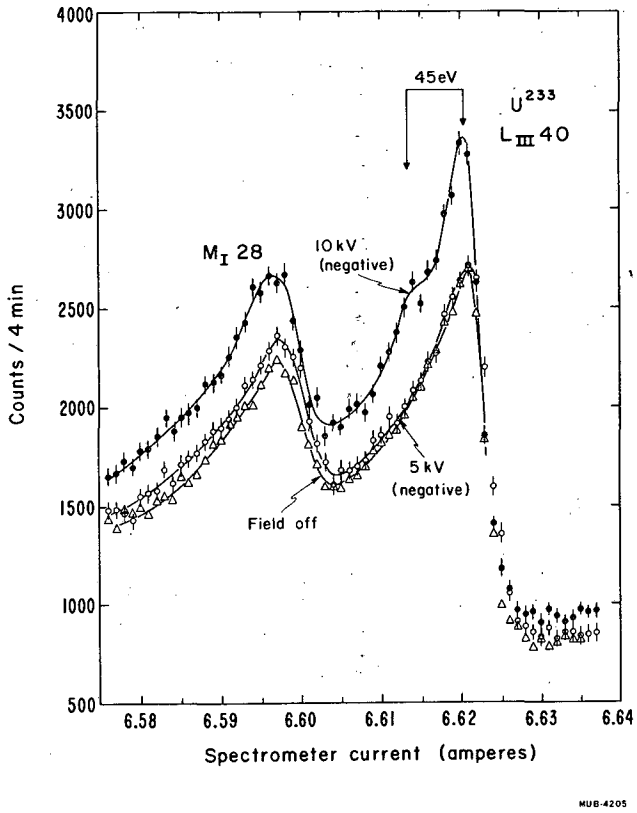

Fig. A.7-1. M_I28 and $L_{III}40$ (U^{233}) lines measured with field off, 5 kV and 10 kV negative potential on the first grid. The $L_{III}40$ line shows a low-energy shoulder when 10 kV is applied to the grid.

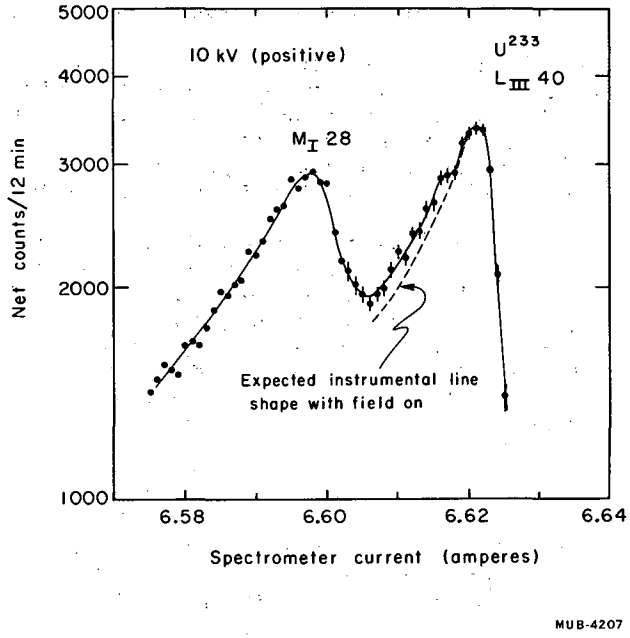

Fig. A.7-2. Semilogarithmic plot of the M_I28 and $L_{III}40$ lines (U^{233}) recorded with 10 kV positive potential on the first grid. The dashed line shows the expected "field on" shape due to instrumental effects alone.

8. ALPHA DECAY OF Gd^{151} AND Gd^{149} †

A. Siivola and G. Graeffe*

In an earlier paper it was predicted that Gd^{151} should have an alpha branching of the order of 10^{-8} with an α-particle energy of about 2.6 MeV.[1] This branching was found in measurements carried out with a grid ion chamber. The observed α-particle energy is 2.60 ± 0.03 MeV, and the α-particles to K x-rays ratio is 0.8×10^{-8}, within a factor of two.

The α-particle energy of Gd^{149} was found to be 3.01 ± 0.02 MeV. The branching ratio was obtained by determining the strength of the source by counting 299-, 347-, and 770-keV γ rays whose relative intensities are known.[2] As a result the alpha branching of Gd^{149} was found to be $(4.6 \pm 1.5) \times 10^{-6}$.

Reduced widths, δ^2, for alpha decay were calculated for all gadolinium isotopes from Gd^{148} to Gd^{152} by the method of Rasmussen.[3] An $\ell = 0$ decay was assumed for all isotopes. Results are shown in a table together with data used in the calculation. As a general conclusion

it can be stated that there seem to be no large differences between the alpha-decay properties of the gadolinium isotopes, and that the experimental uncertainties are still too large to allow any further deductions. During the calculation, it was found that the major source of uncertainty in the reduced width, which can be considered as a final experimental result, is the energy measurement. This, of course, is a reflection of the fact that the barrier-penetration factor is a very steep function of the decay energy. There are many difficulties in low-energy alpha measurements, but the most important one seems to be the lack of suitable energy standards. It should be possible to measure the alpha energies of at least some of the rare earth alpha emitters by using a magnetic spectrograph (Gd^{148}, Tb^{149g}, and Dy isotopes), and in the light of the present experimental results such measurements would be very useful.

Footnotes and References

† Short version of UCRL-11559, to be published in Nucl. Phys.
* Department of Physics, University of Helsinki, Helsinki, Finland.

1. A. Siivola, Ann. Acad. Sci. Fennicae A6, No. 109 (1962).
2. H. J. Prask, J. J. Reidy, E. G. Funk, and J. W. Michelich, Nucl. Phys. 36, 441 (1962).
3. J. O. Rasmussen, Phys. Rev. 113, 1593 (1959); Phys. Rev. 115, 1675 (1959).
4. R. D. Macfarlane and T. P. Kohman, Phys. Rev. 121, 1758 (1961).

Table A. 8-I. Experimental data on the alpha decay of gadolinium isotopes.

A	Ref	E_α[a] (MeV)	$T_{1/2\alpha}$[a] (years)	δ^2 (MeV)	
148	1	3.18 ± 0.01	84 ± 9	0.096	+0.024 -0.021
149	b	3.01 ± 0.02	$(5.5 \pm 1.7) \times 10^3$	0.051	+0.034 -0.024
150	1	2.73 ± 0.01	$(2.1 \pm 0.3) \times 10^6$	0.10	+0.033 -0.025
151	b	2.60 ± 0.03	$4.2 \times 10^7 \times 2^{\pm 1}$	0.16	+0.27 -0.08
152	4	2.14 ± 0.03	$(1.08 \pm 0.08) \times 10^{14}$	0.14	+0.30 -0.10

a. E_α is the α-particle energy and $T_{1/2\alpha}$ the partial alpha half-life.
b. This investigation.

9. ALPHA ACTIVITIES IN PLATINUM

A. Siivola

It has been known for some time that the lightest natural isotope of platinum, Pt^{190}, is an alpha emitter.[1,2] Recently, a weak alpha branch was found in the decay of Pt^{188},[3] and four new alpha-active isotopes (Pt^{186}, Pt^{184}, Pt^{183}, and Pt^{182}) were discovered among the products of high-energy proton bombardments of iridium.[4]

With the Hilac a further study of Pt alpha emitters has been carried out.

Bombardments were done with O^{16}, F^{19}, and Ne^{20} beams, with targets of Yb and Er isotopes and Tm. The target assembly and general technique are the same as used by

Macfarlane in rare earth studies.[5,6] First some of the isotopes discovered by Graeffe[4] were made in $Yb^{174}(O^{16}, xn)Pt^{190-x}$ reactions and his results were reproduced. Mass assignments were obtained from excitation-function measurements, and they were in agreement with Graeffe's suggestions.

In O^{16} bombardments on ytterbium isotopes (Yb^{172}, Yb^{170}, and Yb^{168}) and Ne^{20} bombardments on erbium (Er^{166}, Er^{164}, and Er^{162}) nine new platinum alpha emitters were found; see Table A. 9-I. A sequence of spectra taken in O^{16} + Yb^{170} runs is reproduced in Fig. A. 9-1, and Fig. A. 9-2 gives the spectrum from a full-energy Ne^{20} bombardment on Er^{162} taken at better resolution. Figures A. 9-3 and A. 9-4 represent some of the excitation functions obtained in O^{16} runs.

All these activities are assigned to platinum because they appeared in bombardments listed above, were produced through compound-nucleus reactions, as can be seen from the excitation functions, and were not observed in O^{16} + Tm, F^{19} + Er, and O^{16} + Er bombardments in which isotopes of Ir, Os, and lighter elements are produced. Mass assignments are based on excitation functions obtained in this work and on information on heavy-ion reactions in the rare earth region.[7]

The branching ratios for even isotopes were estimated from the measured intensities of the alpha groups by assuming that the ratio of maximum cross sections for the reactions $(O^{16}, 6n)$ and $(O^{16}, 8n)$ is the same for all ytterbium targets used (Yb^{168}, Yb^{170}, Yb^{172}, and Yb^{174}). In the reaction $Yb^{174}(O^{16}, xn)Pt^{190-x}$ this ratio was found to be 2, by using Graeffe's branching ratios for Pt^{182} and Pt^{184}. That the experimental alpha branchings thus obtained approach unity without exceeding it indicates that the estimate can not be greatly in error.

From the experimental alpha energies, half-lives, and branching ratios, reduced widths, δ^2, were calculated by Rasmussen's method.[8] The results (Table A. 9-I) show a maximum at mass number 178. The origin of this maximum is unknown, and attempts to explain it with theoretical calculations have thus far been unsuccessful.

References

1. W. Porschen and W. Riezler, Z. Naturforsch. 9a, 701 (1954).
2. R. D. Macfarlane and T. P. Kohman, Phys. Rev. 121, 1758 (1961).
3. M. Karras, G. Andersson, and M. Nurmia, Arkiv Fysik 23, 57 (1962).
4. G. Graeffe, Ann. Acad. Sci. Fennicae A6, No. 128 (1963).
5. R. D. Macfarlane and R. D. Griffioen, Nucl. Instr. Methods 24, 461 (1963).
6. R. D. Macfarlane, Phys. Rev. 131, 2176 (1963); also Alpha-Decay Properties of Some Thulium and Ytterbium Isotopes Near the 82-Neutron Closed Shell, Phys. Rev. (to be published).
7. J. M. Alexander and G. N. Simonoff, Phys. Rev. 133B, 93 (1964).
8. J. O. Rasmussen, Phys. Rev. 113, 1593 (1959) and 115, 1675 (1959).

Table A. 9-I. Alpha-active platinum isotopes.

Mass	E_α (MeV)	$T_{1/2}$	Alpha branching	δ^2
190[a]	3.18 ± 0.02	$(5.4 \pm 0.6) \times 10^{11}$ y	1	0.027
188[a]	3.93 ± 0.01	10.2 ± 0.3 d	$(3.0 \pm 0.6) \times 10^{-7}$	0.019
186[a]	4.23 ± 0.02	2.0 ± 0.2 h	1.4×10^{-6}	0.07
184[a]	4.48 ± 0.02	20 ± 2 min	1.5×10^{-5}	
	4.47 ± 0.02	20 ± 2 min		0.10
183[a]	4.74 ± 0.03	6.5 ± 1 min	1.3×10^{-5}	
	4.70 ± 0.02	6.0 ± 1 min		
182[a]	4.82 ± 0.03	2.5 ± 0.5 min	2.3×10^{-4}	
	4.82 ± 0.02	3.1 ± 0.3 min		0.11
181	5.02 ± 0.02	48 ± 2 sec		
180	5.14 ± 0.02	50 ± 5 sec	1.6×10^{-2}	≈ 0.3
179	5.15 ± 0.02	33 ± 5 sec		
178	5.43 ± 0.02	22 ± 1 sec	0.17	≈ 0.4
177	5.52 ± 0.02	6.5 ± 1 sec		
176	5.74 ± 0.02	6 ± 1 sec	0.85	≈ 0.25
175	5.94 ± 0.02	2.3 ± 0.5 sec		
174	6.03 ± 0.02	0.8 ± 0.3 sec	≈1	≈ 0.16
173	6.20 ± 0.04	?		

a. From reference 4.

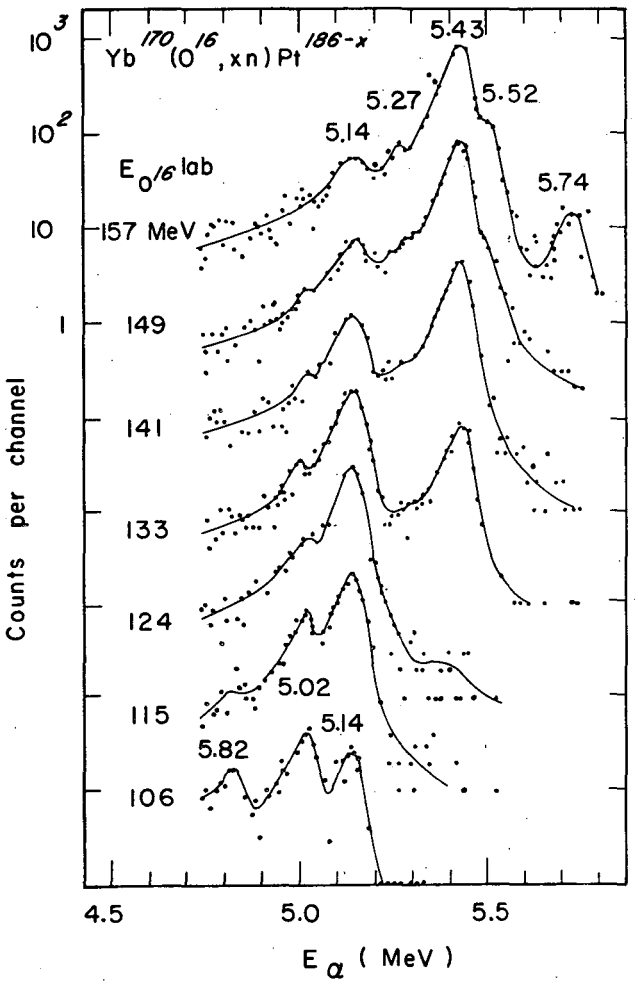

MUB-3151

Fig. A. 9-1. The alpha spectrum of the products of the reaction $Yb^{170}(O^{16}, xn)Pt^{186-x}$ at various bombarding energies. See Table A. 9-I for the identification of the peaks. The bump at 5.27 MeV is a fine-structure group belonging to the 5.43-MeV alpha emitter.

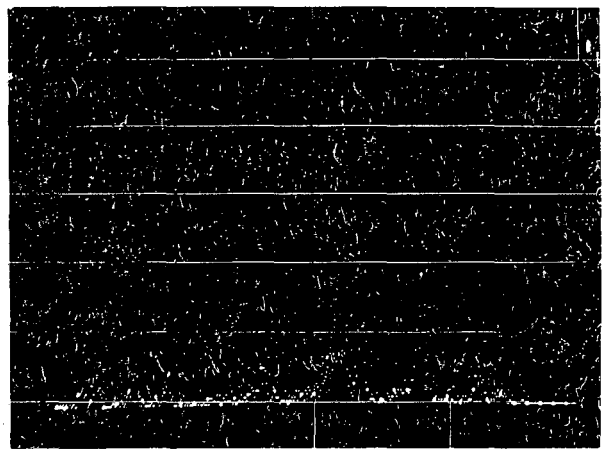

Fig. A. 9-2. The alpha spectrum of the products from a Ne^{20} + Er^{162} experiment. The peaks are, starting from the right, 6.03 Mev (Pt^{174}), 5.94 MeV (Pt^{175}), 5.74 MeV (Pt^{176}), 5.52 MeV (Pt^{177}), 5.43 MeV (Pt^{178}, the most intense group), 5.14 - 5.15 MeV (Pt^{179}, Pt^{180}), and three or four weak lines that belong to the rare earths produced from small impurities in the target.

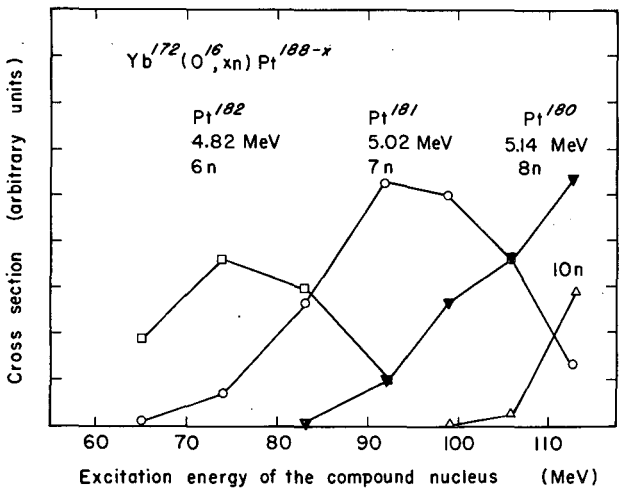

MUB-3152

Fig. A. 9-3. Excitation functions for the reaction $Yb^{172}(O^{16}, xn)Pt^{188-x}$.

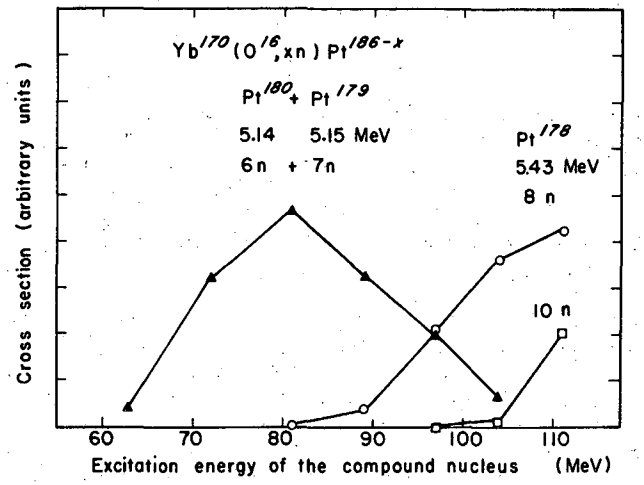

Fig. A. 9-4. Excitation functions for the reaction $Yb^{170}(O^{16}, xn)Pt^{186-x}$. The "missing" 7n reaction was the first indication that the 5.15-MeV line might contain two adjacent isotopes. A definite proof was obtained by measuring the half-life of the alpha group at different bombarding energies, with the result that the group has two different half-lives (Table A. 9-I).

10. ALPHA-ACTIVE GOLD ISOTOPES

A. Siivola

By the same method as in the platinum work reported in the previous paper, several new isotopes of gold have been found. They are listed in Table A. 10-I. The first one, Au^{185}, is the activity observed earlier by Rasmussen et al. [1] and assigned to an isotope of gold with mass number between 183 and 187. The mass assignments in Table A. 10-I are from the measured excitation functions for the reactions F^{19} + $Yb^{168-172}$.

Table A. 10-I. Alpha-active gold isotopes.

Isotope	E_α (MeV)	$T_{1/2}$
Au^{185}	5.07	4.33 min
Au^{183}	5.34	44 sec
Au^{181}	5.60, 5.47	10 sec
Au^{179}	5.84	7.1 sec
Au^{178}	5.91	2.7 sec
Au^{177}	6.11	1.4 sec

References

1. J. O. Rasmussen, S. G. Thompson, and A. Ghiorso, Phys. Rev. 89, 33 (1953).

11. LIGHT POLONIUM ISOTOPES

A. Siivola

By the same method as for the platinum isotopes, the light polonium isotopes have been studied. These isotopes had been discovered previously and were studied by Swedish scientists of the Nobel Institute with heavy-ion bombardments,[1-3] and in Uppsala with proton bombardments of bismuth.[4,6]

Polonium isotopes were produced through the reactions $Re^{185,187}(F^{19}, xn)Po$, and the results are summarized in Table A. 11-I. Mass assignments are based on excitation functions.

The results in Table A. 11-I are in disagreement with earlier data. For Po^{200} the most recent results of the Swedish group[3] are in agreement with this work, and also with the original assignment by Karraker, Ghiorso, and Templeton.[5] The 5.77-MeV activity, earlier assigned to Po^{200}, was observed in the measurements in this work, but its excitation function indicates a considerably lighter mass. The same activity was seen in bombardments in which bismuth isotopes were produced, and it apparently belongs to Bi^{197}. The 5.93-MeV activity is more difficult to explain. It was not present in polonium bombardments in quantities indicated in the spectra of Atterling et al.[2] and Rosenblum and Tyrén.[6] It was, however, observed in bismuth irradiations, the most probable mass number being 193.

Po^{199} (6.06 MeV) and Po^{198} (6.18 MeV) are the same activities as those assigned earlier to Po^{197} and Po^{196}.

All lighter isotopes show no similarities to old data. Tove's results were obtained by analyzing complex decay curves,[4] and it is felt that the method used for this work is more reliable.

References

1. H. Atterling and W. Forsling, Arkiv Fysik 15, 81 (1959).
2. H. Atterling, W. Forsling, and B. Åström, Arkiv Fysik 15, 279 (1959).
3. W. Forsling and T. Alväger, Arkiv Fysik 19, 353 (1961).
4. P. A. Tove, Arkiv Fysik 13, 549 (1958).
5. D. G. Karraker, A. Ghiorso, and D. H. Templeton, Phys. Rev. 83, 390 (1951).
6. S. Rosenblum and H. Tyrén, Compt. Rend. 239, 1205 (1954).

Table A. 11-I. Light polonium isotopes

Isotope	E_α (MeV)	$T_{1/2}$
Po^{200}	5.86	11.4 min
Po^{199}	6.06	4.24 min
Po^{198}	6.18	1.75 min
Po^{197}	6.39	25 sec
Po^{197}	6.30	54 sec
Po^{196}	6.53	5.9 sec
Po^{195}	6.72	1.4 sec
Po^{195}	6.63	3 sec
Po^{194}	6.85	0.5 sec
Po^{193}	7.0	?

12. OBSERVATION OF A SECOND K = 1/2 BAND IN $_{94}Pu^{239}$.†

D. W. Davies and J. M. Hollander

The energy levels of $_{94}Pu^{239}$ have been studied extensively from the beta decay of $_{93}Np^{239}$,[1,2] and Am^{239},[3] and from the alpha decay of $_{96}Cm^{243}$.[4] These levels have been characterized in terms of four intrinsic Nilsson states and of the rotational excitations of these states: 1/2 + [631], ground; 5/2 + [622], 285.5 keV; 7/2 - [743], 391.6 keV; and 7/2 + [624] or 5/2+[633], 511.9 keV. Two very weak γ rays of about 440 and about 490 keV were found in the scintillation spectrum of Np^{239} by Lefevre, Kinderman, and Van Tuyl,[5] and these have not been placed in the Pu^{239} level scheme. In an attempt to gain further information about these and other possible weak radiations in Pu^{239} we have examined the photon spectrum of a carefully purified Np^{239} source with high-resolution lithium-drifted germanium detector systems. Dimensions of the detectors used are 2 $cm^2 \times 7$ mm thick and 6 $cm^2 \times 9$ mm thick. The electronics was standard for these systems.

Figure A. 12-1 shows the relevant portion of the photon spectrum. In all, twelve new γ rays are definitely assigned to the decay of Np^{239}. Energies and relative intensities of the observed γ rays are listed in Table A. 12-I. Calibration was made both with well-known Np^{239} lines[1,2] and with Lu^{177m} and annihilation radiation.[6]

The new radiations are found to define three and probably four new levels, as shown in Fig. A. 12-2. The energies of the new levels can be fitted with the Bohr-Mottelson equation for a K = 1/2 band,

$$E_I = (\hbar^2/2\Im)[I(I+1) + a(-)^{I+1/2}(I+1/2)],$$

with the parameters $\hbar^2/2\Im$ = 5.043 keV and a = 0.48. An independent check on the K value of the upper band can be made by comparing the experimental and theoretical relative intensities of photons connecting this band with the K = 1/2 (ground) band. The theoretical ratios of reduced transition probabilities are given by

$$\frac{B(L, I_i \rightarrow I_f)}{B(L, I_i \rightarrow I_f')} = \left[\frac{\langle I_i L K_i K_f - K_i \,|\, I_i L I_f K_f \rangle + b(-)^{I_f+K_f} \langle I_i L K_i, -K_f - K_i \,|\, I_i L I_f - K_f \rangle}{\langle I_i L K_i K_f - K_i \,|\, I_i L I_f' K_f \rangle + b(-)^{I_f'+K_f} \langle I_i L K_i, -K_f - K_i \,|\, I_i L I_f' - K_f \rangle} \right]^2,$$

where b is a parameter depending on the intrinsic wave functions.[7] In Table A. 12-II the experimental and theoretical branching ratios are compared, for $K_i = K_f = 1/2$. Satisfactory agreement between theory and experiment could be obtained only for dipole radiation and a value of $b = 0 \pm 0.1$.

It is of interest to know the parity of the upper K = 1/2 band. By combining our photon data and information from the scan of the Np^{239} electron spectrum by Ewan et al.[2] we can set an upper limit of 0.14 on the K-conversion coefficient of the 434.7-keV transition. From the Sliv and Band[8] tables the theoretical values are E1, 0.019; M1, 0.29. Thus the 434.7-keV transition is probably an E1 transition and the parity of the upper band is odd. (It is possible that the transition could be an M1-E2 mixture with ≥40% E2 admixture, but so large an E2 admixture would be inconsistent with the branching ratio information in Table A. 12-II).

The present data indicate that the major component of the new K = 1/2 band at 469.8 keV is the intrinsic particle state labeled 1/2-[501] in the Nilsson scheme.[9] Although this state has not yet been reported in studies of nuclei in the heavy-element region, recent calculations by Poggenburg, Mang, and Rasmussen[10] indicate that it should lie at ≈0.7 MeV in Pu^{239}. Support for this assignment is given by the fact that the theoretical decoupling parameter (a in Eq. 1) for state 1/2 - [501] is about +0.9, which is reasonably close to the observed value +0.48.

We cannot exclude the possibility that the observed state is an octupole vibrational excitation rather than an intrinsic particle excitation, or that it is of mixed vibrational-intrinsic character.

The new data are summarized in Fig. A. 12-3 , which also includes the previously known Pu^{239} levels grouped according to the respective rotational bands.

Footnotes and References

† Material condensed from UCRL-11707.

1. J. M. Hollander, W. G. Smith, and J. W. Mihelich, Phys. Rev. 102, 740 (1956).
2. G. T. Ewan, J. S. Geiger, R. L. Graham, and D. R. MacKenzie, Phys. Rev. 116, 950 (1959).
3. W. G. Smith, W. M. Gibson, and J. M. Hollander, Phys. Rev. 105, 1514 (1957).
4. F. Asaro, S. G. Thompson, F. S. Stephens, and I. Perlman, Bull. Am. Phys. Soc. 8, 393 (1957).
5. H. W. Lefevre, E. M. Kinderman, and H. H. Van Tuyl, Phys. Rev. 100, 1374 (1955).
6. P. Alexander, F. Boehm, and E. Kankeleit, Phys. Rev. 133, B284 (1964).
7. G. Alaga, K. Alder, A. Bohr, and B. R. Mottelson, Kgl. Danske Videnskab. Selskab Mat.-Fys. Skr. 29, No. 9 (1955).
8. L. A. Sliv and I. M. Band, Coefficients of Internal Conversion of Gamma Radiation (USSR Academy of Sciences, Moscow-Leningrad, 1956) Part I: K Shell; Part II: L Shell.
9. S. G. Nilsson and B. R. Mottelson, Kgl. Danske Videnskab. Selskab Mat.-Fys. Skr. 1, No. 8 (1959).
10. J. K. Poggenburg, H. J. Mang, and J. O. Rasmussen (Lawrence Radiation Laboratory), unpublished results, August 1964.

Table A. 12-I. Np^{239} transition energies and photon intensities.

Transition energy (keV)		Photon intensity[a]	
This work[b]	Ewan et al.[c]	This work	Ewan et al.[c]
	44.65		
	49.41		
	57.26		
(62)	61.46		1.5
	67.87		
	88.06		
	106.14		13.4
	106.47		
	166.39		
(182.0)	181.71	0.045	
(209.8)	209.76	2.0	2.4
	226.42		
(228.2)	228.20	6.9	7.46
(254.2)	254.41	0.07	0.07
	272.87		0.052
(277.4)	277.62	8.28 ≡	8.28
(285.2)	285.47	0.48	0.37
(315.5)	315.91	0.88	0.88
(334.1)	334.33	1.21	1.17
392.4[d])		0.00091	
429.5		0.0022	
434.7		0.0072	
447.6		0.00015	
454.2		0.00047	
461.9		0.00091	
469.8		0.00062	
484.3		0.00060	
492.3		0.0035	
497.8		0.0018	
~498.7		---	
504.2		0.00045	

a. Arbitrary intensity units, normalized at the value given by Ewan et al. for the 277.6-keV photon. Approximately, 1 intensity unit = 0.017 photon per β decay.
b. Energy values in parentheses were measured for identification only, and are not precise.
c. Reference 2.
d. Our estimated errors for the energies of the new photons range from ± 0.2 keV for the strongest lines to ± 0.5 keV for the weakest lines.

Table A. 12-II. Photon branching ratios from levels of the 469.8-keV band to the ground-state band ($K_i = 1/2$; $K_f = 1/2$)

I_i	I_f	Theoretical relative intensities[a]									Experimental relative intensities
		Dipole radiation, calc. with b = :								Quadrupole radiation calc. with b = 0	
		+5	+1	+0.2	0	-0.2	-1	-5	±∞		
1/2	1/2	1.0	0.03	0.22	0.53	1.2	94	6.1	2.1	--	0.7
	3/2	1.0	1.0	1.0	1.0	1.0	1.0	1.0	1.0	1.0	1.0
	5/2	--	--	--	--	--	--	--	--	0.85	(<0.15)[b]
3/2	1/2	1.0	1.0	1.0	1.0	1.0	1.0	1.0	1.0	1.0	1.0
	3/2	1.6	0.19	0.025	0.18	0.55	30	6.8	2.8	0.93	0.17
	5/2	0.39	0.033	0.73	1.3	2.2	44	4.5	1.3	0.23	2.0
	7/2	--	--	--	--	--	--	--	--	1.1	(<0.025)
5/2	1/2	--	--	--	--	--	--	--	--	3.8	(≤0.05)
	3/2	1.0	1.0	1.0	1.0	1.0	1.0	1.0	1.0	1.0	1.0
	5/2	3.8	8.7	0.003	0.068	0.17	0.64	1.6	2.4	2.4	0.083
	7/2	2.5	33	1.5	0.87	0.49	0.028	0.24	0.85	0.32	1.2
	9/2	--	--	--	--	--	--	--	--	1.3	-----
7/2	3/2	--	--	--	--	--	--	--	--	64	-----
	5/2	6.0	52	2.7	1.6	0.92	0.046	0.50	1.6	4.4	≈1.1
	7/2	7.5	27	0.32	0.053	0	0.17	0.86	3.3	30	(<0.1)
	9/2	1.0	1.0	1.0	1.0	1.0	1.0	1.0	1.0	1.0	1.0
	11/2	--	--	--	--	--	--	--	--	14	-----

a. The E^{2L+1} energy dependence has been removed.
b. Intensities in parentheses are upper limits. These lines were not observed.

Table A. 12-III. Log ft values of Np^{239} beta decays to members of K = 1/2-band

Level energy (keV)	% β decay	Log ft
556.2	$\approx 3\times10^{-3}$	~9.7
505.3	7.1×10^{-3}	9.7
492.6	19.5×10^{-3}	9.4
469.9	$\leq 2.6\times10^{-3}$	≥10.4

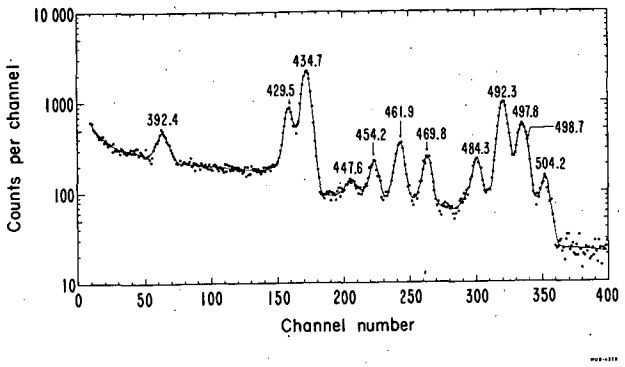

Fig. A. 12-1. Portion of the γ-ray spectrum that includes the new γ rays of Np^{239}. The spectrum was observed with a Ge(Li) detector of dimensions 2 $cm^2 \times 7$ mm deep. A 5.0-mm Pb absorber was interposed between source and detector.

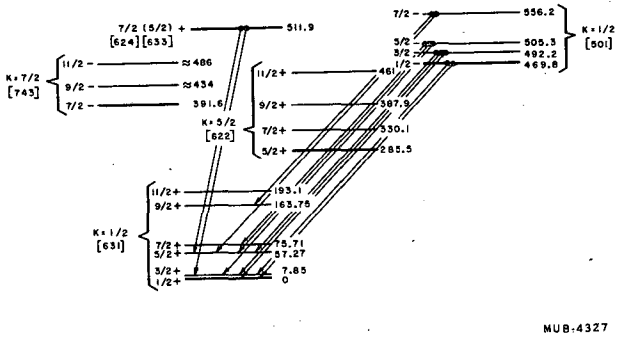

Fig. A. 12-2. Levels of Pu^{239} defined by the new γ rays observed in this study.

Fig. A. 12-3. Level scheme of Pu^{239}, showing all known levels grouped into the respective rotational bands. Only the newly observed transitions are included in this drawing.

13. MEASUREMENTS OF INTERNAL-CONVERSION COEFFICIENTS IN THE DECAY OF U^{237}

T. Yamazaki and J. M. Hollander

Precision measurements of the γ-ray spectrum from U^{237} decay have been carried out with use of a 2 $cm^2 \times 5$ mm lithium-drifted germanium detector. The results, when combined with internal-conversion data taken with the Berkeley 50-cm $\pi\sqrt{2}$ iron-free spectrometer, allow us to calculate the internal-conversion coefficients for most of the prominent transitions. The germanium detector is a very powerful device for measurement of weak γ rays that have been missed in scintillation spectroscopy, and for resolving close-lying γ rays such as are found in the U^{237} spectrum.

The 6.8-day U^{237} was produced by thermal neutron capture of enriched U^{236}. The U^{237} was chemically separated from various fission products. Although extensive chemistry was done, the uranium fraction was found to contain detectable zirconium and niobium, and care

had to be exercised in the assignments of weak lines in the high-energy region. The source for the iron-free spectrometer was prepared by vacuum evaporation.

A typical γ-ray spectrum is presented in Fig. A. 13-1, in which the 332.4- and 335.4-keV doublet (3.0 keV separation), and 368.6- and 370.9-keV doublet (2.3 keV separation) have been analyzed with use of the known photo-peak shape. Besides the prominent γ rays previously reported,[1] we have found six weak gammas. They were identified to belong to U^{237} by following their decays. The results are presented in Table A. 13-I. In obtaining the gamma-ray intensities we used a photo-peak efficiency curve which was determined experimentally by using several intensity standards. The accuracy may be within 5%.

Internal-conversion coefficients were obtained with the assumption $\alpha_K(208) = 2.35$ (the theoretical conversion coefficient for 96% M1 + 4% E2 given by Sliv and Band[2]), because the 208-keV transition has been found from measurements of the L-subshell ratios to be predominantly M1 with about 4% mixture of E2. The K-conversion coefficients so obtained are tabulated in column 3 of Table A. 13-I, and are compared with the Sliv and Band theoretical values in Fig. A. 13-2. The assigned multipolarities are shown in column 4 of Table A. 13-I. The previous assignments given by Rasmussen, Canavan, and Hollander,[1] some of which are indirectly deduced from coincidence measurements and from the decay scheme construction, have been well confirmed.

A proposed decay scheme is presented in Fig. A. 13-3. This is almost the same as that of Rasmussen et al.[1] The two weak γ rays of 293.5 keV and 337.2 keV, reasonably situated in the present level scheme, are expected to be pure E2. With use of the measured intensity of these E2 transitions together with the simple theoretical intensity rules for rotational states, the E2/M1 mixing ratios in the competing transitions can be predicted. The results are

$$\delta^2(335.4) \approx 7.5\times10^{-2},$$
$$\delta^2(368.6) \approx 1.0\times10^{-1},$$
$$\delta^2(370.9) \approx 1.3\times10^{-1}.$$

These values are fairly consistent with those obtained from the K-conversion coefficients.

References

1. J. O. Rasmussen, F. L. Canavan, and J. M. Hollander, Phys. Rev. 107, 141 (1957).
2. L. A. Sliv and I. M. Band, Coefficients of Internal Conversion of Gamma Radiation (USSR Academy of Sciences, Moscow-Leningrad, 1956), Part I: K Shell; Part II: L Shell.

Table A. 13-I. Gamma transitions in Np^{237} from the decay of U^{237}.

Transition energy (keV)	γ-Ray intensity	K-conversion coefficient	Assigned multipolarity
59.45 ± 0.03	≈74[a]	--	E1
164.53 ± 0.05	8.50 ± 0.38	0.198 ± 0.010	E2
207.97 ± 0.06	100	2.35 (assumed)[b]	M1 + E2, $\delta^2 \approx 0.04$
221.0 ± 0.5[c]	0.093 ± 0.005	<0.5	M1 + E2, or E1
234.25 ± 0.07	0.097 ± 0.005	6.3 ± 0.3	M2
267.47 ± 0.08	3.28 ± 0.15	0.80 ± 0.04	E1 + M2[d]
293.5 ± 0.5[c]	0.0106 ± 0.0014	--	E2[d]
332.36 ± 0.1	5.80 ± 0.30	0.062 ± 0.003	E2
335.38 ± 0.1	0.451 ± 0.023	0.57 ± 0.03	M1 + E2, $\delta^2 \approx 0.12$
337.2 ± 1.0[c]	0.032 ± 0.010	--	E2[d]
345.0 ± 0.5[c]	0.0084 ± 0.0010	--	--
365.0 ± 0.5[c]	0.0078 ± 0.0030	--	--
368.59 ± 0.1	0.241 ± 0.020	0.50 ± 0.04	M1 + E2, $\delta^2 \approx 0.05$
370.94 ± 0.1	0.508 ± 0.030	0.47 ± 0.03	M1 + E2, $\delta^2 \approx 0.05$

a. Error may be large because of lack of photo efficiency value at this energy.
b. Theoretical value (Sliv and Band) for 96% M1 + 4% E2.
c. These transitions were seen only in the photon spectrum and hence have larger error associated with the energy value than the other transitions, measured with the iron-free spectrometer.
d. Required from the decay scheme.

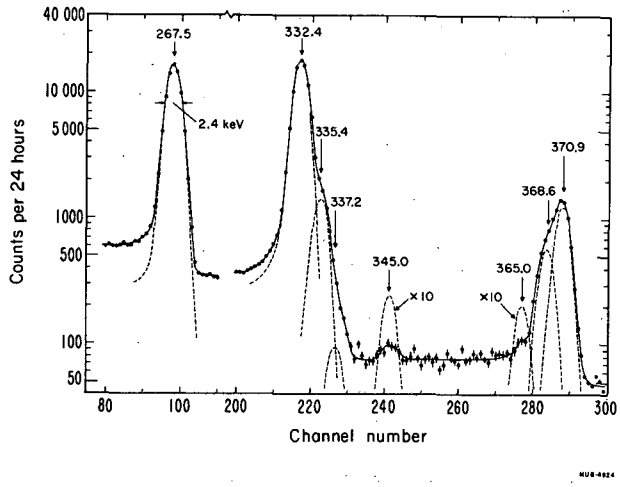

Fig. A. 13-1. γ-Ray spectrum of U^{237}, taken with Ge(Li) detector, 2 cm^2 × 5 mm deep.

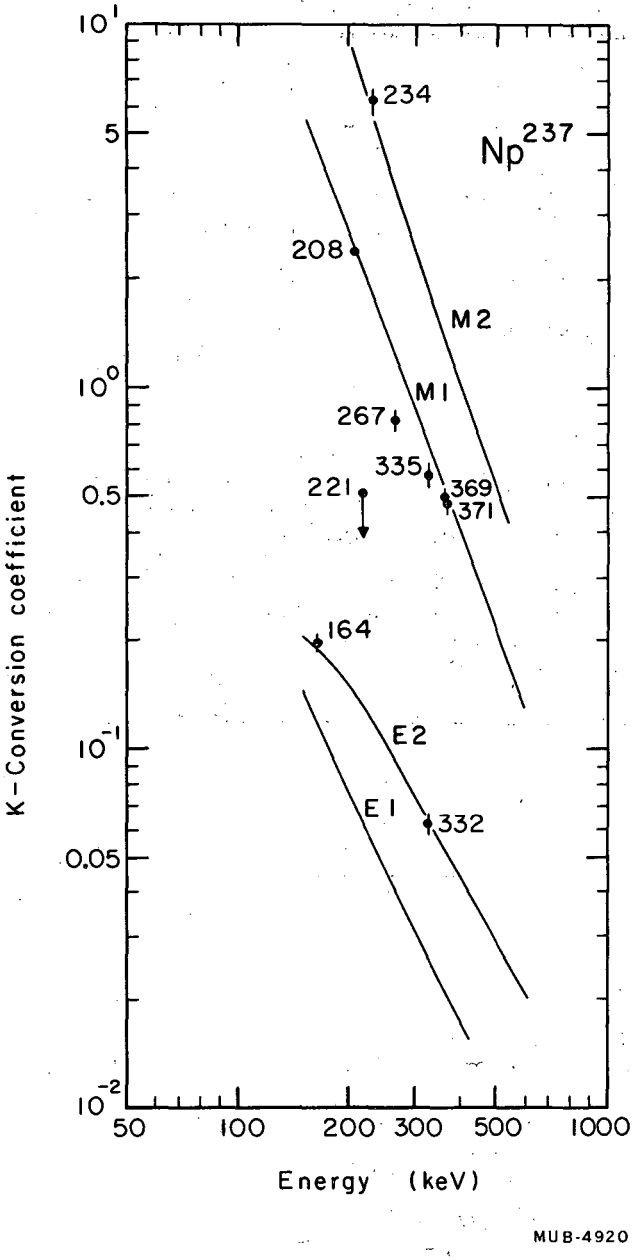

Fig. A. 13-2. Comparison of experimental and theoretical conversion coefficients of U^{237} transitions. Solid lines are the theoretical values, obtained from the tables of Sliv and Band.

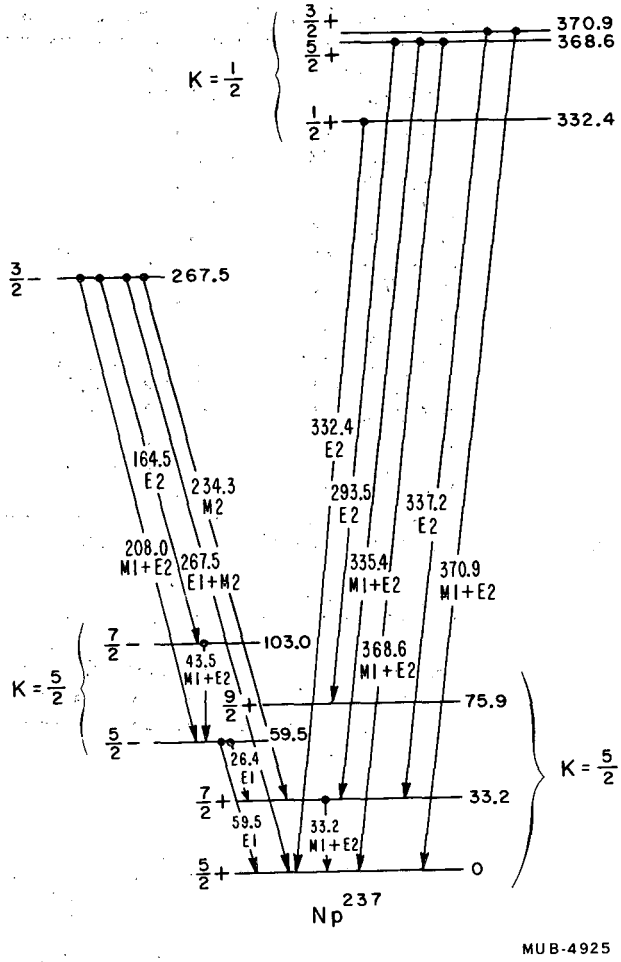

Fig. A. 13-3. Partial-level scheme of Np^{237}, including the transitions studied in this work.

14. MEASUREMENT OF PAIR-PRODUCTION CROSS SECTIONS NEAR THRESHOLD

T. Yamazaki and J. M. Hollander

Experimental determinations of pair-production cross sections, σ_{pair} (E), have in the past been done by means of total photon absorption measurements.[1] For $E > 2.6$ MeV the experimental values are in good agreement with the theoretical values given by Bethe and Heitler.[2] Below 2.6 MeV, however, there are no experimental data because the absorption method, consisting in subtraction of $\sigma_{Compton}$ from σ_{total}, is inaccurate for the low-energy region where σ_{pair} is very small. From a theoretical point of view the region near threshold (2 mc^2) is interesting, because in this region the Bethe-Heitler formula, based on the Born approximation, may not be valid.

We report here on a measurement of the pair-production cross-section curve near threshold, carried out with the use of lithium-drifted germanium γ-ray detectors. The principle of the method is as follows: When a photon of energy kmc^2 ($k>2$) creates an e^+-e^- pair within a germanium crystal, the kinetic energy of the electron pair is nearly completely absorbed, whereas the annihilation photons nearly always escape. Thus, most pair-production events result in a peak at $(k-2)\,mc^2$, called the double-escape peak. Since this peak is formed by a single process (whereas photopeaks and the Compton background are due to multiple events), it is possible by measuring the intensities of the double-escape peaks as a function of incident photon energy to determine the shape of the pair-production cross-section curve. With some corrections, which will be discussed, the absolute values of σ_{pair} (E) can be obtained. Even when the incident photon energy is close to 2 mc^2, the pair peak can be readily identified by its energy, which can be rather accurately determined with the germanium detector systems. The use of a lead absorber will provide further confirmation, if necessary, since it reduces the intensities of photopeaks of lower-energy photons much more effectively than it does double-escape peaks from higher-energy photons.

Used in these measurements was a lithium-drifted germanium detector, 2 $cm^2 \times 5$ mm thick, that has an energy resolution (FWHM) of 2.4 keV at 279 keV. The γ-ray sources were placed at 4 cm from the surface of the detector. Some "singles" spectra obtained in these experiments are shown in Fig. A. 14-1.

For each γ-ray energy, A_{pair} and A_{photo} (areas of pair and photo peaks, respectively) were measured. The quantity

$$\epsilon_{pair} \equiv \eta_{photo}\,(A_{pair}/A_{photo})$$

gives the energy dependence of σ_{pair}. The determination of the photoefficiency function (η_{photo}) was made with use of several γ-ray standards with well-known photon intensities. The isotopes Na^{24} (1.368, 100%; 2.754, 100%), and Co^{60} (1.173, 100%; 1.332, 100%) were used.

In principle, the following corrections to the data must be considered.

a. Finite thickness of the germanium crystal. Because the incident photon flux is reduced in the crystal, the effective thickness

$$d_{eff} = d\left[\frac{1-e^{-\mu d}}{\mu d}\right],$$

where μ is the total absorption coefficient, has an energy dependence. In this case, $\mu d \approx 5\times10^{-2}$ and varies slowly with energy, so this effect is negligible.

b. Absorption of part or all of the annihilation photo energy in the crystal. This reduces A_{pair}, since it shifts the pulse height to higher values. Because this effect always arises from the 511-keV photon, it has no energy dependence and hence is of no importance for relative measurements of σ_{pair}. To obtain absolute values of σ_{pair}, this correction must be applied.

c. Incomplete absorption of e^+-e^- pairs in the finite crystal. A rough estimate of this correction has been obtained from the kinematics and range-energy relations for electrons, and the reduction factor f_3 for this case is given in Table A. 14-I.

Thus, the relative values of the pair-production cross section are given by

$$\sigma_{pair} = \epsilon_{pair}/f_3.$$

In Fig. A.14-2 are plotted these experimental values together with the theoretical curve, which is normalized at high energy. The Bethe-Heitler curve was obtained by numerical integration of the Bethe-Heitler formula (Eq. 21A of ref. 2). It is apparent that the Bethe-Heitler curve shows significant deviation from experiment as the energy becomes lower. Jaeger and Hulme[3] made a more accurate calculation taking into account the interaction between electron and nucleus. This calculation gives larger values than Bethe-Heitler at low energy. Although there is no numerical value available except for Pb at 1.53 MeV and 2.66 MeV, this tendency seems to account for the experimental deviation from the Bethe-Heitler curve.

References

1. See, e.g., C. M. Davisson and R. D. Evans, Rev. Mod. Phys. 24, 79 (1952).
2. H. Bethe and W. Heitler, Proc. Roy. Soc. (London) 146A, 83 (1934).
3. J. C. Jaeger and R. H. Hulme, Proc. Roy. Soc. (London) 153A, 443 (1936).

Table A.14-I. Experimental results.

E_γ (MeV)	Isotope	k	A_{pair}/A_{photo}	η_{photo}	ϵ_{pair}	f_3	σ_{pair}
1.173	Co^{60}	2.30	4.0 ± 1.0 (-2)[a]	8.80	3.5 ± 0.9 (-1)	1.00	3.5 ± 0.9 (-1)[a]
1.278	Na^{22}	2.50	1.1 ± 0.2 (-1)	7.00	7.7 ± 1.4 (-1)	0.99	7.8 ± 1.4 (-1)
1.332	Co^{60}	2.61	1.93 ± 0.10 (-1)	6.45	1.25 ± 0.06 (0)	0.99	1.26 ± 0.06 (0)
1.368	Na^{24}	2.68	2.50 ± 0.20 (-1)	6.05	1.51 ± 0.12 (0)	0.98	1.54 ± 0.12 (0)
1.596	La^{140}	3.12	9.40 ± 0.50 (-1)	4.15	3.90 ± 0.21 (0)	0.97	4.02 ± 0.22 (0)
1.837	Y^{88}	3.59	2.43 ± 0.10 (0)	3.03	7.36 ± 0.30 (0)	0.95	7.75 ± 0.32 (0)
2.318	Nb^{90}	4.54	8.10 ± 0.40 (0)	1.73	1.40 ± 0.07 (1)	0.90	1.56 ± 0.08 (1)
2.754	Na^{24}	5.39	1.50 ± 0.05 (1)	1.15	1.73 ± 0.06 (1)	0.85	2.04 ± 0.07 (1)

a. $4.0 \pm 1.0\ (-2) \equiv (4.0 \pm 1.0) \times 10^{-2}$.

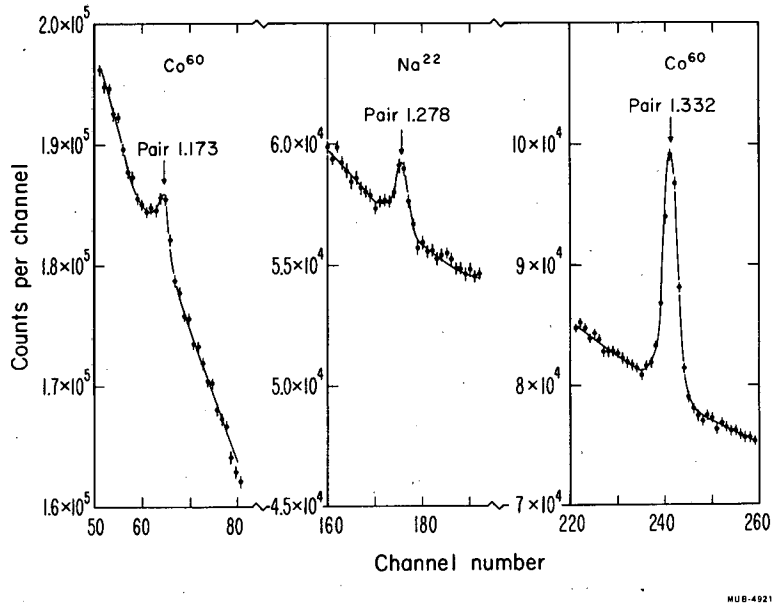

Fig. A. 14-1. "Double-escape" peaks obtained with samples of Co^{60} and Na^{22}, by use of 2 cm^2 × 5-mm-thick Ge(Li) detector system.

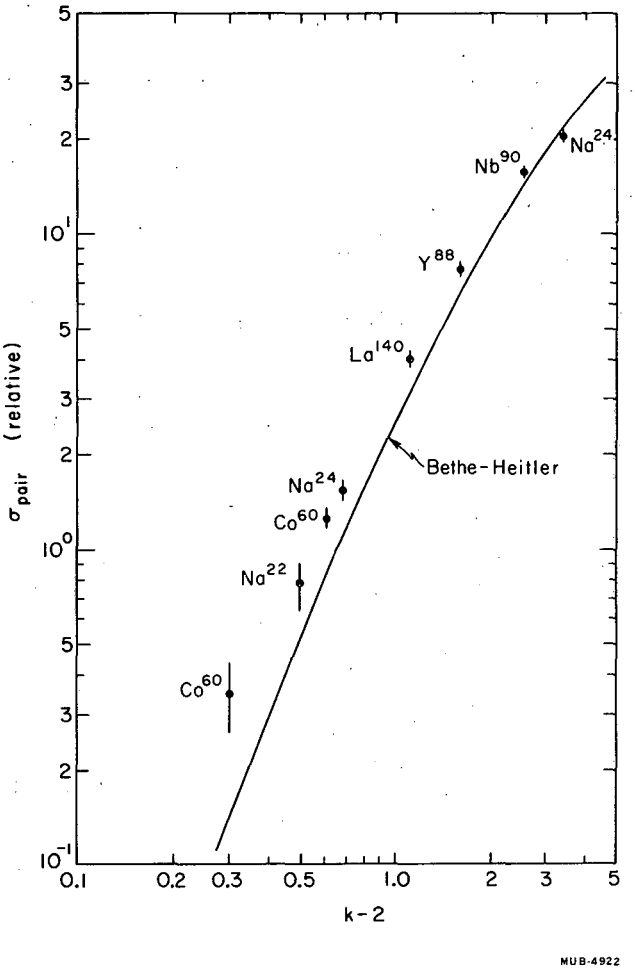

Fig. A. 14-2. Comparison of experimental values of σ_{pair} (relative) with the curve calculated from the theoretical formula of Bethe-Heitler.

15. ENERGY LEVELS OF $_{97}Bk^{249}$

M. D. Holtz, J. M. Hollander, T. Novakov, and R. L. Graham

The results of an experimental and theoretical study of the levels of $_{97}Bk^{249}$ populated by the alpha decay of $_{99}Es^{253}$ have been discussed previously.[1] The internal-conversion electron spectrum was examined with use of the Berkeley 50-cm iron-free $\pi\sqrt{2}$ spectrometer, and the level scheme so obtained is shown in Fig. A. 15-1. It was noted that the observed energy level spacings do not follow the usual I(I+1) energy dependence, but when consideration was taken of the Coriolis interaction among the various bands originating from the $i_{13/2}$ single-particle state, satisfactory agreement between the calculated and observed spacings was obtained.

Since that time additional measurements and calculations have been made. A measurement of the half-lives of the first two excited states in the K=7/2 band combined with a determination of the E2 branching ratios of the transitions deexciting these two levels enabled us to calculate the intrinsic quadrupole moment (Q_0) for these two levels. Also the theoretical half-lives of these states were calculated from the formulas for M1 transition probabilities, both with and without consideration of the Coriolis interaction, and compared with the experimental values;

and finally the M1 interband branching ratios were calculated, both with and without band mixing, and compared with the experimental results.

The lifetimes were measured by using a new method proposed by Novakov et al.[2] This method makes use of an electrostatic preaccelerator system in conjunction with the iron-free spectrometer to measure indirectly the distance that recoil nuclei travel before emitting conversion electrons. Since the recoil velocities can also be estimated, the half-lives can be determined. The half-lives of the 41.8- and 93.8-keV states were found to be $(9 \pm 2) \times 10^{-12}$ sec, and $(5 \pm 1) \times 10^{-12}$ sec, respectively.

The Q_0 values were obtained from the formula $T(E2) = (e^2/60\hbar)(w^5/c)\, Q_0^2 \langle I2KO | I'K' \rangle$, where T(E2) is the E2 gamma transition probability. Since there are three transitions deexciting the 41.9- and 93.7-keV levels, three Q_0 values were obtained. For the 41.9- and 52.0-keV transitions the total conversion coefficient (obtained from the experimental conversion-electron intensities and the theoretical L_I conversion coefficients[3]) and the M1-E2 mixing ratios were involved, while for the pure E2 93.7-keV crossover transition only the total conversion coefficient entered. Because of the large relative error in the E2 branching ratios [$(1.8 \pm 0.5)\%$ E2 and $(2.0 \pm 0.3)\%$ E2] (see reference 4) the crossover transition is expected to give the most accurate result. The three values of Q_0 in order of increasing transition energy are 13.6 ± 2, 15.6 ± 2, and 16.1 ± 1.7 barns. All these values are higher than the theoretical value of 11.5 barns predicted by Szymanski.[5]

A theoretical calculation of the half-lives of the same two excited states was made from the formula for M1 transition probabilities in a deformed region. This formula, given by Nilsson,[6] is based on the unified model, and makes use of the asymptotic quantum numbers. Calculations were made with and without the inclusion of the Coriolis interaction. In the first case, K (the projection of the total spin on the nuclear symmetry axis) is not a good quantum number, and the formula must be applied repeatedly to cover transitions between the admixed components. The results are shown in Table A. 15-I. It is seen that both calculations give good agreement with the experimental data; this agreement indicates that the unified model is valid but that the half-lives are not sensitive enough to the band mixing to test the size of the Coriolis matrix elements.

Similarly the M1 interband branching ratios were calculated with and without the mixing, and the results were compared with the experimental ratios. These results are shown in Table A. 15-II. Again it can be seen that the agreement is quite good, but that the ratios are not very sensitive to the Coriolis mixing.

References

1. Chemistry Division Annual Report, 1963, UCRL-11213, Feb. 1964, Report A. 3.
2. T. Novakov, J. M. Hollander, and R. L. Graham, Nucl. Instr. Methods 26, 189 (1964).
3. L. A. Sliv and I. M. Band, Internal Conversion Coefficients of Gamma Rays, I, II, (Akademia Nauk S. S. S. R., Leningrad 1956, 1958).
4. T. Novakov and J. M. Hollander, Anomalous Subshell Ratios in Mixed M1-E2 Transitions, Nucl. Phys. (in press).
5. Z. Szymanski, Nucl. Phys. 28, 63 (1961).
6. S. -G. Nilsson, Kgl. Danske Videnskab. Selskab Mat.-Fys. Medd. 29, No. 16 (1955).

Table A. 15-I. Comparison of theoretical and experimental M1 transition probabilities in Es^{253} decay.

Transition energy (keV)	$t_{1/2} \times 10^{-12}$ sec (experimental)	$t_{1/2} \times 10^{-12}$ sec (theoretical-- without mixing)	$t_{1/2} \times 10^{-12}$ sec (theoretical-- with mixing)
41.79	9 ± 2	6.3	12.0
51.95	5 ± 1	4.4	8.5

Table A.15-II. Branching ratios of M1 transitions from K = 5/2 to K = 7/2 band.

I initial K = 5/2	I final K = 7/2	Experimental ratio	Theoretical ratio	
			Without mixing	With mixing
7/2 →	9/2 / 7/2	4.7 ± 2.5	3.5	4.1
	9/2 / 7/2	11.4 ± 1.4	14.5	9.9
9/2 →	11/2 / 9/2	2.75 ± 0.25	2.03	2.7
	11/2 / 7/2	32 ± 4.8	29	26
	11/2 / 9/2	5.0 ± 2.5	8.3	5.5
11/2 →	13/2 / 11/2	1.94 ± 0.64	1.53	2.4
	13/2 / 9/2	9.7 ± 7	13	14
13/2 →	15/2 / 13/2	4.5 ± 1.5	1.3	1.9

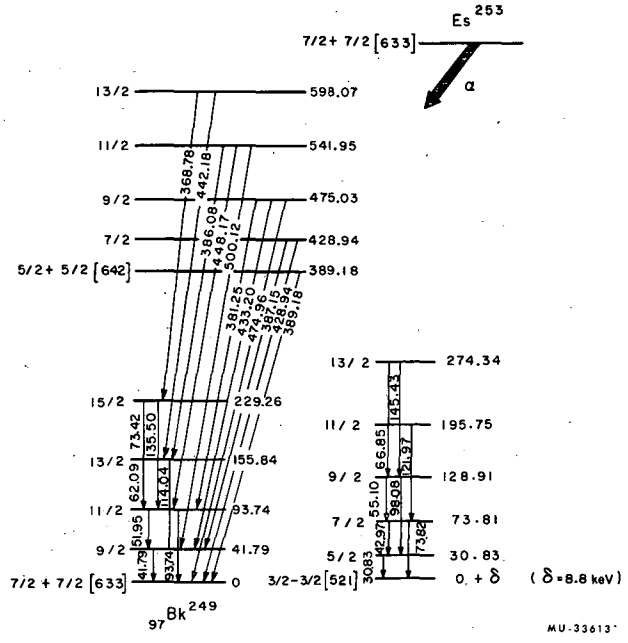

Fig. A.15-1. Decay scheme of $_{99}Es^{253}$.

16. CENTRIFUGAL STRETCHING OF NUCLEI†

R. M. Diamond, F. S. Stephens, and W. J. Swiatecki

The object of this note is to show in a simple way the physical content of the close agreement between the Davydov-Chaban (DC) calculations and the experimental rotational energies described in reference 1 and to suggest a qualitative explanation for the remaining deviations. We shall show that the idea of a spinning nucleus being stretched out under the influence of the centrifugal force, when incorporated in an elementary classical treatment, is capable of reproducing the quantum-mechanical DC calculations[2] and thus of accounting, with remarkable accuracy, for the rotational spectra.

Let us assume, as suggested by Bohr[3] (and DC), that the energy of an axially symmetric nucleus consists of a potential energy, quadratic in the deviation of a deformation parameter β from its equilibrium value β_0, and a kinetic energy of rotation equal to $\hbar^2 I(I+1)$ divided by twice the moment of inertia of the nucleus (a function of β):

$$E = P\,E + K\,E = \frac{1}{2}C\,(\beta-\beta_0)^2 + \frac{\hbar^2}{2\Im(\beta)}\,I(I+1). \qquad (1)$$

If we assume that $\Im$ is proportional to β^2 ($\Im = 3B\beta^2$, where B is a constant) we have a simplified version of the problem that is solved quantum-mechanically by DC. To obtain a quantitative relationship expressing this centrifugal stretching we differentiate Eq. (1) with respect to β, equate the result to zero, thus obtaining the equilibrium value of β, and then substitute this β_{eq} into Eq. (1) to obtain the classical result for the energy E as a function of angular momentum I. A comparison with the DC calculation for the energy spacings shows that, with a suitable choice of B and C, the classical formula reproduces the quantum mechanical result to better than 0.5% over the entire region of spins and nuclei discussed in reference 1.

It is not immediately clear why the classical formula does so well, since the zero-point vibrational energy, included by DC but not in the classical approximation, varies appreciably with I. It is not difficult, however, to make an estimate of the zero-point vibrational energies. The second derivative of Eq. (1) with respect to β, evaluated at β_{eq}, gives the curvature of the effective potential for any I. These curvatures, if used to define new parabolic potentials, lead at once to an estimate of the zero-point vibrational energy as a function of I. Adding this energy to the classical formula based on Eq. (1) gives exactly the DC quantum mechanical solution (DC, Eq. 2. 11) so long as the DC quantum number ν is integral—and this turns out to be an excellent approximation[4] for all but the lowest spins of the worst rotors discussed in reference 1.

The foregoing is, then, a simple, semiclassical derivation of those features of the DC calculation that are essential to the explanation of the energy spectra of reference 1. The simplicity of the semiclassical treatment enables us to go further than DC and to test the effect of different input assumptions, in particular the result of varying the forms of the potential and kinetic energies in their dependence on β.

Examining first the kinetic energy term, one might question the hydrodynamic argument for using moments of inertia proportional to β^2, since, in absolute magnitude, the hydrodynamic moments are wrong by a factor of 6 or so. Fortunately at least a partial test of the β^2 relationship is possible. The moments of inertia derived from the first (2+) rotational energies of nuclei in the region $150 < A < 180$ have been plotted in Fig. A. 16-1 against their respective ground-state equilibrium deformations (β_0), as determined from the appropriate reduced E2 transition probabilities, B(E2;0+ → 2+). The dashed line through the experimental points is a parabola and shows that the points do happen to be approximately representable by a quadratic dependence of $\Im$ on β. Furthermore, Grodzins[5] has shown that this dependence holds over the entire periodic table if $\Im$ varies with mass number approximately as $A^{7/3}$ instead of the expected $A^{5/3}$. This suggests that if the mass parameter B is given this same smooth variation with A, the kinetic energy term in Eq. (1), with $\Im = 3B\beta^2$, may be useful for all even-even nuclei, irrespective of their shape. A different dependence which presents certain advantages would be

$$\Im(\beta) = \Im_{rigid}(B)\,[1-e^{-(\beta/\beta_1)^2}]\,,$$

where β_1 is a parameter. With this choice, the moment of inertia is approximately parabolic for moderate deformations and tends to the rigid-body value for large deformations.

As regards the potential-energy part of Eq. (1), deviations from a parabolic dependence on $(\beta-\beta_0)$ may be expected for large deviations of β from its equilibrium value. The nature of these deviations is suggested by the functional form of the deformation energy used in reference 6 in connection with an interpretation of nuclear masses and deformations. The essential features of this potential are a broad (approximate) parabola in β, representing the restoring potential associated with the nuclear surface tension (modified by the electrostatic repulsion) and a central Gaussian bump of relatively short range, representing shell effects. This bump is negative for nuclei close to magic numbers, stabilizing the spherical shapes, and positive for nuclei between closed shells, producing stable deformations. An important feature is that for large values of β the potential-energy curves of neighboring nuclei are all essentially identical. The immediate prediction is that for rotational states of sufficiently high spin one might expect all nuclei to be forced over against this common part of the potential, with the result that all neighboring nuclei should have similar rotational spacings at high spin. Just such similar behavior at high spins was, in fact, one of the striking features observed for the nine nuclei studied in reference 1.

A second feature of the "mass-formula potential" of reference 6 is that nuclei approaching the region where ground-state deformations disappear (bad rotors) are characterized by a small Gaussian bump; the potential energy tends therefore to be more nearly quadratic in β. Under these conditions the DC equations describe quadrupole surface vibrations of a spherically symmetric nucleus and one knows[3] the solution is essentially a harmonic-oscillator spectrum. With this potential, the semiclassical treatment outlined earlier in this note also gives a series of very nearly equally spaced levels (spaced as $\sqrt{I(I+1)}$ except for the 0+ state, where the zero-point vibrational energy has to be rather carefully considered). One might hope, therefore, that this simplified treatment is capable of tracing in a continuous way the transition of the "rotational" states into the highest-spin member of the "vibrational" multiplets.

We now turn to a qualitative comparison of the energies given by the mass-formula potentials with those given by the DC parabolic potentials. It appears that both of the systematic deviations of the experimental data[1] from the DC solutions are in the direction expected on the basis of the mass-formula potentials. The better rotors (low first-excited states) were fitted very well by DC up to spin 10 or 12, but thereafter usually had smaller level spacings than expected. This can be explained by the decreasing curvature of the potential for large β, which the mass formula predicts for good rotors as they are being driven over against the broad surface-tension parabola.

The other systematic deviation of the experimental data from DC occurs only in nuclei near the "vibrational" region (high first-excited-state energies). Here the lowest spacings, particularly the 2+ to 0+ one, are larger than expected from a DC calculation fitted to the intermediate spin states. Again the data deviate in the direction of the harmonic oscillator; and this, as we have noted before, is what the mass-formula potential predicts when the Gaussian bump is small.

Although the DC kinetic energy expression seems adequate over the region of deformation for which there are data, the mass-formula potential of reference 6 would appear to be a significant improvement over the potential assumed by DC. The indications are that with the mass-formula potential and the simple semiclassical treatment, it may be possible to follow the "rotational" sequence of levels into the region of good "vibrators."

Footnote and References

† Condensation from Phys. Letters 11, 315 (1964).
1. F. S. Stephens, N. Lark, and R. M Diamond, Phys. Rev. Letters 12, 255 (1964); and Nucl. Phys. (in press).
2. A. S. Davydov and A. A. Chaban, Nucl. Phys. 20, 499 (1960).
3. A. Bohr, Kgl. Danske Videnskab. Selskab. Mat.-Fys. Medd. 26, No. 14 (1952).
4. P. P. Day, E. D. Klema, and C. A. Mallmann, Argonne National Laboratory Report ANL-6220, Nov. 1960.
5. L. Grodzins, Phys. Letters 2, 88 (1962).
6. W. J. Swiatecki, in Second International Conference in Nuclidic Masses, Vienna, 1963 (Springer Verlag, Vienna, 1964); W. Myers and W. J. Swiatecki (Lawrence Radiation Laboratory), unpublished work, 1964.

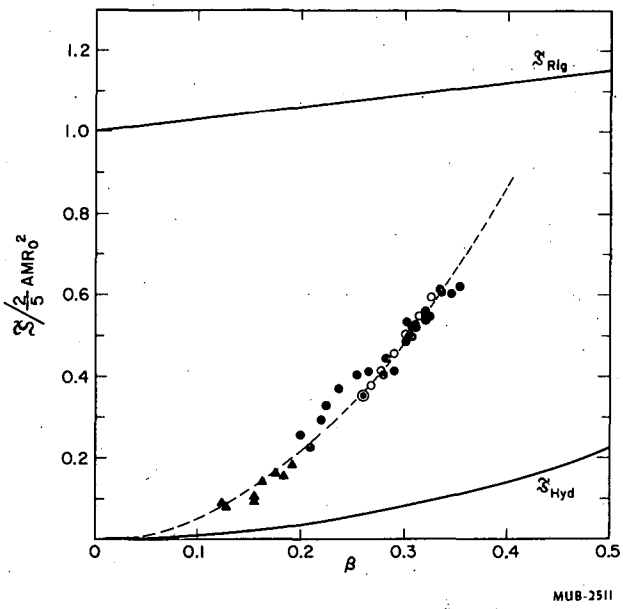

Fig. A. 16-1. Experimental moments of inertia (●) for rotational nuclei (in units of the rigid sphere) plotted against the measured β_0 values; ▲, vibrators; β_0 presumably represents an rms value of β; ———, rigid rotor and hydrodynamic estimates; ----, a parabola passed through the experimental data; O, measured moments of inertia for W^{174} up to spin 14 plotted against the DC-calculated β values. The β_0 value of W^{174} has been roughly measured to be 0.26 ± 0.05.

17. HIGH-SPIN ROTATIONAL STATES IN NUCLEI†

F. S. Stephens, N. Lark, and R. M. Diamond

It is well established that nuclei in the region $150 < A < 190$ have sizable prolate-spheroidal deformations, and consequently have well-defined rotational bands built on the various intrinsic levels. In work reported here high-lying members of the ground-state rotational bands of a number of even-even nuclei in this region have been studied following heavy-ion reactions of the type $Ho^{165}(B^{11}, 4n)Hf^{172}$. Odd-proton-number targets (Tb^{159}, Ho^{165}, and Tm^{169}) and projectiles (B^{11}, N^{14}, and F^{19}) have been used to produce $Yb^{164,166}$, $Hf^{166,168,170,172}$, and $W^{172,174,176}$. The bombarding energy has been adjusted in each case to give predominantly the particular even-even nucleus desired. We have studied the conversion-electron and γ-ray spectra from such targets during the 3-msec beam burst of the Hilac in order to observe the deexcitation of the final nucleus to its ground state.

It was found that at the optimum bombarding energy almost all the intense low-energy transitions could be assigned either to Coulomb excitation in the target or to the ground-state rotational band of the final even-even product nucleus. The latter assignments were made because (a) their energies approximated those of a symmetric rotor,

$$E(I \rightarrow I-2) = \frac{\hbar^2}{2\mathfrak{I}} [I(I+1)-(I-2)(I-1)] = \frac{\hbar^2}{2\mathfrak{I}} [4I-2]; \qquad (1)$$

(b) their intensities were high, and decreased (assuming E2 transitions) in a very regular way with increasing energy (spin); and (c) the lower-energy transitions could be shown to be E2

from their K/L intensity ratio. Direct spin measurements are largely absent, but in a subsequent work[1] three cases were studied in which the first four of these prompt transitions also occurred in low intensity following the beam pulse; that is, held up by an isomeric state. In these three cases, the spins 2+, 4+, 6+, and 8+ were established by angular-distribution measurements.

Those transitions that fit the above requirements and are of outstanding intensity in the spectrum are given "A" classification in Table A. 17-I. In a few cases, such as Hf^{170}, essentially only such transitions are observed in the spectrum. More usually, though, a few apparently extraneous transitions of a moderately low intensity occur at the higher energies; sometimes, as in W^{176}, there is apparently an entire band of additional transitions. As the intensities of the ground-state band transitions decrease with increasing spin, they become at some point no more intense than the extraneous transitions, and it often becomes difficult to decide which of the lines are the members of the ground-state band. We have attempted to do this on the basis of the above requirements and the detailed nature of the excitation functions of the lines. The more certain of these transitions (80% expected to be correct) are labeled "B" in the tables, and those less certain or any that are appreciably weaker than the strongest of the unassigned transitions are given a "C" classification (50% expected to be correct). This last classification does not mean any doubt that the conversion line exists, only that there is some doubt whether it is a member of the ground-state rotational band.

There are a number of models with which these rotational energies can be compared. We have not attempted a thorough examination of all such models, partly because sizable computations are required in some cases, and partly because some general observations have suggested to us certain essential features required in such a model. These observations are: (a) the very nearly identical behavior of the moments of inertia observed at high spin values for the nuclei studied suggests that a very general property of rotating nuclei must be involved; (b) the evidence accumulating from the study of vibrational states in deformed nuclei indicates that the β band is admixed into the ground-state rotational band some 10 times as heavily as is the γ band, and the deviations of the ground-state band from a perfect rotor can be largely accounted for at low spins by a perturbation treatment of such β-ground mixing;[2,3] and (c) the average change in moment of inertia with spin observed in this study is about a factor of 2, which indicates that an attempt to explain this should avoid using perturbation theory. In a model, therefore, we must look primarily for a nonadiabatic treatment of the coupling between β vibrations and rotation. Within the framework of the hydrodynamic model developed by Bohr and Mottelson,[4] the solution of this problem has been given by Davydov and Chaban (DC) in conjunction with their treatment of asymmetric rotors.[5] We have used their treatment, but in accordance with observation (b) above we have set γ (asymmetry parameter) equal to zero and, therefore, have looked only at the effects calculated due to nonrigidity with respect to β deformation. As mentioned by DC this amounts in the ground-state band to accounting for the centrifugal expansion of the nucleus, and hence it seems a priori most consistent with observation (a) above.

As a means of comparing the data with the DC model, we list in Table A. 17-II the level energies as measured and as calculated by adjusting the two parameters, μ and $\hbar\omega_0$, for the best fits. This method is not a very sensitive one, but has the advantage of simplicity and familiarity. In constructing Table A. 17-II, we used only transitions which had been given an A classification in Table A. 17-I. This is primarily because we did not want to affect the entire fit for a particular band with a transition which might be misassigned. In addition, we did not want to obscure the really excellent fits usually possible up to spin 14 or so by including the admittedly more poorly fitted data above these spins. The five nuclei whose first-excited-state energies lie below 115 keV have an overall rms deviation of 0.21%. This is hardly outside our limits of error; however, the systematic nature of the deviations makes it seem likely that this does represent a real difference from the theory. Of the four nuclei whose first excited state is more than 115 keV, W^{172} is fitted almost as well as the previous five, and the considerably poorer fits for the other three, $Hf^{166,168}$ and Yb^{164}, are due almost entirely in each case to the first-excited-state energy. Both this systematic deviation and the other one occurring at the highest spins are in the direction to be explained by better potential energy curves, as discussed elsewhere.[6] We consider the agreement here to be surprisingly good, and considerably better than we could obtain by any other means.

Since our use of the DC calculation, with $\gamma \equiv 0$, accounts for the rotational spacings quite impressively, we were interested to see whether the energy of the β-vibrational band could be correctly predicted when the same restriction was used. Table A. 17-III summarizes the data for all cases we could find in which both the β energy and the 2+ and 4+ ground-state band

members are accurately known. The ratio of the β-band energy (0+ state) to the first-excited-state energy is calculated from the ground-state band members and compared with the experimentally observed ratio. In all cases the DC ratios are high, and the last column gives the percentage error in the calculation. For the rare earths seven cases lie within +8 ±5%. In the one exception, Hf^{178}, the 0+ levels have been assigned as predominantly two-quasi-particle states,[7] and this, if correct, would mean the real β band might lie higher, as predicted. In the heavy elements, all cases fall within the range +20 ±10%. We feel the absolute agreement is not bad, and the higher internal consistency for each group is very encouraging. The absolute B(E2) values connecting the β band and the ground band also appear to be given reasonably well by this model.[8]

In summary it seems that, so far as the presently available data have been analyzed, a simple and reasonably consistent picture can be constructed of a rotating nucleus that can stretch and vibrate along its principal axis. Nothing is assumed or implied in this picture about the gamma vibrational band except, indirectly, that it is not the principal cause of the deviations of the ground-state band from a perfect rotor. We believe this true for the nuclei considered here; however, whether it is true of nuclei in general or not remains to be seen.

Footnote and References

† Condensation of two papers, Phys. Rev. Letters 12, 225 (1964) and Nucl. Phys. (in press).

1. J. Burde, F. S. Stephens, and R. M. Diamond, unpublished work, 1964.
2. F. S. Stephens, B. Elbek, and R. M. Diamond, in Proceedings of the Third Conference on Reactions Between Complex Nuclei, eds. A. Ghiorso, R. M. Diamond, and H. E. Conzett (University of California Press, Los Angeles and Berkeley, 1963), Paper E-8.
3. J. S. Greenberg, D. A. Bromley, G. C. Seaman, and E. V. Bishop, in Proceedings of the Third Conference on Reactions Between Complex Nuclei, eds. A. Ghiorso, R. M. Diamond, and H. E. Conzett (University of California Press, Los Angeles and Berkeley, 1963), Paper E-7; Phys. Rev. Letters 11, 211 (1963).
4. A. Bohr, Kgl. Danske Videnskab. Selskab Mat.-Fys. Medd. 26, No. 14 (1952); A. Bohr and B. R. Mottelson, ibid. 27, No. 16 (1953).
5. A. S. Davydov and A. A. Chaban, Nucl. Phys. 20, 499 (1960).
6. R. M Diamond, R. S. Stephens, and W. J. Swiatecki, Phys. Letters 11, 315 (1964).
7. C. J. Gallagher and V. G. Soloviev, Kgl. Danske Videnskab. Selskab Mat.-Fys. Skr. 2, No. 2 (1962).
8. F. S. Stephens and R. M. Diamond, unpublished data, July 1964.
9. F. S. Stephens, N. Lark, and R. M. Diamond, Phys. Rev. Letters 12, 225 (1964).

Table A. 17-I. Ground-state rotational band transitions. [a]

Transition	Yb^{164}	Yb^{166}	Hf^{166}	Hf^{168}	Hf^{170}	Hf^{172}	W^{172}	W^{174}	W^{176}
2 → 0	122.5 A	101.8 A	158.7 A	123.9 A	100.0 A	94.5 A	122.9 A	111.9 A	108.7 A
4 → 2	261.5 A	227.9 A	312.0 A	261.1 A	220.6 A	213.4 A	254.0 A	243.1 A	239.8 A
6 → 4	374.0 A	337.4 A	426.9 A	371.1 A	320.5 A	319.1 A	350.3 A	349.2 A	350.9 A
8 → 6	461.3 A	430.0 A	509.5 A	456.1 A	400.2 A	408.8 A	419.3 A	432.5 A	440.6 A
10 → 8	528.4 A	506.8 A	564.0 A	522.0 A	462.0 A	483.6 A	469.6 A	498.0 A	508.2 A
12 → 10	574.5 B	567.8 A	593.8 A	569.4 A	510.0 A	543.1 A	512.5 A	551.2 A	557.3 A
14 → 12	606 C	602.7 C	613.4 C	606.5 C	550.3 A	588.6 A	548.5 A	594.0 B	595.1 B
16 → 14		627.8 C			583.7 A	621.9 B	576.2 B		624.2 C
18 → 16					614.3 B	641.8 B	596.8 C		
20 → 18					652 C				

a. The accuracy of these transitions is expected to be ± 0.3%. An additional significant figure has been kept in most of the cases, but this can be useful only in comparing transitions of comparable energy in the same nucleus.

Table A. 17-II. Experimental rotational energies compared with the DC calculation. [a]

Isotope		2+	4+	6+	8+	10+	12+	14+	16+	rms deviation %
W^{176}	Exp	108.7	348.5	699.4	1140	1648	2206			0.20
	Calc	108.7	349.1	698.8	1137	1646	2213			
W^{174}	Exp	111.9	355.0	704.2	1137	1635	2186			0.16
	Calc	111.8	355.8	705.3	1137	1633	2181			
W^{172}	Exp	122.9	376.9	727.2	1147	1616	2129	2677		0.27
	Calc	122.6	378.7	729.3	1147	1617	2126	2668		
Hf^{172}	Exp	94.5	307.9	627.0	1036	1519	2063	2651		0.31
	Calc	94.4	307.5	625.5	1033	1517	2066	2669		
Hf^{170}	Exp	100.0	320.6	641.1	1041	1503	2013	2564	3147	0.22
	Calc	100.0	320.5	639.8	1038	1500	2012	2568	3160	
Hf^{168}	Exp	123.9	385.0	756.1	1212	1734	2304			0.79
	Calc	121.7	384.9	758.6	1216	1740	2315			
Hf^{166}	Exp	158.7	470.7	897.6	1407	1971	2565			1.45
	Calc	153.7	471.3	902.2	1413	1983	2600			
Yb^{166}	Exp	101.8	329.7	667.1	1097	1604	2172			0.12
	Calc	101.9	330.2	667.7	1097	1601	2169			
Yb^{164}	Exp	122.5	384.0	758.0	1219	1748				0.52
	Calc	121.2	384.7	760.3	1222	1752				

a. There are two adjustable parameters, μ and $\hbar\omega_0$, for each nucleus.

Table A. 17-III. Beta-vibrational energies.

Nuclide	$E(2 \rightarrow 0)$ (keV)	$E(4 \rightarrow 2)$ (keV)	$E(0' \rightarrow 0)$ (keV)	$\frac{E(0' \rightarrow 0)}{E(2 \rightarrow 0)_{calc}}$	$\frac{E(0' \rightarrow 0)}{E(2 \rightarrow 0)_{obs}}$	Δ(%)
Pu^{240}	42.87	98.9	858[a]	24.9	20.0	+20
Pu^{238}	44.11	101.9	943.1	26.5	21.38	+19
U^{238}	$\bar{\mu} \sim 0.180$[b]		993	29.0	22.2	+23
U^{234}	43.49	99.8	811.6	20.6	18.66	+10
U^{232}	47.6	109.0	692.9	19.5	14.6	+25
Th^{232}	$\bar{\mu} = 0.232$[b]		730	17.3	14.7	+15
Th^{230}	53.15	120.8	634	16.3	11.9	+27
Os^{188}	155.03	322.94	{1086 1766}	7.2	{7.01 11.4}	{+ 3 -56}
[c](Hf^{178}	93.17	213.42	{1197 1440}	19.6	{12.9 15.5}	{+34 +21})
Er^{166}	80.57	265.1	1460.3	19.5	18.12	+ 7
[c](Gd^{158}	79.5	182.4	1427	20.5	17.9	+13)
Gd^{156}	88.97	199.19	1040	13.0	11.7	+10
Gd^{154}	123.07	248.08	680.6	6.0	5.53	+ 8
Sm^{152}	121.79	244.84	685.0	6.0	5.62	+ 7
[c](Nd^{150}	131	259	687	5.5	5.2	+ 5)

a. References for the data in this table are given elsewhere (reference 9).
b. Precise 2+ and 4+ energies are not available for Th^{232} and U^{238}, but many band members are known. Therefore an average μ value is determined for the band as a whole.
c. Parentheses indicate assignments of less certainty or data of poorer quality than usual.

18. A NEW REGION OF ALPHA ACTIVITY†

R. D. Macfarlane* and A. Siivola

Alpha radioactivity is a mode of decay commonly associated with the heavy elements. In this paper we report the discovery of alpha decay from nuclides in the region of mass 100.

It has long been recognized from atomic mass data that an enhancement of the alpha-decay energies of the tellurium isotopes is present because of the effect of the 50-proton closed shell. The enhancement, however, is not large enough to produce a detectable instability toward α-particle emission among the tellurium isotopes presently known. Some unsuccessful attempts to produce neutron-deficient tellurium alpha emitters by high-energy proton spallation have been previously reported.[1,2] We have obtained results on the alpha activity of the very light tellurium isotopes whose alpha decay energies are additionally enhanced by the N = 50 closed shell.

We bombarded a 90% enriched Ru^{96} target with O^{16} ions from the Berkeley Hilac, and measured α-particle spectra, using techniques described in an earlier paper.[3] Two weak groups of α particles, identified by their energy loss in a thin aluminum leaf, were observed at 3.28 MeV and 3.08 MeV with half-lives of 2.2 sec and 5.3 sec, respectively. The spectrum is shown in Fig. A. 18-1. We established that these activities were due to isotopes of tellurium when we observed that they could not be produced in $Ru^{96} + N^{14}$ bombardments. We obtained mass assignments for these activities from excitation function measurements, using the results of Black on heavy-ion reactions in this mass region to interpret our data.[5] As shown in Fig. A. 18-2, the peak cross section for the production of the 3.28-MeV alpha activity falls at a bombarding energy of 104 MeV. This compares most favorably with that expected for the reaction $Ru^{96}(O^{16}, 5n)Te^{107}$. The excitation function for the 3.08-MeV group peaks at 87 MeV, which is close to the expected value for the reaction $Ru^{96}(O^{16}, 4n)Te^{108}$. The results are summarized in Table A. 18-I.

These nuclides represent the first opportunity to study alpha decay from nuclei where the valence neutrons and protons are in the same single-particle level, in this case, the $g_{7/2}$ level (or $d_{5/2}$). This may give rise to a kind of "super-allowed" alpha decay resulting in large reduced widths. At present we cannot give any estimate of the alpha reduced widths for Te^{107} and Te^{108} because the alpha branchings are not known.

The most alpha-labile tellurium isotope is expected to be Te^{104}, since it can alpha decay to the double closed shell nuclide Sn^{100}. Our first experiments were directed toward producing this nuclide by the reaction $Ru^{96}(O^{16}, 8n)Te^{104}$. Apparently, however, the peak cross section for this reaction as well as the $(O^{16}, 7n)$ and $(O^{16}, 6n)$ reactions is extremely small because of the high neutron binding energies in this region.

We expect that it will also be possible to observe alpha decay from the very neutron-deficient isotopes of iodine and xenon.

Footnotes and References

† A version of UCRL-11765, submitted to Phys. Rev. Letters.

* Department of Chemistry, McMaster University, Hamilton, Ontario.

1. J. O. Rasmussen, S. G. Thompson, and A. Ghiorso, Phys. Rev. 89, 33 (1953).
2. M. Karras, G. Andersson, and M. Nurmia, Arkiv Fysik 23, 57 (1962).
3. R. D. Macfarlane and R. D. Griffioen, Nucl. Instr. Methods 24, 461 (1963).
4. R. P. Black, Heavy Ion Reactions in the Medium Mass Region (thesis), Massachusetts Institute of Technology, 1964.

Table A. 18-I. Summary of results.

Nuclide	E_α (MeV)	$t_{1/2}$ (sec)
Te^{107}	3.28 ± 0.03	2.2 ± 0.2
Te^{108}	3.08 ± 0.03	5.3 ± 0.4

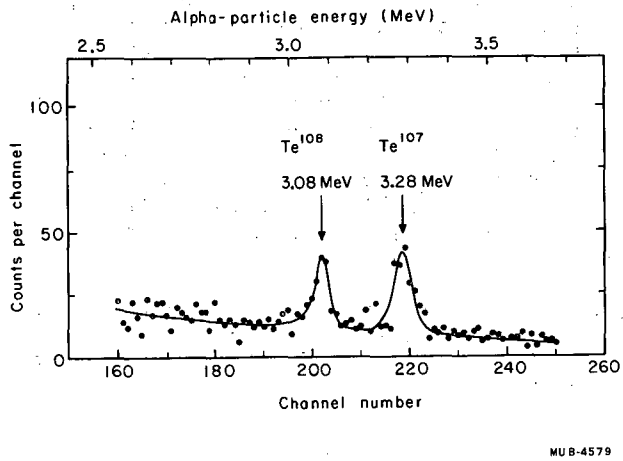

Fig. A. 18-1. Alpha-particle spectrum of the products of the reaction $Ru^{96} + O^{16}$ at a bombarding energy of 95 MeV (lab).

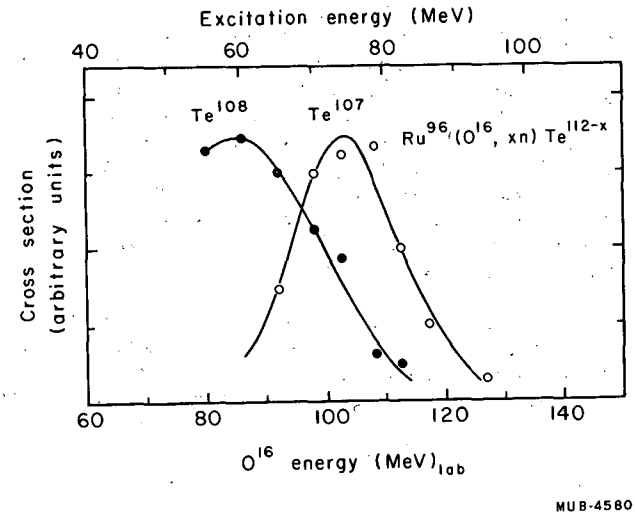

Fig. A. 18-2. Excitation functions for the production of the new Te alpha emitters.

19. DELAYED PROTONS IN THE DECAY OF Te^{108} †

Antti T. Siivola

In a recent study of the alpha activity of Te isotopes, a few counts were observed that apparently did not belong to alpha groups. [1] In order to find out if they possibly were due to proton emission following beta decay of Te, a further study was undertaken.

The experimental apparatus was essentially the same as that used in a number of alpha decay studies at the Berkeley heavy-ion linear accelerator, and it has been described earlier. [2] In this work reaction products were collected on a thin Ni or Al foil. The activity was deposited on a spot approximately 2 mm in diameter. Three millimeters behind the foil was a surface-barrier detector operating at a bias of 60 V, which is enough to stop 4-MeV protons. At this bias the positron pileup extends up to 1.5 MeV.

Tellurium isotopes were produced by the reaction $Ru^{96}(O^{16}, xn)Te^{112-x}$. The targets were 1- to 2-mg/cm^2-thick 95% Ru^{96}, electroplated on 4.5-mg/cm^2-thick Cu. A set of Cu degrader foils was used to control the energy of the beam. Figure A. 19-1 shows the spectrum taken at 85 MeV (lab) bombarding energy. In this case the collector foil was 2.2-mg/cm^2 Ni, which is thick enough to degrade 3.3-MeV alphas of Te^{107} to energies below 1.5 MeV. Three groups are present: 3.7 MeV, 3.4 MeV, and a broad distribution at 2.6 MeV. The energies refer to the kinetic energy of the emitted protons with absorption in the foil taken into account, and they are estimated to be accurate to 0.1 MeV. The same spectrum was measured through 3.7- and 6.8-mg/cm^2 Al foils, and the peaks shifted downwards an amount that can be expected of proton groups with energies given above. This activity was not present when Cu was bombarded with O^{16} ions; neither was it found in $N^{14} + Ru^{96}$ bombardments.

The excitation function for this activity proved to be the same as that for the 3.08-MeV alpha activity described in an earlier report. [1] Also the half-life is the same as that of the alpha group, 5.3 ± 0.4 sec. This means that the proton activity has to be due to the same isotope, Te^{108}, which partly decays through the emission of 3.08-MeV α particles, and whose main decay is positron emission and electron capture to Sb^{108}. The decay curves for both protons and α particles are given in Fig. A. 19-2.

No proton groups that could be assigned to isotopes lighter than Te^{108} were present. In the earlier work, Te^{107} was found by measuring its alpha decay, [1] but it apparently beta

decays mainly to the ground state or to low-lying excited states of Sb^{107}. The proton decay energy of these states has to be less than 2.5 MeV, otherwise they would have been seen. This indicates that the observed protons really originate from excited states of Sb^{108}, because its ground-state proton decay energy has to be less than that of Sb^{107}. The proton binding energies of Te and Sb nuclei for mass numbers less than 110 are not known, so that it is not possible to find out how highly excited the proton-emitting states are. As for the absence of lighter isotopes than Te^{107}, according to mass tables[3] it is possible that their ground states are unstable against proton (or two-proton) emission and have half-lives considerably shorter than 0.1 sec, in which case they cannot be detected by using the present method. For Te^{108}, the mass tables predict a beta-decay energy of 7 to 8 MeV, and for Sb^{108}, a proton binding energy of ≈1 MeV,[3] so that the situation is favorable for delayed proton emission.

During the past year, a large number of delayed proton emitters has been found among the light elements.[4-8] A Russian group has also reported one nuclide in Kr or Br to be a delayed proton emitter,[9] but thus far no experimental data have been published for heavier elements, although Te has been considered as a promising case.[9]

Footnote and References

† A version of UCRL-11834, submitted to Phys. Rev. Letters.

1. R. D. Macfarlane and A. Siivola, A New Region of Alpha Radioactivity (UCRL-11765, Nov. 1964), submitted to Phys. Rev. Letters.
2. R. D. Macfarlane and R. D. Griffioen, Nucl. Instr. Methods 24, 461 (1963).
3. P. A. Seeger, Nucl. Phys. 25, 1 (1961); W. J. Swiatecki (Lawrence Radiation Laboratory), private communication.
4. V. A. Karnaukhov, G. M. Ter-Akopyan, L. A. Petrov, and V. G. Subbotin, Zh. Eksperim. i Teor. Fiz. 45, 1280 (1963) [Translation: Soviet Phys. JETP 18, 879 (1964)].
5. R. Barton, R. McPherson, R. E. Bell, W. R. Frisken, W. R. Link, and R. B. Moore, Can. J. Phys. 41, 2007 (1963).
6. R. McPherson, J. C. Hardy, and R. E. Bell, Phys. Letters 11, 65 (1964).
7. J. C. Hardy and R. I. Verrall, Phys. Letters 13, 148 (1964).
8. P. L. Reeder, A. M. Poskanzer, and R. A. Esterlund, Phys. Rev. Letters 13, 767 (1964).
9. V. A. Karnaukhov and G. M. Ter-Akopyan, Phys. Letters 12, 339 (1964).

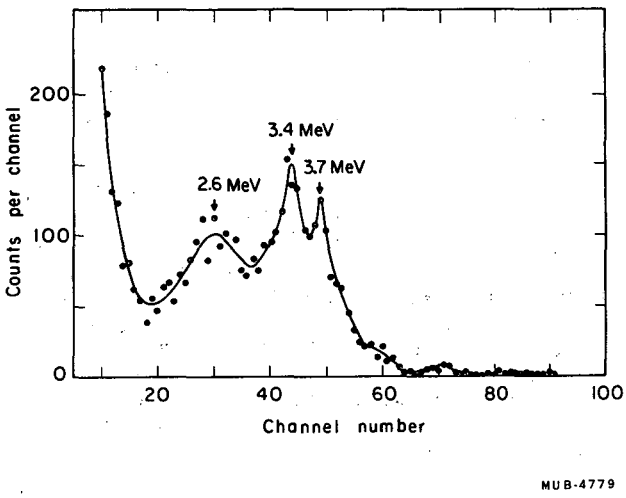

Fig. A. 19-1. Delayed proton spectrum of Te^{108}.

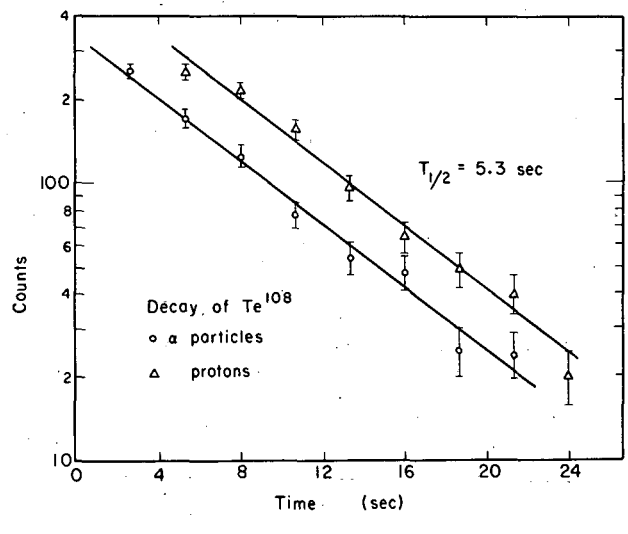

Fig. A. 19-2. Decay curves for Te^{108}. All parts of the proton spectrum (Fig. A. 19-1) were found to decay with the same half-life.

20. GAMMA-RAY SPECTROSCOPY ON 155-DAY LUTETIUM-177 WITH USE OF LITHIUM-DRIFTED GERMANIUM COUNTERS†

J. Blok and D. A. Shirley

We have used recently developed lithium-drifted germanium γ-ray detectors[1] to study the spectrum from the decay of the 155-day isomer of Lu^{177}. This isomer has been shown to be a three-quasi-particle state of an odd proton and an uncoupled neutron pair which gives rise to the very high spin of 23/2.[2,3] The decay scheme was previously proposed by Alexander et al. from work done with a bent-crystal spectrometer.[2] It is shown in Fig. A. 20-1.

We feel that this decay is a particularly important one for nuclear structure theory, involving as it does up to eight members of a rotational band in Hf^{177}, and it seemed worthwhile to confirm the proposed level schemes independently by definitive coincidence measurements and high-sensitivity γ-ray spectroscopy with the newly developed γ-ray counters. In particular we were interested in filling the gap in the $7/2^-$ [514] band in Hf^{177}, in which there was no experimental evidence for the 19/2 state.

In Fig. A. 20-2 we show a γ-ray spectrum of 155-day Lu^{177} obtained with the Ge(Li) counter. Comparison with the bent-crystal data[2] shows that, although not so good for low energies, the resolution of the Ge(Li) counter excels that of the bent-crystal spectrometer for energies above about 300 keV. In two other respects the Ge(Li) counters are far superior to a bent-crystal spectrometer for these reasonably high energies: first, the efficiency is far higher (our experiments were done with sources of less than 1 mCi); secondly, the signal-to-noise ratio is very high for Ge(Li) counters, since there is little background due to incoherent scattering.

In Fig. A. 20-3 we show a spectrum of the region around 420 keV on an expanded scale. One observes a peak at about 426 keV which was not seen by Alexander et al. This peak fits energetically as the cross-over transition between the missing 19/2 level and the 15/2 level in the $K = 7/2^-$ band of Hf^{177}. To establish that this 426-keV γ ray actually was the 19/2 to 15/2 transition, we used two Ge(Li) counters and obtained a spectrum which was in coincidence with this γ ray. Because of the low efficiency of the Ge(Li) counters, the coincidence counting rate was very low; hence only the more prominent γ rays could be seen. Peaks were observed in the coincidence spectrum at 113, 136, 249, and 341 keV, and the other prominent peaks of the singles spectrum either were sharply reduced in intensity or else were completely missing. Thus the 426-keV γ ray must certainly come from the 19/2 to 15/2 transition in the $K = 7/2^-$ band of Hf^{177}. A careful search was made for the transitions which must feed the 19/2 level, namely the 21/2 to 19/2 cascade of about 243 keV or the 21/2 to 19/2 interband transition of about 284 keV. Neither peak could be found; the former because of the high Compton background in the low-energy region, and the latter because resolution from the intense 281-keV peak was impossible. Even without this final proof, however, the position of the 19/2 level appears to be well established.

As an additional independent check of the decay scheme of Alexander et al. we measured the spectra in coincidence with the 105-, 413-, and 418-keV transitions. Prominent peaks were again present or absent in agreement with the above decay scheme.

The excellent resolution obtained at high energies with the Ge(Li) counter enabled us to improve on the γ-ray energies obtained with the bent-crystal spectrometer in the range above about 300 keV. The 511-keV annihilation peak from Na^{22} and the energies of the low-energy γ rays from Lu^{177} given by Alexander et al. were used as calibration standards. The energies thus obtained are used in Table A. 20-I.

Footnote and References

† Shortened version Phys. Letters 13, 232 (1964).

1. A. J. Tavendale, in Proceedings of International Symposium on Nuclear Electronics, Paris, 1963, p. 235.
2. P. Alexander, F. Boehm, and E. Kankeleit, Phys. Rev. 133, B284 (1964).
3. L. Kristensen, M. Jorgensen, O. B. Nielsen, and G. Sidenius, Phys. Letters 8, 57 (1964).

Table A. 20-I. Precise energies and decay-scheme assignments of the γ rays of Lu^{177}. Energies below 318 keV and decay scheme assignments are from reference 2.

Gamma energy (keV)	Decay-scheme assignment	Gamma energy (keV)	Decay-scheme assignment
105.36 ± 0.02	Hf K = 9/2	249.69 ± 0.1	Hf K = 7/2
112.97 ± 0.02	Hf K = 7/2	268.38 ± 0.1	Lu K = 7/2
121.56 ± 0.03	Lu K = 7/2	281.77 ± 0.1	Hf K = 9/2
128.48 ± 0.02	Hf K = 9/2	291.73 ± 0.3	Hf interband
136.68 ± 0.02	Hf K = 7/2	296.13 ± 0.2	Hf K = 7/2
145.59 ± 0.06	Hf interband	299.07 ± 0.3	Hf interband
147.10 ± 0.06	Lu K = 7/2	306.02 ± 0.3	Hf interband
153.25 ± 0.04	Hf K = 9/2	315.54 ± 0.3	Hf interband
159.92 ± 0.08	Hf K = 7/2	318.8 ± 0.2	Lu K = 7/2
171.84 ± 0.08	Lu K = 7/2	327.4 ± 0.2	Hf K = 9/2
174.37 ± 0.06	Hf K = 9/2	341.5 ± 0.3	Hf K = 7/2
177.05 ± 0.08	Hf interband	367.3 ± 0.3	Lu K = 7/2
195.40 ± 0.1	Lu K = 7/2	378.2 ± 0.2	Hf K = 9/2
204.00 ± 0.08	Hf K = 9/2	384.8 ± 0.3	Hf K = 7/2
208.36 ± 0.06	Hf interband	413.6 ± 0.2	Lu K = 7/2
214.32 ± 0.1	Hf K = 9/2	418.2 ± 0.2	Hf K = 9/2
217.98 ± 0.1	Lu K = 7/2	426.2 ± 0.5	Hf K = 7/2
228.48 ± 0.08	Hf interband	465.0 ± 0.5	Hf K = 7/2
233.75 ± 0.1	Hf K = 9/2		

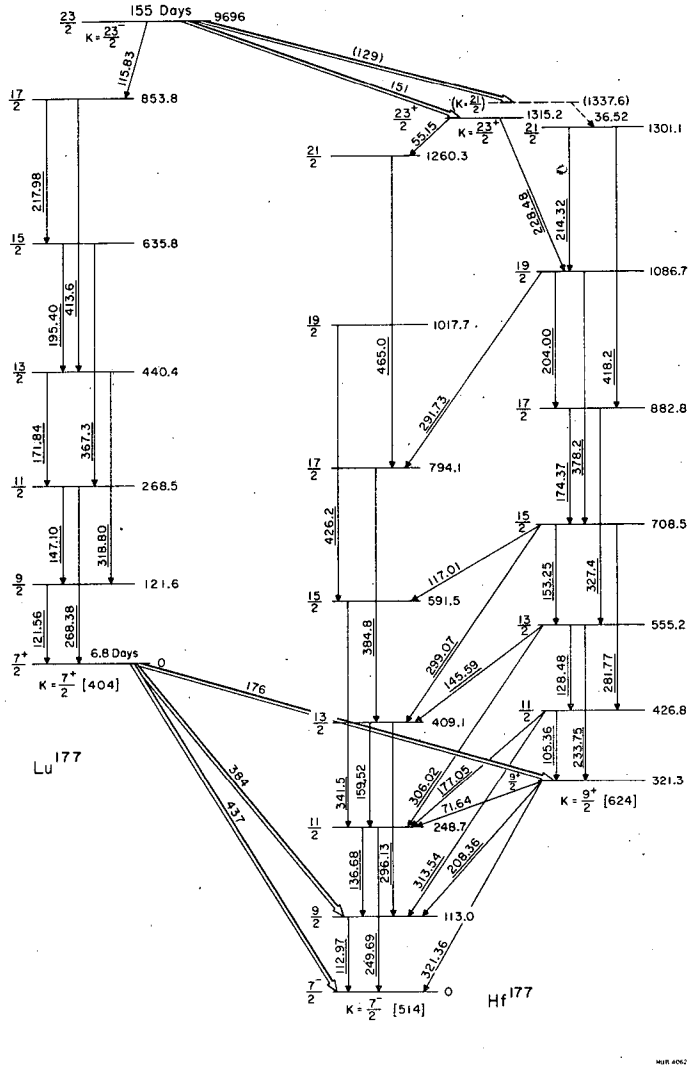

Fig. A.20-1. Decay scheme of Lu^{177} taken from reference 2. We have added the I = 19/2 level of the K = 7/2⁻[514] band and its associated γ ray. Energies of γ rays above 318 keV are ours. Gamma rays observed in this work are underlined.

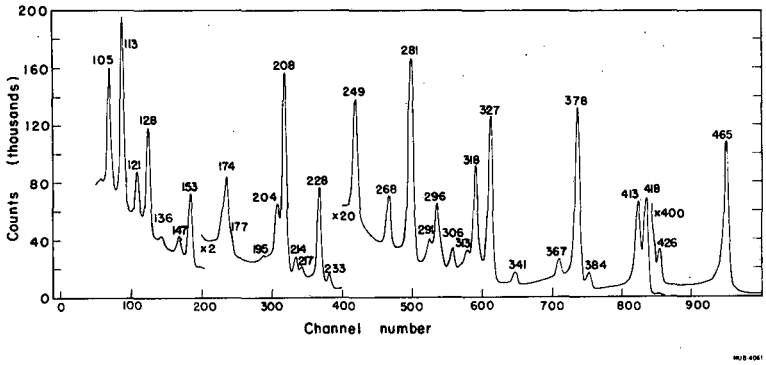

Fig. A. 20-2. γ-ray spectrum of 155-day Lu^{177} with Ge(Li) detectors. The peaks are identified by their energies (in keV).

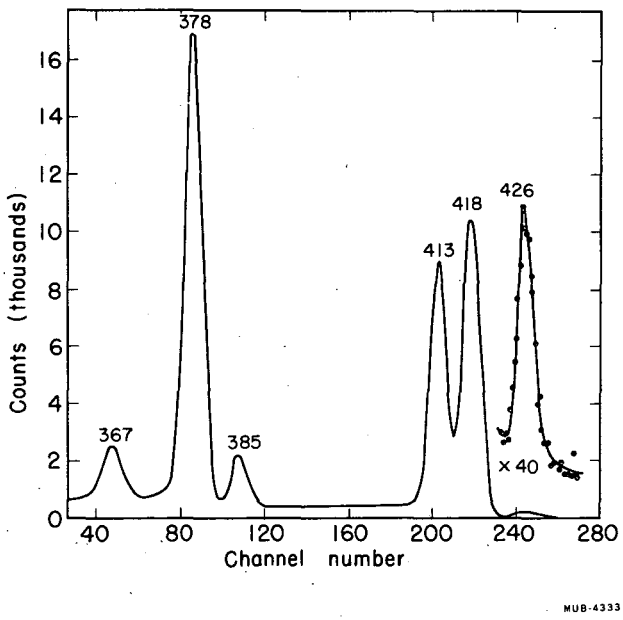

Fig. A. 20-3. Detail of 155-day Lu^{177} γ-ray spectrum showing the 426-keV transition. The experimental points are indicated as filled circles.

21. NUCLEAR MAGNETIC MOMENT OF THE 2084-keV STATE IN CERIUM-140

R. M. Levy and D. A. Shirley

The 2084-keV state of Ce^{140} is of special interest because its long lifetime ($t_{1/2}$ = 3.45 ± 0.06 nsec[1]) allows measurement of its g factor (= magnetic moment/spin), and at the same time this g factor is calculable from quasi-particle theory. Rho has made detailed calculations of the compositions of the states in $^{82}_{58}Ce^{140}$, assuming the 82-neutron core and the 50-proton core to be inert, and considering the $g_{7/2}$ and $d_{5/2}$ proton orbitals. He found, on this theory, a wave function

$$\left|\psi\right\rangle \cong 0.30\left|(d_{5/2})^2\right\rangle_{4+} + 0.91\left|(g_{7/2})^2\right\rangle_{4+} - 0.26\left|(d_{5/2}g_{7/2})\right\rangle_{4+}$$

for the 2084-keV state.[2] Using empirical g factors for the $d_{5/2}$ and $g_{7/2}$ orbitals, he derived a g factor of + 0.92 for this state.

In earlier measurements using integral angular-correlation techniques we had found a g factor of + 1.08 ± 0.10. Values available from other laboratories are + 1.15 ± 0.03,[3] + 1.11 ± 0.04,[4] and + 0.95 ± 0.10.[5] Because a value of + 1.17 would be predicted from naive shell-model considerations, describing this state as $\left|(d_{5/2}g_{7/2})\right\rangle_{4+}$, it seemed desirable to remeasure this g factor, using the more reliable technique of time-differential angular correlation. In this method the time dependence of a function R (derived from coincidence counting rates) is harmonically modulated at twice the Larmor precision frequency.[6]

We studied the 329- to 487-keV cascade. A half-life determination (Fig. A. 21-1) gave $t_{1/2}$ = 3.52 ± 0.10 nsec, in excellent agreement with the literature value. In Fig. A. 21-2 R(t) is plotted for a sample of Ce^{4+} in solution. The Larmor modulation is easily seen. Measurements were also taken on (lanthanum) metallic samples, in which cerium ion cores assume the $4f\ ^2F_{5/2}$ configuration and level. At 298°K the paramagnetism of these ion cores (which behave as free ions, the 4f level being narrow and well below the Fermi surface) enhances the external field by 33 ± 8 %; at 77°K this enhancement becomes a factor of 2.33 ± 0.20. The data from these measurements are shown in Fig. A. 21-3. Our final value for the g factor of the 2084-keV state is g = + 1.014 ± 0.038. This lies between Rho's prediction and the single-particle estimate. It certainly allows us to conclude that Rho's value is not to be rejected in favor of the latter, and, considering the approximate nature of the theory, the agreement is probably quite satisfactory. In fact Rho's model is very much to be preferred on other grounds, as it predicts or fits other properties quite well.

Using a spin of 4 for the 2084-keV state, we find from the g-factor measurement a magnetic moment of μ = + 4.056 ± 0.152 nm.

Footnotes and References

1. W. M. Currie, Nucl. Phys. 32, 574 (1962).
2. Mannque Rho, On the Quasi-Particle Reactions in Spherical Nuclei (Ph. D. Thesis), UCRL-11080, Oct. 1963.
3. N. Kaplan, S. Ofer, and B. Rosner, Phys. Letters 3, 291 (1963).
4. H. J. Körner, E. Gerdau, C. Gunther, K. Auerbach, K. Mielken, G. Strube, and E. Bodenstedt, Z. Physik 173, 203 (1963).
5. M. Schmorak, H. Wilson, P. Gatti, and L. Grodzins, Phys. Rev. 134, B718 (1964).
6. Richard M. Levy, Perturbed Angular Correlation Measurements on Ce^{140} and Pr^{143}, (Ph. D. Thesis), UCRL-11663, Sept. 1964. Derivations and a detailed discussion of the measurements are given.

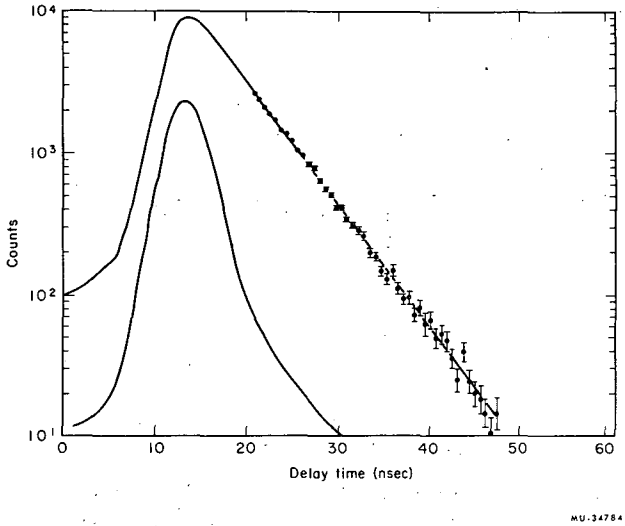

Fig. A. 21-1. Prompt resolution curve and decay curve for the 329-keV to 487-keV cascade in Ce^{140}. The slope gives a half-life of 3.52 ± 0.10 nsec.

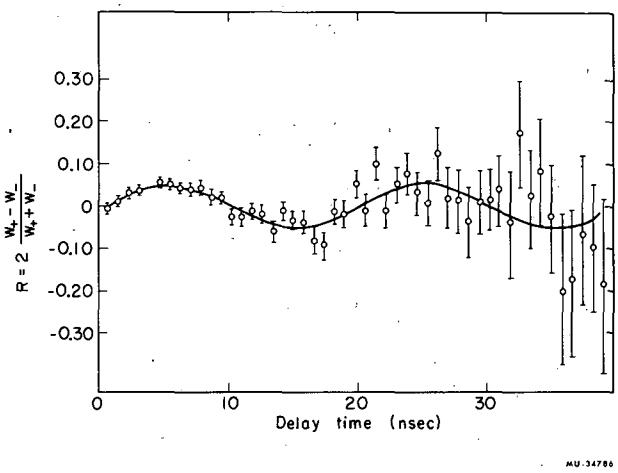

Fig. A. 21-2. Differential rotation of the 2084-keV level in Ce^{140} in an external magnetic field of 42.1 kG. Modulation is at twice the Larmor frequency.

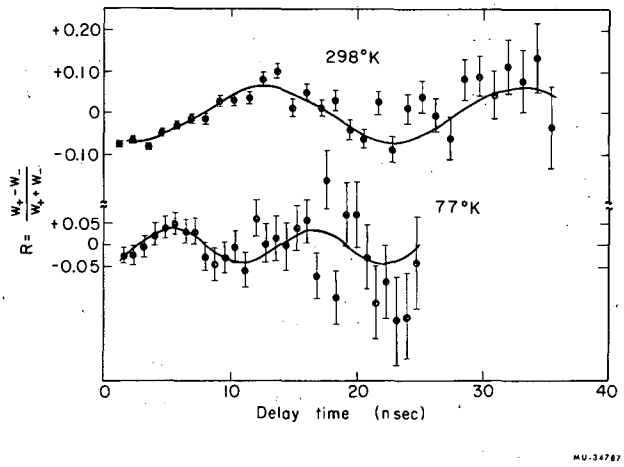

Fig. A. 21-3. Differential measurements of R(t) for Ce^{140} in lanthanum metal. The curves are normalized in time calibration and applied field to show the effect of temperature upon the paramagnetic correction.

22. NUCLEAR ZEEMAN EFFECT IN IRIDIUM-193

J. J. Huntzicker, E. Matthias, S. S. Rosenblum, and D. A. Shirley

Using a lithium-drifted germanium γ-ray detector, we have observed the Mössbauer effect for sources of Ir^{193} in lattices of Fe, Co, and Ni. All experiments were performed at 4°K with a natural Ir metal absorber.

A lithium-drifted germanium detector was used because it made possible the resolution of the 73-keV Mössbauer γ ray from the 64-keV Ir x ray, thus greatly enhancing the signal-to-noise ratio over that obtainable with sodium iodide detectors.

The activity was produced by irradiating 99% enriched Os^{192} metal powder with neutrons at the Vallecitos reactor to get the reactions $Os^{192}(n, \gamma)Os^{193}$. After irradiation the powder was placed in a crucible made of the host material (Fe, Co, Ni) and melted at temperatures of 1600°C, 1520°C, and 1520°C, respectively, for about 30 minutes in an Ar atmosphere. After melting, the samples were annealed at 900°C for 30 min and allowed to cool slowly to room temperature.

Hyperfine structure was observed in all three cases. The principal features of each spectrum were two large absorption areas spaced by 1.22, 0.98, and 0.45 cm/sec in Fe, Co, and Ni, respectively. In Fe, the internal field was large enough to partially resolve further structure, as shown in Fig. A. 22-1.

The proposed hyperfine-level scheme is shown in Fig. A. 22-2. If the 73-keV transition were pure M1 we would expect a six-line spectrum with relative intensities 1:2:3:3:2:1. It is obvious that this is not the case, and there is a strong indication of eight lines. This led us to postulate that there was a large E2 admixture in the transition, an assumption borne out by examination of the relative magnitudes of the $L_I:L_{II}:L_{III}$ subshell conversion coefficients with the help of T. Novakov and J. M. Hollander, at the Berkeley iron-free beta spectrometer.[1] The E2/M1 mixing ratio was found to be $\delta^2 \approx 0.4$.

Fitting Lorentzian shapes to the eight lines (Fig. A. 22-1) and using the known ground-state moment of (0.17 ± 0.03) nm,[2] we calculated the hyperfine field of Ir^{193} in Fe to be 1210 ± 250 kilogauss, in good agreement with the value of Kogan et al.[3] of 1350 ± 300 kG. The fields in Co and Ni are 980 ± 200 and 450 ± 100 kG respectively; the excited-state moment is (0.56 ± 0.11) nm.

This value of the spin-1/2 first-excited-state moment is anomalously small, as is the case in Au^{197}. Both ground states are thought to be $d_{3/2}$ shell-model states, and the first excited states would be $s_{1/2}$ on the simple shell model. This would lead one to think that their excited-state moments would be between the Dirac line (+1.0 nm in this case) and the Schmidt line (+2.79 nm). Experimentally the Au^{197} moment is found to be (+0.37 ± 0.04) nm.[4] The hyperfine fields are essentially what would be predicted on the basis of systematics and a simple theory of conduction-electron polarization.[5] The low nuclear moments, on the other hand, are in rather serious conflict with the simple shell-model picture. In recent calculations by Kisslinger and Sorenson,[6] based on pairing-plus-quadrupole form, a small moment was predicted for the first excited state of Au^{197}. This small moment seemed to arise primarily from configuration mixing and might therefore be expected to be observed in other nuclei in this region.

Footnote and References

1. We are indebted to J. M. Hollander and T. Novakov for communicating these preliminary data.
2. K. Murakawa and S. Suwa, Phys. Rev. 87, 1048 (1952).
3. A. V. Kogan, Y. O. Kulkov, L. P. Nikitin, N. M. Reinov, and M. F. Stelmakh, Zh. Eksperim. i Teor. Fiz. 45, 21 (1963).
4. R. W. Grant, Morton Kaplan, D. A. Keller, and D. A. Shirley, The Nuclear Zeeman Effect in Gold Atoms Dissolved in Iron, Cobalt, and Nickel, UCRL-10847, June 1963.
5. D. A. Shirley and G. A. Westenbarger, Phys. Rev., in press.
6. L. S. Kisslinger and R. A. Sorensen, Rev. Mod. Phys. 35, 853 (1963).

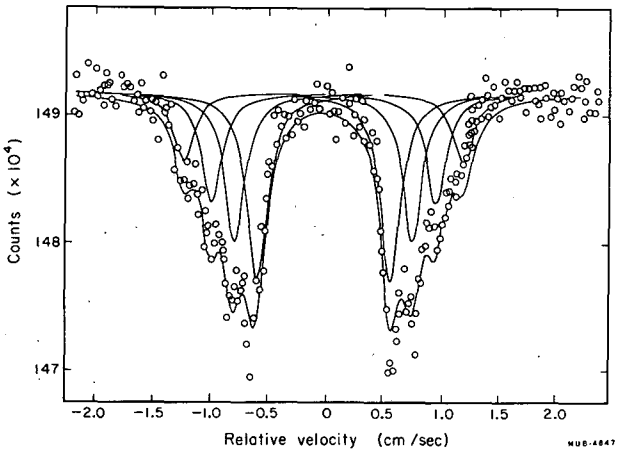

Fig. A. 22-1. Ir^{193} in Fe with Lorentzian fit of eight lines.

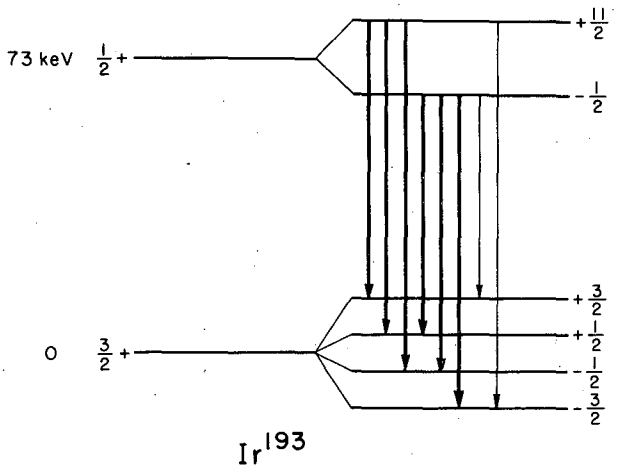

Fig. A. 22-2. Hyperfine level scheme. Note two weak $\Delta M_I = 2$ lines, forbidden for an M1 transition.

23. AN INVESTIGATION OF THE LEVEL SCHEME OF TELLURIUM-125 AND MEASUREMENT OF THE MAGNETIC DIPOLE MOMENT OF ANTIMONY-125 BY NUCLEAR POLARIZATION

N. J. Stone, R. B. Frankel, J. J. Huntzicker, and D. A. Shirley

Two recent developments have increased the effectiveness of nuclear orientation as a technique for studying nuclear properties. The discovery of large induced hyperfine magnetic fields at nuclei of diamagnetic impurities in ferromagnetic materials greatly increased the number of elements to which the technique could be applied, as previously only paramagnetic elements had been oriented. The development of high-resolution lithium-drifted germanium gamma detectors made it possible to study accurately many isotopes whose γ-ray energies could not be resolved with NaI(Tl) crystal detectors. These two advances have been used in conjunction to study the nucleus Sb^{125} and its decay to Te^{125}.

This work was prompted by two particular problems. The reported magnetic dipole moment of Sb^{125} of 3.5 ± 0.5 nm is above the Dirac limit for a $g_{7/2}$ single-proton nucleus, and is considerably higher than that for Sb^{123} (2.55 nm). In this region of the periodic table the addition of a pair of neutrons to a $g_{7/2}$ single-proton nucleus increases the magnetic dipole moment by only a few tenths nm. The previous measurement was made by nuclear orientation, but NaI(Tl) detectors were used to study composite photopeaks with three and four components respectively. We have repeated the experiment with the use of Ge(Li) detectors.

The decay scheme of Te^{125} features two states, at 668 and 633 keV. The high-energy gamma transitions associated with these levels[2-4] have energies of 668 (weak), 633, and 598 keV. These have been interpreted as a single transition to ground ($1/2^+$) from the 668-keV state and two from the 633-keV state to the ground and first excited (35.5 keV, $3/2^+$) states respectively. As both levels are fed by allowed β^- decay Sb^{125} ($7/2^+$), they were both assigned spin $5/2^+$. However, in a Coulomb excitation experiment[5] the 633-keV transition was observed but not that at 598 keV. Following nuclear orientation and coincidence measurements, changes in the decay scheme are suggested to explain this situation.

By use of a contact cooling apparatus similar to that developed by Westenbarger,[6] an alloy of Sb^{125} in Fe was cooled to temperatures down to 0.012°K, and polarized with a small superconducting magnet. Considerable degrees of nuclear polarization were obtained (Fig. A. 23-1) and were measured by observation of the gamma emission in two Ge(Li) detectors placed along and normal to the axis of polarization.

The angular distribution of gamma radiation from oriented nuclei normalized to emission from an unoriented system is given by $W(\theta) = 1 + B_2U_2F_2P_2(\cos\theta)$ + higher terms, where θ is the angle of observation relative to the axis, and $P_2(\cos\theta)$ is a Legendre polynomial. In this experiment the higher terms are small, so that, for observations along the axis, the expression becomes $W(0) = 1 + B_2U_2F_2$. Of the three parameters, only B_2 involves the magnetic hyperfine interaction, μH_{eff}, between the Sb^{125} magnetic dipole moment and the induced hyperfine field, being a weighted summation over a Boltzmann distribution between the hyperfine levels. The exponent in this distribution is given by $\beta = \mu H_{eff}/IkT$, where I is the spin of Sb^{125} and T is the absolute temperature. The temperature is calculated from measurements of the γ-ray anisotropy of a small Co^{60} activity alloyed with the sample, for which all the parameters are known. For Sb in Fe, H_{eff} has been found to be 200 ± 5 kG,[1,7] so that $\mu_{Sb^{125}}$ is the only unknown in B_2. U_2 and F_2 are angular momentum coupling constants and are determined for any decay between levels of known spin provided there are no mixed multipole transitions. The most prominent decay fulfilling these requirements feeds the pure E2 462-keV gamma transition, for which the product $U_2F_2 = -0.468$. Figure A. 23-2 shows W(0) for this γ ray plotted against 1/T and compared with theoretical curves for various values of the nuclear moment. Analysis yields the value $+2.72 \pm 0.15$ nm close to, but slightly larger than, the moment of Sb^{125}, in good agreement with the systematic observation in this region (Fig. A. 23-3). The difference between this result and that of the previous measurement certainly lies in the advantage of observing a single pure multipole transition, rather than a composite peak with consequent uncertainties in relative intensity and multipole admixture. The U_2F_2 products for the other γ rays measured are given by

$$(U_2F_2)_\gamma = 0.468\ [1-W(0)]_\gamma / [1-W(0)]_{462},$$

since B_2 depends only upon the degree of polarization of the parent nucleus at any temperature and is thus the same for all gamma transitions observed. The values of U_2F_2 are given in Table A. 23-I. Also given in the table are the theoretically predicted U_2F_2 values for various spin sequences wherever there is no multipole mixing. Comparing the experimental and theoretical values, one finds the 668-keV gamma measurement is compatible with a $5/2^+$ to $1/2^+$ pure E2 transition; however, the 633-keV γ ray is not. It is possible to fit the observed 633-keV value if the transition is reassigned, as from the 668-keV level to the 35.5-keV level, i.e., $5/2^+$ to $3/2^+$ mixed M1 + E2.

This reassignment can be checked in two ways. First, absence of a transition from the 633-keV state to ground suggests that the spin of this state is 7/2, so that the 598-keV transition becomes $7/2^+$ to $3/2^+$ pure E2. In the gamma spectrum this peak is poorly resolved from a weak transition at 604 keV, which, however, has the same level spin and multipolarity assignments. The observed U_2F_2 for the composite peak agrees well with the proposed decay sequence. A more direct check was afforded by measurement of the gamma spectrum coincident with the 35.5-keV γ ray, by use of a thin Ge(Li) detector to resolve the γ ray from Te x rays. The result (Fig. A. 23-4) shows $95 \pm 5\%$ of the 633-keV transition in coincidence. The Coulomb-excitation observation of a 633-keV transition is now understood as de-excitation of the $5/2^+$ 668-keV state (The 668-keV gamma being weak and scarcely resolved in NaI(Tl).) The 633-keV state, of spin $7/2^+$, would not be excited.

The nuclear polarization measurement also confirmed the assignment of spin $9/2^-$ to the 321-keV state, and indicated spin 9/2 for the 524-keV state. Finally, although many spectra were taken, no sign of a gamma transition at 652 keV was seen. The proposed decay scheme is given in Fig. A. 23-5.

References

1. J. Hess, W. Weyhmann, B. Greenebann, and F. M. Pipkin, Bull. Am. Phys. Soc. 9, 562 (1964).
2. R. S. Narcissi, The Radioactivity of Sb^{125} and Te^{125m} (Thesis), Harvard, 1959.
3. G. Chandra and V. R. Pandharipande, Nucl. Phys. 46, 119 (1963).
4. K. C. Mann, F. A. Payne, and R. P. Chaturvedi, Can. J. Phys. 42, 1700 (1964).
5. L. W. Fagg, E. A. Wolicki, R. O. Bondelid, K. L. Dunning, and S. Snyder, Phys. Rev. 100, 1299 (1955).
6. Gene A. Westenbarger, Polarization of Silver Nuclei in Ferromagnets and the Internal Magnetic Field (Thesis), UCRL-11143, Nov. 1963.
7. B. N. Samiolov et al., in Proceedings of the Ninth International Conference on Low Temperature Physics, Columbus, Ohio, September 1964.

Table A. 23-I. Nuclear orientation of Sb^{125}

E_γ	Spin sequence proposed	$U_2F_2{}_{exp}$	$U_2F_2{}_{theory}$	Mixing ratio
688	$5/2^+ \rightarrow 1/2^+$	-0.33 ± 0.18	-0.47	Pure E2
633	$5/2^+ \rightarrow 1/2^+$ $5/2^+ \rightarrow 3/2^+$	-0.24 ± 0.03	-0.47 --	Pure E2 $\delta\left(\frac{E2}{M1}\right) = {}^{+0.01}$ or > 95
(598 + 604)	$7/2^+ \rightarrow 3/2^+$	-0.47 ± 0.05	-0.42 ± 0.05	Pure E2
462	$5/2^+ \rightarrow 1/2^+$	-0.47 ± 0.03	-0.47	Pure E2
426	$5/2^+ \rightarrow 3/2^+$	$+1.00 \pm 0.01$	--	$\delta\left(\frac{E2}{M1}\right) = {}^{-1.1}_{-0.5}$ or
379	$7/2^- \rightarrow 11/2^-$ $9/2^- \rightarrow 11/2^-$	-0.47 ± 0.20	-0.20 ± 0.02 --	Pure E2 $\delta\left(\frac{E2}{M1}\right)$ neg.
176	$7/2^- \rightarrow 11/2^-$ $9/2^- \rightarrow 11/2^-$	-0.43 ± 0.03	-0.20 ± 0.02 --	Pure E2 $\delta\left(\frac{E2}{M1}\right) = {}^{-1.28}_{-0.67}$ or

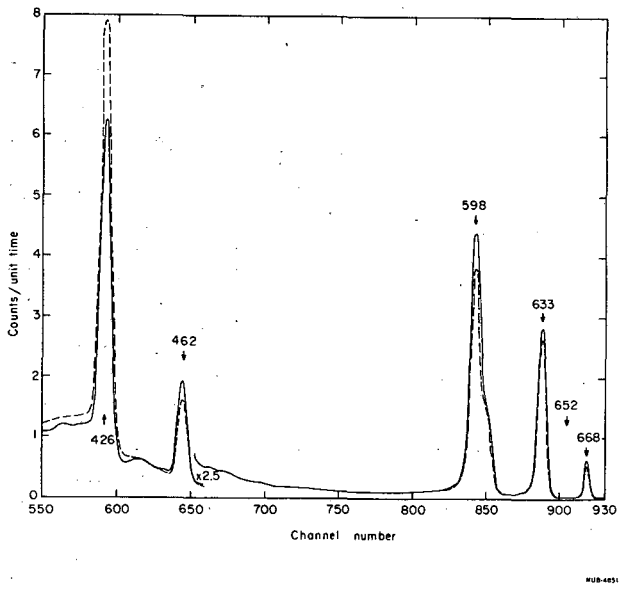

Fig. A. 23-1. Ge(Li) gamma spectrum of Sb^{125} above 400 keV
—— normal intensity
--- intensity at 0.01°K with source polarized.

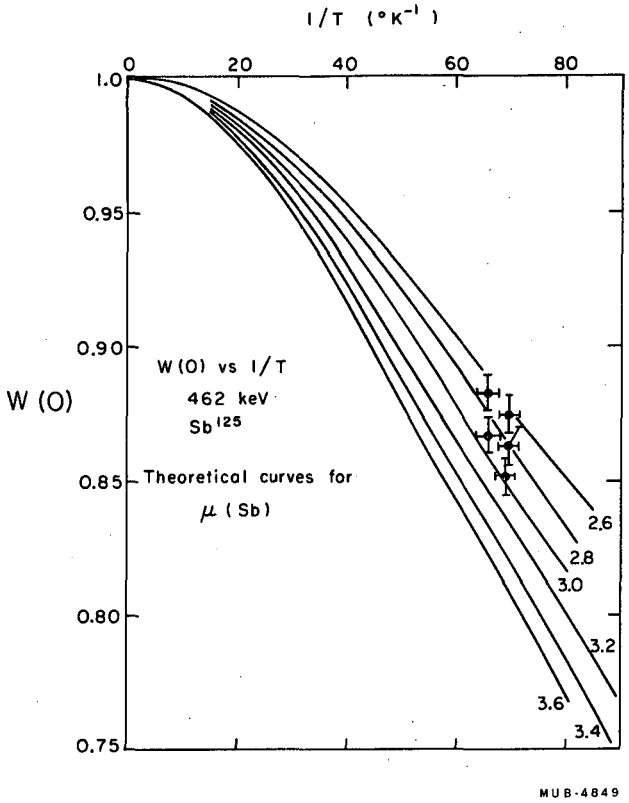

Fig. A. 23-2. Plot of W(0) against 1/T for 462-keV gamma transition of Sb^{125}, and comparison with theoretical curves for various values of the nuclear moment.

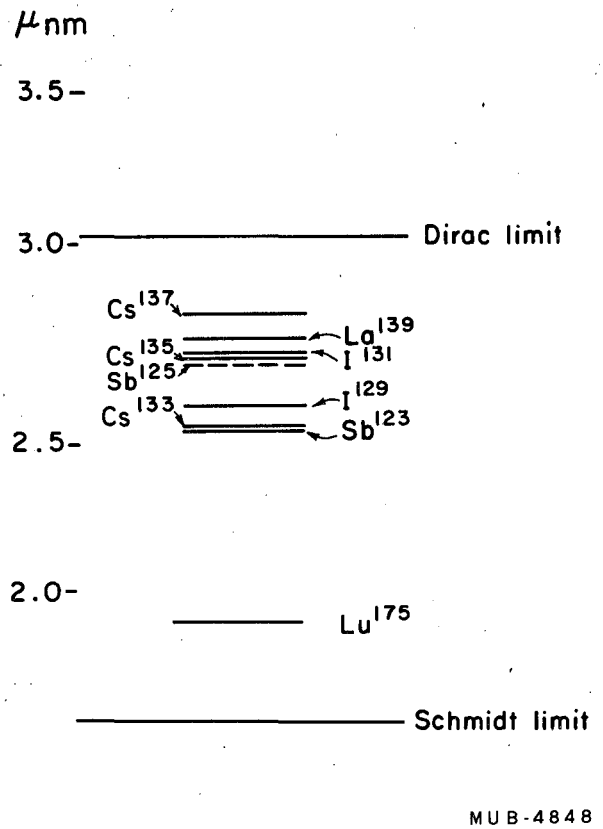

Fig. A. 23-3. Magnetic moments of $g_{7/2}$ single-proton nuclei.

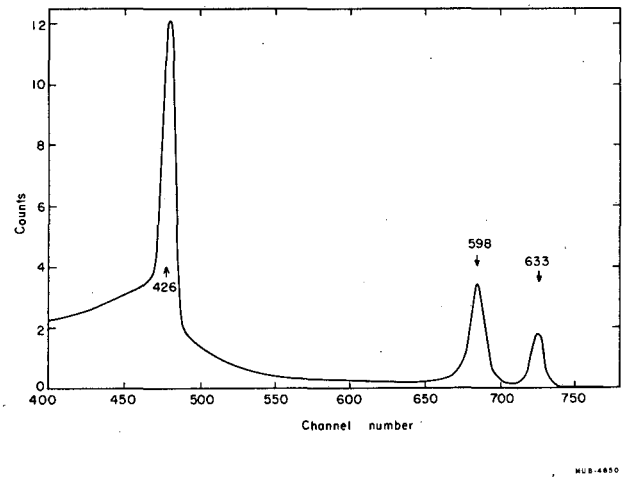

Fig. A. 23-4. Gamma spectrum of Sb^{125} in coincidence with 35.5-keV transition.

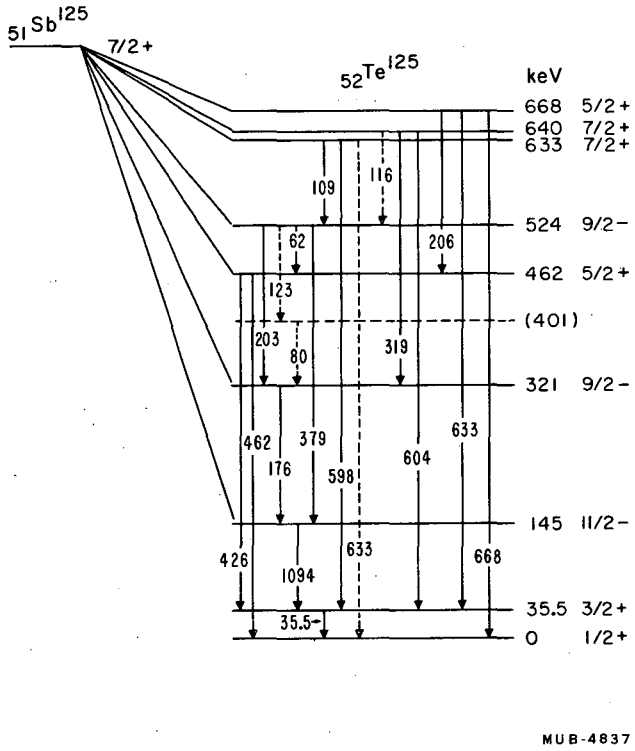

Fig. A. 23-5. Revised decay scheme of Sb^{125}.

24. THE DECAY SCHEME OF EINSTEINIUM-254

W. McHarris, F. S. Stephens, F. Asaro, and I. Perlman

Added information has been obtained about the alpha decay of Es^{254}, allowing us to obtain the somewhat more refined decay scheme shown in Fig. A. 24-1. The biggest advance came in being able to resolve the higher-energy γ rays with a germanium gamma detector, but our data on alpha and electron groups have also been improved. Some of this information is incorporated into Fig. A. 24-1, but some of it appears only in the tables below, since the figure includes only those parts of the decay scheme in which we have the most confidence.

The alpha groups, their intensities, and their hindrance factors are listed in Table A. 24-I according to the rotational band in Bk^{250} that they populate. The working out of the main decay sequence, including the four lowest bands with $K\pi$ = 2-, 4+, 7+, and 5-, has been discussed previously,[1] and will be discussed more thoroughly in a forthcoming article,[2] so we will concentrate here on the aspects having to do with the 6+ band beginning at 406 keV above the ground state in Bk^{250}. The alpha group populating the 406-keV level directly has an energy of 6.114 MeV, the same essentially as Cf^{252}. However, by looking at the alphas (with a solid-state detector) in fast coincidence with gammas whose energy was greater than 275 keV, we were able to see the alphas populating the 6+ band quite clearly, including the 5.99-MeV group to the 6+8 level at $\approx$ 525 keV, previously obscured by Cf^{250} in the source. Also, it was found that the Cf^{250} alone accounted quite well for the fission activity of the source, ruling out appreciable amounts of Cf^{252}.

A gamma spectrum taken with a 3×3-in. NaI scintillator is shown in Fig. A. 24-2. Because of the high background from the daughter, Bk^{250}, in equilibrium in the source, it was taken in fast coincidence (with all alphas), with a resolving time of 100 nsec. A similar spectrum taken with a lithium-drifted germanium detector is shown in Fig. A. 24-3, where the three peaks in the NaI spectrum at 268, 316, and 386 keV have here been split into eleven peaks. All γ rays and their intensities are listed in Table A. 24-II, together with their multipolarities when these are experimentally known.

In Table A. 24-III we list the hindrance factors predicted for each rotational band; these were obtained simply by multiplying the experimental hindrance factors for alpha decay to the proton states[3] in Bk^{249} by the ones for the corresponding neutron states[4] in Cf^{251}. We list also the predicted parameters for fitting the rotational levels to the equation,

$$E_I = E_0 + \frac{\hbar^2}{2\Im} I(I+1).$$

A prediction is included as to the sign of B, the coefficient of an $I^2(I+I)^2$ from that can be included for a better fit. Below these are listed the observed hindrance factors and parameters for the rotational bands in Bk^{250}. One can see that the rotational constant, $\hbar^2/2\Im$, is predicted quite well for the four lowest bands. For the odd-parity bands it has values close to those expected for odd-odd nuclei in general in this region; for the even-parity bands it is much smaller because of Coriolis mixing, but this is predicted by the even-parity bands in Bk^{249}, where there is also extensive Coriolis mixing.

This is not true for the 6+ band; here $\hbar^2/2\Im$ is smaller even than the distorted bands of Bk^{249} would predict. We were able to explain qualitatively the differences between the Bk^{249} and Bk^{250} cases as follows: All the positive-parity proton states in this region originate from the $i_{13/2}$ spherical-shell-model level; these can be singled out and are found to have extraordinarily large contributions to the Coriolis matrix elements between them. For the Bk^{250} calculation one can obtain essentially complete results by considering the 7/2+ and 5/2+ proton states as being mixed with each other and with the other proton states from the $i_{13/2}$ level, namely, with 1/2+, 3/2+, 9/2+, and possibly 11/2+ and 13/2+; the last five states are not known experimentally, so one has to make reasonable guesses as to their positions. In the odd-odd case, however, more states are involved. One gets the following states by coupling the above states with the 7/2+ neutron state: 7+ and 0+ (using the 7/2+ proton state), 6+ and 1+ (5/2+), 5+ and 2+ (3/2+), 4+ and 3+ (1/2+), 8+ and 1+ (9/2+), etc. And the important distinction is that the singlet states (0+, 1+, 2+, etc.) are connected with the triplet states because the 4+ triplet state is connected with the 3+ singlet state through the decoupling parameter of the 1/2+ proton state. Some of these lie fairly close to the 7+ level and especially to the 6+ level, so the higher-order effects become more important than in the odd-mass situation. Another difference involves the change in the Fermi surface; we know that it changes because the 5/2+ and 7/2+ states are

approximately 400 keV apart in Bk^{249} while they are just over 300 keV apart in Bk^{250}. It appears that the blocking caused by the additional quasi particles in Bk^{250} would serve to diminish pairing in the neutrons and hence would cut the matrix element between the 5/2+ and 7/2+ states in this nucleus. Both differences appear to be in the direction of distorting the 6+ band in Bk^{250} more than the 5/2+ band in Bk^{249}. They are now being investigated further.

References

1. W. McHarris, F. S. Stephens, F. Asaro, and I. Perlman, in Chemistry Division Annual Report, 1963, UCRL-11213, Jan. 1964, p. 14.
2. W. McHarris, F. S. Stephens, F. Asaro, and I. Perlman, The Decay Scheme of Einsteinium-254, UCRL-11676, in process.
3. F. Asaro, S. G. Thompson, F. S. Stephens, and I. Perlman, in Proceedings of International Conference on Nuclear Structure, Kingston, 1960, p. 581; also in E. K. Hyde, I. Perlman, and G. T. Seaborg, The Nuclear Properties of the Heavy Elements (Prentice-Hall, 1964), p. 950.
4. F. Asaro, S. Bjørnholm, and I. Perlman, Phys. Rev. 133, B291 (1964).

Table A. 24-I. Alpha-particle energies, intensities, and hindrance factors, grouped according to the rotational bands populated in Bk^{250}.

$K\pi I$ of final state	Excited-state energy (keV)	E_α (MeV)	Intensity (%)	Hindrance factor
7+7	85.5	6.430 ± 0.005	93.0	2.89
7+8	155.9	6.360 ± 0.005	2.91	42.8
7+9	240	6.278 ± 0.005	0.16	309
7+10	≈ 334	6.186 ± 0.010	0.05	≈ 240
5-5	99	6.417 ± 0.005	1.71	136
5-6	169	6.348 ± 0.005	0.74	147
5-7	248	6.270 ± 0.005	0.22	206
5-8	≈ 324	6.195 ± 0.010	0.08	≈ 342
4+4	35.5	6.479 ± 0.005	0.27	1700
4+5	78.1	masked	---	---
4+6	131	6.385 ± 0.005	0.13	1270
4+7	193	6.324 ± 0.005	0.05	1670
4+8	263	6.255 ± 0.010	0.01	3900
2-2	0	6.517 ± 0.010	≤ 0.005	$\geq 1.3 \times 10^5$
6+6	406	6.114 ± 0.005	0.33	22.6
6+7	460	6.061 ± 0.005	0.16	24.7
6+8	≈ 525	5.99 ± 0.02	0.03	61

Table A. 24-II. Gamma rays from Es^{254} decay.

E (keV)	Photon intensity per α particle (%)	Multipolarity (experimentally determined)
≈ 15 to 18 (L x rays)	231[a]	---
43	0.3[b]	M1-E2[b]
63	2.0[a]	E1
104 ($K\alpha_1$)	0.49	---
108 ($K\alpha_2$)		
≈123 ($K\beta$)	0.15	---
150 (2 gammas?)	0.35	---
233?	0.013?	---
249	0.06	---
264	0.11	---
278	0.08	---
284	0.025	---
304	0.14	M1
316	0.30	M1
342	0.016	---
348	0.013	---
377	0.03	---
385	0.10	---

[a] These intensities were obtained from special experiments that compared the L x rays with those of Es^{253} and the 63-keV gamma with the 60-keV gamma of Am^{241}. The intensity under L x rays is that for L vacancies.

[b] This intensity was obtained from a delayed-coincidence experiment.

All other intensities were obtained from Figs. A. 24-2 and A. 24-3, normalized to the 63-keV gamma = 2.0%.

Table A. 24-III. Properties of rotational bands in Bk^{250}.

Neutron states \ Proton states	7/2+[633↑]	3/2-[521↑]	5/2+[642↑]
	Predicted properties		
1/2+[620↑]	$K_\pi = 4+$ $\hbar^2/2\Im = 4.01$ keV B = positive HF = 750	$K_\pi = 2-$ $\hbar^2/2\Im = 5.54$ keV B = negative HF = large	$K_\pi = 3+$ $\hbar^2/2\Im = 5.06$ keV B = positive HF = large
7/2+[613↑]	$K_\pi = 7+$ $\hbar^2/2\Im = 4.30$ keV B = positive HF = 2.0	$K_\pi = 5-$ $\hbar^2/2\Im = 5.83$ keV B = negative HF = 90	$K_\pi = 6+$ $\hbar^2/2\Im = 5.35$ keV B = positive HF = 34
	Experimental properties		
1/2+[620↑]	$K_\pi = 4+$ $\hbar^2/2\Im = 4.26$ keV B = positive HF = 1270	$K_\pi = 2-$ $\hbar^2/2\Im = 5.73$ keV B = ? HF = $\geq 1.3 \times 10^5$	------
7/2+[613↑]	$K_\pi = 7+$ $\hbar^2/2\Im = 4.40$ keV B = positive HF = 2.89	$K_\pi = 5-$ $\hbar^2/2\Im = 5.75$ keV B = negative HF = 136	$K_\pi = 6+$ $\hbar^2/2\Im = 4.00$ keV B = positive HF = 22.6

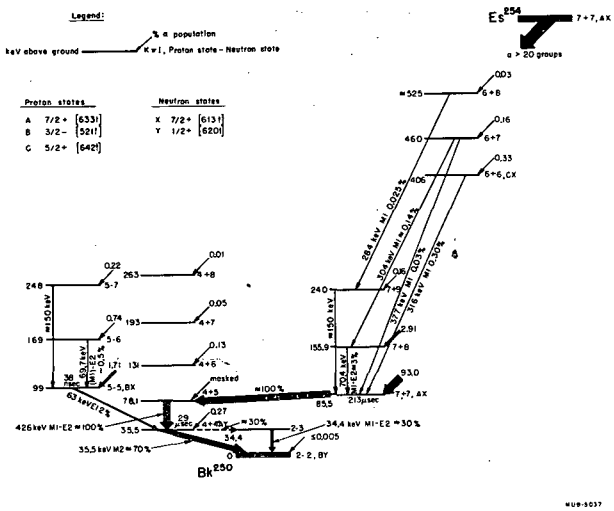

Fig. A. 24-1. Decay scheme of einsteinium-254.

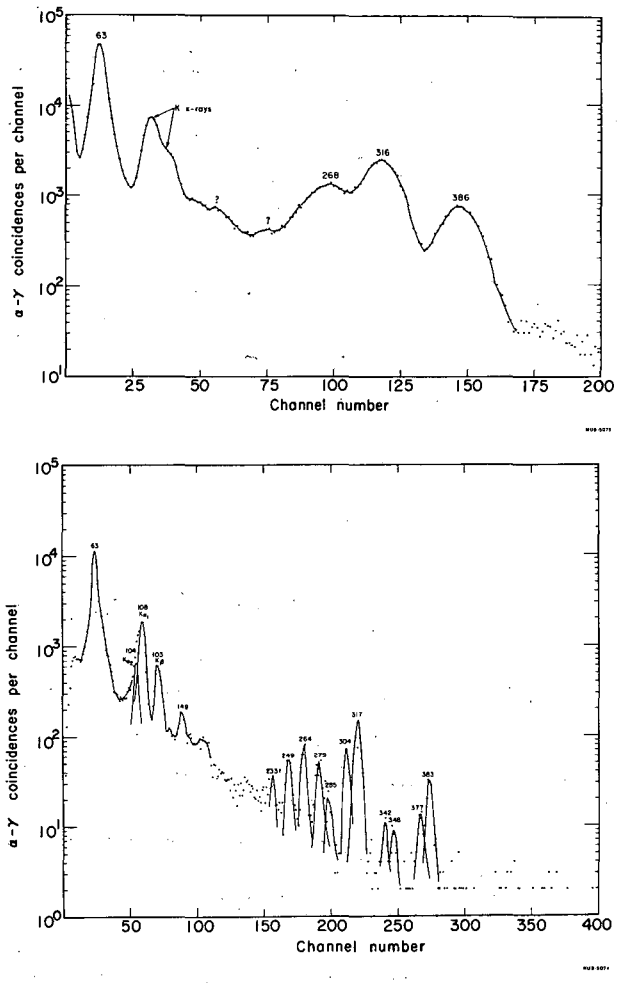

Fig. A. 24-2. Es^{254} γ-ray spectrum taken with a NaI scintillation detector.

Fig. A. 24-3. Es^{254} γ-ray spectrum taken with a Ge gamma detector.

25. DECAY OF MOLYBDENUM-90

J. A. Cooper, J. M. Hollander, M. I. Kalkstein, and J. O. Rasmussen

Bjørnholm et al.[1] have suggested that the ground-state assignment of Nb^{90} is either 8+ or 9+. The log ft value of 5.3 for the decay of Mo^{90} to Nb^{90} (obtained from the positron end point and half-life reported by Diamond[2] and the curves of Feenberg and Trigg[3]) implies that Mo^{90} decays to a state in Nb^{90} of spin 0 or 1. Since only two prominent transitions have been observed[2,4] in the decay of Mo^{90}, it is implied by the above considerations that their multipolarities must be high. Mathur and Hyde[4] measured half-lives of 24 seconds and 10 milliseconds, which suggests multipolarities of either E3 or M3 for the 120-keV transition and E3 for the 250-keV transition. The K conversion coefficient which they reported for the 120-keV transition, ≈ 0.5, agrees best with that predicted for an E2 transition, but their K/L ratio of 3.6 is closest to that predicted for an E3 transition. Even if these transitions were both octupoles, as suggested by their half-lives, angular momentum could not be conserved if the suggested spin difference (7 to 9 units) between the initially populated state and the ground state is correct. Either a higher multipolarity is required for one or both transitions, or additional transitions are required.

This work was therefore undertaken in the hope that a reinvestigation of the conversion electron spectrum with the high-resolution 50-cm-radius $\pi\sqrt{2}$ iron-free spectrometer[5] and the gamma spectrum with lithium-drifted germanium detectors might resolve the above inconsistencies.

The γ rays observed and their relative intensities are listed in Table A. 25-I. Although many other γ rays were observed in addition to the two previously reported, none has an intensity greater than 12% that of the 257-keV γ ray, and therefore none could be in 100% cascade with the 122- and 257-keV transitions.

The only intense electron lines observed in the conversion electron spectrum, other than the strong K and L lines from the 122- and 257-keV transitions, were two complex lines at very low energy, 2 keV and less than 0.2 keV. These lines could not be identified unambiguously, but from their energies and the fact that they decayed with a complex half-life it is thought that these lines are associated with the LXY Auger and L_iL_jX Coster-Kronig transitions. However, we cannot rule out the possibility that a very-low-energy internal conversion line might be mixed in with these other electrons.

The L-subshell conversion ratios are very sensitive indicators of the multipolarities of transitions, and have always been definitive whenever the L lines could be resolved. In this particular case the L lines were not completely resolved, but the complex structure of the line could be analyzed so as to characterize the multipolarity of the corresponding transition.

The experimental L-subshell ratios were compared with the theoretical ratios by comparing the experimental L-line shape (plotted on semi-log paper) with a "theoretical line" constructed by using the theoretical L-subshell conversion coefficients of Rose[6] and Sliv.[7] (The individual L-subshell conversion coefficients for the 122-keV transition were interpolated from log-log plots of Rose's conversion coefficients as a function of gamma energy.) The theoretical composite L-line shape was constructed as follows: First the position of the L_ith line was determined from the position of the K line and the difference between the K and L_i electron binding energies. (The assumption was made that the L-line shapes are the same as that of the closest K line. In the 122-keV L group, this was the K line of the 142-keV transition in Zr^{90}, Fig. A. 25-1, and for the 257-keV L group it was the 257-keV K line.) The relative intensities of the L lines in the composite line were adjusted to agree with the theoretical L-subshell ratios. For the comparison with experiment, this theoretical composite L line was adjusted along the ordinate axis until the best fit of the experimental data points was obtained. The validity of this method of analysis is shown in Fig. A. 25-2, where a comparison is made between the theoretically constructed L group for the known 132-keV E3 transition in Zr^{90} and the experimental L-group points. The agreement is seen to be excellent.

The experimental points for the 122- and 257-keV transitions are compared in a similar manner (Figs. A. 25-3 through A. 25-6) to the theoretical composite lines constructed for different multipolarities. This analysis determines unambiguously the multipolarities of the 122- and 257-keV transitions to be E2 and E3, respectively. In addition, the K/L ratios obtained for the 122-keV transition, 5.76, and for the 257-keV transition, 5.64, agree very well with this

assignment. But the reported half-life of 24 seconds for the 122-keV transition is longer by a factor of 10^7 than that predicted by the single-particle model for an E2 transition of this energy, and thus a gross inconsistency exists. In addition, the two multipolarity assignments are still inconsistent with the expected large spin difference (7 to 9 units) between the state initially populated by the decay of Mo^{90} and the ground state of Nb^{90}.

To explain the very long half-life measured for the 122-keV E2 transition and to conserve angular momentum, we propose a decay scheme (Fig. A. 25-7) in which a very-low-energy (less than 2 keV) transition is postulated as preceding the 122-keV transition. The 24-second half-life is then assigned to this very-low-energy transition and not to the 122-keV transition. The most likely multipolarity of the missing low-energy transition is M2, although E3 is also possible.

A search is presently under way to find evidence bearing on the existence of the postulated low-energy transition.

References

1. S. Bjørnholm, O. B. Nielsen, and R. K. Sheline, Phys. Rev. 115, 1613 (1959).
2. R. M. Diamond, Phys. Rev. 89, 1149 (1953).
3. E. Feenberg and G. Trigg, Rev. Mod. Phys. 22, 399 (1950).
4. H. Mathur and F. Hyde, Phys. Rev. 98, 79 (1955).
5. J. M. Hollander and R. L. Graham, in Chemistry Division Annual Report, 1962, UCRL-10624, Jan. 1963, p. 273.
6. M. E. Rose, Internal Conversion Coefficients (Interscience Publishers, Inc., New York, 1958).
7. L. A. Sliv and I. M. Band, Coefficients of Internal Conversion of Gamma Radiation (USSR Academy of Sciences, Moscow-Leningrad, 1956) Part I: K Shell; Part II: L Shell.

Table A.25-I. Photons of Mo^{90} decay.

Energy (keV)	Relative intensity[a]	
42.76 ± 0.08	0.002	
122.50 ± 0.1	84.	
162.99 ± 0.1	5.9	
202.9 ± 1.	6.7	
257.52 ± 0.15	100.	
323.0 ± 1.	8.9	
420.	< 1.	complex
445.6 ± 1.	10.6	
472.5 ± 1.	2.2	
482. ± 2.	0.1	
486. ± 2.	0.4	
490. ± 2.	0.6	
945.2 ± 1.5	12.2	
992.7 ± 1.5	2.3	
1272.5 ± 1.5	9.4	
1389.0 ± 1.5	5.2	
1457. ± 2.	4.	

a. The relative accuracy of the quoted intensity figures is thought to vary from 10% for the strongest lines to as much as a factor of two for the weaker lines.

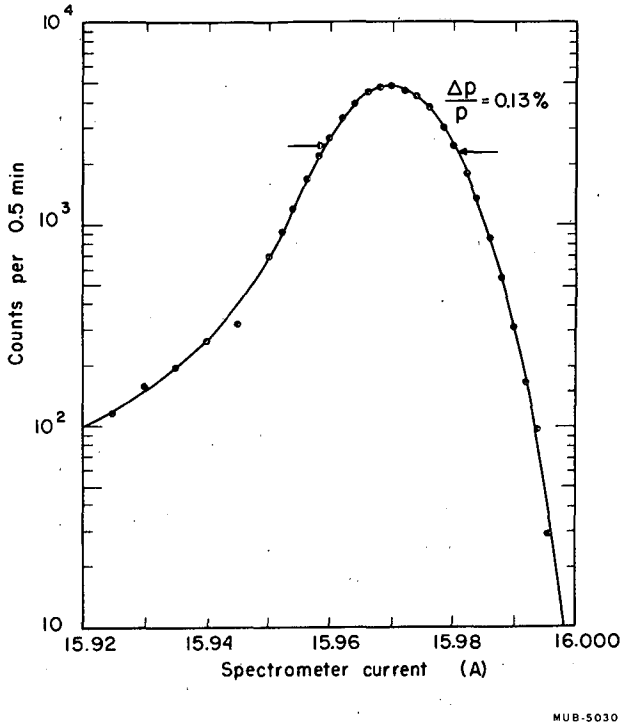

Fig. A. 25-1. K line of 142-keV transition from Nb^{90} decay, measured with 50-cm iron-free $\pi\sqrt{2}$ spectrometer.

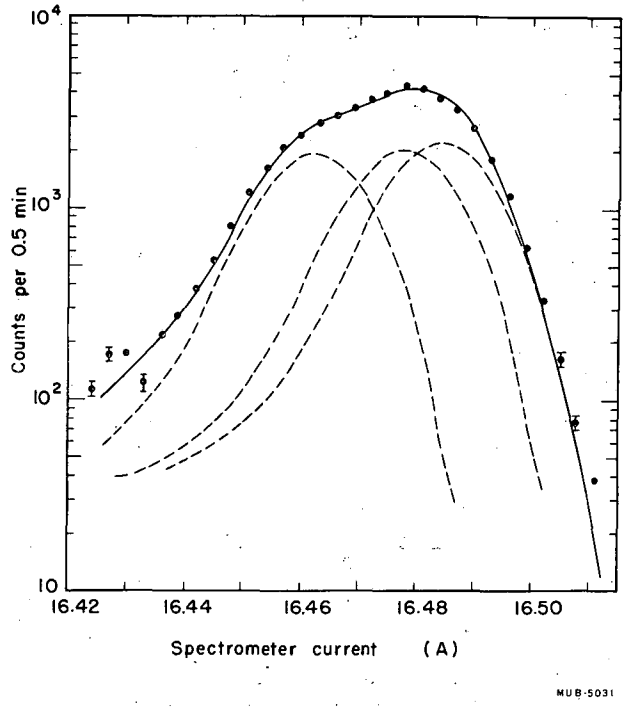

Fig. A. 25-2. Comparison of experimental and theoretical L-group line shapes for 132-keV E3 transition from Nb^{90} decay. Normalization procedure is described in text.

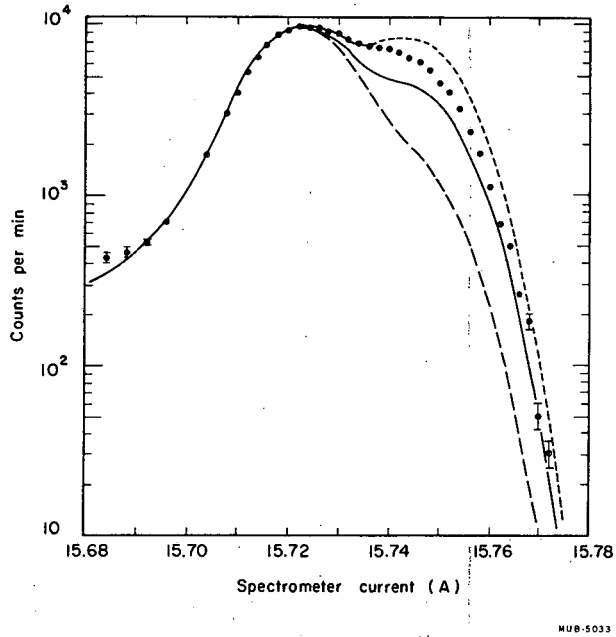

Fig. A.25-3. Comparison of experimental L-group line shape of 122-keV transition of Mo^{90} decay with theoretical composite L-group line for M2 (---), M3 (——), and M4 (· · · ·) multipolarities.

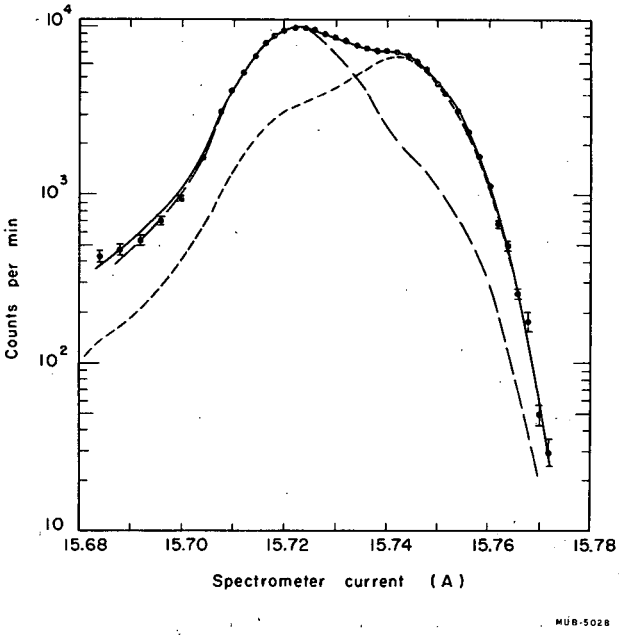

Fig. A.25-4. Comparison of experimental L-group line shape of 122-keV transition of Mo^{90} decay with theoretical composite L-group line for E1 (– – –), E2 (——), and E3 (----) multipolarities.

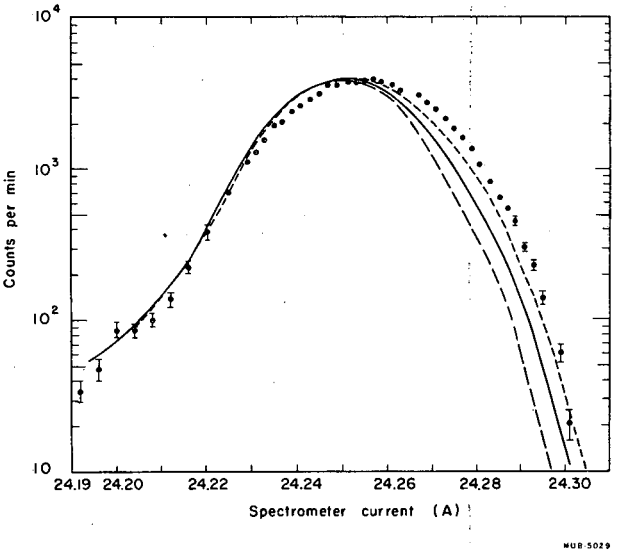

Fig. A.25-5. Comparison of experimental L-group line shape of 257-keV transition of Mo^{90} decay with theoretical composite L-group line for M2 (– – –), M3 (——), and M4 (----) multipolarities.

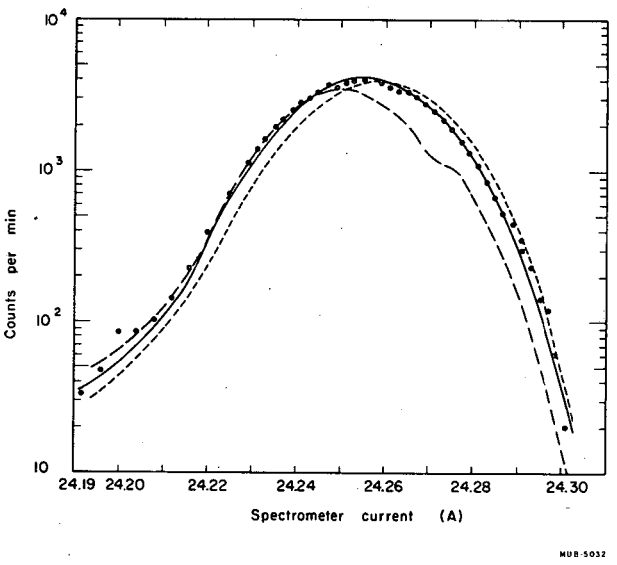

Fig. A.25-6. Comparison of experimental L-group line shape of 257-keV transition of Mo^{90} decay with theoretical composite L-group line for E2 (– – –), E3 (——), and E4 (----) multipolarities.

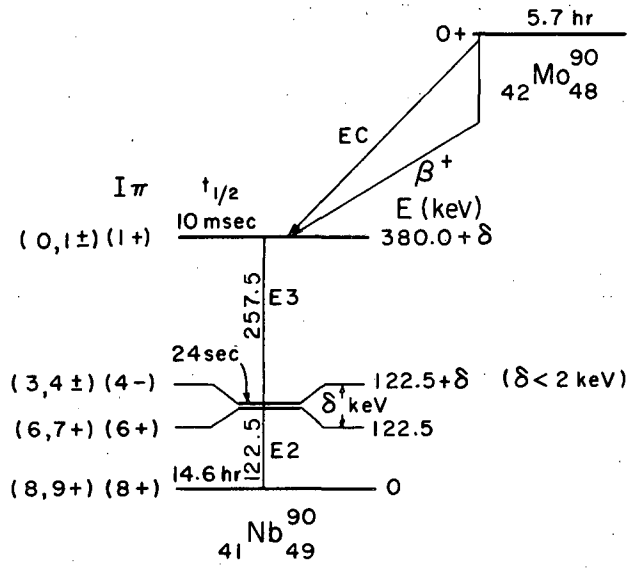

Fig. A. 25-7. Partial decay scheme of Mo^{90}, showing postulated low-energy transition. The preferred state assignments are underlined.

26. THE INFLUENCE OF A RANDOMLY ORIENTED MAGNETIC FIELD ON ANGULAR CORRELATIONS†

E. Matthias, S. S. Rosenblum, and D. A. Shirley

Since the discovery by Samoilov and co-workers[1] that large hyperfine fields can be induced at the nuclei of various atoms by dissolving them in magnetic lattices, considerable interest has been focused on gaining sufficient data to provide a foundation for a theoretical approach to their systematics.

Several techniques have been used, including nuclear polarization, specific heats, NMR, and Mössbauer spectroscopy, but none of these is very generally applicable at present. In this report we discuss the measurement of hyperfine fields by observation of the time dependence of perturbed angular correlations. This technique has two features of special interest: (a) no external polarizing field is necessary, i.e., the sample can be completely demagnetized, and (b) for a demagnetized sample the angular correlation is modulated by at least two frequencies, the Larmor frequency and its first harmonic.

For a demagnetized source the magnetic domains may be taken to be randomly oriented, and the theory is similar to that for a polycrystalline source.[2] It can be shown (in the paper from which this is condensed) that the angular distribution of radiation due to randomly oriented magnetic domains observed by two detectors at a fixed angle to each other is given by

$$W(\theta, t) = \sum_k A_k(1)\, A_k(2)\, G_k(t)\, P_k(\cos\theta), \qquad (1)$$

where θ is the angle between the detectors, and $P_k(\cos\theta)$ are the Legendre polynomials. If the reference system is chosen in such a way that its z axis is the quantization axis for the magnetic interaction Hamiltonian, then $G_k(t)$ has the simple form

$$G_k(t) = \frac{1}{2k+1} \sum_N \exp(-iN\omega_L t), \tag{2}$$

with ω_L = Larmor frequency. We therefore obtain for the real part of the perturbation factor $G_k(t)$ in Eq. (2)

$$G_k(t) = \frac{1}{2k+1} \sum_N \cos N\omega_L t\,. \tag{3}$$

Thus, in a time-differential measurement one observes a superposition of k frequencies with equal amplitudes. In Fig. A. 26-1a the perturbation factors G_2 and G_4 are shown as functions of time.

The integral attenuation factor $\bar{G}_k$ can be obtained from Eq. (2), and is given by

$$\bar{G}_k = \frac{1}{2k+1} \sum_N \frac{1}{1 + (N\omega_L\tau)^2}\,. \tag{4}$$

The theoretical behavior of $\bar{G}_k$ as a function of the interaction strength is demonstrated in Fig. A. 26-1b. In the limit of very strong interaction the attenuation factor approaches a hard-core value of $1/(2k+1)$ which is independent of the nuclear spin, in contrast to the hard-core values for polycrystalline sources.

To demonstrate experimentally the effect of a random magnetic interaction on the angular correlation we performed a time-differential measurement with a sample of In^{111} dissolved in Ni (less than 1 part in 10^{10}). The result is shown in Fig. A. 26-2. The large anisotropy of the 172- to 247-keV cascade in Cd^{111} confirms clearly the prediction of two frequencies for k = 2 [Eq. (3)]. A least-square fit of the data yields a Larmor frequency $\omega_L = (0.995 \pm 0.010) \times 10^8$ sec^{-1}, which gives, with a g factor of $g = -0.318 \pm 0.007$,[3] a magnetic field for Cd dissolved in Ni of

$$|H| = 65.3 \pm 1.6 \text{ kilogauss.}$$

The accuracy of this value is limited by the uncertainty of the time calibration (1%) and by the fact that the g factor is known only within 2%.

Several features of this method are worth pointing out: (a) The presence of a low-frequency (ω_L) component allows the measurement of fields twice as large as would otherwise be possible, with a given instrumental time resolution. (b) Very small fields are also accessible. In this experiment any field between 5 and 500 kG could have been observed. (c) Fields are measured throughout the sample, not just in domain walls. (d) Measurements may be made at any temperature and pressure, provided that the spin-correlation time is long compared with $1/\omega_L$. (e) Induced fields in antiferromagnets may also be measured. (f) Polarization in an external field may be followed independently of frequency shifts by observing the disappearance of the low-frequency component in the correlation function.

Aside from the famous case of Cd^{111}, it appears that there is a fair number of isotopes available which would allow the investigation of internal magnetic fields with the aid of this method.

One of us (E. M.) gratefully acknowledges a fellowship from the Miller Institute for Basic Research in Science, University of California.

Footnote and References

† Shortened version of UCRL-11820.

1. B. N Samailov, V. V. Sklyarevskii, and E. P. Stepanov, Zh. Eksperim. i Teor. Fiz. 36, 448 (1959).
2. A. Abragam and R. V. Pound, Phys. Rev. 92, 943 (1953).

3. E. Matthias, L. Boström, A. Maciel, M. Salomon, and T. Lindquist, Nucl. Phys. 40, 656 (1963).

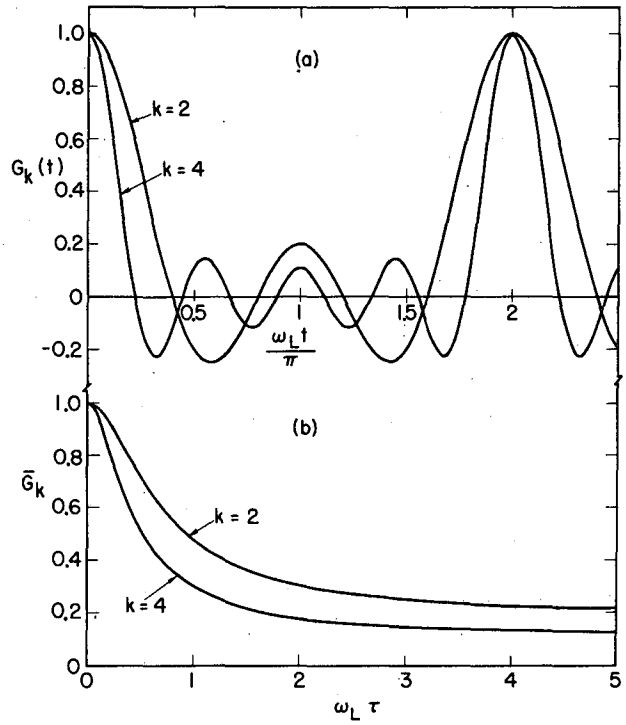

MUB-4657

Fig. A. 26-1. a. Theoretical behavior of the time-differential perturbation factors G_2 and G_4 as a function of time. b. Integral attenuation factors $\bar{G}_2$ and $\bar{G}_4$ plotted as a function of the interaction strength.

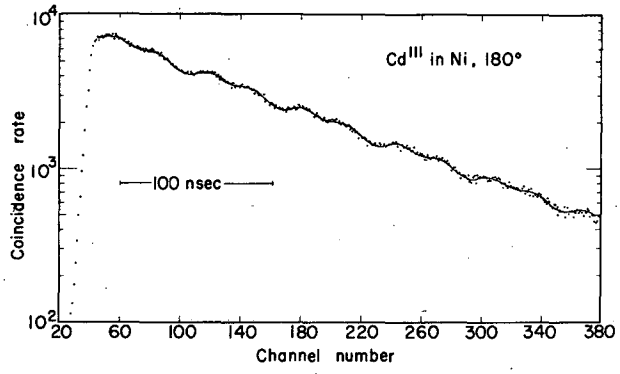

Fig. A. 26-2. Time-differential measurement of a random magnetic interaction with a source of In^{111} dissolved in Ni. The solid curve represents the best fit of the points to the function

$$F(t) = Ne^{-\lambda t}\{1 + a[1 + 2\cos(\omega_L t + \phi) + 2\cos 2(\omega_L t + \phi)]\} + C.$$

B. FISSION

1. FISSION-EXCITATION FUNCTIONS IN INTERACTIONS OF C^{12}, O^{16}, AND Ne^{22} WITH VARIOUS TARGETS†

Torbjørn Sikkeland

The fission cross sections, σ_f, in the bombardment of Cs, Pr, Tb, Ho, Er^{170}, Tm, Yb^{174}, Lu, W^{182}, Au, and Bi with O^{16}, Tm with C^{12}, and Tb with Ne^{22} have been measured as a function of projectile energy. The purpose of these experiments was to obtain experimental values for the ratio Γ_f/Γ_n, where Γ_f and Γ_n are the level widths for fission and neutron evaporation respectively. These values will be compared to theoretical ones in order to extract values for the fission barrier E_f. Such analysis has been performed for the heaviest nuclei, and for nuclei in the closed-shell region around Pb^{208}.[1] It was hoped to extend this analysis to lighter nuclei (outside the closed shell) that can be induced to undergo fission by heavy ions. A more direct comparison with liquid-drop-model calculations can then be made. Also, by the use of heavy ions, the influence of rotation on Γ_f/Γ_n can be enhanced and studied.

The technique consisted of counting coincident fission-fragment pairs with two Au surface-barrier Si detectors. This method should be superior to any other used so far, since a fission event then is not only identified by the energy of the fragments but also by a coincident requirement and by a certain angular correlation between the two fragments. The latter characteristic offers a convenient way of studying fission also of targets lighter than Pb and Bi. In general such targets will have heavy-element impurities such as Pb and Bi, and even U impurities, that might be difficult to eliminate and that have large fission cross sections. However, by proper positioning of the two detectors, one can exclude interference from fission of such impurities.

Absolute values for the fission cross section, σ_f, were obtained by relating the counting rate of elastically scattered ions to that of fission. Errors in σ_f were around 10%.

For the systems studied here we have only fission from complete fusion (CF) reactions. If we denote the cross section for these reactions σ_{CF}, then in a region where first-chance fission is dominant the experimental value for Γ_f/Γ_n will be given by

$$\Gamma_f/\Gamma_n = 1/(\sigma_{CF}/\sigma_f - 1). \qquad (1)$$

We have then ignored charged-particle evaporation. This might introduce an error of as much as 40% in Γ_f/Γ_n at the highest energies for the lighter targets. However, this will not significantly alter the results of the analysis.

Experimental data indicate σ_{CF}/σ_R is nearly independent of target and excitation energy. We adopted the values 0.80 for C^{12}, 0.72 for O^{16}, and 0.60 for Ne^{22}. The total interaction cross section, σ_R, was calculated by using a parabolic approximation for the optical potential. The parameters used were taken from Viola and Sikkeland.[2] Best fit to experimental Γ_f/Γ_n values was obtained with a formula that takes into account the effect of rotation on the level widths. We could not, however, obtain very accurate values for the moments of inertia $\mathcal{I}_e$ and $\mathcal{I}_s$ at the equilibrium and saddle configurations. We used for $\mathcal{I}_e$ the value of the rigid-body moment of inertia for a spherical nucleus, and for $\mathcal{I}_s/\mathcal{I}_e$ the value 0.5.

We found the ratio a_f/a_n to be around 1.2 independent of nuclear type. Here a_f and a_n are the level density parameters for fission and neutron evaporation, respectively, used in the theoretical formula for Γ_f/Γ_n. However, their absolute values could not be determined very accurately. We used for a_n the value 20 MeV^{-1}.

In the analysis we obtained values for the fission barrier E_f for a nonrotating nucleus. We found E_f to be nearly independent of the choice of the other parameters, and hence it could be established fairly uniquely.

The fits to the experimental Γ_f/Γ_n curves are shown in Figs. B. 1-1 and B. 1-2.

The experimental values E_f were corrected for shell energy to yield experimental fission barrier values $E_{f(exp)}^L$ for a liquid drop. These values then could be compared to theoretical values E_f^L for a uniformly charged nonrotating liquid drop.

According to Cohen and Swiatecki[3] the barrier E_f^L is, in the region $1/3 < x < 2/3$, to a good approximation given by

$$E_f^L = 0.38(0.75-x)E_x^0, \qquad (2)$$

where $E_s^0 = 17.8A^{2/3}$ is the surface energy of a spherical liquid drop and $x = (Z^2/A)/(Z^2A)_{crit}$. With the commonly used value 50.13 for $(Z^2/A)_{crit}$, we obtain values for E_f^L that are higher than $E_{f(exp)}^L$. Instead, we obtain a good fit with the value $(Z^2/A)_{crit} = 48.0$. With these values, $E_{f(exp)}^L$ has a standard deviation from E_f^L of around 2 MeV. Huizenga et al. quote the same error in their analysis.[1] There appears to be no systematic deviation of $E_{f(exp)}^L$ from E_f^L in and outside the region of the closed shell. We might conclude from this that no shell and pairing-energy-correction term Δ_n should be introduced in the level-density formula for neutron emission, as was considered by Huizenga et al.[1] Introduction of such a term makes E_f higher in the closed-shell region.

Footnotes and References

† Based on Phys. Rev. 135, B669 (1964).

1. J. R. Huizenga, R. Chandry, and R. Vandenbosch, Phys. Rev. 126, 210 (1962).
2. V. E. Viola, Jr., and T. Sikkeland, Phys. Rev. 128, 767 (1962).
3. S. Cohen and W. J. Swiatecki, The Deformation Energy of a Charged Drop (Aarhus Universitet Press, Aarhus, Denmark, Jan. 1961).

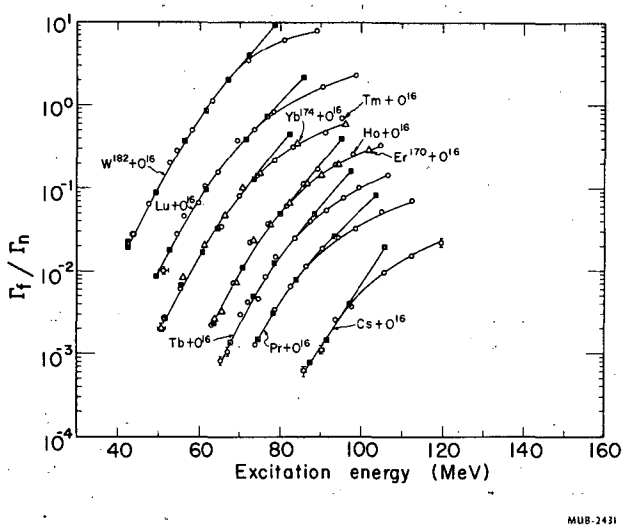

Fig. B. 1-1. Calculated and experimental Γ_f/Γ_n functions for nuclei formed in the bombardments of various targets with O^{16}

■ calculated values

O Δ experimental values

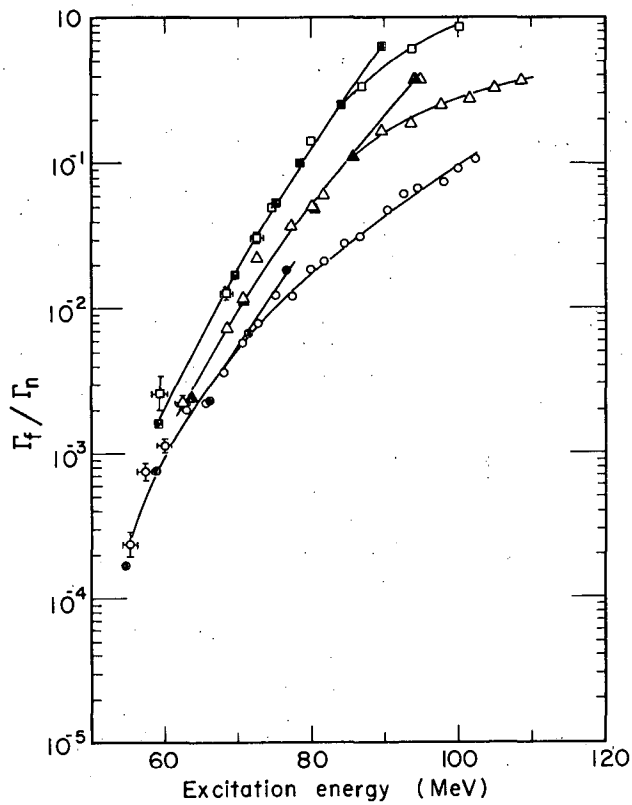

Fig. B. 1-2. Calculated and experimental Γ_f/Γ_n functions for the compound nucleus Re^{181} formed three ways.

Tb + Ne^{22}	□	experimental	■	calculated
Ho + O^{16}	△	experimental	▲	calculated
Tm + C^{12}	○	experimental	●	calculated

2. FISSION BARRIERS OF W, Re, Os, Ir, AND Hg ISOTOPES

Torbjørn Sikkeland, Victor E. Viola, Jr.,* Jack E. Clarkson, and Naftali H. Steiger†

Fission excitation functions have been measured for the systems $Tb^{159} + F^{19}$, $Ho^{165} + N^{14}$, $Y^{174} + C^{12}$, $Lu^{175} + C^{12}$, $W^{182} + C^{12}$, $Tm^{169} + B^{11}$, and $Lu^{175} + B^{11}$. The technique of determining the fission cross section σ_f has been described elsewhere in the Annual Report.

In Figs. B. 2-1 through B. 2-3 are plotted the quantity $\sigma_f/(\sigma_{CF} - \sigma_f)$ vs the excitation energy E of the compound nucleus formed in a complete fusion (CF) of ion and target. Here σ_{CF} is the cross section for CF reactions. For the ratio σ_{CF}/σ_R, where σ_R is the total interaction cross section as obtained from calculations, we used the values 0.82, 0.80, 0.76, and 0.66 for B^{11}, C^{12}, N^{14}, and F^{19}, respectively, independent of E and target used.

For the system studied, fission takes place only after a CF reaction, and, ignoring particle evaporation, we will have at the steep part of the curve, for $\sigma_f/\sigma_{CF}-\sigma_f)$,

$$\Gamma_f/\Gamma_n \approx \sigma_f/(\sigma_{CF} - \sigma_f).$$

Figure B. 2-1 shows the effect of target on Γ_f/Γ_n when the same ion is used. A similar shift towards higher E with decreasing Z and A of the target was also observed with O^{16} as ion.[1] In Fig. B. 2-2 we have compared Γ_f/Γ_n for the same compound nucleus formed two ways. Here at the same value for E the angular momentum, ℓ_{CF}, of the compound nucleus is nearly the same for the two ions. The ions B^{11} and C^{12} are too close in mass to produce a noticeable angular momentum effect on Γ_f/Γ_n. This effect was clearly demonstrated in reference 1, where the same compound nucleus was made with the ions C^{12}, O^{16}, and Ne^{22}.

The effect of neutron binding energy, B_n, and fission barrier, E_f, on Γ_f/Γ_n can be deduced qualitatively from the curves in Fig. B. 2-3. For instance, for the nuclei W^{178} and W^{180} B_n is nearly the same. However, at all values for E, Γ_f/Γ_n is higher for W^{178}, indicating a lower fission barrier for this nucleus.

If, on the other hand, we compare, at the same E and ℓ_{CF}, Γ_f/Γ_n for W^{179} with that for W^{180} we see they are practically equal. Here E_f is lower for W^{179}; however, this is compensated by a smaller value for B_n.

We have fitted theoretical Γ_f/Γ_n values to experimental ones for the system $Ho^{165}+N^{14}$ (see Fig. B. 2-3). The formula used in the calculation has been given in reference 1. In the analysis we obtained the value 25.5 MeV for E_f for W^{179}.

For the other systems, E_f was obtained by fitting theoretical values for the ratio $(\Gamma_f/\Gamma_n)/(\Gamma_f/\Gamma_n)_N$ to experimental ones at the same value for E and ℓ_{CF} at the steep part of the Γ_f/Γ_n curves. Here (Γ_f/Γ_n) refers to the system to be analyzed and $(\Gamma_f/\Gamma_n)_N$ to the system $Ho^{165} + N^{14}$. This way the angular momentum terms are eliminated. However, only values for the difference between two fission barriers are obtained.

In another set of calculations we used as reference E_f and Γ_f/Γ_n for Re^{181} produced by $Tm^{169} + C^{12}$, and that was analyzed in reference 1. The agreement between the values for E_f, for a particular system obtained these two ways, was very satisfactory.

In Table B. 2-I we have given values for E_f for the systems studied in addition to two systems from reference 1.

In columns 4 and 5 are listed experimental and theoretical liquid-drop-model values. The latter ones were calculated from the formula

$$E_f^L = 0.38(0.75 - X)E_S^0,$$

where $E_S^0 = 17.8\ A^{2/3}$ is the surface energy of a spherical liquid drop and $X = (Z^2/A)/(Z^2/A)_{crit}$. For $(Z^2/A)_{crit}$ we used the value 48.0.

Footnotes and References

* Present address: Chemistry Division, Argonne National Laboratory, Lemont, Ill.
‡ Present address: Department of Nuclear Science, Israel Institute of Technology, Haifa, Israel.

1. T. Sikkeland, Phys. Rev. 135, B671 (1964).

Table B. 2-I. Comparison of experimental and liquid-drop-model fission barrier values.

System	Compound nucleus	E_f (MeV)	$E_{f(exp)}^{L}$ (MeV)	E_f^{L} (MeV)	B_n (MeV)
$Tb^{159} + F^{19}$	W^{178}	23.9	22.6	23.4	8.9
$Ho^{165} + N^{14}$	W^{179}	25.5	24.2	24.2	6.6
$Tm^{169} + B^{11}$	W^{180}	27.2	25.9	25.1	8.5
$Tm^{169} + C^{12}$	Re^{181}	24.0[a]	22.9[a]	22.2[a]	8.8
$Er^{170} + O^{16}$	Os^{186}	24.2[a]	23.2[a]	22.7[a]	8.2
$Yb^{174} + C^{12}$	Os^{186}	23.7	22.7	22.7	8.2
$Lu^{175} + B^{11}$	Os^{186}	23.8	22.8	22.7	8.2
$Lu^{175} + C^{12}$	Ir^{187}	21.2	19.8	19.8	8.5
$W^{182} + C^{12}$	Hg^{194}	16.6	14.1	14.2	8.4

a. Data taken from reference 1.

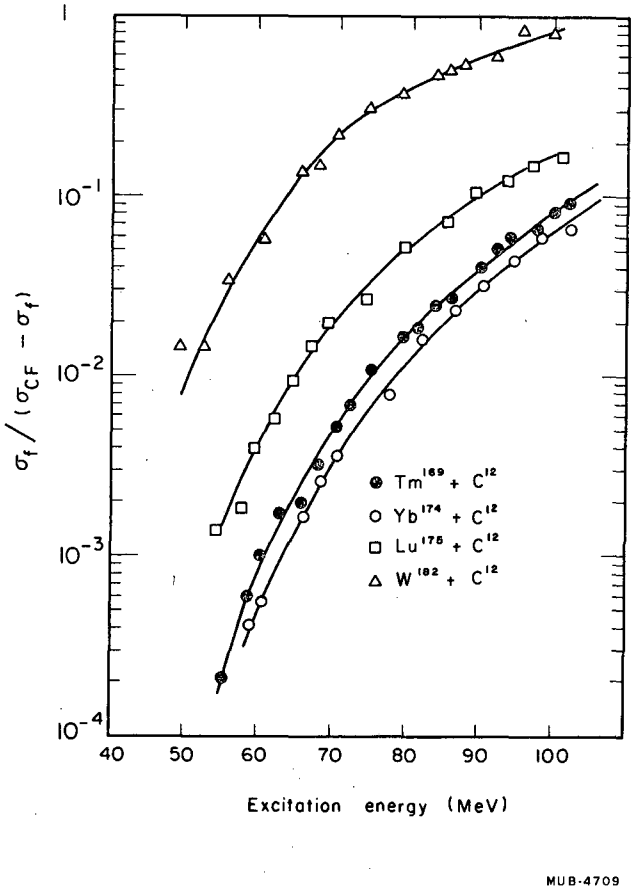

Fig. B. 2-1. Experimental values for the ratio $\sigma_f/(\sigma_{CF}-\sigma_f)$ as a function of the excitation energy, E, of the compound nucleus in the bombardment of various targets with C^{12}.

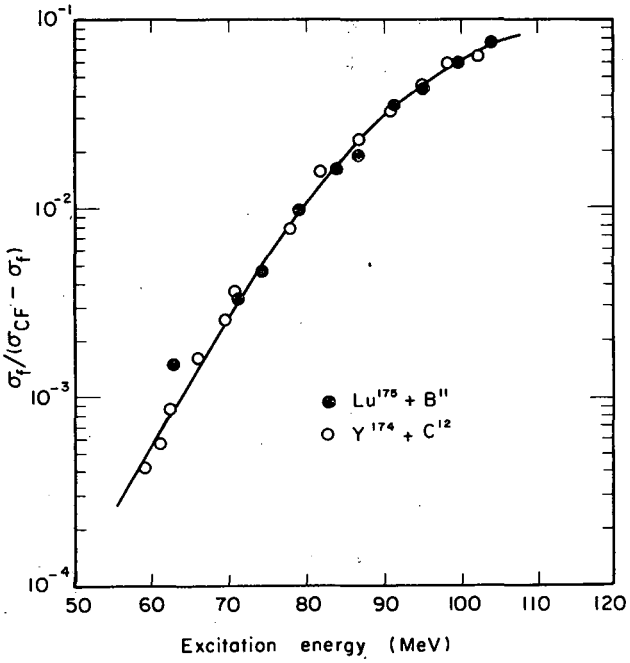

Fig. B. 2-2. Experimental values for the ratio $\sigma_f/(\sigma_{CF}-\sigma_f)$ as a function of the excitation energy, E, of the compound nucleus Os^{186} formed in two ways.

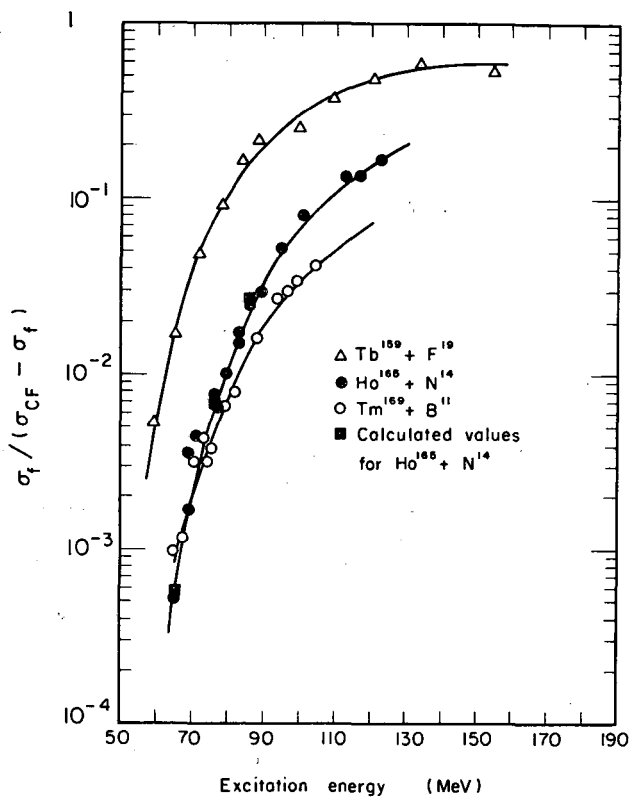

Fig. B. 2-3. Experimental values for the ratio $\sigma_f/(\sigma_{CF}-\sigma_f)$ as a function of the excitation energy, E, of various W isotopes. The solid squares represent calculated Γ_f/Γ_n values for the system $Ho^{165} + N^{14}$.

3. EQUILIBRIUM SHAPES OF ROTATING CHARGED OR GRAVITATING LIQUID MASSES

S. Cohen,* F. Plasil, and W. J. Swiatecki

The study of equilibrium shapes of rotating charged or gravitating liquid masses has been extended somewhat and is nearing completion. The relation of the nuclear problem of a rotating charged drop to the astronomical problem of a rotating gravitating mass has been traced out. In the astronomical case the "threshold energy" for the disintegration of a rotating mass has been calculated (for the first time, we believe). The corresponding asymmetric pear-shaped saddle-point figures (the Poincaré pears) have been traced out beyond previously known degrees of asymmetry. Some progress has been made in understanding probable fate of such rotating masses after disintegration, in particular the role of the binary star configurations of G. H. Darwin.

For the sake of completeness, calculations of the equilibrium configurations have been carried out in a few cases for negative rotational energies.

A paper giving the full account of the calculations is in preparation. It will include tabulations of energies and moments of inertia of the equilibrium shapes.

Footnote

* Present address: Argonne National Laboratory, Argonne, Illinois.

4. FISSION BARRIER OF THALLIUM-201

Donald S. Burnett,* Raymond C. Gatti, Franz Plasil,
P. Buford Price,‡ Wladyslaw J. Swiatecki, and Stanley G. Thompson

A new method involving the detection of fission fragments in mica has been applied to the measurement of the fission cross section of the compound nucleus Tl^{201} produced by bombardments of Au^{197} with helium ions. These data have been interpreted in terms of an expression for the ratio of fission to neutron-emission probabilities similar to those used conventionally, but modified to include the effect of quantum-mechanical barrier penetrability. In this way a height of 22.5 ± 1.5 MeV was found for the fission barrier of Tl^{201}, and a lower limit on the width could be established. The above value of the barrier, when interpreted on the basis of the liquid-drop theory, leads to an accurate determination of the ratio of the electrostatic to the surface energy of nuclei. This serves to establish the constant of proportionality between the "fissionability parameter" x and the value of Z^2/A, $x = (Z^2/A)/(48.4 \pm 0.5)$. This measured barrier height, when added to the ground-state mass of Tl^{201}, gives a saddle-point mass of this nucleus equal to 200.9949 ± 0.0015 mass units (carbon scale).

Footnotes

* Present address: Kellogg Radiation Laboratory, California Institute of Technology, Pasadena, California.
‡ Present address: General Electric Company, Schenectady, New York.

5. FISSION BARRIERS OF POLONIUM-210 AND ANTIMONY-119, 117

R. C. Gatti, A. Khodai-Joopary, and S. G. Thompson

The fission excitation functions of Po^{210} and $Sb^{119(117)}$ produced by bombardment of Bi^{209} and In^{115} (natural indium, 96% In^{115} and 4% In^{113}) by protons and α particles respectively from the Berkeley 88-inch variable-frequency cyclotron were determined. The experimental technique is similar to that used for the determination of the fission barrier of Tl^{201}.[1] The targets were prepared by partial evaporation of 99.9999% pure elements on Al or Cu backing (for water cooling). The targets were thick enough to prevent the penetration of the target by fission fragments from impurities in the backing material.

The results of the measurements of the fission cross sections versus excitation energy for protons on $_{83}Bi^{209}$ and helium ions on $_{49}In^{115}$ are given in Figs. B. 5-1 and B. 5-2 respectively. The corresponding values of $\log \Gamma_f/\Gamma_n$ versus excitation energy are given in Fig. B. 5-3 and B. 5-4 respectively. In order to obtain estimates of the fission barrier and related parameters for Po^{210*}, we used the same approach in fitting the data with a theoretical expression as was used in reference 1. Preliminary results indicate the fission barrier to be $\approx 21.5 \pm 1.0$ MeV. The level-density parameters were $a_f \approx 10.0$ and $a_n \approx 8.0$ MeV^{-1}, and the barrier-penetration factor, $\hbar\omega$, was between 1 and 2 MeV.

In the case of Sb^{119*} ($In^{115}+He^4$) the fission barrier is about 20 MeV higher than the Coulomb barrier for helium ions, and the effect of angular momentum on the fission barrier is large. In Tl^{201}, Po^{210}, and Hg^{198} the angular momentum effects and the contributions of fission after neutron emission are negligible at the excitation energies considered. Using the same theoretical expression as above, but with $\hbar\omega$ fixed at zero, we fitted the data obtained for Sb^{119*}. However, without taking into account angular momentum effects, we could not obtain a good fit to the

data. The best fit is given as the dashed line in Fig. B. 5-4, for which the fission barrier, B_f, is 38 MeV, $a_f = 5.9$, and $a_n = 6.3$ MeV^{-1}. All fits gave small a values (less than 7 MeV^{-1}) and values of a_n greater than a_f, which is opposite to the case of Tl^{201*}, Hg^{198*}, and Po^{210*}. (The calculated threshold for Sb^{119} from the liquid-drop theory with $x_{critical} = 48.4 \pm 0.5$ is 46.7 ± 1.7 MeV). It is likely that the difference is largely due to the influence of angular momentum. We are therefore developing a new program for fitting the data that takes into account the angular momentum effects and contributions of fission after neutron emission.

References

1. Donald S. Burnett, Raymond C. Gatti, Franz Plasil, P. Buford Price, Wladyslaw J. Swiatecki, and Stanley G. Thompson, Phys. Rev. 134, B952 (1964).

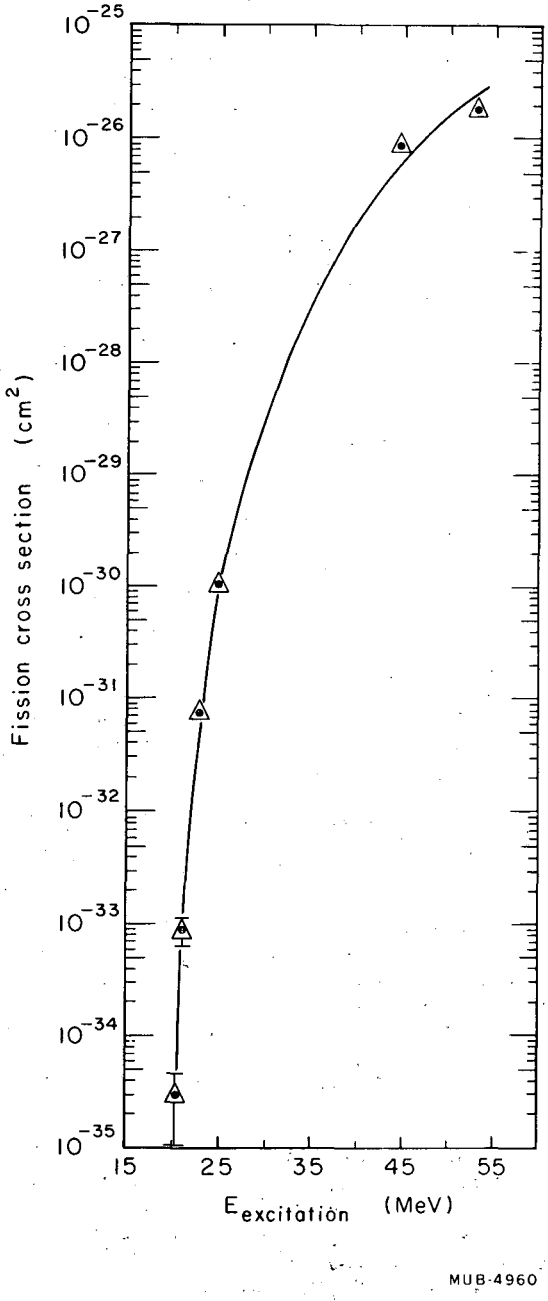

Fig. B. 5-1. Measured fission cross section versus excitation energy for the reaction $_{83}Bi^{209} + {}_{1}H^{1} \rightarrow {}_{84}Po^{210}$.

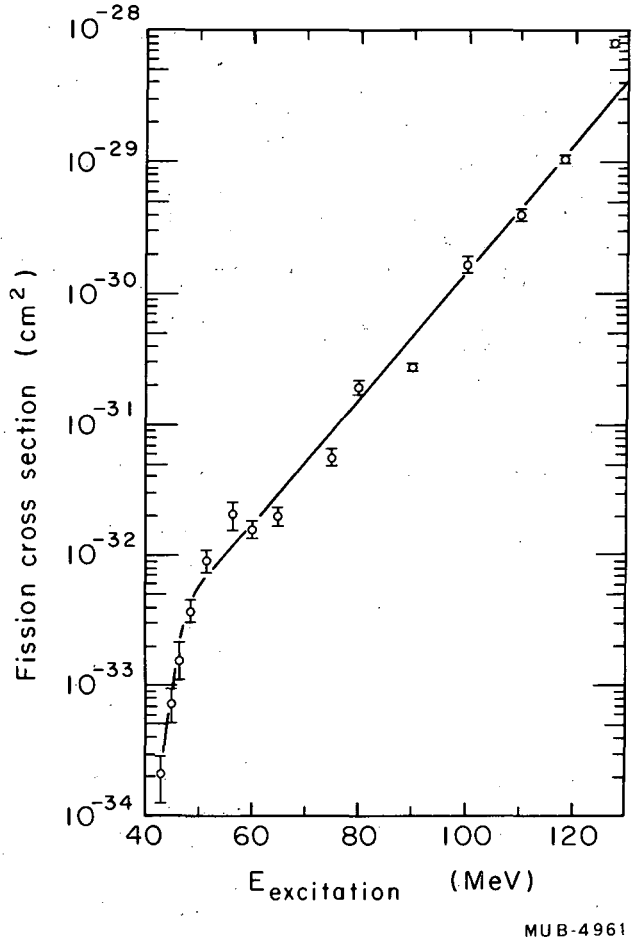

Fig. B. 5-2. Measured fission cross section versus excitation energy for the reaction $_{49}In^{115, 113} + {}_{2}He^{4} \rightarrow {}_{51}Sb^{119, 117}$.

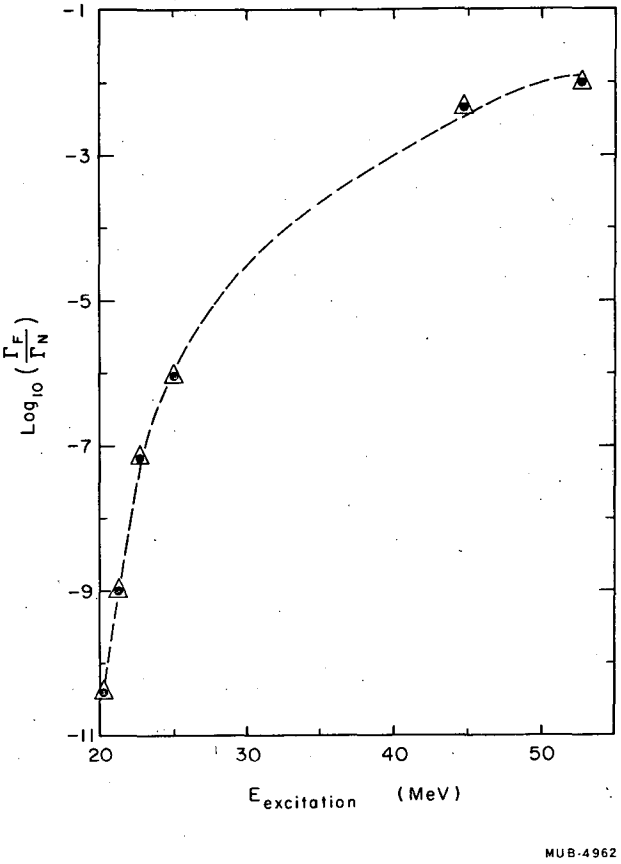

Fig. B. 5-3. $\text{Log}_{10}(\Gamma_f/\Gamma_n)$ versus excitation energy. Experimental points are indicated by triangles. The dashed curve is the theoretical fit for the fission barrier 21.5 ± 1.0 MeV, $\hbar\omega$ between 1 and 2, $a_f \approx 10$ MeV^{-1}, and $a_n \approx 8$ MeV^{-1}.

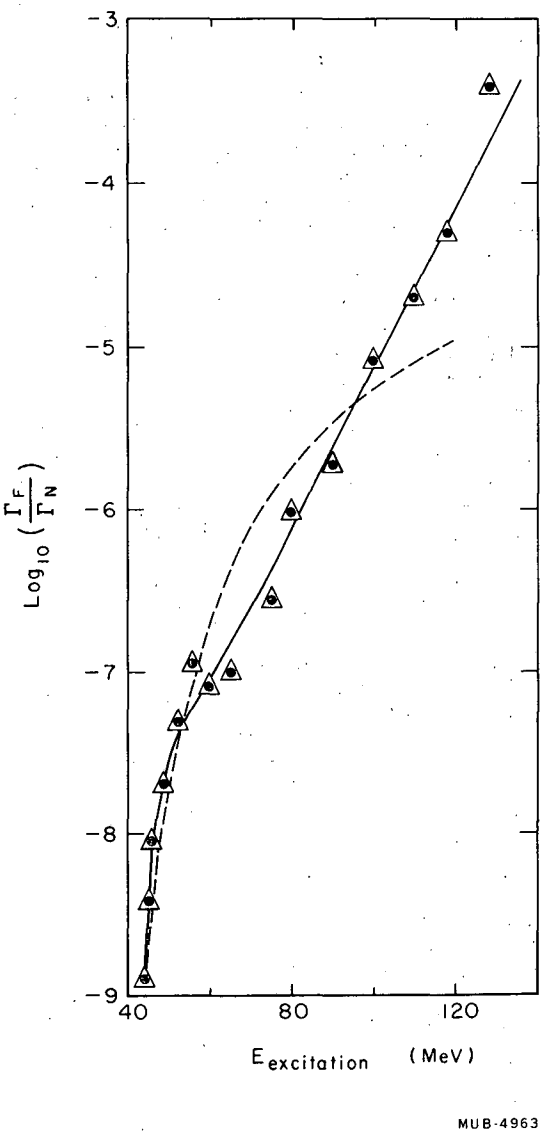

Fig. B. 5-4. $\text{Log}_{10}(\Gamma_f/\Gamma_n)$ versus excitation energy. Experimental points are indicated by triangles which are connected by a solid curve. The dashed curve is the theoretical fit for the fission barrier = 38 MeV, $\hbar\omega = 0$, $a_f = 5.9$ MeV^{-1}, and $a_n = 6.3$ MeV^{-1}.

6. FISSION OF URANIUM-238 AND PLUTONIUM-240 NUCLEI EXCITED BY INELASTIC α-PARTICLE SCATTERING

Harold C. Britt,* Franz Plasil, and Stanley G. Thompson

Direct reactions such as inelastic α-particle scattering can be used to excite fissionable nuclei to excitation energies near the fission threshold. A study of the fission of nuclei in this manner can give information on the properties of the low-lying nuclear states which occur in the distorted fission saddle-point configuration. From an investigation of the level structure at the saddle point of a fissioning nucleus, one can obtain information on the characteristics of nuclei which have deformations much greater than those occurring in normal stable nuclei.

In a study of fission following a direct reaction, the excitation energy of the fissioning nucleus is uniquely determined by the energy of the outgoing direct particle. Therefore, in the (α, α' f) reaction a measurement of the number of coincident fission fragments as a function of the observed number and energy of inelastic α particles gives a measure of the probability of fission for the types of levels excited as a function of the excitation energy available to the fissioning nucleus. Another characteristic of this type of direct reaction is that the fissioning nuclei are formed in states of moderately high angular momentum, so that significant anisotropies can be expected in the angular correlation of the fission fragments relative to the direction of the recoil of the fissioning nucleus. The study of these angular correlations yields information on the average value for the quantum number K for the states which are excited, K being defined as the projection of the angular momentum on the nuclear symmetry axis.

In previous studies the (d, pf) reaction has been used to study both the fission thresholds for "thermally fissionable" nuclei[1] and the angular correlations of the fragments.[2] In the angular correlation measurements for Pu^{239}(d, pf), it was possible to directly measure the two-quasi-particle pairing gap ($2\Delta_0$) for the saddle-point nucleus Pu^{240}, and in addition evidence was found for the existence of low-lying rotational bands built on vibrational states in the region of excitations between the ground state and the onset of two quasi-particle excitations. The major difficulty found in angular correlation experiments on even-even fissioning nuclei produced in the (d, pf) reaction was that the spin of the target nucleus had a large effect on the observed angular correlation. In fact Pu^{239}, which has a spin of 1/2, was the only case investigated for which the angular correlations were large enough to yield detailed information on the saddle-point levels.

In contrast, when the (α, α') reaction is used to produce even-even nuclei at excitations above the fission threshold, the target nucleus has zero spin, and for the same angular momentum transfer, the anisotropies are larger than for the (d, p) case. In addition, the angular momentum transfers in the (α, α') reactions are in general greater than for the (d, p) case, thus further increasing the fission-fragment anisotropies. For these reasons, an investigation has been made of the general properties of (α, α' f) reactions on targets of U^{238} and Pu^{240}.

In these measurements a semiconductor detector was used to measure the energy spectra of inelastic α particles emitted at the laboratory-system angle of 75 deg in coincidence with fission fragments observed in semiconductor detectors at various angles. The incident alpha particles from the 88-inch cyclotron had energies of 40.0 and 38.1 MeV, respectively, for the U^{238} and Pu^{240} measurements. The effective energy resolution for the measurements was approximately 0.4 and 0.5 MeV FWHM, respectively, for the U^{238} and Pu^{240} measurements. The fission detectors were square in shape and each subtended an angle of approximately 20 deg.

Figure B. 6-1, (a) and (b), show the anisotropies, in the reaction plane, obtained for the two targets. Parts (c) and (d) show measurements of azimuthal anisotropies (out of the reaction plane). In Fig. B. 6-1 the angles are measured relative to the symmetry angles for angular correlations measured in the reaction plane. The results have not been corrected for the finite angular resolution of the detectors. A comparison of the anisotropies for Pu^{240} and U^{238} indicates that the dependence on excitation energy is the same to within the statistical accuracy for the two cases if the threshold for U^{238} is taken to be 1.0 ± 0.1 MeV higher than the Pu^{240} threshold. The solid curve drawn through the anisotropies in Fig. B. 6-1 (a) and (b) is the same for both targets except for a shift of 1.0 MeV. The energy resolution and statistical accuracy are not sufficient to allow the observation of structure of the type found in the previous (d, p) measurements.[2]

Figure B. 6-2 shows the coincident spectra observed at 0 and 90 deg relative to the symmetry axis for the two targets. The vertical lines in the Pu^{240} results indicate the positions of the two thresholds measured in the previous Pu^{239}(d, pf) experiment. [1] The lines shown for the U^{238} data are drawn 1.0 MeV higher than for Pu^{240} to account for the difference in the threshold energies, which is indicated by the anisotropy measurements shown in Fig. B. 6-1. These results seem to indicate that for Pu^{240} the amplitude of the second threshold is considerably greater than the amplitude for the first threshold. A similar result is observed in the (d, pf) experiment. [1] In U^{238} the second threshold, if present, contributes to a much smaller extent because of the competition from neutron re-emission at the excitation energy appropriate for that threshold.

In order to obtain reasonable statistical accuracy for the angular correlations, the data were sorted in excitation energy intervals of 0.57 MeV. The angular correlations for the first four excitation energy intervals for the U^{238} data are shown in Fig. B. 6-3. There θ_R is the kinematic recoil angle for the fissioning nucleus. The symmetry angle for the angular correlation is approximately 5 deg less than the kinematic recoil angle in all cases. The angular correlations for the 5.67-MeV group appear to be consistent with fission, primarily through the ground-state $K=0^+$ rotational band. For the 6.82-MeV group the anisotropy has decreased significantly and the angular correlation has broadened because of inclusion of fission through higher vibrational bands. Calculations are now in progress in an attempt to fit the angular correlation results, assuming the presence of $K=0^+$, 1^-, and 2^+ bands in the excitation energy interval represented in Fig. B. 6-3.

Footnote and References

* On leave from Los Alamos Scientific Laboratory, Los Alamos, New Mexico.

1. J. A. Northrup, R. H. Stokes, and K. Boyer, Phys. Rev. 115, 1277 (1959).
2. H. C. Britt, R. H. Stokes, W. R. Gibbs, and J. J. Griffin, Phys. Rev. Letters 11, 343 (1963).

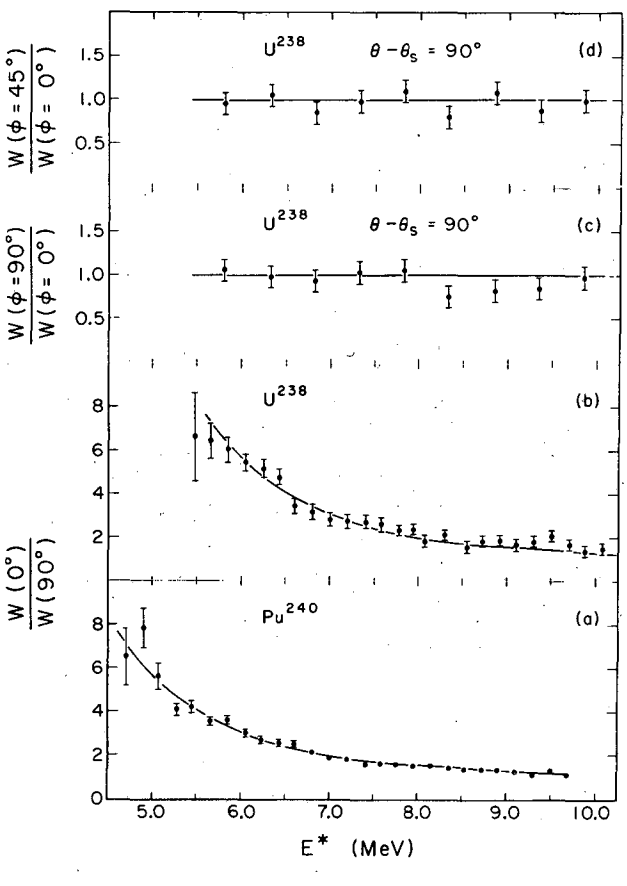

Fig. B. 6-1. Anisotropies of fission fragments emitted in the (α, α' f) reaction on targets of Pu^{240} and U^{238} as a function of the excitation energy available in the fissioning nucleus. All angles are measured relative to the symmetry direction for the angular correlation in the reaction plane. The results have not been corrected for the finite angular resolutions of the detectors.

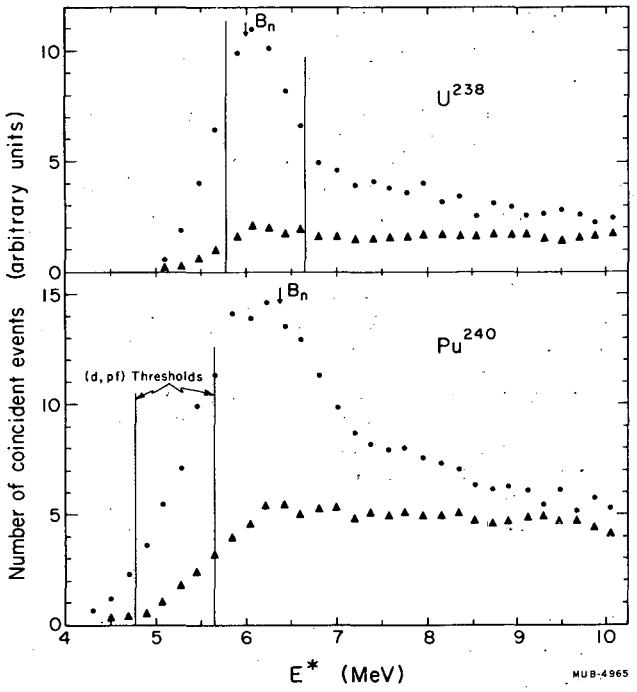

Fig. B. 6-2. Coincident energy spectra observed at 0 (O) and 90 deg (Δ) relative to the symmetry axis. The arrows indicate the neutron binding energies for the two cases. Vertical lines indicate the two thresholds determined in reference 1 for Pu^{240}.

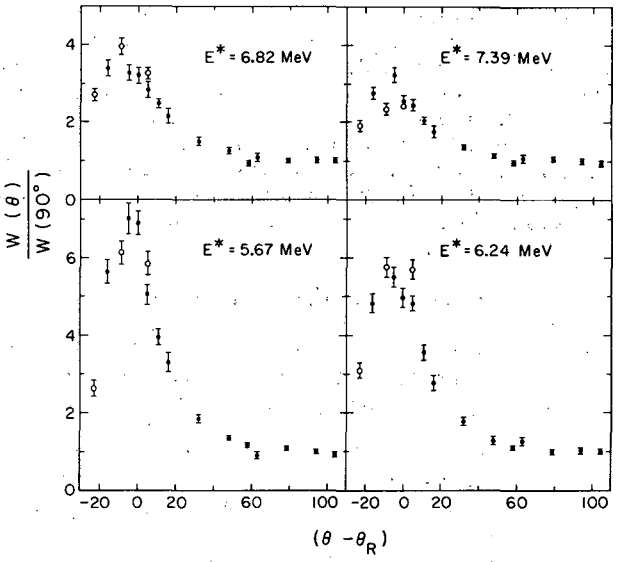

Fig. B. 6-3. Angular correlations of fission fragments emitted in the $U^{238}(\alpha, \alpha' f)$ reaction. The data have been sorted in excitation energy intervals of 0.57 MeV width. The data have not been corrected for the finite energy resolution of the detectors. Open circles indicate points that have been reflected 180 deg.

7. ALPHA PARTICLES EMITTED IN THE SPONTANEOUS FISSION OF CALIFORNIUM-252

Z. Fraenkel and S. G. Thompson

The angular and energy distributions of the α particles emitted in the spontaneous fission of Cf^{252} have been examined in a three-parameter correlation experiment. The experimental apparatus consisted of a fission chamber containing two fixed semiconductor detectors (for the two fission fragments), one movable semiconductor detector (for the α particle), and a 1.5×10^7-fission/min Cf^{252} source on a 100-μg/cm^2 Ni foil backing. A 16-mg/cm^2 Au foil placed in front of the α-particle detector prevented the 6.1-MeV α particles from the alpha decay of Cf^{252} and fission fragments from reaching the detector. Triple-coincidence energy data were processed by a multidimensional analyzer and stored on tape. A total of 2×10^5 events was then analyzed in various ways by means of a computer. A summary and some discussion of the results have been given in Phys. Rev. Letters 13, 438 (1964).

8. PROMPT ELECTRON SPECTRA FROM CALIFORNIUM-252 FISSION FRAGMENTS†

R. L. Watson, H. R. Bowman, S. G. Thompson, and J. O. Rasmussen

Recent measurements of the spectra of prompt γ rays accompanying fission[1] have pointed out the possibility of extending the methods of nuclear spectroscopy into the region spanned by the prompt fission products of Cf^{252}. We have followed up this advance with the measurement of the electron spectra originating from the internal conversion of prompt γ rays from Cf^{252} fission fragments of selected mass in the energy range extending from 30 to 1000 keV. The initial results are quite encouraging with respect to the possibility of charge identification and internal-conversion coefficient measurement, and it is expected that these studies will yield considerable information concerning the de-excitation processes of primary fission fragments.

An inhomogeneous magnetic field of configuration proposed by Malmfors[2] was used to steer the electrons around a block of lead, which shielded the electron detector from fission fragments and γ rays. In our case, a wide range of energies and a large solid angle of electrons precess in trochoidal orbits in the fringing field of a large electromagnet. A weightless Cf^{252} source was mounted inside a brass vacuum chamber, which was positioned between the pole faces of the magnet. A lithium-drifted silicon electron detector was mounted inside the vacuum chamber 90 deg around the magnet from the fission source. This arrangement allowed the detection of electrons without the interference of fission fragments and γ rays. The fragment energies were measured by two phosphorus-diffused silicon detectors mounted on both sides of the fission source on a line perpendicular to the median plane and at a distance of 1.8 cm.

A triple coincidence was required between the two fragments and the electrons. For geometrical reasons only electrons emitted within 1 nsec can precess into the detector. That is, the high magnetic field configuration prevents electrons more distant than about 1 cm from the median plane from reaching the electron detector. The data (E_{f_1}, E_{f_2}, E_β) were recorded individually, event by event, in a multidimensional pulse-height analyzer and stored on magnetic tape. The neutron-corrected masses were then deduced by a method of successive approximations using the coincident fragment energies and the neutron data of Bowman et al.[3] Finally, the electron events were sorted with respect to coincident fragment mass into mass intervals of two units by using an IBM 7094 computer.

The unsorted electron spectrum for the energy region between 30 and 300 keV is shown in Fig. B. 8-1. The highest electron intensity appears at 105 keV. Some structure is apparent although no discrete peaks are discernible. When, however, the electron events are sorted with respect to mass as in Fig. B. 8-2, an improvement in definition is achieved. Although well-defined structure is present, the spectra are obviously quite complex. No discrimination is made between electrons coming from the light fragment and the complementary heavy fragment of each coincident pair. This, in conjunction with a mass resolution of ±2 units, results in the possibility of the existence of components in the spectra arising from 10 to 15 nuclides in each mass interval.

The geometry of the system was such that only electrons which were emitted near 90 deg with respect to the fragment flight path were accepted into the spectrometer; however, the finite size of the fragment detectors and the rather large acceptance angle of the magnetic field introduced considerable angular dispersion from a strictly 90-deg configuration. Those electrons which were accepted having angles other than 90 deg with respect to the fragment trajectory were shifted in energy because of the fragment motion. This effect resulted in a considerable broadening of the electron peaks, and is the predominant contributor to the experimental resolution.

Our initial efforts at analysis of these spectra have been focused on the energy region between 300 and 600 keV for the mass intervals 107 to 111 and 137 to 141. It is interesting to compare these electron spectra (Fig. B. 8-5) with the previously reported gamma spectrum[1] obtained with a NaI detector in this same energy region (Fig. B. 8-3). There is a general similarity between the low-resolution gamma spectra of Fig. B. 8-3 and the electron spectra of Fig. B. 8-5, notably the presence of the three complex peaks in Fig. B. 8-3 (376, 472, and 583 keV), and their counterparts in the electron spectra at the energies expected for K conversion lines.

Recent measurements of the γ-ray spectra in this region with a lithium-drifted germanium detector have resulted in a very great improvement in resolution. Spectra are shown in Fig. B. 8-4 (a) and (b) for the light fragment traveling toward the gamma detector and the heavy fragment traveling toward the gamma detector, respectively. Individual gamma peaks are well resolved, and by comparing part (a) with part (b) the energies can be corrected for Doppler shift and the γ-ray peaks identified with heavy or light fragments. The corresponding peaks in each spectrum have been labeled alphabetically. Inspection of Fig. B. 8-4 shows three peaks identified with light fragments (E, I, L) and twelve identified with heavy fragments located in the region of interest. By use of the γ-ray energies as determined from these spectra, the expected locations of the associated K and L conversion lines have been plotted below the electron spectra in Fig. B. 8-5 on the assumption of a most probable heavy Z of 53 or 54 and a most probable light Z of 44. As a rough guide the line lengths are taken from the intensities of the γ rays in Fig. B. 8-4(b), although we do not wish to imply that all conversion coefficients would be similar.

This initial analysis has been aimed solely at displaying the general structural features and the correspondence between the electron spectra and the gamma spectra from prompt fission fragments. It is expected, however, that further experimental refinements will eventually result in assignments of atomic number for various γ rays and in multipolarity assignments through conversion-coefficient determinations. Further experimentation with conversion electrons may also prove very useful in the determination of fragment excited-state lifetimes.

Footnote and References

† Submitted to Phys. Rev. Letters.

1. H. R. Bowman, S. G. Thompson, and J. O. Rasmussen, Phys. Rev. Letters 12, B522 (1964).
2. K. G. Malmfors, Arkiv Fysik 13, No. 21 (1957).
3. H. R. Bowman, J. C. D. Milton, S. G. Thompson, and W. Swiatecki, Phys. Rev. 129, 2133 (1963).

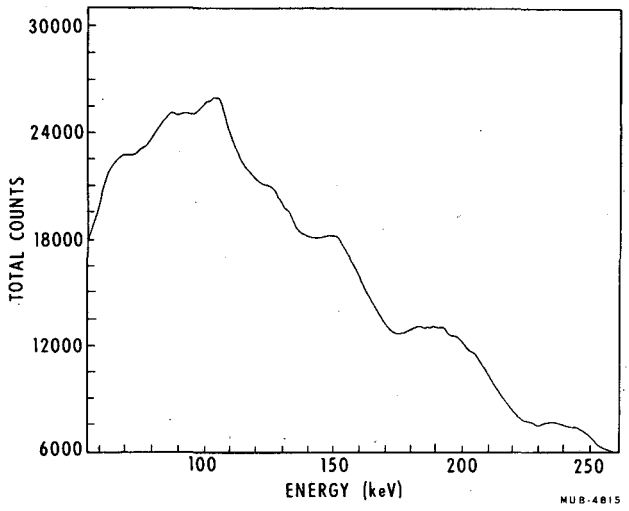

Fig. B. 8-1. Unsorted prompt electron spectrum from Cf^{252} fission fragments.

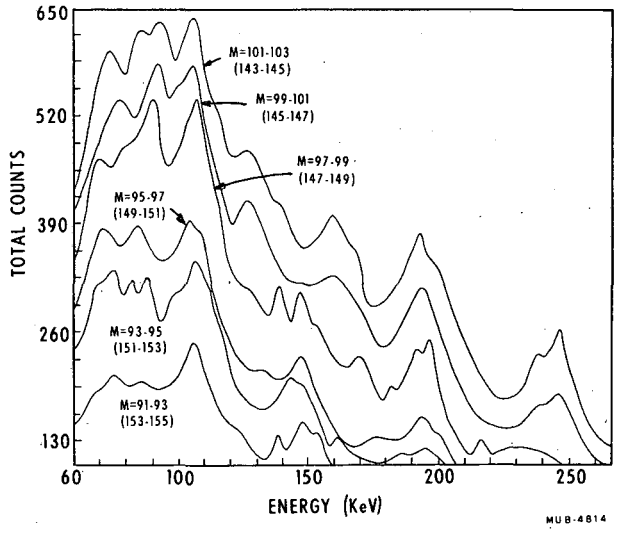

Fig. B. 8-2. Prompt electron spectra from Cf^{252} fission fragments for selected mass intervals.

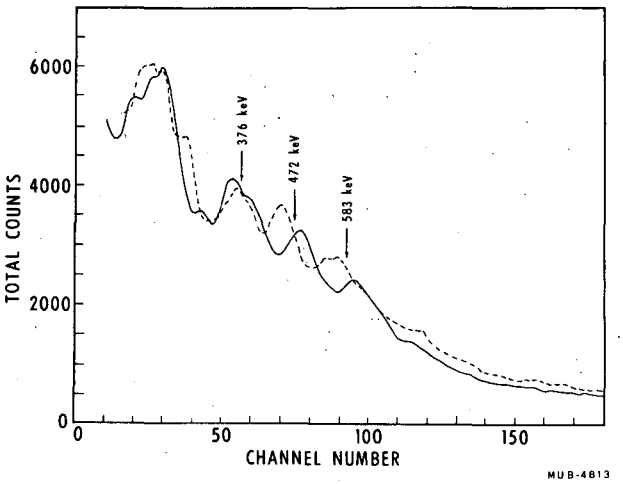

Fig. B. 8-3. Prompt γ-ray spectra from Cf^{252} fission fragments for mass ratio = 1.30.
— heavy fragment moving toward detector
---light fragment moving toward detector

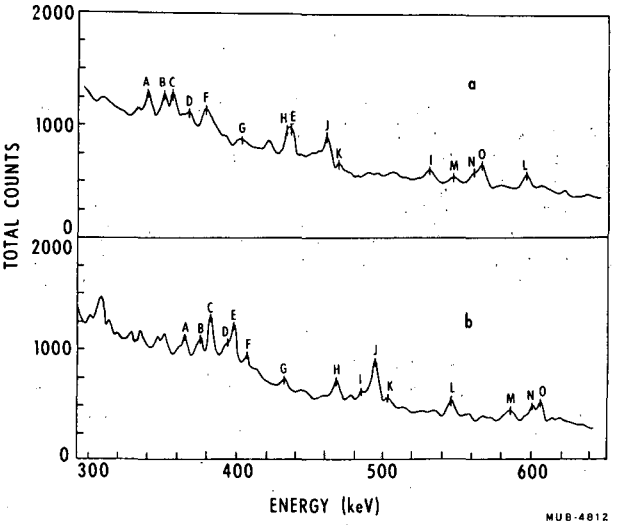

Fig. B. 8-4. Prompt γ-ray spectra from Cf^{252} fission fragments for mass interval 109 to 111 (137 to 139).
(a) light fragment moving toward detector
(b) heavy fragment moving toward detector

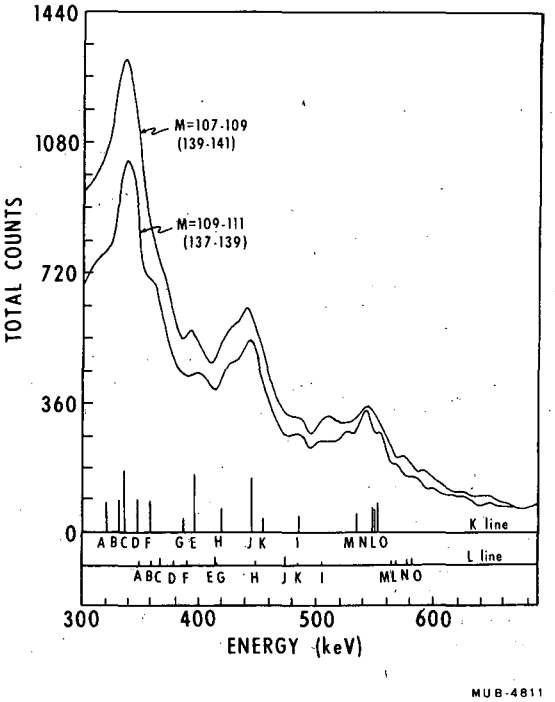

Fig. B. 8-5. Electron spectra showing K and L line positions as determined from γ-ray energies.

9. ENERGY-MASS DISTRIBUTIONS OF Bi, Au, AND W IN He-ION-INDUCED FISSION

F. Plasil, H. C. Britt, and S. G. Thompson

Energy-mass distributions have been measured in the fission of Bi^{209}, Au^{197}, and W^{182} induced with He^4 ions, accelerated by the variable-frequency 88-inch cyclotron. The experimental techniques have been described previously.[1-3] The bombarding energies of the He^4 ions were varied in 20-MeV steps from 40 to 120 MeV for Bi^{209}, from 60 to 120 MeV for Au^{197}, and from 100 to 120 MeV for W^{182}. The shapes and widths of the measured distributions were compared with those calculated from the theory of Nix and Swiatecki,[4] in a manner similar to the one used in references 2 and 3. The overall agreement between calculated and experimental distributions was found not so good as in earlier work.[2, 3]

Some of the data are shown in Figs. B.9-1 through B.9-3. Figure B.9-1 shows experimental and theoretical mass-total kinetic energy distributions for $W^{182} + He^4 = Os^{186}$ at an He^4 energy of 120 MeV, and for $Er^{170} + Os^{16} = Os^{186}$ at an O^{16} energy of 165 MeV. The erbium data are taken from reference 3. The excitation energies of the two compound nuclei are approximately equal. The contour lines pass through regions of equal density of events. The two experiments differ only by the amount of angular momentum involved, and the theoretical and experimental distributions are comparable except for neutron effects. The theory, furthermore, does not include angular momentum effects. It can be seen that although neither of the two experimental distributions is as triangular in shape as the theoretical one is, the $W^{182} + He^4$ case approximates the shape better than the $Er^{170} + O^{16}$ case. Figure B.9-2 shows the variances (experimental and theoretical) of the overall total kinetic distributions $\mu_2(E_T)$ and of the overall mass distributions $\mu_2(A_1)$ as a function of nuclear temperature, θ, for the Os^{186} compound nucleus formed either in He^4 or heavy-ion bombardments. The experimental variances are corrected for neutron effects by the method of reference 2.

Figure B.9-3 shows plots of $\mu_2(E_T)$ and $\mu_2(A_1)$ versus θ for $Bi^{209} + He^4$ (neutron correction is included). Note the substantial disagreement for $\mu_2(E_T)$. This can be compared with a similar plot for the heavy-ion-produced Pb^{198} compound nucleus (from reference 3), in which case the agreement was good.

Several factors have been considered in connection with the disagreements between experiment and theory.

1. Since angular momentum effects have not been considered in the theoretical calculations, the He^4-ion data should be in better agreement with theory than the heavy-ion data. This seems to be true when we consider the overall shape of the distributions (Fig. B.9-1). Thus, from Fig. B.9-1 we see that angular momentum seems to play a definite role in broadening the measured distributions. This may cause fortuitous agreement between experimental and theoretical overall moments in the heavy-ion cases (Figs. B.9-2 and B.9-3).

2. Incomplete momentum transfer between He^4 projectile and target (direct interaction) followed by fission would involve lower θ values for the fissioning nucleus than are estimated. Contributions due to this effect have been shown to be absent by measuring a sample angular correlation and finding fission following direct interaction to be negligible.

3. Prefission neutron emission could also result in lower θ values. Calculations in reference 3 indicate this effect to be small, but an experiment involving the measurements of the angular distributions will be carried out to verify these assumptions. The results of this experiment will, one hopes, give an average temperature at the time of fission.

4. The experimental data may be overcorrected for dispersive effects of neutron emission from fragments. A calculation will be performed to create theoretical distributions with neutron dispersions folded into them in an attempt to treat neutron effects more exactly. However, we are not hopeful that these calculations will show corrections large enough to produce agreement.

Subject to the above reservations on the interpretation of these data and on the knowledge of the nuclear temperature θ, there appears to be a basic difference between experimental and theoretical results.

References

1. Eldon L. Haines, Mass-Energy Relations in the Fission of Highly Excited Heavy Nuclei (Ph. D. Thesis), UCRL-10342, June 1962.
2. Donald S. Burnett, Kinetic Energy and Mass Distributions for Nuclear Fission at Moderate Excitation Energy (Ph. D. Thesis), UCRL-11006, Oct. 1963.
3. Franz Plasil, Energy-Mass Distribution and Angular Momentum Effects in Heavy-Ion-Induced Fission (Ph. D. Thesis), UCRL-11193, Dec. 1963.
4. James R. Nix, Studies in the Liquid-Drop Theory of Nuclear Fission (Ph. D. Thesis), UCRL-11338, April 1964; also J. R. Nix and W. J. Swiatecki, submitted to Nucl. Phys.

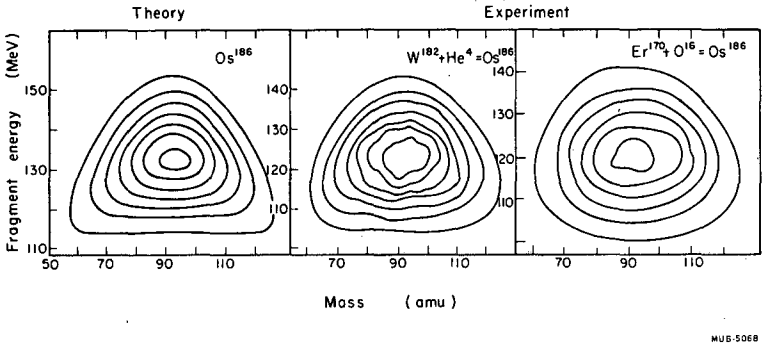

Fig. B.9-1. Theoretical and experimental mass-total kinetic energy distributions resulting from fission of Os^{186} at a nuclear temperature $\theta = 2.0$ MeV. The contour lines pass through regions of constant density of events. The three distributions are normalized.

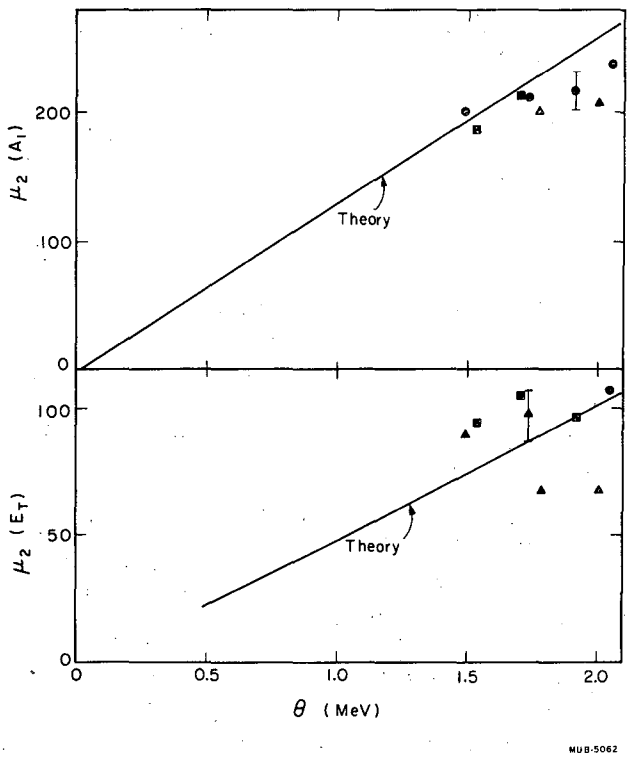

Fig. B.9-2. Theoretical and experimental variances of distributions of overall mass, $\mu_2(A_1)$, and overall total kinetic energy, $\mu_2(E_T)$, as a function of nuclear temperature for the fission of Os^{186}.
● $Er^{170}+O^{16}\rightarrow Os^{186}$ ▲ $W^{182}+He^4\rightarrow Os^{186}$
■ $Yb^{174}+C^{12}\rightarrow Os^{186}$.

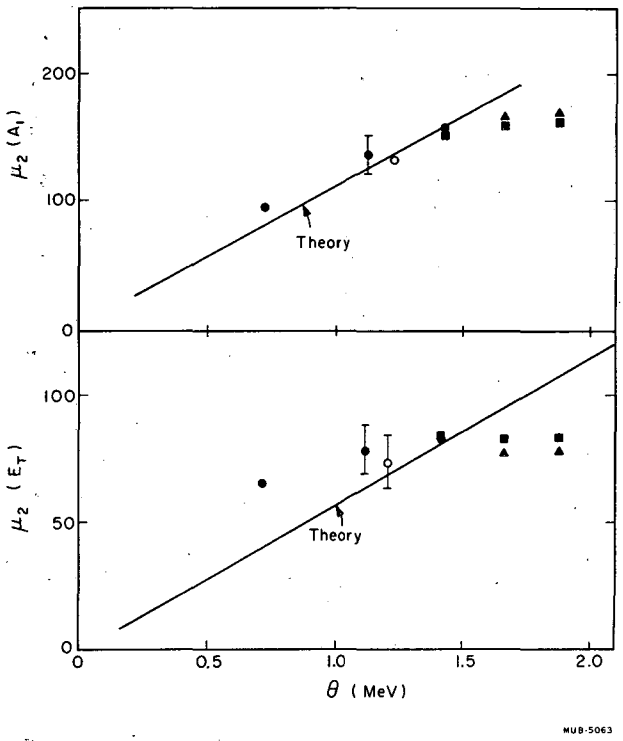

Fig. B.9-3. Theoretical and experimental variances of distributions of overall mass, $\mu_2(A_1)$, and overall total kinetic energy, $\mu_2(E_T)$, as a function of nuclear temperature for the fission of At^{213}. The data were obtained from four separate runs. $Bi^{209} + He^4 \rightarrow At^{213}$.

○ From reference 2 ● Experiment 2
▲ Experiment 1 ■ Experiment 3

10. ANALYSIS OF FISSION-EXCITATION FUNCTIONS OF LIGHT ELEMENTS

Franz Plasil and S. G. Thompson

Fission-excitation functions of several relatively light nuclei induced by heavy ions have been measured by Sikkeland.[1] An analysis of these data requires the inclusion of two important effects.

1. Since during the course of the bombardment projectiles strike the target nucleus with varying impact parameters, ranging from zero to the limit of interaction of nuclear forces, the resulting angular momentum of the compound nucleus ranges from zero to a value L_{max}. In heavy-ion reactions L_{max} can be very large (up to 100 units of $\hbar$). This broad distribution in L_{max} is likely to produce a distribution in B_f, the fission barrier of the compound nucleus. Liquid-drop calculations[2-4] indicate that B_f is very sensitive to the rotational energy of the fissioning nucleus. When the nucleus has an angular momentum value of L_{max}, B_f may, in a typical case, be less than half of the value it would have if the nucleus were not rotating.

2. Because of the high excitation energies involved in heavy-ion bombardments, the possibility of occurrence of fission after neutron emission should be considered.

This work is an attempt to include these two effects in analyzing the data of reference 1. The two objectives are: (a) to compare barriers extracted from excitation-function data with exact rotating-liquid-drop calculations; (b) to obtain estimates of the number of neutrons emitted before fission of the compound nucleus.[5]

The quantity calculated as a function of the excitation energy is σ_f/σ_{CN}, where σ_f is the fission cross section and σ_{CN} is the cross section for the formation of the compound nucleus. This quantity may be compared with σ_f/σ_R, where σ_f is now the measured fission cross section and σ_R is the calculated[6] total reaction cross section. Such a comparison is limited by several complications (direct reactions, charged-particle evaporation, etc.), discussed fully in reference 1. In this work the condition $\sigma_{CN} = \sigma_R$ will be assumed to hold in the region where the excitation function is rising rapidly, and no comparison will be made in the region where the curve for the excitation function is substantially flat. The condition $\sigma_{CN} = 0.72\ \sigma_R$ (independent of bombarding energy) has been used in the analysis of reference 1, and will be used in this work at a later stage for comparison purposes.

The comparison of the measured fission barrier with the calculated fission barrier was complicated by the fact that for any particular set of bombarding conditions a whole range of barriers is produced. Thus, we have assumed in these calculations that the variation of the fission barrier with angular momentum is the same as that predicted by the liquid-drop calculations.[4,5] This assumption reduces the problem to the comparison of one parameter only, i.e., the nonrotating liquid-drop fission barrier, B_f^{nonrot}. According to Cohen and Swiatecki, the liquid-drop expression for B_f^{nonrot} in the region $1/3 < x < 2/3$ is

$$B_s^{nonrot} = 0.38\,(0.75 - x)\,E_s^\circ\,,$$

where

$$E_s^\circ = 17.8\,A^{2/3},\quad x = (Z^2/A)/(Z^2/A)_{crit},\quad \text{and } (Z^2/A)_{crit}$$

is a constant, the value of which is 48.4 according to a recent estimate.[7] Thus the problem of comparing experimental and theoretical B_f^{nonrot} values may be reduced to a re-evaluation of $(Z^2/A)_{crit}$ (see also reference 7). This procedure was used in this work.

A somewhat more detailed description of the methods used in these calculations is presented in reference 5. The following is an outline of the calculation of σ_f/σ_{CN} for any particular excitation energy.

(a) Rotational parameters (L_{max}, etc.) were calculated from bombarding conditions (a classical "triangular" angular momentum distribution was assumed).

(b) Excitation energies following neutron evaporation were calculated for the evaporation chain.

(c) By use of the variable parameter $(Z^2/A)_{crit}$, the value of the fissionability parameter x was calculated, and numerical interpolation in rotational liquid-drop B_f tables of references 5 and 6 was used to calculate the liquid-drop barriers. This two-dimensional interpolation was repeated for many values of angular momentum ranging from zero to L_{max} at fixed intervals, and for many values of x (which varies with the neutrons evaporated).

(d) Branching ratios for the competing processes (fission and neutron evaporation) were evaluated for various angular momenta and for various stages in the evaporation chain. This calculation involved the use of the modified Huizenga and Vandenbosch[8] Γ_f/Γ_n expression (for details see ref. 5; Γ_f and Γ_n are the fission and neutron level widths respectively). This expression involves the level density parameters for fission, a_f, and for neutron emission, a_n. These were chosen to be variables in this calculation (cf. references 1 and 7).

(e) Probabilities for fission for the given values of angular momentum at various stages of the neutron evaporation chain were evaluated by means of the above branching ratios.

(f) The above partial probabilities were integrated numerically over the "triangular" angular momentum distributions, and also over the neutron evaporation chains, giving σ_f/σ_{CN} in the absence of other competing processes. Average values of quantities such as the excitation energy and the angular momentum of the fissioning nucleus were determined during the course of the numerical integrations. The calculation was performed with an electronic computer using a least-squares fitting technique.

The preliminary results for a typical case ($W^{182} + O^{16}$) are presented in Fig. B.10-1 and Table B.10-I. Values of corresponding parameters of Sikkeland, which were obtained from fits to Γ_f/Γ_n values, are also given in Table B.10-I. Here χ^2 is a parameter obtained from the fitting method. Small values of χ^2 are better fits than large values. For values of $(Z^2/A)_{crit} > 50.4$, the fits rapidly become very poor. For values of $(Z^2/A)_{crit} < 48.4$, the number of prefission neutrons increased from less than one to about three at the highest excitation energy. In terms of χ^2, the fits obtained in this region were acceptable, but structure appeared in the calculated excitation function. This region is being studied in more detail.

References

1. T. Sikkeland, Phys. Rev. 135, B669 (1964).
2. G. A. Pik-Pichak, Zh. Eksperim. i Teor. Fiz. 34, 341 (1958).
3. S. Cohen, F. Plasil, and W. J. Swiatecki, in Proceedings of the Third Conference on Reactions Between Complex Nuclei (University of California Press, Berkeley, 1963).
4. S. Cohen, F. Plasil, and W. J. Swiatecki, unpublished results.
5. F. Plasil, UCRL-11193, Dec. 1963.
6. J. R. Huizenga and G. Igo, Nucl. Phys. 29, 462 (1962).
7. D. S. Burnett et al., Phys. Rev. 134, B952 (1964).
8. J. R. Huizenga and R. Vandenbosch, in Nuclear Reactions (North Holland Publishing Co., Amsterdam, 1962).

Table B.10-I. Parameters observed from fits of calculated to experimental excitation functions for fission of W^{182} induced by O^{16}.

	a_n	a_f	a_f/a_n	$(Z^2/A)_{crit}$	χ^2
This work	22.1	24.4	1.11	48.4	0.01475
This work	21.2	27.2	1.28	50.4	0.07290
Reference 1	20.0	25.0	1.25	48.4	---

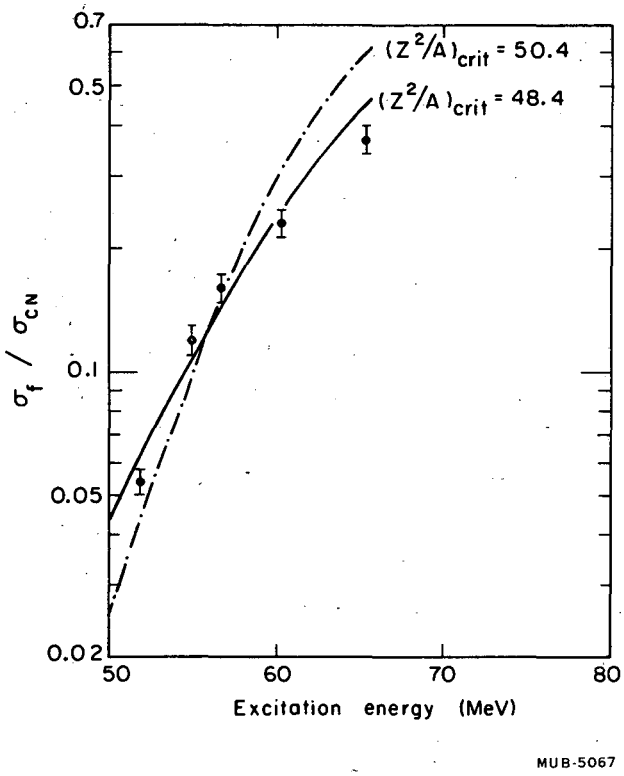

Fig. B.10-1. Calculated (smooth curves) and experimental excitation functions for the reaction $W^{182}+O^{16} \rightarrow Pb^{198} \rightarrow$ fission.

11. INVESTIGATIONS OF THE K x RAYS EMITTED IN THE SPONTANEOUS FISSION OF CALIFORNIUM-252

H. R. Bowman, S. S. Kapoor,* and S. G. Thompson

A direct physical determination of the nuclear charges of the individual primary fragments produced in the spontaneous fission of Cf^{252} has been carried out by simultaneously measuring for each event the kinetic energies of the pair fragments and the energies of the characteristic K x rays emitted nearly along the fission axis, with a high-resolution Li-drifted silicon detector. These measurements also provide information on the mechanism of x-ray emission from the fragments and thereby on the de-excitation process of the fragments.

A weightless amount of Cf^{252} deposited on a thin nickel foil was used in the measurements. The kinetic energies of the pairs of fragments were measured by means of two diffused-junction silicon detectors about 0.05 cm thick placed at a distance of about 1.9 cm on either side of the source foil. A Li-drifted silicon detector having a 3-mm depletion depth was placed about 3.8 cm from the source foil along the direction of the fission detectors to detect the K x rays. The x-ray detector was operated at dry ice temperature to obtain the best energy resolution (FWHM = 3.5 keV). This corresponds to a charge resolution (FWHM) of about 2.7 and 4.0 units for the heavy and the light fragment groups. The energy calibration of the x-ray detector system was made with standard x-ray energy sources. The kinetic energies of both fragments and the coincidence x-ray energies were recorded for each event with a three-dimensional pulse-height analyzer, and were stored event by event in the correlated form on magnetic tape. The data were sorted out with an IBM 7094 computer to obtain the energy distributions of the x rays for the cases in which the fragments of specified masses after the neutron emission were moving at 0 and at 180 deg to the direction of detection of the x rays.

The results have been analyzed to obtain (a) the values of the most probable charge Z_p versus the initial mass M_i of the fragments, (b) the intensities of the x rays per fragment versus the mass M_f of the fragments after neutron emission, and (c) the average time of emission of the x rays from the different fragments. The gross energy spectrum of the K x rays observed from all the fragments is shown in Fig. B.11-1. The typical observed spectra of the x rays when the fragments in the mass interval (M_f) = 139 to 141 are moving at 0 and at 180 deg to the x-ray detector are shown in Fig. B.11-2 (a) and (b). The difference in the energy of the x-ray peaks in the two cases shows that most of the x rays are emitted from the moving fragments, and consequently undergo Doppler shift in the energy. From the measured peak energies, E_1 and E_2, in the two cases, the peak energy E_x of the x ray in the fragment system has been obtained from the relation $E_x = (E_1 + E_2)/2$, for each of the selected fragment mass regions. The width of the observed x-ray energy spectrum arises from the experimental energy resolution, the charge distribution for a single fragment mass, the mass resolution, and finally from the fact that for each value of Z, different x-ray energies arise due to the $K\alpha_1$, $K\alpha_2$, $K\beta_1$, and $K\beta_2$ transitions. For each value of Z, the expected x-ray energy distribution curve was computed by adding four Gaussian distributions, each having the FWHM corresponding to the observed energy resolution and having average energies and intensities as given by Wapstra.[1] From the values of the peak energies of the computed curve and the measured peak energies, E_x, the most probable charge Z_p for each mass region was obtained. The average value, $\overline{M_f}$, of the fragment mass for each mass interval is obtained by $\overline{M_f} = [\int M_f\, P(M_f, x)\, dM]/[\int P(M_f, x)\, dM]$, where $P(M_f, x)$ is the probability of detecting an x ray from mass M_f, and is obtained by unfolding the measured x ray yield function $P'(M_f, x)$ for the experimental mass resolution. The initial mass $\overline{M_i}$ is obtained from $\overline{M_f}$ by use of neutron yield data, and the plot of measured Z_p versus $\overline{M_i}$ is shown in Fig. B.11-3.

On the hypothesis that the Z_p corresponds to the maximum energy released in fission, and using the mass formula of Cameron and Seeger, Milton[2] has calculated the curves for Z_p versus M_i which are also shown in Fig. B.11-3. The two other curves shown in the same figure are calculated on the hypothesis of equal charge displacement and unchanged charge distribution. The $Z_p(M_i)$ function calculated on the basis of the hypothesis of the equal charge displacement with respect to the initial masses of the fragments is seen to be in better agreement with the experimental values.

The analysis of the data to obtain the intensities of the x rays per fragment and the average time of emission of the x rays is in progress. The average time of emission of the x rays is being determined by comparing the measured intensities of the x rays in the direction of and opposite to the direction of motion of the specified fragment masses. The preliminary

results show that the average time of x-ray emission is different for the different fragment masses and varies from about 0.1 nsec to 0.9 nsec. The x-ray intensity per fragment also varies significantly for the different fragment masses.

Footnote and References

* Visitor from Atomic Energy Establishment, Trombay, Bombay, India.

1. A. H. Wapstra, G. J. Nijgh, and R. Van Lieshout, Nuclear Spectroscopy Tables (North-Holland Publishing Company, Amsterdam, 1959).
2. J. C. Douglas Milton, Fission Energy Tables and an Application to Nuclear Charge Division, UCRL-9883 Rev., Jan. 1962.

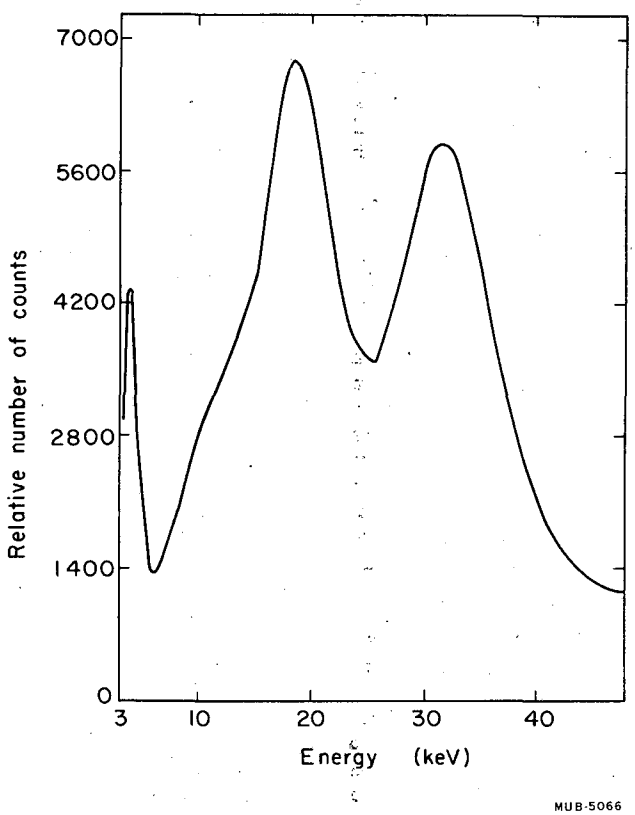

Fig. B. 11-1. The energy distribution of the K x rays from all fragments.

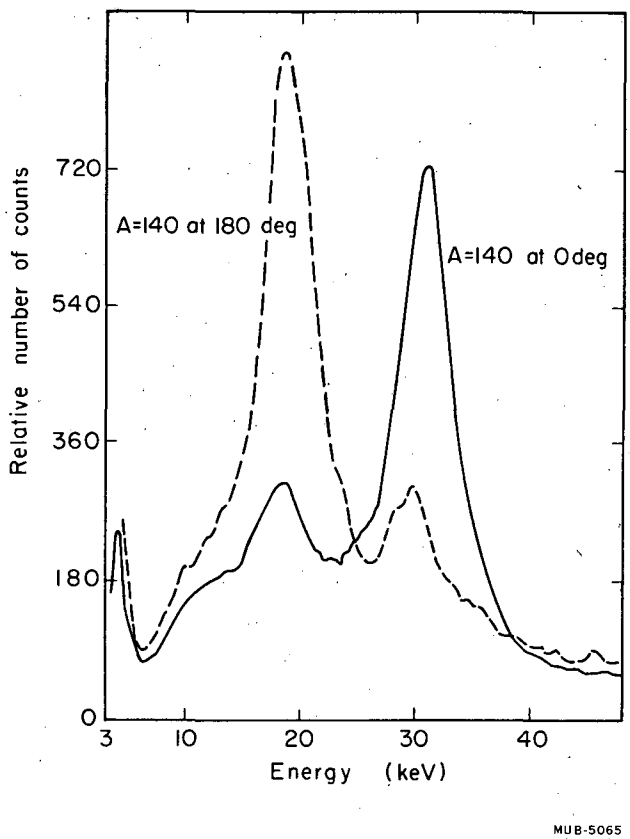

Fig. B.11-2. The energy distribution of the K x rays in coincidence with fragments in the mass interval $M_f = 139$ to 141. The solid line is the distribution for the case in which these heavy fragments are moving in the direction of the x-ray detector. The dashed line is the distribution for the case in which these heavy fragments are moving away from the x-ray detector.

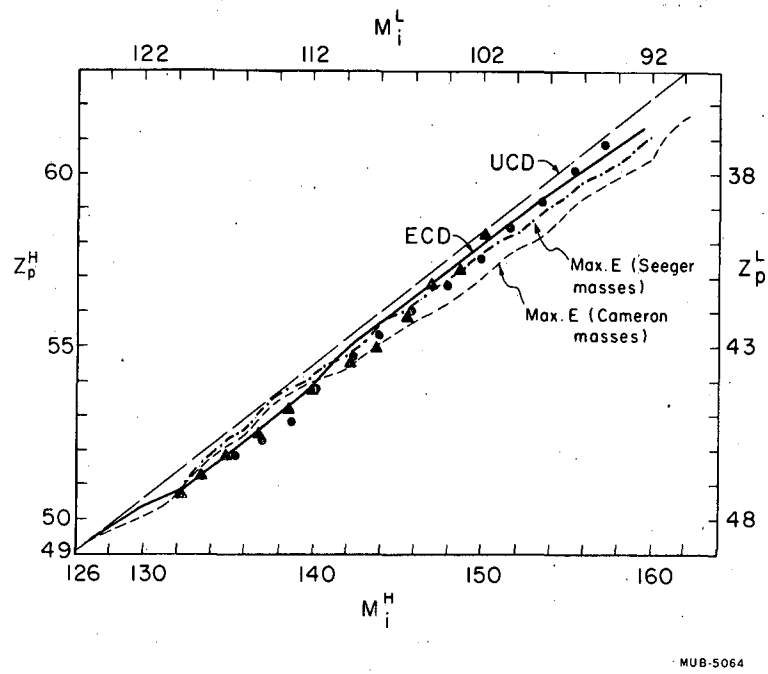

Fig.B.11-3. The plot of measured most probable charge versus initial fragment masses. The data points shown were obtained from the analysis of the heavy (O) and the light (Δ) fragment data respectively. Curves calculated on the hypothesis of equal charge displacement (ECD), unchanged charge distribution (UCD), and the maximum energy released are also shown in the figure.

12. DISTRIBUTION IN ENERGY LOST BY CHARGED PARTICLES IN PASSING THROUGH THIN ABSORBERS†

Mary F. Reed, Nolan F. Mangelson, and George Rogers

The method for calculating the distribution in energy lost by charged particles in passing through thin absorbers, as advanced by Symon,[1] is applicable to protons and heavier charged particles with kinetic energies from approximately 0.01 to 10 times their rest energies. The average energy loss in the absorber may not exceed 0.1 the kinetic energy of the particle. Under these conditions the probability that a particle will lose a large fraction of its kinetic energy in a single collision with the electrons of the absorbing material is small. This method takes only collisions with electrons into account. These collisions are independent events; therefore, particles of a given kind and energy do not all lose exactly the same amount of energy in traversing a given thickness of material.

Symon's method involves the calculation of parameters depending on the mass, atomic number, and energy of the incident particle and the mass number, atomic number, and thickness of the absorbing material. These parameters are then used to extract additional parameters from two graphs. By use of these additional parameters and a third graph, the energy-loss distribution can be calculated. The report describes the calculations in detail and includes the necessary graphs.

Curves giving the variation in full width at half maximum (FWHM) of the energy distribution as a function of absorber thickness for protons, deuterons, and α particles at different energies in silicon and other elements are shown in Figs. B. 12-1, B. 12-2, and B. 12-3.

Footnote and Reference

† Condensation of UCRL-11602, Aug. 1964.

1. K. R. Symon, Fluctuations in Energy Lost by High-Energy Charged Particles in Passing Through Matter (Thesis), Harvard University, Jan. 1948.

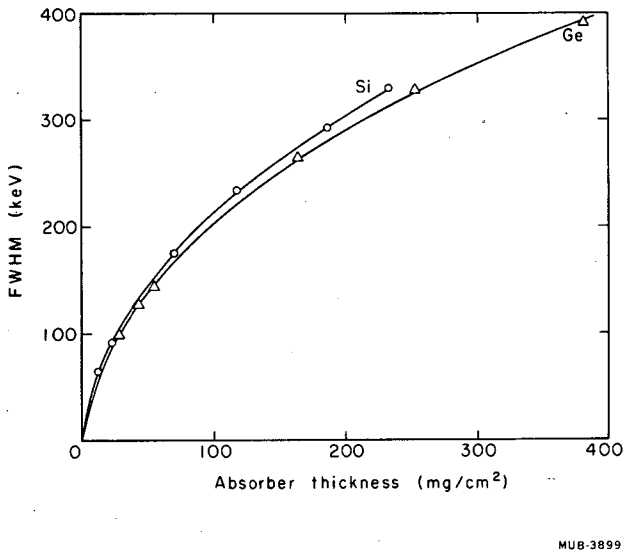

Fig. B. 12-1. Variations of FWHM with absorber thickness for 25-MeV protons in Si and Ge.

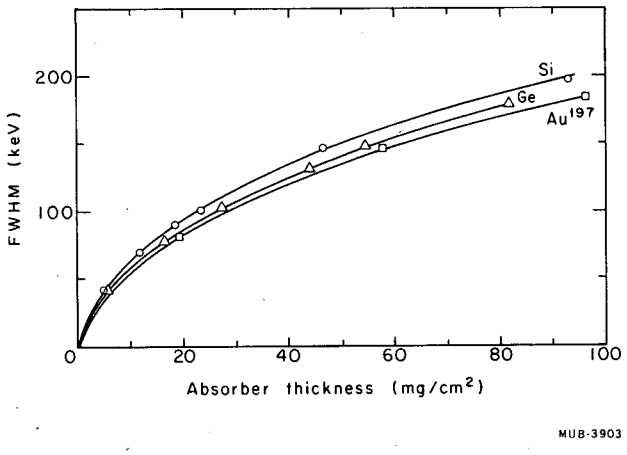

Fig. B. 12-2. Variations of FWHM with absorber thickness for 25-MeV deuterons in Si, Ge, and Au^{197}.

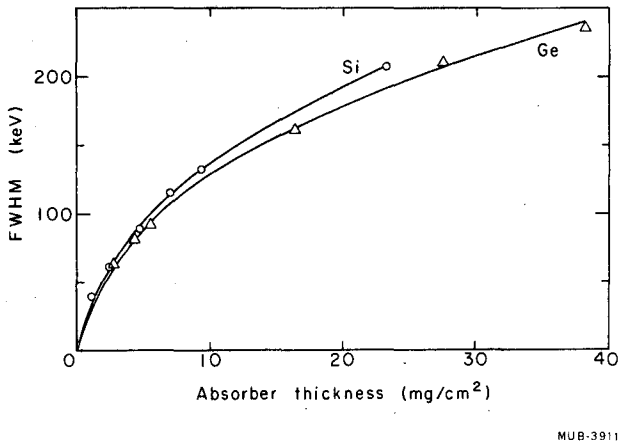

Fig. B. 12-3. Variations of FWHM with absorber thickness for 60-MeV α particles in Si and Ge.

C. NUCLEAR REACTIONS AND SCATTERING

1. FINAL-STATE INTERACTIONS IN THE $He^3(d, t)2p$ REACTION AT 24.7 AND 33.4 MeV†

H. E. Conzett, E. Shield, R. J. Slobodrian, and S. Yamabe*

Recent letters have reported experimental determinations of triton energy spectra from the $He^3(d, t)$ reaction at E_d = 28 MeV[1] and at 20 and 25 MeV.[2] The spectra of reference 1 were obtained with approximately 1.25 MeV energy resolution, and a broad peak near the high-energy end was interpreted as resulting from the formation of an unbound state of He^2 with a mean lifetime $\tau = (0.2 \pm 0.1) \times 10^{-21}$ sec. The observed angular variation of the peak was consistent with a pickup reaction mechanism. The spectra of reference 2 were obtained with an energy resolution of about 0.5 MeV, and consisted of continuum spectra with broad asymmetrical peaking near the high-energy limit. These authors noted a resemblance to neutron spectra from the $D(p, n)2p$ reaction[3,4] whose shape was explained in terms of a final-state interaction[5,6] between the two protons, and they pointed out the necessity both for more precise data and for quantitative calculations in the continued investigation of this $He^3(d, t)2p$ reaction.

We report here experimental results along with calculations based on the 2p final-state interaction interpretation, and we believe this to be the proper explanation of our data.

Triton spectra were measured with an energy resolution of approximately 120 keV at deuteron energies of 24.7 and 33.4 MeV, with the Berkeley variable-energy 88-inch cyclotron. Measured beam ranges in aluminum were converted to energies.[7] The counter assembly consisted of two silicon detectors, a ΔE and E set, with collimation which provided an angular resolution of 0.4 deg.[8] Pulses from these detectors were fed into a particle-identifier system, the output of which was used to gate on a 400-channel pulse-height analyzer whenever a triton identification occurred. The added $(\Delta E + E)$ triton pulse spectrum was then displayed on the analyzer. Also, triton spectra from the $N^{14}(d, t)N^{13}$ reaction were obtained for the purpose of calibration of the energy scale, which we believe to be accurate within 100 keV. Figure C.1-1 exhibits a spectrum at θ_L = 8 deg taken at 33.4 MeV. The observed differential energy spectra are fitted with final-state interaction theoretical curves. The particular form used for the calculations was that of Migdal,[5] in which the 2p wave function includes Coulomb effects, and for comparison we show that of Watson,[9] applicable in the absence of electrostatic effects. The center-of-mass differential cross section is given by

$$\frac{d^2\sigma}{dE d\Omega} = g(\theta) \frac{2\pi}{v} |T(E_{2p})|^2 \rho(E_T), \tag{1}$$

where E_{2p} is the relative energy of the two protons in their own c.m. system, E_T is the corresponding c.m. triton energy, $g(\theta)$ is an angular dependent factor peculiar to the reaction mechanism, v is the relative velocity of the initial particles, and $\rho(E_T)$ is the phase-space factor of the observed particles, in this case the tritons. $T(E_{2p})$ is the transition matrix element, which gives the "enhancement" of the cross section due to the final-state interaction (or correlation) of the two protons. In Migdal's treatment this is just proportional to $|\phi_{2p}(q)|$, the 2p wave function, where q is the relative momentum.

To fit our data we have used the expressions

$$|T|^2 \propto \frac{C(\eta)\,(E_{2p})^{1/2}}{C^2(\eta)\,E_{2p} + \frac{\hbar^2}{m_p}\left[-\frac{1}{a_p} - \frac{h(\eta)}{R} + \gamma E_{2p}\right]^2}, \tag{2}$$

where $C(\eta) = 2\pi\eta/(e^{2\pi\eta}-1)$ is the so-called Coulomb penetration factor, a_p is the scattering

length, $\eta = e^2/\hbar v$ and $h(\eta) = \mathrm{Re}\,\frac{\Gamma'(-i\eta)}{\Gamma(-i\eta)} - \ell n\eta$, $R = \hbar^2/m_p e^2$, and $\gamma = 3.4\times10^{11}$ MeV^{-1} cm^{-1}, and also

$$|T|^2 \propto \sin^2\delta_0/E_{2p}\,, \tag{3}$$

where δ_0 was taken to be the singlet s-wave p-p phase shift, as defined in the expression for the scattering amplitude

$$f(\theta) = f_c(\theta) + 1/(2ik)\, e^{2i\zeta_0}\,(e^{2i\delta_0} - 1), \tag{4}$$

where $\zeta_0 = \mathrm{Arg}\,\Gamma(1 + i\eta)$, and finally,

$$\rho(E_T) = C(E_T)^{1/2}\,(E_{max} - E_T)^{1/2},$$

where E_{max} is the maximum triton energy in the c. m. system. Expression (2) corresponds to the treatment by Migdal,[5] and expression (3) is due to Watson.[9] The theoretical c. m. spectra were converted to the laboratory system by using the appropriate Jacobian determinant and experimental values for $g(\theta)$. The high-energy region of the lab spectra is quite insensitive to the angular dependence $g(\theta)$, particularly at small lab angles. It is clear from Fig. C. 1-1 that expression (2) is most consistent with the data for a value of $a_p = -7.7$ F, which is the scattering length obtained from low-energy p-p scattering experiments.[8]

A triton spectrum from this $He^3(d, t)2p$ reaction obtained with very good statistical accuracy and high-energy resolution could be used to determine independently a value of a_p. A difference from the already established value could provide quantitative information on the question of spectrum distortion due to a p-t final-state interaction, and this is of interest with respect to the determination of the n-n scattering length, recently extracted from just such final-state interaction spectra from the D(n, p)2n reaction.[10, 11]

We thank J. Meneghetti and E. Cory for their assistance in the design and construction of the gas target chamber, and we are indebted to D. A. Landis and F. S. Goulding for their contribution in the setting up of the electronics.

Footnotes and References

† Condensation of paper in Phys. Rev. Letters 13, 625 (1964).
* Now at the Physics Department, Osaka University, Osaka, Japan.
1. O. M. Bilaniuk and R. J. Slobodrian, Phys. Letters 7, 77 (1963).
2. K. P. Artjomov, V. J. Chuev, V. Z. Goldberg, A. A. Ogloblin, V. P. Rudakov, and J. N. Serikov, Phys. Letters 12, 53 (1964).
3. C. Wong, J. Anderson, C. Gardner, J. McClure, and M. Nakada, Phys. Rev. 116, 164 (1959).
4. B. V. Rybakov, V. A. Sidorov, and N. A. Vlasov, Nucl. Phys. 23, 491 (1961).
5. A. B. Migdal, Soviet Physics-JETP 1, 2 (1955).
6. W. H. Heckrotte and M. MacGregor, Phys. Rev. 111, 593 (1958).
7. C. Williamson and J. P. Boujot, Tables of Range and Rate of Energy Loss of Charged Particles of Energy 0.5 to 150 MeV, Report CEA-2189, Center of Nuclear Studies, Saclay.
8. R. H. Stokes, J. A. Northrup, and D. Boyer, Rev. Sci. Instr. 29, 61 (1958); W. L. Briscoe, Rev. Sci. Instr. 29, 401 (1958); F. S. Goulding, D. A. Landis, J. Cerny, III, and R. H. Pehl, IEEE Trans. Nucl. Sci. NS-11, 388 (1964).
9. Kenneth M. Watson, Phys. Rev. 88, 1163 (1952).
10. M. Cerineo, K. Ilakovac, I. Slaus, P. Tomas, and V. Valkovic, Phys. Rev. 133, B948 (1964).
11. V. K. Voitovetskii, I. L. Korsunskii, and Y. F. Pazhin, Phys. Letters 10, 107 (1964).

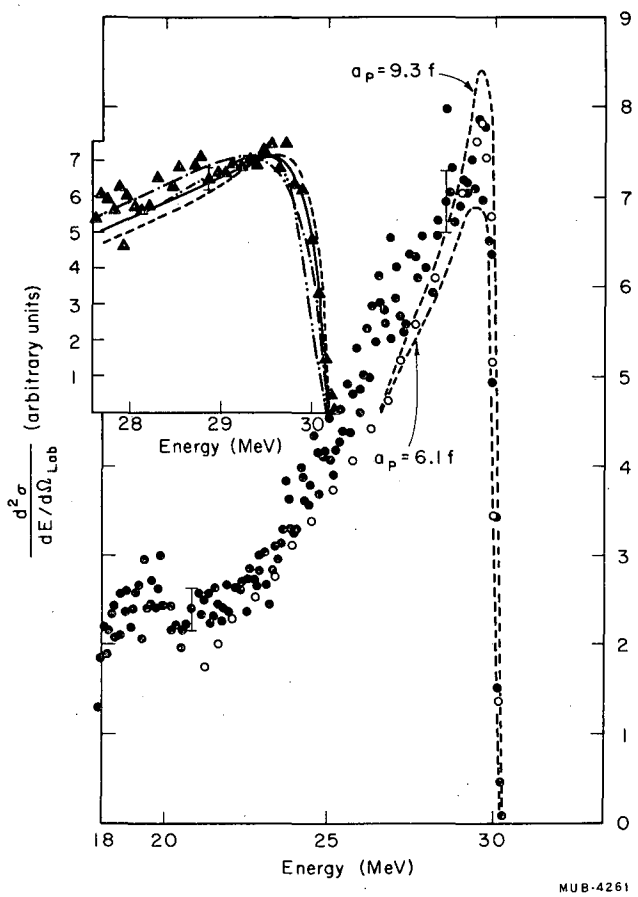

Fig. C. 1-1. $_3$ Triton spectrum of the reaction $He^3(d, t)2p$ at θ_L = 8 deg, E_d = 33.4 MeV. Solid dots are the experimental points. Open circles correspond to the calculated spectrum, with a_p = - 7.7f. The dashed lines are calculated spectra with the indicated values of a_p. The high-energy side of the spectrum is shown via a magnified energy scale on the upper left; the solid triangles are the experimental points, the solid line is the calculated spectrum with a_p = - 7.7 f, the dashed line was calculated with a_p = - 9.3 f, the dash-dot line was calculated with a_p = - 6.1 f, and the dashed double-dot line corresponds to expression (3) with a_p = - 7.7 f.

2. A MICROSCOPIC DESCRIPTION OF INELASTIC SCATTERING: APPLICATION TO NICKEL ISOTOPES†

Norman K. Glendenning and Marcel Vénéroni*

The usual method of analyzing inelastic alpha scattering has been to adopt the early Bohr-Mottleson description of the nuclear states. We shall refer to this as the macroscopic picture. The alternative is to use detailed wave functions describing the nucleon motion. Excitation of states differing only in the coordinates of a single nucleon was considered earlier.[1] Recently Sanderson and Wall[2] have used Gillet's wave functions for Ca^{40} to obtain a macroscopic description of the excitation of the 3^- collective states. Such collective states are built up from a superposition of many single-nucleon excitations.

In the distorted-wave (first) Born approximation the inelastic scattering amplitude for excitation of the state J in an even nucleus is given by the matrix element between the distorted waves in the incident and outgoing channels of

$$\left\langle \Psi_J^M(A) \middle| V(\mathbf{r}, A) \middle| \Psi_0(A) \right\rangle \equiv \mathcal{F}_J(r)\, Y_J^{M*}(\hat{\mathbf{r}}).$$

Here V is the interaction between the incident nuclide (coordinate r) and the nucleus (A), whose wave functions are denoted by Ψ. This equation serves to define the form factor $\mathcal{F}_J(r)$ once a nuclear model and nucleus-alpha interactions, V, have been chosen. In the macroscopic picture, V has the deformation of the nucleus. The corresponding form factors for λ-pole deformations are

$$\mathcal{F}_J(r) \propto \begin{cases} \delta_{J\lambda}\,\beta_\lambda\, R\, \partial V(r)/\partial r, & \text{one } \lambda \text{ phonon,} \quad (1a) \\ \beta_\lambda^2\, R^2/2\, \partial^2 V(r)/\partial r^2, & \text{two } \lambda \text{ phonons,} \quad (1b) \end{cases}$$

for one- and two-phonon states. Both of these refer to the direct excitation of the final state. The two-step scattering going through an intermediate state cannot be easily evaluated in the distorted-wave method, although it poses no problem in the general coupled-channel solution of the scattering.

Following a method developed earlier,[1] the form factors in the microscopic description can be obtained in the closed form

$$\mathcal{F}_J(r) = -V_0 \exp(-\beta\nu/(\beta+\nu)\, r^2) \sum_{m=0}^{\bar{m}} D_m (\beta r/\sqrt{\nu})^{2m+J}. \quad (2)$$

These can of course have more complicated structures than the form factors of the macroscopic model. To what extent the two descriptions yield similar form factors is mentioned below. The ingredients of the model that lead to the form of Eq. (2) are (a) harmonic oscillator wave functions for bound nucleons (parameter $\nu = m\omega/\hbar \approx A^{-1/3}$) and (b) Gaussian force between alpha particle and nucleons: $V_0 \exp(-\beta r^2)$. The upper limit on the polynomial is $\bar{m} = 2N$, where N is the oscillator quantum number of the highest shell used in calculation of the nuclear structure. For the nuclear states described in the first paragraph the coefficients D_m are certain linear combinations of elementary (single-particle) excitations. We will give more details in a fuller report.

We have computed the form factors of many excited states of all the even isotopes of nickel from mass 58 to 66, using the wave functions computed by Arvieu et al.[3] For any variation of ν and β (within reasonable limits, at least) the qualitative features of the form factors remain unchanged. The qualitative shape and the magnitude of the form factors depend on the degree of correlation among the nucleons. For example, the form factor of the lowest 2+ level is always larger than for any of the other levels of this spin. Its shape is roughly that corresponding to the one-phonon shape of Eq. (1), while that of the second 2+ level is always reduced in magnitude, and has usually the shape characteristic of a two-phonon level.

In the figures we give a sample of our results. It is interesting to note that the form factor of the $J = 2_1$ level, usually associated with one phonon of excitation, has the one-phonon shape, while that of the 2_2 level has the two-phonon shape in Ni^{62} but the one-phonon shape in Ni^{58}. The 0_2 has a form factor with two nodes having no precise counterpart in the macroscopic picture, but corresponding in spirit to the two-phonon shape, while the 4_1 level has a form factor corresponding to a single four-pole phonon state rather than to a state of two quadrupole phonons.

The differential cross sections for several levels have been computed. The well depth, V_0, of the α-nucleon interaction was chosen as 52 MeV to obtain agreement with the cross section for the transition to the 2_1 level. The other two parameters have values $\nu = 0.214\ F^{-2}$ and $\beta^{-1/2} = 2.5$ F. While 2.5 may at first sight seem to be a rather long range, one knows that the α radius is about 1.7 F and its range of influence must certainly extend beyond this, perhaps by a substantial fraction of the nucleon-nucleon force range. The optical-model parameters used reproduce the elastic scattering. Two sets were used, as shown in the table. Both give substantially the same results for both the elastic and inelastic differential cross sections, so that

we were unable to discriminate between them as we had hoped to do.

In our calculations so far we have found that the angular distributions for alpha scattering are not sufficiently sensitive to the interior region to yield any information therefrom, a result consistent with the lack of sensitivity to the two sets of optical-model parameters and implying that the particles that do penetrate beyond the surface region are absorbed. The absolute cross sections of course do depend on the magnitudes of the form factors in the surface region, but this is a weaker dependence on nuclear structure than one would hope for.

Perhaps the absorption of nucleons will be sufficiently small that one can investigate the details of the nuclear wave functions. We are investigating currently what are the best experimental conditions that still yield the sensitivity we want.

We wish to thank Dr. Bernard G. Harvey et al. for kind permission to use their data before publication. To Jeannette Mahoney we are indebted for operating the optical-model elastic scattering code.

Footnotes and References

† Condensation of paper to be submitted to Phys. Letters.

* Summer visitor during 1964 at UCLRL. On leave from Laboratory of Nuclear Science, M.I.T., Cambridge, Mass. Permanent address Laboratoire de Physique Théorique, Orsay, France.

1. N. K. Glendenning, Phys. Rev. 114, 1297 (1959).
2. E. Sanderson and N. S. Wall, Phys. Letters 2, 173 (1962).
3. R. Arvieu, E. Baranger, M. Véneroni, M. Baranger, and V. Gillet, Phys. Letters 4, 119 (1963).

Table C. 2-I. Two sets of optical-model parameters which reproduce the elastic scattering of alpha particles on Ni^{62} at 50 MeV.[a]

V	W	r_0	r_1	a	b
50	21	1.3	1.2	0.572	0.58
101	42	1.2	1.2	0.563	0.58

[a] The potential has the form $V_{Coul}(r) + V f(\frac{r-R}{a}) + W f(\frac{r-R}{b})$, where $R = r_0 A^{1/3} + r_1$, and f is the Woods-Saxon shape. The Coulomb potential is that of a uniform sphere of radius $r_0 A^{1/3}$.

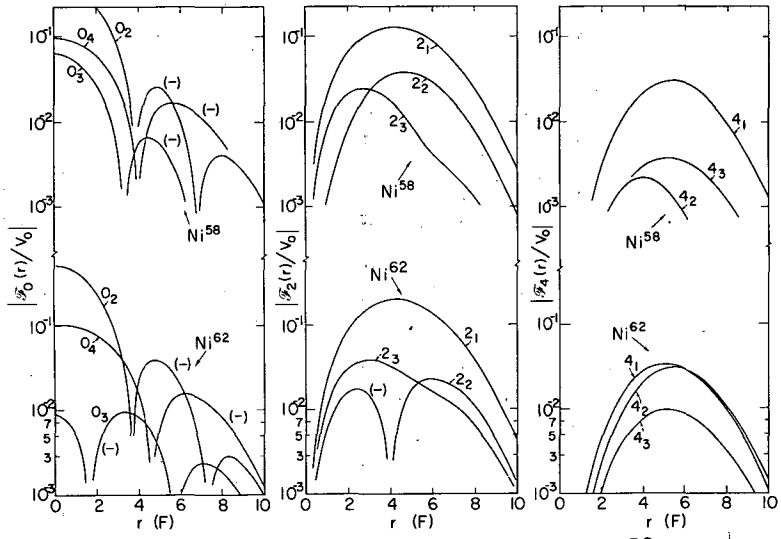

Fig. C.2-1. Form factors for some levels in Ni^{58} and Ni^{62} computed from the microscopic wave functions. The (-) signs indicate a change of sign in the form factor which we cannot otherwise show on a logarithmic plot.

3. THE POLARIZATION OF 40-MeV PROTONS ELASTICALLY SCATTERED FROM DEUTERONS*

H. E. Conzett, H. S. Goldberg, E. Shield, R. J. Slobodrian, and S. Yamabe†

The recent development of a variable-energy polarized proton beam at the Berkeley 88-inch cyclotron has made it possible to extend measurements[1] of the proton polarization induced in the elastic scattering of protons from deuterons below 100 MeV. Polarized protons, available at energies from 12 to 60 MeV with polarization ranging from 80 to 100%, are produced as recoil protons (near 130 deg c.m.) from a liquid-nitrogen-cooled gaseous hydrogen target placed in the alpha-particle beam.

It is expected that determinations of polarization in nucleon-deuteron scattering at energies below 100 MeV should provide information useful to the understanding of the very marked difference between the polarization induced in nucleon-nucleon scattering and that resulting from the scattering of the nucleon from a few-nucleon system.[2] Kowalski and Feldman[3] have recently made an impulse approximation (IA) calculation of the polarization in p-d scattering at 150, 90, and 40 MeV; we have measured the polarization at 40 MeV in order to make a direct comparison with their prediction.

The experiment was carried out in two steps, the first of which was to determine the polarization of the 40-MeV proton beam. The known[4] 99% polarization (near 130 deg c.m.) of 10-MeV protons scattered from He^4 was taken as our starting point. The same c.m. energy is achieved with 40-MeV α particles incident on a hydrogen target; so, with this condition fulfilled, recoil protons taken at 23.5 deg (133 deg c.m.) with respect to the direction of the incident alpha beam provided a 20-MeV beam polarized to 99%. We then measured the left-right asymmetry, $\epsilon = (L-R)/(L+R)$, in the scattering of this beam from He^4. For elastic scattering, the asymmetry is given by $\epsilon(\theta) = P_1 P(\theta)$, where P_1 is the fractional polarization of the proton beam and $P(\theta)$ is the proton polarization that would be induced in the scattering of unpolarized protons by the target. Thus, from $\epsilon(\theta) = 0.99\, P(\theta)$ we determined that the maximum polarization in p-He^4 scattering at 20 MeV occurs at $\theta_{c.m.} = 126$ deg with a value of $+0.82 \pm 0.03$. The sign is given in accord with the Basle convention (positive polarization in the direction of $\vec{k}_{in} \times \vec{k}_{out}$). The procedure was repeated at an alpha beam energy of 80 MeV, which produced at 126 deg c.m. a 41-MeV beam of recoil protons with a polarization $P_1 = +0.82 \pm 0.03$ and an intensity of approx-

imately 4×10^7 protons/sec for 10 μA of incident α particles. This beam was then scattered from a deuterium gas target at a mean energy of 40.3± 0.6 MeV, and the measured asymmetries gave the polarizations $P(\theta) = \epsilon(\theta)/0.82$.

Eight detectors, consisting of CsI crystals mounted on Dumont 6363 photomultiplier tubes, were used to record simultaneously asymmetries at four scattering angles. Pulses from each detector were routed to separate quadrants of two 400-channel pulse-height analyzers. Figure C.3-1 shows pulse-height-analyzer spectra taken at equal left and right scattering angles in the forward hemisphere, and one sees, in addition to the peak of elastically scattered protons, a peak of recoil deuterons. Such recoil-deuteron asymmetries gave the asymmetries of the associated backward scattered protons, and thus provided consistency checks on the back-angle proton data.

Our results are presented in Fig. C.3-2. Also shown are the results calculated by Kowalski and Feldman[3] in the approximation that the scattering process is a superposition of the single scatterings of the incident nucleons from each of the target nucleons. Multiple scattering effects and pickup scattering[5,6] were not included. The CA curve results from the Chew form of the IA, applicable to regions of small momentum transfers. The LA (linear approximation) curve results from including larger momentum transfers but not considering off-the-energy-shell effects. Finally, the FA curve results from the inclusion of off-the-energy-shell scattering. Even though one ignores the angular region of pickup scattering, $\theta_{c.m.} > 130$ deg, our results do not agree quantitatively with any one of the calculated curves. In fact, the discrepancy between experimental and calculated results increases in going to the more complete versions of the calculation. The FA result provides the best fit to data at 150 MeV,[6] so the nonapplicability of the IA at 40 MeV or the importance of multiple scattering corrections[7] at this energy is indicated.

We acknowledge the invaluable assistance of the accelerator technicians under the direction of J. R. Maneghetti in setting up the polarized proton beam facility, and that of D. A. Landis and F. S. Goulding in the design of the electronics.

Footnotes and References

* Shortened version of article in Phys. Letters 11, 68 (1964).
† Now at the Physics Department, Osaka University, Osaka, Japan.

1. H. E. Conzett, G. Igo, and W. J. Knox, Phys. Rev. Letters 12, 222 (1964).
2. For data at energies below 20 MeV see references in ref. 1; at 46MeV a p-p polarization of 0.012± 0.013 has been reported by J. N. Palmieri et al., Ann. Phys. 5, 299 (1958).
3. K. L. Kowalski and D. Feldman, Phys. Rev. 130, 276 (1963).
4. L. Rosen and J. E. Brolley, Jr., Phys. Rev. 107, 1454 (1957); R. I. Brown, W. Haeberli, and J. X. Saladin, Nucl. Phys. 47, 212 (1963).
5. G. F. Chew and M. L. Goldberger, Phys. Rev. 77, 470 (1950).
6. H. Postma and R. Wilson, Phys. Rev. 121, 1229 (1961).
7. G. F. Chew and G. C. Wick, Phys. Rev. 85, 639 (1952).

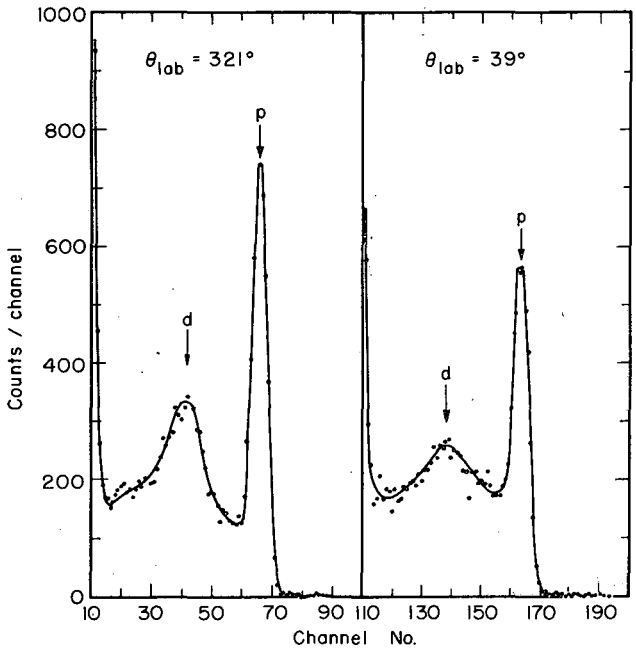

Fig. C. 3-1. Pulse-height spectra taken at equal right and left scattering angles (θ_{lab} = 39 deg), showing the elastic proton peak (p) and the recoil deuteron peak (d).

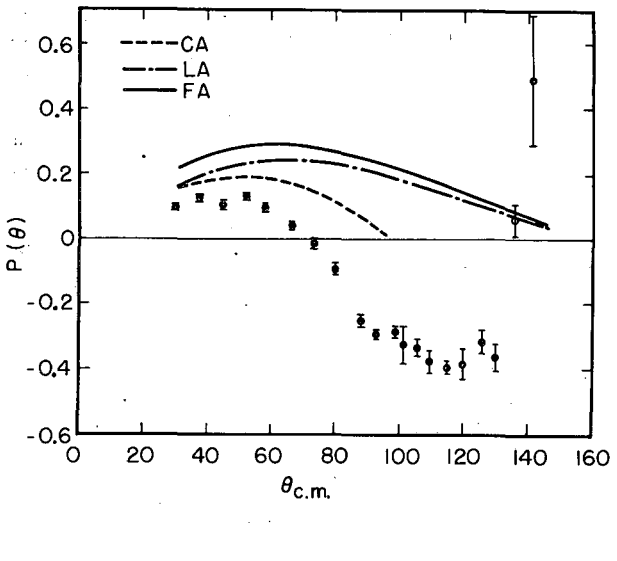

Fig. C. 3-2. Proton polarization, P(θ), in p-d elastic scattering at 40 MeV. The curves labeled CA, LA, and FA are results from impulse-approximation calculations of reference 3.

4. NUCLEAR SPECTROSCOPY WITH TWO-NUCLEON TRANSFER REACTIONS

Norman K. Glendenning

In the reactions considered, a pair of nucleons is transferred between a nucleus and a light nuclide. The pair is presented to or taken away from the nucleus in a specifically correlated condition predicted by the properties of the light nuclides involved. Nuclear states will have greatly varying proportions of the appropriate correlation, thus accounting in part for the wide range of intensities observed for levels in a given nucleus. In addition, strongly excited states must have a parentage based on the lighter nucleus. The wave functions obtained from a microscopic model must reproduce the observed intensities, which depend on rather intimate details. These reactions therefore provide a severe check of the wave functions.

A measure of the appropriate correlations and parentage is provided by structure amplitudes, G, which we have introduced and defined in a fuller report.[1]

In any microscopic nuclear model, the correlations are reflected in the wave functions by mixtures of several of the basic states of the model. Once these wave functions have been obtained by a nuclear structure calculation, the structure amplitudes can be constructed. This has been illustrated by a number of examples. To make a conclusive check on whether the wave functions correctly reproduce the observed intensities, one would have to carry out a calculation of the transfer amplitude which carries the information on the scattering states and the kinematics, but does not depend on the nuclear structure. However, the structure amplitudes

alone are sufficient to suggest which states will be strongly populated, and with what multipolarity.

The following example will serve to show how a wave function containing only small admixtures nonetheless contains important correlations that are absent in the dominant configuration taken alone. The reaction is $C^{12}(\alpha, d)N^{14}$ going to the ground state. True[2] has calculated the ground-state wave function to be

$$\chi = 0.9666\,(p_{1/2}{}^2) + \cdots .$$

For many purposes this wave function would be considered pure, since it has only 7% admixtures of other configurations. However, for those phenomena that are sensitive to the correlations between nucleons the admixtures are important. The projection of the relevant part of the center-of-mass motion from the above wave function is shown in Fig. C. 4-1. For comparison the projection for the pure configuration above is also shown. In the important surface region there is a factor of 1.5 to 2 enhancement due to the correlations, and in the cross section this makes a factor of 3 to 4.

References

1. N. K. Glendenning, Nuclear Spectroscopy With Two-Nucleon Transfer Reactions, Phys. Rev. (in press).
2. W. W. True, Phys. Rev. 130, 1530 (1963).

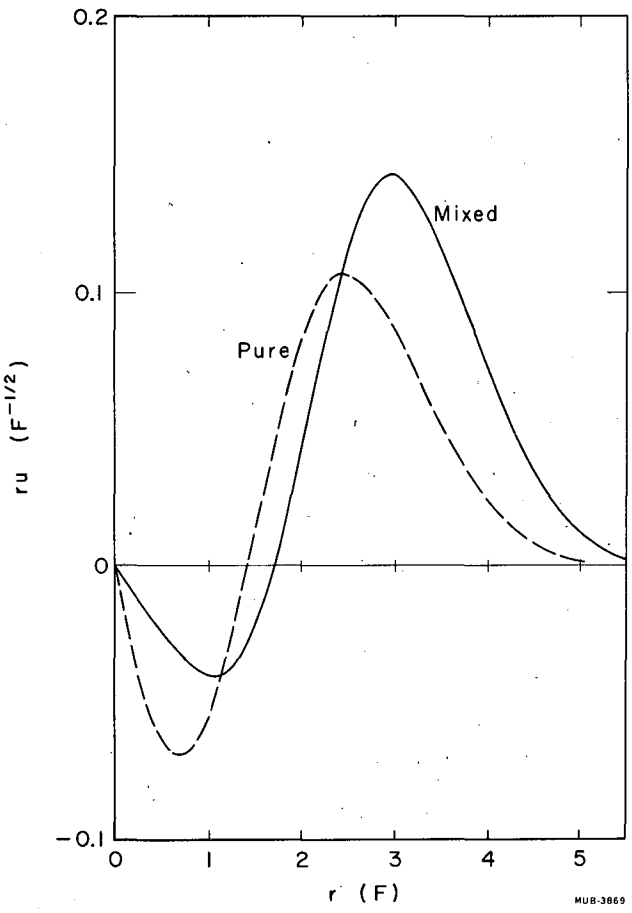

Fig. C. 4-1. Projection of the N^{14} ground-state wave function for the center of mass of the last neutron and proton appropriate to the $C^{12}(\alpha, d)N^{14}$ reaction. The L = 0 part is shown for the configuration mixed wave function and for the dominant configuration alone.

5. THE ELASTIC SCATTERING OF α PARTICLES BY HELIUM BETWEEN 53 AND 120 MeV*

P. Darriulat,† G. Igo, H. G. Pugh, and H. D. Holmgren‡

Using the 88-inch cyclotron and the 17-inch scattering chamber, we have measured the differential cross section for elastic scattering of α particles by He^4 at center-of-mass angles between 10 deg and 90 deg at laboratory-system bombarding energies of 53.40± 0.15, 58.49± 0.16, 63.91± 0.18, 69.91± 0.20, 77.55± 0.22, 99.60± 0.28, and 119.86± 0.34 MeV. The relative and absolute cross sections are both accurate to 1 or 2%, and the scattering angles are known within ±0.02 deg. The results are shown in Fig. C. 5-1.

The angular distribution at 53.40 MeV is very similar to that at 47.1 MeV,[1] with maxima at 90 deg and at about 55 deg. As the energy is increased the angular distributions change systematically: a maximum appears at about 30 deg and moves slowly to smaller angles, while the 55-deg maximum decreases until barely a trace of it remains at 119.86 MeV. The cross section at large angles decreases rapidly as the energy increases; however, the maximum at 90 deg persists at all energies though its width decreases slowly with increasing energy.

These angular distributions were analyzed in terms of complex phase shifts, $\delta_\ell \equiv \mathrm{Re}(\delta_\ell) + i\,\mathrm{Im}(\delta_\ell)$, with the IBM 7094 computer. The fits to the differential cross sections are shown in Fig. C. 5-2.

The real parts of the phase shifts are shown in Fig. C. 5-3, together with those obtained at lower energies;[2, 3] the imaginary parts of the phase shifts and the calculated total reaction cross sections are shown in Fig. C. 5-4.

The following simple argument indicates how the real parts of the phase shifts may be understood in terms of a two-body effective potential.

The phase shifts (Fig. C. 5-3) all start from zero at zero energy, since Be^8 has no bound states. As the energy increases each partial wave's phase shift begins to deviate from zero in the positive direction, at an energy corresponding to an impact parameter of about 5 F, and then passes through resonance. This behavior implies that the nuclear interaction must be attractive at large radii. Above the resonance the $\ell = 0$ and $\ell = 2$ phase shifts decrease monotonically, eventually becoming negative at impact parameters of 1 to 2 F. This latter behavior indicates that the interaction has a repulsive core of radius 1 to 2 F. For the higher partial waves the centrifugal barrier prevents investigation of the central regions of the potential; the $\ell = 4$ phase shift has hardly begun to decline at 120 MeV and the higher phase shifts are still rising.

We have analyzed the smooth energy dependence of the phase shifts, using a potential constructed by adding two Saxon-Woods potentials: a real repulsive core and a complex attractive potential of longer range. We first attempted to fit the phase shifts, using the same potential for each partial wave. This attempt failed: it was found that a more attractive outer region was required for the higher angular momenta. We therefore used a different set of potential parameters for each partial wave. The best fits obtained in this way are shown in Fig. C. 5-3. The real parts of the potentials are quite well defined by the phase shifts. They are displayed in Fig. C. 5-5, which shows only those parts of each potential corresponding to a total potential (centrifugal + nuclear) smaller than 60 MeV, the maximum c.m. energy available for the measurements.

It is interesting to examine the potentials we have obtained in the light of theoretical predictions.[4] Calculations of the interaction have used the cluster approximation, in which the α particles are assumed to be in their ground state and unpolarized, while the interaction results from the nucleon-nucleon forces which operate between nucleons in the two clusters. Antisymmetrization of the wave function with respect to the nucleon coordinates and spins introduces terms due to one-nucleon and two-nucleon exchange between the clusters, and the total potential is the sum of three parts: a static local direct attractive long-range potential and two nonlocal ℓ-dependent potentials arising from the exchange terms. Approximations are then made which

are valid at low energies to convert the nonlocal ℓ-dependent potentials into local ℓ-dependent potentials, which have short ranges and are mainly repulsive. The final potential has a strongly repulsive core which becomes weaker for higher ℓ, together with a weakly attractive ℓ-independent outer region.

These results are in qualitative agreement with our findings: the extreme tail of the potential seems to be almost the same for the $\ell = 0$, 2, and 4 partial waves. The repulsive core is less strong for the $\ell = 2$ wave than for the $\ell = 0$ wave, again consistent with the prediction. It would appear that at radii below about 2F the potential is dominated by the exchange terms, and at radii greater than about 4 F by the ℓ-independent direct terms, while between 2 F and 4 F the direct and exchange terms are comparable.

Footnotes and References

* P. Darriulat, G. Igo, H. G. Pugh, and H. D. Holmgren, The Elastic Scattering of Alpha Particles by Helium between 53 MeV and 120 MeV, Phys. Rev. (to be published).

† NATO fellow on leave from C. E. N., Saclay, France.

‡ University of Maryland, College Park, Md., partly supported by the U. S. Office of Naval Research.

1. H. E. Conzett, G. Igo, H. C. Shaw, and R. J. Slobodrian, Phys. Rev. 117, 1075 (1960).
2. T. A. Tombrello and L. S. Senhouse, Phys. Rev. 129, 2252 (1963) and references therein.
3. A. T. Berztiss (University of Melbourne), private communication.
4. I. Shimodaya, R. Tamagaki, and H. Tanaka, Progr. Theoret. Phys. (Kyoto) 27, 793 (1962).

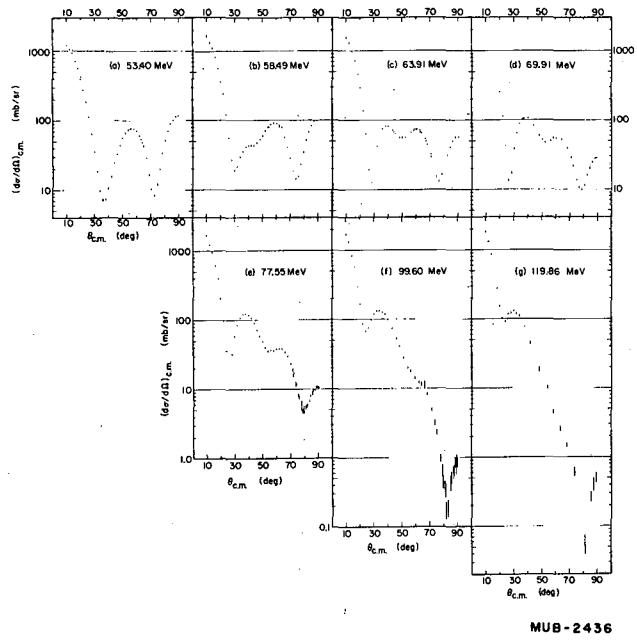

Fig. C. 5-1. The differential cross section in the center-of-mass system, $(d\sigma/d\Omega)_{c.m.}$, for elastic scattering of α particles by helium at laboratory-system bombarding energies of (a) 53.40 ± 0.15 MeV, (b) 58.49 ± 0.16 MeV, (c) 63.91 ± 0.18 MeV, (d) 69.91 ± 0.20 MeV, (e) 77.55 ± 0.22 MeV, (f) 99.60 ± 0.28 MeV, and (g) 119.86 ± 0.34 MeV. The measurements made at $\theta_{c.m.} > 90$ deg are shown at the corresponding angles less than 90 deg.

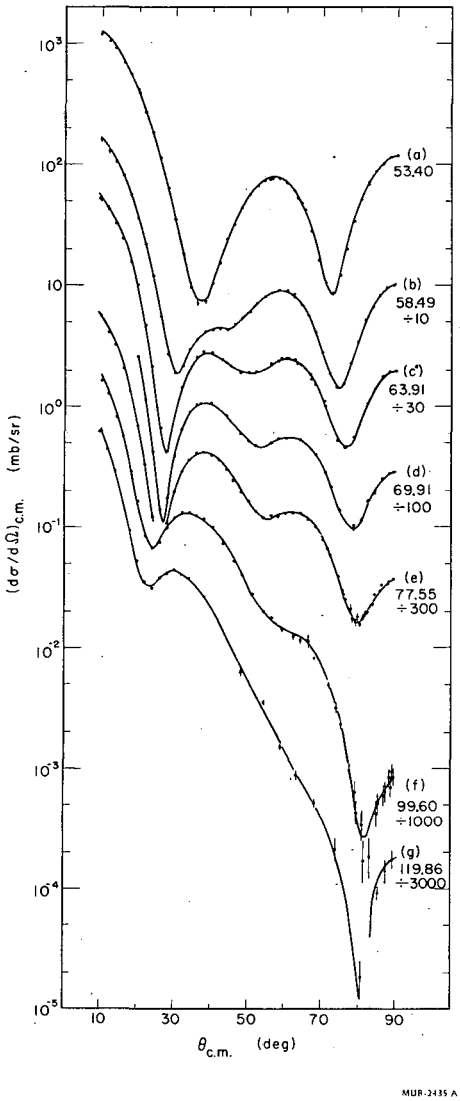

Fig. C. 5-2. The fits to the differential cross sections in the center-of-mass system, $(d\sigma/d\Omega)_{c.m.}$, given by the phase shifts.

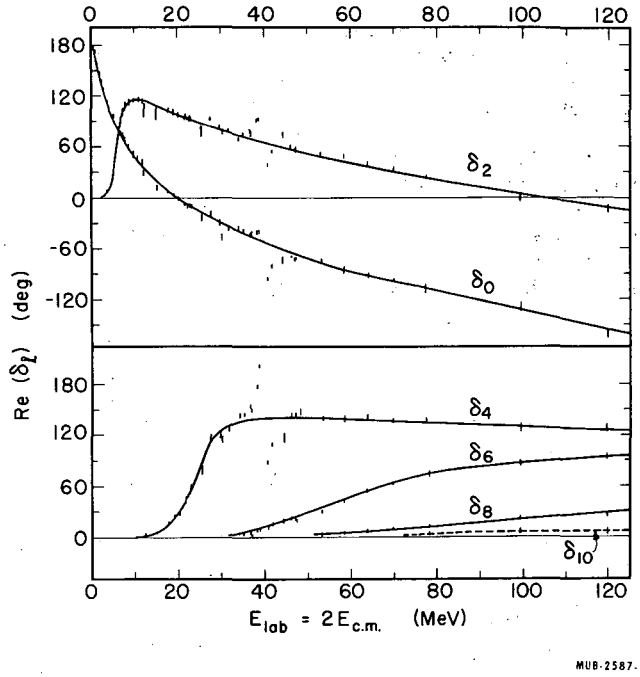

Fig. C. 5-3. The real parts of the phase shifts $\mathrm{Re}(\delta_\ell)$ plotted as a function of the lab bombarding energy E_{lab}. The phase shifts below 53.4 MeV were obtained from references 2 and 3. The solid curves are fits given by the potentials illustrated in Fig. C. 5-3.

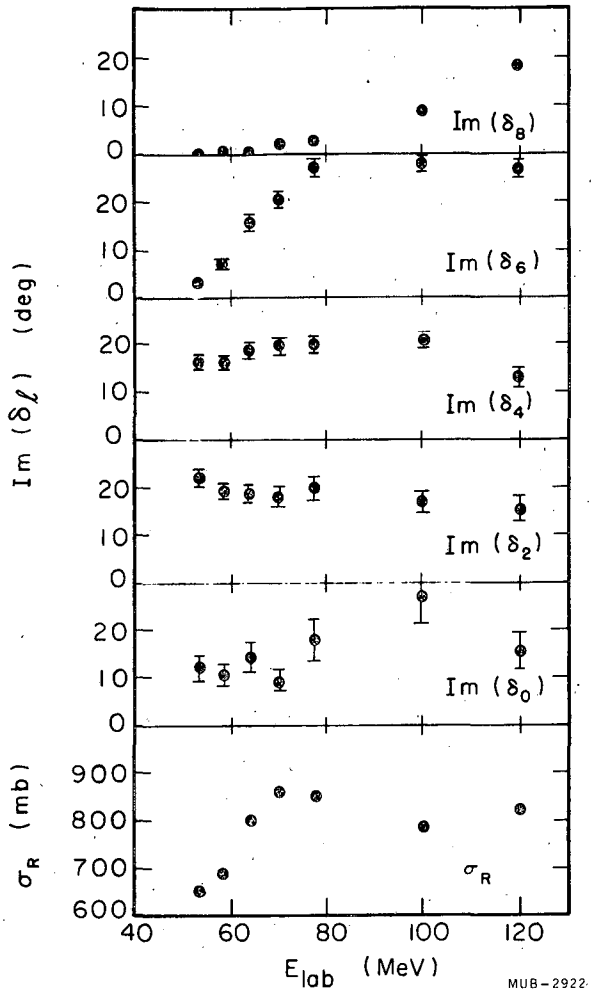

Fig. C. 5-4. The imaginary parts of the phase shifts Im(δ_ℓ) and the total reaction cross sections σ_R calculated from them, plotted as a function of the laboratory-system bombarding energy, E_{lab}.

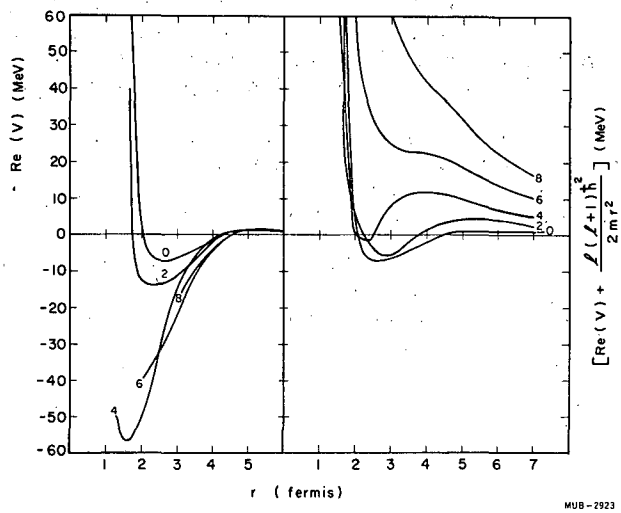

Fig. C. 5-5. The real parts of the potentials V used to fit the phase shifts, shown with and without the centrifugal barrier added, plotted against the interaction radius r.

6. INELASTIC SCATTERING OF 50.9-MeV ALPHA PARTICLES FROM Ne^{20}

A. Springer and B. G. Harvey

Besides the well-investigated regions of high permanent deformation in the heavy nuclei, there is mounting evidence of a small pocket of similarly deformed nuclei in the light nuclei with partially filled $d_{5/2}$ shell such as Ne^{20} and Mg^{24}.

Considerable evidence of rotational band structure in Ne^{20} has been obtained through a comprehensive set of experiments by the Chalk River group.[1] In the heavier elements, multiple Coulomb excitation has been one of the most profitable methods of investigating complex rotational band structure. A potentially powerful method for obtaining further evidence of the detailed band structure is inelastic alpha scattering.

The application of the Austern and Blair model in analyzing the scattering of alphas from Ca^{40} that proceeds primarily by single excitation is discussed in a previous paper.[2] The more complicated case of double excitation is also treated by Austern and Blair[3] but had not been used to analyze any experimental data previous to the investigation of Ne^{20} (which is to follow).

Alpha-particle energy spectra were measured at 1-deg intervals from 11 to 43 deg c.m. for 50.9-MeV α particles scattered from a gas target containing 98.1% Ne^{20} at 10 cm pressure The overall energy resolution varied from 160 to 210 keV, with the best resolution obtained at small angles. The counter used was a 0.06-in. -thick lithium-drifted silicon detector.

A parameterized phase analysis was performed on the elastic scattering differential cross section. The method used is fully described elsewhere.[4] The Austern and Blair model describes the inelastic scattering to second order of the nuclear deformation β as an adiabatic process, and gives the inelastic scattering amplitude from a 0^+ state to a state of spin I and z projection M_I as

$$f_{(Im;\,00)} = \frac{i}{2}(2I+1)^{1/2} \sum_{\ell\ell'} I^{\ell-\ell'}(2\ell'+1)^{1/2} e^{i(\sigma_\ell+\sigma_{\ell'})} \left\langle \ell' I\text{-}M_I M_I \middle| \ell 0 \right\rangle \left\langle \ell' I 00 \middle| \ell 0 \right\rangle Y_{\ell_1}^{-M_I}(\theta, 0) \left(C_1(I)\frac{\partial \eta_\ell}{\partial \ell} - \frac{k}{2} C_2(I) \frac{\partial^2 \eta_\ell}{\partial \ell^2} \right),$$

where $C_1(I)$ is the matrix element of the coordinate describing collective motion, and $C_2(I)$ is the corresponding matrix element of the second power of this coordinate. The first and second derivatives are evaluated at $\bar{\ell} = (\ell + \ell')/2$, and $Y_{\ell'}^{-M_I}(\theta, 0)$ is a spherical harmonic evaluated at θ, the scattering angle in the center-of-mass system, and $\phi = 0$. This form is justified in Blair's Yugoslavia-lecture notes.[3]

The experimental differential cross sections for excitation of the 2^+ and 4^+ members of the ground-state rotational band are shown with the corresponding Austern and Blair model angular distributions in Fig. C. 6-1. The double-excitation and single-excitation matrix elements are related by the spherical harmonic addition rule and so the double-excitation contribution from a pure rotational model can be calculated and compared with the measured values. The data support the rotational character of the lowest band of states.

It has also been pointed out that the low-lying negative-parity states in Ne^{20} may be due to K = 0 and K = 2 rotational bands based on an octupole surface vibration.[1] Comparisons of the differential cross sections and first-order Austern and Blair angular distributions, shown in Fig. C. 6-2, strongly support this. In each case the 3^- member of the band is the most highly populated state and has the angular distribution corresponding to a single-excitation octupole transition, while in the K = 0 band the 1^- is weakly excited with the phase opposite that of a dipole transition, indicating double excitation through the 3^- state. All that can be said of the 2^- member of the K = 2 band is that it is weakly excited and does not show any regular oscillations. Similar behavior of single and double excitation is reported in Coulomb excitation of rotational bands in U^{238} (reference 5)(see Fig. C. 6-3).

Two higher positive-parity K = 0 bands have been suggested.[1] Since no members of these bands have enhanced excitation, it is not likely that these bands are based on a single-phonon quadrupole vibration. Further evidence of this is that the 0^+ at 6.71 MeV and the 2^+ at 7.46 MeV both appear to proceed by double excitation of comparable strength.

References

1. A. E. Litherland, J. A. Kuehner, H. E. Gove, M. A. Clark, and E. Almqvist, Phys. Rev. Letters 7, 98 (1961).
2. A. Springer and B. G. Harvey, Inelastic Scattering of 50.9-MeV Alpha Particles from Calcium-40 (UCRL-11708, Dec. 1964), submitted to Phys. Letters.
3. J. S. Blair, Yugoslavia Summer Meeting of Physicists, 1962.

4. Arthur Springer, Scattering of 50.9-MeV Alpha Particles from Ne^{20} and Ca^{40} (Ph. D. Thesis), UCRL-11691, to be issued.
5. Earl K. Hyde, Nuclear Models and Their Application to the Heavy Elements, UCRL-8783 Rev., March 1963, p. 167.

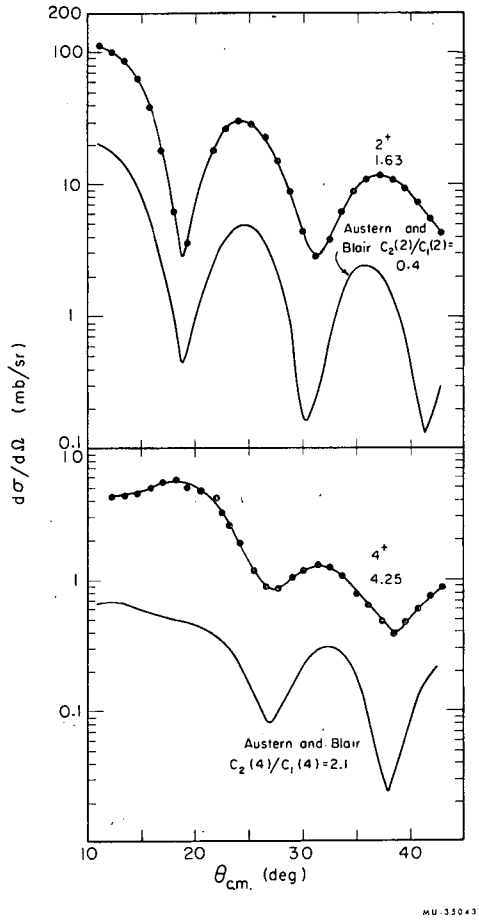

Fig. C. 6-1. The differential cross sections for excitation of the 2^+ and 4^+ of the ground-state rotational band are compared with the Austern and Blair model for mixed single and double excitation.

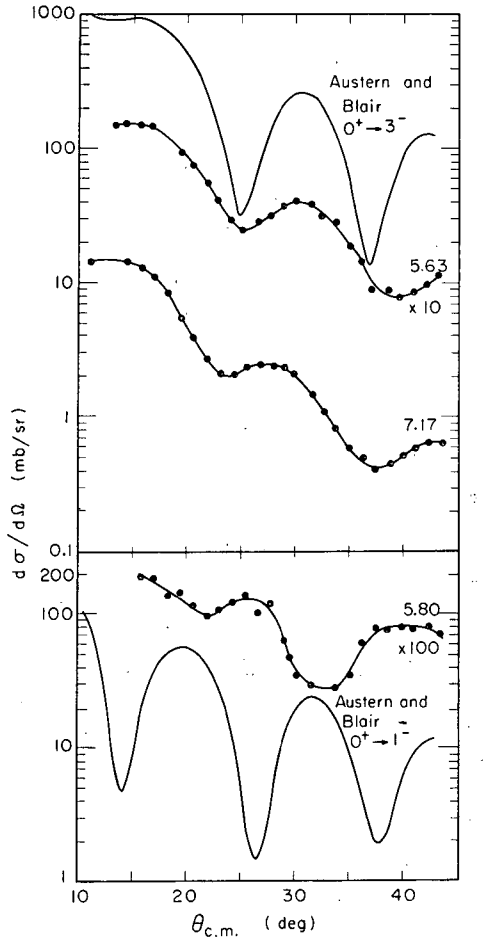

Fig. C. 6-2. The 1^- and 3^-'s of the negative parity bands are compared with the Austern and Blair model for single excitations.

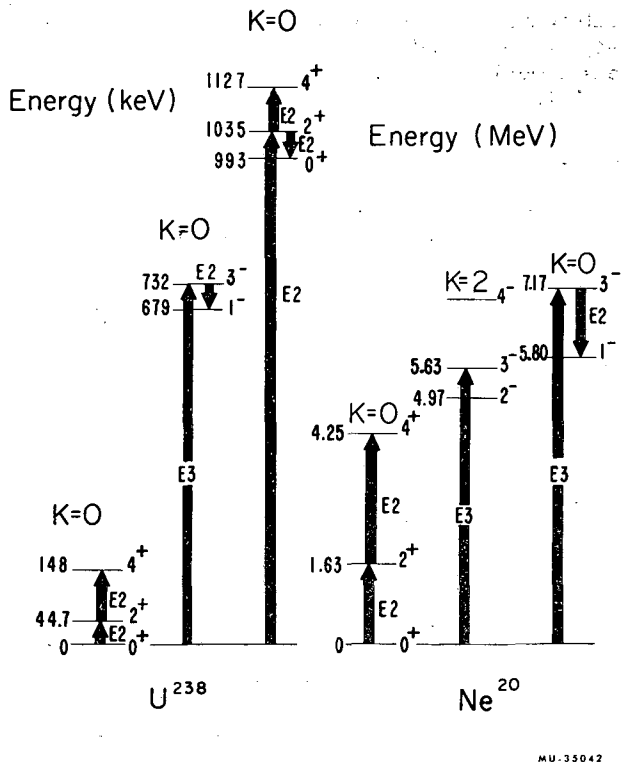

Fig. C. 6-3. Coulomb excitation of U^{238} is compared with inelastic scattering from Ne^{20}. The arrows indicate the dominant modes of excitation.

7. INELASTIC SCATTERING OF 50.9-MeV α PARTICLES FROM Ca^{40}†

A. Springer and B. G. Harvey

A series of simple models[1] has been developed to obtain nuclear spectroscopic information from α-particle scattering data. The model developed by Austern and Blair[1] generalizes the Drozdov-Blair-Sharp-Willets diffraction model[2] to arbitrary multipole excitation, allows the amplitude of the ℓth outgoing partial wave to be complex, and includes Coulomb distortion. In the work presented here this model has been used for the first time to obtain information from experimental data.

Alpha-particle energy spectra were measured at 1-deg intervals from 11 to 62 deg in the center-of-mass system for 50.9-MeV α particles scattered from 0.64 mg/cm^2-thick natural Ca (97% Ca^{40}). The overall energy resolution of 115 keV was obtained by using a 0.06-in.-thick lithium-drifted silicon detector at 300 V bias.

The data have been analyzed as follows. The elastic-scattering amplitude has the form

$$f(\theta) = f_c(\theta) + \frac{i}{2k} \sum_{\ell=0}^{\infty} e^{2i\sigma_\ell}(2\ell+1)(1-\eta_\ell)\, P_\ell(\cos\theta),$$

where $f_c(\theta)$ is the Coulomb amplitude, σ_ℓ is the Coulomb phase shift for the ℓth partial wave, η_ℓ is the amplitude of the ℓth outgoing partial wave, $P_\ell(\cos\theta)$ is the Legendre polynomial of order ℓ, and k is the relative wave number. η_ℓ has been assumed to have the form

$$\eta_\ell = \epsilon + B\Delta\frac{d\epsilon}{d\ell} + i\left(A\Delta\frac{d\epsilon}{d\ell} + D\Delta^2\frac{d^2\epsilon}{d\ell^2}\right), \qquad \text{where } \epsilon = (1+e^{(L-\ell)/\Delta})^{-1},$$

and L, Δ, A, B, and D are parameters which have been determined by a search program[3] from the elastic differential cross section. This fit is shown in Fig. C. 7-1.

The Austern and Blair model describes the inelastic scattering in the first order of the nuclear deformation β as an adiabatic process, and gives the inelastic scattering amplitude for a transition from a 0^+ state to a state of spin I and z projection M_I as

$$f_{IM\,00} = +(i/2)(2I+1)^{1/2}C(I)\sum_{\ell\ell'} I^{\ell-\ell'}(2\ell'+1)^{1/2} i(\sigma_\ell+\sigma_{\ell'})\left\langle \ell' I\text{-}M_I\, M_I \mid \ell 0\right\rangle\left\langle \ell'\, I\, 0\, 0 \mid \ell\, 0\right\rangle(\partial\eta_\ell/\partial\ell)Y_{\ell'}^{-M_I}(\theta, 0),$$

where $C(I) = B_I R_0/(2I+1)^{1/2}$. The quantities in brackets are Clebsch-Gordan coefficients. The derivative is evaluated at $\bar{\ell} = (\ell+\ell')/2$, and $Y_{\ell'}^{-M_I}(\theta, 0)$ is a spherical harmonic evaluated at θ, the scattering angle in the center-of-mass system and $\phi = 0$. This form comes from the distorted-wave formulation by replacing the radial integral with $\left(\frac{-iE}{2}\right)\frac{\partial\eta_\ell}{\partial\ell}$.

Angular distributions have been calculated for angular momentum transfers of 0 through 5, with the parameters from Fig. C. 7-1. The experimental differential cross sections of almost all the states excited fall into distinct groups corresponding to angular momentum transfers of 2 through 5. The experimental and calculated angular distributions corresponding to odd angular momentum transfer are shown in Fig. C. 7-2; those corresponding to even angular momentum transfer are shown in Fig. C. 7-3. Table C. 7-I summarizes the spins, parities, and reduced transition probabilities extracted by this method.

The two states around 8.5 MeV are of special interest because a state at 8.5 MeV had previously been reported[4] as the second 5^- calculated by Gillet and Sanderson[5] to have an excitation of 8 MeV. Since neither state has an angular distribution resembling an angular momentum transfer of 5, this raises some doubt about the original assignment, and may mean that the second 5^- level in Ca^{40} has not yet been seen.

The Austern and Blair model is easy to use and seems from a spectroscopic standpoint to be as powerful as the more sophisticated models. The least-squares fit to the elastic

angular distribution and the calculation of the inelastic angular distributions can be made in 3 minutes on an IBM 7094 computer.

Footnotes and References

† Condensation of paper submitted to Phys. Letters.

1. J. S. Blair, paper given at Yugoslav Summer Meeting of Physicists, 1962, and private communication.
2. J. S. Blair, D. Sharp, and L. Wilets, Phys. Rev. 125, 1625 (1962).
3. A. Springer, Scattering of 50.9-MeV Alpha Particles (Ph. D. Thesis, in preparation).
4. D. Blum, P. Barreau, and J. Bellicard, Phys. Letters 4, 109 (1963).
5. V. Gillet and E. Sanderson, Phys. Letters 2, 173 (1962).

Table C.7-I. Spins, parities, and reduced transition probabilities.

Q value		J^π		$\beta_J R_0$
3.73		3^-		0.85
3.90		2^+		0.34
4.48		5^-		0.35
5.25		$?^-$		
5.62		$?^-$		
5.90		3^-		0.18
6.28		3^-		0.40
6.58		3^-		0.31
6.94	either	$2^+, 3^-$	< for	2^+ 0.21
			for	3^- 0.36
		$2^+, 1^-$		
7.92		4^+		0.29
8.11		2^+		0.24
8.38		4^+		0.24
8.59		2^+		0.19
9.87				

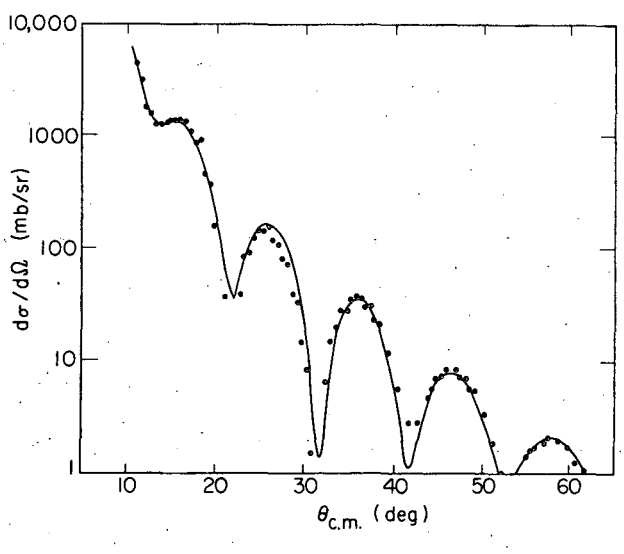

Fig. C.7-1. The best fit obtained to the Ca^{40} elastic scattering cross section with the parameters L = 16.7, Δ = 1.15, A = 0.66, B = 1.51, D=-1.92. The parameters are described in the text.

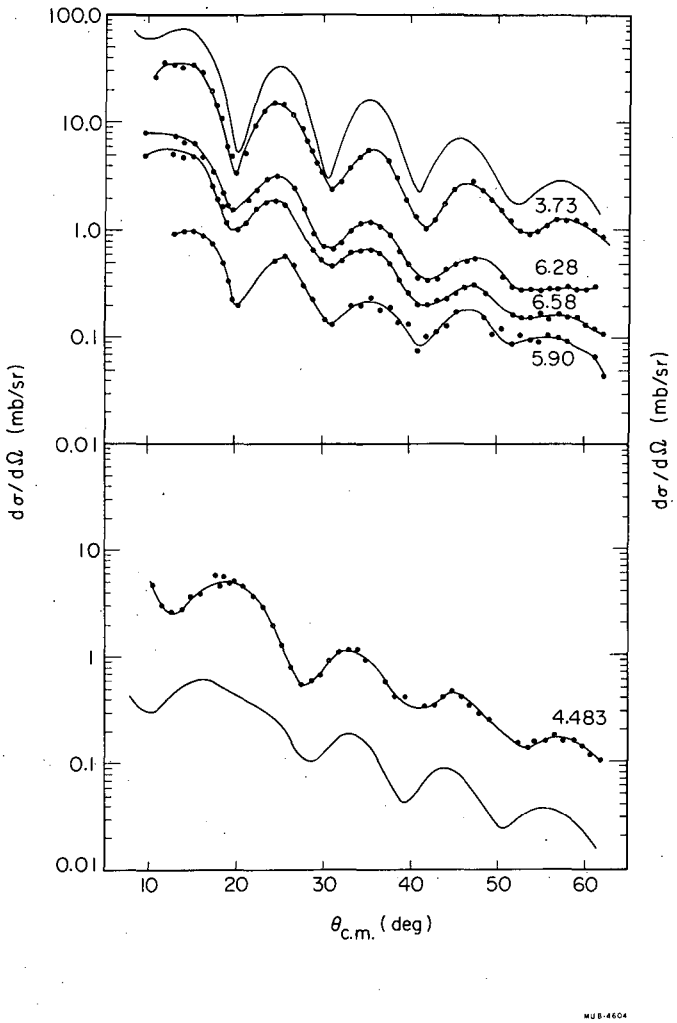

Fig. C.7-2. Angular distributions from Austern and Blair model and similar experimental inelastic differential cross sections. Upper curves, 0 + → 3-; lower curves, 0 + → 5-.

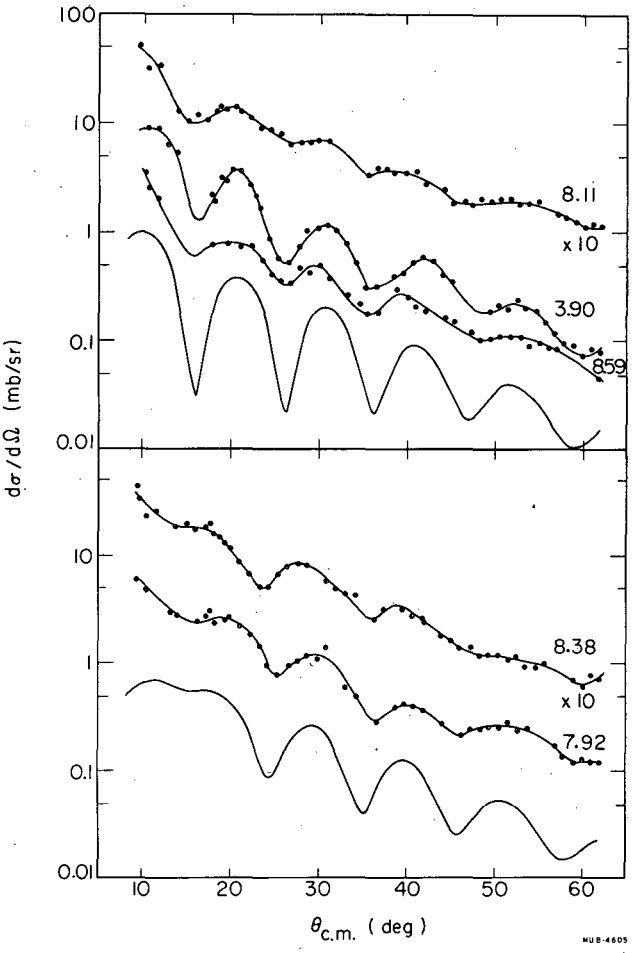

Fig. C.7-3. Angular distributions from Austern and Blair model and similar experimental inelastic differential cross sections. Upper curves, 0 + → 2+; lower curves, 0 + → 4+.

8. COMPARISON OF THE O^{16}(p, t) AND (p, He^3) REACTIONS POPULATING ANALOG FINAL STATES IN O^{14} AND N^{14}†

Richard H. Pehl and Joseph Cerny

Detailed comparative measurements of direct-interaction transitions from an initial state to analog final states provide a sensitive experimental test of the charge independence of nuclear forces. Since few comparisons of direct transfer reactions to analog final states have been made and none under unambiguous direct reaction conditions, we have investigated the O^{16}(p, t) O^{14}[g. s., 0^+, T = 1] and O^{16}(p, He^3)N^{14*}[2.31 MeV, 0^+, T = 1] transitions induced by 43.7-MeV protons. Previous two-nucleon transfer investigations of the mass-14 isobaric triad have been reported, utilizing the C^{12}(He^3, n) O^{14}(g. s.) and C^{12}(He^3, p) N^{14*}(2.31 MeV) reactions at bombarding energies up to 2.6 MeV,[1] 1.8 to 5.5 MeV,[2] and 6 to 11 MeV.[3] However, rigorous comparison of these low-energy measurements is handicapped by the relatively larger Coulomb effects and interference between the compound nucleus and direct-reaction contributions to the

transitions. A further difficulty arises in comparing the absolute cross sections, since two different detecting systems must be employed.

The (p, t) and (p, He^3) measurements were induced by a beam of 43.7-MeV protons from the Berkeley 88-inch cyclotron. A new type of particle identifier[4] fed by a 40-mg/cm^2 transmission, 480-mg/cm^2 stopping semiconductor counter telescope distinguished the reaction products. A typical particle-identifier spectrum is shown in Fig. C.8-1. Total energy pulses were fed into a Nuclear Data analyzer which was appropriately gated so that the triton and He^3 spectra were recorded simultaneously, each spectrum in a 1024-channel group. The deuteron-triton valley and the entire α-particle spectrum of the identifier were also recorded in the analyzer to measure any small but possible loss of the t and He^3 groups in question. The average energy resolution was 190 keV for the tritons and 240 keV for the He^3.

Figure C.8-2 presents absolute cross-section measurements of the $O^{16}(p, t)O^{14}$(g. s.) and $O^{16}(p, He^3)N^{14*}$(2.31 MeV) transitions; the (p, He^3) differential cross sections have been multiplied by the theoretically required factor of 1.88, as is discussed below. Representative statistics are shown on Fig. C.8-2. Our independent absolute cross sections should be accurate to ± 10%; however, since the spectra were obtained simultaneously, the relative errors should be given primarily by the statistics. Although the differential cross sections vary by a factor of 100 over the angular range investigated, only slight departures from exact agreement are apparrent. Also shown in Fig. C.8-2 are two-nucleon DWBA fits, which are discussed elsewhere.[5, 6]

In Born approximation, the ratio of these differential cross sections is given by

$$\frac{d\sigma(p, t)}{d\sigma(p, He^3)} = \frac{k_t}{k_{He^3}} \frac{|M_t|^2}{|M_{He^3}|^2} .$$

Assuming pure isospin states for all nuclei involved in the transitions and an isospin-conserving interaction, the theoretical ratio is

$$\frac{|M_t|^2}{|M_{He^3}|^2} = \frac{C(t_p Tt_t; \tau_p, \tau_t - \tau_p)^2}{C(t_p Tt_{He^3}; \tau_p, \tau_{He^3} - \tau_p)^2} = 2$$

(T is the isospin of the transferred pair). Since the ratio of k_t/k_{He^3} is 0.94, the (p, t) reaction should be favored by a factor of 1.88 over the (p, He^3) reaction.

The ratio of the integrated cross sections (11-90° c. m.) for these transitions, after correction for the phase-space and isospin coupling factors, is $\sigma(p,t)/\sigma(p, He^3)$ = 0.905 mb/0.807 mb = 1.12/1. This excellent agreement between the absolute cross sections, and the angular distributions, implies a strongly charge-independent interaction operator. Further, the analog states of O^{14} and N^{14} must be extremely similar. In addition to the principal $[(p_{1/2})^2]0^+$, T = 1 component in these states, there can be admixtures of 0^+ states of T ≠ 1 and admixtures of other 0^+, T = 1 states. Since these amplitudes enter linearly into the matrix elements, though appropriately weighted by transition-dependent factors, the matrix-element ratio is a sensitive measure of differing amplitude and phase admixtures in the analog states.

Footnotes and References

† Condensation of article in Phys. Rev. Letters 12, 619 (1964).

1. D. A. Bromley, E. Almqvist, H. E. Gove, A. E. Litherland, E. B. Paul, and A. J. Ferguson, Phys. Rev. 105, 957 (1957).
2. G. V. Din, H. M. Kuan, and T. W. Bonner, Nucl. Phys. 50, 267 (1964).
3. H. W. Fulbright, W. Parker Alford, O. M. Bilaniuk, V. K. Deshpande, and J. W. Verba, University of Rochester Report No. NYO-10034, Feb. 1962 (unpublished).
4. F. S. Goulding, D. A. Landis, J. Cerny, and R. H. Pehl, Nucl. Instr. Methods (in press).
5. Norman K. Glendenning (Lawrence Radiation Laboratory), private communication. A detailed description of these calculations will be published.
6. J. Cerny and R. H. Pehl, Phys. Rev. Letters 12, 619 (1964).

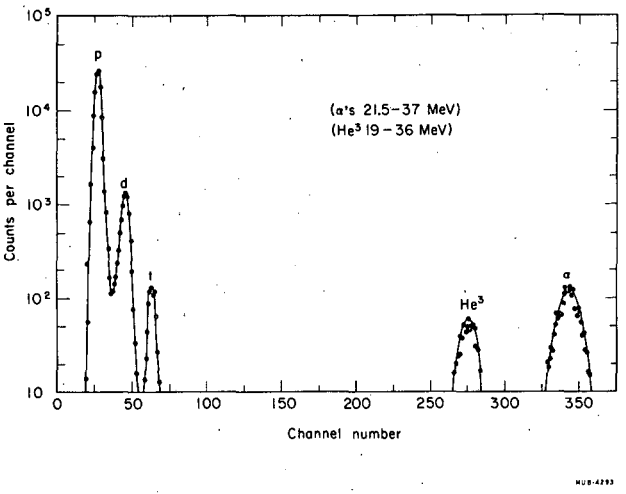

Fig. C.8-1. Particle identifier spectrum from 43.7-MeV protons on O^{16}.

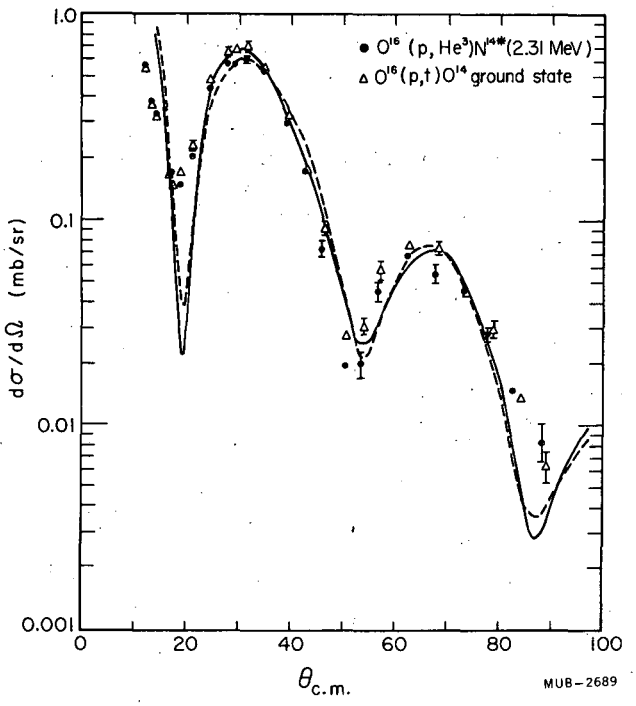

Fig. C.8-2. Angular distributions for the $O^{16}(p,t)O^{14}$[g. s., 0^+, T = 1] and O^{16} (p, He^3)N^{14*} [2.31 MeV, 0^+, T= 1] transitions; the latter cross sections have been multiplied by 1.88. The solid and dashed lines are L=0, two-nucleon transfer DWBA fits to the(p,t) and (p, He^3) transitions, respectively (reference 5).

9. T=2 STATES IN THE T_Z=0 NUCLEI O^{16} AND Ne^{20} AND THE T_Z=1 NUCLEI N^{16} AND F^{20}†*

Joseph Cerny, Richard H. Pehl, and Gerald T. Garvey‡

Both the (p, t) and (p, He^3) reactions when employed on targets with isobaric spin greater than zero can produce states with $T > T_Z$ in the residual nucleus through pickup of the two nucleons in a $^1S_0$, T=1 configuration. We wish to report observations of the two lowest T= 2 states in O^{16} and Ne^{20} through the (p, t) reaction on O^{18} and Ne^{22}, respectively. Further, the analogous ability of the (p, He^3) reaction on these targets to locate the same T=2 states in the product T_Z = 1 isobars N^{16} and F^{20} is demonstrated.

These (p, t) and (p, He^3) reactions were induced by a beam of 43.7-MeV protons from the Berkeley 88-inch cyclotron. A 50-mg/cm^2 transmission 780-mg/cm^2 stopping counter telescope, which was turned at an angle of 25 deg to the flight path of the scattered particles, fed a new type of particle identifier.[1] Total energy pulses were fed into a Nuclear Data analyzer so that the triton and helium-3 spectra were recorded simultaneously, each spectrum in a separate 1024-channel group. Resolutions (FWHM) of 150 keV for tritons and 200 keV for helium-3 were obtained.

Figure C.9-1 shows energy spectra from the $O^{18}(p,t)O^{16}$ and $O^{18}(p, He^3)N^{16}$ reactions, while Fig. C.9-2 shows spectra for $Ne^{22}(p,t)Ne^{20}$ and $Ne^{22}(p, He^3)F^{20}$. The helium-3 spectra

have been shifted relative to the tritons to indicate the expected correlation of analog states. The 0+, T=2 states are sharp, having widths defined by the experimental resolution. [The states tentatively identified as 2+, T=2 are discussed in Phys. Letters 12, 234 (1964).] Strong population in both spectra of many T=1 analog states is also apparent.

Within the framework of charge independence of nuclear forces, these (p, t) and (p, He^3) transitions populating analog T=2 states proceed from identical initial to final states via only ^1S, T=1 pickup. Hence their cross sections, in the limit of no Coulomb mixing or distortions in the final states, should be identical apart from a constant factor. One therefore expects quite similar angular distributions in these experiments for transitions to pairs of T=2 analog states.

The 0+ → 0+, L=0 (p, t) transitions possess characteristic angular distributions at this energy, peaking at ≈ 26° to 32° c.m. for light targets. Figure C.9-3 presents the O^{18}, Ne^{22} (p, t) O^{16}, Ne^{20} ground state and the alleged lowest T=2 state angular distributions; also shown are the O^{18}, Ne^{22}(p, He^3) N^{16}, F^{20} lowest T=2 state angular distributions. As expected, all the angular distributions of the levels indicated as 0+, T=2 parallel those of the known L=0 (T=0) ground-state transitions. The absolute cross section, apart from statistics, should be accurate to ± 10%; the statistical error varied from 4 to 25%.

Table C.9-I presents the predicted and experimental values for the excitations of the 0+, T=2 analog levels in these T_z = 1 and 0 isobars; in addition, values for the T=2 states in Mg^{24}, Ti^{44} and Fe^{52} are included. The predicted values are obtained by adding to the mass difference between the ground states of the isobars the appropriate Coulomb energy corrected for the neutron-hydrogen atom mass difference.

The agreement between the predicted and experimental excitations shown in Table C.9-I is quite good and is sufficient to indicate the absence of strong Thomas-Ehrman shifts or widely different spatial wave functions, relative to lower T states, in these generally particle-unstable T=2 states. The data on the mass 16 and 20 isobars are displayed in Fig. C.9-4, which also illustrates the good agreement among the observed excitations of the 2+, T=2 isobaric analog states.

Footnotes and References

† Condensation of Phys. Rev. Letters 12, 726 (1964) and Phys. Letters 12, 234 (1964).

* Supported in part by the Higgins Scientific Trust Fund.

‡ Palmer Physical Laboratory, Princeton University, Princeton, N. J.

1. F. S. Goulding, D. Landis, J. Cerny, and R. H. Pehl, A New Particle Identifier Technique for Z=1 and Z=2 Particles in the Energy Range > 10 MeV (UCRL-11245, Feb. 1964), Nucl. Instr. Meth. (in press).

Table C.9-I. Comparisons of the predictions based on Coulomb energies to the experimentally determined excitation energies for the lowest-lying T=2 states.

Nucleus	Prediction from Coulomb energy differences (MeV)	Experimental value (MeV)
N^{16}	10.04	9.9_1 ± 0.1
O^{16}	23.13	22.9^1 ± 0.1
F^{20}	6.38	6.4_3 ± 0.1
Ne^{20}	16.59	16.8^3 ± 0.1
Mg^{24}	15.30 ± 0.05	15.4 ± 0.12
Ti^{44}	9.44 ± 0.1	9.35 ± 0.12
Fe^{52}	8.46 ± 0.1	8.54 ± 0.12

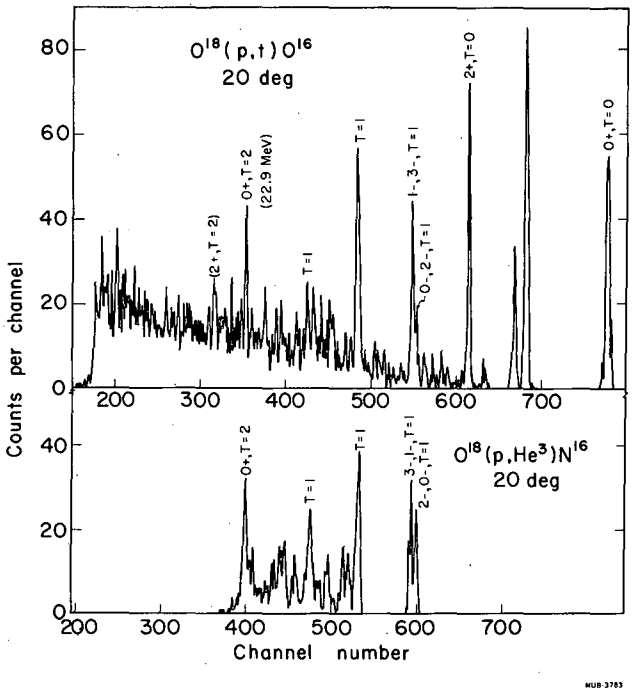

Fig. C.9-1. Top: Triton energy spectrum at 20 deg from the $O^{18}(p,t)O^{16}$ reaction. Bottom: He^3 ion energy spectrum at 20 deg from the $O^{18}(p, He^3)N^{16}$ reaction. The spectra have been lined up to match the analog states of O^{16} and N^{16}. Some low-lying T=1 and 2 states are indicated; the states labeled T=2 are analogs of C^{16}.

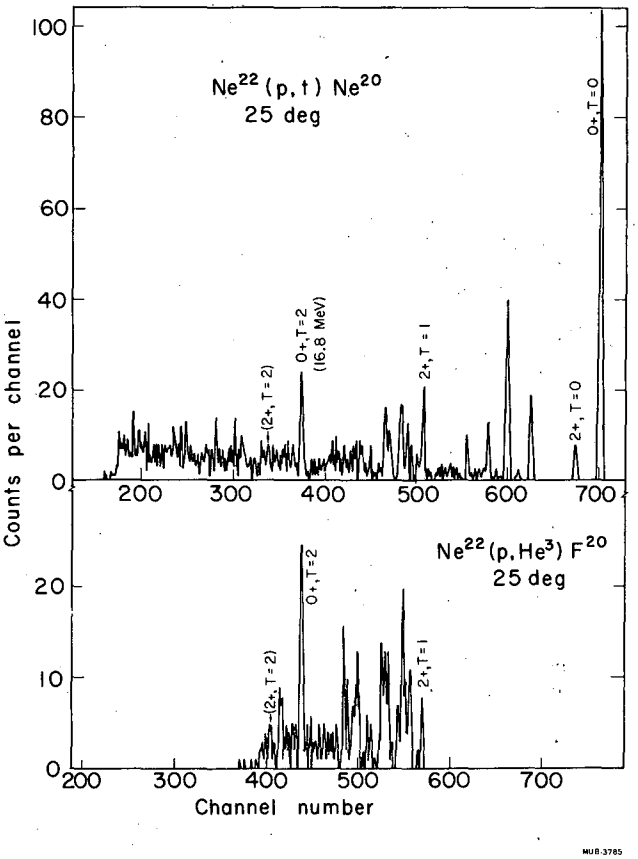

Fig. C.9-2. Top: Triton energy spectrum at 25 deg from the $Ne^{22}(p,t)Ne^{20}$ reaction. Bottom: He^3 ion energy spectrum at 25 deg from the $Ne^{22}(p, He^3)F^{20}$ reaction. The spectra have been lined up to match the analog states of Ne^{20} and F^{20}. Some low-lying T=1 and 2 states are indicated; the states labeled T=2 are analogs of O^{20}.

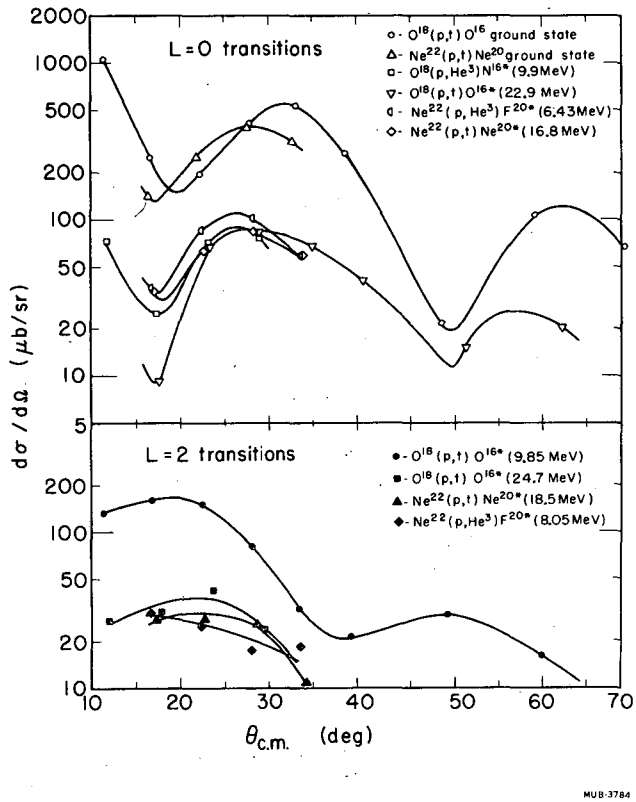

Fig. C.9-3. Angular distributions of tritons and He^3 ions from some of the reactions induced by 43.7-MeV protons on O^{18} and Ne^{22}.

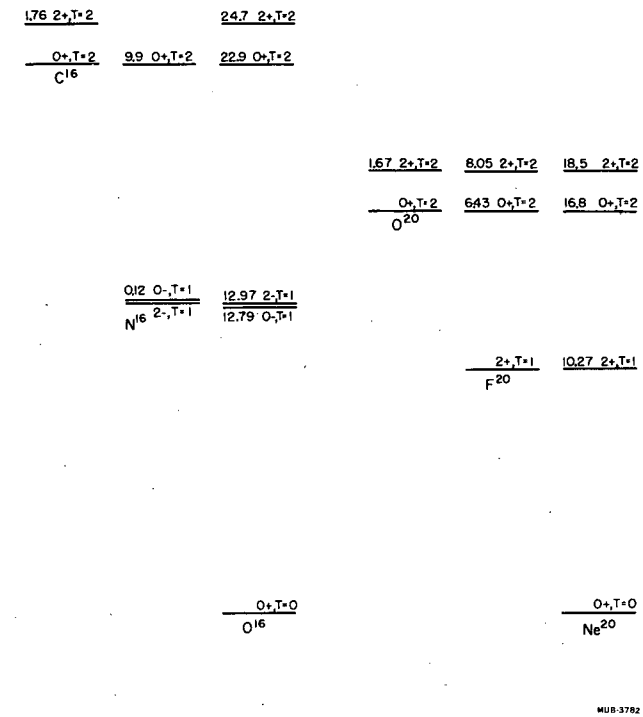

Fig. C.9-4. Schematic representation of the mass-16 and mass-20 isobars, emphasizing the correlation of the T=2 states. The excited states of C^{16} and O^{20} are from reference 4.

10. THE $C^{12}(\alpha, d)N^{14}$ REACTION†

Richard H. Pehl, Ernest Rivet,* Joseph Cerny, and Bernard G. Harvey

The two-nucleon transfer reaction, (α, d), leading to states of N^{14} is especially interesting for two reasons.

(a) A detailed investigation may provide the basis for an understanding of the observed selectivity of final-state population in α, d (or He^3, p) reactions in general, since extensive theoretical studies of this nucleus, most recently by True,[1] provide the wave functions necessary for cross-section predictions. A paper by Glendenning[2] delineates and tests this possibility.

(b) High-resolution studies of the $C^{12}(\alpha, d)N^{14}$ reaction, continuing to high excitation (>15 MeV), can extend our knowledge of the N^{14} levels, particularly exploring states of two excited nucleons around the target "core" that are inaccessible in single-nucleon transfer experiments.

The $C^{12}(\alpha, d)N^{14}$ reaction was induced by a beam of 53-MeV α particles from the Berkeley 88-inch spiral-ridge cyclotron. Particles were detected by a counter telescope that consisted of two Li-drifted surface barrier counters: a 14-mil transmission counter backed by a 120-mil stopping counter. To increase the effective counter thickness the counter telescope was rotated 40 deg with respect to a radial line from the center of the scattering chamber. Deuterons of up to 37.5 MeV could be stopped by this system. The reaction products were distinguished by a new type of particle identifier.[3] The average energy resolution for the deuterons was 170 keV. (Optimum resolution was 145 keV.)

Figure C.10-1 shows a deuteron energy spectrum at 60 deg. The angular range studied

covered from 12 to 80 deg (lab), and the observable excitation in N^{14} extended up to 21 MeV at small angles. The $C^{12}(\alpha, d)N^{14}$ reaction should preferentially populate those N^{14} levels whose configurations are an unchanged C^{12} core coupled to a neutron-proton pair, since direct-stripping transitions involving excitation of the core are relatively unlikely.[4] Further selectivity of the (α, d) reaction arises from the fact that the wave function of the neutron-proton pair in the captured state must have a high degree of overlap with the wave function of that neutron-proton pair in the α particle.[2] Extensive theoretical studies of the N^{14} nucleus have been made,[1,5,6] and in general our results are in excellent agreement with the shell-model assignments.

Above 11 MeV excitation a number of levels are populated fairly strongly. The large, broad peak centered at 12.76± 0.10 MeV probably corresponds to the same level (or levels, since the peak appears to be a doublet or triplet) as Sachs et al.[7] identified at 13 MeV from an investigation of the $C^{12}(B^{11}, Be^{9})N^{14}$ reaction (E_B 11 = 115 MeV). However, their tentative assignment, $(d_{5/2})^2$ 4+, T=1, appears doubtful, since the (α, d) reaction also populates this level. Nagatani and Bromley have also observed a strong population to a state at 13 MeV in the $C^{12}(\alpha, d)N^{14}$ reaction (E_α = 42 MeV).[8] A more likely assignment is a 4+, T=0 state of strongly mixed $(d_{3/2}\, d_{5/2})$ and $(p_{1/2}\, f_{7/2})$ configurations, which is calculated to fall in this region. Another large peak arises at 15.1± 0.10 MeV. The only T=0 high-spin configuration in this excitation region that has not been correlated with a specific level is the $(d_{5/2}\, f_{7/2})6-$, T=0 configuration that is calculated to lie at about 15 MeV.[1]

Footnotes and References

† Condensation of paper to be published in Phys. Rev. (Jan. 11, 1965).
* Now at the University of Montreal, Montreal, Quebec.

1. W. W. True, Phys. Rev. 130, 1530 (1963), and private communication.
2. N. K. Glendenning, UCRL-11353, to be published in Phys. Rev.
3. Reference 1 of paper C.9.
4. J. Cerny, B. G. Harvey, and R. H. Pehl, Nucl. Phys. 29, 120 (1962).
5. E. K. Warburton and W. T. Pinkston, Phys. Rev. 118, 733 (1960).
6. I. Talmi and I. Unna, Ann. Rev. Nucl. Sci. 10, 353 (1960).
7. M. W. Sachs, C. Chasman, and D. A. Bromley, in Proceedings of the Asilomar Conference on Reactions Between Complex Nuclei, ed. by Ghiorso, Conzett, and Diamond (University of California Press, 1963), p. 77.
8. D. A. Bromley (Yale University), private communication, 1964.

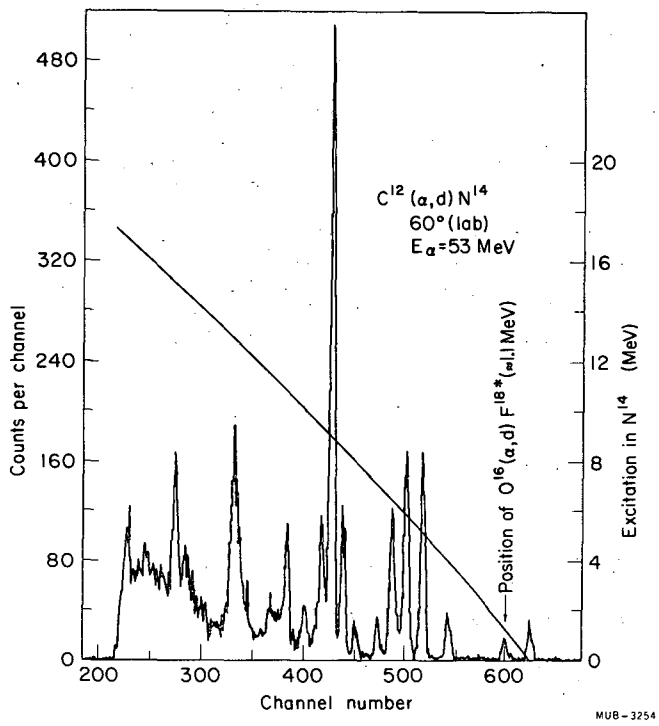

Fig. C. 10-1. Deuteron energy spectrum from the $C^{12}(\alpha, d)N^{14}$ reactions at 60 deg.

11. COMPLETION OF THE MASS-9 ISOBARIC QUARTET VIA THE THREE-NEUTRON PICKUP REACTION $C^{12}(He^3, He^6)C^{9\dagger}$

Joseph Cerny, Richard H. Pehl, Fred S. Goulding, and Donald A. Landis

Besides general interest in the existence of highly neutron-deficient isotopes,[1] considerable immediate importance[2] is attached to the accurate measurement of masses of certain $T_z = -3/2$ nuclei, e. g. C^9, which complete $T = 3/2$ isobaric spin quartets and provide a new test of the charge independence of nuclear forces. We wish to report a new nuclear reaction—that of three-neutron pickup via (He^3, He^6) transitions—permitting measurement of the mass of C^9, which completes an isobaric quartet for the first time.

The Berkeley 88-inch variable-energy cyclotron was used for these experiments. Alpha particles of 70 MeV were used to set up the electronics through the $Mg^{26}(He^4, He^6)Mg^{24}$ and $Mg^{26}(He^4, Li^6)Na^{24}$ reactions. A new type of particle identifier[3] fed by a 50-mg/cm^2 transmission—180-mg/cm^2 stopping semiconductor counter telescope distinguished the reaction products. A typical particle identifier spectrum for Mg^{26}+ He^4 is shown in Fig. C. 11-1. Single-channel analyzers on the dE/dx counter eliminated all He^4 >46 MeV prior to identification. Total energy pulses for both He^6 and Li^6 were fed into a Nuclear Data analyzer, each spectrum in a 1024-channel group, and used to establish an energy scale. The lines 2-3 and 5-6 on Fig. C. 11-1 bounded the particle identifier spectrum corresponding to the He^6 and Li^6 energy spectra, respectively. Energy spectra of particles bounded by lines 1-2 and 3-4 were also recorded in 1024-channel groups to prevent any possible loss of He^6 ions. An average He^6 energy resolution of 190 keV (FWHM) was obtained.

Because of the large negative Q value ($\approx$ -32 MeV) of the $C^{12}(He^3, He^6)C^9$ reaction, a beam of 65-MeV He^3 ions was used. However, to establish the general properties of this three-neutron pickup reaction, the $Mg^{26}(He^3, He^6)Mg^{23}$ reaction—involving known target and product nuclei—was first investigated. This reaction was observed with the $Mg^{26}(He^3, He^6)Mg^{23*}$ (0.449 MeV) transition dominating the ground-state transition at forward angles; the cross

section of the former is presented in Table C. 11-I. Carbon targets were then bombarded and both $C^{12}(He^3, He^6)C^9$ and $C^{12}(He^3, Li^6)B^9$ spectra recorded. Figure C. 11-1 also shows the identifier spectrum from C^{12} + He^3. Single-channel analyzers were reset to eliminate all He^3 > 22 + MeV and He^4 > 28 MeV from reaching the identifier. Measurement of the Li^6 spectra in conjunction with a pre-established pulser energy scale provided the energy calibration for each run.

Figure C. 11-2 presents the energy spectrum of $C^{12}(He^3, He^6)C^9$. At present only the ground-state transition has been definitely observed, and its cross section is also given in Table C. 11-I. It is apparent that the $C^{12}(He^3, He^6)C^9$ and $Mg^{26}(He^3, He^6)Mg^{23}$*(0.449 MeV) cross sections are comparable and quite small, both peaking forward and reaching about 1 μb/sr. The mass excess of C^9 on the C^{12} scale was determined to be 28.95± 0.15 MeV; hence, as expected,[1] C^9 is stable with respect to proton emission. Sharper energy limits could not be set from these data because of transient difficulties in maintaining a constant He^3 beam energy.

Within the framework of charge independence of nuclear forces, it can be shown[2,5] that the masses of an isobaric multiplet are related by

$$M = a + bT_z + c\,T_z^2 .$$

Measurement of the C^9 mass excess enables us to make the initial check of this relation, since, previously, at most only three members of an isobaric multiplet have been available. The other three members of the mass 9, T = 3/2 quartet are Li^9(T_z = +3/2, mass excess 24.965± 0.020 MeV),[6] Be^9(T_z = +1/2, excitation of T = 3/2 state 14.392± 0.005 MeV),[7] and B^9(T_z = -1/2, excitation of T = 3/2 state 14.668± 0.016 MeV).[8] Since the experimental error is greatest for the C^9 mass, the coefficients were obtained from the Li^9, Be^9, and B^9 states and used to predict the mass excess of C^9 to be 29.00± 0.08 MeV. Excellent agreement between this prediction and the experimental mass is apparent. In fact, though the mass equation has been applied[2,9] to investigate certain relationships between different i-spin multiplets within a given A, this is the most accurate check of the equation for a specific mass number.

Unfortunately, as has been pointed out,[2] this quadratic mass relation is not an extremely sensitive test of charge independence, because such a relation would also hold for charge-dependent forces, provided only that they are two-body forces. Hence further confirmation of this formula for T = 3/2 quartets or T = 2 quintets,[9,10] permitting an analysis of the resulting b and c coefficients and their change with mass number (see, for example, reference 11), would appear to be a most fruitful course to evaluate accurately any charge dependence of nuclear forces.

Footnotes and References

† Condensation of Phys. Rev. Letters 13, 726 (1964).
1. V. I. Goldanskii, Nucl. Phys. 19, 482 (1960).
2. D. H. Wilkinson, Phys. Letters 12, 348 (1964).
3. Reference 1 of paper C. 9.
4. Mylar targets were used at two angles to attempt a preliminary measurement of O^{13}.
5. E. P. Wigner and E. Feenberg, Rept. Progr. Phys. 8, 274 (1941); S. Weinberg and S. B. Treiman, Phys. Rev. 116, 465 (1959).
6. R. Middleton and D. J. Pullen, Nucl. Phys. 51, 50 (1964).
7. T. Lauritsen, B. Lynch, and G. Griffiths, Bull. Am. Phys. Soc. 8, 597 (1963).
8. F. S. Dietrich and J. W. Davies, Bull. Am. Phys. Soc. 8, 598 (1963); also C. A. Barnes, private communication.
9. G. T. Garvey, J. Cerny, and R. H. Pehl, Phys. Rev. Letters 13, 548 (1964); D. H. Wilkinson, Phys. Letters 11, 243 (1964).
10. J. Cerny, R. H. Pehl, and G. T. Garvey, Phys. Letters 12, 234 (1964).
11. D. H. Wilkinson, Phys. Rev. Letters 13, 571 (1964).

Table C.11-I. Differential cross sections for the $Mg^{26}(He^3, He^6)Mg^{23*}$ (0.449 MeV) and $C^{12}(He^3, He^6)C^9$ g. s. transitions. The absolute accuracy of the cross sections should be ±25%; statistical errors are indicated.

$Mg^{26}(He^3, He^6)Mg^{23*}$		$C^{12}(He^3, He^6)C^9$	
Angle, c. m. (deg)	σ (μb/sr)	Angle, c. m. (deg)	σ (μb/sr)
16.2	1.0 ±0.2	15.8	1.6 ±0.4
24.6	0.59± 0.14	20.7	1.3 ±0.2
36.4	0.50± 0.16	20.7 (see 4)	1.4 ±0.3
		25.7 (see 4)	1.3 ±0.2
		33.9	0.23± 0.07

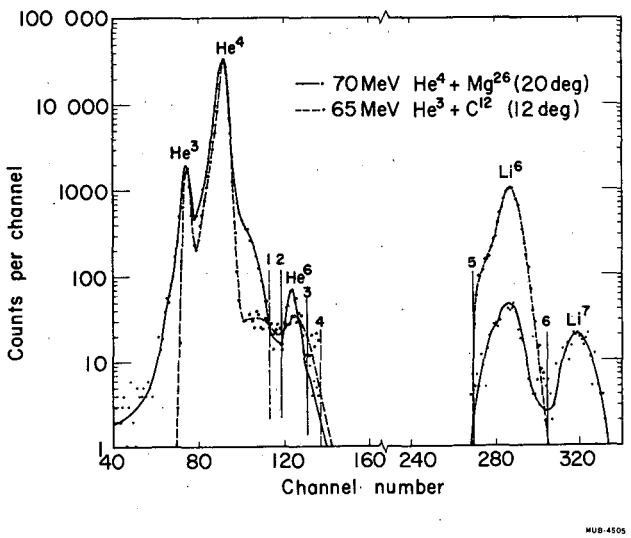

Fig. C.11-1. Particle identifier spectra from 70-MeV He^4 on Mg^{26} (at 20 deg) and 65-MeV He^3 on C^{12} (at 12 deg). Lines 1 through 6 represent discriminator settings as determined from the He^4 + Mg^{26} data. The spectrum for He^3 + C^{12} arises when all discriminators but number 1 are set.

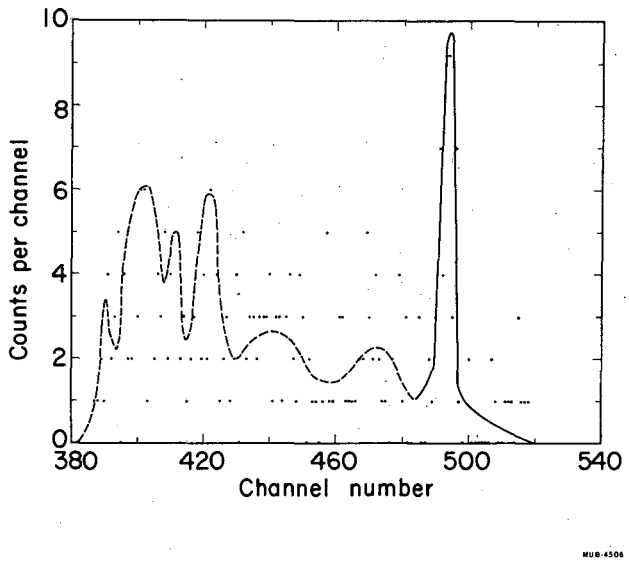

Fig. C.11-2. An energy spectrum from $C^{12}(He^3, He^6)C^9$ at 12 deg. The dashed line at lower channels than the C^9 g.s. peak merely represents an average of the scattered counts in this region.

12. OCTUPOLE STATES IN N^{15} AND O^{16}

André Bussière,* Norman K. Glendenning, Bernard G. Harvey, Jeannette Mahoney, John R. Meriwether, and Daniel J. Horen

Many examples are known of nuclear energy levels some of whose properties can be described by a moderately weak coupling of an odd particle to a strongly collective vibrational level of an even-even nuclear core.[1] The 6.134-MeV 3- level of O^{16} has an enhanced E3 transition strength to the ground state.[2] In inelastic helium-ion scattering from O^{16}, the 6.134-MeV level is strongly excited,[3] and the angular distribution of the scattered particles is characteristic of an $\ell = 3$ transition.

According to the weak coupling model, there should be two strong octupole levels in N^{15} with spins 5/2+ and 7/2+, formed by coupling a $p_{1/2}$ proton hole to an octupole vibration of the nucleus which is related to the octupole level of O^{16}.[2] These two levels should be found at excitations not far from 6.1 MeV. They should have octupole strengths equal to each other and equal to that of the 6.1-MeV level of O^{16}. The angular distributions for all three levels should have the same shape. N^{15} has 5/2+ levels at 5.276 and 7.16 MeV and a 7/2+ level at 7.57 MeV.[4]

The elastic and inelastic scattering by N^{15} and O^{16} of 40.6-MeV helium ions from the Berkeley 224-cm spiral-ridge cyclotron was studied with equipment that has been previously described.[3] Spectra taken at an angle of 24 deg in the laboratory system are shown in Fig. C.12-1. The levels of N^{15} at 5.276 and 7.57 MeV were found to be strongly excited; excitation of the 7.16-MeV level was weak at all angles. We assume that the 5.304-MeV level of N^{15} (which would be unresolved) does not contribute significantly to the observed peak at 5.3 MeV, because its spin is 1/2 instead of 5/2 and because the $\ell = 1$ transitions in O^{16} and N^{14} are weaker than the $\ell = 3$ transitions. The 6.06-MeV 0+ level of O^{16} is assumed not to contribute significantly to the observed peak at 6.1 MeV. The angular distributions for particles elastically scattered from N^{15} and O^{16} are shown in Fig. C.12-2. They are quite similar in shape.

Optical-model fits to the elastic angular distributions were made for N^{15} and O^{16} with the computer program GULLEY.[5] The best parameter sets are shown in Table C.12-I. The notation in the table is conventional; r_0 is the parameter relating the nuclear radius to the mass number A. The helium ion is given a radius r_α so that the optical potential radius $R = r_0 A^{1/3} + r_\alpha$; the diffuseness parameter of the real potential, V, is a_0 and that of the imaginary potential, W, is b_0. The Woods-Saxon shape was used for the real and imaginary parts. The calculated angular distributions are shown as solid curves in Fig. C.12-2.

The parameters of Table C.12-I were used to calculate the inelastic angular distributions for the three $\ell = 3$ levels. The DWBA curves, shown in Fig. C.12-3 as dashed lines, were normalized to the experimental cross sections at the 40-deg maximum. In this way it was found that the octupole deformation parameter β_3 was equal to 0.31 for each of the three levels. Thus the macroscopic model mentioned in the first paragraph yields a consistent interpretation of the experimental results.

The question that we have not yet examined in detail is whether the microscopic wave functions obtained from the shell-model calculations mentioned below also yield a consistent interpretation. Qualitatively it appears that this would be possible. The 6.134-MeV level of O^{16}, according to the shell-model calculations of Elliott and Flowers,[2] has a large amplitude for the configuration $s^4 p^{11} d_{5/2}$. The shell-model calculations by Halbert and French[6] assign the configuration $s^4 p^{10} d_{5/2}$ to the 5.27- and 7.57-MeV levels of N^{15}. Thus all three levels can be formed from their respective ground states by promotion of a $p_{1/2}$ nucleon to the $d_{5/2}$ shell. In the 5.27-MeV level it is a proton that is promoted; in the 7.57-MeV level it is a neutron.[6] We have observed similar angular distributions and octupole strengths for excitation of the 5.10-MeV 2- and 5.83-MeV 3- levels of N^{14}, both of which can be formed from the ground state by a $1p_{1/2}$ to $1d_{5/2}$ promotion. The form factor for these single-particle transitions is

$$F(r) \propto r^3 \exp[-(\nu\gamma/\nu+\gamma)\, r^2],$$

where $\gamma^{-1/2}$ is the range of the nucleon-alpha potential, and $\nu(A^{-1/3}F^{-2})$ is the nuclear size parameter.[7] This function has one maximum at

$$r = \left(\frac{3}{2}\,\frac{\gamma+\nu}{\gamma\nu}\right)^{1/2},$$

or about 3 F. It looks roughly like the form factor, $\partial V/\partial r$, used in the macroscopic description and therefore would yield similar angular distributions. The actual intensity we do not discuss here. In any case the similarity in inelastic helium-ion angular distributions and octupole strengths for all these levels shows that their wave functions are very closely related to each other.

Footnotes and References

* NATO Fellow. On leave from Laboratoire de Physique Nucléaire, Orsay (S. et O.), France.

1. A. de Shalit, Phys. Rev. 122, 1530 (1961); A. Braunstein and A. de Shalit, Phys. Letters 1, 264 (1962); B. F. Bayman and L. Silverberg, Nucl. Phys. 16, 625 (1960); M. Harvey, Nucl. Phys. 48, 578 (1963); N. K. Glendenning, Phys. Rev. 119, 213 (1959); J. Vervier, Nuovo Cimento 28, 1412 (1963); M. Bouten and P. van Leuven, Nucl. Phys. 32, 499 (1962).
2. A. M. Lane and E. D. Pendlebury, Nucl. Phys. 15, 39 (1960); G. E. Brown, J. A. Evans, and D. J. Thouless, Nucl. Phys. 24, 1 (1961); J. P. Elliott and B. H. Flowers, Proc. Roy. Soc. (London) 242, 57 (1957).
3. B. G. Harvey et al., Nucl. Phys. 52, 465 (1964).
4. T. Lauritsen and F. Ajzenberg, "Energy Levels of the Light Nuclei," Nuclear Data Sheets, May 1962.
5. R. H. Pehl, Studies in Nuclear Spectroscopy by Two-Nucleon Transfer Reactions (Ph. D. Thesis), UCRL-10993, Aug. 1963.
6. E. C. Halbert and J. B. French, Phys. Rev. 105, 1563 (1957).
7. N. K. Glendenning, Phys. Rev. 114, 1297 (1959).

Table C.12-I. Optical parameters for interaction of 40.6-MeV helium ions with N^{15} and O^{16}.

	V (MeV)	W (MeV)	r_0 (F)	r_a (F)	a_0 (F)	b_0 (F)
N^{15}	-45.1	-15.1	1.30	1.20	0.586	0.500
O^{16}	-45.7	-15.2	1.30	1.20	0.606	0.500

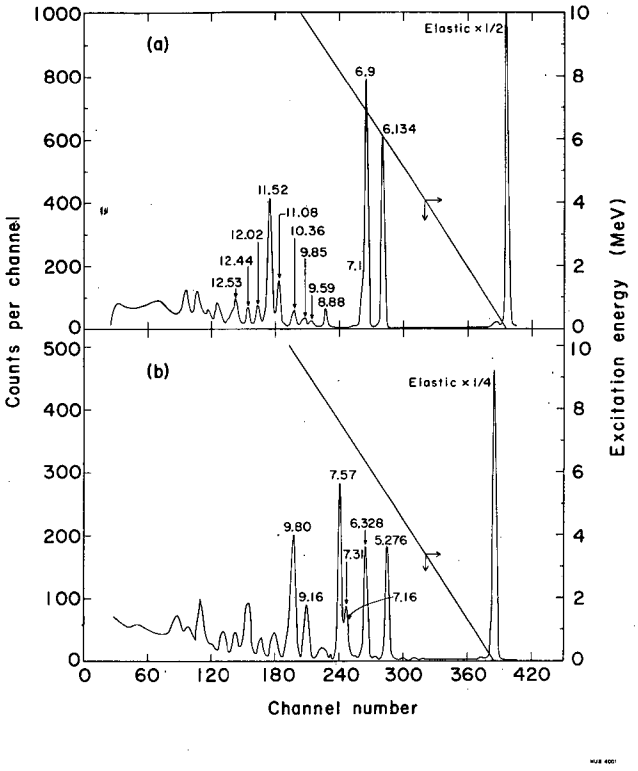

Fig. C.12-1. Energy spectra of 40.6-MeV helium ions scattered from O^{16} (upper) and N^{15} (lower) at 24 deg (lab).

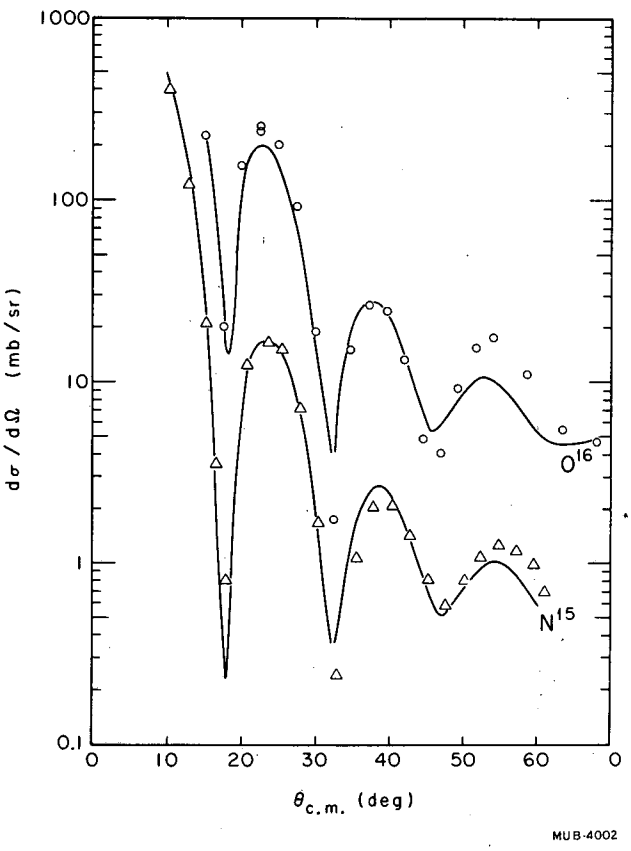

Fig. C.12-2. Experimental and calculated angular distributions for elastic scattering of 40.6-MeV helium ions from N^{15} and O^{16}. The solid line represents the theoretical curve.

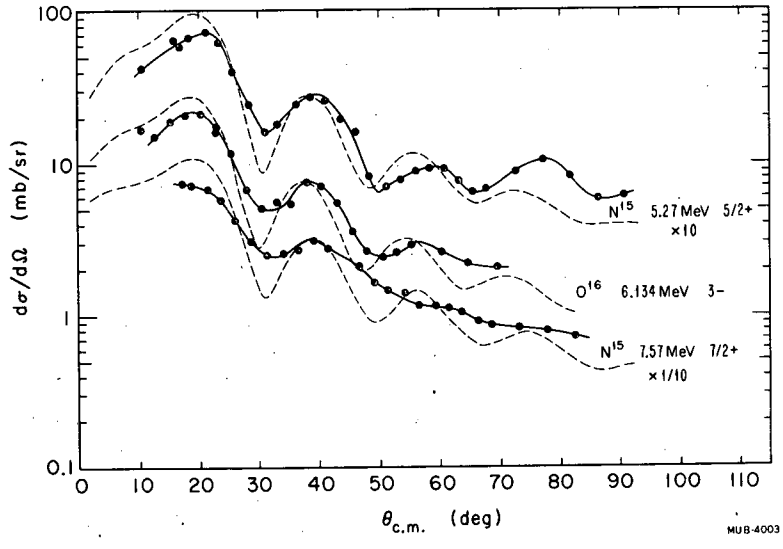

Fig. C.12-3. Angular distributions for 5.27- and 7.57-MeV levels of N^{15} and the 6.134-MeV level of O^{16}. The dashed curves are DWBA calculations for $\ell = 3$, normalized to the experimental curves at the 40-deg maximum.

13. ENERGY VARIATION OF THE PHASE RULE IN α-PARTICLE SCATTERING

J. R. Meriwether, A. Bussière de Nercy,† B. G. Harvey, J. Mahoney, and D. J. Horen

Recently, the use of elastic and inelastic α-particle scattering data to obtain nuclear spectroscopic information has been the subject of a number of theoretical and experimental investigations. Initial application of the Drozdov-Blair-Sharp-Wilets diffraction model[1] to extract information pertaining to spins, parities, and reduced radiative transition probabilities of excited states was relatively successful. Among other things, this model predicts that for the inelastic scattering of α particles, the angular distributions corresponding to odd values of the angular momentum transfer L should be in phase with the elastic angular distribution, while those for even angular momentum transfer should be out of phase. Considerable evidence has been accumulated in support of this model as regards excitations of the first 2+ and 3- states in even-even nuclei, which are believed to arise from single quadrupole and octupole oscillations, respectively. However, several groups have observed that the angular distributions for the alpha groups leading to excitation of the second 2+ and first 4+ levels in medium-weight even-even nuclei, which are assumed to arise from two-phonon excitation, are in some cases out of phase with the elastic group and in other cases in phase.[2]

Blair has indicated that expansion of the diffraction model to second order in the deformation could reproduce the "in phase" characteristic.[1] Recent coupled-channel calculations by Buck have shown that the two-phonon states can be excited either by a direct two-phonon mechanism or by a multiple process.[3] This author found that, for the scattering of 43-MeV α particles by Ni^{58}, the magnitude of the direct and multiple processes for excitation of the 4+ level are comparable.[3] Furthermore, the angular distributions for the two processes, although shifted slightly in opposite directions, were nearly in phase with that for excitation of the first 2+ level. However, as the result of destructive interference, the combined effect of the two excitation mechanisms resulted in an angular distribution which was out of phase with that arising from excitation of the first 2+ level. To fit the experimental data, Buck found it necessary to multiply the predicted contribution from the direct process by a factor of 1.5, and suggested that this might be attributable to a contamination of the 4+ level with a single 4+ phonon component.

Most measurements to date have been made with α particles of energy less than about 48 MeV. It was the purpose of this experiment to investigate the energy dependence of the various mechanisms which have been proposed. By use of the Berkeley 224-cm variable-energy cyclotron, angular distributions for the scattering of 25-, 33-, 50-, 85- and 100- MeV α particles by thin Ni^{62} targets have been measured. The particle detectors were of the lithium-drifted silicon type, varying in thickness from 0.051 cm to about 0.35 cm and gave overall resolutions from 65 keV at 25 MeV to 300 keV at 100 MeV. Angular distributions for scattering to the ground, 1.17-MeV (first 2+), and combined 2.303- and 2.336-MeV (second 2+ and first 4+, respectively) states in Ni^{62} are shown in Fig. C.13-1 for three incident α-particle energies, 33, 50, and 100 MeV. In addition to the data obtained in this work, the results of others[5] are available for 44 MeV. The data show:

a. The angular distribution resulting from excitation of the first 2+ level is out of phase with the elastic distribution over the incident α-particle energy range of 25 to 100 MeV.
b. The angular distribution for the combined excitation of the second 2+ and first 4+ levels is about one-quarter cycle out of phase with the elastic distribution at 25 MeV and is in phase at 100 MeV; there appears to be a smooth variation from out-of-phase to in-phase as one increases the incident α-particle energy.

Comparison of the data, at small angles in the center-of-mass system, with the diffraction model for incident α-particle energies of 50 MeV indicates that the angular momentum transfer involved in excitation of the doublet at 2.3 MeV is L = 4, which would imply that the main contribution arises from excitation of the 4+ level. Complications could arise from the presence of an unresolved 2+ component if its phase were opposite from the phase of the 4+ component and if the relative cross sections for L = 2 and L = 4 varied strongly as a function of bombarding energy. The variation of phase of the angular distribution of a pure L = 4 excitation cannot be explained by the diffraction model. Whether or not a coupled-channel analysis could explain this phenomenon is not yet clear, as the variation of the relative magnitudes of the direct and multiple processes as a function of energy was not discussed in the paper by Buck.[3]

The results reported here clearly indicate the need for additional α-particle scattering measurements, as well as further coupled-channel calculations, as a function of energy of the incident α particles.

Footnote and References

† NATO Fellow, on leave from Laboratoire de Physique Nucléaire, Orsay (S. et O.), France.

1. S. I. Drozdov, Zh. Eksperim. i Teor. Fiz. 36, 1875 (1959) [translation: Soviet Phys.-JETP 9, 1335 (1959)]; J. S. Blair, Phys. Rev. 115, 928 (1959); J. S. Blair, D. Sharp, and L. Wilets, Phys. Rev. 125, 1625 (1961); J. S. Blair, in Proceedings of the Conference on Direct Interactions and Nuclear Reaction Mechanisms, Padua, Italy, September 3-8, 1962 (Gordon and Breach Science Publishers, New York, 1963), p. 669.
2. R. Beurtey, P. Catillon, R. Chaminade, M. Crut, H. Faraggi, A. Papineau, J. Saudinos, and J. Thirion, Compt. Rend. 252, 1756 (1961); H. Broek, T. Braid, J. Yntema, and B. Zeidman, Nucl. Phys. 38, 305 (1962); Phys. Rev. 126, 1514 (1962).
3. B. Buck, Phys. Rev. 127, 940 (1962).
4. G. Bruge, J. C. Faivre, M. Barloutaud, H. Faraggi, and J. Saudinos, Phys. Letters 7, 203 (1963).

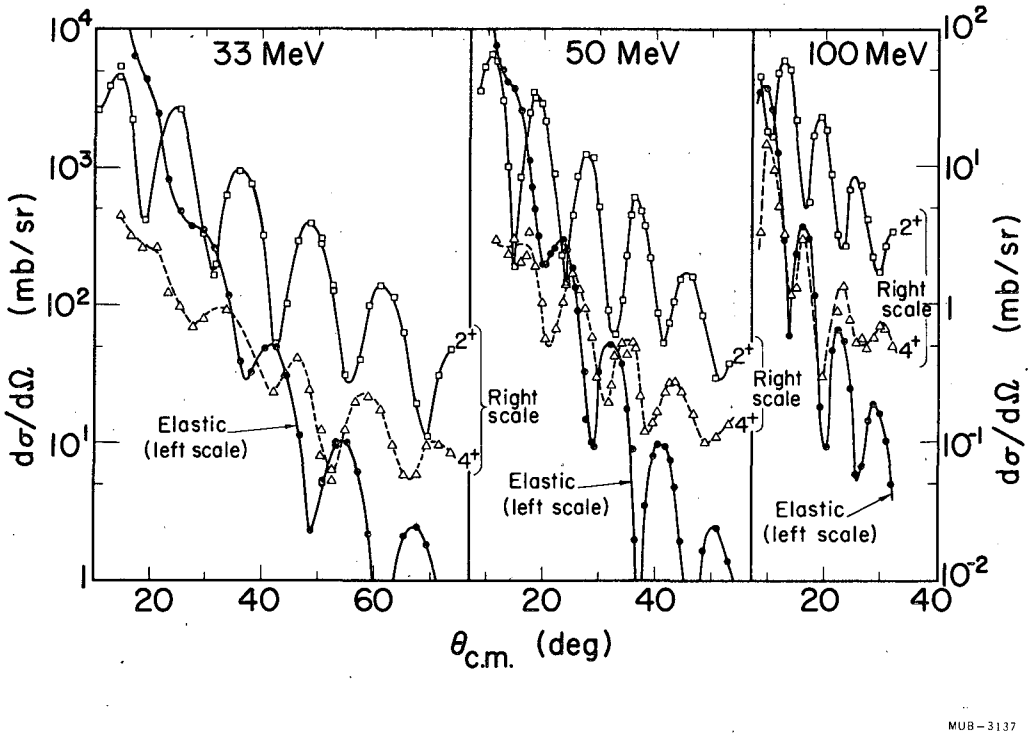

Fig. C. 13-1. Angular distributions of α particles, with incident energies of 33, 50, and 100 MeV, scattered by the ground, 1.17-MeV (2+) and combined 2.303- and 2.336-MeV (second 2+ and first 4+, respectively) states in Ni^{62}.

14. ELASTIC α - α SCATTERING NEAR 40 MeV †

H. E. Conzett, R. J. Slobodrian, S. Yamabe,* and E. Shield

A recent phase-shift analysis[1] of the α-α elastic scattering data available between 23 and 47 MeV[2,3] has indicated a rapid energy variation of the s-, d-, and g-wave phase shifts near 40 MeV. This behavior contrasts markedly with their otherwise rather smooth dependence on energy from 23 to 120 MeV,[1,2,4] and might be interpreted as evidence for resonances corresponding to 0+, 2+, and 4+ states of Be^8 (with appreciable widths for decaying to two α particles). However, since the threshold energy for the first reaction channel ($He^4 + He^4 \rightarrow Li^7 + p$) is 34.7 MeV, and several other reaction channels open near 40 MeV, the possibility exists that threshold effects may be responsible for the suggested behavior of these phase shifts. It is apparent that analyses of data more closely spaced in energy are needed before this question can be resolved.

The variable-energy feature of the Berkeley 88-inch cyclotron has simplified considerably just such an experimental investigation. Thus, we have measured differential cross sections for α - α scattering over c. m. angles from 16 to 100 deg at nine energies between 37 and 43 MeV. The energy resolution was better than 200 keV, and the angular resolution was approximately 0.25 deg. Angular distributions determined at 39, 40, and 41 MeV are shown in Fig. C.14-1, where they demonstrate the very rapid variation with energy previously seen in less detail.[3] The insert in Fig. C.14-1 shows the excitation curve for α - α scattering at the c. m. angle $\theta = 56$ deg ($\theta_{lab} = 28$ deg), which is near the position of the first zero of the Legendre polynomial $P_2(\cos\theta)$. This is clear evidence for rapid changes in the g- or s-wave phase shifts or both in the energy interval shown.

A phase-shift analysis has been carried out, making use of a computer program developed by P. Darriulat.[4] The c. m. cross section can be calculated from the scattering amplitude for charged identical bosons

$$d\sigma/d\Omega = |f(\theta)|^2 ,$$

$$f(\theta) = f_M(\theta) + f_N(\theta),$$

where $f_M(\theta)$ is the Mott scattering amplitude and

$$f_N = \frac{1}{ik} \sum_{\ell,\ \text{even}} (2\ell+1)\, e^{2i\zeta_\ell}\, (e^{2i\delta_\ell} - 1)\, P_\ell(\cos\theta),$$

where $\zeta_\ell = \text{Arg}\ \Gamma(\ell+1+i\eta)$ and where, in turn, $\eta = \frac{4e^2}{\hbar v}$, e in the charge of the electron, $\hbar$ in Planck's constant divided by 2π, and v is the relative velocity. The computer program minimizes a χ^2 function that contains both the error of the experimental cross section and the error due to the angular uncertainty (± 0.2 deg in the c. m. system in the present case).

The analysis by Berztiss[1] was performed under the assumption that the contribution of inelastic processes is small, and therefore he used real phase shifts δ_ℓ. Above 34.7 MeV several reaction channels open up, and particularly the reaction

$$He^4 + He^4 \rightarrow Be^7 + n$$

may lead to appreciable absorption, requiring, for a rigorous analysis, the use of complex phase shifts: $\delta_\ell = \alpha_\ell + i\beta_\ell$. Large variations of the real part of the phase shifts are expected in the neighborhood of thresholds for reactions, even if the imaginary parts are relatively small.[5] Two acceptable sets of phase shifts reproduce the experimental angular distributions. One of them, set #1, is the continuation through the studied energy region of the existing phase shifts. The second set, #2, was obtained by using as starting points values calculated by hand for angular distributions obtained in an earlier experiment.[3]

Figure C.14-2 shows the result of the phase-shift analysis on the $\ell = 2$ partial wave for set #1, together with a comparison with the results of Berztiss analysis. The rapid variation of $\alpha_2 = \text{Re}(\delta_2)$ over the investigated region can be associated with the opening of a reaction channel around 38 MeV, as shown by $|\eta_2| = e^{-2\beta_2}$, plotted along with α_ℓ in the same figure.

Finally, Fig. C.14-3 shows the reaction cross section as a function of energy, obtained through the present analysis for both sets of phase shifts. It is still premature to discard the phase shift set #2 because of an excitation function measurement recently performed at this Laboratory[6] at several fixed angles. This measurement showed two sharp resonances of the $\ell = 2$ partial wave around 34 MeV, and thus a reconsideration of set #2 may be advisable. In any event it is worth while to point out that a reaction cross-section measurement near 43 MeV would probably solve the ambiguity. There both solutions yield reaction cross sections that differ by almost a factor of two.

Footnotes and References

† Expanded version of paper to be published in Proceedings of Congrès International de Physique Nucléaire, Paris, July 1964.

* Permanent address: Physics Department, Osaka University, Osaka, Japan.

1. A. T. Berztiss (University of Melbourne), private communication.
2. E_a = 23 to 38 MeV: D. J. Bredin, W. E. Burcham, D. Evans, W. M. Gibson, J. S. C. McKee, D. J. Prowse, J. Rotblat, and J. N. Snyder, Proc. Roy. Soc. (London) A251, 143 (1959).
3. E_a = 37 to 47 MeV: H. E. Conzett, G. Igo, H. C. Shaw, and R. J. Slobodrian, Phys. Rev. 117, 1075 (1960).
4. P. Darriulat, H. D. Holmgren, G. Igo, and H. G. Pugh, The Elastic Scattering of Alpha Particles by Helium between 53 MeV and 120 MeV, Phys. Rev. (to be published).
5. Fernando B. Morinigo, Nucl. Phys. 36, 529 (1962).
6. H. E. Conzett, P. Darriulat, H. Pugh, E. Shield, and R. J. Slobodrian, Bull. Am. Phys. Soc. 9, 703 (1964), Abstract B. 4.

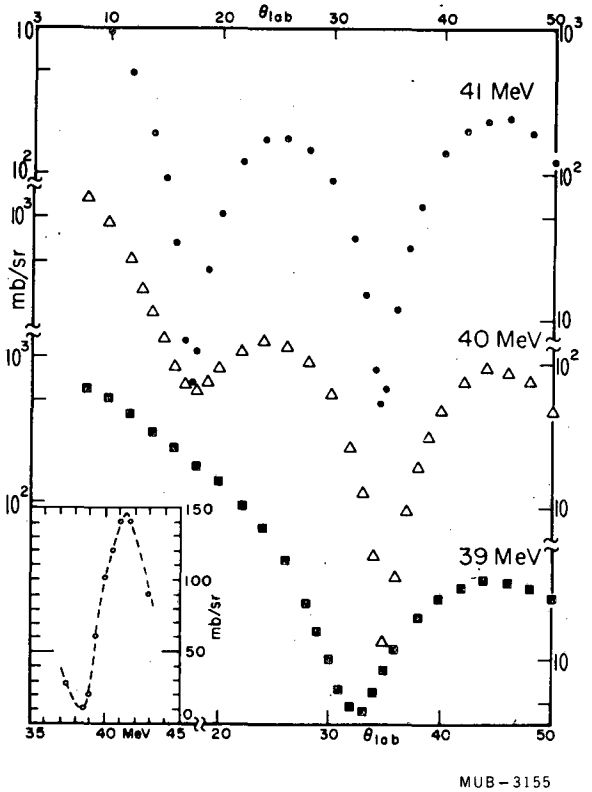

Fig. C.14-1. Center-of-mass differential cross sections for indicated lab energies. The insert shows the excitation curve for the c.m. angle, θ = 56 deg.

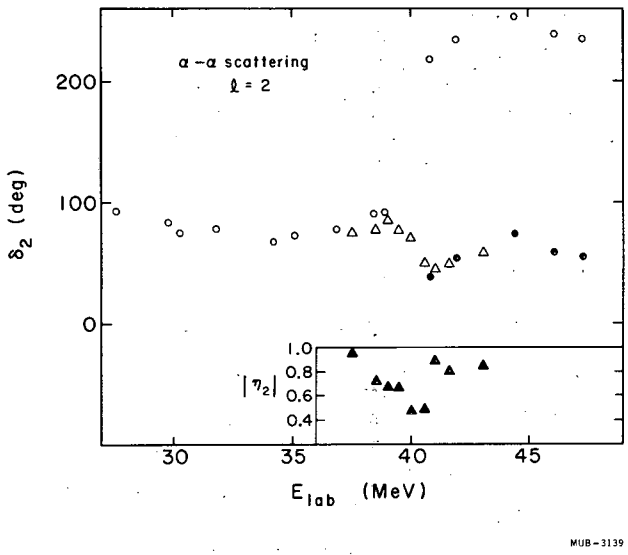

Fig. C. 14-2. The $\ell = 2$ phase shift as a function of lab energy. The open dots are from reference 1. The solid dots represent the open dots displaced by π radians. The open triangles are the $\mathrm{Re}(\delta_2) = a_2$ obtained from the present analysis. The solid triangles show the absorption in the $\ell = 2$ channel; $|\eta_2| = \ell^{-2\beta_\ell}$.

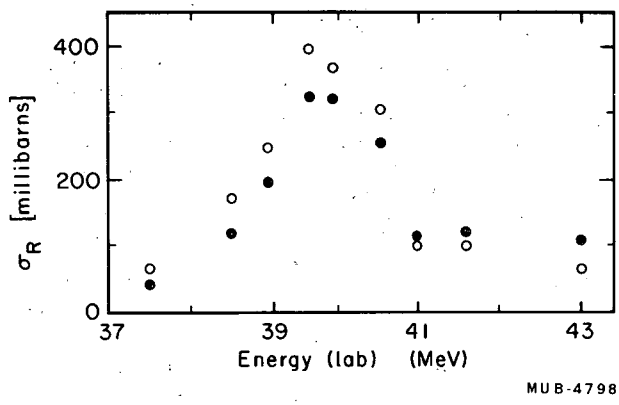

Fig. C.14-3. The reaction cross section, σ_r, as a function of energy, calculated from phase-shift sets 1 and 2. O, Solution 1; ●, Solution 2.

D. PHYSICAL CHEMISTRY

1. ENERGY LEVELS OF 4+ ACTINIDES†

John G. Conway

In recent years there has been considerable success in interpreting the spectra of 3+ actinides in solids[1] and solutions[2] and relating these results to the free-ion calculations. The U^{4+} ion has also been treated in the same way,[3] and Axe has reported on Pa^{4+}.[4]

The complete f^n matrices were made available by Koster and Nielsen.[5] The configurations f^3, f^4, f^5, and f^6 were diagonalized for various values of χ and E/F_2; $\chi (=\zeta/F_2)$ was used instead of ζ, and energy was used in units of $F_2(E/F_2)$ because in this form the results may be compared with those for other atoms. In all cases the $5f$ hydrogenic wave function was used. This is the same assumption as was made in the interpretation of the 3+ ions.

The only available data are for solutions or powdered solids, and all the data are at low resolution and room temperature; hence the energy is of low accuracy, and not all the Stark components are resolved.

Figure D. 1-1 is a plot of the calculated and the experimental levels. The parameters used are listed in Table D. 1-I.

It can be seen that even with the crude data it is possible to derive a set of parameters that can give a satisfactory explanation of the data. Several conclusions can be drawn from such a set of calculations. First, the magnitude of the crystal-field splitting is not so great as to overlap the level positions of the various free ions. This indicates that there is every reason to expect experiments on these ions to yield information about crystal-field parameters, as do experiments on the 3+ ions. Second, one gets a feeling for the magnitude of the Slater parameters and spin-orbit constants. The values of the parameters derived here are probably within 5% of the final values.

Footnotes and References

† Shortened version of J. Chem. Phys. 41, 904 (1964).

1. H. Lämmermann and J. G. Conway, J. Chem. Phys. 38, 259 (1963); J. G. Conway, J. Chem. Phys. 40, 2504 (1964).
2. W. T. Carnall and B. G. Wybourne, J. Chem. Phys. 40, 5428 (1964).
3. J. G. Conway, J. Chem. Phys. 31, 1002 (1959); R. McLaughlin, ibid. 36, 2699 (1962).
4. J. D. Axe, Lawrence Radiation Laboratory Report UCRL-9293, July 1960.
5. G. F. Koster and C. W. Nielson, a magnetic tape entitled "Energy Matrices for All Configurations of Equivalent f Electrons," Massachusetts Institute of Technology, Cambridge, Massachusetts.

Table D. 1-I. Slater parameters and spin-orbit constants for Np^{4+}, Pu^{4+}, Am^{4+}, and Cm^{4+}.

Ion	Pa^{4+}	U^{4+}	Np^{4+}	Pu^{4+}	Am^{4+}	Cm^{4+}
f^n	$5f^1$	$5f^2$	$5f^3$	$5f^4$	$5f^5$	$5f^6$
F_2	···	206	223.8	242.9	282.1	307.0
ζ	1490	1870	2193.	2429.	2821.	3042.

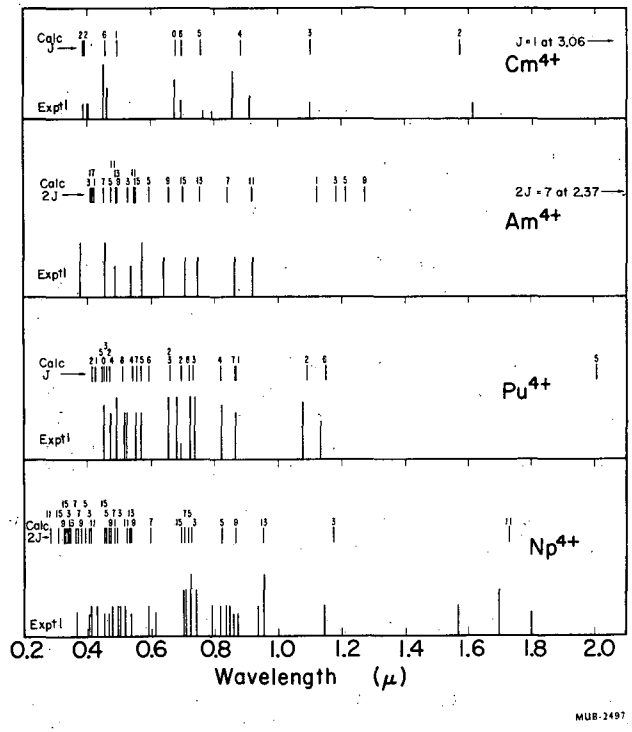

Fig. D. 1-1. Experimental and calculated levels for Np^{4+}, Pu^{4+}, Am^{4+}, and Cm^{4+}. For Np^{4+} and Am^{4+}, the numbers associated with the calculation are equal to 2J. For Pu^{4+} and Cm^{4+}, the numbers are the J values.

2. RED GLOW OF CURIUM†

Ralph G. Gutmacher, E. Kenneth Hulet, and John G. Conway

Curium has been observed to glow with a bright red color on anion-exchange columns and in various compounds. A spectroscopic study has been made of 200 mg of Cm^{244} on Dowex-1 resin and in 10 M lithium chloride solutions. The strongest glow on the resin is at 6065 and 6240 A. In the solution the strongest glow is at 5989 A. A calculation of where the various energy levels should occur for Cm^{+3} shows that there can be only one assignment to this red glow. That is a transition from the first excited state, $^6p_{7/2}$, to ground, $^8s_{7/2}$. The magnitude of the crystal field splitting of the excited level is much larger than expected. Most actinides have splittings of a few hundred cm^{-1}, whereas the splitting of the glow is on the order of 900 to 1000 cm^{-1}.

Footnote

† Shortened version of abstract in J. Opt. Soc. Am. 54, 1403 (1964).

3. HYPERFINE STRUCTURE OF EuI†

Y. Bordarier,* B. R. Judd, and M. Klapisch*

A theoretical analysis has been made of the hyperfine structures of the twelve levels of EuI $4f^7(^8S)6s6p$, using intermediate-coupled eigenfunctions obtained from a least-squares fit of the energies of the levels. Relativistic effects for the 6p electron are calculated throughout by tensor-operator techniques; radial correction factors are taken from Casimir's work.[1] The effective Hamiltonian for each level is, as usual, taken to be of the form

$$A\underset{\sim}{I}\cdot\underset{\sim}{J} + 3B((\underset{\sim}{I}\underset{\sim}{I})^{(2)}\cdot(\underset{\sim}{J}\underset{\sim}{J})^{(2)})/2I(2I-1)J(2J-1).$$

The observed A values[2] are compared to theory in Table D. 3-I. Two calculations (α and β) have been performed: α, employing only two hyperfine parameters (a_s for the 6s electron and a_f for the core ^8S); and β, in which the contribution from the 6p electron is no longer derived from the spin-orbit coupling parameter ζ_p, but included as an additional parameter. The values of a_f (-2.35 for α, -2.52 for β) are in reasonable agreement with that deduced from the spectra of EuI $4f^7(^8S)6s^2$ and EuIII $4f^7(^8S)$ (namely -2.05), and also with that deduced from the two levels $^9S_4$ and $^7S_3$ of EuII $4f^7(^8S)6s$ (namely -2.37). Almost all of a_f comes from core polarization.

The hyperfine-structure anomalies Δ fall into a consistent pattern (see Table D. 3-II), and permit one to obtain a value of Δ(s) for a single s electron that agrees with that of Baker and Williams[3] (-0.65%) after allowance is made for the recent correction[4] to $\mu(153)/\mu(151)$, the ratio of the magnetic moments of ^{153}Eu and ^{151}Eu. Calculated and experimental values of B are set out in Table D. 3-III for those levels for which measurements have been made. The single parameter which is necessary for each isotope can be further analyzed, and the quadrupole moments Q (without Sternheimer corrections) are deduced to be $Q(151) = 1.16 \pm 0.08$ b and $Q(153) = 2.92 \pm 0.20$ b. These are some 20% larger than those of Krebs and Winkler,[5] though the combined limits of error only just fail to meet. Their values were obtained from an analysis of the single level $^9P_5$ of EuII $4f^7(^8S)6p$, which may possibly be subject to undetermined perturbations. It is noteworthy that the calculated B value of $y^8P_{9/2}$, the only level listed in Table D. 3-III with the coupling $(6s6p)^1P$, is much larger than the experimental value; and this effect is also observed for the ^1P levels of 6s6p in other atoms (for example, Hg, Ba, and Yb).

Footnotes and References

† Brief form of UCRL-11745 [submitted to Proc. Roy. Soc. (London)].

* Laboratoire Aimé Cotton, C.N.R.S., Bellevue, S. et O., France.

1. H. B. G. Casimir, On the Interaction Between Atomic Nuclei and Electrons (Freeman and Co., San Francisco, 1963).
2. W. Müller, A. Steudel, and H. Walther, Z. Phys. (to be published).
3. J. M. Baker and F. I. B. Williams, Proc. Roy. Soc. (London) A267, 283 (1962).
4. P. G. H. Sandars and G. K. Woodgate, private communication.
5. K. Krebs and R. Winkler, Naturwiss. 47, 490 (1960).

Table D. 3-I. Values of A for ^{151}EuI $4f^7(^8S)6s6p$ (in mK).

Level	Calculated A		Observed
$^{10}P_{11/2}$	30.70	30.90	31.13 ± 0.10
$^{10}P_{9/2}$	34.35	34.62	34.138 ± 0.008
$z^8P_{9/2}$	22.16	21.69	22.18 ± 0.01
$y^8P_{9/2}$	- 8.32	- 7.71	- 7.68 ± 0.11
$^{10}P_{7/2}$	32.55	32.36	32.32 ± 0.02
$y^8P_{7/2}$	- 7.57	- 6.95	- 7.1 ± 0.2
$^6P_{7/2}$	1.09	0.54	$0 < A < 2.2$
$y^8P_{5/2}$	- 4.68	- 4.11	$-5 < A < 0$
$^6P_{5/2}$	-18.98	-19.74	-19.72 ± 0.05

Table D. 3-II. Hyperfine-structure anomalies.

Level	$\Delta/\Delta(s)$ (Theory)	Δ(Observed)	$\Delta(s)$ (Calculated)
$^{10}P_{9/2}$	0.88	-0.57 ± 0.12%	-0.64 ± 0.14%
$z^8P_{9/2}$	0.88	-0.40 ± 0.20%	-0.45 ± 0.23%
$^{10}P_{7/2}$	1.18	-0.75 ± 0.12%	-0.64 ± 0.10%

Table D. 3-III. Values of B for EuI $4f^7(^8S)6s6p$ (in mK).

Level	B for ^{151}Eu		B for ^{153}Eu	
	Theory	Experiment	Theory	Experiment
$^{10}P_{11/2}$	13.19	13.5 ± 1.5	33.26	---
$^{10}P_{9/2}$	-16.56	-16.79 ± 0.10	-41.75	-42.13 ± 0.12
$z^8P_{9/2}$	10.01	9.65 ± 0.15	25.23	24.62 ± 0.15
$y^8P_{9/2}$	13.75	8.6 ± 1.2	34.65	---
$^{10}P_{7/2}$	5.28	5.25 ± 0.20	13.30	13.27 ± 0.15
$^6P_{5/2}$	-12.78	-11.8 ± 0.4	-32.23	---

4. THE CRYSTAL STRUCTURE OF SODIUM FLUOSILICATE†

Allan Zalkin, J. D. Forrester,* and David H. Templeton

Sodium fluosilicate came to our attention as the result of hydrolysis of a sample of XeF_4 in a Pyrex vessel. The hexagonal crystals were found with orthorhombic crystals of $NaBF_4$ as a residue after evaporation of the solution. In seeking the identity of these crystals we discovered contradictions in the literature concerning sodium fluosilicate which led us to undertake the determination of the structure.

According to x-ray powder diffraction data, sodium fluosilicate has the same crystal structure as Na_2GeF_6 (Cox,[1] Cipriani[2]), Na_2TiF_6, Na_2MnF_6, Na_2PtF_6, Li_2SiF_6 (Cox[1]), Na_6PdF_6, Na_2RhF_6 (Cox et al.[3]), and Na_2IrF_6 (Hepworth et al.[4]). A determination of this structure was reported by Cipriani,[2] but we believe it to be in error because of incorrect choice of symmetry.

Crystals of Na_2SiF_6, found as crusts on lava at Vesuvius, are known as the mineral malladrite (Palache et al.[5]).

Crystals of Na_2SiF_6 were prepared by dissolving $(NH_4)_2SiF_6$ in water, adding NaOH solution, and heating briefly. On cooling, numerous well-formed small crystals of sodium fluosilicate were obtained.

A "single crystal" (later found to be twinned) with the shape of a hexagonal prism and of approximate dimensions $0.08 \times 0.08 \times 0.08$ mm was used for collecting the intensity data.

The 270 independent reflections permitted by the space group in the sphere of reflection with $\sin\theta/\lambda$ less than 0.596 ($2\theta < 50$ deg) were measured with counting times of 20 sec each. Of these, only two were recorded as zero intensity. A correction for twinning was made.

The primitive cell contains three formula units Na_2SiF_6, and is trigonal with dimensions $a = 8.859 \pm 0.002$ Å, $c = 5.038 \pm 0.002$ Å. The density is calculated as 2.74 g/cm^3, compared with 2.755 measured by Stolba.[6] Axial dimensions and ratios are compared with other work in Table D. 4-I.

An initial inspection of the film data gave the impression that a sixfold symmetry axis was present. The superior precision of the counter measurements showed on the contrary that the crystal had Laue symmetry $\bar{3}$m, in agreement with Cipriani.[1] The mirror symmetry of this Laue group is oriented with a plane perpendicular to the primitive a axis, as indicated by the full symbol $\bar{3}$m1 rather than $\bar{3}$1m. Our final structure has the symmetry of space group P321.

The sodium atoms are in two independent threefold sets, and each fluorine octahedron is free to rotate about its threefold axis. The atoms are distributed in the final sets of positions; the atomic parameters are shown in Table D. 3-I.

Space group P321

Si(1) in 1(a): 0, 0, 0.
Si(2) in 2(d): 1/3, 2/3, z; 2/3, 1/3, $\bar{z}$.
Na(1) in 3(e): x, x, 0; $\bar{x}$, 0, 0; 0, $\bar{x}$, 0.
Na(2) in 3(f): x, x, 1/2; $\bar{x}$, 0, 1/2; 0, $\bar{x}$, 1/2.
F(1), F(2), and F(3) each in 6 (g): x, y, z; $\bar{y}$, x-y, z; y-x, $\bar{x}$, z; y, x, $\bar{z}$; $\bar{x}$, y-x, $\bar{z}$; x-y, $\bar{y}$, $\bar{z}$.

It was noticed that we were calculating much larger differences between F(hkℓ) and F(khℓ) than were found in our experimental data. This fact suggested twinning such that hkℓ and khℓ are interchanged in position. This can be accomplished by rotation about c or by reflection in (100). Because of the possibility that the crystals may be optically active, these twin laws in principle are distinguishable by optical methods, but we have no evidence for choosing between them.

By trial we found the best agreement by assuming 59% of one twin and 41% of the other. Introduction of the correction for twinning made a substantial reduction in the largest discrepancies, but caused only small changes in the structure. No atom was moved as much as 0.1 Å

as a result of this correction. The change from isotropic to anisotropic temperature factors made little improvement in the agreement and moved no atom more than 0.01 Å.

The crystal structure is shown in Fig. D. 4-1. There are two independent kinds of SiF_6^{-2} ions, but their dimensions are equal and their shapes are regular-octahedral within the accuracy of the experiment. The mean Si-F bond distance is observed as 1.68 Å. Correction for thermal motion with the assumption that F rides on Si increases this distance to 1.695 ± 0.005 Å. Several measurements of this bond distance in other crystals have given values in the range 1.65 to 1.75 Å (Gossner and Kraus,[7] Ketelaar,[8] Hoard and Vincent,[9] Hoard and Williams[10]).

The F-Si-F bond angles are 90 or 180 deg within 2 deg or less, with standard deviations estimated as 1 deg.

Each sodium atom is in an "octahedral" hole, with six fluorine neighbors at distances which are only approximately equal. These distances range from 2.18 to 2.45 Å, with standard deviations of 0.01 Å. The average Na-F distance is 2.32 Å. The F-Na-F angles deviate by nearly as much as 30 deg from the 90- or 180-deg values they would have if the coordination polyhedron were a regular octahedron.

This structure of Na_2SiF_6 is remarkably similar to that found by Stanley[11] for $K_2S_2O_6$: a = 9.785 Å, c = 6.295 Å, c/a = 0.643, space group P321. If the pair of S atoms in each dithionate ion is considered as a single atom, then the two structures have atoms in the same sets of positions, with K corresponding to Na, S_2 corresponding to Si, and O corresponding to F.

Footnotes and References

† Brief form of paper in Acta Cryst. 17, 1408 (1964).

* Present address: Imperial Chemical Industries, Ltd., Runcorn, Cheshire, England.

1. B. Cox, J. Chem. Soc. 1954, 3251.
2. C. Cipriani, Rend. Soc. Mineralog. Ital. 11, 58, (1955).
3. B. Cox, D. W. A. Sharp, and A. G. Sharpe, J. Chem. Soc. 1956, 1242.
4. M. A. Hepworth, P. L. Robinson, and G. S. Westland, J. Chem. Soc. 1958, 611.
5. C. Palache, H. Berman, and C. Frondel, Dana's System of Mineralogy (John Wiley and Sons, New York, 1951), vol. 2, p. 105.
6. Stolba, Z. anal. Chem. 11, 199 (1872).
7. E. Gossner and O. Kraus, Z. Kristallogr. 88, 223 (1934).
8. J. A. A. Ketelaar, Z. Kristallogr. 92, 155 (1935).
9. J. L. Hoard and W. B. Vincent, J. Am. Chem. Soc. 62, 3126 (1940).
10. J. L. Hoard and M. B. Williams, J. Am. Chem. Soc. 64, 633 (1942).
11. E. Stanley, Acta Cryst. 9, 897 (1956).

Table D. 4-I. Final coordinates and estimated standard deviations.[a]

	x	σ(x)	y	σ(y)	z	σ(z)
Si(1)	(0)	---	(0)	---	(0)	---
Si(2)	(1/3)	---	(2/3)	---	0.5062	0.0012
Na(1)	0.3790	0.0010	(0.3790)	---	(0)	---
Na(2)	0.7143	0.0009	(0.7143)	---	(1/2)	---
F(1)	0.0870	0.0018	-0.0918	0.0017	0.8099	0.0014
F(2)	0.4442	0.0012	-0.4006	0.0013	0.7007	0.0014
F(3)	0.2299	0.0015	-0.2599	0.0015	0.3098	0.0014

[a] Parentheses indicate coordinates which are not independent parameters.

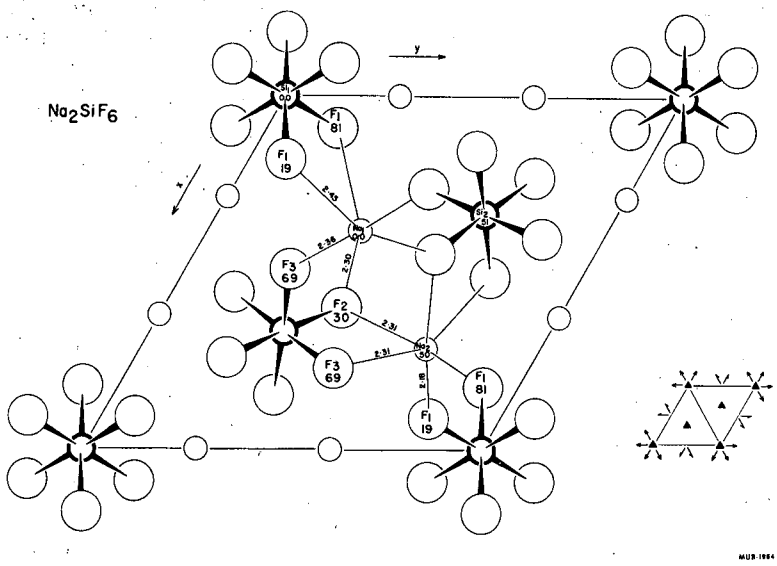

Fig. D. 4-1. Crystal structure of Na_2SiF_6. The z coordinates (× 100) are indicated for some of the atoms, and the lengths (in Å) are given for some of the interatomic distances.

5. CRYSTAL AND MOLECULAR STRUCTURE OF FERRICHROME A†

Allan Zalkin, J. D. Forrester,* and David H. Templeton

Ferrichrome A, a product of the metabolism of the smut fungus Ustilago sphaerogena, is a ferric hydroxamate and a cyclic hexapeptide consisting of residues of the amino acids glycine, serine, and ornithine.[1] It is related in structure to several substances which are growth factors for certain micro-organisms.[2-4] Its structure is also of interest for possible clues to the structures of proteins. By x-ray diffraction methods we have determined the crystal structure and have found the molecular structure (Fig. D. 5-1) to be in agreement with deductions from chemical evidence.[1-5]

Crystals of composition $C_{41}H_{58}N_9O_{20}Fe \cdot 4H_2O$ are monoclinic, space group $P2_1$, with $a = 11.02 \pm 0.02$, $b = 13.26 \pm 0.03$, $c = 18.22 \pm 0.01$ Å, $\beta = 99.48°$, $Z = 2$. The density calculated from the x-ray data, $D_x = 1.42$, is to be compared with $D_m = 1.45$ g cm^{-3}.[2] Diffraction measurements were made by scintillation counting with a crystal about $0.1 \times 0.1 \times 0.2$ mm. Because MoKα radiation gave low counting rates, we recorded the intensities of 3115 independent reflections with FeKα radiation; of these, only 56 were recorded as zero. To determine the absolute configuration of the structure we measured the intensities of 71 pairs ($hk\ell$ and $h\bar{k}\ell$) with CuKα radiation, which iron atoms scatter with a large phase shift (anomalous dispersion effect). Significant intensity differences were observed for 40 pairs, and in each case the sign of the difference is explained by our final structure. This test shows that we have the correct absolute configuration and at the same time is strong evidence for the correctness of the structure determination.

The position of the iron atom was guessed correctly from the Patterson function and later confirmed with the anomalous-dispersion data. The structure was determined by repeated electron density calculations alternated with least-squares refinement.

The electron density maps were excellent for most of the structure, but suggested disorder for a few atoms. One water molecule was distributed among three sites so close together

that only one at a time could be occupied. The oxygen atom of one serine side chain, the methyl carbon and alpha carbon of one methyl glutaconic acid residue, and the oxygen atoms of the terminal carboxyl group of another glutaconic acid were each assigned two sites corresponding to two ways of twisting each of these groups. An electron-density difference function calculated at this point showed peaks which can be explained as the result of anisotropic thermal motion or as the result of slight shifts associated with the disorder of neighboring atoms. Other peaks were found in correct positions for about 40 hydrogen atoms on those parts of the structure for which the effects of disorder and anisotropic motion are less severe.

The molecular shape is shown in Fig. D. 5-2. The sequence of amino acid residues in the cyclic peptide is -Orn-Orn-Orn-Ser-Ser-Gly-. The configuration of the ring is trans at each peptide linkage. The absolute configuration of each of the five asymmetric alpha carbon atoms is the same as that commonly found in other peptides of biological origin, and which is described conventionally as left-handed. The absolute configuration of the three hydroxamate rings at the iron atom (Fig. D. 5-3) is that of a left-handed propeller. In such a ring structure there are two distinct ways in which the polarities of the C-N bonds can be arranged: either all the same way or one different from the other two. We find the more symmetrical structure in which the polarities are the same in the three rings, as shown in Fig. D. 5-3.

We recognize two hydrogen bonds within the molecule. One of length 2.99 Å bridges the peptide ring and joins the alpha nitrogen of one ornithine residue to the carbonyl oxygen of one serine residue. This bond distance corresponds to a weak bond. In the flat representation of this ring (Fig. D. 5-1) there seems to be the possibility of a second hydrogen bond across the ring, but the folding of the ring in the actual structure does not permit this. A second hydrogen bond of length 2.79 Å joins the alpha nitrogen of the second ornithine residue to the oxygen atom of the delta nitrogen of this same residue.

Several other hydrogen bonds connect various oxygen atoms with water molecules which in turn are connected to other ferrichrome molecules. There is disorder in some of these bonds, because they involve some of the atoms with alternate sites.

Bond distances and angles which do not involve hydrogen atoms are in good agreement with the expected values, with standard deviations of the distances of ≈0.02 Å. The six oxygen neighbors of the iron atom are at distances ranging from 1.96 to 2.07 Å. The bond angles at the iron atom which would be 90 deg for a regular octahedron range from 78 to 101 deg.

We thank Prof. J. B. Neilands for providing the crystals for this investigation and for helpful discussions concerning the molecular structure.

Footnotes and References

† Condensed form of Science 146, 261 (1964).

* Present address: Imperial Chemical Industries, Ltd., Runcorn, Cheshire, England.

1. T. Emery and J. B. Neilands, J. Am. Chem. Soc. 83, 1626 (1961).
2. J. B. Neilands, Bact. Rev. 21, 101 (1957).
3. V. Prelog, Pure Appl. Chem. 6, 327 (1963).
4. O. Mikeš and J. Turková, Chem. listy 58, 65 (1964).
5. S. J. Rogers, R. A. J. Warren, and J. B. Neilands, Nature 200, 167 (1963).

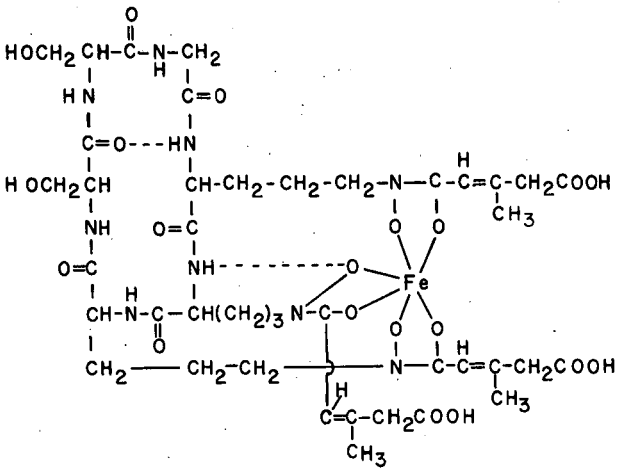

Fig. D. 5-1. Ferrichrome A.

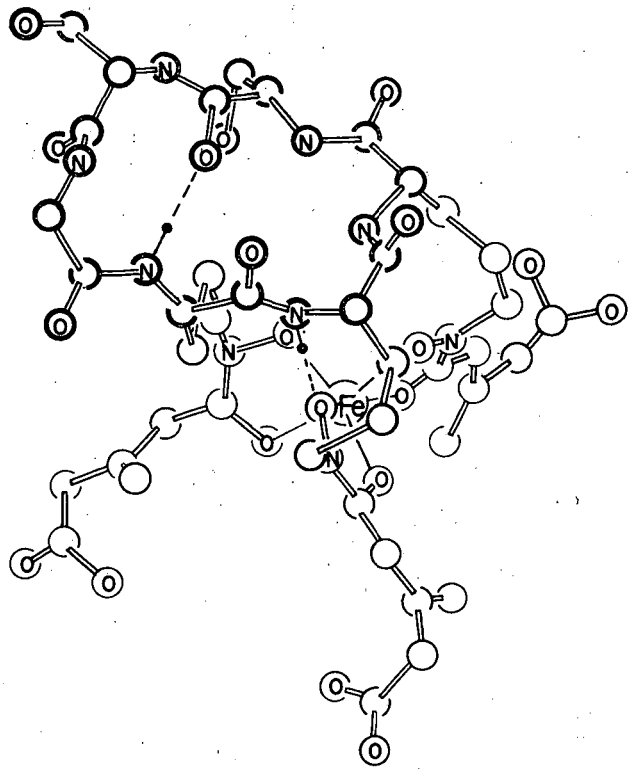

Fig. D. 5-2. Molecular shape of ferrichrome A; only one of the two configurations is shown for the disordered atoms, which are the oxygen at the upper left corner, the carboxyl at the far right, and the center of the methyl glutaconic acid residue at the lower left.

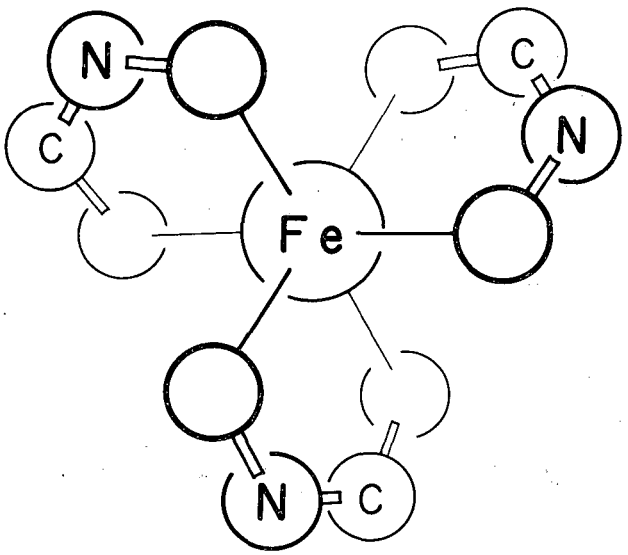

Fig. D. 5-3. Absolute configuration around the iron atom (left-handed coordination propeller about Fe) in Ferrichrome A.

6. THE CRYSTAL STRUCTURE OF CESIUM AQUOPENTACHLORORUTHENATE

Ted E. Hopkins, Allan Zalkin, David H. Templeton, and Martyn G. Adamson

A series of aquopentachlororuthenates with cations of potassium, rubidium, cesium, and tetraphenylarsenic have been prepared. The crystal structure of only the potassium salt has been reported.[1]

A single prismatic crystal 0.14×0.021×0.02 mm was used. Accurate cell dimensions and reflected intensities were determined with a General Electric XRD-5 goniostat with a scintillation counter and Mo Kα radiation (λ = 0.70926 Å, Kα1). There were 525 independent reflections, which were measured with 10-second counts, and 95 recorded as zero intensity.

The unit cell contains four formula units of $Cs_2RuCl_5H_2O$. It is face-centered orthorhombic with dimensions a = 7.986 Å, b = 17.289 Å, c = 7.400 Å; D_x = 3.65 g/cm^3. The space group was found to be Amam.

A three-dimensional Patterson function was calculated from the observed intensities, and the cesium-ruthenium and ruthenium-chlorine vectors were identified. Least-squares refinement of the structure resulted in a final value for R of 7%, with all atoms being allowed anisotropic temperature factors. Except for one set of chlorine atoms, all the atoms are in special positions 4(c): 1/4, y, 0; 3/4, -y, 0; + (0, 0, 0; 0, 1/2, 1/2). A set of four chlorines are in the general positions 16(h): ± (x, y, z; -x, -y, z; 1/2 -x, y, z; 1/2 + x, -y, z) + (0, 0, 0; 0, 1/2, 1/2). The y parameters are, for Cs(1), 0.4715; Cs(2), 0.7534; Ru, 0.1153; Cl(1), 0.2490; and O, 0.9936. For Cl(2) the x parameter is 0.4605, y is 0.1112, and z is 0.2222.

The bond angles and distances are shown in Fig. D.6-1. It was found that the six atoms surrounding the ruthenium do not lie at the corners of a regular octahedron. The packing of the atoms is illustrated in an aclinic projection of the unit cell in Fig. D.6-2.

Reference

1. T. S. Khodashova, Zh. Strukt. Khim. 1, 333 (1960).

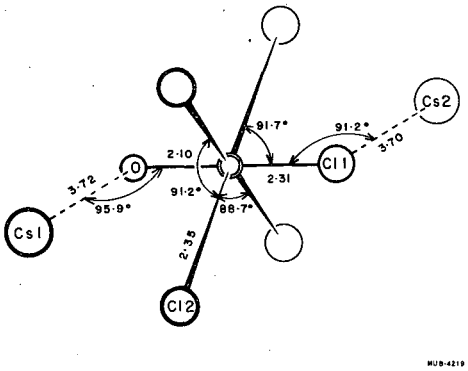

Fig. D.6-1. Bond angles and distances.

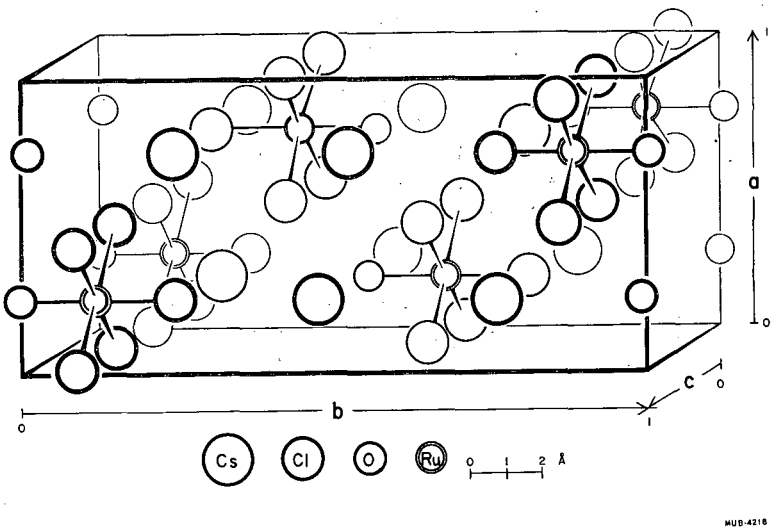

Fig. D.6-2. Aclinic projection of the unit cell.

7. POTASSIUM PERXENATE NONAHYDRATE†

Allan Zalkin, J. D. Forrester,* David H. Templeton,
Stanley M. Williamson, and Charles W. Koch

Several salts of the unstable perxenic acid have been isolated and identified. Sodium perxenate exists in several crystalline forms,[1,2] and the structures of $Na_4XeO_6 \cdot 8H_2O$[3,4] and $Na_4XeO_6 \cdot 6H_2O$[5] have been determined. Perxenate salts of barium[6,7] and of calcium, lithium, and cesium[7] have been prepared, but their structures are unknown. We have now prepared a potassium salt and characterized it as $K_4XeO_6 \cdot 9H_2O$ by determination of its crystal structure.

The solubility of potassium perxenate appears to be much greater than that of the sodium perxenates at a given concentration of OH^-. The disproportionation reaction of xenic acid in potassium hydroxide solution failed to give crystals under conditions analogous to those under which $Na_4XeO_6 \cdot 8H_2O$ was easily crystallized. Appelman and Malm have described other failures to obtain potassium perxenate.[6] We obtained the potassium salt by the following procedure. A concentrated solution of reagent-grade KOH was treated with a small amount of $KMnO_4$(s) and was heated at 70° for three days, i.e., until the purple color was no longer present. The solution (10.04 M) was decanted from the sediment and was used without further treatment. Prolonged exposure to the atmosphere was avoided, and all experiments were carried out in Pyrex ware. After thorough degassing, 200 µl of the base and 750 µl of 0.1082 M xenic acid, prepared by dissolution of XeO_3(s), were mixed in vacuum at 0°. By gas-evolution measurements similar to those previously described,[8] it was determined that 26.06 µmole of Xe(VIII) was prepared. No crystals were obtained by cooling the solution to 0°. We removed 400 µl of H_2O via vacuum distillation and added 200 µl of the xenic acid. This increment of 21.64 µmole of xenic acid produced only an additional 5.61 µmole of Xe(VIII). When this solution was cooled slowly to 5°, well-defined colorless transparent crystals appeared. After equilibrium at 5° was established, about three-fourths of the mother liquor was removed. The crystals in the remaining solution were stable and insoluble at room temperature. Before crystallization the concentrations were [Xe(VIII)] = 0.042 and $[K^+]$ = 3.39.

Crystals were studied by the same x-ray techniques as we used for sodium perxenate.[5] The crystals of the potassium salt are considerably more stable in x rays than $Na_4XeO_6 \cdot 6H_2O$, but less so than $Na_4XeO_6 \cdot 8H_2O$. The measurements include 1412 independent reflections; of these, we recorded 95 as zero. No correction was made for absorption or extinction.

The symmetry is orthorhombic, space group $Pbc2_1$ (C_{2v}^5), with a = 9.049 ± 0.004, b = 10.924 ± 0.004, c = 15.606 ± 0.006 Å, Z = 4, d_x = 2.35 g/ml. Each atom is in general positions 4(a): x, y, z; -x, -y, 1/2 + z; -x, 1/2 + y, z; x, 1/2 - y, 1/2 + z. Further refinement, with potassium atoms assigned anisotropic thermal parameters, reduced R to 0.058.

The composition is assigned as $K_4XeO_6 \cdot 9H_2O$ on the basis of the good agreement with the x-ray data.

Atomic coordinates are listed in Table D.7-I. The XeO_6^{-4} ion is in the shape of a regular octahedron within experimental accuracy, with average Xe-O distance 1.86 ± 0.01 Å, in excellent agreement with 1.864 ± 0.012 Å (reference 4) and 1.84 ± 0.02 Å (reference 5) found in the two sodium salts. The bond angles that would be 90 deg for a regular octahedron range from 88.8 to 91.2 deg (σ = 0.7 deg). The four independent potassium atoms have respectively 6, 6, 7, and 7 water molecules and 2, 1, 1, and 2 oxygen atoms of perxenate as neighbors, as indicated in Fig. D.7-1, at distances ranging from 2.67 to 3.22 Å. These neighbors are at the corners of very irregular polyhedra, and some other neighbors are not much more distant. An intricate network of hydrogen bonds connects the entire structure.

Footnotes and References

† Condensation of J. Am. Chem. Soc. 86, 3569 (1964).

* Present address: Imperial Chemical Industries, Ltd., Runcorn, Cheshire, England.

1. J. G. Malm, B. D. Holt, and R. W. Bane, in Noble Gas Compounds, H. H. Hyman, Ed. (University of Chicago Press, Chicago, Ill., 1963), p. 167.
2. S. Siegel and E. Gebert, ibid., p. 193.
3. W. C. Hamilton, J. A. Ibers, and D. R. Mackenzie, Science 141, 532 (1963).
4. J. A. Ibers, W. C. Hamilton, and D. R. Mackenzie, Inorg. Chem. 3, 1412 (1964).

5. A. Zalkin, J. D. Forrester, D. H. Templeton, S. M. Williamson, and C. W. Koch, Science 142, 501 (1963).
6. E. H. Appelman and J. G. Malm, J. Am. Chem. Soc. 86, 2141 (1964).
7. C. W. Koch and S. M. Williamson, unpublished work.
8. S. M. Williamson and C. W. Koch, in Noble Gas Compounds, H. H. Hyman, Ed. (University of Chicago Press, Chicago, Ill., 1963), p. 158.

Table D.7-I. Atomic coordinates and thermal parameters[a]

Atom	x	y	z	B (Å^2)
Xe	0.249	0.988	0.250	1.1[b]
K(1)	0.628	0.987	0.339	2.1[b]
K(2)	0.846	0.238	0.958	2.9[b]
K(3)	0.307	0.227	0.026	3.2[b]
K(4)	0.877	0.989	0.139	1.9[b]
O(1)	0.403	0.101	0.251	2.4
O(2)	0.094	0.878	0.253	2.4
O(3)	0.138	0.096	0.316	2.0
O(4)	0.176	0.058	0.151	2.2
O(5)	0.323	0.918	0.351	1.6
O(6)	0.360	0.881	0.188	2.3
W(1)[c]	0.654	0.839	0.190	1.9
W(2)	0.850	0.136	0.297	1.9
W(3)	0.873	0.829	0.369	2.2
W(4)	0.692	0.046	0.506	3.0
W(5)	0.997	0.243	0.111	2.0
W(6)	0.967	0.980	0.972	2.7
W(7)	0.376	0.470	0.002	3.1
W(8)	0.493	0.262	0.886	3.1
W(9)	0.606	0.150	0.124	2.8

a. Standard deviations correspond to 0.02 Å or less for coordinates and 0.3 Å^2 or less for B.
b. Value equivalent to average of anisotropic parameters.
c. "W" indicates oxygen atom of water molecule.

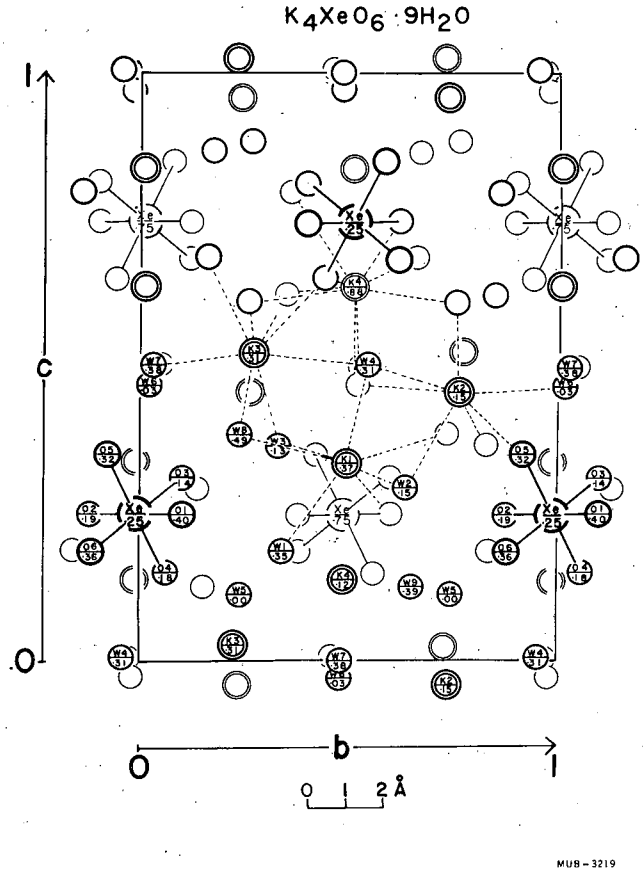

Fig. D.7-1. Crystal structure of $K_4XeO_6 \cdot 9H_2O$ viewed down the a axis. The designation and x coordinate are indicated on some of the atoms. Broken lines connect potassium atoms to their neighbors.

8. THE CRYSTAL AND MOLECULAR STRUCTURE OF A COBALT CHELATE†

J. D. Forrester,* Allan Zalkin, and David H. Templeton

The crystal and molecular structure of di(tetra-n-butyl ammonium) cobalt(II) bis-(maleonitrile dithiolate) has been determined from an x-ray diffraction study of a single crystal specimen. This substance is a salt:

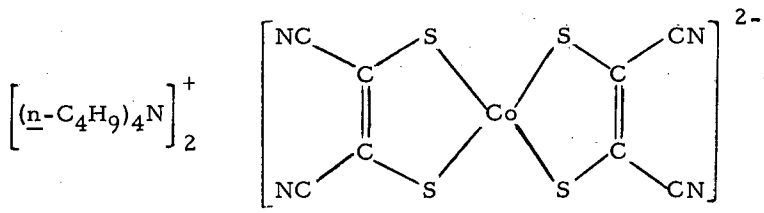

An x-ray structure determination was completed very recently by Eisenberg et al. [1] on a related substance, $[(CH_3)_4N]_2^+ [Ni(MNT)_2]^{2-}$, and our work is in very close agreement with this.

Maki et al. [2] have recently used the results of the present crystallographic investigation in a detailed report on the electronic structures of several members of this series of compounds.

x-Ray photographs obtained by the Weissenberg technique and copper radiation established the diffraction symmetry of the crystal. Intensities were measured for 2213 independent reflections with a General Electric XRD-5 goniostat equipped with a scintillation counter and a pulse-height discriminator, with MoKα radiation.

A convenient primitive unit cell contains one formula unit $[(n\text{-}C_4H_9)_4N]_2^+ [Co(S_2C_4N_2)_2]^{2-}$ and is triclinic with dimensions a = 10.77 ± 0.01, b = 12.35 ± 0.01, c = 9.81 ± 0.01 Å, α = 88.5 ± 0.1, β = 114.8 ± 0.1, γ = 93.5 ± 0.1 deg, V = 1182.0 Å^3. With one formula unit per unit cell, the density calculated from the x-ray data is 1.16 g/cm^3, in comparison with the value of 1.14 g/cm^3 found by flotation methods with a mixture of benzene and carbon tetrachloride. The space group is PT. With the exception of the Co atom, which is in a special position, 1 (a) 0, 0, 0, all the atoms are in general twofold positions, 2 (i) ±(x, y, z). Preliminary positions were found for 26 atoms by Fourier methods.

A least-squares refinement of these atoms, each having an isotropic temperature factor of the form $\exp(-B\lambda^{-2}\sin^2\theta)$, and using 1627 terms each with unit weight, resulted in a conventional unreliability factor R = 0.11. Several errors in the data taking and in the card punching were corrected, and the Co atom was given an anisotropic temperature factor. Four cycles of refinement with all 2213 terms included resulted in R = 0.142. The terms were weighted so that the 1823 nonzero terms were given unit weight and the 390 zero terms were given 1/4 weight.

An electron-density difference function, with all the atoms except hydrogen subtracted out, was calculated with the results of this refinement used for the terms with $\sin\theta/\lambda < 0.4$. With the exception of several peaks due to an incorrect description of the thermal motion of the sulfur atoms, the highest peaks in this function all corresponded to reasonable positions for the 36 independent hydrogen atoms, all in twofold general positions. Further refinement of all the atoms reduced R to 0.091.

A projection down the b axis of the overall structure is shown in Fig. D. 8-1. The planar $Co(MNT)_2^{2-}$ ion has a center of symmetry at the cobalt atom, and the two tetra-n-butyl ammonium ions are related to each other by a center of symmetry. The ions are interlaced to form layers in the bc plane.

The dimensions of the anion are illustrated in Fig. D. 8-2 and are in close agreement with those found in the complex $[(CH_3)_4N]_2^+ [Ni(MNT)_2]^{2-}$ by Eisenberg et al. [1]

The anion is very closely planar, and deviations from planarity are small enough to be chemically insignificant.

The chemically equivalent but crystallographically nonequivalent bonds in the anion are equal, to better than two standard deviations. Although the ion is required to have only a center of symmetry, the geometry is such that it does not differ significantly from mmm.

The arrangement of the sulfur atoms around the cobalt atom is very close to square, although the S-metal-S angle within the five-membered ring is found to be somewhat greater than 91 deg in both this structure determination and that by Eisenberg et al. [1]

The cobalt atoms are very well separated, as the nearest distance of approach is the shortest lattice distance, 9.81 Å. Three of the butyl chains adopt the trans conformation but one adopts a gauche conformation, presumably to improve the packing and to avoid too close approach to the Co atom.

The four C-N bonds are equal to within the experimental accuracy and have an average value of 1.52 ± 0.01 Å.

We thank Prof. A. H. Maki and Dr. N. Edelstein for providing us with excellent crystals of the material and for their co-operation in and helpful discussion of the problem.

Footnotes and References

† Brief form of paper in Inorg. Chem. 3, 1500 (1964).
* Present address: Imperial Chemical Industries, Ltd., Runcorn, Cheshire, England.

1. R. Eisenberg, J. A. Ibers, R. J. H. Clark, and H. B. Gray, J. Am. Chem. Soc. 86, 113 (1964).
2. A. H. Maki, N. Edelstein, A. Davison, and R. H. Holm, J. Am. Chem. Soc. 86, 4580 (1964).

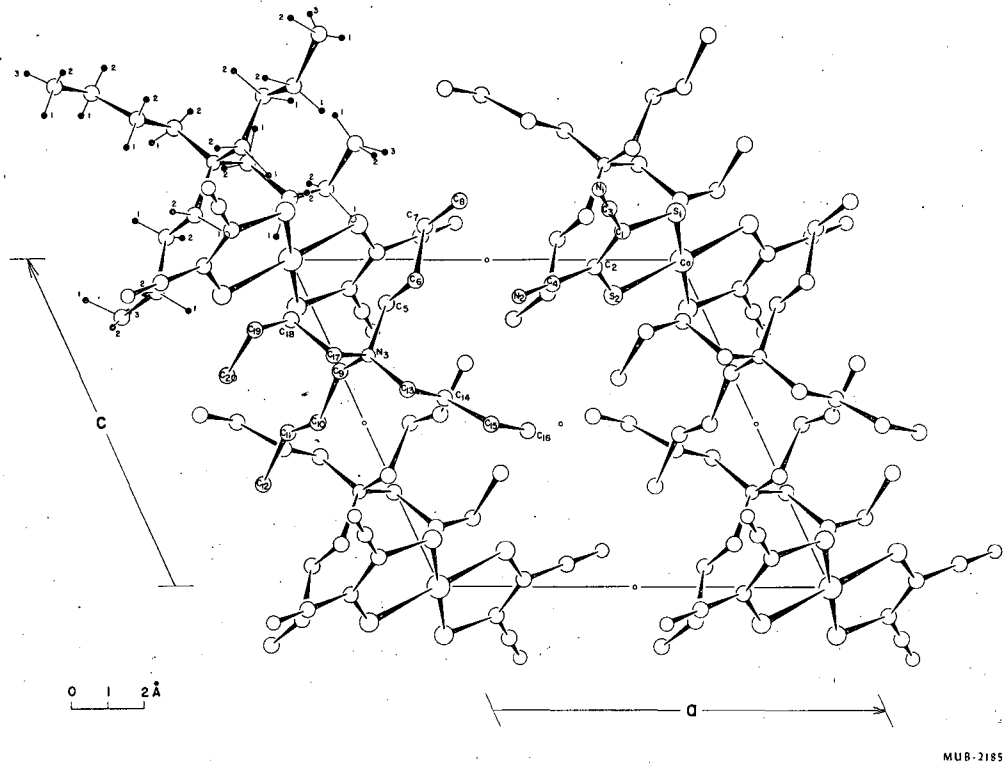

Fig. D. 8-1. Projection of the structure of $[(n\text{-}C_4H_9)_4N]_2^+ Co(S_2C_4N_2)_2^{2-}$ down the b axis. The small black circles represent examples of each type of hydrogen atom.

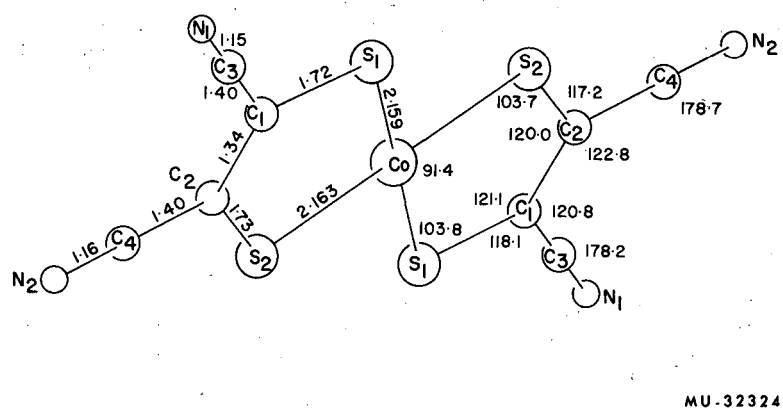

Fig. D. 8-2. Dimensions of the $Co(MNT)_2^{2-}$ ion.

9. THE CRYSTAL AND MOLECULAR STRUCTURE OF A COPPER CHELATE†

J. D. Forrester,* Allan Zalkin, and David H. Templeton

In a previous paper,[1] we reported our work on the structure of $[(n\text{-}C_4H_9)_4N]_2 \cdot Co(S_2C_4N_2)_2$, a member of a series of compounds of general formula $R'_z(M'S_4C_4R_4)^{-z}$, where z = 0, 1, 2; M' = Co, Ni, Cu, Pd, Pt, Zn, Rh; R = CN, CF_3, C_6H_5, etc., and R' = $(n\text{-}C_4H_9)_4N^+$, $(CH_3)_4N^+$, etc. We report in this paper a structure determination of another member of the series, viz., $(n\text{-}C_4H_9)_4N^+ Cu(S_2C_4N_2)_2^-$. We were encouraged to examine this material, as it had considerably different electron spin resonance (ESR) properties from the first structure, and interpretation of these phenomena would be aided considerably by some knowledge of the structure.

Maki et al.[2] have already used the results of this crystallographic study in a detailed review of the electronic structures of several members of this family of compounds.

Experimental Procedure

x-Ray Diffraction

Dr. N. Edelstein kindly supplied us with some well-formed needle-like dark red crystals of the complex $(n\text{-}Bu_4N)^+ Cu(S_2C_4N_2)_2^-$. The melting point, analysis, and preparation of these crystals are described in a paper by Davison et al.[3]

x-Ray photographs obtained by the Weissenberg technique and copper radiation established the diffraction symmetry of the crystal. A single crystal, in the form of a long thin plate of approximate dimensions $0.27 \times 0.11 \times 0.07$ mm, mounted about a b^* axis, was used for collecting the intensity data.

The space group permits 2803 independent reflections in the sphere with $\sin\theta/\lambda$ less than 0.482 ($2\theta < 40$ deg), and of these, 1834 were measured with counting times of 10 sec each; 396 were assigned zero intensity. No corrections were made for either absorption or extinction.

Results

Unit Cell and Space Group

A body-centered unit cell contains eight formula units $(n\text{-}C_4H_9)_4N\ Cu(S_2C_4N_2)_2$ and is monoclinic with dimensions $a = 15.59 \pm 0.02$, $b = 13.83 \pm 0.01$, $c = 27.94 \pm 0.03$ Å, $\beta = 93.86 \pm 0.03$ deg, $V = 6010.5$ Å^3.

Reflections are absent unless $h+k+\ell = 2n$, and $hO\ell$ reflections are absent unless $\ell = 2n$. This is consistent with either the centric space group $I2/c$ (C_{2h}^6) or the noncentric space group Ic (C_s^4). The success of our structure determination confirms our choice of the former.

With eight formula units of $(n\text{-}C_4H_9)_4N\ Cu(S_2C_4N_2)_2$ in the unit cell, the density calculated from the x-ray data is 1.30 g/cm^3. This compares with the value of 1.30 g/cm^3 found by a flotation method using a mixture of benzene and carbon tetrachloride.

Determination of the Structure

When all the data had been collected, the observed intensities were corrected for Lorentz and polarization effects, and a three-dimensional Patterson function was calculated by using the 1143 terms whose intensities were measured as two counts or greater. Plausible positions for the copper atom and the four independent sulfur atoms, all in general positions, were found from the Patterson function by inspection of the highest peaks around the origin and by using our knowledge of the geometry of the anion as found in the cobalt compound.

A three-dimensional electron density Fourier was calculated, with phases based on the copper and the four sulfur atoms. This function readily revealed the locations of the other 29 heavier atoms. The copper and the sulfur atoms were given anisotropic temperature factors.

The 33 hydrogen atoms were included in two cycles of least-squares refinement in which only the heavy atoms were refined, followed by two cycles in which the heavy atoms were held fixed and the hydrogen atom positions were refined. R fell to 0.106 after these four cycles of refinement, and all but 9 of the 33 hydrogen atoms were satisfactorily located. The remaining eight were rather imprecisely located in extended areas of electron density in the difference function, and the least-squares refinement had moved them, through admittedly small distances, to unsuitable locations. Refinement with all 70 atoms included, but only the 34 heavy atoms allowed to refine, resulted in a final value of R of 0.104.

Description of the Structure

The stacking of the $Cu(MNT)_2^{-1}$ ions is shown in a projection down the a axis in Fig. D. 9-1, and the arrangement of the tetra-n-butyl ammonium ions is shown in a similar projection in Fig. D. 9-2. An overall picture of the projection is directly obtainable by inserting the contents of Fig. D. 9-1 into the almost unoccupied central rectangle in Fig. D. 9-2. The two figures illustrate the nature of the molecular arrangement in the structure. The anions are stacked in columns whose axes are parallel to a and these columns are surrounded by a latticework of cations making the two parts of the structure quite independent, with very little overlap in the bc plane. This arrangement is very different from that found both in $[(C_4H_9)_4N]_2\ Co(S_2C_4N_2)_2$ by Forrester et al.[1] and in $[(CH_3)_4N]_2\ Ni(S_2C_4N_2)_2$ by Eisenberg et al.,[4] where the metal atoms are separated by about 10Å.

A side view of the column of stacked anions is shown in Fig. D. 9-3. The four copper atoms per unit cell per stack are almost exactly above each other in the a direction, whilst the anions are rotated in such a way as to give the stack mm symmetry in the bc projection.

The $Cu(MNT)_2^{-1}$ Ion

The dimensions of the anion are illustrated in Fig. D. 9-4 and compare well to those found for the doubly charged anion in $[(C_4H_9)_4N]_2\ Co(S_2C_4N_2)_2$. Despite the difference in the oxidation state, there is no significant difference in the molecular dimensions of the two anions, with standard deviations of about 0.02 Å.

The anion is approximately planar, but deviations from planarity are considerably greater than in the $Co(MNT)_2^{-}$ ion. The ion appears to be approximately boat-shaped, with only

one sulfur atom deviating to any extent from this shape. Deviations range from 0.05 Å on one side of the plane to 0.11 Å on the other, and because of the shape of the ion no attempt was made to calculate a least-squares plane through it.

The four sulfur atoms around the copper are considerably distorted out of the plane, but in an irregular fashion. However, this arrangement is very close to square planar, and the Cu-S-Cu angles within the rings are again found to be somewhat greater than 90 deg, as found in previous studies (Forrester et al.,[1] Eisenberg et al.[4]).

The chemically equivalent but crystallographically nonequivalent bonds in the anion are equal, to better than two standard deviations. Crystallographically, the ion is not required to have any symmetry, but its geometry is such that it does not differ very much from mmm (D_{2h}) symmetry.

In sharp contrast with the Co chelate, in which the closest distance of approach of the metal atoms is 9.81 Å, the copper atoms in this structure have nearest copper neighbors at 4.026 ± 0.005 and 4.431 ± 0.006 Å. This is consistent with the ESR results found by Maki et al.,[2] as it allows the necessary coupling needed to explain the observed phenomena in the copper compound. No atom from the cation except hydrogen (nearest at 4.74 Å) approaches closer than 5.0 Å to the copper atom, although some 14 different atoms from adjacent anions are at distances between 3.6 and 5.0 Å from the copper.

The Tetra-n-Butyl Ammonium Ion

The configuration of this ion can be seen in Fig. D. 9-2. All the butyl chains adopt the trans conformation. With the exception of one chain these angles are very small, showing that the chains are very nearly planar.

The four C-N bonds are equal to within the experimental accuracy and have an average value of 1.52 ± 0.01 Å. The six tetrahedral angles at the nitrogen atom (C-N-C) average 109.5 deg with a spread of ± 5 deg. Both these results are in excellent agreement with the values found in the cobalt compound.

As described earlier, 24 of the hydrogen atoms were located from the difference Fourier in very suitable locations and their parameters refined by least-squares methods. The remaining 12 hydrogen atoms were also located from the difference Fourier. However, their parameters were not refined, but merely used in the least-squares analysis to calculate structure factors. The mean C-H bond length (36 values) is 0.94 Å, somewhat smaller than the value of 1.09 Å usually taken as the standard interatomic separation. With the exception of the hydrogen atoms associated with the end carbon atoms, all the hydrogen bond angles are within 20 deg of the tetrahedral angle. This is consistent with the estimated standard deviations of the hydrogen atom positional parameters.

We thank Prof. A. H. Maki and Dr. N. Edelstein for providing us with excellent crystals of the material, and for their co-operation in and helpful discussion of the problem.

Footnotes and References

† Condensation of article in Inorg. Chem. 3, 1507 (1964).

* Present address: Imperial Chemical Industries, Ltd., Runcorn, Cheshire, England.

1. J. D. Forrester, A. Zalkin, and D. H. Templeton, Inorg. Chem. 3, 1500 (1964).
2. A. H. Maki, N. Edelstein, A. Davison, and R. H. Holm, J. Am. Chem. Soc. 86, 4580 (1964).
3. A. Davison, N. Edelstein, R. H. Holm, and A. H. Maki, Inorg. Chem. 2, 1227 (1963).
4. R. Eisenberg, J. A. Ibers, R. J. H. Clark, and A. B. Gray, J. Am. Chem. Soc. 86, 113 (1964).

$(C_4H_9)_4N \cdot Cu(S_2C_4N_2)_2$

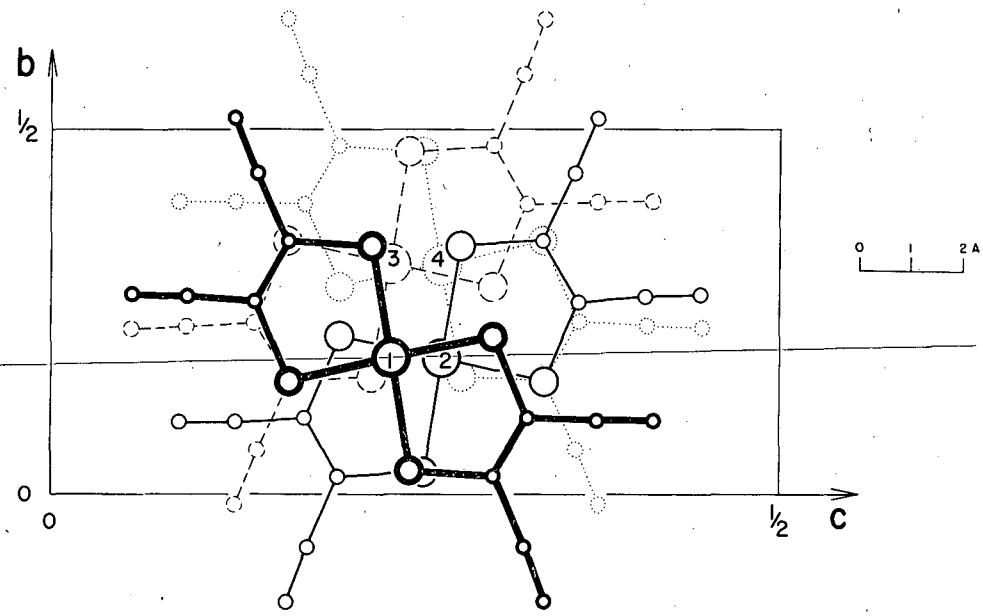

MUB-2344

Fig. D. 9-1. A projection down the a axis, showing the stacking of the $Cu(MNT)_2^{-1}$ anions as viewed down a stack. The copper atoms labeled 1, 2, 3, and 4 have x co-ordinates of 1.14, 0.86, 0.64, and 0.36 respectively.

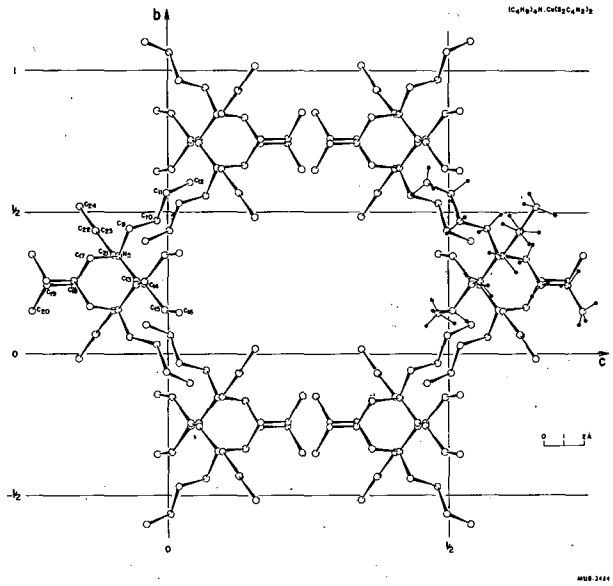

Fig. D. 9-2. A projection down the a axis, showing the latticework arrangment of the tetra-n-butyl ammonium ions. The small black circles are representative of each type of hydrogen atom. The stacked anions shown in Fig. D. 9-1 fit exactly into the almost unoccupied rectangle in the center of this figure.

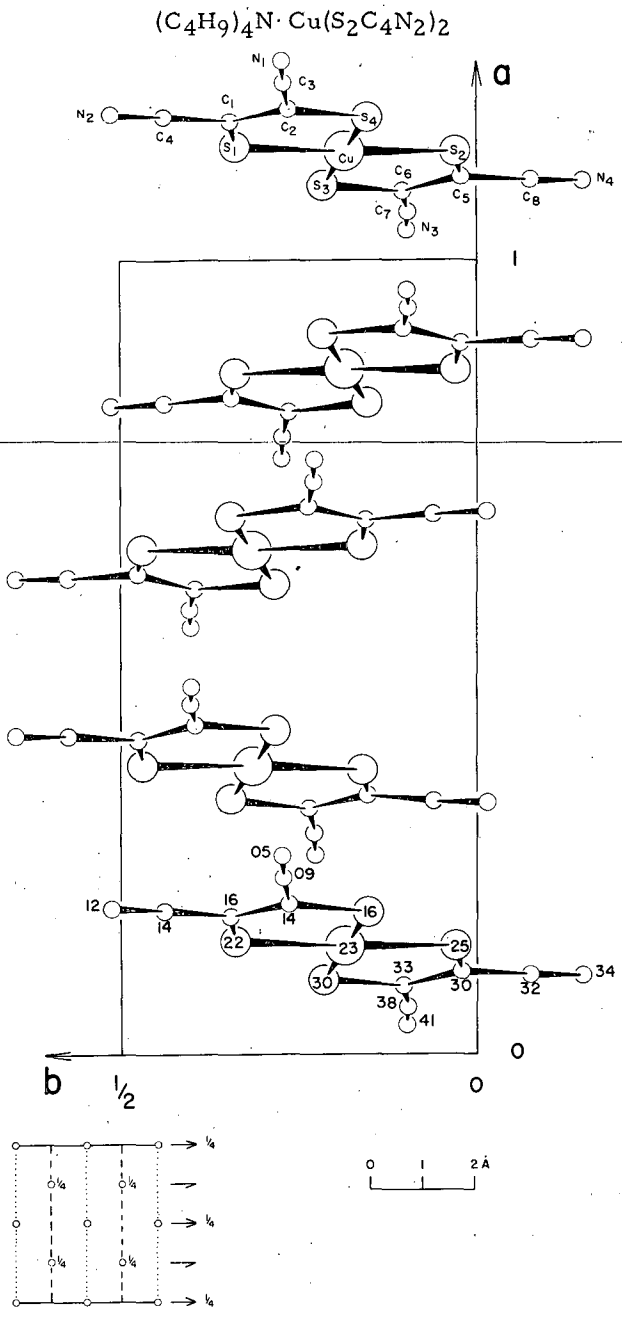

Fig. D. 9-3. A projection down the c axis, showing the stacking of the $Cu(MNT)_2^{-1}$ anions from the side. The figures beside some of the atoms are the z co-ordinates (×100).

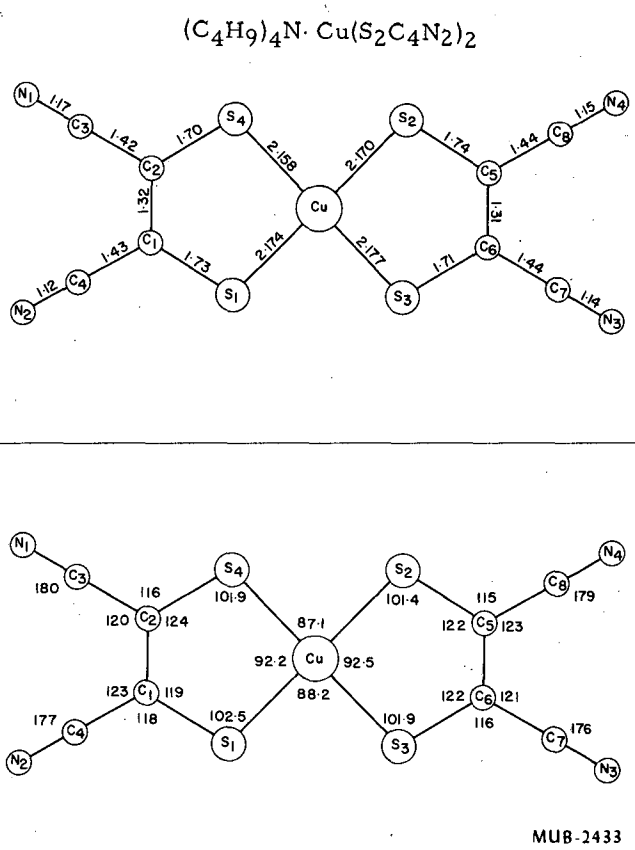

Fig. D. 9-4. The molecular dimensions of the $Cu(MNT)_2^{-1}$ anion.

10. THE CRYSTAL STRUCTURE OF OSMIUM TETROXIDE

Tatzuo Ueki, Allan Zalkin, and David H. Templeton

The crystal structure of osmium tetroxide was investigated previously by x-ray photographic methods[1], but oxygen positions were not determined from the intensity data. The complete structure has now been established with intensity data from the direct counting technique. The new study shows that the old unit cell must be doubled and that the wrong space group had been chosen.

The crystals are transparent, with a low melting point (about 40°) and high vapor pressure.[2] They are monoclinic, space group C 2/c, with

$$a = 9.379 \pm 0.005 \text{ Å } (9.39 \text{ Å}),$$

$$b = 4.515 \pm 0.002 \text{ Å } (4.52 \text{ Å}),$$

$$c = 8.632 \pm 0.003 \text{ Å } (8.66 \text{ Å}),$$

$$\beta = 116.6 \pm 0.05 \text{ deg } (116.7 \text{ deg}),$$

$$V = 330.7 \text{ Å}^3$$

The values in parentheses are from Zalkin and Templeton,[1] changed to the new setting. With Z = 4 the calculated density is 5.10 g/cm^3, compared with 4.95 observed by Krauss and Schrader.[3]

The atomic positions were determined from the Patterson function. Least-squares refinement reduced R to 0.082 for 479 independent reflections and gave the coordinates listed in Table D. 10-I.

The deviations from tetrahedral symmetry of the molecule are not experimentally significant. This result is in accord with the interpretation of Raman and infrared spectra by Woodward and Roberts[4] and Dodd.[5] The average Os—O bond distance is 1.74 ± 0.02 Å, uncorrected for thermal motion. The rms interatomic distance is larger, because of thermal motion, by an amount which is estimated at 0.02 Å (with the assumption that oxygen rides on osmium), but the magnitude of this correction is doubtful because of the low precision of the thermal parameters. An early electron-diffraction study[6] gave 1.66 Å for the Os—O distance, but this result is likely to be in error because of failure of the Born approximation.[7] A check on our result is given by the consistency of the isoelectronic sequence WO_4^{-2}, ReO_4^-, OsO_4, with bond distances W—O = 1.79 Å[8,9] and Re—O = 1.77 Å.[10]

The crystal structure (Fig. D. 10-1) can be described approximately as cubic closest packing of oxygen atoms, with osmium in tetrahedral holes. The pseudo-cubic pseudo cell corresponding to the close-packed oxygen structure has axes which are related to the monoclinic axes by the matrix $\frac{1}{2}\ 0\ \frac{1}{4}\ /\ 0\ 1\ 0\ /\ 0\ 0\ \frac{1}{2}$. From a different point of view, the structure can be described less accurately as cubic closest packing of OsO_4 molecules, an arrangement which is common in crystals of spherical or nearly spherical molecules. The axes of the pseudo cell describing this packing are derived from the monoclinic axes by the matrix $\frac{1}{2}\ 0\ -\frac{1}{2}\ /\ \frac{1}{2}\ 1\ \frac{1}{2}\ /\ \frac{1}{2}\ -1\ \frac{1}{2}$. In this packing each osmium atom has 12 osmium neighbors at distances ranging from 4.52 to 5.20 Å. The intermolecular O—O distances exceed 2.98 Å and are consistent with weak intermolecular forces indicated by the high vapor pressure and low melting point.

Footnote and References

† Brief version of paper to be published in Acta Cryst.

1. A. Zalkin and D. H. Templeton, Acta Cryst. 6, 106 (1953).
2. E. Ogawa, Bull. Chem. Soc. Japan 6, 302 (1931).
3. F. Krauss and G. Schrader, Z. Anorg. Chem. 176, 391 (1928).
4. L. A. Woodward and H. L. Roberts, Trans. Faraday Soc. 52, 615 (1956).
5. R. E. Dodd, Trans. Faraday Soc. 55, 1480 (1959).
6. L. O. Brockway, Rev. Mod. Phys. 8, 260 (1936).
7. R. Glauber and V. Schomaker, Phys. Rev. 89, 667 (1953).
8. A. Zalkin and D. H. Templeton, J. Chem. Phys. 40, 501 (1964).

9. M. I. Kay, B. C. Frazer, and I. Almodovar, J. Chem. Phys. 40, 504 (1964).
10. J. C. Morrow, Acta Cryst. 13, 443 (1960).

Table D. 10-I. Final coordinates and estimated standard deviations.

Atom	x	y	z	σ(x)	σ(y)	σ(z)
Os	0	0.2601	1/4	---	0.0004	---
O(1)	0.121	0.038	0.190	0.003	0.007	0.004
O(2)	0.115	0.476	0.425	0.003	0.006	0.003

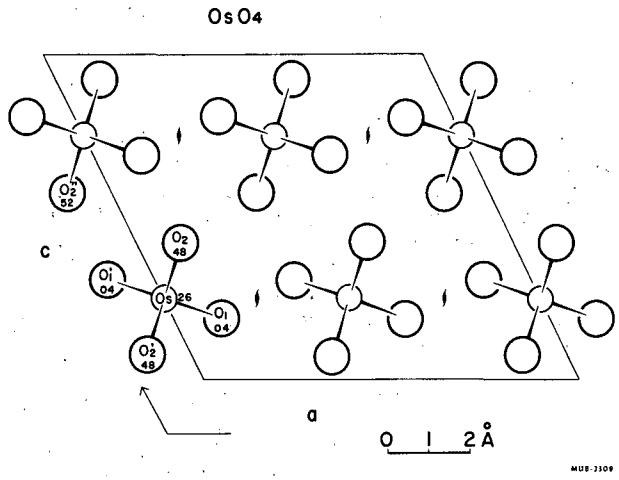

Fig. D. 10-1. Crystal structure of OsO_4. The y coordinates (multiplied by 100) are indicated for some atoms.

11. MISSING BAND IN THE SPECTRUM OF THE TRIPOSITIVE AMERICIUM ION†

John G. Conway and B. R. Judd

Calculations using the complete energy matrices developed by Koster and Nielson[1] for f^6 predict that the transition $^7F_0 \rightarrow {}^5D_1$ of Am^{3+} lies at roughly 17 500 cm^{-1}. The first experiments[2] failed to demonstrate the existence of this transition, and we therefore decided to calculate its transition probability. We expect it to be almost pure magnetic dipole in character, because forced electric dipole transitions of the type [J=0] → [J=1] within the 4f and 5f shells should be anomalously weak.[3] On using the detailed eigenfunctions for $^7F_0$ and $^5D_1$ that come from diagonalizing the complete f^6 matrices, we find, however, that the matrix elements of the magnetic dipole operator $\underset{\sim}{L}+2\underset{\sim}{S}$ that couple these two levels comprise positive and negative parts that almost exactly cancel, apparently accidentally. The intensity of the transition is depressed by roughly three orders of magnitude below what we would normally expect, thereby accounting for its absence in the reported scheme.[2]

Subsequent observations by Carnall, Fields, and Wybourne[4] have indeed revealed an extremely weak transition at 17 000 cm^{-1} in aqueous solutions of Am^{3+}, thereby confirming that the apparent absence of such a transition in the earlier experiments was due to an anomalously low transition probability, and not to any inadequacy in the calculation of the positions of the energy levels.

Footnote and References

† Brief form of published letter, J. Chem. Phys. 41, 1526 (1964), with additional comments.
1. G. F. Koster and C. W. Nielson, "Energy Matrices for All Configurations of Equivalent f Electrons" (recorded on magnetic tape), MIT, Cambridge, Massachusetts.
2. J. G. Conway, J. Chem. Phys. 40, 2504 (1964).
3. G. S. Ofelt, J. Chem. Phys. 37, 511 (1962); B. R. Judd, Phys. Rev. 127, 750 (1962).
4. W. T. Carnall, P. R. Fields, and B. G. Wybourne, J. Chem. Phys. 41, 2195 (1964).

12. AZIDE COMPLEXES OF PALLADIUM(II)†

Ray G. Clem and E. H. Huffman

Studies have been made of azide complexes of palladium in aqueous and in alcohol solutions, with the near-ultraviolet region of the spectrum, which indicate that, in addition to the species previously reported[1] there are 5:1 and 6:1 azide-to-palladium species. As the azide-to-palladium ratio is increased from 4:1 to 10:1 in aqueous solution the absorption spectra from 290 mμ to 350 mμ exhibit peaks (unlike the case in the visible region) which shift to longer wavelengths (Fig. D. 12-1). At ratios higher than 10:1 the peak absorbances remain at 315 mμ, although the maximum absorbance is not shown until a ratio of 150:1 for azide to palladium is attained. The molar absorptivity coefficient, based on the palladium content, is 18 300 at this ratio. The shift in wavelength is probably explained by the conversion of all $[Pd(N_3)_2Cl_2]^{-2}$ species to $Pd(N_3)_4^{-2}$. The absorption curve shown in Fig. D. 12-1 for a ratio of 4:1 azide to palladium in ethanol exhibits a peak at the same wavelength as do the curves for all ratios from 3:1 to 7:1 in ethanol for either 10^{-3} M or 10^{-5} M palladium(II).

Application of the molar ratio method of Yoe and Jones[2] to solutions in ethanol over the concentration range from 5×10^{-5} M to 1×10^{-3} M Pd^{+2} gives sharp breaks in the curves indicative of the formation of five- and six-coordinate complexes, as shown in Fig. D. 12-2. The six-coordinate break first appears on increasing the concentration to 1×10^{-3} M Pd^{++}, and appears only between 300 mμ and 340 mμ. Although it is clear that five- and six-coordinate complexes exist, it is not certain that pentaazido and hexaazido species account for these. Pearson and Basolo have shown that chloride in some cobalt(III) species can be replaced by hydroxide even in acid solutions,[3] and they have further inferred that azide may undergo methanolysis with similar subsequent reactions between cobalt(III) complexes and methoxide.[4]

The precipitate which is sometimes formed on adding azide to a palladium(II) solution has been identified as $Pd(N_3)_2$.

Footnotes and References

† Brief version of paper in J. Inorg. Nucl. Chem. (to be published).
1. F. G. Sherif and K. F. Mickail, J. Inorg. Nucl. Chem. 25, 999 (1963).
2. J. H. Yoe and A. L. Jones, Ind. Eng. Chem., Anal. Ed. 16, 111 (1944).
3. R. G. Pearson and F. Basolo, J. Am. Chem. Soc. 78, 4878 (1956).
4. R. G. Pearson, P. M. Henry, and F. Basolo, J. Am. Chem. Soc. 79, 5379 (1957); ibid 79, 5382 (1957).

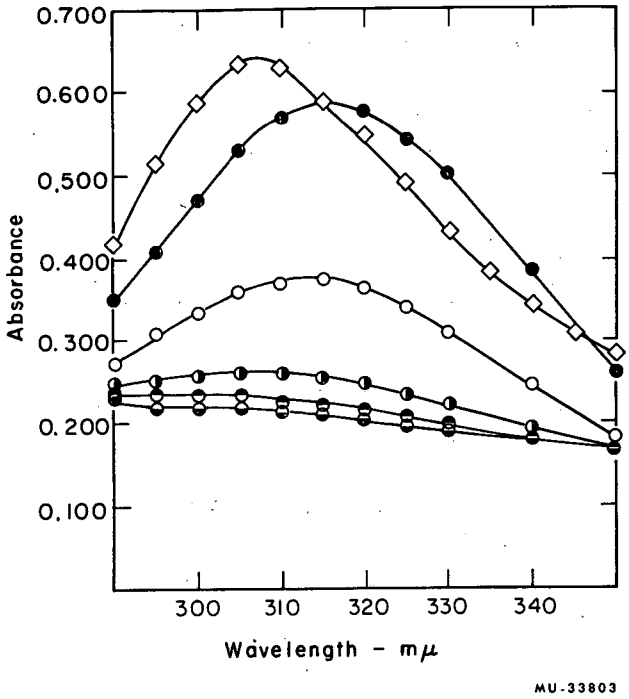

Fig. D. 12-1.

◇ 1×10^{-3} M Pd^{+2} and 4×10^{-3} M N_3^- in 99.0% ethanol

◒ 4×10^{-4} M Pd^{+2} and 16×10^{-4} M N_3^- in water

◒ 4×10^{-4} M Pd^{+2} and 24×10^{-4} M N_3^- in water

◑ 4×10^{-4} M Pd^{+2} and 28×10^{-4} M N_3^- in water

○ 4×10^{-4} M Pd^{+2} and 40×10^{-4} M N_3^- in water

● 4×10^{-4} M Pd^{+2} and 60×10^{-4} M N_3^- in water

All measurements made in 0.1-cm cells

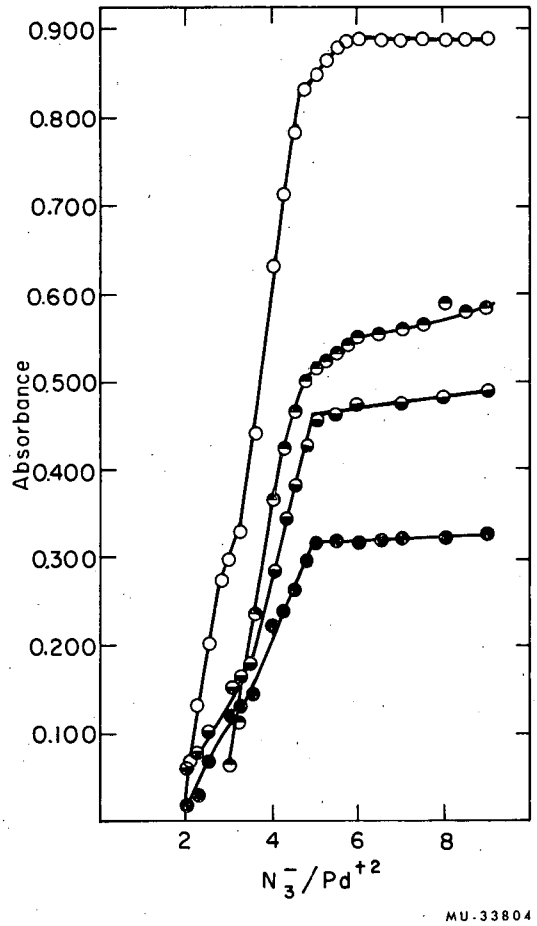

Fig. D. 12-2.

○ 1×10^{-3} M Pd^{+2}; λ = 300 mμ; 0.1 cm. cell

◒ 1×10^{-3} M Pd^{+2}; λ = 340 mμ; 0.1 cm. cell

◒ 5×10^{-5} M Pd^{+2}; λ = 300 mμ; 1.0 cm. cell

● 5×10^{-5} M Pd^{+2}; λ = 340 mμ; 1.0 cm. cell

The 1×10^{-3} M Pd^{+2} solution contains 1% water by volume from dilution of the stock palladium solution, and the 5×10^{-5} M Pd^{+2} solution contains 0.05% water.

13. DETERMINATION OF AZIDE ION BY HYDROGEN ION TITRATION AFTER OXIDATION WITH NITRITE†

Ray G. Clem and E. H. Huffman

A simple and accurate method for the determination of azide ion has been based upon the reaction

$$2H^+ + N_3^- + NO_2^- = H_2O + N_2 + N_2O \quad ,$$

in which the hydrogen ion consumed is measured by titration. Although the reaction has been used for other means of determining azide,[1] this simple approach does not appear to have been used before, though it offers several advantages. Large amounts of chloride and thiocyanate do not interfere and the titrants, perchloric acid and sodium hydroxide, are stable. The precision is comparable to that of other weak acid—strong base titrations. The azide must be in a solution free of metal ions which hydrolyze at pH 8—9; procedures for meeting this condition have been presented for silver, lead, and palladium azides.

Silver azide is metathesized with sodium thiocyanate, the pH is adjusted to the phenolphthalein end point, standard perchloric acid and nitrite are added, and the excess acid is titrated to the phenolphthalein end point in the presence of the silver thiocyanate precipitate. Hydrazoic acid is distilled from lead azide with perchloric acid and the analysis continued as with silver azide after adjustment of the pH. Only about 5% of the azide can be recovered from palladium azide by direct distillation. The addition of chloride, a stronger complexing agent in acid, releases the azide, which can then be distilled and determined.

Footnote and Reference

† Brief version of UCRL-11777, submitted to Anal. Chem.

1. F. Feigl, Spot Tests in Inorganic Chemistry, 5th ed. (translated by R. E. Oesper) (Elsevier, New York, 1958), p. 287.

14. SPECTROPHOTOMETRIC DETERMINATION OF PALLADIUM WITH AZIDE†

Ray G. Clem and E. H. Huffman

A spectrophotometric method for the determination of palladium has been developed which utilizes the absorptivity of the tetraazidopalladium(II) complex at 315 mμ after extraction into n-butyl alcohol at pH < 2.7 and back-extraction into an aqueous azide solution at pH 6.5. The method offers advantages in sensitivity, color stability, speed, accuracy and, especially, lack of interference from a large number of commonly interfering cations, though silver, lead and platinum must be removed prior to analysis. The standard deviation over the optimum range from 1.3 to 4.6 ppm is 0.03 ppm.

Spectrum scans are shown in Fig. D. 14-1 for the palladium azide complex in water and in n-butyl alcohol, as well as for the reagents. Beer's law is obeyed by the aqueous solution over the concentration range from 1 to 5 ppm. A phosphate buffer system of pH 6.5 was chosen because of its high capacity in the optimum pH region shown in Fig. D. 14-2. Although weak phosphate complexing of palladium(II) is shown in Fig. D. 14-3, phosphate does not interfere with color development by the stronger azide complexing. The effect of pH on extraction into n-butyl alcohol is shown in Fig. D. 14-4 with 10 ml each of aqueous and organic phases and concentrations for azide and phosphate of 0.1 M and 0.5 M respectively. Chloride strongly complexes palladium but the complex is not extracted; to achieve quantitative recovery by extraction the chloride concentration should be below 0.002 M.

Footnote

† Condensation of UCRL-11604 accepted for publication in Anal. Chem.

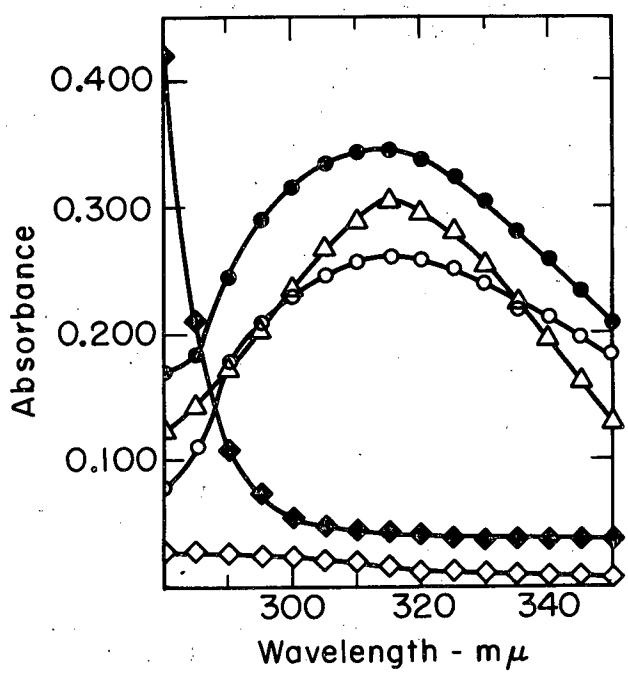

MUB-3814

Fig. D. 14-1. Absorption spectra of analytical species and reagents.
- 5 ppm Pd in n-BuOH; pH 2.25, aq. phase
- 5 ppm Pd in n-BuOH; pH 1.81, aq. phase
- 2 ppm Pd, back extracted, pH 6.5
- 1.0 M NaN_3
- 1.0 M phosphate

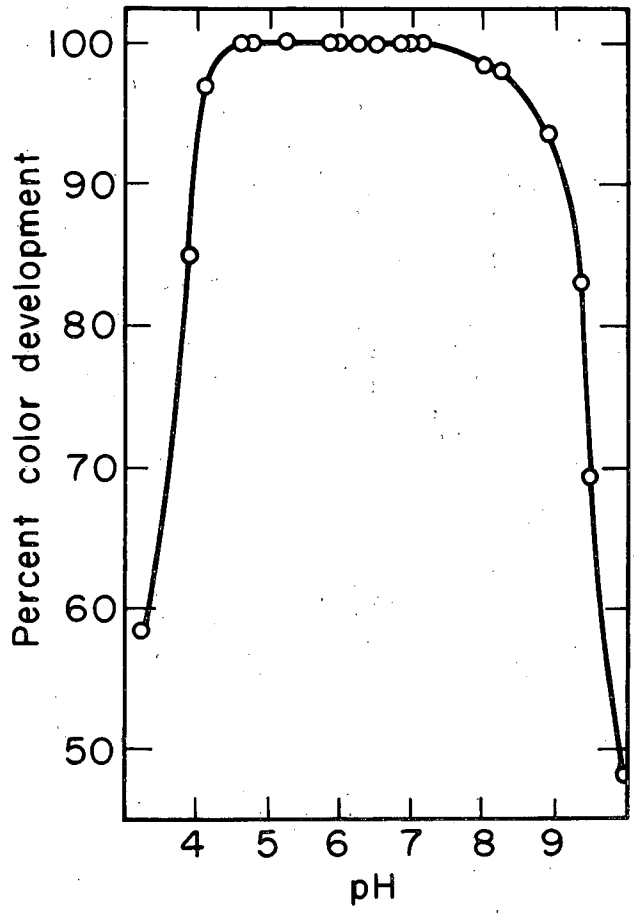

MUB-3815

Fig. D. 14-2. Effect of pH on color development.

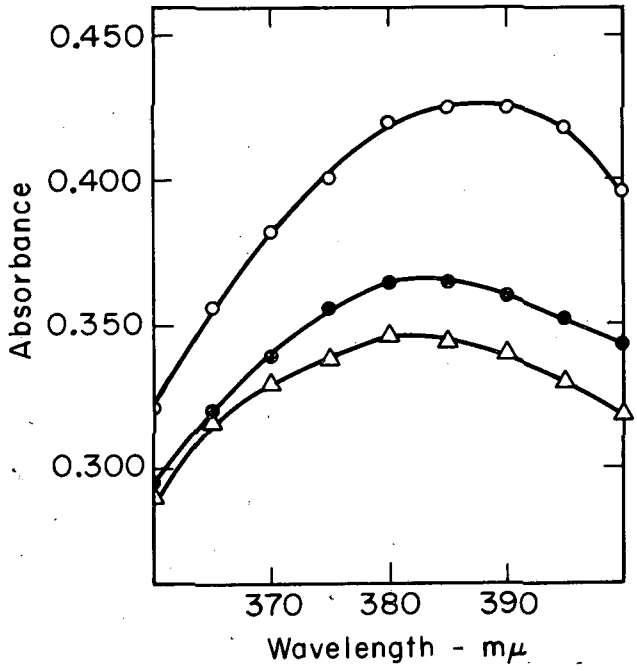

MUB-3816

Fig. D. 14-3. Effect of phosphate on absorbance-wavelength curve of 4×10^{-3} M Pd^{+2}

○ 0.5 M H_3PO_4

● 0.1 M H_3PO_4

△ 0.0 M H_3PO_4

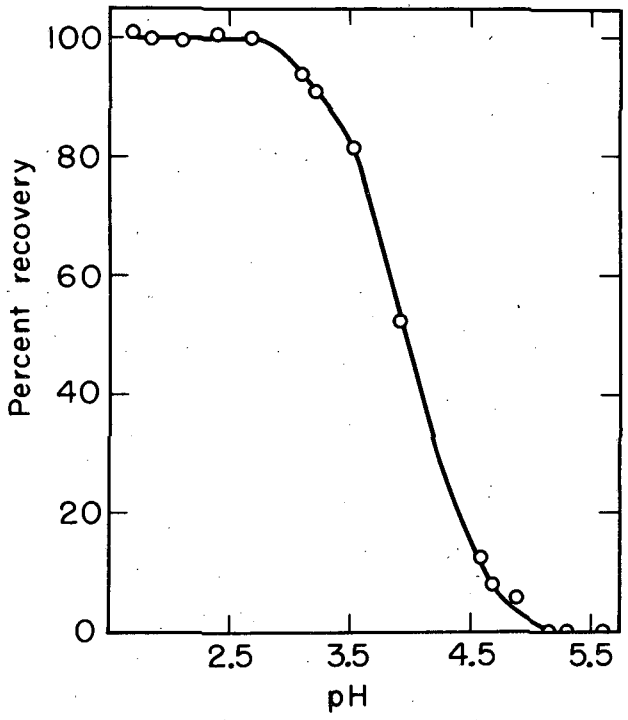

MUB-3817

Fig. D. 14-4. Effect of pH on extraction with n-butyl alcohol.

15. CONFIGURATION INTERACTION IN THE $4f^3$ CONFIGURATION OF PrIII†

K. Rajnak

The analysis of the complex spectra of the rare earth elements has usually been carried out by determining the values of the Slater integrals F_2, F_4, and F_6,[1] and the spin-orbit coupling constant ζ which best reproduce the experimental spectrum. Inherent in the method is the assumption that the energy levels may be described in terms of a pure f^N configuration. Attempts have been made to improve on this approximation by including the additional parameters α, β, and γ arising from the linear theory of configuration interaction.[2-6] This has led to considerable improvement, but, in many cases, the differences between calculated and experimental spectra are still several hundred cm^{-1}. It has recently been shown[7] that the "nonlinear" effects, arising from interaction with configurations differing from ℓ^N in the quantum numbers of only one electron, may be accounted for by adding several new parameters to those discussed above. Such effects have been considered in d-electron systems,[6,8] but until the recent work of Sugar[9] on the spectrum of doubly ionized Pr ($4f^3$), sufficient data have not been available to allow determination of the many parameters of the nonlinear theory for systems of f electrons.

Interaction of the configuration ℓ^N with $\ell^{N-1}\ell'$ and $\ell'^{4\ell'+1}\ell^{N+1}$ leads to a correction to the electrostatic matrix element between the states ψ and ψ' of ℓ^N which may be written as

$$C(\psi,\psi') = \Sigma_{kk'}\ X(kk',\ell')\ Y(kk',\ell'),$$

where

$$X(kk',\ell') = \Sigma_{k'' \text{ even} > 0}\ (2k''+1) \begin{Bmatrix} k & k' & k'' \\ \ell & \ell & \ell' \end{Bmatrix} \times (\psi \| \sum_{h\neq i\neq j} (\{U_h^{(k)}\ U_i^{(k'')}\}^{(k')} U_j^{(k')})^{(0)} \| \psi').$$

The parameter $Y(kk',\ell')$ is a function of the radial integrals $R^k(\ell\ell,\ell\ell')$ and $R^{k'}(\ell\ell,\ell\ell')$ and the energy separations between the interacting configurations ℓ^N and $\ell^{N-1}\ell'$ or $\ell'^{4\ell'+1}\ell^{N+1}$.

The coefficients $X(kk',\ell')$ were computed for $\ell'=1$ and 3. Least-squares fits to the 38 experimental energy levels of the $4f^3$ configuration of PrIII were then carried out with various combinations of parameters. The resulting parameter values are shown in Table D. 15-I, where the rms deviation σ is defined as

$$\sigma = \sqrt{\frac{\Sigma_i \Delta_i^2}{N-K}}\ .$$

Here Δ_i is the deviation of the ith level, N is the number of levels, and K is the number of free parameters. As soon as the parameter Y(22, 3) is included the upper $^2D_{5/2}$ level at 27597.13 cm^{-1} begins to deviate by considerably more than the expected $\pm 2\sigma$. When this level is excluded from the calculation, its calculated position is always the same, 355 ± 10 cm^{-1} above the experimental level. Consequently, the assignment of this level is extremely doubtful, and it was excluded from the final calculation, No. 6. The energy levels, eigenvectors, and g values resulting from this calculation are given in Table D. 15-II.

With the exception of the upper $^2D_{5/2}$ level, an excellent fit to the energy levels of the $4f^3$ configuration of PrIII has been obtained by including both linear and nonlinear parameters of configuration interaction. These values of the parameters should provide at least a first estimate to be used as guide in the analysis of other rare earth spectra. It is also possible to draw some conclusions regarding the relative magnitudes of the various mechanisms of configuration interaction. It seems that the two competing types of p interactions, $4f^3 \rightarrow 4f^2np$ and $np^6 4f^2 \rightarrow np^5 4f^4$, come close to cancelling in PrIII, while interactions of the type $4f^3 \rightarrow 4f^2 n'f$ are quite large.

Although these conclusions will not necessarily hold for all rare earth ions, they do provide a starting point for other analyses, particularly if the data are not complete enough to allow one to fit all of the possible parameters. Before conclusions drawn from the study of PrIII can really be generalized to other rare earths, however, a similar analysis of an ion at

the other end of the series should be carried out. Unfortunately, the necessary data are not available at present.

The author is grateful to Professor Racah for pointing out that, contrary to a statement in reference 7, three parameters are necessary to account for p interactions. The program for calculation of the angular matrix elements was written by J. M. Eusebio and Les Wilson of the Mathematics and Computing group. The author is particularly grateful to Tom Clements of that group for development of the fitting routine, and to C. W. Nielson for a magnetic tape of f^N matrices.

Footnote and Reference

† Condensed from paper in J. Opt. Soc. Am. (in press).

1. E. U. Condon and G. H. Shortley, The Theory of Atomic Spectra (Cambridge University Press, New York, 1935).
2. R. F. Backer and S. Goudsmit, Phys. Rev. 46, 948 (1934).
3. D. Layzer, dissertation, Harvard Univ., Cambridge, Massachusetts, 1950 (unpublished).
4. R. E. Trees, Phys. Rev. 83, 756 (1951); 84, 1089 (1951); 85, 382 (1952).
5. G. Racah, Phys. Rev. 85, 381 (1952); Lunds Univ. Arssk. Avd. 2:50, 31 (1954).
6. R. E. Trees and C. K. Jørgensen, Phys. Rev. 123, 1278 (1961).
7. K. Rajnak and B. G. Wybourne, Phys. Rev. 132, 280 (1963).
8. R. E. Trees, Phys. Rev. 129, 1220 (1963).
9. Jack Sugar, J. Opt. Soc. Am. 53, 831 (1963).

Table D. 15-I. Parameter values for the $4f^3$ configuration of PrIII (in cm^{-1}).

Parameter	Calculation number					
	1	2	3	4	5	6[a]
E^0	10966.	10608.	11262.	14976.	15152.	15030.
E^1	4291.39	4261.5	4369.3	4906.4	4869.2	4863.4
E^2	21.44	21.14	20.60	19.62	19.65	19.79
E^3	398.1	406.7	414.5	419.2	412.8	410.1
ζ	644.9	642.7	657.3	666.9	664.0	665.0
α		16.72	26.26	31.69	33.14	31.65
β			- 890.1	- 963.1	- 894.7	- 839.7
γ				-3072.	-3230.	-3164.
Y (22, 1)					6660	6250
Y (42, 1)					4560	6150
Y (44, 1)					-1430	2100
Y (22, 3)					-11200	-14280
Y (44, 3)					-10300	- 4380
σ	± 500	± 406	± 338	± 149	± 59	± 29

a. The $b^2D_{5/2}$ level was excluded from this calculation.

Table D.15-II. Calculated energy levels, eigenvectors, and g factors for the $4f^3$ configuration

J	Observed energy (cm^{-1})	Calculated minus observed energy	Eigenvector	g factor
1/2	18693.65	-7.48	$0.2240\|^4D\rangle +0.9746\|^2P\rangle$	0.632
	23465.43	36.18	$-0.9746\|^4D\rangle +0.2240\|^2P\rangle$	0.036
3/2	9370.66	-34.08	$.0430\|^4S\rangle +0.0104\|^4D\rangle -0.9730\|^4F\rangle +0.0518\|^2P\rangle -0.2132\|^2D1\rangle +0.0570\|^2D2\rangle$	0.424
	10950.24	-1.68	$-0.9748\|^4S\rangle -0.0131\|^4D\rangle -0.0632\|^4F\rangle -0.2098\|^2P\rangle +0.0391\|^2D1\rangle -0.0032\|^2D2\rangle$	1.964
	17095.63	-26.37	$-0.1792\|^4S\rangle +0.1169\|^4D\rangle +0.1896\|^4F\rangle +0.6348\|^2P\rangle -0.7040\|^2D1\rangle +0.1399\|^2D2\rangle$	1.045
	20856.86	-13.16	$-0.1244\|^4S\rangle +0.0762\|^4D\rangle -0.1154\|^4F\rangle +0.7287\|^2P\rangle +0.6355\|^2D1\rangle -0.1748\|^2D2\rangle$	1.099
	23091.70	-6.21	$0.0150\|^4S\rangle +0.9075\|^4D\rangle -0.0003\|^4F\rangle -0.1090\|^2P\rangle +0.1251\|^2D1\rangle +0.3856\|^2D2\rangle$	1.136
	26921.49	29.06	$-0.0090\|^4S\rangle -0.3959\|^4D\rangle +0.0097\|^4F\rangle +0.0862\|^2P\rangle +0.1944\|^2D1\rangle +0.8932\|^2D2\rangle$	0.866
5/2	10138.18	-15.29	$0.0031\|^4D\rangle -0.9893\|^4F\rangle +0.0133\|^4G\rangle -0.1402\|^2D1\rangle +0.0187\|^2D2\rangle +0.0191\|^2F1\rangle +0.0264\|^2F2\rangle$	1.032
	14187.35	3.69	$0.0056\|^4D\rangle -0.0162\|^4F\rangle -0.9961\|^4G\rangle +0.0012\|^2D1\rangle +0.0114\|^2D2\rangle -0.0540\|^2F1\rangle -0.0665\|^2F2\rangle$	.573
	19046.09	-24.63	$0.0218\|^4D\rangle +0.1402\|^4F\rangle -0.0044\|^4G\rangle -0.9896\|^2D1\rangle -0.0198\|^2D2\rangle +0.0116\|^2F1\rangle +0.0038\|^2F2\rangle$	1.197
	23245.99	19.24	$0.9016\|^4D\rangle +0.0064\|^4F\rangle +0.0175\|^4G\rangle +0.0114\|^2D1\rangle +0.4224\|^2D2\rangle -0.0552\|^2F1\rangle -0.0711\|^2F2\rangle$	1.337
	27597.13	363.51	$-0.4314\|^4D\rangle +0.0125\|^4F\rangle +0.0252\|^4G\rangle -0.0273\|^2D1\rangle +0.8761\|^2D2\rangle -0.0978\|^2F1\rangle -0.1875\|^2F2\rangle$	1.217
	34193.20	0.42	$-0.0113\|^4D\rangle +0.0337\|^4F\rangle -0.0799\|^4G\rangle +0.0090\|^2D1\rangle +0.2304\|^2D2\rangle +0.4627\|^2F1\rangle +0.8515\|^2F2\rangle$	.874
	62882.19 (calc.)		$-0.0146\|^4D\rangle -0.0028\|^4F\rangle +0.0155\|^4G\rangle -0.0091\|^2D1\rangle -0.0033\|^2D2\rangle -0.8774\|^2F1\rangle +0.4791\|^2F2\rangle$	.857
7/2	10859.06	5.44	$0.0021\|^4D\rangle +0.9666\|^4F\rangle +0.0310\|^4G\rangle -0.0213\|^2F1\rangle -0.0340\|^2F2\rangle -0.1966\|^2G1\rangle +0.1563\|^2G2\rangle$	1.216
	13887.60	-3.98	$0.0007\|^4D\rangle +0.2331\|^4F\rangle -0.4935\|^4G\rangle -0.0058\|^2F1\rangle -0.0064\|^2F2\rangle +0.6384\|^2G1\rangle -0.5427\|^2G2\rangle$	0.931
	15443.48	-13.95	$-0.0050\|^4D\rangle +0.1003\|^4F\rangle +0.8673\|^4G\rangle +0.0345\|^2F1\rangle +0.0469\|^2F2\rangle +0.3818\|^2G1\rangle -0.2974\|^2G2\rangle$	0.965
	24886.51	-37.99	$0.9978\|^4D\rangle -0.0038\|^4F\rangle +0.0079\|^4G\rangle -0.0535\|^2F1\rangle -0.0372\|^2F2\rangle +0.0056\|^2G1\rangle +0.0001\|^2G2\rangle$	1.428
	34944.64 (calc.)		$-0.0567\|^4D\rangle -0.0344\|^4F\rangle +0.0514\|^4G\rangle -0.4127\|^2F1\rangle -0.9058\|^2F2\rangle +0.0457\|^2G1\rangle +0.0072\|^2G2\rangle$	1.143
	39940.72	-23.10	$0.0034\|^4D\rangle -0.0069\|^4F\rangle +0.0189\|^4G\rangle +0.0376\|^2F1\rangle -0.0542\|^2F2\rangle -0.6363\|^2G1\rangle -0.7684\|^2G2\rangle$	0.890
	62601.47 (calc.)		$0.0332\|^4D\rangle +0.0048\|^4F\rangle -0.0124\|^4G\rangle +0.9076\|^2F1\rangle -0.4144\|^2F2\rangle +0.0324\|^2G1\rangle +0.0466\|^2G2\rangle$	1.143
9/2	0.00	-3.97	$-0.0026\|^4F\rangle -0.0067\|^4G\rangle -0.9861\|^4I\rangle +0.0151\|^2G1\rangle -0.0134\|^2G2\rangle -0.0534\|^2H1\rangle +0.1560\|^2H2\rangle$	0.732
	10032.92	14.54	$0.3155\|^4F\rangle +0.1280\|^4G\rangle -0.1490\|^4I\rangle -0.3176\|^2G1\rangle +0.2652\|^2G2\rangle +0.2930\|^2H1\rangle -0.7777\|^2H2\rangle$	0.986
	11761.69	4.47	$0.8874\|^4F\rangle -0.0205\|^4G\rangle +0.0535\|^4I\rangle -0.1533\|^2G1\rangle +0.1084\|^2G2\rangle -0.1350\|^2H1\rangle +0.3932\|^2H2\rangle$	1.250
	15705.13	5.44	$-0.2394\|^4F\rangle +0.7394\|^4G\rangle +0.0332\|^4I\rangle -0.4149\|^2G1\rangle +0.3694\|^2G2\rangle -0.1118\|^2H1\rangle +0.2715\|^2H2\rangle$	1.139
	16763.98	-8.14	$0.2355\|^4F\rangle +0.6579\|^4G\rangle -0.0167\|^4I\rangle +0.5446\|^2G1\rangle -0.4317\|^2G2\rangle -0.0145\|^2H1\rangle -0.1680\|^2H2\rangle$	1.144
	26979.66	82.02	$0.0030\|^4F\rangle +0.0568\|^4G\rangle +0.0032\|^4I\rangle -0.0152\|^2G1\rangle -0.0934\|^2G2\rangle +0.9352\|^2H1\rangle +0.3366\|^2H2\rangle$	0.912
	39225.60	-1.27	$0.0137\|^4F\rangle -0.0204\|^4G\rangle +0.0004\|^4I\rangle +0.6375\|^2G1\rangle +0.7656\|^2G2\rangle + 0.0766\|^2H1\rangle +0.0318\|^2H2\rangle$	1.110
11/2	1398.34	-0.95	$0.0063\|^4G\rangle +0.9952\|^4I\rangle +0.0338\|^2H1\rangle -0.0904\|^2H2\rangle -0.0132\|^2I\rangle$	0.966
	12494.63	-3.07	$-0.2056\|^4G\rangle +0.0951\|^4I\rangle -0.3590\|^2H1\rangle +0.9044\|^2H2\rangle -0.0444\|^2I\rangle$	1.097
	17409.58	12.57	$-0.9722\|^4G\rangle -0.0135\|^4I\rangle +0.1804\|^2H1\rangle -0.1483\|^2H2\rangle -0.0052\|^2I\rangle$	1.263
	24357.98	18.47	$0.0569\|^4G\rangle -0.0145\|^4I\rangle +0.3774\|^2H1\rangle +0.1193\|^2H2\rangle -0.9165\|^2I\rangle$	0.950
	28101.77	-13.28	$0.0958\|^4G\rangle +0.0101\|^4I\rangle +0.8337\|^2H1\rangle +0.3711\|^2H2\rangle +0.3974\|^2I\rangle$	1.066
13/2	2893.14	8.85	$0.9983\|^4I\rangle -0.0198\|^2I\rangle +0.0549\|^2K\rangle$	1.079
	16089.14	15.38	$0.0564\|^4I\rangle +0.0890\|^2I\rangle -0.9944\|^2K\rangle$	0.935
	25391.75	37.50	$0.0148\|^4I\rangle +0.9958\|^2I\rangle +0.0900\|^2K\rangle$	1.076
15/2	4453.76	23.41	$0.9949\|^4I\rangle +0.1004\|^2K\rangle -0.0065\|^2L\rangle$	1.199
	17642.06	-2.91	$-0.1000\|^4I\rangle +0.9791\|^2K\rangle -0.1770\|^2L\rangle$	1.064
	25244.61	-23.30	$-0.0114\|^4I\rangle +0.1767\|^2K\rangle +0.9842\|^2L\rangle$	0.945
17/2	26447.88	-51.84	$1.0000\|^2L\rangle$	1.059

16. CONFIGURATION INTERACTION IN CRYSTAL FIELD THEORY†

K. Rajnak and B. G. Wybourne*

The effect of configuration interaction on the validity of the usual method of expanding the crystal field potential V in terms of spherical harmonics is examined with use of second-order perturbation theory. It is shown that most types of interactions give rise to a simple linear scaling of the crystal field parameters, i.e., the usual crystal field matrix element

$$(n\ell^N\psi | V_q^k | n\ell^N\psi')$$

is replaced by

$$(1 + \Delta)\ (n\ell^N\psi | V_q^{(k)} | n\ell^N\psi'),$$

where Δ is independent of ψ and ψ'. In this case the factor $(1 + \Delta)$ is absorbed in the crystal field parameters if they are determined empirically from the experimental data. However, electrostatically correlated crystal field interactions involving single electron excitations, either from a closed shell into the incomplete ℓ^N shell or from the ℓ^N shell into an unfilled shell, may be represented by effective interactions, the angular dependence of which is not included in the usual theory. The effect of these interactions is to make Δ dependent on ψ and ψ'. In the limit of LS coupling, this results in crystal field parameters which are constant within a given multiplet but differ from one multiplet to another. It is also shown that electrostatically correlated crystal field interactions lead to a scaling of the Slater integrals F^k which differs from one crystal to another. Such effects are similar to those which Wong et al.[1] have interpreted in terms of changes in covalent bonding from crystal to crystal.

The clearest evidence of overt configuration interaction effects would seem to come from the work of Eisenstein,[2,3] who has shown that in rare earth crystal spectra, where the theory has been applied in considerable detail, it is not possible to find a single set of crystal field parameters that will adequately describe the crystal field levels deriving from different "free ion" states. The variation in the crystal field parameters for different LS multiplets explains, at least in part, why crystal field calculations limited to levels derived only from the ground multiplet usually lead to very satisfying results though the same parameters give an inadequate description of the splittings of higher states.

This theory has been developed within the framework of the electrostatic model. The qualitative features of the results do not, however, depend explicitly upon the validity of the model. Regardless of the precise nature of the potential we may make an expansion in terms of spherical harmonics. The electrostatic model enters the theory only as a particular model for calculating the coefficients in the expansion.

Footnotes and References

† Condensed from J. Chem. Phys. 41, 565 (1964).

* Argonne National Laboratory, Argonne, Ill.

1. E. Y. Wong, O. Stafsudd, and D. Johnston, J. Chem. Phys. 39, 786 (1963).
2. J. C. Eisenstein, in International Conference on Paramagnetic Resonance, Jerusalem, 1962, edited by W. Low (Academic Press Inc., New York, 1963).
3. J. C. Eisenstein, J. Chem. Phys. 39, 2128, 2134 (1963).

17. ABSORPTION SPECTRUM OF ASTATINE†

Ralph McLaughlin

The absorption spectrum of atomic astatine was recorded by utilizing a highly sensitive method of spectrographic detection. The goal of this approach was the placement of as large an amount of astatine as possible into as small a volume as possible in such a manner that light

which is transmitted through this volume will interact with as many atoms of astatine as possible. (For a cylindrical volume consideration of Beer-Bougner's Law indicates that to achieve maximum sensitivity it is the radius which must be made as small as possible and not the volume.)

The absorption cell illustrated in Fig. D. 17-1 was used in an effort to achieve this goal. The astatine was distilled off the Bi target onto the Pt disk represented by the cylinder in the figure. After evacuation a seal-off was made at point A. The cell was next placed in a liquid nitrogen bath such that when the Pt disk was heated the astatine was trapped to the right of point B. A second seal-off was then made at point B. The astatine was now confined to a cylinder 0.5 mm in radius and 5 cm long.

In addition to building up a high concentration of astatine the hope was that it could be rendered atomic (molecular astatine would be expected to have a lower absorption coefficient than atomic astatine). Consideration of the thermal decomposition of other halogen molecules as a function of temperature would indicate that at 600° C most At_2 molecules would dissociate. Hence the optical cell was next enclosed in a furnace and heated to this temperature (a later effort to obtain the spectrum of molecular astatine at lower temperatures was unsuccessful).

The spectrum obtained with this absorption cell is displayed in Fig. D. 17-2. Spectrograms were taken as the astatine decayed and it was verified that the change in line intensity with time was consistent with the half-life of At^{210}. Wavelength measurements determined that the transitions occurred at 2244.01 Å and at 2162.25 Å. By analogy with other halogens these lines can be assigned to the transitions $^2P_{3/2}^0 - {}^4P_{5/2}$ and $^2P_{3/2}^0 - {}^4P_{5/2}$ between configurations $6p^5$ and $6p^47s$. Calculation of the amount of astatine produced during the bombardment indicates that this method is capable of detecting as little as 0.2 ng of this element.

Credit for the construction of the quartz capillary absorption cell goes to Dane H. Anderberg and Harry S. Powell.

Footnote

† Condensed from J. Opt. Soc. Am. 54, 965 (1964).

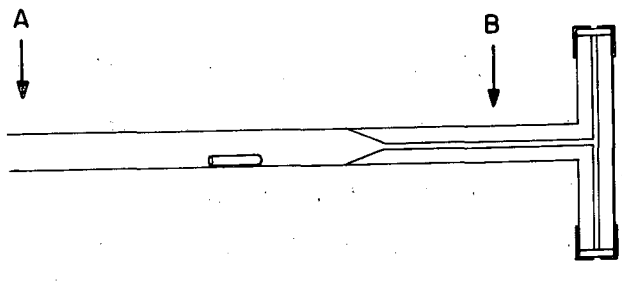

Fig. D. 17-1. Quartz capillary absorption cell. The coatings on either end mask the cell so that light may pass only through the internal hole and not through the quartz walls. A and B indicate the points at which seal-offs were made as described in the text. The cylinder represents the Pt disk which contains the astatine.

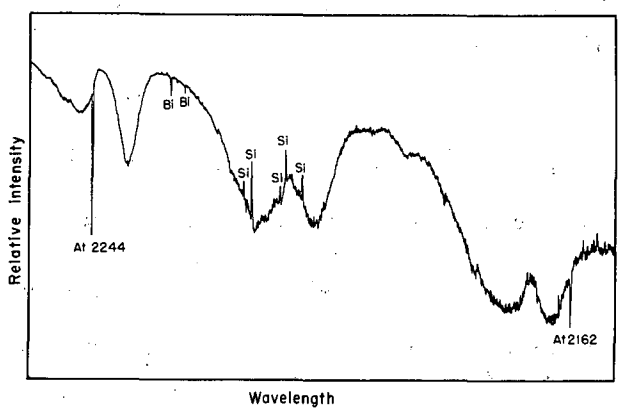

Fig. D. 17-2. Densitometer tracing taken of exposure made 35.42 h after bombardment. The broad absorption features are of unknown origin. The Si emission lines are produced in the hydrogen discharge which was the source of the continuum.

18. RADIATION-CHEMICAL OXIDATION OF PEPTIDES IN THE SOLID STATE†

Michael E. Jayko, Winifred Bennett-Corniea, and Warren M. Garrison

The yield for destruction of amino-acid residues in the radiation-induced decomposition of solid peptides has been described by Alexander and Hamilton[1] and by Bowes and Moss[2] as not being significantly greater under oxygen than under vacuum. However, neither of the reported studies was undertaken to determine optimum conditions for radiation-chemical reaction in a heterogeneous peptide-oxygen system. The dose rate in the one study was confined to the relatively high value of $\approx 5 \times 10^{21}$ eV/g/min, and in the other study, the solids were in a nondispersed form.

We have therefore re-examined this question by irradiating a polypeptide, gelatin, and a polyamino acid, poly-D, L-alanine,[3] as highly dispersed fluffs (average bulk density ≈ 0.05 g/cc) in vacuo and in an oxygen atmosphere under γ rays at the relatively low dose rate of 1×10^{16} eV/g/min. Oxygen uptake and carbon dioxide production were followed mass-spectrometrically. Dose was determined by extrapolation on the basis of the ratio of the electron densities of the solids and the Fricke dosimeter.[4] The validity of the extrapolation for the low-density solids and the geometries used here was established experimentally in a series of control runs in which the density and the volume of the irradiated samples were varied from about 0.025 g/cc to 0.6 g/cc and from 1 cc to 80 cc respectively. Chemical analysis of the irradiated peptides following a 3-hour hydrolysis in 2 N hydrochloric acid established ammonia and α-keto-acid(s) as principal degradation products. The quantitative procedures were those developed in our previous studies of the radiolytic oxidation of polypeptides in aqueous solution.[5]

The very striking result shown in Tables D. 18-I and D. 18-II is the remarkably high G values for oxygen uptake and for oxidative degradation of both gelatin and poly-D, L-alanine. The removal of oxygen at an energy requirement of only 1.5 to 2 eV per molecule as observed in the present work implies (a) that a radical chain oxidation is involved or (b) that low-lying excited states are produced and that such states are chemically quenched by molecular oxygen. That the degradation yields in oxygen are independent of pressure from 650 mm down to 20 mm, as shown in Table D. 18-II, indicates that energy absorption by oxygen is not a major contributing factor. The production of ammonia and carbonyl products in the radiolysis of gelatin and poly-alanine under oxygen can be formulated in terms of a chain oxidation involving the radical species $RCONH\dot{C}R_2$ as the chain carrier. The peptide radicals react with oxygen to form peroxy radicals via

$$O_2 + RCONH\dot{C}R_2 \rightarrow RCONHC(O_2)R \qquad (1)$$

or

$$O_2 + RCONH\dot{C}R_2 \rightarrow RCON{=}CR_2 + HO_2, \qquad (2)$$

and further reaction of the radical products of steps 1 and 2 at the labile C-H bond[5,6]

$$RCONHCHR_2 + R'O_2(HO_2) \rightarrow RCONH\dot{C}R_2 + R'O_2H(H_2O_2), \qquad (3)$$

would then lead to chain propagation and to formation of ammonia and carbonyl products following dissolution,[5]

$$RCONHC(OOH)R_2 + 2H_2O \rightarrow RCOOH + NH_3 + R_2CO + H_2O_2 , \qquad (4)$$

$$RCON{=}CR_2 + 2H_2O \rightarrow RCOOH + NH_3 + R_2CO . \qquad (5)$$

The terminating step of the oxidation chain would be of the type

$$RCONH\dot{C}(O_2)R_2 + HO_2 \rightarrow RCONHC(OOH)R_2 + O_2 . \qquad (6)$$

Comparison of the data of parts A and B of Table D. 18-I shows that the long-lived $RCONH\dot{C}R_2$ radicals present in gelatin and polyalanine following radiolysis in vacuo[7,8] do not

initiate chain oxidation during postirradiation exposure to oxygen. The explanation seems to lie in the fact that the instantaneous concentration of peroxy radicals produced on exposure of the pre-irradiated peptides to oxygen is very much higher than under the condition in which the peptide radicals are formed in the presence of oxygen over a 40-hour irradiation period. Hence, under the first condition the peroxy radicals react preferentially via the terminating step (6).

Although a radical chain mechanism appears to explain staisfactorily the yields of ammonia and carbonyl function observed in the radiolysis of polypeptide fluffs under oxygen, we have been unable on the basis of a chain mechanism to account for the production of carbon dioxide as a major degradation product. In fact, the very preferential effect shown in Table D. 18-I of an oxygen atmosphere on carbon dioxide yields suggests that some other mechanism is involved in the formation of this product. One possibility is that radiolysis of the peptide aggregate gives rise to low-lying excited states which, as suggested by Mason,[9] may be represented as the enolized form of the peptide bond, i. e., ~C(OH)=N~ or ~C(R)=C(OH)-NH~ or both. Such states would not lead to net chemical change in the radiolysis of peptides in vacuo. However, in the presence of molecular oxygen we envisage a chemical quenching of the excited state,

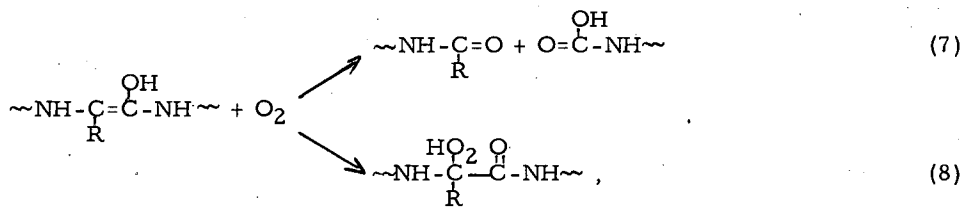

(7)

(8)

where carbon dioxide is derived from Reaction 7 via HOOC-NH~ = CO_2 + NH_2~ and where reaction 8 provides an alternate path for production of ammonia and carbonyl products. Current studies of the effects of temperature on product yields will provide a basis for determining the relative importance of radicals and excited states in peptide radiolysis.

We wish to thank Aldo Sciamanna for the help he gave us with the mass spectrometer.

Footnotes and References

† Condensed from Science 146, 250 (1964).
1. P. Alexander and L. D. G. Hamilton, Radiation Res. 13, 214 (1960).
2. J. H. Bowes and J. A. Moss, Radiation Res. 16, 211 (1962).
3. One percent solutions of gelatin (Eastman, lime processed) in water and poly-D, L-alanine (Yeda, mol wt 2000) in glacial formic acid were dialyzed against distilled water, quick-frozen in liquid nitrogen, and vacuum-dried at about -5°C.
4. C. J. Hockanadel and J. A. Ghormley, J. Chem. Phys. 21, 880 (1953).
5. W. M. Garrison, M. E. Jayko, and W. Bennett, Radiation Res. 16, 483 (1962).
6. W. M. Garrison and B. M. Weeks, Radiation Res. 17, 341 (1962).
7. R. C. Drew and W. Gordy, Radiation Res. 18, 552 (1963).
8. T. Henriksen, T. Sanner, and A. Pihl, Radiation Res. 18, 147 (1963).
9. R. Mason, Faraday Soc. Discussions 7, 129 (1959).

Table D. 18-I. Product yields in the γ radiolysis of gelatin and poly-D, L-alanine in the solid state. A, irradiated in vacuo and then exposed to oxygen prior to chemical manipulation. B, irradiated in oxygen at a pressure of 50 mm Hg. Dose = 1.44×10^{20} eV/g. G = molecules per 100 eV absorbed energy.

	G(>C = 0)	$G(NH_3)$	$G(CO_2)$	$G(-O_2)$
A. Evacuated				
gelatin	2.3 ± 0.3	8.1 ± 0.5	0.63 ± 0.03	———
poly-D, L-alanine	4.8 ± 0.3	5.6 ± 0.3	0.41 ± 0.01	———
B. Oxygen atmosphere				
gelatin	17.9 ± 0.9	42.1 ± 1.8	15.7 ± 3.0	72.7 ± 0.5
poly-D, L-alanine	24.3 ± 0.7	30.9 ± 1.7	33.8 ± 0.5	52.3 ± 0.9

Table D. 18-II. Effect of oxygen pressure on product yields in the γ radiolysis of gelatin. Dose = 1.44×10^{20} eV/g. G = molecules per 100 eV absorbed energy.

Pressure (mm Hg)	G(> C = 0)	$G(NH_3)$	$G(-O_2)$
20	17.9 ± 0.9	42.1 ± 1.8	70.8
50	18.8 ± 0.9	42.5 ± 2.0	72.4 ± 0.5
600	16.4 ± 1.0	40.0 ± 2.5	———

19. THE EFFECT OF CUPRIC ION ON THE RADIATION CHEMISTRY OF AQUEOUS GLYCINE†

Rodney L. S. Willix and Warren M. Garrison

The principal actions of ionizing radiations on neutral solutions of the simple amino acids may be represented in terms of the radiation-induced step[1, 2]

$$H_2O \rightsquigarrow H_2O_2, H_2, OH, H^+, e^-_{aq} \quad (1)$$

followed by[3, 4]

$$e^-_{aq} + NH_3^+CH_2CO_2^- \rightarrow NH_3 + \dot{C}H_2CO_2^- , \quad (2)$$

$$OH + NH_3^+CH_2CO_2^- \rightarrow H_2O + NH_3^+\dot{C}HCO_2^- , \quad (3)$$

$$NH_3^+\dot{C}HCOO^- + \dot{C}H_2CO_2^- \rightarrow NH_2^+{=}CHCO_2^- + CH_3CO_2^- , \quad (4)$$

$$2NH_3\dot{C}HCO_2^- \rightarrow NH_2^-{=}CHCO_2^- + NH_3^+CH_2CO_2^- , \quad (5)$$

$$H_2O + NH_2^+{=}CHCO_2^- \rightarrow NH_3 + CHOCO_2H \quad (6)$$

$$H_2O + NH_2^+{=}CHCO_2^- \rightarrow NH_3 + CH_2O + CO_2 \, . \quad (6a)$$

The amino acid cations, $NH_3^+CH_2CO_2H$, undergo the analogous reactions, but capture of e_{aq}^- by the acid form of the amino acid occurs in competition with its conversion reaction,[5]

$$e_{aq}^- + H^+ \rightarrow H \, , \quad (7)$$

where $k_7 \approx 2\times10^{10}$ $M^{-1}sec^{-1}$. The H atoms formed in reaction(7)are subsequently removed via

$$H + NH_3^+CH_2CO_2H \rightarrow H_2 + NH_3^+\dot{C}HCO_2H \, . \quad (8)$$

The effects of transition metal ions such as Cu^{+2} on the radiation chemistry of the amino acids are of particular significance because (a) the free Cu^{+2} ion has been shown to react rapidly with e_{aq}^- by simple capture,[6]

$$e_{aq}^- + Cu^{+2} \rightarrow Cu^{+1} \, , \quad (9)$$

with $k_9 \approx 3\times10^{10}$ $M^{-1}sec^{-1}$, and because (b) such ions are effectively chelated by the amino acid according to the pH-dependent equilibria

$$Cu^{+2} + NH_3^+CH_2CO_2^- \rightleftarrows [Cu(NH_2CH_2CO_2^-)]^{+1} + H^+ \, , \quad (I)$$

$$[Cu(NH_2CH_2CO_2^-)]^{+1} + NH_3^+CH_2CO_2^- \rightleftarrows [Cu(NH_2CH_2CO_2^-)_2] + H^+ \, , \quad (II)$$

with $K_I = 10^{8.5}$, $K_{II} = 10^7$ at 20°C.[7] Hence, there arises the interesting chemical and biological question of whether the glycine-Cu(II) chelates react with e_{aq}^- by analogous simple capture,

$$e_{aq}^- + [Cu(NH_2CH_2CO_2^-)_2] + H_2O \rightarrow [Cu(NH_2CH_2CO_2^-)]^{+1} + NH_3^+CH_2CO_2^- + OH^- \, , \quad (10)$$

or by a path that leads to chemical degradation of the ligand by reaction akin to Step (2), i.e.,

$$e_{aq}^- + [Cu(NH_2CH_2CO_2^-)_2] + H_2O \rightarrow [Cu(NH_3)(NH_2CH_2CO_2^-)]^{+1} + \dot{C}H_2CO_2^- + OH^- \, , \quad (11)$$

where Eqs. (10) and (11) represent overall stoichiometries.

We have studied the effects of cupric ion on the radiation-induced degradation of glycine in oxygen-free solutions over the pH range 3 to 9. Ammonia was determined by the absorption at 410 mμ on the addition of Nessler reagent to the 0.08 N H_2SO_4 solution from a Conway cell. Glyoxylic acid and formaldehyde were identified by paper chromatography of their 2:4 dinitrophenylhydrazone derivatives against authentic material with butanol/ammonia and methanol/heptane respectively as the ascending solvents. Their amounts were determined by the method of Johnson and Scholes[8] with the modification that the target solution was first passed through a Dowex-50 column to remove copper and glycine. Gas analyses were made by adjusting the pH to < 1 with H_2SO_4, removing the material volatile at -79°C, and analyzing the contents in a mass spectrometer after a total pressure measurement. All irradiations were carried out with the 200-Ci Co^{60} γ facility (dose rate 5.3×10^{16} eV $cc^{-1}min^{-1}$), at room temperature. The dose rate was determined with the Fricke dosimeter [10^{-3} M Fe(II), 0.8 N H_2SO_4], by use of the values $G[Fe(III)] = 15.6$ and $\epsilon_{Fe(III)} = 2130$ at 3050 Å and 22°C. With γ rays we assume the 100-eV yields of OH and e_{aq}^- in Reaction (1) to correspond to $G_{OH} = 2.2$, $G_{e^-} = 2.3$.[9]

Over the pH range 3 to 6, the ammonia yield from 0.3 M glycine decreases with increasing concentrations of divalent copper, and approaches a limiting steady value of $G \approx 2.2$ at Cu(II) concentrations above ≈0.03 M (Figs. D. 19-1 and D. 19-2). The stoichiometry

(Table D. 19-I) of radiation-chemical change is given by

$$2Cu(II) + NH_2CH_2CO_2H + H_2O \rightarrow 2Cu(I) + 2H^+ + CHOCO_2H(CH_2O + CO_2) + NH_3 , \quad (12)$$

with $G(NH_3) \approx G(RCHO) \approx 2.2 \approx G_{OH}$. A consistent explanation is that at pH < 6 the reducing species in the form of e^-_{aq} or H is preferentially scavenged by Cu^{+2} or $[Cu(NH_2CH_2CO_2^-)]^{+1}$ to give cuprous ion without net chemical effect on glycine. Glycine degradation at pH < 6 is ascribed wholly to OH attack via Reaction (3) followed by the stoichiometry

$$Cu(II) + NH_2\dot{C}HCO_2H \rightarrow Cu(I) + NHCHCO_2H + H^+ , \quad (13)$$

and by Reaction (6) or (6a) along with some contribution from the back reaction

$$Cu(I) + H_2O_2 \rightarrow Cu(II) + OH + OH^- . \quad (14)$$

The finding (Fig. D. 19-3) that $G(NH_3)$ does not drop to nil at pH 4 on addition of formate ion which is an effective scavenger for OH,[9]

$$OH + HCOO^- \rightarrow H_2O + CO_2^-$$

($k \approx 10^9\ M^{-1}sec^{-1}$), suggests (a) that the Cu^{+1} in Reaction (14) is present in the chelate form $[Cu(NH_2CH_2CO_2^-)]^{+1}$, and as a result the OH radical is liberated in close proximity to a glycine molecule and is not then available for scavenging by moderate concentrations of formate in the bulk, or (b) that a relatively long-lived excited water molecule[10] is formed with $G \approx 0.8$ and reacts preferentially with glycine—for example,

$$H_2O^* + NH_2CH_2CO_2H \rightarrow NH_2\dot{C}HCO_2H + H_2O + H , \quad (15)$$

$$H_2O^* + [Cu(NH_2CH_2CO_2^-)]^{+1} \rightarrow Cu^{+1} + NH_3 + CHOCO_2H + H . \quad (16)$$

As the pH of the glycine-Cu(II) system is increased above pH 6, the concentration of the bis-glycinato-Cu(II) chelate increases sharply,[7] and at pH 8.5 essentially all the Cu^{+2} is so bound. The carbonyl yield, $G(CHOCO_2H) + G(CH_2O)$, remains essentially constant with increasing alkalinity (Table D. 19-I), indicating that oxidation by OH via Steps (3) and (13) retains the stoichiometry given by Eq. (12). The abrupt increase in $G(NH_3)$ and $G(CO_2)$ over the pH range 6 to 9 is associated with the onset of a competing reaction of e^-_{aq} that leads to glycine deamination. One possibility, of course, is that the uncharged bis-glycinato-Cu(II) chelate is relatively unreactive towards e^-_{aq} as compared with Cu^{+2} and $[Cu(NH_2CH_2CO_2^-)]^{+1}$, so that reaction of e^-_{aq} with the zwitterion via Step (2) becomes the dominant process at high pH values. We note, however, that solutions of preformed bis-glycinato-Cu(II) at pH 8 also give $G(NH_3) \approx 5.0$ (and maximal yields of the other products), even though the concentration of free glycine in such solutions is less than 10^{-4} M. We conclude therefore that bis-glycinato-Cu(II) scavenges e^-_{aq}, and propose Reaction (11) as satisfying the overall experimental requirements. The addition of formate to the glycine-Cu(II) system at pH 8.6 reduces $G(NH_3)$ from ≈5.0 to a limiting value of about 3.3 (see Fig. D. 19-3). Assuming Reaction (14) or (15) and (16) contributes $G(NH_3) \approx G(RCHO) \approx 0.8$, we than have $G_{e^-_{aq}} = 3.3 - 0.8 \approx 2.5$, in satisfactory agreement with current findings.[9]

The carboxymethylene radical formed in Reaction (11) is a strong oxidizing agent, and one might anticipate that it would abstract hydrogen as proposed for the Cu-free system (Reaction 4). However, in the presence of Cu(II) the product stoichiometries require $\dot{C}H_2CO_2^-$ to be removed by the equivalent of

$$\dot{C}H_2CO_2^- + Cu(II) + H_2O \rightarrow Cu(I) + CH_3OH + CO_2 . \quad (18)$$

Reaction (18) is analogous to the recently reported oxidation of methyl radicals (from t-butyl hydroperoxides) to methanol by cupric ion in aqueous solution.[11]

Footnotes and References

† Condensation of paper (UCRL-11728) submitted to J. Phys. Chem.

1. G. Czapski and A. O. Allen, J. Phys. Chem. 66, 262 (1962).
2. E. J. Hart and J. W. Boag, J. Am. Chem. Soc. 84, 4090 (1962).
3. B. M. Weeks and W. M. Garrison, Radiation Res. 22, 249 (1964).
4. B. M. Weeks and W. M. Garrison, Radiation Res. 9, 291 (1958).
5. E. J. Hart, S. Gordon, and J. K. Thomas, J. Phys. Chem. 68, 1271 (1964).
6. S. Gordon, E. J. Hart, M. S. Matheson, J. Rabani, and J. K. Thomas, J. Am. Chem. Soc. 85, 1375 (1963).
7. H. Dobbie, W. O. Kermack, and H. Lees, Biochem. J. 59, 240 (1955).
8. G. R. A. Johnson and G. Scholes, Ind. Eng. Chem. Anal. Ed. 79, 217 (1954).
9. A. O. Allen, Radiation Res. Suppl. 4, 54 (1964).
10. See also M. Anbar and D. Meyerstein, J. Phys. Chem. 68, 1713 (1964).
11. H. E. De La Mare, J. K. Kochi, and F. F. Rust, J. Am. Chem. Soc. 85, 1437 (1963).

Table D. 19-I. Product yields from 0.30 M glycine, 0.03 to 0.04 M Cu(II) solutions[a] (dose = 10^{19} eV cc^{-1}).

pH	$G(NH_3)$	$G(CHOCO_2H)$	$G(CH_2O)$	$G(CO_2)$	$G(H_2)$	$G(CH_3CO_2H)$	$G(\frac{\text{succinic}}{\text{acid}})$
3.0	2.2 ± 0.2	1.8	0.53	0.5		0.04	0.07
8.5	5.0 ± 0.2	1.8	0.77	3.7	0.45	0.12	0.24
		2.1	0.85				
a. Preformed 0.02 M bis-glycinato Cu(II)							
8.4	5.0 ± 0.2	2.2	0.54	3.1			

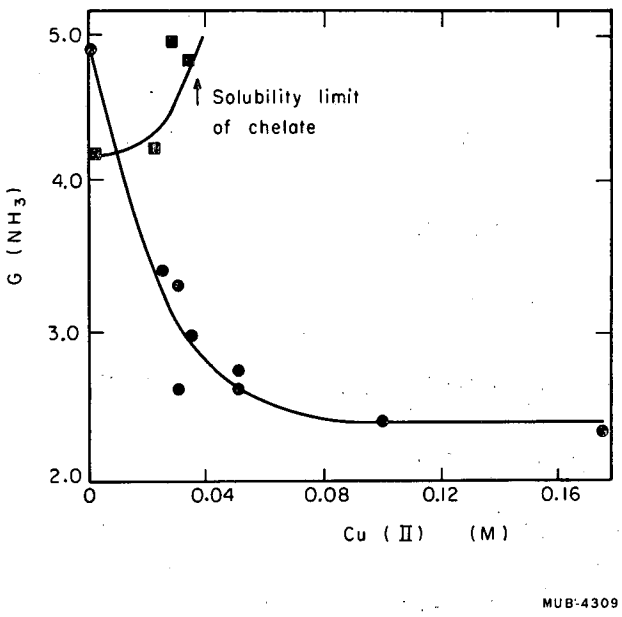

Fig. D. 19-1. Yield of ammonia as a function of cupric ion concentration in 0.3 M glycine solutions.
● pH 3.0 ■ pH 8.5

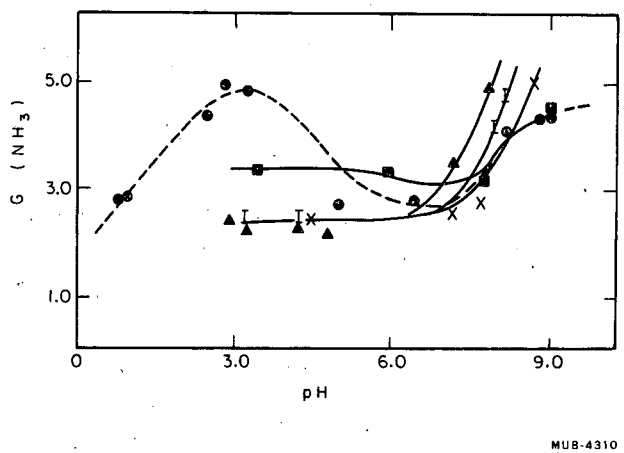

Fig. D. 19-2. Yield of ammonia as a function of pH in 0.3 M glycine solutions.
---● glycine
—— glycine plus ■ 0.025, X 0.030, I 0.035, ▲ 0.040 M Cu(II)

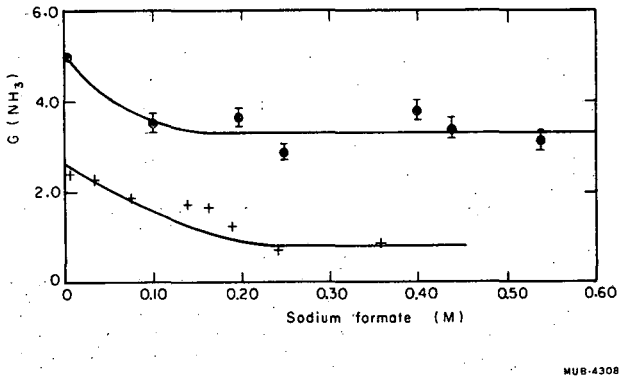

Fig. D. 19-3. Effect of formate ion on ammonia yield in 0.3 M glycine solutions.
● pH 8.6, 0.035 M Cu(II),
† pH 4.0, 0.040 M Cu(II).

20. A MARKED EFFECT OF CONFORMATION IN THE RADIOLYSIS OF POLY-α-L-GLUTAMIC ACID IN AQUEOUS SOLUTION†

Harvey A. Sokol, Winifred Bennett-Corniea, and Warren M. Garrison

Compounds containing the peptide bond undergo chemical degradation at the N-C linkage on irradiation in aqueous solution under oxygen. The schematics of the radiation-induced reactions are given by[1]

$$H_2O \longrightarrow H^+, e^-_{aq}, OH, \quad (1)$$

$$e^-_{aq} + O_2 + H_2O \rightleftarrows HO_2 + OH^-, \quad (2)$$

$$OH + RCONHCHR_2 \rightarrow H_2O + RCONH\dot{C}R_2, \quad (3)$$

$$O_2 + RCONH\dot{C}R_2 \rightarrow RCONHC(\dot{O}_2)R_2, \quad (4)$$

$$HO_2 + RCONHC(\dot{O}_2)R_2 \rightarrow H_2O_2 + O_2 + RCON{=}CR_2, \quad (5)$$

$$2RCONHC(\dot{O}_2)R_2 \rightarrow H_2O_2 + O_2 + 2RCON{=}CR_2, \quad (6)$$

$$2HO_2 \rightarrow H_2O_2 + O_2. \quad (7)$$

The dehydropeptides, $RCON{=}CR_2$, as a class are readily hydrolyzed,

$$RCON{=}CR_2 + 2H_2O \rightarrow RCOOH + NH_3 + R_2CO, \quad (8)$$

in dilute mineral acid under the conditions conventionally employed to liberate ammonia from organic amides.[1,2] Hence, regardless of the relative rates of Reactions (5) and (6), each $RCONH\dot{C}R_2$ radical yields one molecule of ammonia on hydrolysis of the irradiated system.[3] The over-all stoichiometry of Steps (1) to (7) plus the hydrolysis steps is given by

$$RCONHCHR_2 + O_2 + 2H_2O \rightarrow RCOOH + NH_3 + R_2CO + H_2O_2 . \quad (9)$$

The yield of Reaction (9) for a particular peptide system depends on the relative reactivities of the peptide chain and of the side-chain loci towards OH attack.

We report here a study of the γ-ray-induced oxidation of poly-α-L-glutamic acid (PGA) over the pH range 3.5 to 9. Dilute solutions of PGA (Pilot Chemicals, Lot G-9, molecular weight, 140 000) were irradiated under oxygen at 1 atmosphere at a γ-ray dose rate of 1.2×10^{18} eV/g/min. The irradiated solutions were hydrolyzed in 2 N H_2SO_4 under nitrogen for 3 hours at 100°C prior to analysis.[4,5] The anticipated products of Reaction (9)--ammonia and α-keto-glutaric acid--are formed and pyruvic acid is also present as a major product.

Yields of these products from 0.15% PGA solution over the pH range 3.5 to 9 are summarized in Fig. D.20-1. It is seen that the yield of α-ketoglutaric acid is essentially pH-independent, in accord with the schematics of Eqs. (5) and (6), whereas G(pyruvic) and G(NH_3) increase sharply with pH over the very narrow range pH ≈ 4.5 to pH ≈ 6. That this effect is not a result of incomplete scavenging of OH radicals at pH < 6 is shown by the fact that product yields at both pH 4 and pH 7 are independent of the PGA concentration from 0.15% down to at least 0.015%. Nor does it appear that the sharp break in the pH-yield curves is directly related to changes in hydrogen-ion concentration or degree of ionization of side-chain carboxyl groups, per se. This is shown by results obtained with N-acetylglutamic-α-methyl ester, a radiation-chemical model for the single-residue segment of the PGA chain; ammonia and carbonyl yields from 0.05 M solutions of this low-molecular-weight peptide derivative of glutamic acid are essentially independent of pH over the entire range pH 3 to 8, with G(NH_3) ≈ G(>C=O) ≈ 2. The evidence is that pyruvic acid and ammonia are produced as a result of OH attack at a side-chain locus and that the chemical consequences of such attack, unlike reaction at the peptide chain, is dependent on the macromolecular conformation of PGA. Consider the reactions

$$OH + >CHCH_2CH_2COOH \rightarrow H_2O + >CHCH_2\dot{C}HCOOH , \quad (10)$$

$$O_2 + >CHCH_2\dot{C}HCOOH \rightarrow >CHCH_2CH(\dot{O}_2)COOH , \quad (11)$$

where $>CHCH_2CH_2COOH$ represents the side chain of the glutamic acid residue. Peroxy radicals of the type formed in Reaction (11) are relatively long-lived and are subsequently removed through

$$HO_2 + >CHCH_2CH(\dot{O}_2)COOH \rightarrow O_2 + >CHCH_2CH(OOH)COOH \quad (12)$$

and the disproportionation

$$2\ >CHCH_2CH(\dot{O}_2)COOH \rightarrow >C=CH_2 + (COOH)_2 + >CHCH_2CH(OOH)COOH \quad (13)$$

Degradation reactions akin to Reaction (13) have been described by Russell[6] and by Durup et al.[7] It is seen that the product $>C=CH_2$ in the above nomenclature corresponds to the acrylic acid derivative $RCONHC(=CH_2)R$ [a tautomeric form of the dehydropeptide, $RCON=C(CH_3)R$] which on hydrolysis yields ammonia and pyruvic acid.

Now, a unique characteristic of the radiation chemistry of a macromolecular substance in aqueous solution is that each molecule undergoes reaction with a relatively large number of OH radicals even at the lowest practicable dosages. For example, with a 0.15% solution of PGA, a γ-ray dose of 3×10^{18} eV/g produces but one OH per 100 glutamic acid residues, but at the same time this corresponds to about 20 OH radicals per PGA molecule (140 000 mol wt). However, at pH > 6, PGA has the random coil configuration and the various segments of the macromolecule are free to interact both intermolecularly and intramolecularly. Hence we find at pH > 6 no essential differences between the macromolecule and the low-molecular-weight model from the standpoint of product yields. But, as the pH of the solution is decreased, PGA undergoes a coil → helix transition over the pH range 6 to 4.5,[8] which as we have noted is the significant pH range of Fig. D.20-1. With PGA in the helix form, the peroxy radicals are frozen in a fixed spatial arrangement and it is obvious that the probability of Reaction (13) is greatly reduced; hence Reaction (12) is favored and as a result G(NH_3) and G(pyruvic) decrease, as seen in Fig. D.20.1.

Footnotes and References

† Condensation of UCRL-11733, submitted to J. Phys. Chem.

1. (a) W. M. Garrison, M. E. Jayko, and W. Bennett-Corniea, Radiation Res. 16, 483 (1962); (b) W. M. Garrison and B. M. Weeks, Radiation Res. 17, 341 (1962).
2. J. P. Greenstein and M. Winitz, Chemistry of the Amino Acids (John Wiley and Sons, Inc. New York, 1961), p. 843.
3. There is some evidence (reference 1 b) that peroxy radicals of certain peptides give the amide directly without intermediate formation of the dehydropeptide, e.g.,

$$HO_2 + RCONHC(O_2)R_2 \xrightarrow{H_2O} RCONH_2 + R_2CO + O_2 + H_2O_2 .$$

4. E. J. Conway and A. Berne, Biochem. J. 27, 419 (1933).
5. T. E. Friedemann and G. E. Haugen, J. Biol. Chem. 147, 415 (1943).
6. G. A. Russell, J. Phys. Chem. 49, 1483 (1956).
7. M. Durup, J. Durup, F. Kuffer, and M. Magat, in Proceedings of the Second International Conference on Peaceful Uses of Atomic Energy, Geneva, 1958, 29, 143.
8. See, for example, J. Applequist and J. L. Breslow, J. Am. Chem. Soc. 85, 2869 (1963).

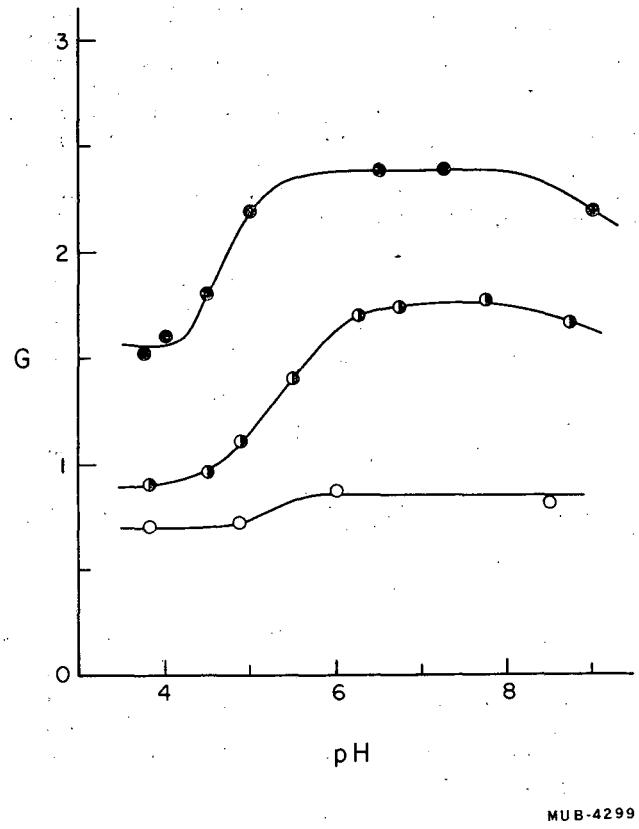

Fig. D.20-1. Effect of pH on the yield of ammonia (●), total α-keto acids (◑), and α-ketoglutaric acid (○) in the γ radiolysis of 0.15% poly-α-L-glutamic acid. G = molecules/100 eV.

21. RADIOLYTIC DEGRADATION OF AQUEOUS CYTOSINE: ENHANCEMENT BY A SECOND ORGANIC SOLUTE†

Ahmad Kamal* and Warren M. Garrison

Scholes and Weiss[1,2] and Eckert and Monier[3] have shown that the OH radical reacts rapidly with the pyrimidine bases by addition at the 5,6 double bond to give the hydroxyhydropyrimidyl radical:

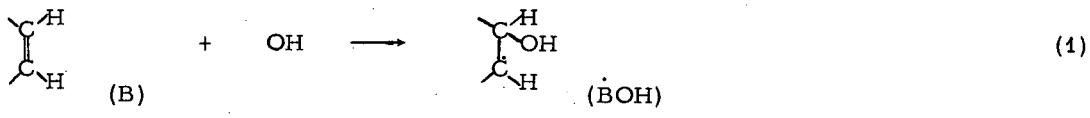

(1)

The 100-eV yield for base destruction, G(-B), in oxygenated 10^{-3} M solutions of thymine, uracil, and cytosine under γ rays approximates the primary yield of OH radicals ($G \approx 2.4$) formed in the radiation-induced step[4]

$$H_2O \longrightarrow OH + H^+ + e^-_{aq} .$$

The hydrated electron, e^-_{aq}, reacts preferentially with molecular oxygen to form O_2^-, which is unreactive towards the pyrimidine bases.

In the absence of oxygen, the G value for destruction of the pyrimidine and purine bases has been found to be about one-third that observed in oxygenated neutral solution. Latarjet et al.[5] report $G(-B) \approx 0.8$ for oxygen-free 10^{-3} M thymine solutions under γ rays, and the datum of Ponnamperuma et al.[6] gives $G(-B) = 0.95$ for aqueous cytosine under similar irradiation conditions. As we have noted, the evidence is that the OH radical is quantitatively scavenged via Reaction (1) at relatively low concentrations of the pyrimidine bases, and Hart et al.[7] have established by physical methods that the reactions of e^-_{aq} with the pyrimidines are among the fastest of known radical-molecule reactions. It would appear then that some type of reconstitution reaction is acting to reduce the G value for base destruction in the oxygen-free system. If, as seems likely, the hydrated electron, e^-_{aq}, also adds to the labile 5,6 position,

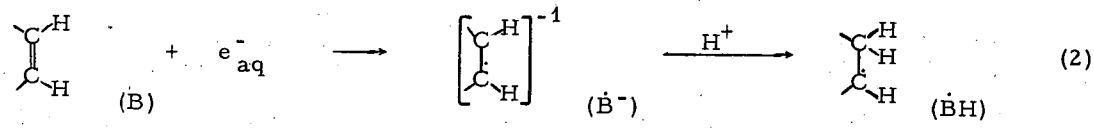

(2)

then the reconstitution reaction may be interpreted in terms of water regeneration via $\dot{B}H + \dot{B}OH \rightarrow 2B + H_2O$, or $\dot{B}H + \dot{B}OH \rightarrow B + BH_2O$ followed by $BH_2O \rightarrow B + H_2O$, or both. On this basis it follows that addition of a second organic solute that is preferentially reactive towards OH via $RH + OH \rightarrow \dot{R} + H_2O$ would lead on replacement of OH by $\dot{R}$ in Reaction (1) to an enhancement in G(-B), since the possibility for self-protection through water elimination would be excluded. This increase in G(-B) would correspond to an increase in the yield of products saturated at the 5,6 position.

Cytosine was chosen for study here because the dihydrocytosine derivatives obtained on saturation of the 5,6 double bond hydrolyze readily to give the corresponding 5,6 dihydrouracil derivatives and ammonia,[8] a product conveniently followed analytically. Sodium formate and ethanol were used as second solutes; each of these compounds is relatively inert towards e^-_{aq} and at the same time is extremely reactive towards OH via $HCOO^- + OH \rightarrow \dot{C}OO^- + H_2O$ and $CH_3CH_2OH + OH \rightarrow CH_3\dot{C}HOH + H_2O$.[4,7] The effects of added formate and ethanol on ammonia yields in the γ radiolysis of oxygen-free 0.06 M solutions of cytosine at pH ≈ 7 are shown in Fig. D.21-1. We see that $G(NH_3)$ increases abruptly with increasing solute concentration and reaches a limiting value of approximately 2.9 at the higher formate concentrations.

If our interpretation of this enhancement is correct, the hydrated electron, e^-_{aq}, is removed via Reaction (2) and the OH radical is converted to the $\dot{C}OO^-$ radical, which in turn is removed via the analog of Reaction (1), viz.,

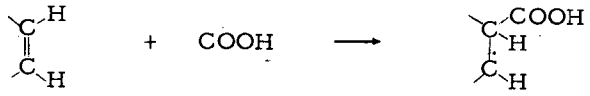

(3)

The radical products of Reactions (2) and (3) then undergo disproportionation to yield the 5,6-dihydrocytosine derivatives:

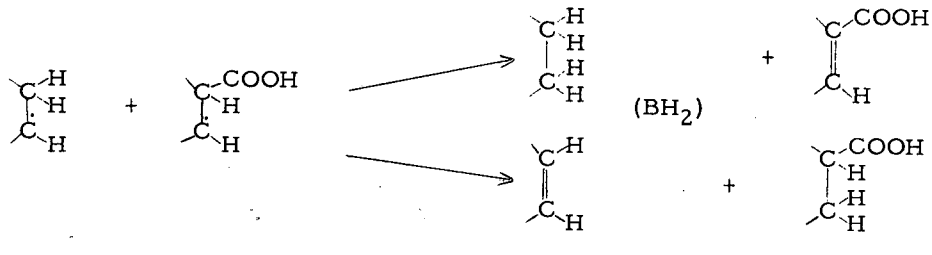

(4)

(5)

These hydrolyze spontaneously to ammonia and the corresponding dihydrouracil derivatives. To confirm the formation of the hydrouracil nucleus, the irradiated cytosine formate solutions were passed through Dowex-50 in the acid form to quantitatively remove cytosine.[9] The water effluent was freeze-dried, redissolved in water at pH ≈ 7, and then read spectrophotometrically over the range 210 to 350 mμ in 0.1 N sodium hydroxide against an unirradiated sample that had undergone the identical treatment. As shown in Fig. D. 21-2, the absorption spectrum of the irradiation products corresponds closely to the absorption spectra of authentic dihydrouracil and dihydrouracil-6-carboxylic acid.

Since the spectra of these substances are almost identical, other methods had to be employed to distinguish their relative contribution to the absorption given by the product material. Advantage was taken of the fact that the effect of base on the optical absorption of hydrouracil and its derivatives is associated with the production of enol forms which are unstable and are rapidly hydrolyzed with characteristic first-order rates to give the corresponding ureido acid. Batt et al.[10] have reported half-times of 5.0 and 11.1 minutes, respectively, for the hydrolysis of hydrouracil and hydrouracil-6-carboxylic in 0.1 N sodium hydroxide. The irradiation products whose initial absorption spectrum in 0.1 N sodium hydroxide is shown in Fig. D. 21-2 showed a decrease in optical density at λ_{max} = 230 mμ corresponding to a half-time of ≈12.1 minutes over a minimum of three half-time periods. Reaction (4) seems to occur preferentially over Reaction (3). Preliminary spectrophotometric determinations of $G(B'H_2)$, based on $\epsilon_{max} \approx 8 \times 10^3$,[10] gave values considerably below that expected on the basis of the indicated mechanism. Apparently $B'H_2$ undergoes a slow hydrolytic dark reaction to form the corresponding ureido acid. However, the ureido acids revert to the original hydrouracil derivatives in the presence of dilute mineral acid.[10] Treatment of the irradiated cytosine solutions with 0.1 N hydrochloric acid for several hours prior to analysis gave $G(B'H_2) \approx 2.4$, in good agreement with the reaction mechanisms described here.[11]

These findings would appear to cast some doubt on recent proposals regarding the nature and locus of the primary radiobiological lesion. Various authors have commented on the fact that the pronounced enhancement by oxygen of the radiation-induced degradation of the pyrimidines and purines in aqueous solution is closely paralleled by the two- to threefold increase in radiobiological damage effected by oxygen. And, it has been suggested[11] that this similarity in oxygen response is a strong argument in favor of a common radiation chemical process. However, we have found here that radicals of certain organic substances are as effective as oxygen in increasing the degradation of cytosine in irradiated aqueous solution. The possibility that organic radicals in anoxic biological systems under irradiation are equally effective in the enhancement of cytosine degradation cannot be dismissed. Hence, the interpretation of the oxygen effects in radiobiology in terms of the radiation chemistry of pure base-water systems may prove misleading.

Footnotes and References

† Condensation of UCRL-11561, submitted to Nature.

* Present address: Central Laboratories, 35 P. N. H. Lines, Karachi, Cantt (Pakistan).

1. G. Scholes, J F. Scholes, J. F. Ward, and J. Weiss, J. Mol. Biol. 2, 379 (1960).
2. G. Scholes and J. Weiss, Nature 185, 305 (1960).

3. B. Ekert and R. Monier, Nature 188, 309 (1960).
4. A. O. Allen, Radiation Res. Suppl. 4, 54 (1964).
5. R. Latarjet, B. Ekert, and P. Demerseman, Radiation Res. Suppl. 3, 247 (1963).
6. C. Ponnamperuma, R. M. Lemmon, E. L. Bennett, and M. Calvin, Science 137, 605 (1962).
7. E. J. Hart, J. K. Thomas, and S. Gordon, Radiation Res. Suppl. 4, 74 (1964).
8. M. Green and S. C. Cohen, J. Biol. Chem. 228, 601 (1957).
9. W. E. Cohn, Science 109, 377 (1949).
10. R. D. Batt, J. K. Martin, J. McT. Ploeser, and J. Murray, J. Am. Chem. Soc. 54, 3663 (1954).
11. See, for example, G. Hems, Radiation Res. 13, 777 (1960), and also reference 5.

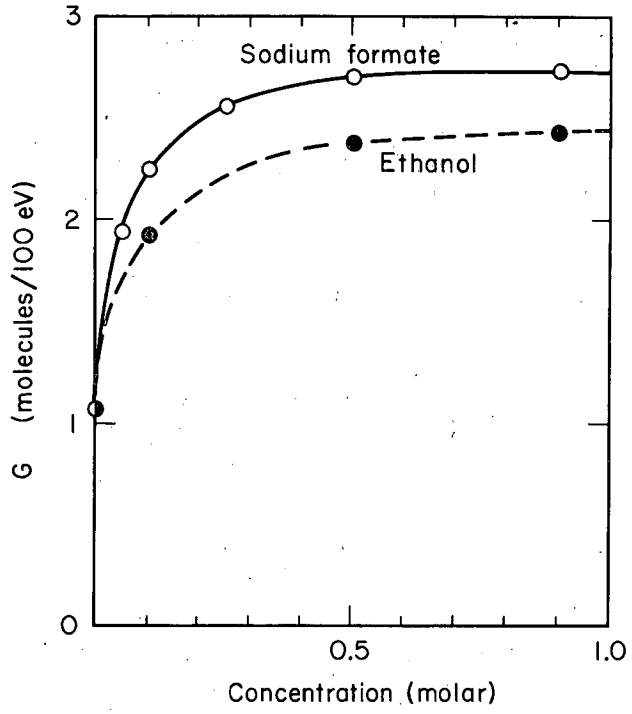

MUB-3540

Fig. D.21-1. Effect of second-solute concentration on $G(NH_3)$ in the γ radiolysis of 0.05 M cytosine, evacuated, pH 7 ± 0.3. Cytosine (Calbiochem., A grade, Lot 35887) was purified by fractional recrystallization from cold water. Solutions were irradiated in evacuated Pyrex ampoules under Co^{60} γ rays at a dose rate of 1.2×10^{18} eV/g/min for a total dose of 6.5×10^{18} eV/g. Ammonia was separated by the Conway diffusion method following addition of 1 ml of sample to 9 ml of 10 N potassium carbonate. The diffusates were assayed by means of the Nessler reaction.

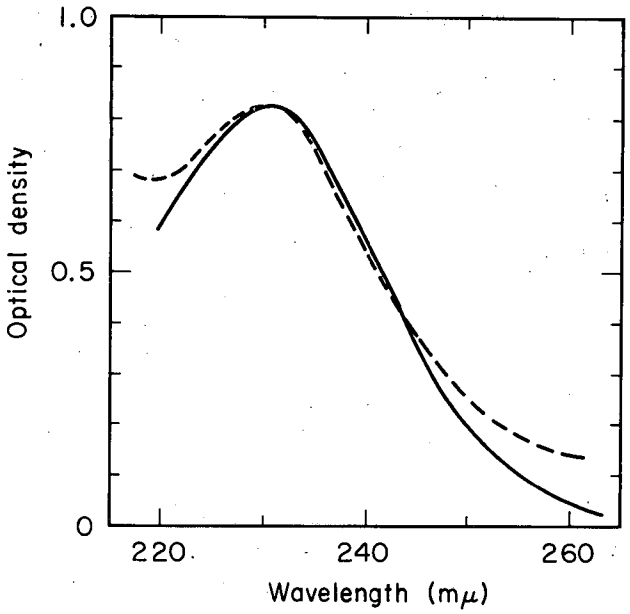

MUB-3539

Fig. D.21-2. Absorption spectrum in 0.1 N sodium hydroxide of the dihydrouracil derivatives formed in the γ radiolysis of 0.05 M cytosine is given by dashed line. The solid line represents the normalized spectrum of authentic dihydrouracil and dihydrouracil-6-carboxylic acid, which are practically indistinguishable with the Beckman DB spectrophotometer.

2.2. A STUDY ON THE STABILITY OF XENON TRIOXIDE IN BASIC SOLUTIONS

Charles W. Koch and Stanley M. Williamson

The chemistry of XeO_3 in alkaline solution has previously been described in some detail.[1,2,3] The significance of the research in basic solution is shown by the stability of the XeO_3 in neutral or acidic solution as opposed to the instability of the species and salts thereof in basic solution, and by the usefulness of the instability as a method of preparation of various salts of the yet unobtained paraperxenic acid, H_4XeO_6.

In our previous work[3] on this problem, we observed that XeO_3 in sodium hydroxide solution ranging from 0.25 to 4.2 M gave oxygen and xenon gas in the ratio of 1.0 along with the production of $Na_4XeO_6 \cdot 8H_2O$ or, under some conditions, $Na_4XeO_6 \cdot 6H_2O$.[4] In a more detailed study[5] on the nature of this apparent disproportionation reaction of XeO_3 with subsequent decomposition of a lower-oxidation-state oxide [presumably Xe(IV)] we have observed that XeO_3 outwardly behaves very differently in KOH than it does in NaOH solutions.

In order to follow the stoichiometry of the reaction between XeO_3 and KOH, a glass vessel with two 1-ml fingers was attached to a separation train and Toepler pumping system that has been previously described.[3] The glass vessel was mounted on a standard taper joint at such an angle that rotation would cause the two individual solutions to mix. Before mixing they were degassed so the system was a closed one in which Xe could be quantitatively separated from the O_2 and water vapor. Each of the gases could be measured directly in a gas buret. The quantities of materials used for a reaction ranged from 200 to 750 µl of about 0.1 M XeO_3 and enough 10 M KOH to make the hydroxyl concentration range from 0.03 to 3.6 M after mixing. The amounts of reactants for any one experiment were known exactly.

The KOH was treated with $KMnO_4$ at 70° until it had all decomposed and (or) been reduced by any reducing agent impurities (e.g., Cl^-) to MnO_2. Moderate care was taken to exclude CO_2, and the reactions described here were run at room temperature. The resulting concentration of manganese was so low that no pink color was ever observed because of oxidation to MnO_4^- by the XeO_3 or perxenate anion.

The data in Table D.22-I show that the overall reaction is more complex than the simple disproportionation of XeO_3 followed by the decomposition of Xe(IV). Instead of obtaining a 50% yield of perxenate from XeO_3 and KOH we have observed that a 25 to 33% yield is obtained over a range of 0.3 to 3 M KOH. The smaller yield is the result of an alternative reaction, by which XeO_3 can decompose without giving rise to an increased amount of perxenate. With the occurrence of both reactions the O_2/Xe values are greater than unity. As the decomposition progresses a yellow insoluble compound is formed. Appelman and Malm[6] have described this as an explosive compound with a formula of $K_4XeO_6 \cdot 2XeO_3$. In alkaline solution this yellow substance decomposes slowly, yielding an oxygen-to-xenon ratio approaching 1.5. The explosive character of this substance, which we have also observed, and the proximity of the O_2/Xe ratio to 1.5 in the later stages of decomposition when the yellow solid is still present in the reaction mixture, also suggests that the precipitate may be a potassium xenate salt. When the colorless homogeneous perxenate solution that remains is treated with an additional increment of XeO_3 (Table D.22-I, Exp. 2b and 3b), the yellow precipitate forms within a few minutes and is present in slowly diminishing amount until all degassing has ceased. It appears from these measurements that as the reaction proceeds the increasing perxenate concentration diminishes the relative production of perxenate. Experiment 5 shows that when the initial KOH concentration is as low as 0.03 M, perxenate no longer is stable and the O_2/Xe ratio approaches 1.5. Also in this experiment no yellow colored solution or precipitate is observed.

In one experiment when the resulting perxenate solution contained 33.8 µmoles of perxenate, 2008 µmoles of K^+, and 950 µl H_2O, the solution was reduced to half volume in a desiccator. Slow chilling to 5° produced well-defined, colorless transparent crystals. The x-ray crystal structure of this colorless compound has been determined and the formula established as $K_4XeO_6 \cdot 9H_2O$, potassium perxenate nonahydrate.[7] The crystals of the potassium perxenate were found to be considerably more stable in x rays than was $Na_4XeO_6 \cdot 6H_2O$, but less so than was $Na_4XeO_6 \cdot 8H_2O$. In none of these salts has any explosive character been observed.

References

1. J. G. Malm, B. D. Holt, and R. W. Bane, Noble-Gas Compounds, H. H. Hyman, Ed. (University of Chicago Press, Chicago, 1963), p. 167.
2. E. H. Appelman, ibid., p. 185.
3. S. M. Williamson and C. W. Koch, ibid., pp. 158 and 181.
4. A. Zalkin, J. D. Forrester, D. H. Templeton, S. M. Williamson, and C. W. Koch, Science 142, 501 (1963).
5. C. W. Koch and S. M. Williamson, J. Am. Chem. Soc. 86, 5439 (1964).
6. E. H. Appelman and J. G. Malm, J. Am. Chem. Soc. 86, 2141 (1964).
7. A. Zalkin, J. D. Forrester, D. H. Templeton, S. M. Williamson, and C. W. Koch, J. Am. Chem. Soc. 86, 3569 (1964).

Table D.22-I. Experimental data.

Expt.	μmoles XeO_3 initial	μmoles KOH initial	Total Vol. μl	Temp. °C	μmoles O_2	evolved Xe	$\left[\frac{O_2}{Xe}\right]_{collected}$	$\left[\frac{O_2}{Xe}\right]_{remaining}$	% Rxn.	Total Time hrs.
1	20.50	2540	700	25±1	2.66	2.19	1.22	1.53	10.7	2.3
		$\left[\frac{\Sigma O_2}{\Sigma Xe}\right]_{collected} = 1.27$			4.12	3.39	1.21	1.61	27.2	4.8
					12.06	9.28	1.30	3.1	72.5	21.4
2(a)	27.05	2008	950	24±1	8.34	7.26	1.15	1.63	26.9	6.2
		$\left[\frac{\Sigma O_2}{\Sigma Xe}\right]_{collected} = 1.25$			14.53	10.96	1.33	2.01	67.6	19.4
(b)	500μl H_2O removed by vacuum distillation; added additional 54.00 μmoles XeO_3 + 500 μl H_2O									
		$\left[\frac{\Sigma O_2}{\Sigma Xe}\right]_{collected} = 1.33$			7.35	6.13	1.20	1.54	11.4	1.8
					22.53	17.19	1.31	1.67	43.2	7.2
					22.71	16.23	1.40	1.97	73.2	18.9
3(a)	80.82	2008	950	26±2	45.10	38.00	1.19	1.78	47.0	68.5
		$\left[\frac{\Sigma O_2}{\Sigma Xe}\right]_{collected} = 1.25$			12.21	8.85	1.38	1.88	57.9	145.9
					8.93	6.00	1.49	1.97	65.4	237.4
(b)	400 μl H_2O pumped off; 21.64 μmoles XeO_3 + 200 μl H_2O added.									
		$\left[\frac{\Sigma O_2}{\Sigma Xe}\right]_{collected} = 1.33$			4.23	3.30	1.28	1.54	15.2	21.2
					11.49	8.67	1.32	1.73	55.3	87.5
					5.60	4.06	1.38	1.99	74.1	159.3
4	27.05	250	775	25±2	9.13	7.79	1.17	1.63	28.8	6.7
		$\left[\frac{\Sigma O_2}{\Sigma Xe}\right]_{collected} = 1.34$			8.46	6.32	1.34	1.78	52.2	40.1
					9.65	6.22	1.55	1.99	75.2	162.1
5	27.05	25	850	24±1	8.81	6.22	1.42	1.53	23.0	21.6
		$\left[\frac{\Sigma O_2}{\Sigma Xe}\right]_{collected} = 1.46$			25.61	17.20	1.49	1.70	86.6	69.2
					2.94	2.12	1.39	2.1	94.4	166.8

23. ANION EXCHANGE IN CONCENTRATED SOLUTIONS†

C. H. Jensen* and R. M. Diamond

The purpose of this work was to study the variation of selectivity of anion-exchange resin with the nature of the resin group and of the macroelectrolyte, and to see if rules of behavior could be found similar to those for cation exchange.[1,2]

The equation for the exchange of a halide tracer ion, A^-, with a univalent macro-ion, B^-, on an ion-exchange resin can be written

$$A + \overline{B} = \overline{A} + B . \tag{1}$$

In the usual way, combination of the equilibrium expression

$$1 = \frac{(\overline{A})(B)}{(A)(\overline{B})} = \frac{[\overline{A}][B]}{[A][\overline{B}]} \frac{\overline{\gamma}_A \gamma_B}{\gamma_A \overline{\gamma}_B} = K_{A/B} \Gamma_{A/B} \tag{2}$$

with the definition of the distribution coefficient

$$D \equiv \frac{[\overline{A}]}{[A]} \tag{3}$$

leads to

$$D = \frac{[\overline{B}]\, \overline{\gamma}_B \gamma_A}{[B]\, \overline{\gamma}_A \gamma_B} . \tag{4}$$

For dilute solutions, where resin invasion is negligible and the activity coefficient ratios are essentially constant, Eq. (4) reduces to the well-known form, $D \alpha [B]^{-1}$. As can be seen in Figs. D.23-1 through D.23-3, this is obeyed in dilute solution for all the tracers with the types of resins and eluting solutions studied.

Furthermore the elution order is the same in all cases, F < Cl < Br < I. In this sequence, the position of the small F^- is mainly due to the better hydration available in the aqueous phase, while that of the large I^- is probably mainly due to its disturbance of the water structure and the possibility of water-structure-enforced ion pairing with the resin ammonium groups in the resin phase.[3,4] But it can be seen that the degree of separation of the halide tracers varies with the nature of the macro-anion and of the resin group.

In particular, as can be observed by comparing Figs. D.23-1 and D.23-2, a compression of the halide separation factors occurs if a tertiary amine rather than a quaternary ammonium group is used as the resin group. Dowex-4 is such a weak-base resin, and so in slightly acid solutions has R_3NH^+ as the active site. The resulting ammonium ion is still a large ion, but it has a special site, the hydrogen, which probably carries much of the ion's charge, and which can hydrogen-bond to water and to other bases. That is, the ion has a hydrophilic side compared to the quaternary ammonium group, and so cannot participate in water-structure-enforced ion pairing as well as can the quaternary ion, thereby decreasing its attraction for large ions like I^-. But it has the possibility of (hydrogen-) bonding, even though weakly, to small basic anions such as F^-, and so making the resin phase more attractive to such ions than are strong-base resins. For both reasons, the halide elution sequence should be compressed over that with a quaternary ammonium-type resin, and Figs. D.23-2 and D.23-3 show only a tenfold spread in D from F^- to I^- with Dowex-4 and eluting solutions of LiCl or NMe_4Cl below a few hundreths molar in concentration, compared with the 250-fold range in D with Dowex-1.

Furthermore, as can be seen in Figs. D.23-1 through D.23-3, all the tracers deviate from the mass-action slope of -1 as the external salt solution concentration is increased. These deviations indicate a breakdown in the dilute solution assumptions made in the derivation of Eq. (4). One effect is the entrance of nonexchange electrolyte into the resin phase at high concentration of external solution. This resin-invasion electrolyte acts, to a first approximation, as additional cationic sites for the anions (increase of $[\overline{B}]$ in Eq. 4), and so contributes to a gradual increase above the ideal mass-action line of slope -1 for all the tracer anions. More important, however, are the increasingly stronger interactions of the anions with the aqueous cations and with the resin groups as the amount of water available to hydrate each ion decreases. That is, as the external aqueous-phase concentration is increased, ion hydration gradually tends to become cation solvation (complexing) by the aqueous phase macro-cation and by the resin group. With the halide anions and simple cations such as the alkali-metal ions, these interactions are not chemical complex-ion formation, but more transient types of electrostatic association. Two such types, a temporary contact ion pairing of the bare ions and an association through one or

more polarized water molecules (localized hydrolysis), have been discussed in an earlier paper on cation exchange.[1] The strength of such electrostatic associations depends upon the crystallographic size of the ions, decreasing from Li > Na > K > Rb > Cs and from F > Cl > Br > I. It should be remembered that the very different type of water-structure-enforced ion pairing has precisely the opposite behavior, becoming more important the larger the ion, and occurring noticeably only with ions as large as NMe_4^+ (possibly Cs^+) and I^- (Br^-).

If, as the aqueous-phase concentration increases, the interactions of the tracer anion of interest with the resin group are stronger than those with the aqueous-phase macro-cation, the anion will increasingly prefer the resin phase, and conversely, if the aqueous-phase cation interactions are the stronger, the anion will go preferentially into that phase. But in an ion-exchange reaction, it must be remembered, both anions are competing for the best solvating medium; the exchange goes in such a direction as to provide the most favorable situation--the lowest free energy--for the system as a whole, and this will usually be determined by the smallest ion, that which needs solvation the most.

With these considerations in mind, we can take up the experimental results in concentrated salt solutions. Figure D.23-1 shows the behavior of tracer F^-, Br^-, and I^- on a quaternary ammonium resin with LiCl as the macro-electrolyte. As the external-solution concentration increases, the aqueous phase remains the more favorable one for solvating the anions, for with decreasing water activity, ion hydration is gradually replaced by complexing with the lithium ion. Fluoride is complexed more strongly than Cl^-, and enough so that it is held in the aqueous phase more strongly relative to Cl^- in concentrated LiCl than in dilute solution, so that the curve for F^- tracer shows a slight negative deviation from the mass-action slope of -1 in concentrated solutions. Furthermore, the dilute-solution selectivity order F < Cl < Br < I is greatly enhanced in concentrated LiCl solutions as the larger halides are pushed out of the aqueous phase into the resin in order to permit the smaller anions to achieve their solvation by complexing with the Li^+ in the concentrated external solution.

However, it should be possible to greatly change this selectivity order by changing the nature of the resin group and of the macro-cation. Obviously, as already mentioned for the dilute solution case, the replacement of the quaternary ammonium cation of the strong-base resin with a group capable of (hydrogen-) bonding to the (smaller) anions would more nearly equalize the distribution coefficients of the halide ions. And this effect should be even more significant in concentrated solutions, where the anion-cation interactions become more important relative to anion-water solvation than in dilute solution. A comparison of the results given in Fig. D.23-1 for the quaternary ammonium ion resin and in Fig. D.23-2 for the tertiary amine resin shows indeed this result; the 250-fold range in distribution coefficients from F^- to I^- for Dowex-1 in dilute solution is increased 80 times in going to 10 M LiCl, while the tenfold spread of D's with Dowex-4 in dilute solution increases only by a factor of about 5 at 10 M LiCl. Furthermore, the ability of the R_3NH^+ resin group to hydrogen-bond to the small electronegative anions means that even F^- can obtain solvation in the resin phase comparable to that available in the aqueous phase (from the Li^+), and so yields a small positive deviation from the ideal mass-action curve in concentrated LiCl.

By going to a still better complexing resin group or to a more poorly complexing macro-cation, it should be possible to reverse the elution order of the halides in concentrated solution. The latter approach was tried, substituting tetramethyl ammonium chloride for lithium chloride, and using Dowex-4 resin. Now, as the water activity falls, the tertiary amine resin group can provide stronger interactions for the smaller anions than does the macro-cation in the aqueous phase, although unfortunately, the water activity does not fall as rapidly with NMe_4Cl concentration as with LiCl. As can be seen in Fig. D.23-3, the distribution curves for F^-, Br^-, and I^- tracers, instead of diverging at higher macro-electrolyte concentrations as in the previous cases, come together at 6 M NMe_4Cl. Although no region of inverted selectivity order was actually observed, the behavior found certainly supports the ideas presented, and somewhat more forcing conditions (perhaps the use of NEt_4Cl as macro-electrolyte) would appear capable of yielding such an inverted sequence.

Footnotes and References

† Shortened version of UCRL-11806.
* Summer visitor, 1962, NSF High School Teachers Research Participation Program. Permanent address: Cabrillo College, Aptos, California.

1. D. C. Whitney and R. M. Diamond, Inorg. Chem. 2, 1284 (1963).
2. D. C. Whitney and R. M. Diamond, Ion-Exchange Studies in Concentrated Solutions. II. Alkaline Earth Cations with a Sulfonic Acid Resin, J. Inorg. Nucl. Chem., in press.
3. B. Chu, D. C. Whitney, and R. M. Diamond, J. Inorg. Nucl. Chem. 24, 1405 (1962).
4. R. M. Diamond, J. Phys. Chem. 67, 2513 (1963).

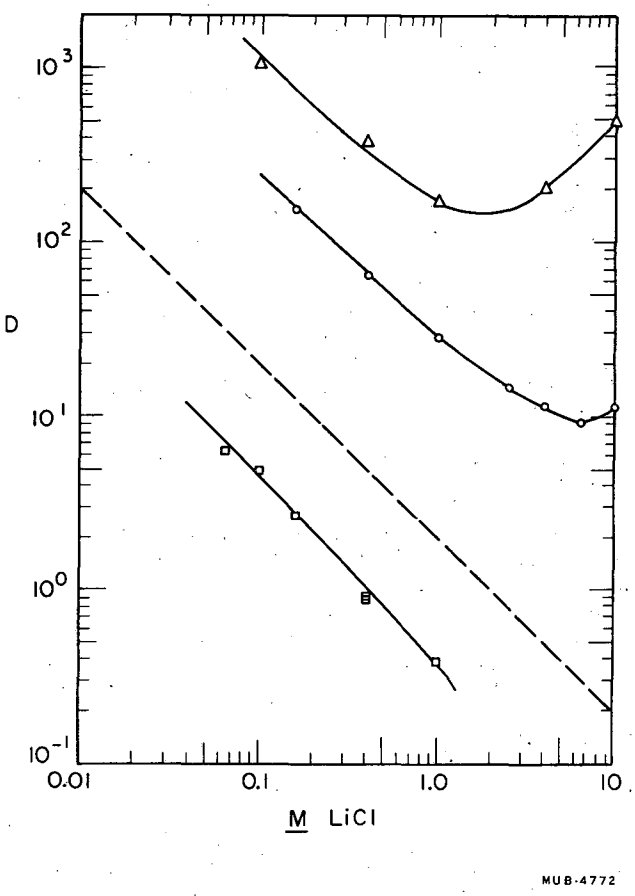

Fig. D.23-1. Plot of log D vs log LiCl molarity with Dowex-1 resin for tracer. F^-, □; Br^-, O; I^-, △.

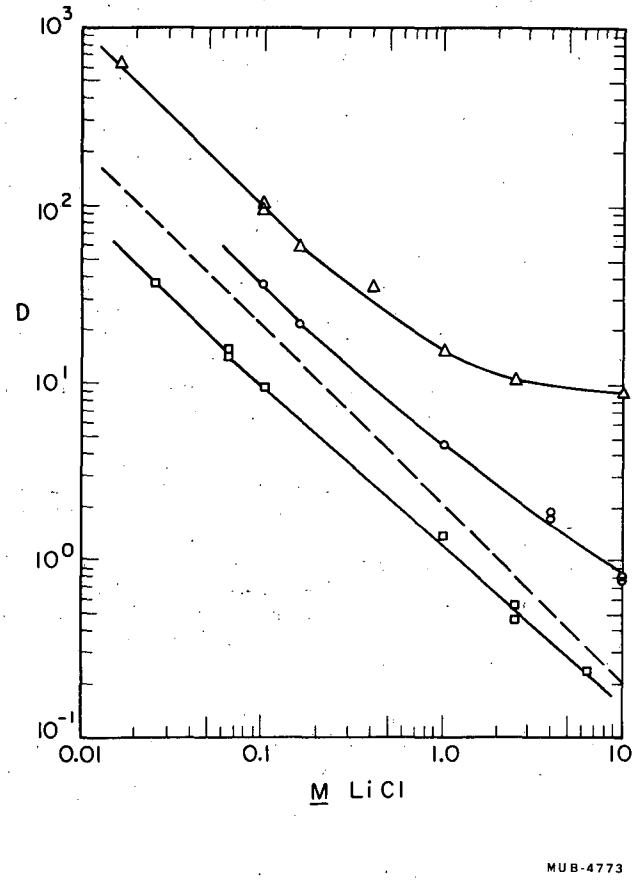

Fig. D.23-2. Plot of log D vs log LiCl molarity with Dowex-4 resin for tracer. F^-, □; Br^-, O; I^-, △.

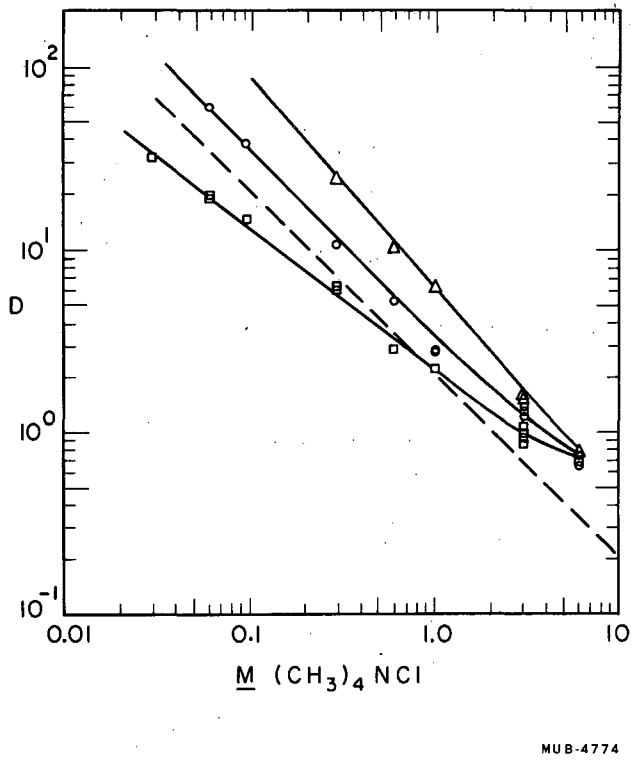

Fig. D. 23-3. Plot of log D vs log NMe_4Cl molarity with Dowex-4 resin for tracer. F^-, □; Br^-, O; I^-, △.

24. ION-EXCHANGE STUDIES IN CONCENTRATED SOLUTIONS: The Nature of the Resin Sulfonate—Cation Bond in Strong Acid Solutions†

D. C. Whitney* and R. M. Diamond

The distribution ratios of lanthanide elements between HCl solutions and sulfonic acid ion-exchange resins were shown several years ago to pass through a minimum at 4 M HCl, followed by a steep rise at higher concentrations.[1] An even steeper rise occurs with solutions of $HClO_4$ above 4 M.[2] A very strong interaction with the resin is implied, and the work reported in this paper is an attempt to determine the nature of the interaction. This was accomplished through the use of two trivalent cations of essentially identical size but with coordination spheres greatly differing in lability, i.e., Fe(III) (0.64 Å), with essentially instantaneous ligand exchange, and Cr(III) (0.69 Å), with an approximately 32-hour half-life for H_2O exchange in strong acid solution.[3] By observation of the behavior of these ions, the nature of their bonding to the resin from strong acid solutions has been elucidated.

It was subsequently determined that Fe(III) has somewhat anomalous behavior in dilute $HClO_4$ solutions (< 1 M), so Sc(III) (0.81 Å), a somewhat larger but equally labile ion, was used to check the Fe results.

The experimental data are plotted with solid symbols used as log D vs log M $HClO_4$ for Dowex-50W in Fig. D. 24-1. The main point of interest is that since in dilute solution the tripositive ions fall into a normal selectivity order they must all be exhibiting the same type of bonding to the resin sites. Moreover, Boyd and Soldano have shown[4] that Cr(III) retains its

primary hydration shell of six water molecules in the resin phase under such dilute solution conditions. This leads to the conclusion that all three of the ions in this study retain at least their first shell of water molecules inside the resin in dilute $HClO_4$ (< 1 M), and that the cations, if bonding to a specific resin sulfonate group, do so through at least one H_2O "bridge" in their primary hydration shell.

Consider now the behavior of the exchange resin in more concentrated $HClO_4$ solutions. It is seen in Fig. D. 24-1 that the plots of D for Fe, Sc, and Cr are essentially similar up to about 2 M $HClO_4$. At this point the Fe and Sc curves begin to deviate upward from a straight line, going through a minimum at 3.5 M, after which they turn up sharply. The values for Cr, on the other hand, keep on dropping until a more or less constant value of D is attained over the region of 4 to 10 M $HClO_4$.

Since Fe and Cr are of substantially identical size and are both hexaquo ions, any explanation of the difference in their behavior must be connected with the difference in the labilities of the aquo-ions. The relatively long half-life for water exchange by $Cr(H_2O)_6^{+++}$ means that in our distribution experiments this ion exists primarily as the hexaquo complex even in concentrated $HClO_4$. On the other hand, $Fe(H_2O)_6^{+++}$ tends to surrender some of its waters of hydration in the dehydrating atmosphere of the concentrated $HClO_4$ solutions, even though its high charge density strongly requires coordination (solvation) by basic (electron-donating) species. Under these conditions, it seems reasonable that the labile ions, seeking solvation, would enter the resin phase and use sulfonate ions to complete their primary solvation shells, forming bonds directly between the cation and the resin sulfonate anion. This solvation by the resin would result in a rise in the D's for most tripositive ions in concentrated $HClO_4$ solutions. On the other hand, the $Cr(H_2O)_6^{+++}$ ion, because of the slow kinetics of its water exchange, would keep its hydration shell during the period of time of these experiments, even in very concentrated acid solutions. Thus $Cr(H_2O)_6^{+++}$ could not bond directly to the sulfonate groups and would tend to remain in the aqueous phase to a greater extent than would the labile cations.

The foregoing ideas can be checked by carrying out a study of the change in distribution ratio with time. Since the $Cr(H_2O)_6^{+++}$ does slowly undergo exchange of its waters of hydration, it would be expected that in solutions of low water activity another solvating group, specifically a resin sulfonate anion, could replace a water molecule if given enough time. Thus it might be predicted that the distribution ratio of Cr tracer would gradually increase with time, as resin sulfonate groups gradually entered the first hydration shell of more and more chromium ions, until values of the distribution ratio approaching those for Fe were obtained. Scandium and iron, on the other hand, would be expected to maintain the same D over these periods of time, since they are undergoing continuous exchange between H_2O and sulfonate groups in a state of dynamic equilibrium.

Distribution ratios at several different acid molarities taken over a period of several weeks are shown in Fig. D. 24-1 with open symbols, and are listed in Table D. 24-I. It can be seen that essentially no differences occur in any of the points with the exception of those for Cr tracer in 7.5 M $HClO_4$, where a roughly exponential increase with time occurs for the first week; results for longer times are probably incorrect (on the low side) due to degradation of Dowex-50W by the $HClO_4$.

It thus appears that some rather definite conclusions can be made about the bonding of tripositive ions such as Sc, Fe, the lanthanides and actinides, etc., to sulfonic acid ion-exchange resins. In dilute solutions, the ions retain their primary hydration shell, and to whatever extent they are actually bonded to the resin sulfonate groups, this must be through at least the primary hydration shell. As the water activity falls, and in the absence of complexing anions in the aqueous phase, those ions which lose at least one of their first-shell waters of hydration may replace it with a resin sulfonate group, forming a cation-sulfonate group bond and thus yielding very high distribution ratios. Those ions which, under the conditions of the experiment do not lose their primary hydration shell, whether for kinetic reasons or because of the strength of the water-ion bond, will not go as strongly into the resin phase and so will exhibit lower distribution ratios than the former ions. Exactly the reverse behavior will occur in the presence of strongly complexing anions.

Footnotes and References

† Brief form of J. Phys. Chem. 68, 1886 (1964).

* Present address: Shell Development Co., Emeryville, California.

1. R. M. Diamond, K. Street, and G. T. Seaborg, J. Am. Chem. Soc. 76, 1461 (1954).

2. G. R. Choppin and A. Chetham-Strode, J. Inorg. Nucl. Chem. 15, 377 (1960).
3. J. P. Hunt and H. Taube, J. Phys. Chem 19, 602 (1951).
4. G. E. Boyd and B. A. Soldano, J. Am. Chem. Soc. 75, 6105 (1953).

Table D.24-I. Time studies of the distribution of trivalent tracers between Dowex-50W and $HClO_4$.

Acid molarity	Time	D for Fe(III)	D for Cr(III)
0.226	15 m	5.5×10^3	1.6×10^4
0.226	4 h	5.7×10^3	1.4×10^4
0.226	7 d	4.0×10^3	1.7×10^4
1.63	15 m	4.6×10^1	4.8×10^1
1.63	4 h	5.2×10^1	4.8×10^1
1.63	7 d	4.0×10^1	4.9×10^1
7.47	15 m		5.2×10^0
7.47	4 h	8.2×10^1	6.7×10^0
7.47	7 d	7.4×10^1	
7.47	24 h		8.9×10^0
7.47	4 d		1.3×10^1
7.47	5 d		1.5×10^1
7.47	7 d		1.8×10^1
7.47	14 d		2.0×10^1
7.47	28 d		2.1×10^1

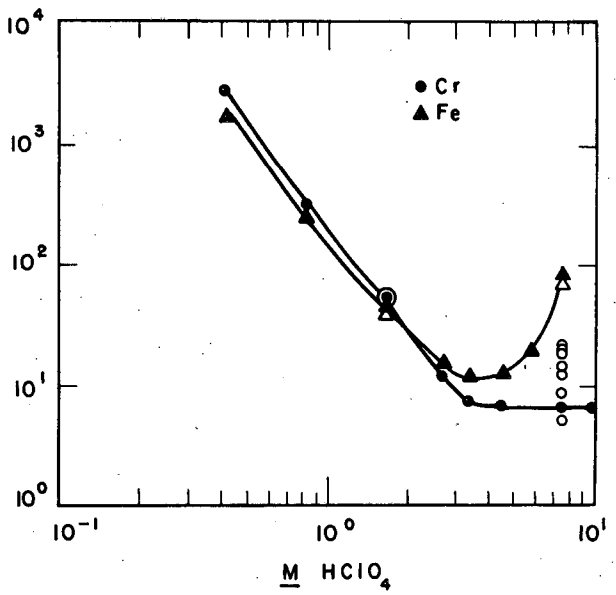

Fig. D.24-1. Variation of distribution ratio on Dowex-50W with $HClO_4$ molarity for the tripositive ions: ▲, Fe; ●, Cr; ■, Sc. Open symbols are time studies; see Table D.25-I.

25. THE EXTRACTION OF ACIDS BY BASIC ORGANIC SOLVENTS: Trioctyl Phosphine Oxide-$HClO_4$ and Trioctyl Phosphine Oxide-$HReO_4$†

T. J. Conocchioli,* M. I. Tocher, and R. M. Diamond

Two previous papers have described the extraction of aqueous $HClO_4$, $HReO_4$, and HBr by solutions of tributyl phosphate in CCl_4.[1,2] In these systems the extracted acid species was $H_3O^+ \cdot 3TBP \cdot yH_2O \ldots X^-$, where $0 \leq y \leq 3$. That is, the TBP is not basic enough to take the proton alone out of the water phase, but extracts a partially hydrated hydronium ion; water is a stronger base than TBP. The extractant used in the present study was tri-n-octyl phosphine oxide (TOPO), a stronger base than TBP. Thus it might be expected to compete better with water for the proton, and so permit less water in the extracted complex. The choice of TOPO was also influenced by the fact that it has only one basic site—the phosphoryl oxygen—as opposed to TBP, which has three ester oxygens in addition to the terminal oxygen.

It is assumed that the TOPO-water system is maintained independently of any TOPO-acid system, so that TOPO molecules bonded to water are not readily available for acid extraction. Therefore, the initial investigation was of the extraction of pure water by TOPO. The equation for this extraction may be written

$$nTOPO_{(o)} + H_2O = H_2O \cdot nTOPO_{(o)}, \quad (1)$$

where (o) indicates the organic phase. The corresponding concentration constant is

$$K_{H_2O} = [H_2O \cdot nTOPO]/[TOPO]^n(H_2O). \quad (2)$$

Fig. D.25-1 shows a plot of log organic-phase water vs log initial TOPO. The curve is linear from 0.001 to 0.1 M TOPO, with a slope of 1.0. Correction to equilibrium TOPO yields a value of n = 1.0 and $K'_{H_2O} = 0.56$, which means that at TOPO concentrations below 0.1 M in CCl_4 36% of the total TOPO is bonded to H_2O, and the water-TOPO complex contains only one TOPO. This is analogous to the earlier studied TBP-CCl_4 system,[1] and the larger value of K'_{H_2O} is an indication of the greater basicity of TOPO over TBP.

Above 0.1 M TOPO, the curve rises more steeply than a slope of unity. This rise indicates either the introduction of a new TOPO-H_2O complex or the breakdown of the assumptions made for dilute solutions.

The next series of experiments had to do with the $HClO_4$ extraction itself. Concentrations of acid from 0.01 to 11 M $HClO_4$ were equilibrated with dilute solutions of TOPO in CCl_4 ranging from 0.01 to 0.1 M, and the organic-phase acid content was determined at each external (aqueous) acid concentration. Perrhenate tracer extractions from macro-concentrations of $HClO_4$ were used to extend the range of aqueous acid concentrations investigated toward more dilute solutions, namely down to 0.001 M $HClO_4$.

From a log-log plot of the organic acid concentration vs the aqueous acid activity, with the equilibrium TOPO and water activity held constant, it can be determined whether the extracting species is an ion pair or a pair of dissociated ions. Such a plot is shown in Fig. D.25-2 for the tracer $HReO_4$ out of dilute $HClO_4$, and the slope of 1.0 obtained indicates an ion pair.

Thus the extraction may be expressed as

$$H^+ + X^- + yH_2O + nTOPO_{(o)} = H^+ \cdot nTOPO \cdot yH_2O \ldots X^-_{(o)}, \quad (3)$$

with the corresponding equilibrium constant

$$K_{HX} = (H^+ \cdot nTOPO \cdot yH_2O \ldots X^-)/(TOPO)^n (H_2O)^y (H^+X^-) . \quad (4)$$

The value of n can be determined from a log-log plot of the organic acid vs the equilibrium TOPO concentration at a fixed aqueous acid activity. Such a plot is shown in Fig. D.25-3 for dilute aqueous $HClO_4$, and yields n = 3.

Finally, determinations were made of the amount of H_2O extracting with $HClO_4$. Solutions of 0.05 and 0.1 M TOPO were equilibrated with aqueous solutions of acid ranging from 0.01 to 11 M in $HClO_4$ and the amounts of H^+ and H_2O in the organic phase were measured, the latter by the Karl Fischer method. The water values, however, include the water dissolved in CCl_4 alone, which quantity may be calculated as the product of the solubility of pure water in CCl_4, the aqueous water activity, and the volume fraction of CCl_4. To determine the number of water molecules extracted per proton, y, however, these values also had to be corrected for the amount of water involved in the TOPO-H_2O complex. This can be calculated from Eq. (2) by assuming that the TOPO-H_2O system is maintained independently of the TOPO-acid-H_2O system, and that no other TOPO-acid complex exists. In Fig. D.25-4 is shown a plot of the water bound in the acid complex, $[H_2O]_{acid}$ vs $[H^+]_{(o)}$. It can be seen that the curve passes through the origin and that its slope is initially 1.

Thus, for the system of dilute $HClO_4$-H_2O-TOPO, water best solvates the proton, and the H_3O^+ ion is extracted over a considerable range of TOPO and acid concentrations. The species present is $H_3O^+ \cdot 3TOPO \ldots ClO_4^-$,

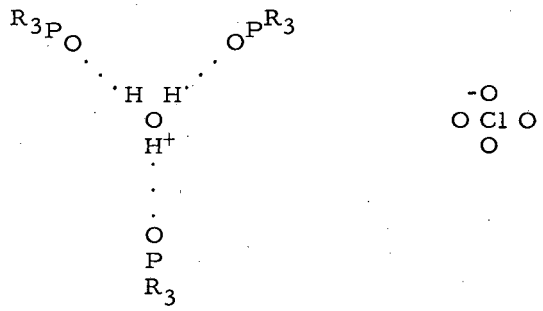

an ion pair in the CCl_4 diluent. This trisolvated species is similar to the one proposed for the extraction of $HClO_4$ by dilute TBP (a weaker base) in CCl_4, except that the TOPO has displaced the water molecules from about the hydronium ion.[1,2] But as the acid concentration is increased, the water activity falls and the amount of free TOPO decreases, so that a transition occurs to a monosolvated species, $TOPOH^+ \ldots ClO_4^-$, and probably the hydrate, $TOPOH^+ \cdot OH_2 \ldots ClO_4^-$, with concentrated acid.

Footnotes and References

† Brief form of a paper (of same title) accepted by J. Phys. Chem.

* Present address: Chemistry Department, Brookhaven National Laboratory, Upton, Long Island, New York.

1. D. C. Whitney and R. M. Diamond, J. Phys. Chem. 67, 209 (1963).
2. D. C. Whitney and R. M. Diamond, J. Phys. Chem. 67, 2583 (1963).

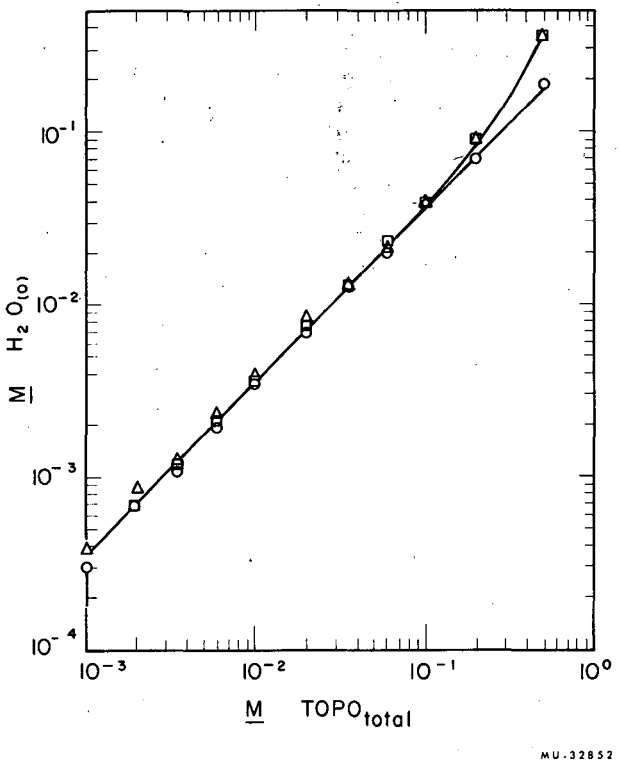

Fig. D.25-1. Variation of water content in organic phase (CCl_4 diluent) with TOPO concentration, corrected for solubility of H_2O in CCl_4: □, Karl Fischer;), 2.75-μ peak in infrared; △, 3.0-μ peak in infrared.

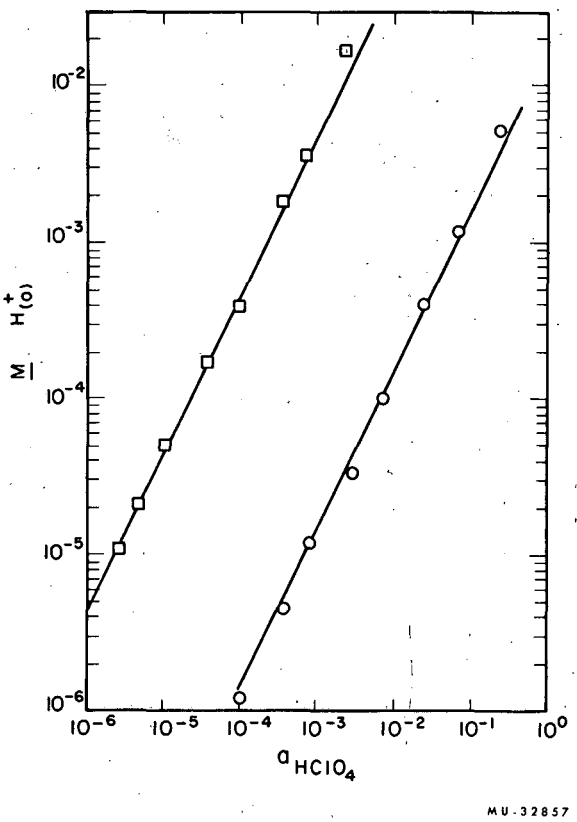

Fig. D.25-2. Variation of organic-phase acid content (measured by $HReO_4$ tracer, CCl_4 diluent) with aqueous $HClO_4$ activity for fixed TOPO concentrations of: □, 0.1 M; O, 0.01 M. Both lines drawn with slopes of 1.0.

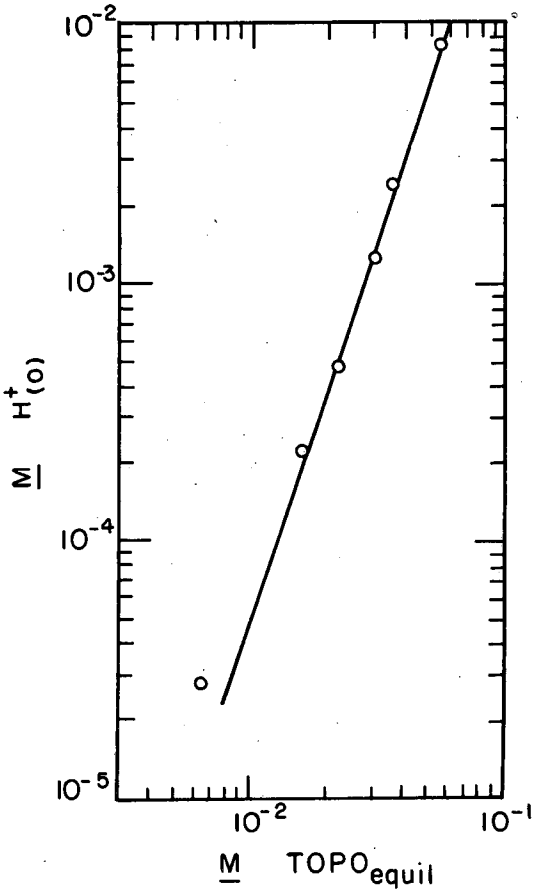

Fig. D.25-3. Variation of organic-phase acid content (measured by $HReO_4$ tracer, CCl_4 diluent) with equilibrium TOPO concentrations for aqueous $HClO_4$ activity of 2.8×10^{-3}. Line drawn with slope of 3.0.

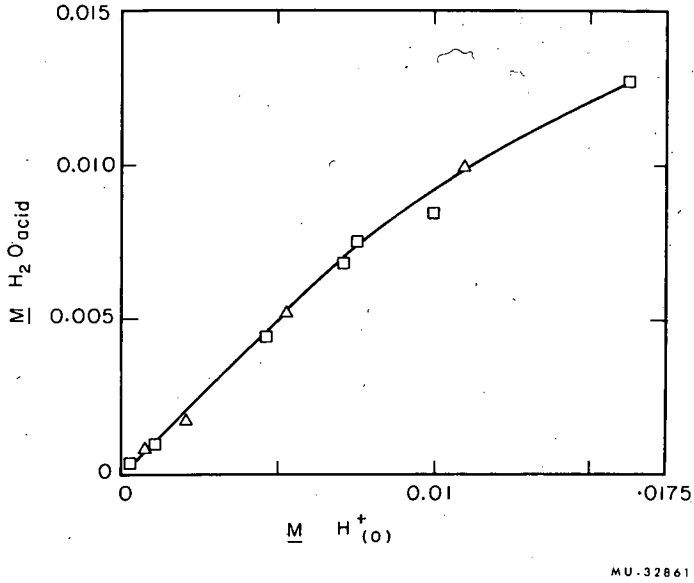

Fig. D.25-4. Variation of organic-phase water content (CCl_4 diluent; M H_2O_{acid} does not include H_2O dissolved in CCl_4 nor complexed in TOPO·H_2O) with organic phase $HClO_4$ acid content: □, 0.1 M TOPO; △, 0.05 M TOPO.

26. MOLECULAR BEAM ELECTRIC RESONANCE EXPERIMENTS ON LiF, LiCl, LiBr, LiI, AND NaF

Alvin J. Hebert, Troy L. Story, Jr., Francis W. Breivogel, Jr., Craig D. Hollowell, and Kenneth Street, Jr.

The molecular beam electric resonance method has been used to investigate the molecular properties of several dipolar diatomic molecules, as described below. Values are reported for rotational constants, B_v, dipole moments, μ_v, quadrupole coupling constants, $(eq\Omega)_v$, and spin-rotation and spin-spin interaction constants, c, of molecules in different vibrational states, v, and in low rotational states.

The apparatus and methods used in these investigations, discussed in detail elsewhere,[1] may be briefly described as follows:

The apparatus, shown schematically in Fig. D.26-1, consists of a consecutive arrangement of four connecting high-vacuum chambers. The source chamber houses a 6-in. -long 3/8-in. -diameter tube of 0.015-in. wall thickness into which a 0.25×0.004-in. slit has been cut to define the beam. The beam is produced by placing the desired salt in the tube and passing a few hundred amperes of ac current through it, thus heating the salt until vapor effuses through the slit at an adequate rate.

The effusing vapor passes out of the source chamber through a small opening into a buffer or separating chamber and then on through another small opening into the main chamber. The main chamber houses a beam collimator and hot-wire beam ionizer and accelerator as well as two 12-in. -long inhomogeneous electric deflecting fields of the dipole–two wire analog type for quantum state selection. The deflecting fields and collimator system allow only molecules in the desired rotational and magnetic quantum states to reach the hot-wire ionizer-accelerator.

The main chamber also houses a homogeneous electric field region into which one may introduce radio-frequency or microwave signals to induce the desired magnetic-quantum-number or rotational-quantum-number transitions respectively. The electric field in this 10-in. -long region is homogeneous to better than 2 parts in 10^5.

The ionized positive ions are accelerated out of the main chamber, through a 5-cm-radius 60-deg mass-analyzing magnet, and into the electron multiplier chamber, where a 14-stage electron multiplier amplifies the positive ion current by approximately 10^6. The electron multiplier output can be fed either into an electrometer with recorder output or into a pulse amplifier and counter with provision for digital recording and graphing.

Lithium Fluoride

Radio-frequency spectra observed for the lowest vibrational states of $^6Li^{19}F$ and $^7Li^{19}F$ are consistent with the following values (all hyperfine constants are given in kc/sec):[2]

$^6Li^{19}F$: $\mu_v = 6.28397 \pm 0.08630\,(v + 1/2) + 0.000535\,(v + 1/2)^2 \pm 0.001$ Debye

	v = 0	v = 1	v = 2
eqQ	8.5 ± 0.8	8.6 ± 1.2	7.1 ± 2.0
c_{Li}	0.71 ± 0.08	0.71 ± 0.12	0.73 ± 0.20
c_F	36.75 ± 0.4	36.08 ± 0.5	35.66 ± 0.7
c_3	4.307 ± 0.08	4.224 ± 0.12	4.140 ± 0.20
c_4	0.00 ± 0.15	0.00 ± 0.20	0.00 ± 0.40

$^7Li^{19}F$: $\mu_v = 6.28383 \pm 0.08153\,(v + 1/2) + 0.000445\,(v + 1/2)^2 \pm 0.001$ Debye

	v = 0	v = 1	v = 2
eqQ	415.6 ± 0.4	406.1 ± 0.6	396.5 ± 0.8
c_{Li}	1.87 ± 0.04	1.84 ± 0.04	1.79 ± 0.04
c_F	32.68 ± 0.16	32.20 ± 0.22	31.84 ± 0.24
c_3	11.382 ± 0.020	11.173 ± 0.030	10.964 ± 0.030
c_4	0.00 ± 0.08	0.00 ± 0.11	0.00 ± 0.14

Lithium Chloride

Observations of the radio-frequency spectra of $^6Li^{35}Cl$ and $^6Li^{37}Cl$ have resulted in the following molecular constants (all hyperfine constants are given in kc/sec):[3]

$^6Li^{35}Cl$: $\mu_v = 7.08532 + 0.08683\,(v + 1/2) + 0.00056\,(v + 1/2)^2 \pm 0.001$ Debye

$(eqQ)_{Cl}$	-3072.12 ± 1.1	-3478.69 ± 1.2	-3872.86 ± 2.1
c_{Cl}	2.34 ± 0.19	2.26 ± 0.20	2.26 ± 0.36

$^6Li^{37}Cl$: $\mu_v = 7.08533 \pm 0.08635\ (v + 1/2) + 0.00064\ (v + 1/2)^2 \pm 0.001$ Debye

	v = 0	v = 1	v = 2
$(eqQ)_{Cl}$	-2420.81 ± 1.4	-2739.56 ± 1.5	-3051.90 ± 2.7
c_{Cl}	1.75 ± 0.23	1.82 ± 0.25	1.77 ± 0.45

The observation of J = 1 → J = 0 microwave transitions yielded the following rotational constants (Mc/sec):

$^6Li^{35}Cl$	$^6Li^{37}Cl$
$B_0 = 23971.088 \pm 0.006$	$B_0 = 23781.615 \pm 0.009$
$B_1 = 23682.420 \pm 0.007$	
$B_2 = 23396.844 \pm 0.012$	

Lithium Bromide

The observation of radio-frequency spectra for three or more vibrational states of ^6LiBr led to the following values:[4,5]

$^6Li^{79}Br$: $\mu_v = 7.22624 \pm 0.08318\ (v + 1/2) + 0.00057\ (v + 1/2)^2 \pm 0.001$ Debye

$(eqQ)_v = 37.015 + 2.918\ (v + 1/2) - 0.039\ (v + 1/2)^2 \pm 0.005$ Mc/sec

$c_{Br} = 9.2 \pm 0.2$ kc/sec

$^6Li^{81}Br$: $\mu_v = 7.22611 + 0.08312\ (v + 1/2) + 0.00060\ (v + 1/2)^2 \pm 0.001$ Debye

$(eqQ)_v = 30.912 + 2.442\ (v + 1/2) - 0.034\ (v + 1/2)^2 \pm 0.005$ Mc/sec

$c_{Br} = 9.9 \pm 0.2$ kc/sec

The observation of J = 1 → J = 0 microwave transitions yielded the following rotational constants (Mc/sec):

$^6Li^{79}Br$	$^6Li^{81}Br$
$B_0 = 19090.296 \pm 0.006$	$B_0 = 19057.005 \pm 0.006$
$B_1 = 18882.820 \pm 0.009$	$B_1 = 18850.050 \pm 0.020$
$B_2 = 18677.242 \pm 0.055$	$B_2 = 188645.035 \pm 0.217$

The radio-frequency spectra of $^7Li^{79}Br$ yielded the following constants for the ground (v = 0) vibrational state:

$\mu = 7.2648 \pm 0.001$ Debye

$(eqQ)_{Li} = 210 \pm 3$ kc/sec

$(eqQ)_{Br} = 38.365 \pm 0.003$ Mc/sec

$c_{Li} = 0.5 \pm 0.3$ kc/sec

$c_{Br} = 7.8 \pm 0.3$ kc/sec

Lithium Iodide

Radio-frequency spectra obtained for the first two vibrational states of $^6Li^{127}I$ resulte in the following molecular constants:[5,6]

	v = 0	v = 1
μ (D)	7.4285 ± 0.001	7.5120 ± 0.001
eqQ_I (Mc/sec)	-198.780 ± 0.005	-207.453 ± 0.010
c_I (kc/sec)	7.7 ± 0.4	7.8 ± 0.6

The observation of J = 1 → J = 0 microwave transitions yielded the following rotational constants:

$$B_0 = 15,304.895 \pm 0.005 \text{ Mc/sec}$$
$$B_1 = 15,153.316 \pm 0.009 \text{ Mc/sec}$$

Sodium Fluoride

The molecular constants determined for $^{23}Na^{19}F$ from the radio-frequency spectra are (all hyperfine constants are given in kc/sec):[7]

$$\mu_v = 8.12349 + 0.06436\,(v + 1/2) + 0.00037\,(v + 1/2)^2 \pm 0.001 \text{ Debye}$$
$$(eqQ)_0 = -8440.1 \pm 1.5$$
$$(eqQ)_1 = -8327.9 \pm 1.5$$
$$(eqQ)_2 = -8220.5 \pm 2.0$$
$$c_{Na} = 1.4 \pm 0.5$$
$$c_F = 2.0 \pm 0.3$$
$$c_3 = 3.85 \pm 0.25$$
$$c_4 = 0.0 \left\langle {}^{+0.4}_{-0.1} \right.$$

The observation of J = 1 → J = 0 microwave transitions gave the following rotational constants (Mc/sec):

$$B_0 = 13029.811 \pm 0.002$$
$$B_1 = 12894.543 \pm 0.003$$
$$B_2 = 12760.674 \pm 0.004$$

References

1. A. J. Hebert, A Molecular Beam Electric Resonance Spectrometer and the Radio-Frequency Spectra of Lithium Fluoride (Ph. D. Thesis), UCRL-10482, Sept. 1962.
2. A. J. Hebert, C. D. Hollowell, and K. Street, Jr., The Radio-Frequency Spectra of LiF by the Molecular Beam Electric Resonance Method (UCRL-11026, Sept. 1963), to be submitted for publication.
3. T. L. Story, A. J. Hebert, and K. Street, Jr., Radio-Frequency and Microwave Spectra of LiCl by the Molecular Beam Electric Resonance Method (UCRL-11805, Nov. 1964), to be submitted for publication.
4. A. J. Hebert, F. W. Breivogel, Jr., and K. Street, Jr., J. Chem. Phys. 41, 2368 (1964).
5. F. W. Breivogel, Jr., The Radio-Frequency and Microwave Spectra of LiBr and LiI (Ph. D. Thesis), UCRL-11665, Sept. 1964.
6. F. W. Breivogel, Jr., A. J. Hebert, and K. Street, Jr., The Radio-Frequency and Microwave Spectra of $^6Li^{127}I$ by the Molecular Beam Electric Resonance Method, J. Chem. Phys. 41, 2368 (1964).
7. C. D. Hollowell, A. J. Hebert, and K. Street, Jr., The Radio-Frequency and Microwave Spectra of NaF by the Molecular Beam Electric Resonance Method, J. Chem. Phys. 41, 3540 (1964).

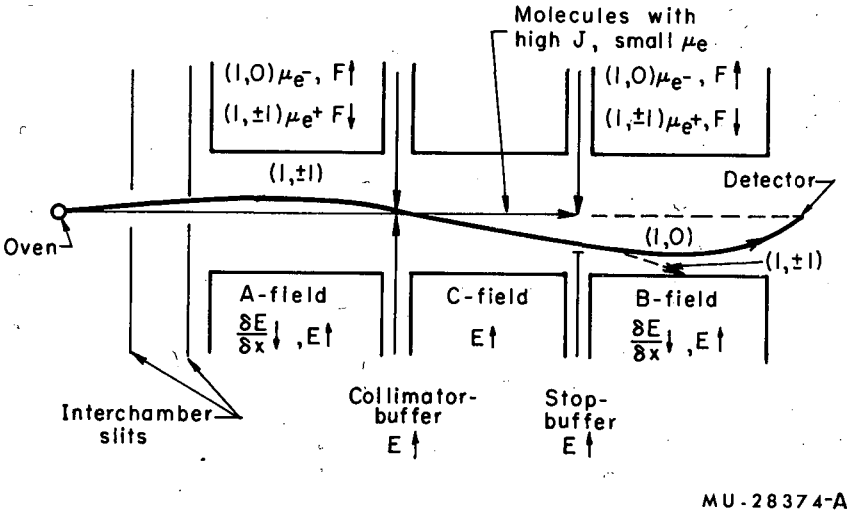

Fig. D. 26-1. Apparatus. Dipolar molecules passing through the inhomogeneous A and B fields experience a force $F = \mu_e \delta E/\delta x$, where μ_e is the effective electric moment and $\delta E/\delta x$ is the electric field gradient.

27. NONDESTRUCTIVE ACTIVATION ANALYSIS WITH LITHIUM-DRIFTED GERMANIUM DETECTORS

S. G. Prussin, J. A. Harris, and J. M. Hollander

The recent development of high-resolution lithium-drifted germanium γ-ray detectors suggests the application of these devices for nondestructive trace analysis by activation. Because of the poor resolution of the commonly used sodium iodide scintillation detectors, nondestructive activation analysis has not been widely applicable, and many analyses have required considerable time in postirradiation chemical separations to reveal the presence of even the prominent photopeaks from certain elements. The far superior energy resolution obtainable with the new germanium detectors may in many cases eliminate the need for chemical separations, since γ rays differing in energy by less than 5 keV can be distinguished. The very favorable signal-to-noise ratio characteristics of these detectors may be expected to provide an increased sensitivity for trace constituents.

In order to assess the potential of these detectors for nondestructive analysis, we have determined the concentrations of several trace constituents in some high-purity aluminum samples by neutron activation analysis.

The lithium-drifted germanium detector used for analysis has dimensions 6 $cm^2 \times 9$ mm (depletion layer), and is operated at approximately 77°K with a bias voltage of 720 volts. The line width obtained for the 122-keV γ ray of Co^{57} was approximately 4 keV (FWHM). The photoelectric efficiency of this detector relative to a 3×3-in. (diam.) NaI(Tl) crystal for the 279-keV γ ray of Hg^{203} at a distance of 2.5 cm from the face of the detectors is approximately 1.3×10^{-2}.

Samples of approximately 400 mg of 99.9% and 99.999% pure aluminum were irradiated for 2-hour periods at a thermal neutron flux of about 5×10^{12} n $cm^{-2}sec^{-1}$ in the Livermore LPTR reactor. The cadmium ratio at the irradiation position was R_{Cd} = 12 to 13, and the fast flux above 3.5 MeV was approximately 7×10^{10} n $cm^{-2}sec^{-1}$. The samples were available for spectral studies within 2 hours after the end of irradiation.

The γ-ray spectra of the 99.9% pure aluminum clearly showed the presence of Na^{24}, Cu^{64}, Mn^{56}, and Ga^{72}. Gamma spectra of the sample taken with the germanium detector and a 3×3-in. (diam) NaI(Tl) crystal are shown in Fig. D. 27-1. The high resolution of the germanium detector made the qualitative determination of Ga^{72} possible without the necessity of decay-curve analysis of the composite photopeak at about 840 keV. The quantitative analysis of Na, Cu, Mn, and Ga was performed by comparison with standards irradiated together with the aluminum samples. The results of the nondestructive analysis of the two aluminum samples are given in Table D. 27-I.

The values given for Na^{24} have not been corrected for contribution from the secondary reaction $Al^{27}(n,\alpha)\ Na^{24}$, the latter accounting for more than 90% of the sodium activity produced in the sample of 99.999% pure aluminum. The sensitivities for analysis of Na, Cu, Mn, and Ga in the purer aluminum is limited by the production of Na^{24} by the (n, α) reaction on aluminum. However, it appears possible to determine with ease levels of these impurities down to about one-quarter the concentrations in the higher-purity aluminum.

This method is presently being extended to the analysis of other elements.

Table D. 27-I. Results of nondestructive neutron-activation analysis of two aluminum samples.

Impurity	Concentration (in ppm)	
	99.9% Al	99.999% Al
Na	209	105
Cu	950	22
Mn	3.7	0.98
Ga	195	> 20

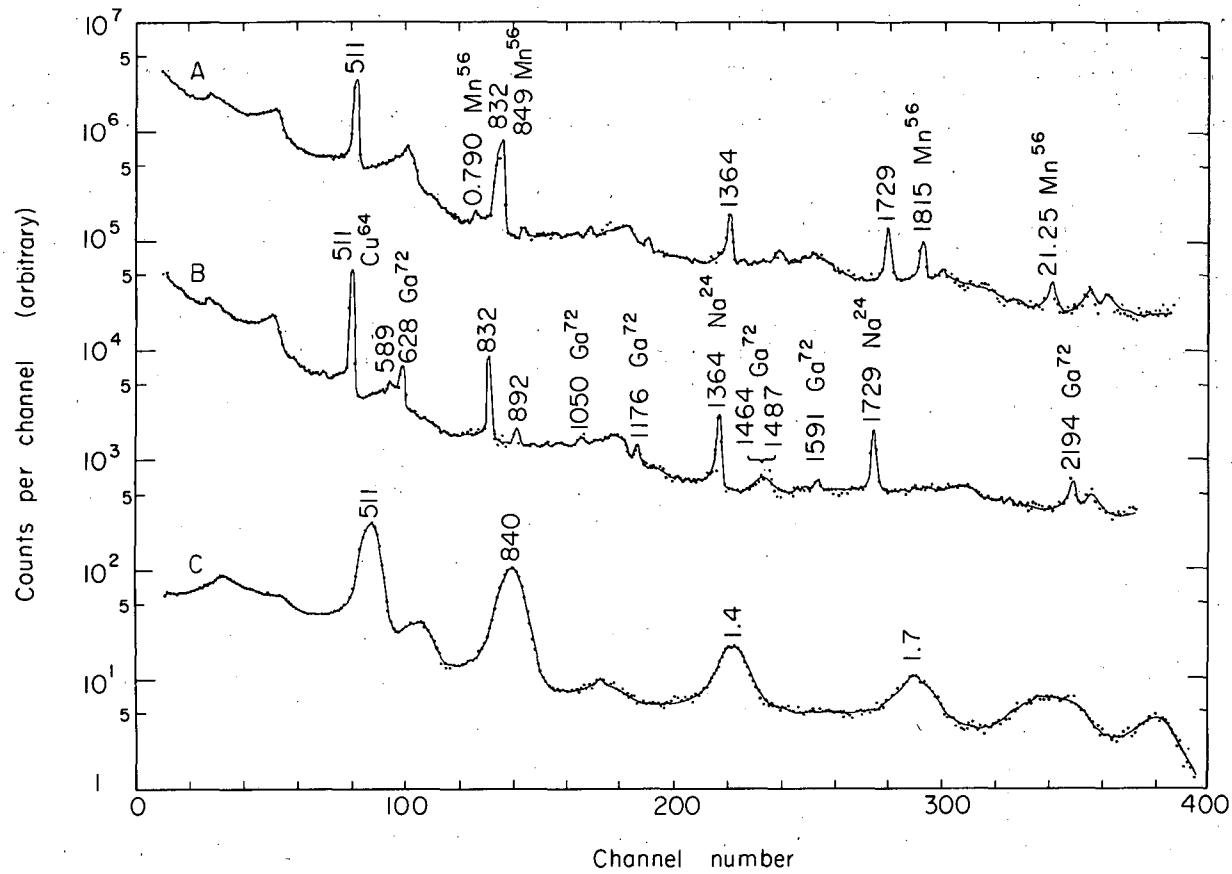

Fig. D. 27-1. Gamma-ray spectra of the irradiated 99.9% pure aluminum. Spectra A and B were obtained with a Ge(Li) detector. Spectrum C was obtained with a 3×3-in. (diam) NaI(Tl) crystal. The spectra were recorded at the following times after the end of a 2-hr irradiation: A = 5.2 hr, B = 54.7 hr, C = 5.7 hr. MUB-5034

28. THE CERIUM MAGNESIUM NITRATE TEMPERATURE SCALE

R. B. Frankel, N. J. Stone, and D. A. Shirley

Cerium magnesium nitrate (CMN) is of great importance in low temperature research. It may be adiabatically demagnetized to about 0.003° K, [1] and because its susceptibility follows Curie's law down to 0.005° K, it serves as a useful thermometer. Below 0.005° K, deviations from Curie's law occur and the temperature T^* obtained by measuring the susceptibility $T^* = C/\chi$, where C is the Curie constant, must be related to the absolute temperature by methods based on the second law of thermodynamics. This has been done by Daniels and Robinson[1] for CMN. Because the shape of the sample can determine the demagnetizing field, it is convenient to introduce $T^{\circledast}$, the magnetic temperature for a spherical sample. The $(1/T^{\circledast}$ vs $1/T)$ correlation according to Daniels and Robinson is shown in Fig. D. 28-1. Also shown is the $(1/T^{\circledast} - 1/T)$ correlation obtained by de Klerk, [2] based on a reinterpretation of Daniels and Robinson's data.

We have aligned 34-hr Ce^{137m} in CMN and measured the anisotropy of the 255-keV γ ray as a function of $1/T^*$. The transition sequence is $11/2 - \xrightarrow[255\ keV]{M4} 3/2+$ and is well known. [3,4] In addition, the Hamiltonian for alignment of Ce^{137m} in CMN is known from the

work of Kedzie et al.[5] to be $H = B(S_xI_x + S_yI_y)$. The data are shown in Fig. D. 28-2, in three separate experiments using different samples, corrected to 1/T using the $(1/T^{*})$ vs 1/T) correlation of Daniels and Robinson. The solid curve is theoretical and was calculated by using the value of B that best fitted the data in the range $0 \leq 1/T \leq 200$. The data show very anomalous behavior at $1/T \leq 250$. This is evidence for a breakdown of Daniels and Robinson's $(1/T^{*} - 1/T)$ correlation at the lowest temperatures.

Based on our data and the theoretical curve, a new $(1/T^{*}$ vs 1/T) correlation was made. This is given in Table D. 28-I and is shown in Fig. D. 28-1 as curve D. We suggest that the lowest temperature is 0.002° K. Figure D. 28-3 shows the anisotropy data replotted with the new temperature scale.

This result is of importance in nuclear alignment experiments and in experiments in which CMN is the coolant and thermometer in the T = 0.003° K range. For example, experiments have recently been reported in which searches were made for a superfluid transition in He^3.[6,7] These experiments will require a reinterpretation on the basis of the new temperature scale for CMN.

References

1. J. M. Daniels and F. N. H. Robinson, Phil. Mag. 44, 630 (1953).
2. D. de Klerk, in Handbuch der Physik Vol. 15 (Springer-Verlag, Berlin, 1956), p. 38.
3. J. N. Haag, D. A. Shirley, and D. H. Templeton, Phys. Rev. 121, 591 (1961).
4. R. B. Frankel, D. A. Shirley, and N. J. Stone, Phys. Rev. 136, B577 (1964).
5. R. W. Kedzie, B. Abraham, and C. D. Jefferies, Phys. Rev. 108, 54 (1957).
6. A. C. Anderson, G. L. Salinger, W. A. Steyert, and J. C. Wheatley, Phys. Rev. Letters 6, 331 (1961).
7. V. P. Peshkov, Soviet Phys. JETP 19, 1023 (1964).

Table D. 28-I. $(1/T^{*} - 1/T)$ correlation according to Daniels and Robinson (DR) and Frankel, Shirley, and Stone (FSS).

$(\frac{H}{T})_{initial}[kG(O_K)^{-1}]$	$\frac{1}{T}^{*}$	$(\frac{1}{T})_{DR}$	$(\frac{1}{T})_{FSS}$
1.0	20	20	20
1.9	40	40	40
2.9	60	60	60
3.8	80	80	80
4.6	100	100	100
5.4	120	120	120
6.2	140	140	140
6.9	160	160	160
7.8	180	182	181
8.75	200	223	210
9.2	210	231	221
9.7	220	249	232
10.2	230	266	249
10.8	240	284	266
11.4	250	300	287
12.1	260	312.5	305
12.8	270	319	322
13.5	280	322.5	358
14.2	290	324	383
15.5	300	324	430
18.0	310	324	500
18.8	312	324	520

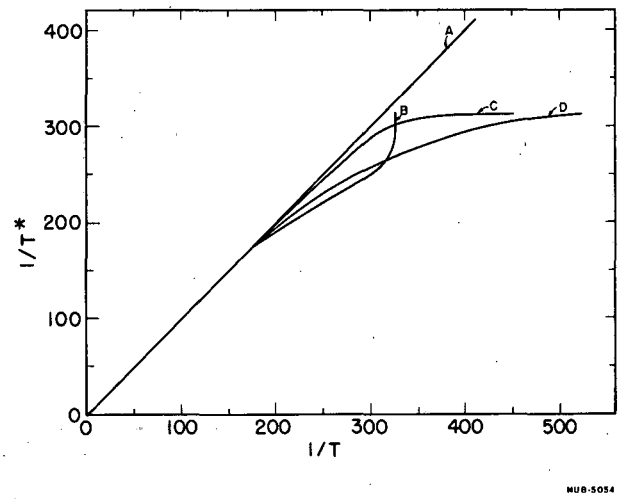

Fig. D. 28-1. $(1/T^{*}$ vs 1/T) correlations:
Curve A: $1/T^{*} = 1/T$
Curve B: Daniels and Robinson
Curve C: de Klerk
Curve D: Frankel, Stone, and Shirley.

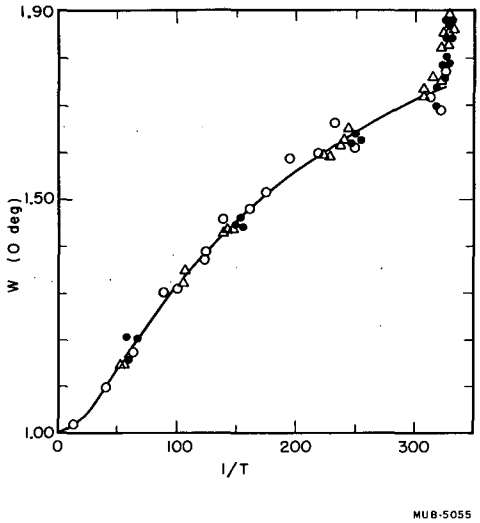

Fig. D. 28-2. Anisotropy of the 255-keV γ ray from Ce^{137m} in CMN at 0 deg to the crystal "C" axis plotted as a function of 1/T by use of Daniels and Robinson's $(1/T^{*} - 1/T)$ correlation. The solid curve is theoretical.
O, 4/15/64 data; △, 9/11/64;
●, 11/17/64.

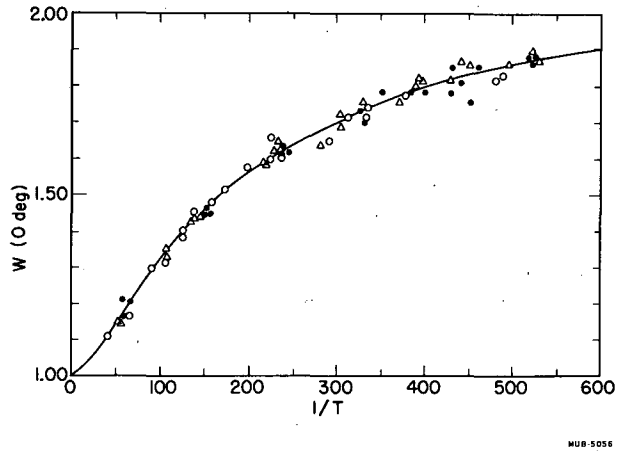

Fig. D. 28-3. Anisotropy of the 255-keV γ ray from Ce^{137m} in CMN at 0 deg to the crystal "C" axis plotted as a function of 1/T by use of the empirical $(1/T^{*} - 1/T)$ correlation.
O, 4/15/64 data; △, 9/11/64;
●, 11/17/64.

29. APPEARANCE POTENTIALS OF SOME DOUBLY CHARGED MOLECULE IONS†

Amos S. Newton and Aldo F. Sciamanna

Surprisingly little attention has been given to the occurrence and characteristic properties of doubly charged ions in the mass spectra of molecular species.[1] Many of them fragment into two singly charged ions, but the total initial contribution of doubly charged ions to mass spectra of molecules taken with 70-eV electrons may be 10% or more of the total ions.[2]

Morrison and co-workers have studied the appearance potentials of a number of stable doubly charged molecule ions of organic materials as well as the rare gases.[3-5] They have shown the threshold law for formation of a multiply charged ion is an n th-power increase in the ion current with electron energy over the appearance potential,[3] where n is the multiplicity of charge on the ion. Literature values of multiply charged ions are, in general, poor, owing to use of the incorrect threshold law.[6]

Appearance potentials of doubly charged molecule ions were taken with a Consolidated Electrodynamics Corporation Model 21-103A mass spectrometer. Helium, krypton, or argon was introduced simultaneously with the compound under investigation as an internal standard for the electron energy scale. The spectroscopic values of the ionization potentials for formation of He^{+} (24.580 eV), Kr^{++} (38.56 eV), and Ar^{++} (43.38 eV) were used. From separate runs on the pure compounds, with normal operating conditions, the fraction of the total mass spectrum represented by M^{++} ions was estimated. N_2^{++} and O_2^{++} were run with the mixed isotopically labeled species, $^{14}N^{15}N$ and $^{16}O^{17}O$ respectively. Benzene and cyanogen were run with the normal carbon isotope peak of each respective compound.

Typical ionization efficiency curves for O_2^{++} and $C_2N_2^{++}$ are shown in Figs. D. 29-1 and D. 29-2, showing the linear extrapolation obtained when the square root of the ion peak height is plotted against the electron energy.

In Table D. 29-I the appearance potentials of M^{++} found in this work are tabulated. Values in parenthesis are from Dorman and Morrison.[5] The ionization potential of the singly charged ion is also given as well as the ratio of these values. In the last column, the yield of the doubly charged molecule ion is given as percent of total ionization. Values of M^{+} are spectroscopic (s), photoionization values (p),[7] or from electron impact studies (e^-).[6]

From the data in Table D. 29-I, together with good data on the rare gases and a few other molecules from the literature[5] shown in Table D. 29-II, one immediately sees that for most of the compounds the ratios of the appearance potentials for the doubly and singly charged ions are close to 2.75. If one assumes the ratio to be 2.75 ± 0.05, more than half the compounds are covered. Some of the exceptions such as He (s electrons only involved), and NO and O_2 (these molecules have unpaired electrons) are expected. For some of them, such as NH_3, the lowest state of the doubly charged ion may be a repulsive state and for others the lowest state may be either forbidden for a Frank-Conden transition or possess such a low transition probability it is not seen. There is no obvious theoretical reason why the ratio of the appearance potentials of M^{++} and M^{+} should not be specific for each particular molecule, and the observation that the ratios cluster about 2.75 is strictly empirical. In any case, unless there are obvious factors involved, an estimation by use of the ratio 2.75 should give a figure for the appearance potential of M^{++} within about 1 eV.

The other obvious conclusion to be drawn from the data is that the yield (fraction of total ions observed) of the doubly charged ions when 70-eV electrons are used increases with the number of delocalized or nonbonding electrons in the molecule. Thus the yield of M^{++} increases in the order $CO_2 < COS < CS_2$.

Footnote and References

† Condensed version of a paper to be written for submission to J. Chem. Phys.

1. F. L. Mohler, E. G. Bloom, E. J. Wells, Jr., J. H. Lengel, and C. E. Wise, J. Res. Natl. Bur. Std. 42, 369 (1949).
2. J. Olmsted III, K. Street, Jr., and A. S. Newton, J. Chem. Phys. 40, 2114 (1964).
3. F. H. Dorman, J. D. Morrison, and A. J. C. Nicholson, J. Chem. Phys. 32, 378 (1960).
4. F. H. Dorman and J. D. Morrison, J. Chem. Phys. 34, 1407 (1961).
5. F. H. Dorman and J. D. Morrison, J. Chem. Phys. 35, 575 (1961).
6. F. H. Field and J. L. Franklin, Electron Impact Phenomena (Academic Press, Inc., New York, 1957).
7. K. Watanabe, J. Chem. Phys. 26, 542 (1957).

Table D. 29-I. Appearance potentials of some doubly charged molecule ions.

Compound	A. P. $_{(M^{++})}$ [a]	A. P. $_{(M^{+})}$ [b]	$\frac{\text{A. P.}_{(M^{++})}}{\text{A. P.}_{(M^{+})}}$	$\frac{M^{++}}{\Sigma \text{ Ions}} \times 100$
N_2	42.72 (43.5)	15.557 (s)	2.746	2.69%
NO	39.00 (39.8)	9.25 (p)	4.22	1.86
O_2	37.20	12.075 (p)	3.08	0.61
CO_2	38.00 (36.4)	13.79 (s)	2.76	1.24
COS	30.45	11.0 (e^-)	2.77	2.37
CS_2	27.45	10.08 (p)	2.72	3.94
HCN	36.51	13.8 (e^-)	2.65	0.73
C_2N_2	35.71	13.7 (e^-)	2.61	2.18
NH_3	33.96 (33.7)	10.18 (p)	3.35	0.08
C_4H_4O (Furan)	25.30	8.89 (p)	2.84	0.82
C_4H_4S (Thiophene)	24.48	8.862 (p)	2.76	1.00
C_4H_4NH (Pyrrole)	23.3 ± 0.5	8.20 (e^-)	2.84	1.70
C_6H_6 (Benzene)	25.49 (26.0)	9.245 (p)	2.76	1.30
C_6H_5N (Pyridine)	25.45	9.23 (p)	2.76	0.30
$C_6H_5NH_2$ (Aniline)	21.19	7.70 (p)	2.75	1.81

a. Estimated probable error, ± 0.2 eV.
b. (s) = spectroscopic value, (p) = photoionization value, (e^-) = electron impact value.

Table D. 29-II. Literature data on doubly charged molecule ions.

Molecule	A. P. $_{(M^{++})}$ [a]	A. P. $_{(M^{+})}$ [b]	$\frac{\text{A. P.}_{(M^{++})}}{\text{A. P.}_{(M^{+})}}$	$\frac{M^{++}}{\Sigma \text{ Ions}} \times 100$
He	79.983 (s)	24.580 (s)	3.213	< 0.01%
Ne	62.63 (s)	21.559 (s)	2.905	0.11
Ar	43.38 (s)	15.755 (s)	2.75_3	11.85
Kr	38.56 (s)	13.996 (s)	2.75_5	15.08
Xe	33.3 (e^-)	12.127 (s)	2.74	15.10
CO	(41.8)	14.01 (p)	2.97	0.61
HCl	(35.5)	12.85 (s)	2.76	---
DBr	(33.2)	12.09 (s)	2.75	---
HI	(30.0)	10.39 (s)	2.89	---
$C_6H_5CH_3$	(24.5)	8.82 (p)	2.78	---

a. Data from references 6 and 7. Values in brackets have a probable error of ± 0.5 eV.
b. (s) = spectroscopic value, (p) = photoionization value.

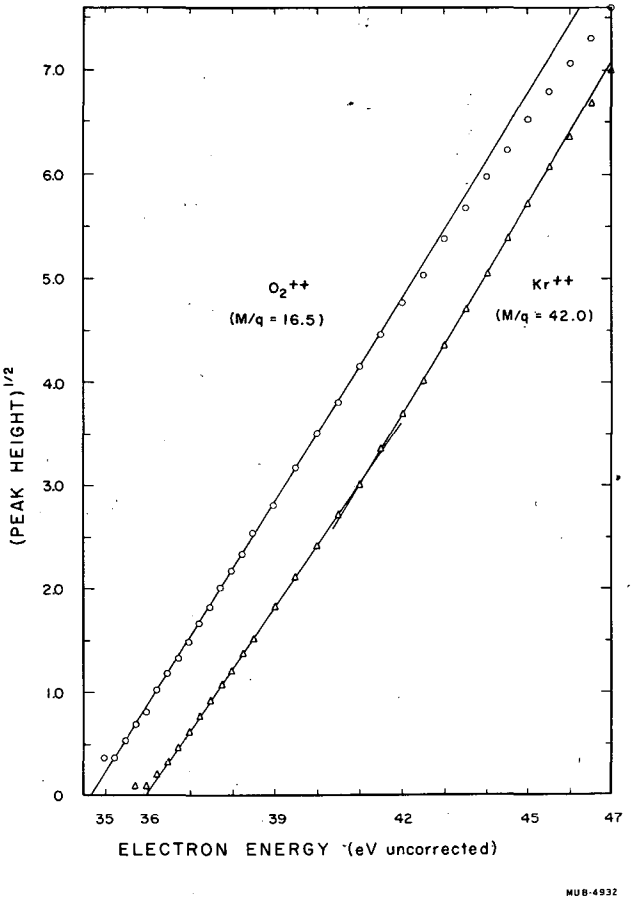

Fig. D. 29-1. Ionization efficiency curve for O_2^{++} with Kr^{++} as a comparison standard.

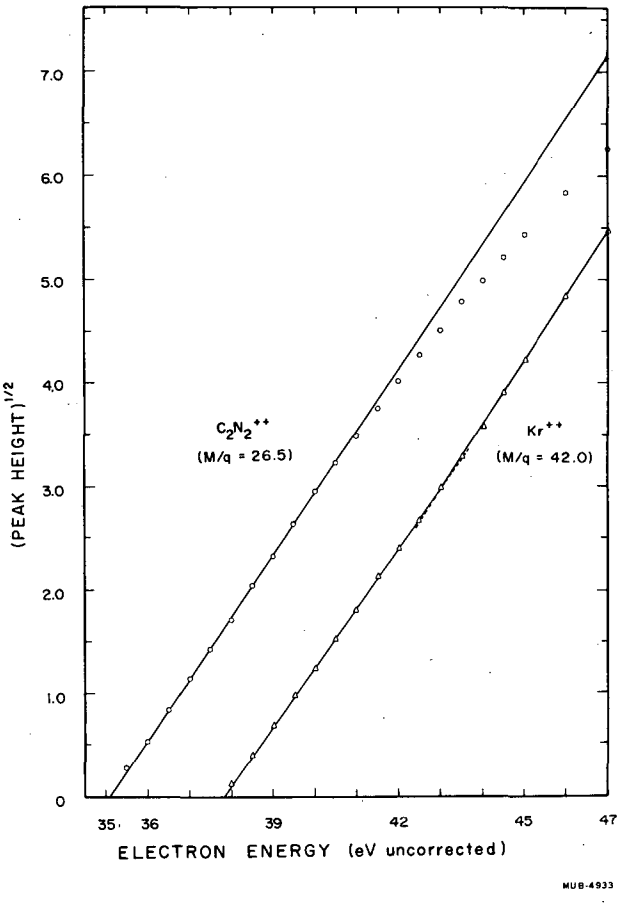

Fig. D. 29-2. Ionization efficiency curve for $C_2N_2^{++}$ with Kr^{++} as a comparison standard.

30. CONTROL OF RESPONSE SENSITIVITY IN GAS CHROMATOGRAPHY USING HOT-WIRE THERMAL CONDUCTIVITY DETECTORS

Amos S. Newton and Aldo F. Sciamanna

The use of gas chromatography in analytical work can be simplified by controlling the detector sensitivity over long periods of time or by being able to accurately select a given sensitivity. In principle then only a table of relative sensitivities for various materials need be available to provide a complete calibration. The procedure should provide control to better than 1% to be acceptable.

The variables, other than the specific properties of the carrier gas and the sample injected, which affect the sensitivity of response of a hot-wire thermal conductivity cell, are (a) the filament current, (b) the carrier gas flow rate, and (c) the ambient temperature of the cell.

These variables were investigated with the setup shown in Fig. D. 30-1. The power supply was a Power Designs Model 4005 which could be used in either a constant-voltage (0 to

50 V) or constant-current (0 to 500 mA) mode. R_1 was a by-pass resistor so that in the constant current mode, P_1 acted as a fine current control. In the constant voltage mode, P_2 acted as a fine control on the current. R_7 was a precision 0.5-ohm resistor and J_1 a jack for a 0- to 160-mV potentiometer for accurate measurement of the bridge current. The rest of the network is fairly standard.[1] The cell used was a Gow-Mac Cell Model 9193, with either four W or four W-2 filaments.

Considering the extensive use of cells of this type, little has been done on the effect of bridge current on sensitivity, and some misinformation is in print. Dal Nogare and Juvet state that sensitivity increases with the applied voltage and the current squared,[2] while Keulemans states that doubling the bridge current increases the sensitivity fivefold.[3] Recently Robinson and Rosie have reported that the response increases as the cube of the bridge current.[4]

Careful measurements at constant helium flow and constant detector temperature have shown that for the detector used, the sensitivity, S, increases as the 3.05 power of the current, I:

$$S = kI^{3.05} . \qquad (1)$$

As shown in Fig. D.30-2 for the Gow-Mac cell with either W or W-2 filaments, this relation holds to within 1% from a bridge current of 25 mA to a bridge current of 320 mA, covering a factor of 4000 in sensitivity. The constant k depends upon the specific filaments used.

Dal Nogare and Juvet state that the sensitivity is inversely proportional to the carrier gas flow rate.[2] We find this to be true, and at constant detector current and temperature, the relation is

$$S \times FR = C, \qquad (2)$$

in which S is the sensitivity of the detector, FR is the flow rate of the carrier gas, and C is a constant, the value of which depends on the units used for S and FR. As shown in Fig. D.30-3, Eq. (2) applies to within close to 1% for helium as the carrier gas and flow rates of 30 to 100 ml per minute. Equation (2) is also inherently assumed in the work of Dimbat, Porter, and Stross.[1]

Keulemans[3] states that the sensitivity of a thermal conductivity detector increases with decrease of temperature of the cell block (ambient temperature). This has been investigated and the sensitivity is found to increase slightly with increase of block temperature between 70 and 175°C. With the W-2 filaments the sensitivity increases linearly with temperature, increasing at a rate of 0.12%/degree at 100°C, as shown in Fig. D.30-4. Thus accurate temperature measurement of the cell block temperature is not a factor in determining the sensitivity, but close control of the temperature necessary for low noise levels of the detector bridge.

Sensitivity of a hot-wire thermal conductivity detector is largely determined by the bridge current and the flow rate of carrier gas. The exponent n is an empirically determined constant of the cell and is slightly larger than 3:

$$S = kI^n,$$
$$S = C/FR .$$

These can be combined to yield an overall equation

$$S = k'I^n/FR.$$

In order to control the sensitivity to within 1%, the flow rate must be measured to within 1% or less, and the current measured to within less than 0.3% (at 100 mA). In order that all the error not be in one factor, obviously each must be measured more accurately than this. As the cell current can readily be measured to within less than 0.1% with a potentionmeter, the measurement of accurate carrier gas flow rate becomes the limiting factor in controlling the sensitivity.

References

1. M. Dimbat, P. E. Porter, and F. H. Stross, Anal. Chem. 28, 290 (1956).
2. S. Dal Nogare and R. S. Juvet, Gas-Liquid Chromatography (Interscience Publishers, New York, 1962).
3. A. I. M. Keulemans, Gas Chromatography (Reinhold Publishing Corp., New York, 1957).
4. D. Robinson and D. M. Rosie, Response of Hot Wire Thermal Conductivity Cells, presented at Pittsburgh Conference on Analytical Chemistry and Applied Spectroscopy, Pittsburgh, March 2, 1964.

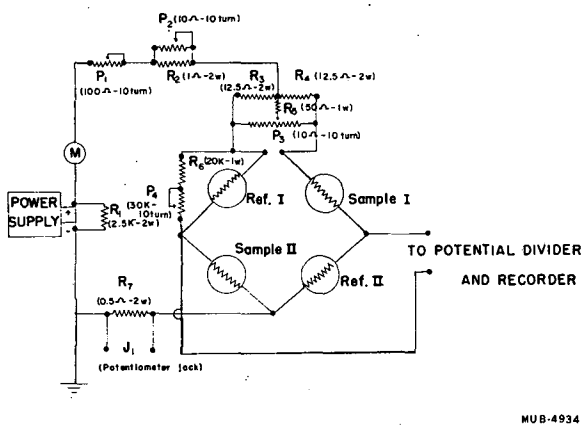

Fig. D.30-1. Schematic of bridge and power supply for gas chromatograph.

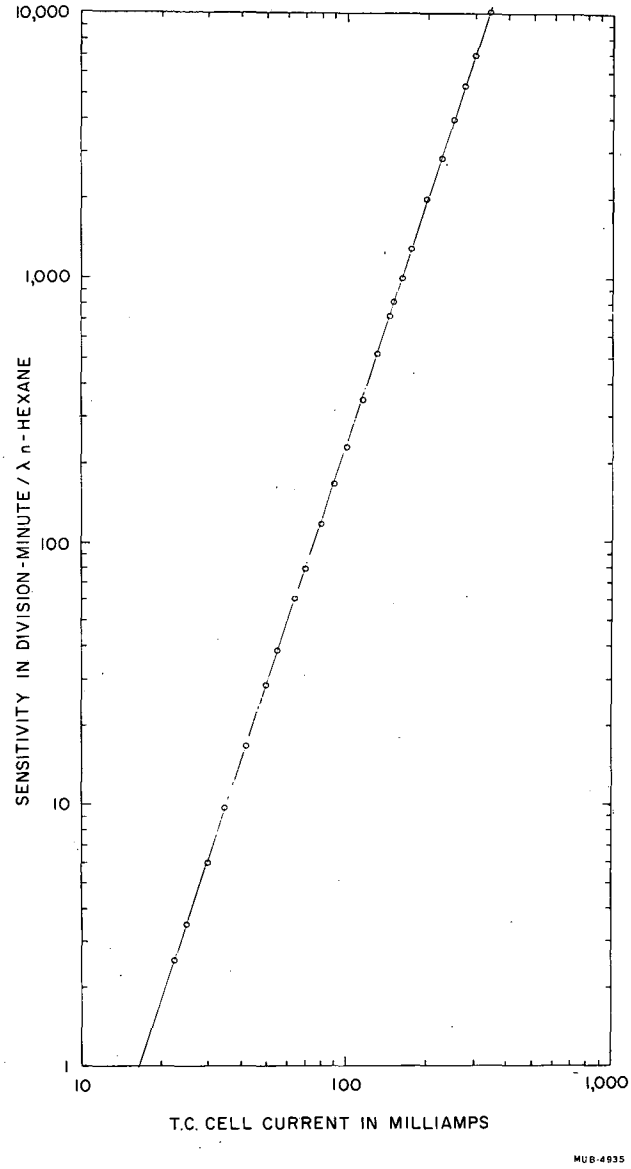

Fig. D.30-2. Variation of sensitivity of a hot-wire thermal conductivity (T.C.) cell with bridge current.

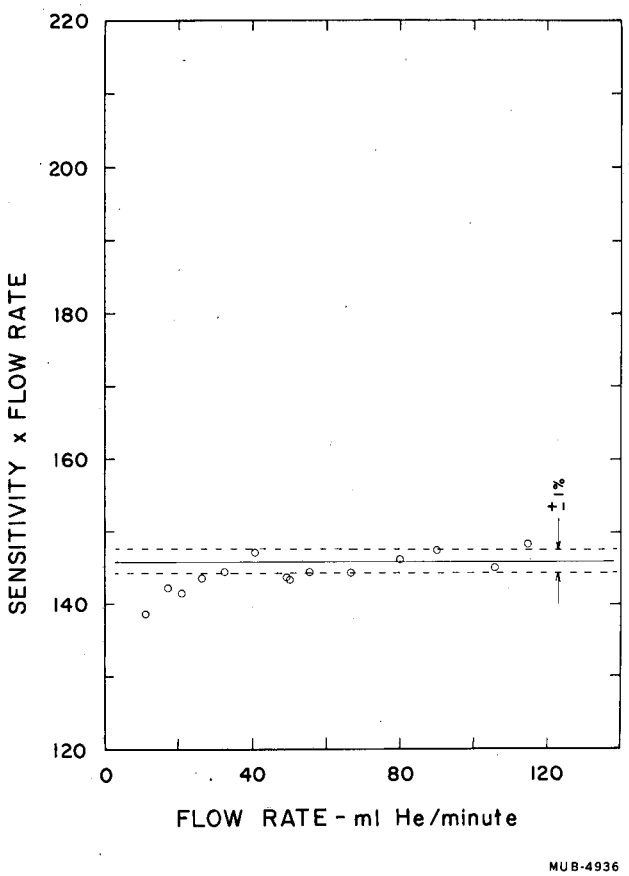

Fig. D.30-3. Variation of sensitivity of T.C. cell with flow rate of carrier gas.

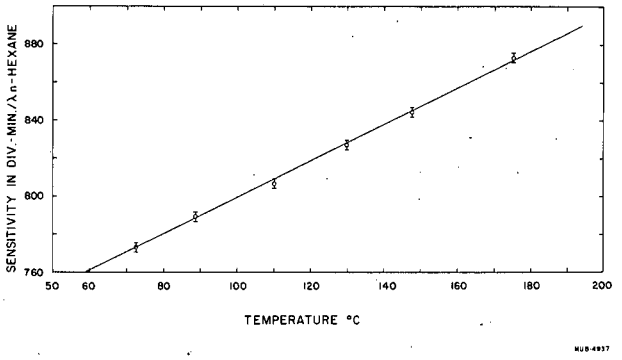

Fig. D.30-4. Effect of cell block temperature on sensitivity of a hot-wire thermal conductivity detector.

31. DETERMINATION OF THE EXCITATION FUNCTIONS FOR FORMATION OF METASTABLE STATES OF SOME RARE GASES AND DIATOMIC MOLECULES BY ELECTRON IMPACT†

John Olmsted III, Amos S. Newton, and K. Street, Jr.

A molecular beam apparatus for the study of excitation of metastable states of atoms and molecules by low-energy electron impact has been developed. The apparatus, shown schematically in Fig. D.31-1, generates a molecular beam, which traverses an electron beam perpendicular to its path and then impinges on a detector (a surface of low work function), which is the first stage of an electron multiplier. Metastable states of atoms or molecules, impinging on the detector surface, undergo Auger de-excitation with ejection of an electron. The metal surface used in the work described here was a silver-magnesium alloy with a work function of about 4.5 eV.

The electron gun was a retarding-potential-difference gun similar to that described by Fox, Hickam, Grove, and Kjeldaas.[1] In operation a 23-cps square wave of 0.055 V peak-to-peak amplitude was applied to the constant negative potential of the retarding grid. The anode current of this gun thus possessed a 23-cps component made up entirely of electrons within a small energy range (somewhat greater than 0.055 eV); this component could be measured by ac amplification of the voltage developed across a load resistor.

In the detector, the same 23-cps square-wave generator as supplied the retarding grid of the gun gated the signal to the counting network, so that separate counters registered the

signal in the negative and positive portions of the square wave. The difference between these two counts was thus the signal derived from those electrons of small energy spread at the voltage set on the gun.

The excitation function for formation of metastable neon atoms is shown in Fig. D. 31-2. It shows two distinct resonance maxima, the first coincident with the $2p^5 3s$ states and the second with the $2p^5 3p$ states. The curve is in agreement with that of Dorrestein[2] except our threshold breaks and resonance peaks are more sharply defined owing to better energy resolution.

It is necessary to explain the shape of this curve, since between the first metastable state ($2p^5 3s$ at 16.62 eV) and the onset of the lowest $2p^5 3p$ state at 18.38 eV the possible modes of excitation are extremely limited and the rise in this region is not explicable on the assumption of pure L-S coupling. However, it is known that there is a considerable mixing of the $^1p_1$ and $^3p_1$ states, since the $^3p_1 - {}^1s_0$ transition has a lifetime of the same order of magnitude as the $^1p_1 - {}^1s_0$ transition.[3,4] Accordingly in Fig. D. 31-3 a diagram of the neon levels in the region of interest is shown, with levels designated both in the L-S coupling system and the J_c-j system (electronic core coupled with the excited electron). The selection rule $\Delta J = 0, \pm 1, 0 \not\rightarrow 0$, together with the Laporte selection rule for dipole radiation, $\Delta(\Sigma l_i) = \pm 1$, assures the metastability of the $^3P_0$ and $^3P_2$ states.

In the region from 16.72 to 18.38 eV, there are no states that can be populating these 3p states by cascade processes, so the rise in cross section observed between 17.5 and 18.4 eV must be due to direct excitation to the $^3P_0$ and $^3P_2$ states. It is suggested that these states form two maxima, at 17.05 eV and somewhat higher than 18.38 eV, the threshold of the second resonance peak. The second maximum can be explained if (a) the observed curve is the sum of two curves, one peaking at higher energy, or (b) the individual peaks both possess twin peak character owing to different mechanisms of exciting each.

Calculations by Penney for excitation of analogous excited states in mercury show the maximum of the $^3P_2$ state of mercury to be displaced about 1.5 eV above that of the $^3P_0$ state, with neither showing a twin peaked character.[5] The sum is not twin peaked owing to both the low relative cross section and the broad character of the excitation function to the $^3P_0$ state. In neon the cross section and width could, however, be such that the sum exhibits a twin peaked character.

Evidence for double peak character in the excitation of spectral lines by slow electrons exists.[6,7] In these cases, the twin peaked character observed is explained by the initial peak's being excited by electron exchange and the second broad maximum by a direct interaction. To use this explanation for our results on neon requires that there be an intermediate character to the coupling. Such intermediate character is known from other considerations to exist in neon.[3,4]

Excitation curves for argon and krypton were also run, and these show behavior similar to neon, though the resonance peaks are less distinct in the background of total excitation to metastable peaks. An analysis is more difficult than for neon owing to the closer spacing of higher states that can cascade to the lower metastable states.

The molecules H_2, N_2, and CO were excited by electron impact to metastable states, as shown in Figs. D. 31-4 through D. 31-6. For H_2 the threshold at about 11.7 V corresponds to excitation to the metastable $C^3\pi_u$ state. The curve remains high after the initial resonance excitation because successive vibrational levels of this state can be excited in the energy region between this state and higher states which can cascade to this state. Lichten observed similar behavior for H_2 excitation by slow electrons.[8]

In N_2 a metastable state at about 11.8 eV was observed which was assigned to the yet undesignated E triplet state of nitrogen. In CO the $a^3\pi$ state at 6.0 eV was not observed, owing to its short lifetime of 10 μsec. A state at about 10.5 eV was excited, and is probably the $b^3\Sigma^+$ state, but the curve does not have the shape expected for a resonance excitation. The assignment of this excitation to the $b^3\Sigma^+$ state is provisional at this time.

Footnote and References

† Condensed from paper to be published in J. Chem. Phys.

1. R. E. Fox, W. M. Hickam, D. J. Grove, and T. Kjeldaas, Jr., Rev. Sci. Instr. 26, 1101 (1955).
2. R. Dorrestein, Physica 9, 447 (1942).
3. G. H. Shortley, Phys. Rev. 47, 295 (1935).
4. A. Gold and R. S. Knox, Phys. Rev. 113, 834 (1949).
5. W. G. Penney, Phys. Rev. 39, 467 (1936).
6. H. Maier-Liebnitz, Z. Physik 95, 499 (1936).
7. O. Thieme, Z. Physik 78, 412 (1933).
8. W. Lichten, J. Chem. Phys. 26, 306 (1957).

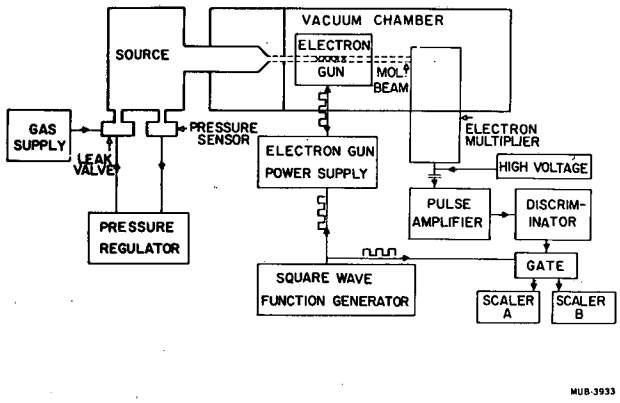

Fig. D.31-1. Block diagram of molecular beam apparatus for triplet state excitation studies.

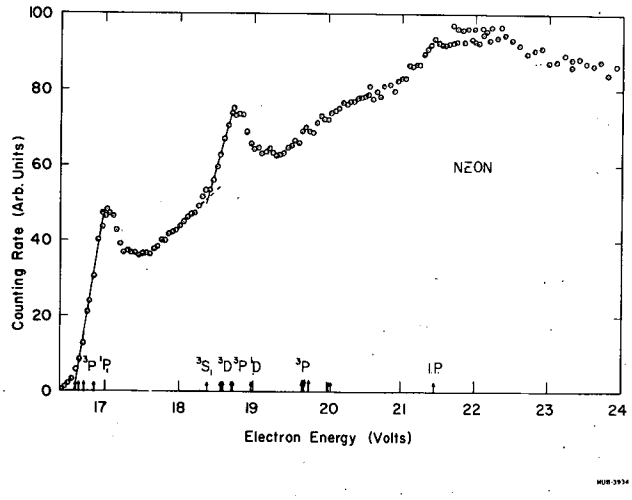

Fig. D.31-2. Excitation function for metastable states of neon. Energies of the first several excited levels are indicated.

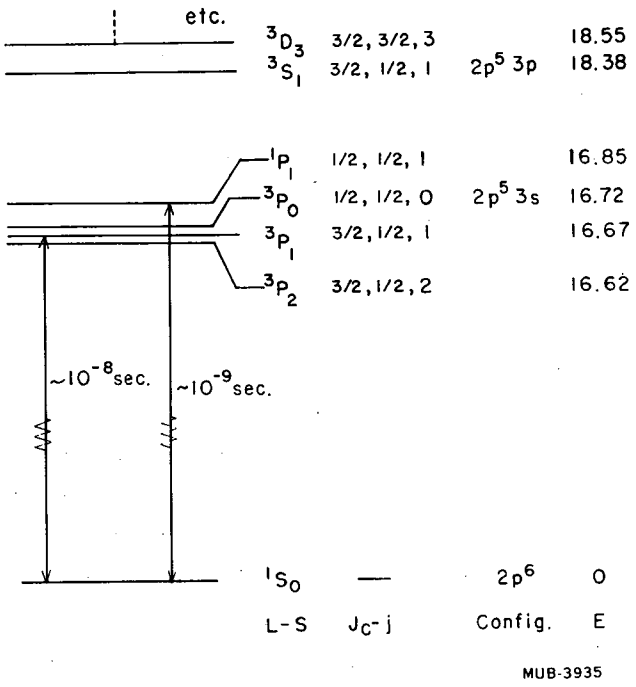

Fig. D.31-3. Low-lying electronic levels of the neon atom. Both L-S and J_C-j coupling designations are shown.

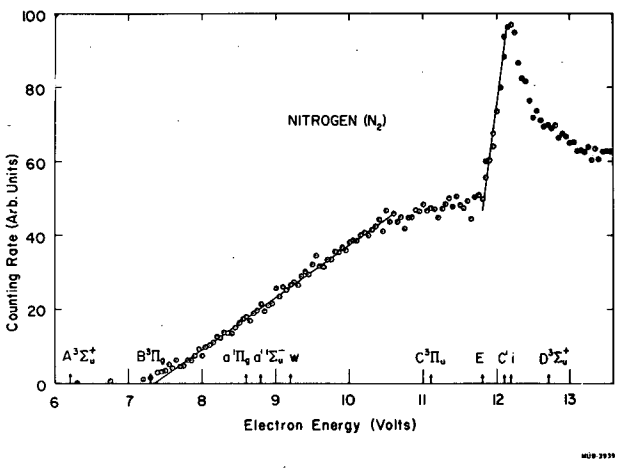

Fig. D.31-5. Excitation function for metastable states of molecular nitrogen.

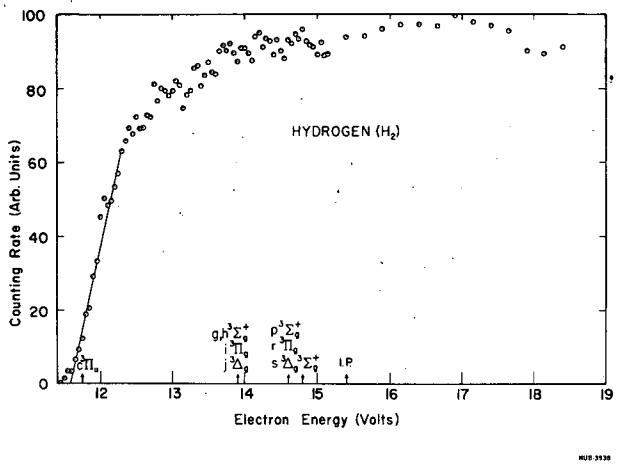

Fig. D.31-4. Excitation function for metastable states of molecular hydrogen.

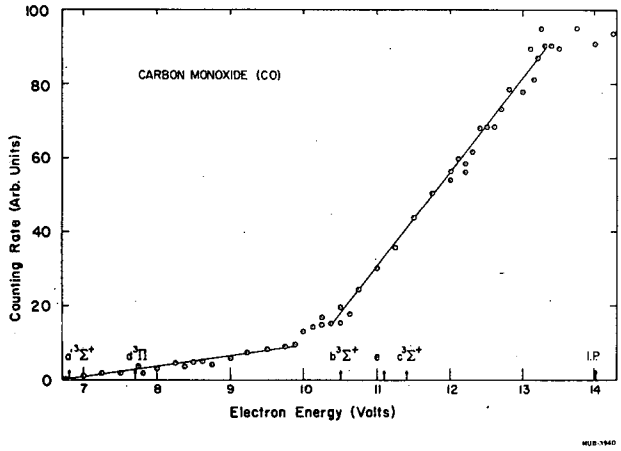

Fig. D.31-6. Excitation function for metastable states of carbon monoxide.

32. PARAMAGNETIC RESONANCE OF Fe^{3+} IN POLYCRYSTALLINE FERRICHROME A†

H. Hollis Wickman,* Melvin P. Klein, and D. A. Shirley

The Ferrichrome A molecule[1] is obtained from the smut fungus Ustillago sphaerogena, and although it is related in structure to substances that are growth factors in several microorganisms[2] its precise biological function is not known. Recently, Zalkin, Forrester, and Templeton[3] have determined the complete molecular structure by x-ray diffraction. The coordination about the iron is roughly octahedral, resulting from the three hydroxamic acid residues, and is expected to have low overall crystal-field symmetry. The paramagnetic resonance experiments reported here were undertaken to provide us with a set of reasonably accurate eigenfunctions for the Fe^{3+} in ferrichrome A; these were required to make a detailed analysis of the relaxation phenomena encountered in Mössbauer resonance studies.[4] While analyzing these experiments we have become aware of several symmetry properties of the spin Hamiltonian usually invoked to account for the strong resonances observed with a g factor of 4.3 which are attributed to $^6S_{5/2}$ ions such as Fe^{3+}. Thus we discuss the analysis of our spectra in somewhat greater detail than would otherwise be necessary.

At room temperature a strong resonance, of 400 Oe line width, was observed at 1550 Oe, corresponding (for a 9-kMc/sec spectrometer) to a g factor of 4.3. A resonance at this position is not unique to ferrichrome A, but has been observed in several Fe^{3+} compounds.[5,6] The observed line width was, however, greater by nearly a factor of 10 than those previously reported, and was not explicable by the usual theory. To minimize relaxation broadening we repeated the experiments at temperatures down to the helium range, without finding any qualitative changes, but at lower temperatures new resonant areas grow in. At 1.0° K there are particularly conspicuous resonances near g values of 1.0, 1.3, and 9.6. The low-temperature spectra are shown in Fig. D.32-1.

Castner, Newell, Holton, and Slichter[5] have given a clear discussion of the origins of an Fe^{3+} resonance at g = 4.3. In the interpretation of a spin resonance experiment on iron in glass they gave lucid arguments showing that a Hamiltonian of the form

$$\mathcal{H} = E(S_x^2 - S_y^2) + g\beta \vec{H} \cdot \vec{S} , \qquad (1)$$

with $E \gg g\beta H$, will split a state with effective spin S = 5/2 into three doublets, of which the one of intermediate energy has an isotropic g value of 4.286. They noted that addition of a crystal field operator of the form $D[S_z^2 - 1/3\ S(S+1)]$ to the above Hamiltonian has the effect, for $D \ll E$, of broadening the line. Because the outstanding unexplained feature of the ferrichrome A spectrum was the broadness of the main line, and because the hyperfine structure of the Mössbauer spectra arose presumably from all the electronic levels of Fe^{3+}, it seemed worth while to consider a Hamiltonian of the more general form

$$\mathcal{H} = D[S_z^2 - 1/3\ S(S+1)] + E(S_x^2 - S_y^2) + g\beta \vec{H}\cdot\vec{S} = \mathcal{H}_0 + g\beta \vec{H} \cdot \vec{S} . \qquad (2)$$

We shall assume for this discussion that the crystal field terms are large compared with the Zeeman terms. This $\mathcal{H}_0$ is the most general crystal field Hamiltonian of second powers of spin operators. We shall find it convenient to define the parameter $\lambda = E/D$ and to write $\mathcal{H}_0$ in units of D,

$$\mathcal{H}_0 = S_z^2 - 1/3\ S(S+1) + \lambda\,(S_x^2 - S_y^2) . \qquad (3)$$

On diagonalizing $\mathcal{H}_0$ in the J = 5/2 manifold of the $Fe^{3+}3d^5;{}^6S_{5/2}$ level, we find three Kramers' doublets $\psi_i^{\pm}$, given in $|J_z\rangle$ representation by

$$\psi_i^{\pm} = a_i |\pm 5/2\rangle + b_i |\pm 1/2\rangle + c_i |\mp 3/2\rangle , \quad \text{with } i = 1, 2, 3. \qquad (4)$$

The a_i, b_i, and c_i are functions of the single parameter λ. The range of physically distinct values for λ is restricted to $\lambda \leq 1/3$. In addition, only positive values of λ need be considered. These symmetries are most easily displayed by writing $\mathcal{H}_0$ in the form

$$\mathcal{H}_0 = AS_x^2 + BS_y^2 + CS_z^2 \quad , \tag{5}$$

with A + B + C = 0. A coordinate system may be chosen such that $|C| \geq |B|, |A|$, and it is always possible to choose B > A. In this system $\mathcal{H}_0$ assumes the conventional form after the substitutions C = 2D/3, B = E - D/3, and A = -E-D/3. Now we see $\lambda = E/D = (B - A)/3C$, or $|\lambda| \leq 1/3$, since $|B - A| \leq |C|$. With our choice of A, B, and C, we find that E is always positive. Thus the sign of λ determines the sign of D. By diagonalizing $\mathcal{H}_0$ for positive λ in the range $0 \leq \lambda \leq 1/3$ we obtain the complete range of physically distinct eigenvalues and eigenfunctions for $D \geq 0$. For $D \leq 0$ we need only invert the energy levels. A positive D means, of course, that in the limit $\lambda = 0$ the state $|S_z = \pm 1/2\rangle$ lies lowest in energy.

We have plotted in Fig. D.32-2 the variation with λ of the effective g factors for the three crystal-field Kramers' doublets considered separately as having effective spins of 1/2. We note that Castner et al. used the Hamiltonian $\mathcal{H} = E(S_x^2 - S_y^2)$, which is identical--aside from a scale factor and a rotation of axes--to $\mathcal{H}_0$ with $\lambda = 1/3$. This is easily checked by substituting 1/3 for λ in Eq. (3), and replacing S(S + 1) by $S_x^2 + S_y^2 + S_z^2$. Thus, while the description of a Hamiltonian as having only a D term is physically meaningful, implying axial symmetry, it is never necessary to invoke a crystal-field Hamiltonian with only a large E term and D = 0. This is one example of a physical problem in which one may or may not choose to order the principal axes of the system according to the magnitude of the influence of the Hamiltonian in each direction; if one does so choose, E need never be larger in magnitude than D. An analogous case occurs in nuclear quadrupole interaction, for which an asymmetry parameter η is introduced to describe deviations from axial symmetry, and η need never exceed unity.[7]

From Fig. D.32-2 we find that the variation of the upper-level g values is small. In the middle level the g values vary from highly anisotropic to isotropic as λ increases from 0 to 1/3. For the lower level the g values vary considerably and assume the same values at $\lambda = 1/3$ as those of the upper level, except for a relabeling of the axes. [There is complete symmetry between the g values of the different levels for the ranges $0 \leq \lambda \leq 1/3$ and $1/3 \leq \lambda \leq 1$, within trivial relabeling and a scale factor in λ. In fact, by combining these two ranges we exhaust all the distinct physical possibilities for the system including both signs for D. This may easily be shown analytically by reference to the Hamiltonian, Eq. (3).] If higher-order crystal-field operators may be neglected, the calculation summarized by Fig. D.32-2 should suffice to account for the dominant features of the resonance data. Let us consider first the line width of the main "isotropic" line at g = 4.3. The absorption actually occurs over the range $g = 4.3^{+0.67}_{-0.51}$, taking the crossing point, maximum, and minimum in the derivative curve. This is consistent with a $|\lambda|$ of 0.23, for which three closely spaced lines are expected. In a polycrystalline sample spectrum these would appear as a broad resonance at approximately the average of their g values.

This value of λ requires the appearance of lines originating from the lower level; the principal values at $\lambda = 0.23$ for the effective g tensor of this level are 9.3, 1.7, and 1.0. These lines are expected even in polycrystalline samples, because their intensities are derived from the large g_y of 9.3 in this level. Indeed the lowest-temperature spectra show features of this type, namely the "humps" at 9.6, 1.3, and 1.0. The growth of these absorptions with decreasing temperatures establishes λ (and thus D) as positive. The lack of accurate agreement is probably due in part to the inherent difficulty of assigning g values based on a broad resonant area extending over a region of 7000 gauss. Again, neglect of the Zeeman energy, with consequent admixing of higher doublets, is less valid in the high-field region. The observed line width of the main resonance is compatible with a range of about 0.10 in λ, and the fit to experiment of the principal values of the lower-level g tensor may be improved somewhat by varying λ. For example, a λ of 0.25 gives g values of 9.45, 1.32, and 0.86. Even without an exact fit and in spite of the various approximations discussed above, our data require λ to be in the range $\lambda = 0.25 \pm 0.04$. We conclude that the Hamiltonian proposed in Eq. (2) gives an adequate description of the observed spectra. It seems particularly valuable to do these resonance experiments at vey low temperatures, especially if one is studying large biologically active molecules in which the spin correlation time is likely to be long.

Footnotes and References

† Short form of UCRL-11685, submitted to J. Chem. Phys.

* Present address: Bell Telephone Laboratory, Semiconductor Development Division, Murray Hill, N. J.

1. T. Emory and J. B. Neilands, J. Am. Chem. Soc. 83, 1626 (1961).
2. J B. Neilands, Bacteriol. Rev. 21, 101 (1957).
3. A. Zalkin, J. D. Forrester, and David H. Templeton, Science 146, 261 (1964).
4. H. Hollis Wickman, Melvin P. Klein, and D. A. Shirley, Magnetic Hyperfine Structure in the Mössbauer Spectrum of Paramagnetic Fe^{3+} in Ferrichrome A (to be submitted to Phys. Rev.).
5. T. Castner, Jr., G. S. Newell, W. C. Holton, and C. P. Slichter, J. Chem. Phys. 32, 668 (1960).
6. R. Aasa, B. G. Malmstrom, P. Saltman, and T. Vangaard, Biochim. Biophys. Acta 75, 203 (1963); J. J. Windle, A. K. Wiersema, J. R. Clark, and R. E. Feeney, Biochemistry 2, 1341 (1963); R. G. Shulman and W. M. Walsh, Jr., Bull. Am. Phys. Soc. 8, 199 (1963).
7. See, for example, M. H. Cohen and F. Reif, Solid State Physics (Academic Press, New York, 1958), p. 4.

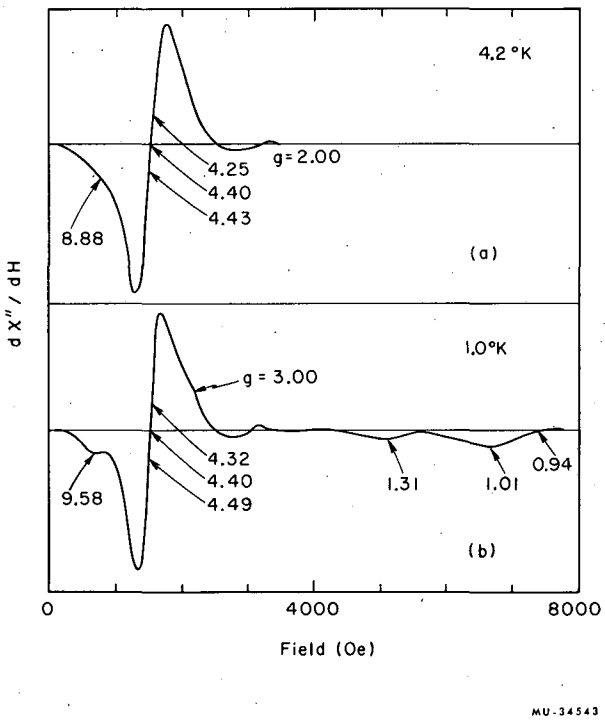

Fig. D. 32-1. The X-band paramagnetic-resonance spectrum of ferrichrome A at 4.2° K and at 1.0° K. Note additional structure at the lower temperature.

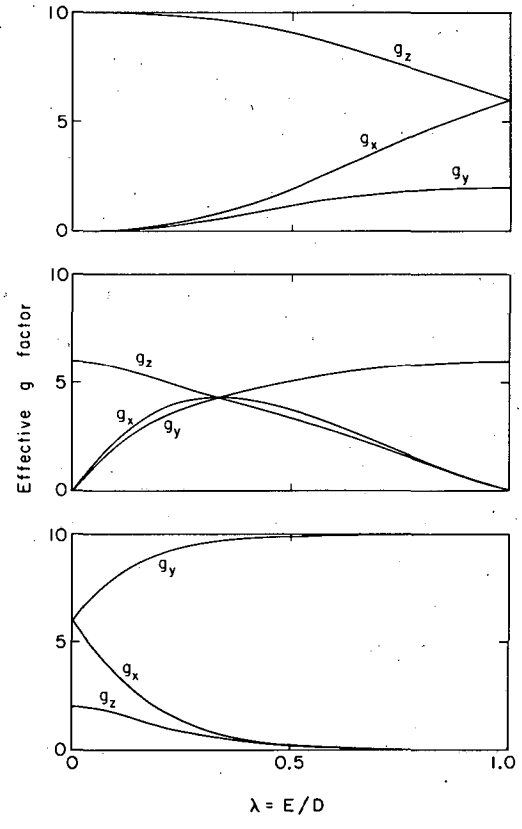

Fig. D. 32-2. The effective g values for the spin Hamiltonian $\mathcal{H} = D S_z^2 - 1/3\, S(S+1) + E(S_x^2 - S_y^2)$ operating within a $J = 5/2$ manifold (with $g_J = 2.00$), plotted against $\lambda = E/D$. Except for the order of the energy levels, the range $1/3 \leq \lambda \leq 1$ is redundant. The symmetry around $\lambda = 1/3$ is easily displayed by changing the sign of D (thus inverting the order of the levels) making the transformation $y \to x$, $z \to y$, $x \to z$, and substituting $\lambda' = 1/2\lambda$ for λ.

33. OBSERVATION OF ELECTRONIC RELAXATION IN MÖSSBAUER SPECTROSCOPY

H. Hollis Wickman,* Melvin P. Klein, and D. A. Shirley

One of the most interesting and useful features of the Mössbauer effect is the possibility of observing individual nuclear Zeeman components in γ-ray transitions. This is most easily done by using a specimen in which the resonant atoms exhibit hyperfine structure (hfs). The Hamiltonian governing such a situation might, for example, have the form

$$H = A\vec{S}\cdot\vec{I} + (\text{crystal field terms}),$$

where A is the hfs constant, S is the electronic spin of the ion or atom in question, and I is the nuclear spin of the nuclear ground or excited state. The crystal field terms can play a pivotal role in relaxation phenomena, as discussed below.

A most fundamental question affecting Mössbauer spectra is whether the electron correlation time τ_c (a function of spin-lattice, spin-spin, etc. relaxation times) is larger or smaller than or about equal to $(\Delta\nu_{ij})^{-1}$, the time associated with the frequency difference between hfs components i and j, determined by $E_k = h\nu_k$. For $\tau\Delta\nu_{ij} \gg 1$, resonant absorption may occur at the two frequencies, ν_i and ν_j. For $\tau\Delta\nu_{ij} \ll 1$ a single absorption will be observed, at a position intermediate between ν_i and ν_j. Before the experiments presented here were undertaken only these two extreme types of behavior had been seen, although many cases of each type were known. In fact it was common practice to decide that a substance was paramagnetic if only one line was observed (i.e., $\tau\Delta\nu \ll 1$) or, for example, antiferromagnetic if a resolved hfs spectrum was seen ($\tau\Delta\nu \gg 1$).

For ferrichrome and ferrichrome A, containing Mössbauer-resonant Fe^{57} the spectra changed markedly from 300° K, where only one very broad line was found, to 77° K, where evidence appeared for six weak lines (the full Fe^{57} hfs spectrum). We therefore extended the measurements to 4.2° K and below, with substantial clarification of the spectra as τ increased. Several measured spectra are shown in Figs. D. 33-1 and D. 33-2.

The physical situation here is analogous to one encountered in NMR spectroscopy, and we have treated it with a theory analogous to the Bloch theory. In fact the differential equations employed have the same form. By solving the Bloch equations with certain boundary conditions, we have obtained theoretical curves for various values of the correlation time τ, including the range that is relevant to ferrichrome and ferrichrome A. These are shown in Figs. D. 33-3 and D. 33-4. We conclude that, using the Mössbauer effect, we have observed an intermediate case of exchange ($\tau\Delta\nu \approx 1$).

Footnote

* Present address: Bell Telephone Laboratory, Semiconductor Development Division, Murray Hill, N. J.

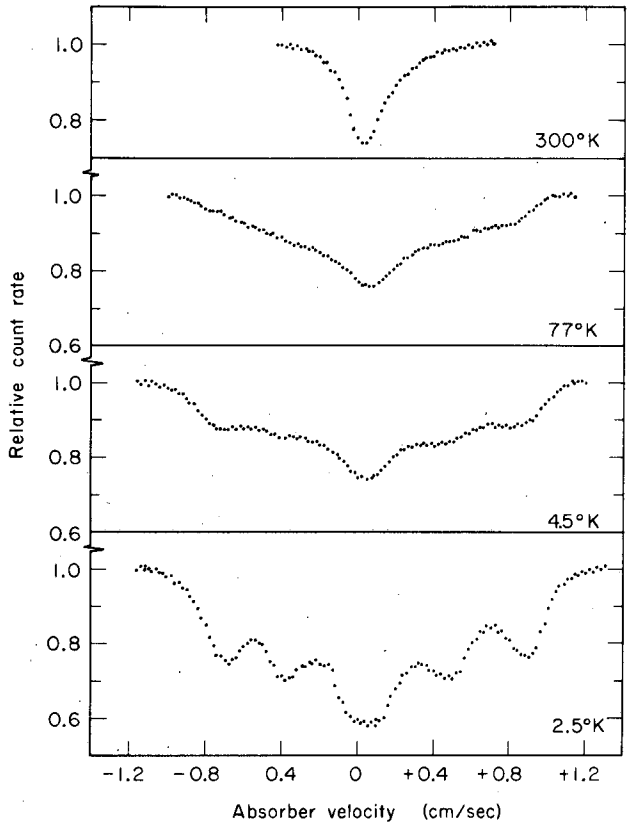

Fig. D. 33-1. Mössbauer spectra of ferrichrome at several temperatures. At highest temperatures sites are averaged by short relaxation time, which increases with decreasing temperature. The full six-line spectrum of Fe^{57} is evident at 2.5° K.

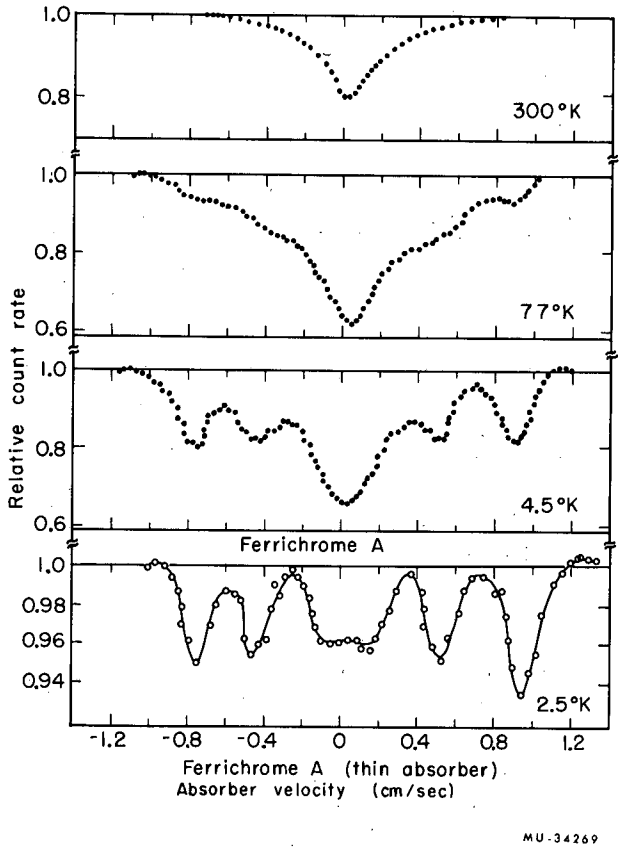

Fig. D. 33-2. Similar to Fig. D. 33-1, but for ferrichrome A. Note improvement of spectrum, relative to ferrichrome, at each temperature due to longer correlation time.

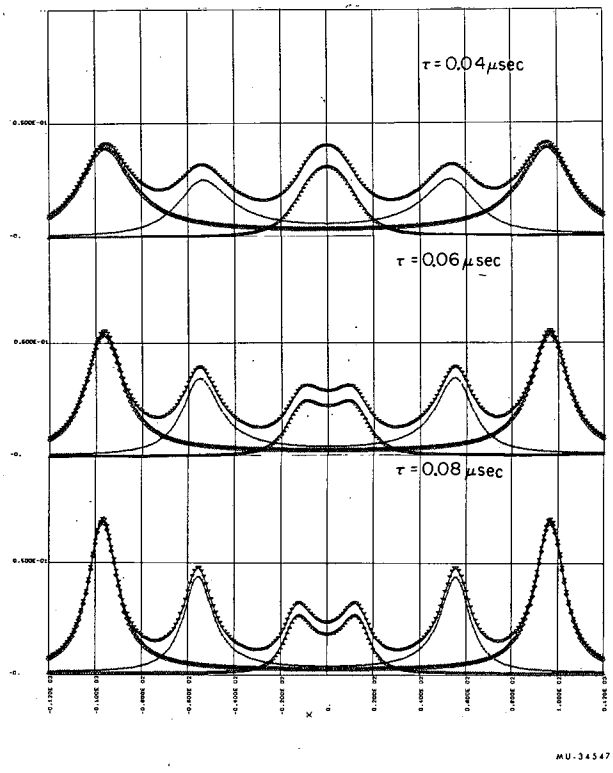

Fig. D. 33-3. Relaxation spectra calculated from the modified Bloch equations.

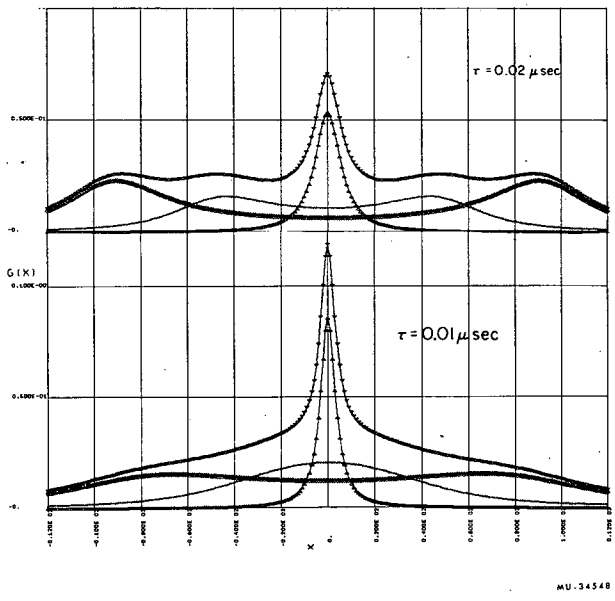

Fig. D. 33-4. Relaxation spectra for shorter τ, calculated from the modified Bloch equations.

E. INSTRUMENTATION

1. THE DESIGN, CONSTRUCTION, AND OPERATION OF A DIFFERENTIAL MICROMANOMETER*

Peter R. Rony† and Kenneth W. Lamers

A differential micromanometer capable of measuring 0.1 μ Hg to an accuracy of ± 1% has been designed, constructed, and tested. The micromanometer is being used as a Wrede-Harteck gauge, a device that converts an atom concentration into a pressure differential in a low-pressure gaseous system.

The pressure difference is sensed by a membrane manometer constructed as a differential capacitor that forms two legs of a resonant-bridge network excited by a radio-frequency source (Fig. E.1-1). The bridge output (2.762 Mc) is amplified and fed to a phase-sensitive detector that determines the direction of unbalance and develops a dc voltage that can be (a) used in a feedback-loop system to restore the diaphragm to its null position, or (b) used in an open loop system and recorded directly.

The most favorable system found to date consists of a Decker Corporation Model 306-2A pressure transducer operated open loop with our bridge and electronics. Differential pressures as low as 0.05 μ Hg can be measured with a zero drift of about 0.03 μ Hg or less per hour (approximately 0.001 μ Hg/min) in a room thermally regulated to within ± 0.5 °C. Differential pressures of 0.0005 μ Hg are detectable. With a more sensitive transducer, such as a Decker Corporation Model 306-2G, it may be possible to increase the sensitivity by almost an order of magnitude over the above figures. An attenuator in the amplifier section extends the 306-2A system to differential pressures as large as 35 μ Hg.

The micromanometer is calibrated electrostatically. The diaphragm constant, K, in the formula $\Delta P = K V^2$ is determined to ± 1% by comparing the readings produced by a known pressure differential, as measured with an accurate McLeod gauge, and a voltage of known magnitude applied to one side of the differential capacitor. Once the gauge constant is known, the system can be calibrated daily by applying a series of known voltages and plotting the recorder reading vs the square of the voltages (Fig. E.1-2). This method of calibration eliminates completely the effect of changes of bridge voltage, bridge constant, amplifier gain, diaphragm tension, and recorder calibration. It takes 5 minutes to perform and need be applied as little as two times per day.

In the pressure region of 0.1 to 35 μ Hg, the system is an excellent secondary pressure standard, being much more convenient and generally more accurate than a McLeod gauge.

Footnotes

* Brief version of UCRL-11218, Pt. I (Oct. 1964) and UCRL-11218, Pt. II (to be issued).
† Address after April 1965, Monsanto Corporation, St. Louis, Missouri.

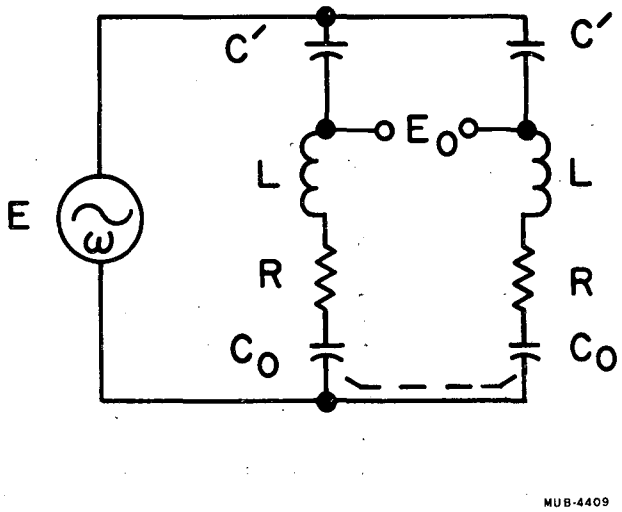

Fig. E.1-1. Capacitance bridge with two resonant arms excited by a radio-frequency source.

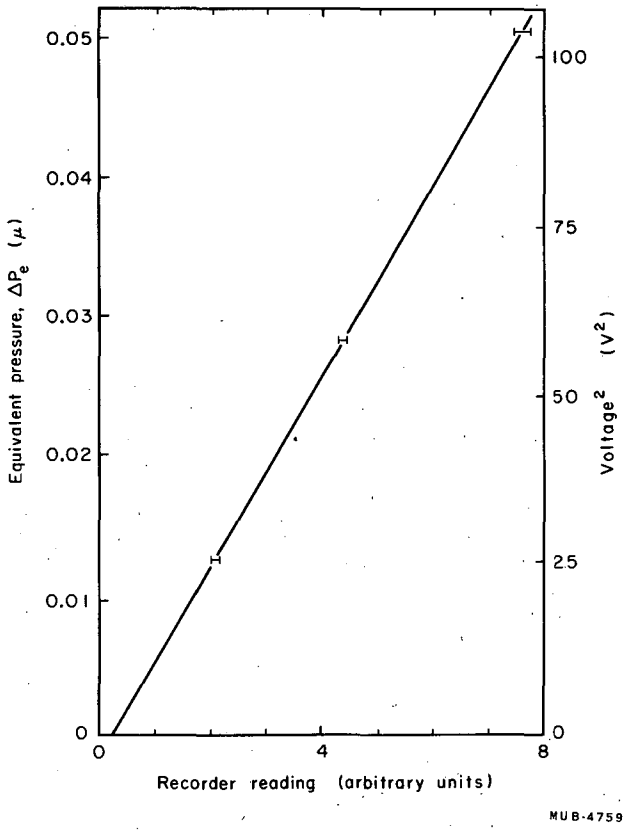

Fig. E.1-2. Typical calibration curve for most sensitive scale. Gauge constant was 4.85×10^{-4} μ Hg/volt^2. Noise and dc drift was less than 0.001 μ Hg/min. Ambient pressure in system was 0.001 μ Hg. The zero offset, due to an incorrect choice of recorder zero reading, is of no importance.

2. EXPERIMENTAL INSTRUMENTATION FOR THE 88-INCH CYCLOTRON

F. S. Goulding, D. A. Landis, and R. P. Lothrop

The past year has seen considerable changes in the instrumentation for experiments and also in the accuracy of energy measurements using solid-state detectors at the 88-inch cyclotron. Some of these advances are summarized in the following paragraphs.

a. Particle Identifier

The unit described in the preceding report has been improved in minor circuit details, and continues to give excellent particle discrimination. In recent experiments using a thin (4 mil) ΔE detector, the identifier has given excellent separation for particles which include He^3, He^4, He^6, Li^6, Li^7, Li^8, Be^8, and Be^9 (all at the same time). No adjustment of the identifier has been required in 1 year of operation.

b. Analyzer Routing Systems

In using the particle identifier, as well as in multidetector experiments, it is necessary to split the multichannel analyzer memory into many small groups. We have now modified the 4096-channel analyzers to permit operation in modes where the memory can be split into up to 32 groups.

c. Multiple Single-Channel Analyzers

Several units have been constructed, each containing four or more single-channel analyzers. These, used on detector signals, or on the outputs of the identifier, drive the routing system of the analyzers.

d. Multiple-Detector Experiments

Improvements in the process for producing Li-drifted silicon detectors have made practicable multiple counter arrays in scattering experiments. Recent experiments in which improvements in counting rate were desirable have used as many as eight detectors in the scattering chamber. This technique is particularly useful in studies of variation of cross section as the energy of the cyclotron beam is varied in small increments. It is also being used in $\alpha,\alpha\gamma$ experiments where the inefficiency of the Li-drift Ge detectors makes it desirable to detect as many α's as possible to raise the coincidence rate.

e. A Pulse Generator as an Energy Standard

A unit containing four stable pulse generators has recently been used for energy-calibration purposes at the cyclotron. To use this for absolute energy measurements it is essential to equip preamplifiers with accurately calibrated test capacitors, which has now been done. As measurements of pulse voltage and capacity can be carried out with an accuracy of better than 0.1%, we should be able to achieve energy calibration within 0.1% (i.e., 50 keV in 50 MeV). Unfortunately, it appears that the amount of energy absorbed in silicon per hole-electron pair (ϵ) is not known to this degree of accuracy. At present we can rely on the energy calibration to better than 1%, but after one more experiment, we will be able to define the value of ϵ to about 0.25%, and our energy calibration will not be worse than this figure. This technique permits easy setup of experiments, and facilitates rapid identification of unknown peaks.

f. Energy Resolution in Cyclotron Experiments

The best energy resolution figures obtained with Li-drifted silicon detectors are

(i) at 40 MeV (α's), 43 keV, (ii) at 85 MeV (α's), 130 keV.

A large part of the spread must be attributed to spread in energy of the cyclotron beam itself.

Until recently, the resolution at higher energies was much worse than this (e.g., 280 keV at 85 MeV). We also observed that the linearity of a plot of channel number vs energy was poor at high energies. These two effects appear to be due to a combination of long detector charge-collection time and inappropriate choice of amplifier-shaping networks.

In a recent experiment using 1.5 μsec delay-time differentiation and a 0.5-μsec integrator, the improved energy resolution figure (i.e., 130 keV at 85 MeV) was obtained. Time did not permit an accurate linearity check, but there were indications that linearity had improved at the same time as resolution.

Many of the measurements described here and the development of the techniques have been the result of cooperation with the experimental staff at the cyclotron. In particular, B. G. Harvey, J. Merriwether, H. Pugh, J. Cerny, and D. Pehl have contributed to this work.

3. STUDIES ON SILICON—SILICON DIOXIDE SYSTEM†

R. Y. Deshpande*

The use of silicon dioxide is a standard technique for the protection of silicon p-n junctions and as a mask for diffusions. The electrical effects introduced by the oxide on devices

therefore have considerable practical importance. We have been studying the effect of ambients on the electrical behavior of the oxide and the semiconductor interface. The ambients studied were nitrogen, oxygen, and nitrogen plus 5% hydrogen. Typical "field-effect" measurements were carried out and the density of charge under the oxide and the carrier mobility were measured. The results are summarized in the following table. The temperature at which the devices were pulled out of the furnace are indicated in the table.

Recently we have been studying the temperature dependence of conductivity of the interface. From the results of these experiments the activation energies of the various impurity levels introduced in the system have been estimated. These results are also given in the table. Knowledge of surface charge density and carrier mobility enables us to calculate some of the parameters of the system. The possibility of the formation of quenched-in defects has been suggested to explain the results. It is felt that these results will throw more light on the electrical nature of the oxide-semiconductor system and hence on the device characteristics.

Type of device	Room-temperature conductivity (ohm^{-1}-cm^{-1}/sq)	Surface charge-density (C/cm^2)	Effective carrier mobility (cm^2/volt-sec)	Activation energy (eV)	$\frac{d\sigma}{dT}$
N(600°C)	7×10^{-8}	7.0×10^{-8}	1.0	0.39	+ ve
O(600°C)	1.7×10^{-6}	2.4×10^{-7}	7.0	0.31	+ ve
H(500°C)	1.8×10^{-5}	3.0×10^{-8}	600	<0.10	- ve

Footnotes

† Condensed version of R. Y. Deshpande, The Effect of Ambients on the Charge Density and Carrier Mobility in a Silicon—Silicon Dioxide Interface, UCRL-11419, May 1964.
* I. A. E. A. Fellow from Atomic Energy Establishment, Trombay, Bombay, India.

4. LITHIUM-DRIFTED GERMANIUM DETECTORS†

W. L. Hansen and B. V. Jarrett

Techniques have been developed by which a large number of germanium γ-ray detectors have been produced. The best energy resolution obtained has been shown to be the sum of input tube noise and charge-collection statistics, with no apparent detector noise contribution. For this best case, the energy resolution of 122-keV γ's (Co^{57}) was 2.1 keV, and for 1.3-MeV γ's (Co^{60}) was 3.5 keV, when an amplifier with a measured pulser noise of 2.0 keV was used.

Much of the development effort has been directed toward the production of very thick junctions (> 1 cm) and depleted volumes greater than 6 cm^3. It has been found that, with rare exceptions, charge-collection efficiency in thick junctions is very voltage-dependent, and that energy resolution is much poorer than expected. Gamma-ray probing has shown this effect to be most prominent in the center of zone-leveled crystals, and several good thick detectors have been made by using only the outside 1 cm of the crystal. Temperature-vs-conductivity plots and other techniques indicate that this effect is largely due to the presence of the fast diffusers such as copper or nickel or both. Typical energy resolutions obtained for 1-cm-depletion detectors made by using the outside parts of crystals have been 2.8 keV for Co^{57} and 4.2 keV for Co^{60} γ rays.

It is clear now that the principal limitation to making very thick high-resolution γ detectors is the quality of the starting material. Efforts are being made to improve the material now available and to find new sources of supply. As it is unlikely that high-quality material will become available commercially in the near future, we are proceeding with the development of our own crystal-growing facilities.

Footnote

† Condensation of William L. Hansen and Blair V. Jarrett, Techniques for the Fabrication of Lithium-Drifted Germanium Gamma Detectors, UCRL-11589, Aug. 1964.

5. SUBGROUPING MULTICHANNEL ANALYZERS ON A PERIODIC BASIS

Richard G. Leres

Multichannel analyzers in general are not equipped to subgroup themselves on a time basis during data accumulation. Most manufacturers provide for multidetector subgrouping, where each detector routes itself into a specific quadrant or half of the analyzer memory, but periodic subgrouping is not possible without further instrumentation.

A device has been developed and tested which will subgroup multichannel analyzers at accelerator beam rates. This unit, a Gating and Sequential Subgrouping External Router (acronym: GASSER), performs subgrouping and controlling functions on a maximum of four RIDL model 34-12B 400-channel analyzers. GASSER provides a total of 12 gates or subgroup periods, individually variable from several μsec to 2 sec. A patching arrangement at the rear of the unit allows the 12 gates to be triggered sequentially or independently, as the experimenter desires. Also at the rear patch panel are buffered positive and negative gate outputs for auxiliary uses.

A wired switching array on the front panel provides complete flexibility in routing any gate to any analyzer subgroup. Indication of mispositioned switches is accomplished with an illuminated sign. Other front-panel controls allow both PHA (pulse-height analysis) and time (multiscaler) modes of operation, choice of subgroup size in terms of channels, and monitoring of all primary signals. An electromechanical countdown register driven by an electrometer controls the dwell time per channel in time-mode operation. A single multilead cable is used to connect each analyzer to GASSER.

Modifications performed on 34-12B analyzers were designed to cause the least intrusion on existing circuitry and to permit the analyzer (when not connected to GASSER) to function completely and exactly as the manufacturer intended.

It is believed that, with effort comparable to that expended on the 34-12B, almost any solid-state pulse-height analyzer that makes provisions for split-memory operation can be modified to operate in a time mode subgroup fashion.

6. MÖSSBAUER EFFECT INSTRUMENTATION

Ronald Zane

A method for performing Mössbauer effect experiments in the multiscaler mode of operation of pulse-height analyzers has been developed.

A tuning-fork frequency standard is used to provide an extremely precise and stable "clock" frequency. An integrated circuit scaler (using Fairchild microLogic) simulates the address scaler in the pulse-height analyzer, and is used to generate a "start" pulse when the analyzer has stepped through all channels. The simulated address scaler also generates a low-frequency square wave, which in turn is integrated to produce a triangle wave to serve as a reference for a closed-loop drive system which produces the relative velocity between source and absorber needed to produce the Mössbauer effect. Thus, in the multiscaler mode of operation the triangular relative velocity is precisely synchronous with the "clock" frequency, and exactly fills the pulse-height analyzer with two absorption spectra which are mirror images of each other.

The advantages of multiscaler-mode operation are numerous. The multiscaler mode produces an inherently straight-line spectrum base line. The straight base line increases the experimenter's ability to resolve low-intensity or broad absorption lines while at the same time permitting well over 90% efficiency in use of the counting time. In pulse-height-analyzer mode of operation nonlinearities and small oscillations of the triangular velocity wave produced variations in the count rate which were inversely proportional to the derivative of the variations and nonlinearities. Thus, large counting-rate errors, which tended to mask out and distort the absorption spectra, were produced by relatively small deviations in the triangular velocity wave shape. In multiscaler mode nonlinearities and small oscillations of the triangular velocity wave drive produce variations in channel-to-velocity linearity that are directly proportional to the nonlinearity of the triangular velocity wave shape. Thus, small velocity base nonlinearities are produced by small velocity wave nonlinearities.

At present, measurement accuracy is limited to about 1% by the use of the Fe^{57} spectrum as a "standard" for velocity calibration. A method for calibration of velocity transducers is being developed which will rely on the measurement of the Doppler shift in monochromatic light reflected from the moving system. The Doppler-shift technique should substantially improve the accuracy of velocity measurements.

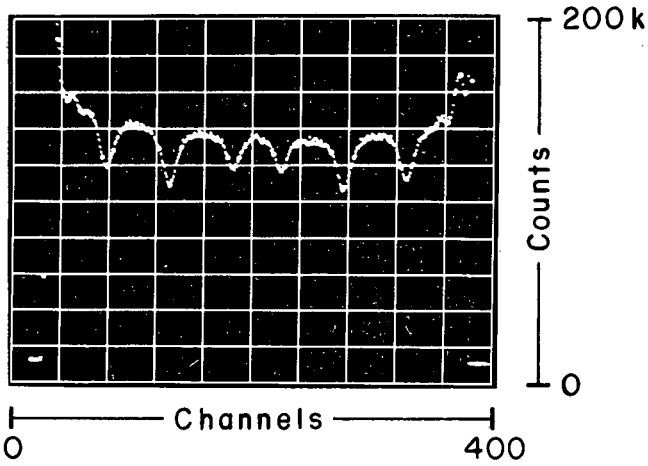

Fig. E.6-1. Fe^{57} spectrum, pulse-height-analyzer mode, 200 000 counts full scale, 400 channels.

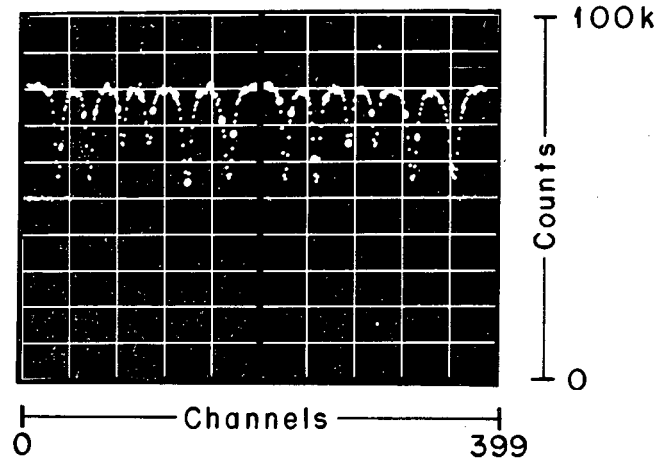

Fig. E.6-2. Fe^{57} spectrum, multiscaler mode, 100 000 counts full scale, 400 channels.

7. A NEW TYPE OF BEAM INTEGRATOR

D. A. Landis and F. S. Goulding

The recent advent of the insulated-gate transistor, which can be employed as an electrometer, led us to develop a new beam-integrator circuit which is presently in use at the 88-inch cyclotron. The block diagram (Fig. E.7-1) illustrates some unusual functions of this instrument. Many beam integrators use an operational amplifier with a feedback capacitor to integrate the beam charge. In general, these instruments recognize when the output level exceeds (or goes below) a fixed level and shorts out the integrating capacitor to remove the accumulated charge before starting a new integrating period. The short is usually applied by a mechanical contact, and the low operating speed of this device limits the dump rate to a low value.

In the arrangement shown in Fig. E.7-1 a diode pump and capacitor arrangement is used to restore the charge in C_f at the end of each integrating period. Since this can be accomplished in a microsecond or so, the dump rate can be quite high. The circuit of Fig. E.7-1 is designed

for a dump rate from 1 to 500 cps. Two diode pumps are connected to the input, and either of these may operate depending upon the direction of the input current. The leakage current of the diodes CR_1 and CR_2 and the input insulated-gate transistor Q_1 determine the minimum current sensitivity of the circuit. With Si diodes FD-300 for CR_1 and CR_2 and a commercial MOS transistor (Siliconix X5-2N3631), the effective value of leakage current in the input circuit can be kept below 10^{-11} A, permitting 1% accuracy in measuring currents of 10^{-9} A. (For complete details of the instrument, refer to drawing number 11X3400 P-1.)

In this type of instrument it is more important to measure the integrated charge than the input current. In the design of Fig.E.7-1 the current is indicated on a meter by using a counting rate meter to measure the dump rate. A gated scaler is used to sum the dump pulses and thereby record the total beam charge in the measured period.

The stability of the integrating circuit is not affected by slow drifts in the integrating amplifier or discriminator threshold, or in the stability of the feedback capacitor C_f. What does affect the stability is the amount of charge applied to the input through the diode pumps. Capacitors C_1 and C_2 are switched from 10 pF to 0.1 μF for the different current-integrating ranges, and are stable polystyrene capacitors. The voltage pulses V_1 and V_2 are about 10 volts in amplitude and are developed from stable reference zeners, and are compensated for changes in voltage drop in CR_1 and CR_2 due to temperature.

The zero drift in the gate to source voltage for the insulated-gate transistor after initial warm-up is less than 3 mV for a 24-h period. This affects the stability of the charge fed back through CR_1 or CR_2 by 0.03%. Lack of complete temperature compensation of CR_1 and CR_2 results in an additional change of about 0.03% for 10°C change of temperature.

The instrument is easy to operate and has a minimum of controls. The controls consist of a zero adjust, a test current pushbutton that connects a positive or negative test current for checking each integrating range, an ohmmeter button, and a current-meter sensitivity switch. The six integrating ranges are from 10^{-10} coulomb to 10^{-6} coulomb per dump, and the current ranges are from 5×10^{-10} to 5×10^{-4} full scale.

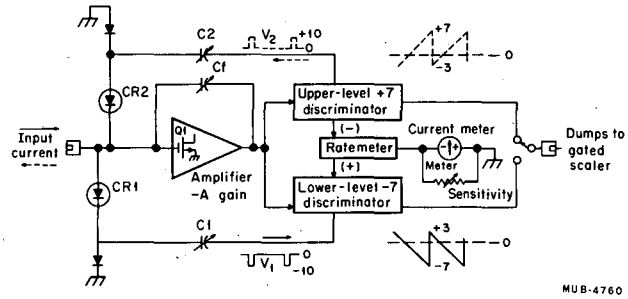

Fig.E.7-1. Block diagram of beam integrator.

8. COMPUTER INSTALLATION AT THE 88-INCH CYCLOTRON*

Lloyd B. Robinson

A PDP-5 digital computer, with 8192 words of core storage and fast arithmetic hardware, has been purchased for use in experiments at the 88-inch cyclotron. The computer is directly linked to a 4096-channel two-dimensional pulse-height analyzer (PHA), and initially will be used to provide a fast memory dump for the PHA, producing graphical plots and performing routine computations on the data. The link between computer and analyzer allows the computer to control data-taking and readout of the analyzer, with or without human intervention. (See Fig.E.8-1.)

The computer is expected to allow more efficient use of experimental time, since complete graphical and CRT display of a series of runs will be immediately and continuously available, in addition to a considerable amount of reduced data. This will help the experimenter to modify experimental conditions at once, when new or unexpected results arise, since he will be able to keep in much closer touch with the incoming data.

Computations on data will be facilitated by the use of a CRT display with a "light pen." The light pen makes it easy for the experimenter to select specific portions of data from an analog display, and provides an easy method for choosing between alternatives in a program.

Control of the PDP-5 by untrained operators is facilitated by a special switch panel, somewhat less complex than the control panel of a pulse-height analyzer. This switch panel will allow one of several programs to be selected by merely setting a rotary switch and pressing a button. Usually, of course, the computer will be controlled from a typewriter keyboard.

Additional input-output devices attached to the computer include a dual magnetic tape deck and 60-character-per-second paper tape punch and reader.

The computer memory is directly accessible to external devices, and in some experiments that are too large for the 4096-channel PHA, additional digital encoders will allow the PDP-5 to be used as a 6000-channel PHA.

The computer will be especially valuable in multiparameter experiments. In some of these experiments, the number of possible channels exceeds the capacity of any conceivable magmetic core memory, so that magnetic tape storage of each event has often been necessary, with sorting and analyzing being done after the experiment. The computer offers a much more attractive technique.[1] Since most of the data in many multiparameter experiments falls in a small fraction of the total number of possible channels, it is useful to let the computer assign core memory only to channels in which data are actually accumulating. This allows most of the data in even very complex experiments to be held immediately available for display and computation. If the core storage is still inadequate, any remainder can be put on magnetic tape.

A computer is of course especially convenient for arithmetic calculations, and FORTRAN programs have already been written to allow calculation of particle dynamics on the PDP-5. However, it is expected that the use of the PDP-5 as a control for input and output devices will be of more importance than its use as a calculator. Some complex computations will be made possible because of the easy communication between the experimenter and the machine, but in general the PDP-5 will be complementary to, rather than competitive with, the larger computing facilities at LRL.

Footnote and Reference

* Shortened form of UCRL-11458.

1. I. N. Hooton, Associative Storage for Nuclear Physics, EANDC Conference on Automatic Aquisition and Reduction of Nuclear Data, Karlsruhe, Germany, July 1964.

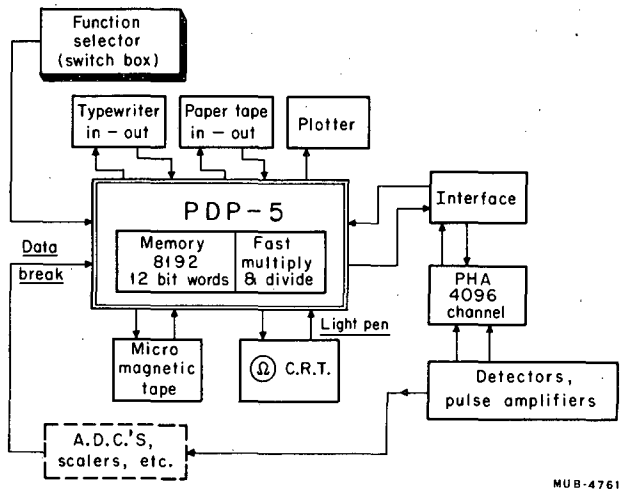

Fig. E.8-1. On-line computer installation at 88-inch cyclotron.

9. SILICON RADIATION DETECTORS

Robert P. Lothrop, Morris D. Roach, and Harry E. Smith

A. Diffused Silicon Devices

The major problem in the fabrication of diffused silicon devices is the control of surface states at the quartz-silicon interface. The original process used an accurately controlled gallium diffusion to effect control over the donors that appear at the interface.[1] During the past year, studies have shown that control over the surface states may be effected by the proper choice of the gaseous ambient during the end of the final high-temperature diffusion.[2] As a result, typical diffused devices no longer require a precisely controlled gallium diffusion, and may be fabricated with greater ease while high performance standards are maintained.

The fabrication process is as follows:

Wafers are sawed from suitable p-type silicon. The p+ back contact is made by diffusing boron, from a BI_3 vapor source, with the wafer at 1000°C in a reducing atmosphere. The boron-rich layer is removed from one surface and thermal quartz is grown in water vapor with the wafer at 1000°C and atmospheric pressure. The desired geometry is etched into the quartz layer and the wafers are phosphorus-diffused at 900°C. The phosphorus is predeposited briefly (30 sec) from oxygen saturated with $POCl_3$, and then, while the wafers are still at temperature, the ambient is changed to yield the desired surface states. Final fabrication steps are the painting of the quartz layer with silicone varnish, and the evaporation of gold contacts.

Typical detectors fabricated by this technique are:[3]

1. Natural alpha: 1000 to 5000 ohm-cm; p-type; 12 to 18 mm diameter, FWHM to 14 to 20 keV.
2. Fission fragment: 200 to 600 ohm-cm; p-type.
3. dE/dX: 300 to 5000 ohm-cm; p-type; 4 to 10 mils thick.

B. Lithium-Drifted Silicon Devices

The major problem in the fabrication of lithium-drifted devices is the control and protection of the exposed junction edges and intrinsic surface. During the last year a polyurethane

coating was found which, when used on properly prepared surfaces, yields devices with a long useful life and excellent characteristics. Work has also been carried out toward the development of quartz passivated devices and of devices with thin windows on both sides. Although the results show promise, they do not, as yet, meet present standards.

The development of an automatic lithium-drift apparatus[4] has made it possible to drift reproducibly to desired depths with 100% yield, requiring only a few minutes of operator time.

Typical lithium-drifted devices have the geometry shown in Fig.E.9-1 and are fabricated as follows: Wafers cut from p-type silicon are heated in high vacuum to 350°C, and lithium is evaporated onto one surface and diffused. The wafers are masked and etched to form a lithium mesa 14 mm in diameter, and gold is evaporated on the back side to form suitable contacts for drifting. The wafers are then drifted, lapped, and stained to assure that the sensitive diameter is no less than 12 mm. A well 0.003 in. deep is etched and a thin gold entrance window evaporated. Finally the exposed junction edges and intrinsic surface are washed and coated with polyurethane, and the device is evaluated.

Typical devices[3] fabricated by this process are 12 mm minimum in sensitive diameter, and range from 1/2 to 3 mm thick in 0.5-mm steps.

It is of interest to note that cooled 3-mm-thick detectors exhibit 3.2 keV line width for 60-keV gammas, and 4 to 5 keV for betas.

References

1. William L. Hansen, Frederick S. Goulding, and Robert P. Lothrop, Compensated-Surface Oxide-Passivated Silicon Junction Radiation Detectors, UCRL-10578, Dec. 1962.
2. R. Y. Deshpande, The Effect of Ambients on the Charge Density and Carrier Mobility in a Silicon—Silicon Dioxide Interface, UCRL-11419, May 1964.
3. Fred S. Goulding, A Survey of the Applications and Limitations of Various Types of Detectors in Radiation Energy Measurement, UCRL-11302, Feb. 1964.
4. Fred S. Goulding and W. L. Hansen, An Automatic Lithium Drifting Apparatus for Silicon and Germanium Detectors, UCRL-11261, Feb. 1964.

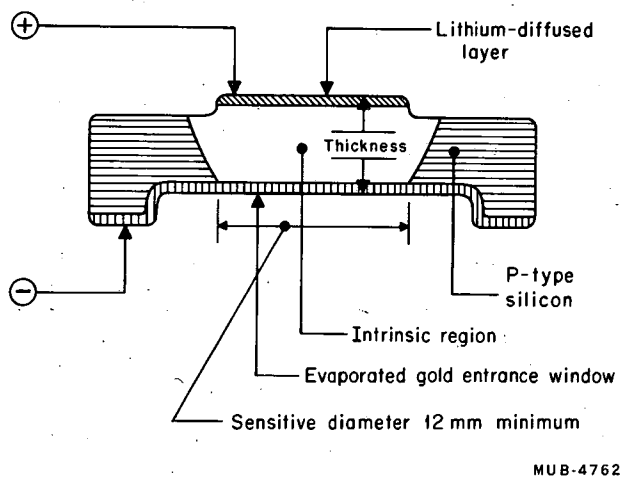

Fig.E.9-1. Lithium-drifted silicon device. Thickness: 0.5 to 3 mm in 0.5-mm steps.

10. SEMICONDUCTOR PROBE FOR INVESTIGATING ACCELERATOR BEAM PULSES*

H. E. Conzett, L. B. Robinson, and R. N. Burger

In the operation of the Berkeley 88-inch sector-focused (isochronous) cyclotron,[1] a knowledge of the phase of the beam with respect to the rf accelerating voltage has been important, both for reasons of theoretical interest and for diagnosis of machine operation. A determination of the radial variation of the phase of the circulating beam provides a measure of the degree to which the isochronous condition--that of maintaining constant phase throughout the acceleration process--has been achieved; these phase values can be compared with those calculated from measured or computed knowledge of the magnetic field. Also, these phase measurements provide the means through which trim-coil adjustments to the field can be made in order to best achieve the isochronous condition for the several different particles and many different energies available.[2]

Instruments used for this kind of measurement have typically been direct beam pickup probes with the pulses amplified and displayed on a sampling oscilloscope.[3] Such an oscilloscope samples a small part of each of a series of recurring pulses, and thus displays a pulse shape which constitutes an average over many separate pulses. Hence, detailed information on possible variations of beam intensity among different rf cycles, as well as within a single cycle, may be lost.

In order to circumvent these disadvantages, a probe has been designed which utilizes the favorable characteristics of the semiconductor detector,[4] namely, the fast charge-collection time ($\approx$ 1 nsec) and the inherent amplification provided by the formation of one electron-hole pair (in silicon) for each 3.6 eV of energy loss in the detector. For example, an 80-MeV α particle loses 4.9 MeV in traversing a 250-μ depletion region of a silicon detector, and so provides approximately 1.5×10^6 electron-hole pairs for collection. The large output pulse can be examined without amplification by a fast oscilloscope that does not require sampling.

Diffused silicon detectors with oxide-protected junction edges were used. All were made of high-resistivity silicon (4000 ohm-cm p-type) with phosphorus-diffused N^+ fronts and boron-diffused P^+ backs.[5] Detector thicknesses ranged from 100 to 250 μ, so that the detectors were fully depleted at bias voltages less than 200 V. All detectors used would support a bias voltage of 300 volts with a few μA of leakage current.

For a detector made of p-type material the calculated maximum collection time for a charge produced in the detector varies from 0.2 nsec for a detector 100 μ thick to 4 nsec for a thickness of 250 μ when the applied voltage is 200 volts.

To avoid the need for amplification, with the resulting increase in rise time, a detector 250 μ thick was mounted directly in the external cyclotron beam. A mechanical shutter allowed the beam to strike the detector for about 50 msec at 1-sec intervals. With a 33-MeV α-particle beam of the order of 0.1 μA average intensity, each beam pulse produced 10- to 20-nsec electrical pulses of about 10 volts amplitude across the detector load. The detector output appeared to vary linearly with beam intensity even at this high level. The pulses were displayed on a Tektronix 519 oscilloscope which had a calibrated rise time of 0.27 nsec for single pulses, but has only about 9 V/cm sensitivity.

Examples of the results obtained[6] are shown in Figs. E.10-1 and E.10-2. Figure E.10-1 displays the detector response to single beam pulses with the cyclotron oscillator set at the resonant frequency, f_0, and at nearby frequencies. These pulses can be compared and correlated with independently determined information on the distribution in phase of the internal beam pulses.[6,7] The pulses of Fig. E.10-1 were produced with a 250-μ detector operating with applied voltage just large enough to fully deplete it. The long tails on the pulses were probably caused by the long collection time for electrons produced near the back of the detector. Figure E.10-2 shows examples of some 60 to 70 beam pulses per oscilloscope sweep. Modulations of the beam over several to many rf cycles are apparent. Clearly, investigation of beam modulation with respect to variations of the cyclotron parameters will provide information useful to the operation and understanding of the machine.

The semiconductor detector has proved very useful in providing detailed information about the external beam of the Berkeley 88-inch cyclotron. It should be possible to adapt it for

use as an internal beam probe, also. Applications to beam monitoring or beam studies on other accelerators may be enhanced by such simple changes as, for example, scattering the beam from a target foil into the detector.

We are very indebted to Frederick S. Goulding and William L. Hansen for advice and assistence concerning the use of the Si detector, to Roy F. Burton and Donald R. Elo for the design of the probe assembly, and to Hermann A. Grunder and Frank B. Selph for providing us with examples of their results prior to publication.

Footnotes and References

* Shortened version of report in Nucl. Instr. Methods (to be published).
1. Elmer L. Kelly, Nucl. Instr. Methods 18, 19, 33 (1962).
2. H. A. Grunder and F. B. Selph, in Proceedings of International Conference on Sector-Focused Cyclotrons, CERN, May 1963, 63-19, p. 9.
3. Charles G. Dols, Nucl. Instr. Methods 18, 19, 595 (1962); W. H. White, Jr., B. Duelli, and R. J. Jones, Nucl. Instr. Methods 18, 19, 60 (1962).
4. G. L. Miller, W. M. Gibson, and P. F. Donovan, Ann. Rev. Nucl. Sci. 12, 189 (1962); Fred S. Goulding, Nucleonics 22, No. 5, 54 (1964).
5. William L. Hansen and Frederick S. Goulding, Oxide-Passivated Silicon p-n Junction Particle Detectors, UCRL-11227, Jan. 1964.
6. Hermann A. Grunder and Frank B. Selph, Operation of the 88-Inch Cyclotron, UCRL-11477, June 1964.
7. A. A. Garren and Lloyd Smith, reference 2, page 18.

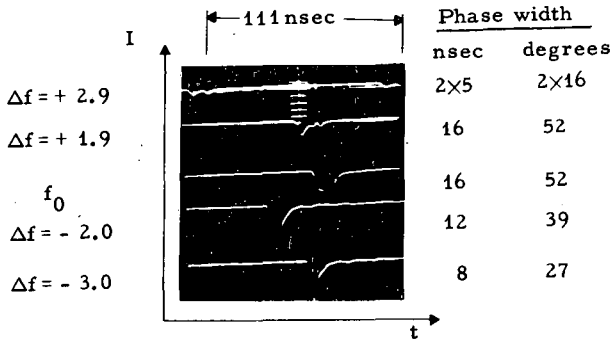

Fig. E.10-1. Detector response to external beam of 65-MeV α particles. The cyclotron resonant frequency was $f_0 = 8965.6$ kc/sec. Between successive single sweeps the only experimental parameter changed was the cyclotron oscillator frequency. Changes in pulse shape and width under small frequency changes, Δf, are clearly seen. For example, derived information on the beam phase width is indicated on the right. The oscilloscope sweep was not synchronized with the cyclotron oscillator.

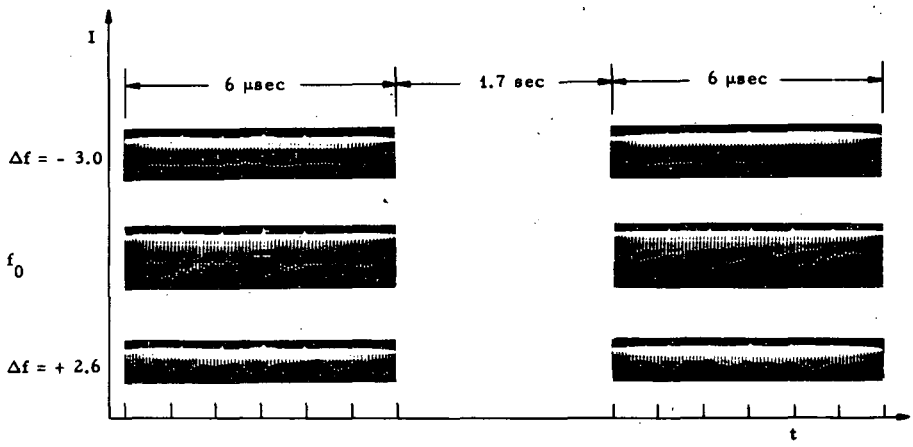

Fig. E.10-2. Detector response to external beam of 80-MeV α particles over 60 to 70 cyclotron rf cycles. The resonant frequency was $f_0 = 9986.6$ kc/sec. Changes in the beam modulation envelope under small frequency changes, Δf, are evident.

11. HEWLETT-PACKARD DIGITAL RECORDER MODEL 562A INSIGNIFICANT-ZERO SUPPRESSION

A. A. Wydler

Users of the Model 562A recorder have frequently expressed concern regarding their overlooking small amounts of data. The recorder prints columns of 0's when no data are present and also in all columns superior in value to that of the data. It is very easy to overlook the presence of 8's or 3's in a field of 0's. Eliminating the insignificant zeroes will overcome the difficulty and is applicable for use with pulse-height analyzers such as RIDL, Victoreen, or other equipment employing similar logic levels. To make such universal usage possible, this modification is installed within the cabinet of the digital recorder. Two circuit cards are inserted in spaces reserved for analog operation; total cost is less than $90. A switch mounted on one of these cards disables column 6 when analyzers of only 10^5 storage capacity are used.

A positive level on all input lines represents a BCD "0," some other character is produced when one or more lines are negative. Therefore an "AND" gate can be used to detect the presence of a "0." Each group of data (Fig. E.11-1) is capable of being inverted by a normally cut-off transistor controlled by its corresponding "AND" gate. These control transistors are operated in series to allow for suppression of 0's in order of descending significance. Because of the unique design of the circuit cards, any character may be substituted for a suppressed zero, i.e., dashes may be placed in one or more columns as an aid in aligning channel address with data, or a digit may be inserted to identify the particular machine producing the data. Commonly this identification is done in column 6.

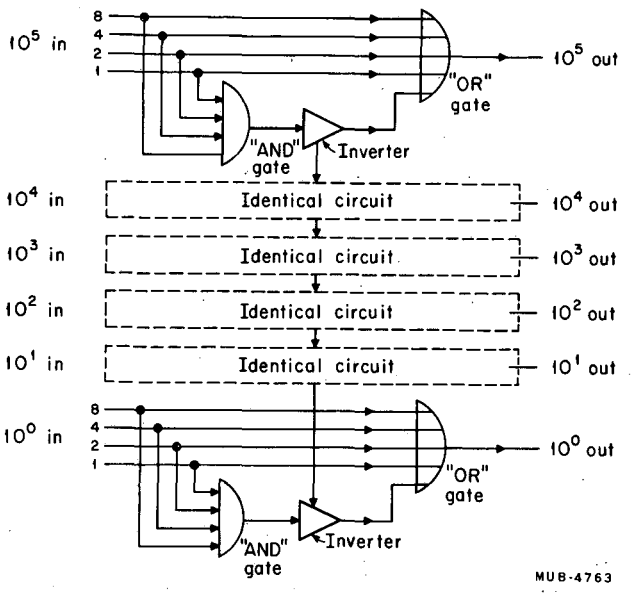

Fig. E.11-1. Circuit for suppressing insignificant zeroes.

12. HEWLETT-PACKARD DIGITAL RECORDER MODEL 562A MODIFICATION TO PRODUCE LEADER PAPER

A. A. Wydler

Frequently the Model 562A recorder is operated automatically and unattended to print accumulated data. A shortcoming of operating in this manner is that the end of print cycle "n" is adjacent to the start of "n + 1." This causes unnecessary difficulty in editing or rapid evaluation of the data.

Unfortunately, because of the mechanical design of this recorder, no simple method has been devised to remedy the above difficulty. However, for a moderate cost of less than $70 it is possible to insert automatically ten spaces between each group of data without interferring with previously programmed operations. If desired, a switch is included to disable this modification.

To accomplish this a circuit board is inserted in the normally unused column 12 position of the recorder. A reed relay on this board (Fig. E.12-1) interrupts the normal column reset return and prevents the retention of data. Upon receipt of a print command, a "POSITIVE INHIBIT" signal inverted and stretched by Q1 and Q2 is applied to Q3 and Q4, a Schmitt trigger. The reed relay closes and normal operation is resumed.

Receiving no print command for 0.5 sec, the stretcher discharges, restoring the Schmitt to its steady state. The reed relay opens and a positive trigger is generated at the collector of Q4. This trigger is delayed for 2 msec to insure the opening of the relay, and applied to Q7, Q8, and Q9. A negative "set" pulse from Q7 places all columns in the "blank" position. A 2-sec pulse from Q8 and Q9, through Q10, is then applied to the recorder clutch Flip-Flop, energizing the clutch solenoid, thereby producing leader paper.

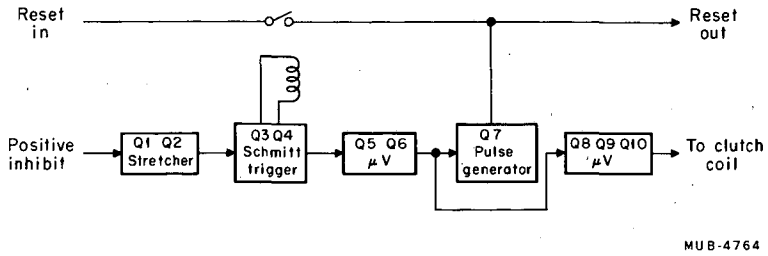

Fig. E.12-1. Arrangement of modification for producing leader paper.

13. INSTRUMENT DEVELOPMENT PROGRAM

W. W. Goldsworthy

Projects completed in the past year consist of the design of a high-performance transistorized linear amplifier having considerable application in high-resolution energy measurements, especially those employing semiconductor detectors; the design of a highly stable semilogarithmic amplifier system; and the packaging of several instruments into modular units.

Linear Amplifier in Modular Package

This is a versatile amplifier packaged in RIDL and National Lab standard modules which can be employed for nuclear or other pulse or complex wave amplification. Extreme flexibility is provided by the selectable differentiation, integrating, input polarity, and gain ranges. Integrating time constants of 0.05, 0.1, 0.2, 0.5, 1.0, 2.0, and 5.0 μsec; RC differentiation time constants of 0.5, 1.0, 2.5, 5.0, and 5k μsec; single line-shaping time constants of 0.2, 1.0, and 4.0 μsec; double line-shaping time constants of 0.2, 1.0, and 4.0 μsec; gains of from 1 to 400; and input polarity selection are all selectable with front panel controls.

Some additional features of this amplifier are its ±10-volt output, its 50-nsec rise time, and its ability to deliver a nonintegrated double-delay-line shaped crossover timing pulse output while delivering integrated single-or double-line differentiated pulses to pulse-height analysis circuitry.

The exceptionally rapid recovery from overload and high pulse rates, together with low noise contribution, greater flexibility, and excellent stability of this amplifier makes its use attractive in a wide variety of amplifying applications.

Semilogarithmic Amplifier System

(A paper on this subject was presented at the Eleventh Nuclear Science Symposium, held in Philadelphia on 28-30 October 1964. The IEEE Proceedings will contain this paper in full; an expanded abstract is given here.)

This report describes an amplifier system having the capability of compressing several-decade pulse-height ranges into several linear step gain ranges covering only a single decade.

Rather than employing the usual frequency, voltage, and temperature-dependent low-voltage semiconductor switching and conduction characteristics, this amplifying system utilizes the reproducible, easily calibrated, abrupt, high-level limiting characteristics of a transistor operational feedback amplifier.

The several cascaded stages of this amplifier, whose individual outputs drive a pulse adder, use these abrupt, high-level limiting characteristics to determine the boundaries between several well-defined linear step gain ranges as a function of pulse amplitude. The gain in each of these ranges is established by that gain available prior to the point where limiting occurs in the amplifier system.

Such an amplifying system has great application in the measurement of wide-range nuclear or other pulse-height spectra, where the relatively poor resolution uniformity of multi-channel analyzers dictates either an unreasonable number of available channels or some sort of compression amplifier. Figure E.13-1 displays a wide complex nuclear spectrum derived by employing the described semilogarithmic amplifier system.

The block diagram of a three-step compression amplifier using this principle is shown in Fig.E.13-2. Typical gain and output characteristics of the three-step ranges are expressed by the following relationships.

1. Range 1.

$$E_0 = K_t E_I (G_2 G_3 + G_2 + 1) \approx 0 - 3.3 \text{ V.}$$

(No limiting) $A_1 = G_2 G_3 + G_2 + 1.$

2. Range 2.

$$E_0 = K_t (E_I G_2 + E_1 + K_3) \approx 3.3 - 6.6 \text{ V.}$$

(Stage 3 limiting) $A_2 = G_2 + 1.$

3. Range 3.

$$E_0 = K_t [E_1 + 2K_3] \approx 6.6 - 10 \text{ V.}$$

(Stage 2 and 3 limiting) $A_3 = 1.$

Here E_0 = output voltage,
K_t = arbitrary gain constant of output stages,
E_1 = input voltage,
$K_3 = K_2 = 10$ = limiting voltage constant,
G_2 = gain, stage 2,
G_3 = gain, stage 3,
A_1 = differential gain, range 1,
A_2 = differential gain, range 2,
A_3 = differential gain, range 3.

The use of this amplifying system appears quite attractive for many types of wide-range high-resolution analysis, since it possesses qualities of good resolution uniformity, ease of calibration, stability, and reproducibility.

Modular Packaging

Several other instruments were designed into RIDL Designer Series modules. These instruments were to provide specific functions desired in an experimental program.

One such instrument provides for the simultaneous alpha-fission spectra display on a multichannel analyzer, where the lower 97% of the channels are employed for alpha spectra and the top 3% are employed for fission-count storage.

Another instrument, for the monitoring of elution columns, consists of a solid-state detector and amplifier followed by an integral and a differential rate meter. This instrument, which drives a multichannel recorder, is capable of providing simultaneous and continuous alpha-beta or alpha-fission monitoring while at the same time cataloguing elution sample number and number of drops per sample.

Also designed was a time-mode analyzer programmer employed for half-life studies. This instrument provides for a continuous time-interval stepping range, at from 250 μsec to 16 sec per step, allowing for an extremely wide range of half-life studies.

Aside from these instruments already discussed are those instruments in which existing designs were repackaged to conform with the modular concept. These consist of a single-channel analyzer, an expander amplifier, a dual pulse generator, and a dual detector bias supply.

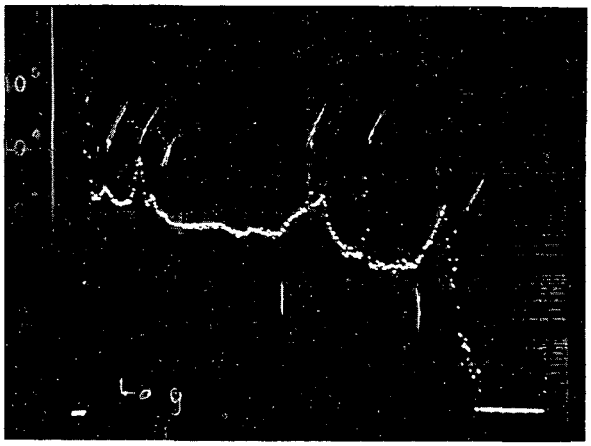

Fig. E.13-1. Spectrum derived by use of semilogarithmic amplifier system.

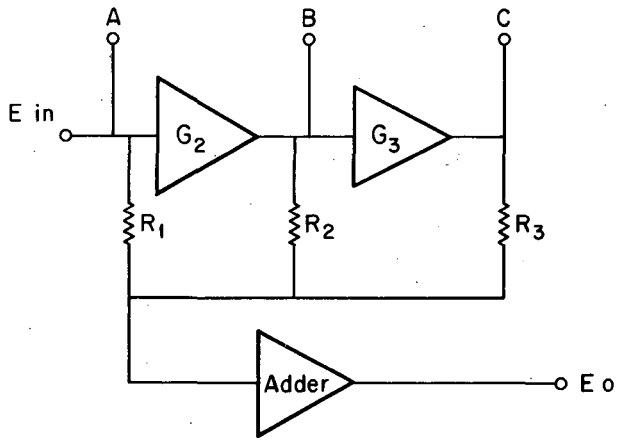

Fig. E.13-2. Block diagram of three-step compression amplifier.

14. AUTOMATIC SPECTROGRAM MEASURING AND RECORDING

Kenneth C. Ward and Michiyuki Nakamura

A spectrogram measuring and recording system for use with the Grant Instruments Spectrum Line Comparator is in use by the Optical Spectroscopy group.[1] The centers of the line images of the spectra are automatically detected and accurately located and then recorded on magnetic tape. The basic method of measurement is not new,[2-5] but reading of the spectra is more rapid than previously accomplished, the maximum rate being sixteen spectra per second. A computer program allows rapid evaluation of spectra data by comparison with reference

spectra. Tables of known spectra wavelengths have been reproduced within desired experimental accuracy.

The measuring and recording system consists of a Grant Comparator, an electronics network which stores information from the comparator, a Precision Instruments Incremental Tape Recorder which receives the stored information, and a computer program for reducing the data to tables of wavelengths.

Pertinent electrical components in the comparator are the following:

(a) photomultiplier with output signal proportional to spectra photo transmission;
(b) 18-binary-digit shaft position encoder which locates the comparator table position to within a micron;
(c) a dc motor for driving the comparator table at any of four constant speeds; and
(d) a dc-supplied 100-watt projection lamp.

A separate rack of diverse electrical trappings processes and records the signals from the comparator and provides dc power for the projection lamp and for the comparator drive motor. The photomultiplier signal is treated by a peak detector, a peak-height- or intensity-measuring device, and a spectrum line-width measuring circuit. The 18 digits of table-position information are transformed from Gray binary to conventional binary code, then stored in the memory upon command from the peak detector. An array of 24 binary-coded decimal thumb-wheel switches on the control panel places the spectrogram identification information on the tape. A programmer logic circuit automates the measuring and recording procedure. The identification information is recorded. Next, reference spectra of known wavelength are recorded. Then an adjacent spectrogram of unknown spectral wavelengths is scanned. This sequence of data constitutes one file on the tape, and is the unit of information upon which the computer operates.

The reference spectra wavelengths are punched on IBM cards and fed to the computer with the tape. A least-squares linear fit of comparator table position versus wavelength is then computed by operating on the taped reference-spectra center locations. By use of this calibration of table position, wavelengths are then assigned to each of the unknown spectra.

The apparatus has proven useful when a large number of spectra must be measured to the accuracy mentioned. Scanning a spectrogram is rapid, a 10-inch plate requiring two minutes for each traverse. Desired accuracy has been achieved. Measurement of wavelengths of thorium, with nine thorium lines on the same spectrogram used as reference, showed that

(a) spectra center measurements may be reproduced to within one micron on the spectrographic plate,
(b) measured values of wavelength agree with tabulated values[6] within 0.0008 Å (average of absolute values of errors).
tographic films.

This instrument has also been used to measure x-ray diffraction photographic films.

References

1. LRL drawing numbers 13X1100 through 13X1199.
2. G. R. Harrison, Automatic Measurement, Reduction and Recording of Wavelengths from Spectrograms, J. Opt. Soc. Am. 25, 169-178 (1935).
3. G. R. Harrison, Photoelectric Measurement of Spectrum Lines, J. Opt. Soc. Am. 30, 343-347 (1940).
4. D. W. Steinhaus, Photoelectric Comparator for Wavelength and Intensity Measurements of Spectra, J. Opt. Soc. Am. 49, 468-470 (1959).
5. David Steinhaus and Rolf Engleman, Automatic Comparator for Measurement of Line Spectra, J. Opt. Soc. Am. 53, Abstract FA15, p. 1349 (1963).
6. W. F. Meggers and Stanley, Wavelengths from Thorium Halide Lamps, J. Res. N. B. S. 61, 95-103 (August 1958).

15. AN ELECTRICALLY CONTROLLED VARIABLE-GAIN PULSE AMPLIFIER USING DIFFERENT CONTROLLING ELEMENTS†

Helenio Arque Almaraz*

The ideal solution to the problem of automatically controlling the gain of an amplifier is the all-electric gain control, in which an electrical signal controls the gain of the amplifier.

A two-transistor amplifier, with the emitter resistance of the second transistor employed as the gain control element, is analyzed in the original article (UCRL-11481). Different types of variable-resistance control elements are considered and typical circuits utilizing the variable resistance elements are given. Figure E.15-1 shows a variable-gain amplifier utilizing a field-effect transistor (FET) as the variable resistance element. With the FET biased at 0 V_{ds} (drain-source voltage), the useful drain-source resistance range of the FET varies from 900 ohms at 0 V_{gs} (gate-source voltage) to 2.1 kΩ at 1.6 V_{gs}. The FET is capable of following V_{gs} variations at a 100-kc rate. The incremental linearity of the variable resistance is better than 0.08%. The amplifier shown in Fig. E.15-1 is capable of accepting ±1 volt input pulses with gain-change capabilities of ±21%.

An important application for the electrically controlled variable-gain amplifier is in system-gain stabilization. Many system stabilizers control the overall gain of the system by altering the high voltage of multiplier phototubes or proportional counters. This technique is not applicable to systems using semiconductor detectors. The semiconductor counters used for fission-fragment, x-ray, and particle detection must be operated at a bias voltage at which charge-collection efficiency is constant, but not in a region where leakage current increases abruptly.

It was shown that an electrically controlled variable-gain pulse amplifier inserted between the preamplifier and the main amplifier was the answer to semiconductor detector-system stabilization. This inserted amplifier is a self-contained unit that can be added to existing systems without disturbing or changing its components. This method can also be applied to detector systems that use multiplier phototubes or proportional counters.

Footnotes

† Short version of paper (UCRL-11481, June 1964) submitted to Nucl. Instr. Methods.
* Now at Instituto Venezolano de Investigaciones Cientificas, Caracas, Venezuela.

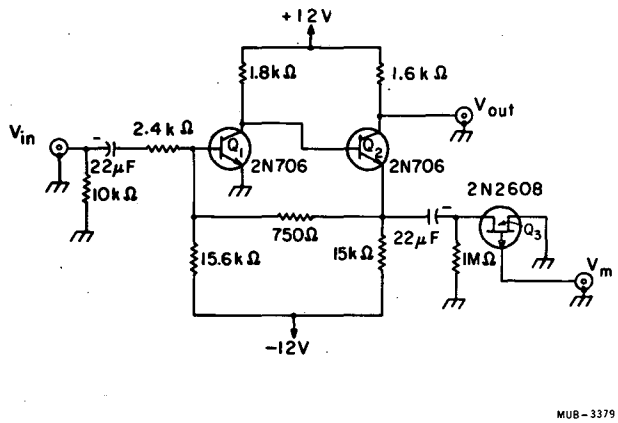

Fig. E.15-1. Two-transistor variable-gain amplifier utilizing a 2N2608 field-effect transistor as control element.

16. A TEMPORARY PULSE-STORAGE UNIT†

Helenio Arque Almaraz*

The problem of storing pulses for short periods is present in many systems dealing with nuclear-particle detection. A unit capable of storing pulses for periods up to 1 msec, without any appreciable loss of relative pulse amplitude, could be the answer to the problem. The temporary pulse-storage unit (stretcher) built at this Laboratory meets this requirement.

A description of the temporary storage unit, which utilizes a capacitor-type storage device, electronic switches, and conventional timing circuits, is given in the original report (UCRL-11539).

Two models of the temporary pulse-storage unit have been built at this Laboratory. One uses a peak detector to obtain the reference for the timing circuits, the other model receives its timing reference from a zero-crossover double-delay-line circuit. In both models very stable multivibrators are used in the timing circuits, otherwise temperature instabilities cause time jitter and a resultant degradation in the resolution of the overall system. Energy resolutions better than 0.1% are reported for systems that use the temporary pulse-storage unit.

Footnotes

† Short version of paper (UCRL-11539, July 1964) submitted to Nucl. Instr. Methods.
* Now at Instituto Venezolano de Investigaciones Cientificas, Caracas, Venezuela.

17. A DIGITAL GAIN STABILIZER FOR A MULTIPARAMETER PULSE-HEIGHT-RECORDING SYSTEM†

Michiyuki Nakamura and Richard L. LaPierre

A method for stabilizing semiconductor-detector systems, and hence realizing the full resolution of the detector, has been developed.

The basic system concepts, as well as a mathematical analysis of the stabilizer's properties, have been reported by Ladd and Kennedy.[1] The digital stabilizer divides the region of any selected peak of a multichannel analyzer spectrum into two segments. Counts occurring in the lower segment of the selected peak add counts to the contents of a reversible scaler, whereas counts occurring in the upper segment subtract counts from the scaler's content. As the position of the peak shifts owing to gain changes, the relative counting rates of the two segments change, thus producing a net increase or decrease of the reversible scaler's contents. A digital-to-analog converter generates a control voltage which is proportional to the contents of the reversible scaler.

We have used this control voltage to operate a variable-gain amplifier[2] inserted between the preamplifier and the main linear amplifier of our stabilized system.

A limitation in any system similar to the one described by Ladd and Kennedy is the large number of interconnections and switches needed for a flexible system. It can be shown that in order to use, for example, three channels on either side of a peak for stabilization, four decimal switches plus six toggle switches might be required.

Unless we took a different approach to selecting a peak and the number of channels to either side, our control panel would become formidable and contribute to operator errors, particularly since we would be stabilizing four parameters simultaneously.

We therefore used a null detection scheme for detecting and sorting pulses that fall within the neighborhood of a reference peak. The significance of this approach is manifested by the simple control panel used to introduce stabilization. A photograph of our control panel for stabilizing four parameters (dimensions) is shown in Fig. E.17-1. The operator dials in the channel location of the reference peak with the group of three selected channel decimal

thumb-wheel switches. The other decimal switch, labeled ± window width, selects the number of channels adjacent to the peak to be included for stabilization. The stabilization trigger switch permits stabilization on a peak in the spectrum (self) or on a specially introduced reference peak (coinc).

During the past year the stabilizer has been used primarily in the study[1] of the gamma-ray spectra resulting from the spontaneous fission of Cf^{252}.[3] Stability of peak channel numbers to 0.1% or better is obtained over extended periods of time without significant loss in resolution. The ability of the stabilizer to eliminate system drifts allows the experimenter to combine results from similar experiments conducted at different times. As long as similar detectors are used, compatible results are obtained by using the same selected channel and window-width numbers for the stabilizing peak. The gain of the system, and hence the results, are duplicated by the stabilizer's holding of the reference peak at the same address location.

We have just completed the check of our prototype model of a general-purpose stabilizer for use with any analyzer. This general-purpose stabilizer utilizes integrated circuits. The chief advantages of this model will be its compactness and the price savings realized over the cost of discrete components. The circuitry is laid out on six printed-circuit boards which are approximately 5×7 in.

Footnote and References

† Short version of paper (UCRL-11494, June 1964) submitted to Nucl. Instr. Methods.

1. J. A. Ladd and J. M. Kennedy, A Digital Spectrum Stabilizer for Pulse Analyzer Systems, Chalk River Project Report CREL-1063, Dec. 1961.
2. Helenio Arque Almaraz, An Electrically Controlled Variable-Gain Pulse Amplifier Using Different Controlling Elements, UCRL-11481, June 1964.
3. H. R. Bowman, S. G. Thompson, and J. O. Rasmussen, Gamma-Ray Spectra from Spontaneous Fission of Cf^{252}, Phys. Rev. Letters 12, 195 (1964).

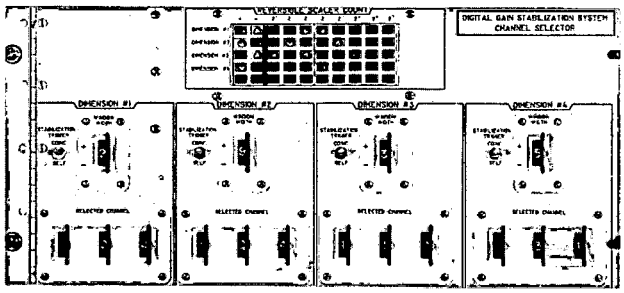

Fig. E. 17-1. Control panel used for stabilizing four parameters (dimensions).

18. 88-INCH CYCLOTRON OPERATION AND DEVELOPMENT

Hermann A. Grunder,* Frank B. Selph, Hogil Kim, Elon Close, and David J. Clark

General Development

Development of new beams and facilities has proceeded at the 88-inch cyclotron during the past year. Three particles are now available to the experimenters: protons from 10 to 50 MeV, α particles from 25 to 130 MeV (including D and H_2^+ at half these energies), and He^3 from 20 to 80 MeV. As each new beam is developed, all machine settings are recorded, and measurements are made on beam parameters such as internal phase width, virtual source positions, and emittances for extracted beam. For most of the beams, reference settings have been obtained in steps of 5 MeV or less. Development to April 1964 is given in a previous report.[1]

The experimental facilities of the 88-inch cyclotron are shown in Fig. E.18-1. Beams used by the experimenters are delivered to the five caves by the beam-transport system.

The machine runs three 8-hour shifts per day, 7 days a week. Isotope production is carried out in the high-level cave (HLC), using about 20% of the cyclotron time. Nuclear chemistry and physics in other caves use about 40%. Biomedical groups use Cave 3 for about 4%. The remainder of the scheduled time, 36%, is used for beam development, and for scheduled maintenance and repairs.

Cave 1 beams have the best energy resolution, about 0.15%, with the switching magnet, Ms, used for energy analysis. Cave 5 contains the polarized proton beam, produced by α particles incident on a hydrogen target.

Several mechanical and electrical improvements have been incorporated during the past year. A persistent leak was located at a sleeve gasket where the ion source comes down through the magnet. Its repair reduced the tank pressure from 33×10^{-6} mm to 7×10^{-6} mm. This improves the operation of dc and rf voltage electrodes. Another improvement was the replacement of magnetic components in the rf tuning panels by nonmagnetic material. This reduced the heating above 14 Mc/sec. The deflector septum will handle 2 kW of beam power at the extraction radius. A water-cooled copper septum is being developed to increase this capability.

Some internal-beam foil burns were made to study the vertical profile of the beam near the extraction radius (see Fig. E.18-2). They show the beam to be slightly above the center line of the machine. The vertical extent of the beam is 0.25 to 0.5 in. The increase in vertical height between 38 and 39 in. is due to the passage through the coupling resonance: $\nu_r = 2\nu_z$.

A water-cooled dummy dee has been installed, as shown in Fig. E.18-3. This electrode is at ground potential and is opposite the dee in the center region. It concentrates the accelerating electric field of the dee. This will improve the third-harmonic mode of acceleration, which is useful for low energies and heavy ions. It is also one component in a future system for injecting the beam axially through the magnet.

Phase Width and Energy Spread of External Beam

A silicon particle detector[2] was used to observe external beam pulses. The signal of about 10 volts could be used to observe individual pulses on a Tektronix 519 oscilloscope. The signal could also be used to feed a sampling oscilloscope to show the average pulse shape. Figure E.18-4 shows the 519 display of pulses at frequencies near resonance. At frequencies below resonance the lagging part of the beam is favored and the leading edge of the pulse is clipped off by phase loss. Above resonance, more leading beam appears, giving a phase width of more than 50 deg. Further above resonance the beam is clipped. The 519 display of the external beam is again shown in Fig. E.18-5 over a longer time interval. The beam is modulated at about 0.5 Mc/sec on resonance. By moving off resonance slightly it is seen that the modulation is mainly in the leading part of the beam, while the lagging part is stable. This may be due to arc instability affecting the first part of a pulse.

An external beam pulse is shown on a sampling oscilloscope in Fig. E.18-6. The beam is 65-MeV α particles. Measurements were made at the same time on the energy spread of this beam with a solid-state detector. The energy spectrum is shown in Fig. E.18-7. The measurement was made in Cave 2 with no energy-analyzing slit. The cyclotron was tuned by use of valley coils, frequency, and dee voltage. The energy spectrum of Fig. E.18-7 has the best energy resolution obtained on this type of run, about 240 kV full width at half maximum. Various beam-pulse shapes and energy spreads were obtained for different tuning conditions. The beam pulse and energy spectrum for another tuning condition are shown in Figs. E.18-8 and E.18-9. Figure E.18-8 shows the beam pulse with two peaks in time (or phase). The corresponding energy spectrum in Fig. E.18-9 shows two energy peaks, with an overall spread of some 800 kV. The figures show that small changes in tuning can cause large changes in the phase distribution and energy spread of the external beam. The cause of these changes is believed to be the change in radial precession phase and amplitude of the beam entering the electrostatic deflector. The best energy resolution appears to coincide with a single peak in the phase distribution.

Regenerative Deflector Design and Construction

A program is under way for the installation of an electrostatic regenerative extraction system on the 88-inch cyclotron. The regenerative extraction method has been used widely for synchrocyclotrons and also for the Birmingham 40-inch cyclotron. This method increases the turn separation by a resonant excitation of the radial betatron motion. It is expected to reduce

the heating of the septum and increase the extraction efficiency. In addition to this, it has been proved that the method may give better energy resolution. The regenerator does this by extracting the high-energy component of the beam more quickly and delaying the low-energy component.

With the successful operation of the Birmingham 40-inch cyclotron electrostatic regenerative beam extractor[3] used as a guide, the possibility of designing a regenerative beam extractor for the 88-inch cyclotron was investigated theoretically. Analytically it has been proved that for the 88-inch cyclotron a regenerator positioned at a valley-to-hill boundary gives the best regenerative action, while one positioned at a hill-to-valley boundary gives the worst regenerative action. This has been checked numerically by using suitably modified existing orbit codes whose magnetic field input is based on a reconstruction of fields used in actual developed beams. However, after consideration of the external beam line and the final deflection problem, it was decided to place the center of the regenerator at 90 deg, the center of a valley. One of the best results of these computer studies is shown in Fig. E.18-10. For a given dee voltage, one-half of the 0.5-in. square of phase space has a turn-to-turn separation of 0.040 in. at extraction radius. Instability in the vertical motion does not occur until after the extraction radius. In actual operation, a spread in rf phase of the beam produces a spread in energy gain per turn; therefore one should overlap figures such as Fig. E.18-10. The extraction efficiency should be more than 50%, while the energy spread will be 0.1 to 0.2%.

A model regenerator was constructed by the 88-inch cyclotron engineering group. The regenerator is 24 in. long, curved to match the equilibrium orbit, and the spacing of the electrodes is 2.5 to 3.0 cm. It is the same size as the final regenerator. The model was simplified mechanically to allow a preliminary regeneration test without a deflector. Figure E.18-3 shows the arrangement. A ΔR probe was used to obtain turn-separation measurements in the cyclotron. One of the results of these measurements is given in Fig. E.18-11. Clear regenerative action can be seen from this figure. Current collected by the outer electrode of the ΔR probe indicates that the necessary 0.2-in. turn separation has been obtained at the expected regenerator voltage. Having shown the practicality of a regenerative extraction system for the 88-inch cyclotron, we are now in the process of fabricating the complete system, and it is expected that this will be available in the spring of 1965.

The new deflector will have three sections instead of two. This will allow some adjustment of the virtual radial source position by changing voltages on the end sections in opposite directions. A test on this steering method was made with the present two-section deflector. With an 80-MeV α beam the source could be moved 0.2 in. by this method. This can be useful in moving the virtual radial sources of all particles and energies to a common point for good external beam optics.

Footnote and References

* Present address: University of Basel.

1. Hermann A. Grunder and Frank Selph, Operation of the 88-Inch Cyclotron, UCRL-11477, June 1964.
2. H. E. Conzett, L. B. Robinson, and R. N. Burger, Semiconductor Probe for Investigating Accelerator Beam Pulses, UCRL-11492, June 1963.
3. H. Kim, G. H. Mackenzie, W. B. Powell, and P. J. Waterton, in Proceedings of an International Conference on Sector-Focused Cyclotrons, CERN, April 1963, p. 73.

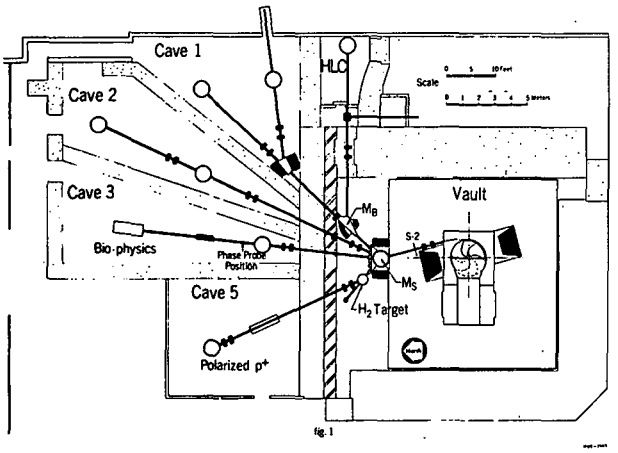

Fig. E.18-1. 88-inch cyclotron and experimental area.

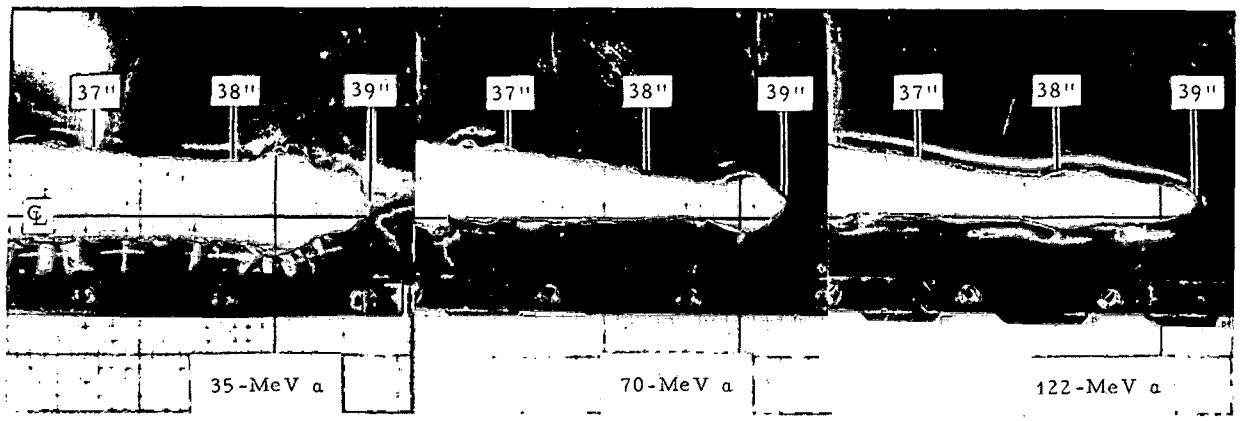

Fig. E.18-2. Internal beam profiles as shown by foil burns.

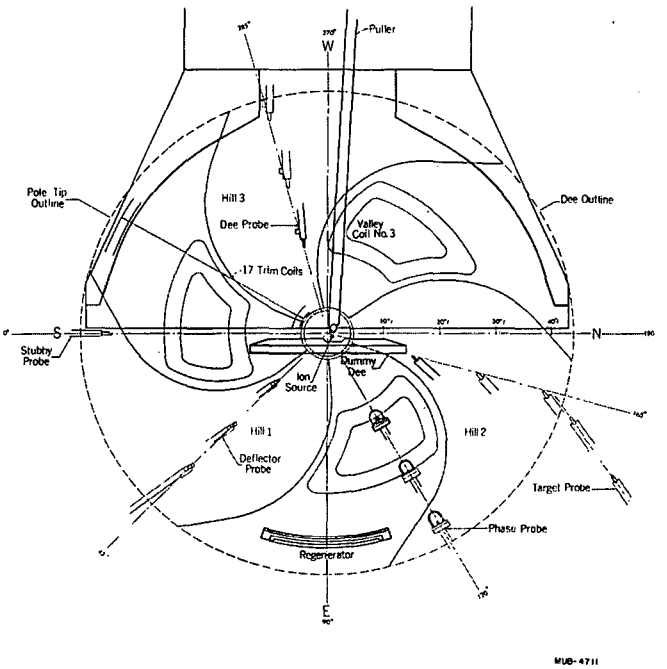

Fig. E. 18-3. 88-inch cyclotron internal beam region, showing regenerator test arrangement.

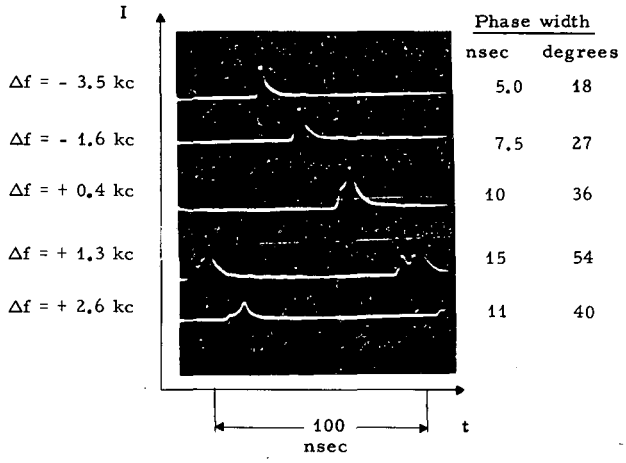

Fig. E.18-4. External beam pulses on 519 scope; 80-MeV α particles at frequencies near resonance.

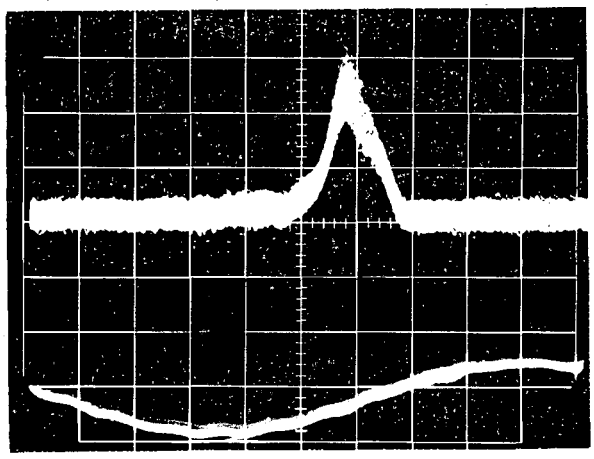

Fig. E.18-6. External beam pulse on sampling scope; 65-MeV α particles.

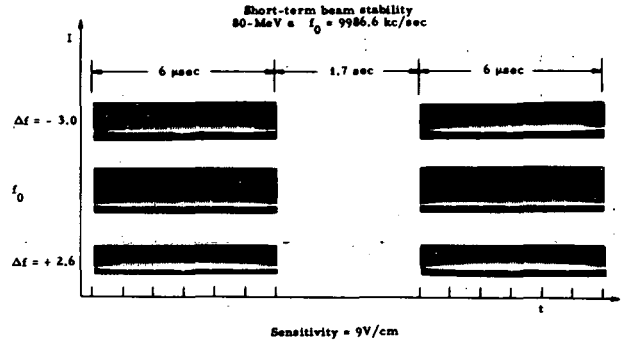

Fig. E.18-5. External beam pulses on 519 scope, showing short-term stability; 80-MeV α particles at frequencies near resonance (f_0 = 9986.6 kc/sec). Sensitivity = 9 V/cm.

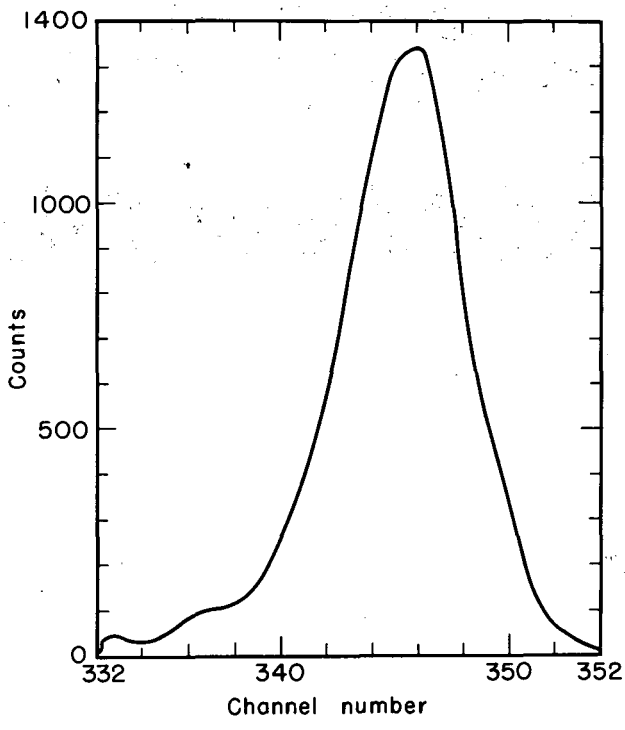

Fig. E. 18-7. Energy spectrum of unanalyzed external beam. Conditions the same as for Fig. E. 18-6.

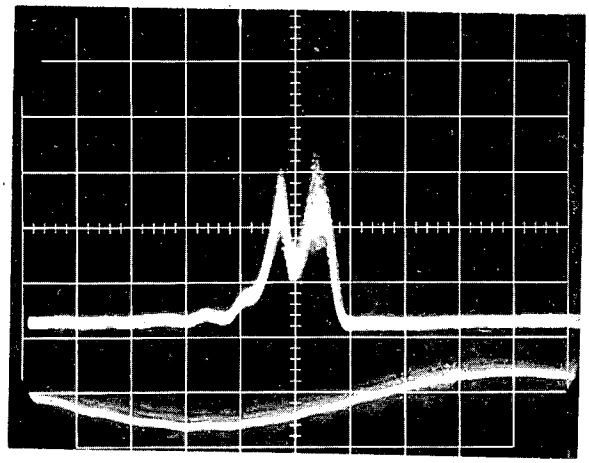

Fig. E.18-8. External beam pulse on sampling scope; 65-MeV α particles.

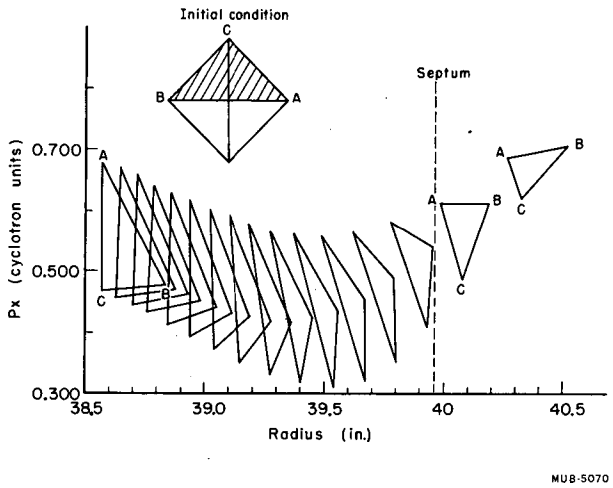

Fig. E.18-10. Computed radial-motion phase plot, for successive turns at 21 deg azimuth showing turn separation produced by regenerator. Regenerator at 90 deg azimuth, starting at 37.2 in. radius.

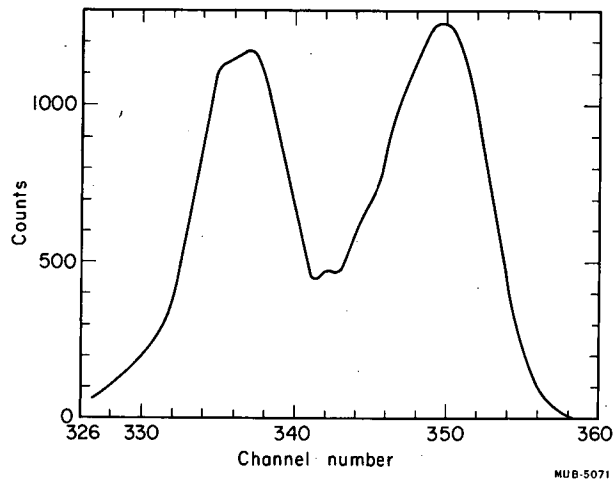

Fig. E.18-9. Energy spectrum of unanalyzed external beam. Conditions the same as for Fig. E.18-8.

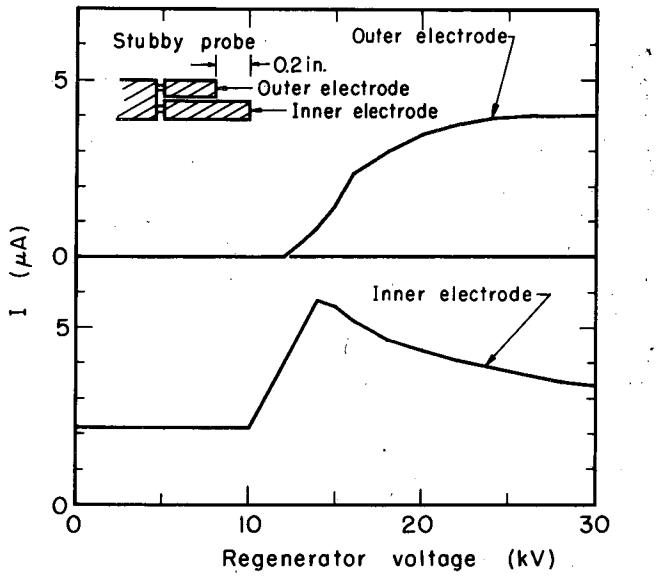

Fig. E. 18-11. Experimental measurement (with "stubby probe") of turn separation during regenerator test; 40-MeV α; probe position, 3 deg azimuth at 39.3 in. radius; dee voltage 45 kV. When current is collected by outer electrode, turn separation is greater then 0.2 in.

F. CHEMICAL ENGINEERING

1. THE ELECTROMAGNETIC LEVITATION OF METALS†

Peter R. Rony*

A variety of subjects connected with the electromagnetic levitation of metals has been considered. A complete theoretical description of the phenomenon is given, leading to the basic equations for the lifting force and power input for a metal sphere levitated in an inhomogeneous sinusoidally alternating magnetic field,

$$\frac{\vec{F}}{W} = -\frac{3G(x)}{2\rho\mu_0}(\vec{B}\cdot\nabla)\vec{B},$$

$$P = \frac{3\pi R\, H(x)}{\sigma\,\mu_0^2}(\vec{B}\cdot\vec{B}),$$

where

$$x = R\left(\frac{1}{2}\omega\mu\sigma\right)^{1/2},$$

ρ is the metal density, σ is the electrical conductivity, μ is the permeability, and R is the radius, B is the magnetic-field strength, ∇ is the vector del operator, and ω is the radian frequency of the magnetic field. G(x) and H(x) are shown in Figs. F. 1-1 and F. 1-2.

Both the force and power cannot be simultaneously controlled with the current-control knob of an induction heater. The suspended metal is suitably controlled either by operating at lower frequencies and supplying additional heat with an electron beam, plasma-arc torch, high-frequency induction heater, or reflection furnace, or by operating at high frequencies and employing high-thermal-conductivity gases such as hydrogen and helium to cool the metal.

Values indicating the ease of levitation of 1-cm-radius spheres of more than 50 different metals at 0°C and at their respective melting points are given (Fig. F.1-3). When frequencies in the 10- to 100-kc/sec range are used, the density of the metal chiefly determines the ease of levitation. Refractory, semiconducting, or dielectric materials can be levitated either by heating them to high temperatures to decrease their electrical resistivity or by coating a light and inert metal of high melting point with the material to be studied.

Liquid sodium surrounded by a mineral oil of almost identical density can be used to study the magnetic-field distribution of levitation coils. Liquid mercury can be used to determine the ability of levitation coils to suspend high-temperature liquid metals.

Although the use of this technique with large commercial quantities of liquid metals appears discouraging, the levitation of long rods or plane sheets of liquid metals does appear to be feasible, provided that these configurations are not dynamically unstable.

More attention should be given to the improvement of commercial levitation equipment through the use of variable frequencies, solid-state circuits, and high-permeability magnetic core materials with low losses. The ideal levitation power supply would have a variable frequency for the range of 500 cps to 50 kc/sec, a decade capacitor bank, and the capability of producing a square of sine-wave alternating magnetic field up to several kilogauss over a 75 cm^3 volume.

Footnotes

† Abstract of UCRL-11411, May 1964, presented at the seventh Annual Vacuum Metallurgists Conference held June 29 through July 1, 1964 in New York City and sponsored by the Vacuum Metallurgy Division of the American Vacuum Society.

* Present address: Monsanto Company, St. Louis, Missouri.

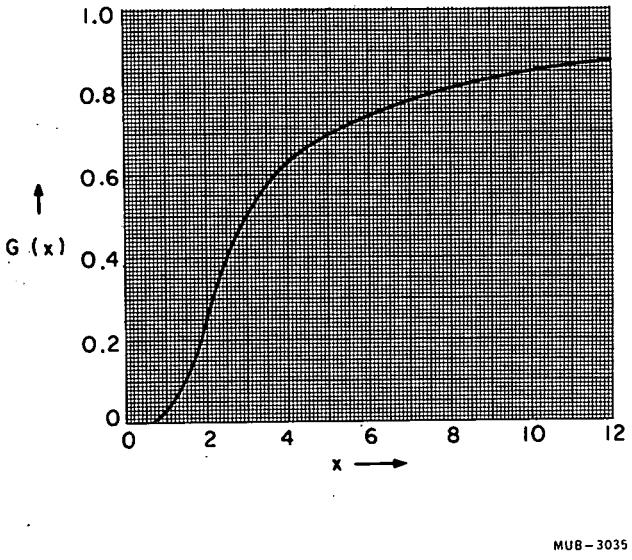

Fig. F.1-1. G(x) plotted as a function of x (high values of x), where

$$G(x) = 1 - \frac{3}{2x}\,\frac{\sinh 2x - \sin 2x}{\cosh 2x - \cos 2x}\,.$$

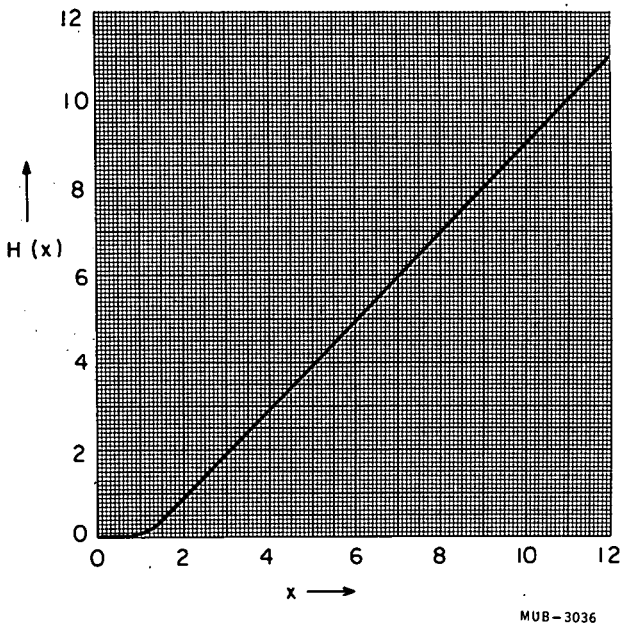

Fig. F.1-2. H(x) plotted as a function of x (high values of x), where

$$H(x) = \frac{x(\sinh 2x + \sin 2x)}{\cosh 2x - \cos 2x} - 1\,.$$

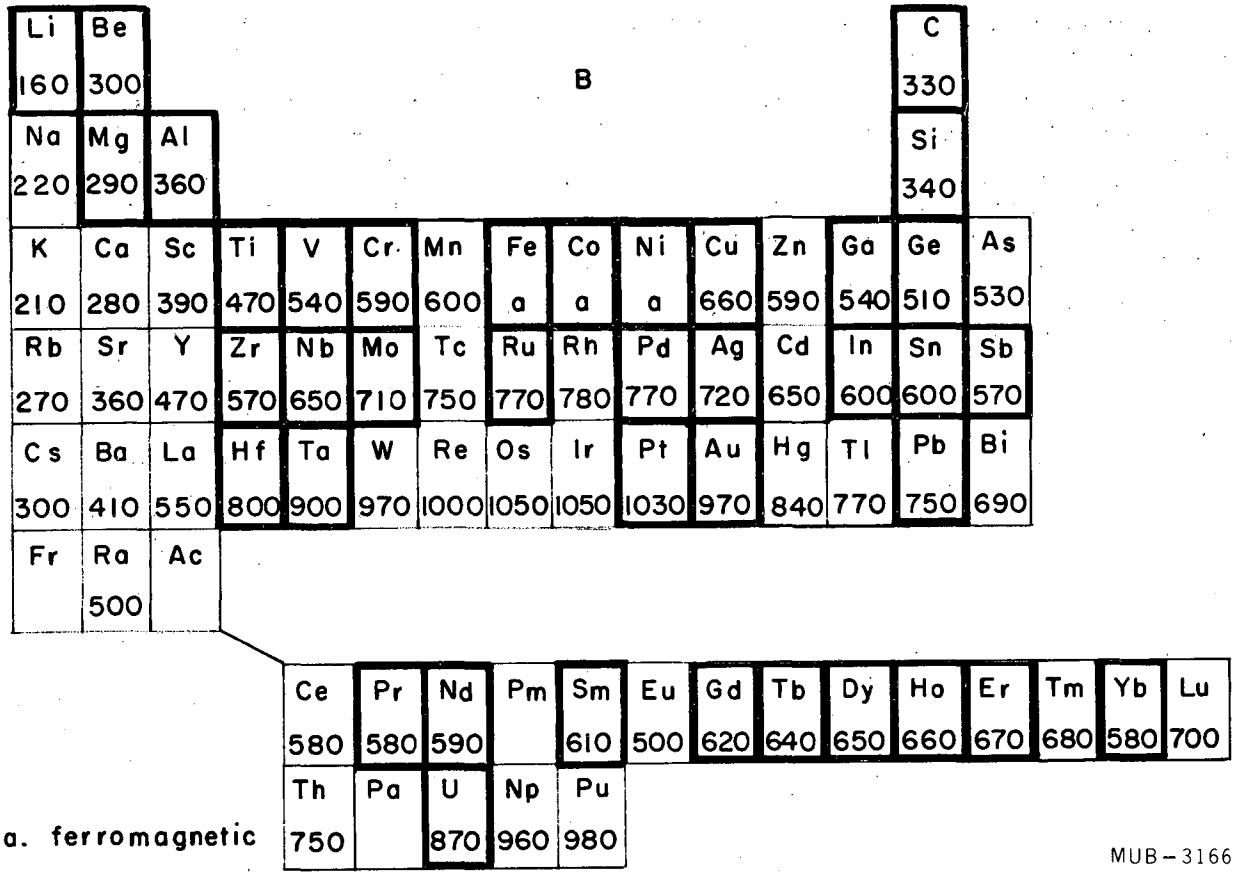

Fig. F.1-3. The elements in the dark boxes have been levitation melted. The figures are the approximate values of the magnetic field (in gauss) required to levitate solid metal spheres of 1-cm radius at 0°C when G(x) = 1.

2. EFFECT OF INERT GAS CONCENTRATION IN TURBULENT GAS-PHASE MASS TRANSFER IN PIPES†

D. T. Wasan* and C. R. Wilke

The study is concerned with steady-state mass transfer in vaporization of a liquid (or solid) A from the wall of a tube over a transfer section of finite length Z_L. A binary mixture consisting of varying amounts of diffusing species A and inert gas B enters with a fully developed velocity distribution as shown in Fig. F.2-1. Component A is maintained at a constant concentration (vapor pressure) at the wall over the entire section. To simplify mathematical treatment of the process, mass transfer is assumed to occur by diffusion and correction in the radial direction and by correction in the axial direction. With the foregoing assumptions the turbulent diffusion-convection equation for species A may be written as

$$V_z \frac{\partial p_A}{\partial z} = \left[D + E(r)\right] \frac{\partial^2 p_A}{\partial r^2} + \left[\frac{D + E(r)}{r} + \frac{\partial E(r)}{\partial r}\right] \frac{\partial p_A}{\partial r} + \left(\frac{D + E(r)}{P - p_A}\right) \left(\frac{p_A}{r}\right)^2 . \quad (1)$$

For the solution of Eq. (1), velocity V_z and eddy diffusivity E (assumed equal to the eddy viscosity) are obtained as a function of radial position from relations developed previously.

Equation (1) is put into dimensionless form and solved numerically by a four-point explicit method with a rectangular network. In the numerical solution there are obtained concentration profiles, local mass-transfer coefficients and Stanton numbers over a range of distances down the pipe, partial pressures of inert gas B, Schmidt numbers, and Reynolds numbers. Average Stanton numbers based on the log mean mass transfer driving force are computed separately from the concentration profiles. Details of the computation procedure are described elsewhere.[2]

Figure F.2-2 shows the typical variation of the local Stanton number with downstream distance. A significant difference between the terminal Stanton number and the log mean average value is obtained for the pipe of length equal to approximately 18 diameters. The terminal Stanton number closely approaches the result predicted by the authors' analogy treatment.[3] Similar results were obtained over a range of Schmidt numbers from 0.2 to 2.5.

Figure F.2-3 shows the variation of the log mean average Stanton number with the concentration of inert gas B for several Schmidt numbers over a tube 17.7 diameters long. The major conclusion is that the Stanton number is independent of the inert gas concentration. Previous experimental evidence on this point has shown much uncertainty and disagreement among various studies, probably in large part because of the extreme difficulty of obtaining accurate measurements at low mol fractions of inert gas. It is believed the present computer simulation of the problem provides a definitive answer.

Notation

A	diffusing species
B	stagnant species
C_A	molar concentration of species A
C_{A_W}	molar concentration of species A at the wall
C_{avg}	averaged molar concentration of species A
d	diameter of a pipe
D	molecular diffusivity
E	eddy diffusivity
k_c	$N_A/(C_{A_W} - C_{avg})$, mass transfer coefficient based on molar concentration difference
N_A	molar flux of species A in the radial direction
N_{A_W}	molar flux of species A at the wall
P	total pressure
p_A	partial pressure of species A
p_{A_i}	partial pressure of species A in the inlet
p_{A_W}	partial pressure of species A at the wall
r	radial distance
R	radius of pipe
U	time-averaged mass velocity in axial direction
U_0	averaged velocity
V	time-averaged molar velocity in the radial direction
V_r	radial velocity
V_z	time-averaged molar velocity in z direction
X_f	film pressure factor or log mean volume fraction of inert species B between bulk stream and the wall
Z	axial direction
Z_L	length of pipe
ν	kinematic viscosity
Re	Reynolds number $U_0 d/\nu$
Sc	Schmidt number ν/D
St	Stanton number $k_c X_f/U_0$

Footnotes and References

† Based on UCRL-11629, September 1964.

* Present address: Chemical Engineering, Illinois Institute of Technology, Chicago, Illinois.

1. D. T. Wasan, C. L. Tien, and C. R. Wilke, A. I. Ch. E. J. 9, 567 (1963).
2. D. T. Wasan and C. R. Wilke, UCRL-11629, September 1964.
3. D. T. Wasan and C. R. Wilke, Intern. J. Heat Mass Transfer 7, 87 (1964).

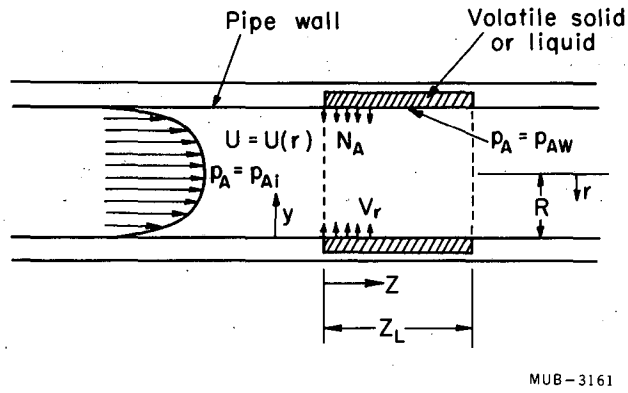

Fig. F.2-1. Schematic diagram of the diffusion-convection model.

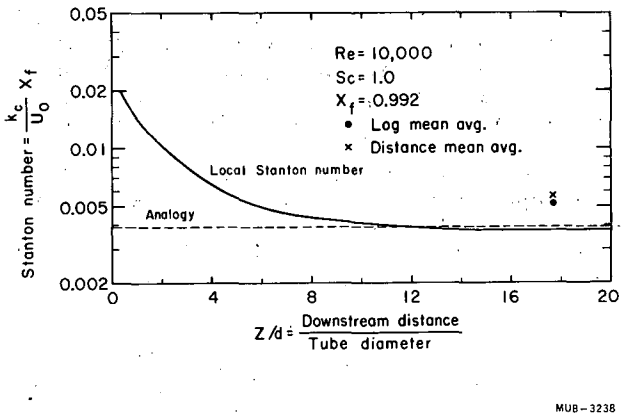

Fig. F.2-2. Variation of Stanton number with downstream distance at Sc = 1.0.

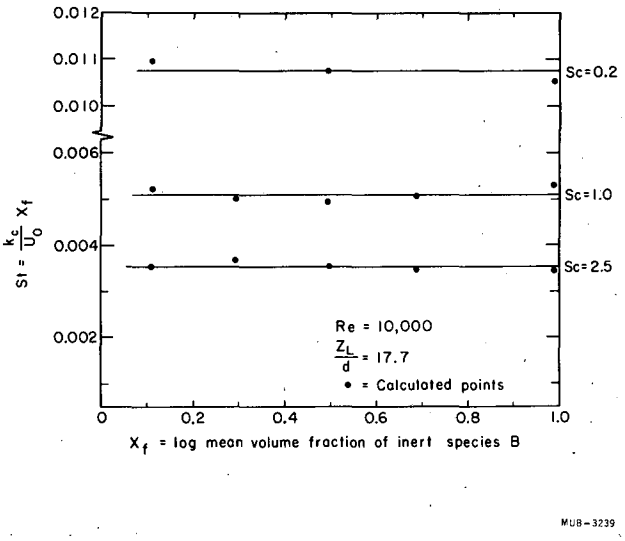

Fig. F.2-3. Effect of inert gas concentration on transfer coefficient for $Z_L/d = 17.7$.

3. MEASUREMENT OF THE VELOCITY OF GASES IN A FIELD OF VARIABLE COMPOSITION AND TEMPERATURE†

Robert M. Davis, D. T. Wasan, and C. R. Wilke

An experimental study is undertaken to observe the effects of mass transfer on the fully developed turbulent velocity field in a pipe. Water is vaporized from the wetted walls of a short cylindrical section. A hot-wire anemometer is used to measure the time-averaged velocity distribution (velocities ranging from 0.2 to 6 feet per second) of a gas stream with variable composition and temperature which flows through the pipe.

The conventional theory for hot-wire anemometry is extended to include the effects of natural and forced convection on gases having variable fluid properties. An appreciable effect of gas composition and free convection on the hot-wire calibration is predicted as shown in Fig. F.3-1. Experimental observations appear to substantiate the theoretical analysis, which indicates a divergence from the linear relationship between $\sqrt{u}$ and $I^2R_w/\Delta t$ at very low velocities.

With the modified hot-wire anemometer technique velocity measurements were taken for fully developed air flow into a short section of porous pipe 7.5 in. in diameter and 24 in. in length. For measurements with mass transfer the walls were wetted with water at 25°C and 50°C. Mass transfer rates varied from 1.0×10^{-6} g mol/cm^2-sec to 5.0×10^{-6} g mol/cm^2-sec. In other tests the walls were dry. Reynolds numbers ranged from 9000 to 17 000 in the study.

Figure F.3-2 shows the measured velocities in relation to the generalized correlation developed by Wasan, Tien, and Wilke.[1] No appreciable effect on the velocity distribution appears to result from the mass transfer in the range of conditions of the study. The measurements are in good agreement with the generalized correlation in the region very near the wall.

Notation

g_c	conversion constant	$\frac{\text{ft - lb}}{\text{lb - force sec}}$
I	electrical current flowing through wire	(mA)
R_w	wire resistance	(ohms)
u	fluid velocity	(ft/sec)
u_τ	friction velocity = $\sqrt{\tau_w g_c/\rho}$	(ft/sec)
y	distance from pipe wall	(ft)
Δt	temperature difference between wire and gas	(°F)
ν	kinematic viscosity	(ft^2/hr)
ρ	fluid density	(lb/ft^3)
τ	shear stress	(lb/ft^2)
u^+	dimensionless velocity (u/u_τ)	
y^+	dimensionless distance (yu_τ/ν)	

Footnote and Reference

† Based on UCRL-11552, Aug. 1964.

1. D. T. Wasan, C. L. Tien, and C. R. Wilke, A. I. Ch. E. J. 9, 567 (1963).

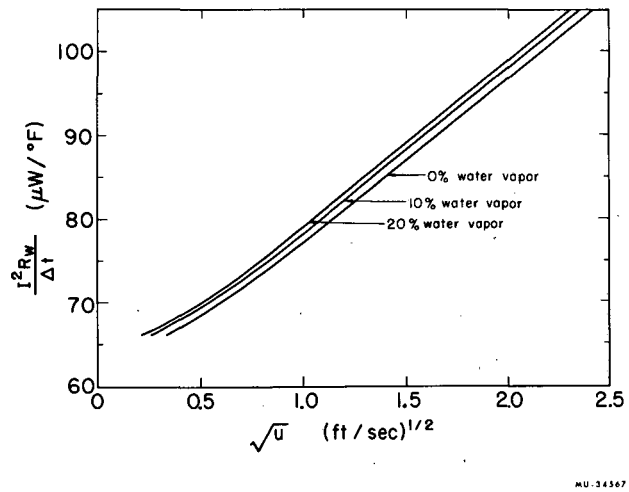

Fig. F.3-1. Effect of water vapor on hot-wire anemometer calibration curve for air according to theory. Wire diameter = 0.00025 in.; wire length = 0.10 in.; wire mean film temperature = 152°C.

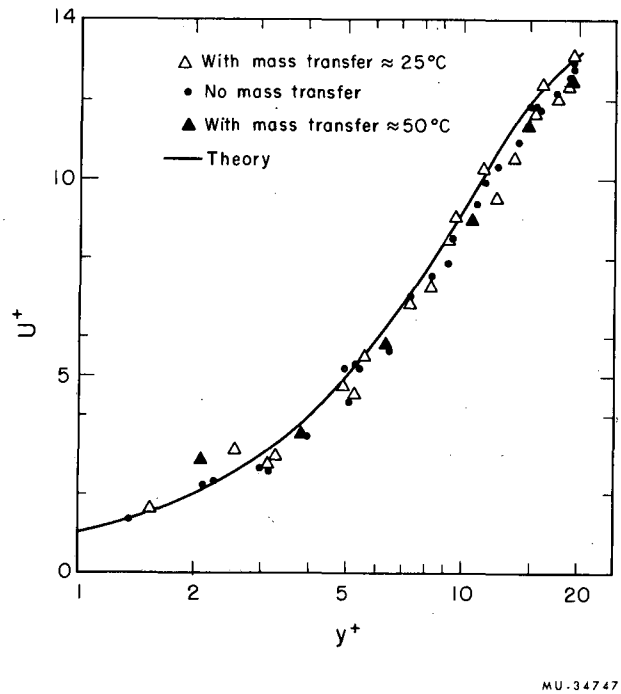

Fig. F.3-2. Comparison of velocity distribution measurements with and without mass transfer with the generalized correlation (reference 1).

4. A NEW CORRELATION FOR THE PSYCHROMETRIC RATIO†

C. R. Wilke and D. T. Wasan

The wet bulb thermometer is considered to be a long cylinder placed perpendicular to the gas stream. The absorbent wick or covering of the bulb is saturated with a liquid phase corresponding to a vapor whose composition in the gas stream is to be measured. Since the gas stream is unsaturated with respect to the vapor, liquid evaporates from the bulb with an accompanying cooling effect. A dynamic equilibrium between the rates of heat and mass transfer to and from the bulb may be expressed in terms of the psychrometric ratio β:

$$\beta = \frac{k_g p_{Bm} M_m C_p}{h_c^*} = \frac{(t_g - t_s)(1+a)\gamma M_m p_{Bm} C_p}{M_v \lambda_s (p_g - p_s)}. \qquad (1)$$

The present analysis applies the same framework of equations as used in the authors' analogy treatment for mass and heat transfer in pipes[2] to the wet bulb problem. In this approach the Stanton numbers may be expressed as

$$St_h = \frac{h_c^*}{GC_p} = \frac{C_h}{1 + [F(Pr) - 13.0]\sqrt{C_h}} \qquad (2)$$

and

$$St_m = \frac{k_g M_m p_{Bm}}{G} = \frac{C_m}{1 + [F(Sc) - 13.0]\sqrt{C_m}}, \qquad (3)$$

where F(Sc), F(Pr) = numerical functions of Schmidt and Prandtl numbers tabulated in reference 2; C_m and C_h are assumed equal in the present case.

The psychrometric ratio may be expressed as a ratio of the Stanton numbers:

$$\beta = \frac{1 + [F(Pr) - 13.0]\sqrt{C_h}}{1 + [F(Sc) - 13.0]\sqrt{C_h}}. \qquad (4)$$

In Eq. (4) it is assumed that the effective drag coefficient is for skin friction in flow over cylinders and that the Prandtl and Schmidt number functions are those developed for pipe flow and tabulated elsewhere.

Equation (4) is applied to existing wet bulb data in the following manner. From the extensive correlation of McAdams[3] for heat transfer between air streams and cylinders values of C_h are computed for various Reynolds numbers from Eq. (2). The resulting relation between C_h and Reynolds number is shown in Fig. F.4-1. With the drag coefficients of Fig. F.4-1 the psychrometric ratio may be computed at various Prandtl, Schmidt, and Reynolds numbers by Eq. (4). Existing wet bulb data for systems of essentially constant Prandtl number (mainly air streams) are compared in Fig. F.4-2 with the results predicted by Eq. (4). It is noted that the data agree well with the theoretical expression for high velocities, but that the theory predicts a significant dependence of β on Reynolds number. Experimental evidence suggests that β is independent of gas velocity.

To obtain a simple practical relation for β, the drag coefficient for $Re = 10^5$ and simple power-function approximations for F(Sc) and F(Pr) are substituted in Eq. (4) to give

$$\beta = \frac{1 + 0.7(Pr^{0.77} - 1)}{1 + 0.7(Sc^{0.77} - 1)}. \qquad (5)$$

Equation (5) predicts the data shown in Fig. F.4-2 with an average deviation of 7.0%.

Notation

C_h	effective skin friction drag coefficient under heat transfer	P_g	partial pressure of the vapor in the gas stream, atm
C_m	effective skin friction drag coefficient under mass transfer	P_{Bm}	log mean of the inert partial pressure, atm
C_p	heat capacity of the gas stream, Btu/lb - °F	t_g	dry bulb temperature, °F
F	functional notation	t_s	wet bulb temperature, °F
G	gas stream mass velocity, lb/hr - ft^2	α	radiative heat transfer corrective term
h_c^*	conductive heat transfer coefficient in absence of mass transfer, Btu/hr - ft^2 - °F	β	psychrometric ratio defined by Eq. (1)
		γ	convective heat transfer corrective term
k_g	gas-phase mass transfer coefficient, lb - mol/hr - ft^2 - atm	λ_s	latent heat of vaporization per lb basis, Btu/lb
M_m	mean molecular weight of the gas stream, lb	Pr	Prandtl number $C_p\mu/k$
M_v	molecular weight of the diffusing vapor, lb	Re	Reynolds number dU_0/ϕ
p_s	partial pressure of vapor at the surface, atm	Sc	Schmidt number ν/D
		St_h	heat-transfer Stanton number h_c^*/C_pG
		St_m	mass-transfer Stanton number $k_gP_{Bm}M_m/G$

Footnotes and References

† Summary of paper to be presented at joint meeting of A. I. Ch. E. and Institution of Chemical Engineers, London, June 1965; based in part on UCRL-11629, Sept. 1964.

1. D. T. Wasan, C. L. Tien, and C. R. Wilke, A. I. Ch. E. J. 9, 567 (1963).
2. D. T. Wasan and C. R. Wilke, Intern. J. Heat Mass Transfer 7, 87 (1964).
3. W. H. McAdams, Heat Transmission (McGraw-Hill Book Co., Inc., New York, 1942), p. 221.

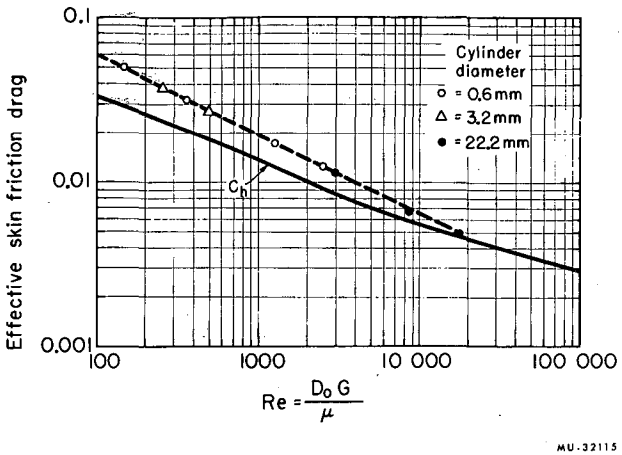

Fig. F.4-1. Variation of effective frictional drag with Reynolds number.

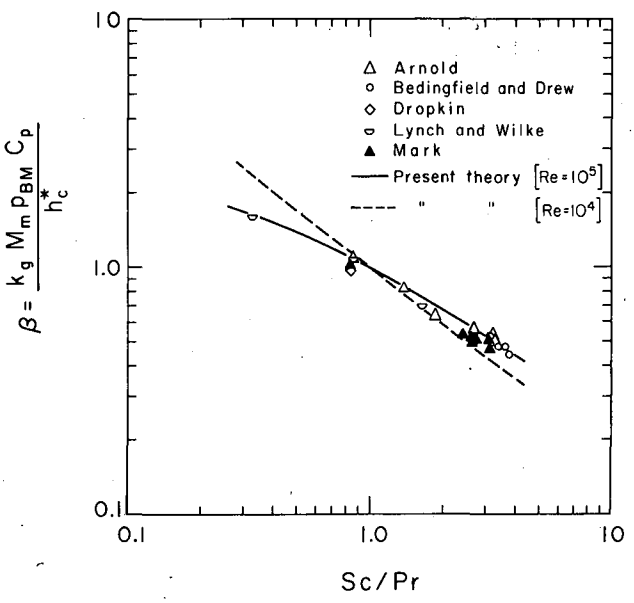

Fig. F.4-2. Comparison of proposed equation for the psychrometric ratio with the experimental data.

5. GAS-LIQUID MASS TRANSFER IN COCURRENT FROTH FLOW†

J. M. Heuss, C. J. King, and C. R. Wilke

Gas-liquid mass transfer processes are often carried out in equipment providing counter- or cross-current flow; however, cocurrent flow is just as suitable when equilibrium is not closely approached between the product streams or where one stream is not altered substantially in composition. Also, flooding does not occur in cocurrent operation.

At high flow rates and for liquid-to-gas flow ratios that are equal volume or higher, two-phase gas-liquid flow in a pipe occurs as a stable froth. The visible high degree of agitation and high throughputs suggest that the froth flow regime should be highly effective for mass transfer. Heat transfer in two-phase flow is also of considerable interest. There is an analogy between heat and mass transfer in individual phases. For mass transfer it is possible to measure individual phase coefficients--something which is not possible in heat transfer studies.

The apparatus shown in Fig. F.5-1 was employed for the measurement of rates of absorption of oxygen and ammonia from air into water during froth flow. Test sections of various lengths were employed and samples of bubble-free liquid were withdrawn slowly from taps at the wall. Ammonia contents of water samples were measured by electrical conductivity cells, while oxygen contents were monitored with polarographic cells.

Pressure-drop measurements were also obtained. Data taken over sections of different lengths indicated that the pressure drop per unit length became constant quite rapidly, thus verifying stable flow in the test sections. Pressure-drop data were analyzed by means of the Bankoff homogeneous flow model.[1] A better correlation was obtained through use of $U_{hom} = \frac{L+G}{\rho_L (1-\alpha) + \rho_G \alpha}$ as a mean velocity instead of $U_{tp} = \frac{L}{\rho_L} + \frac{G}{\rho_G}$, as has been employed previously. L and G are liquid and gas flow rates, respectively (lb/hr ft^2); ρ_L and ρ_G are liquid and gas densities (lb/ft^3); and α is void fraction. U_{hom} is more closely related to the velocity of the liquid phase, which carries the bulk of the kinetic energy.

The ammonia absorption data proved to be almost entirely gas-phase-controlled, and yielded as a correlation

$$k_G a = 0.016\, a^{2\pm 0.3}\, U_{hom}^{\,3.2\pm 0.2}, \qquad (1)$$

where k_G is the individual gas-phase mass-transfer coefficient (lb moles/hr ft^2 atm) and a is interfacial area (ft^2 per ft^3 of flow volume). Bubble size distributions may be estimated from the photographic data of James and Silberman.[2] The interfacial area for spherical bubbles is

$$a = 6a/d_{SV}, \qquad (2)$$

where

$$d_{SV} = \sum_i N_i d_i^{\,3} / \sum_i N_i d_i^{\,2}, \qquad (3)$$

with N_i being the number of bubbles with diameter d_i per unit volume. The absolute magnitude of $k_G a$ in Eq. (1) is in agreement with a model postulating transient molecular diffusion within spherical bubbles. The exponent on U_{hom} indicates that $d_{SV} \approx U_{hom}^{-1.6}$, which is in agreement with the photographic observations of James and Silberman and the previous findings of Vermeulen et al.[3] for dispersions in a rapidly stirred vessel. Equation (1) indicates that $k_G \approx a$, which may be due to a breakup effect at high voidage.

For oxygen absorption it was found that

$$k_L a \approx U_{hom}^{4.1\pm 0.25}\, a^{-2.0\pm 0.25}. \qquad (4)$$

With use of the estimate of d_{SV} from the ammonia results, a was removed from $k_L a$. The resulting dimensionless equation for k_L is then

$$\left(\frac{k_L d_{ds}}{D_L}\right) = 0.0316 \left(\frac{2R_p U_{hom} \rho_L}{\mu_L}\right)^{0.9} \left(\frac{1}{a}\right)^3, \qquad (5)$$

where

$$d_{ds} = \sum_i N_i d_i^{\,2} / \sum_i N_i d_i, \qquad (6)$$

μ_L is liquid viscosity, D_L is liquid diffusivity, and R_p is pipe radius. The Schmidt group should also be included to some power for a general correlation, but the dependence was not measured in this study. The exponent on the Reynolds group is typical for characterization of the turbulence level in flow processes. The exponent on the voidage may indicate a damping effect upon turbulence in the liquid at high void fractions.

For both phases the mass transfer rate increases faster than does the throughput, so that the length of a transfer unit decreases as the residence time decreases. This is an unusual situation in mass transfer, and results primarily from bubble size effects. As the turbulence level is increased, k_L is increased. The average bubble size is also decreased, which serves to increase both the interfacial area and k_G and also serves to increase k_L further.

Footnote and References

† Submitted to A. I. Ch. E. J.; condensation of UCRL-11570, Aug. 1964.

1. S. G. Bankoff, Trans. A. S. M. E. 82, 265 (1960).
2. W. James and E. Silberman, University of Minnesota Technical Paper No. 26, Series B, 1958.
3. T. Vermeulen, G. M. Williams, and G. E. Langlois, Chem. Eng. Progr. 51, 85F (1955).

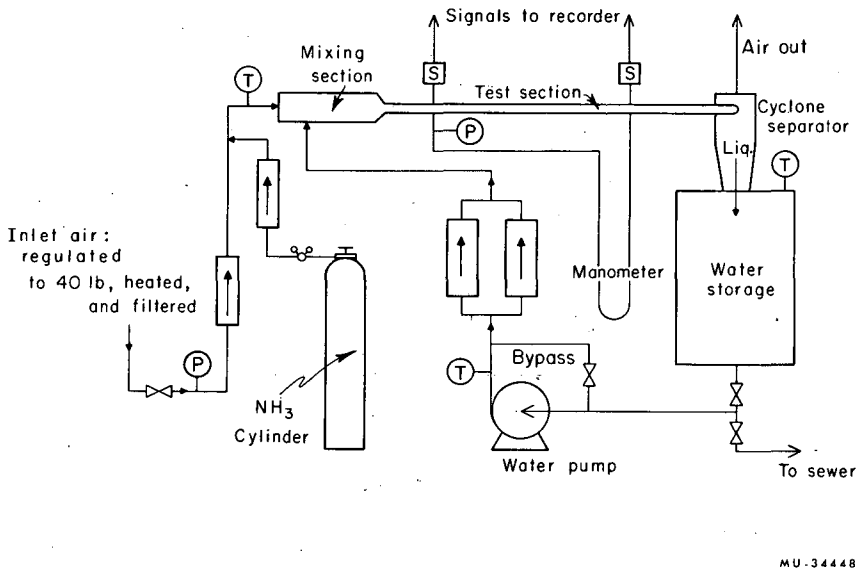

Fig. F.5-1. Apparatus used to measure absorption rates.

G. THESIS ABSTRACTS

On the following pages the abstracts of theses issued in 1964 are given as they appeared in the original documents.

Papers elsewhere in this report cover work described in theses by:

Robert M. Davis (M. S.)	Paper F.3
Jon M. Heuss (M. S.)	Paper F.5
Richard M. Levy (Ph.D.)	Paper A.21
Tatzuo Ueki (M. S.)	Paper D.10
Darshanlal T. Wasan (Ph.D.)	Paper F.2

1. SPINS OF Gd^{153}, Dy^{159}, AND Pm^{148} AND HYPERFINE STRUCTURES OF Pm^{148} AND Er^{165}

Dolores E. Ali
(Ph.D. Thesis)

(From UCRL-11536)

Ground state nuclear spins of Gd^{153}, Dy^{159}, and Pm^{148} have been measured by the atomic-beam magnetic-resonance flop-in method. The spins and nucleon state assignments are

Gd^{153}	Dy^{159}	Pm^{148}
$I = 3/2$	$I = 3/2$	$I = 1$
$3/2+\|651\rangle$	$3/2-\|521\rangle$	$g_{7/2}(f_{7/2})^{-3}_{5/2}$

The spin of Er^{165} was also verified to be $I = 5/2$.

The hyperfine-structure interaction constants, a and b, of Pm^{148} and Er^{165} have also been measured by this method. The results are

Pm^{148} $(I = 1)$	Er^{165} $(I = 5/2)$
$a = +1038(75)$ Mc	$a = \pm 195(6)$ Mc
$b = -98(103)$ Mc	$b = \mp 3502(115)$ Mc
	$b/a < 0$.

From the measured interaction constants of Pm^{148} and Er^{165}, the nuclear magnetic dipole moments (μ_I) and electric quadrupole moments (Q) have been inferred to be

Pm^{148}	Er^{165}
$\mu_I = +2.07(21)$ nm	$\mu_I = \pm 0.652(29)$ nm
$Q(\text{uncorr}) = +0.246(251)$ b	$Q(\text{uncorr}) = \pm 2.22(9)$ b
	$Q/\mu > 0$

Only the uncorrected quadrupole moments are given because the Sternheimer shielding has a large uncertainty. The magnetic moment of Pm^{148} was calculated from the $\langle 1/r^3 \rangle$ value, $4.87/a_0^3$, and the measured dipole interaction constant. The Fermi-Segre formula and the direct measurement of the magnetic moment of Er^{167} were used to calculate the dipole moment of Er^{165}.

These experiments have established the sign of the magnetic moment of Pm^{148} to be positive. Also, the electronic g_J for the $J = 7/2$ level of promethium has been measured, and this value when combined with the data for Pm^{147} and Pm^{151} gives a weighted mean of $g_J = -0.8278(1)$.

The spins of Gd^{153} and Dy^{159} and the moments of Er^{165} serve as a test of the collective-model predictions for the nuclear properties of deformed nuclei. The Pm^{148} measurements are consistent with the shell-model predictions for the spin and moments of this odd-odd nuclide.

2. THE RADIO-FREQUENCY AND MICROWAVE SPECTRA OF LiBr AND LiI

Francis William Breivogel, Jr.
(Ph.D. Thesis)

(From UCRL-11665)

The molecular-beam electric-resonance method has been used to obtain the radio-frequency and microwave spectra of Li^6Br^{79}, Li^6Br^{81}, and Li^6I^{127} and the radio-frequency spectrum of Li^7Br^{79}. Values were obtained for the quadrupole coupling constants and spin-rotation constants for Br^{79} in Li^6Br^{79} and Li^7Br^{79}, for Br^{81} in Li^6Br^{81}, for I^{127} in Li^6I^{127}, and for Li^7 in Li^7Br^{79}. The molecular electric dipole moment was measured for Li^6Br^{79} and Li^6Br^{81} in the $v = 0$, 1, and 2 states, for Li^6I^{127} in the $v = 0$ and $v = 1$ states, and for Li^7Br^{79} in the $v = 0$ state. For Li^6Br^{79} and Li^6Br^{81} values were obtained for Y_{01}, Y_{11}, and Y_{21}. Values for Y_{01} and Y_{11} were obtained for Li^6I^{127}.

A new computer program was written to interpret the spectra obtained. This program took into account second-order quadrupole effects and the Stark-quadrupole interaction.

An attempt was made to correlate the ionic polarizabilities of the alkali halides with the experimental dipole moments using an ionic model.

3. A SOLVENT EXTRACTION STUDY OF PROTON SOLVATION

Teresa Jean Conocchioli
(M. S. Thesis)

(From UCRL-10971)

The extraction of $HClO_4$ and HNO_3 into dilute solutions of tri-n-octyl phosphine oxide (TOPO) in carbon tetrachloride and nitrobenzene is studied, and the nature of the extracting species is determined. In the extraction of dilute $HClO_4$ (≤ 0.2 M) into dilute TOPO (≤ 0.1 M) in CCl_4, the extracting species are TOPO $\cdot$ H_2O and $H_3O^+ \cdot 3\,\overline{TOPO}\ldots ClO_4^-$. The predominant species in the extraction of HNO_3 (≤ 0.3 M) is anhydrous and is TOPO $\cdot$ HNO_3. In the extraction of both dilute $HClO_4$ and HNO_3 into $\overline{TOPO}$ in nitrobenzene, the extracting species is $H_3O^+ \cdot 3\,\overline{TOPO} \cdot yH_2O + X^-$, in which y is probably 0 but may be as large as 3, and in which X^- is the anion. The results of the extraction are interpreted on the basis of the evaluation of the relative basicities of all components in each system and of the dielectric constant of the inert diluent.

4. RECOIL STUDIES OF NUCLEAR REACTIONS OF Ir, Bi, AND Pb^{208} WITH O^{16}

Paul D. Croft
(Ph.D. Thesis)

(From UCRL-11563)

Range-energy curves for 6 to 12 MeV At and Po recoils in Al leaf and Al_2O_3 have been determined using nuclear reactions of O^{16} with Ir to produce the recoils. Al leaf foils of

~0.15 mg/cm^2 and Al_2O_3 foils of 0.007 mg/cm^2 were used. Ranges in mg/cm^2 are 7 to 11% larger in Al_2O_3 than in Al. The range-energy curves obtained were compared with theoretical predictions and were used to transform measured ranges for Po, At, Rn and Fr into recoil energies.

Projected range distributions in stacked Al_2O_3 foils were determined for the α-active products from the reactions $Bi^{209}(O^{16}, X)Y$ at various bombarding energies from 76 to 163 MeV and $Pb^{208}(O^{16}, X)Y$ at 123 and 163 MeV. The products, Y, identified were $Po^{206, 208, 210}$, $At^{209, 211}$, $Rn^{210, 211, 212}$ and Fr^{212}.

The nature of X could be exactly specified only for the Bi bombardments near the Coulomb barrier where the results indicate that Po^{210} and At^{211} are formed by p and 2p transfers, with the residual N^{15} and C^{14} being ejected in a preferentially backward direction. These processes give the recoils energies and ranges up to about 3 times the values possible from a compound nucleus reaction. For both Pb and Bi targets at bombarding energies above about 1.3 times the Coulomb barrier, the range distributions for the products generally peak at ranges from one-quarter to one-half the compound nucleus range, but most have a long-range tail. With the help of angular distribution experiments, it was possible to clarify in a qualitative way the mechanisms at the higher energies. No evidence was obtained which indicates that α transfer might be a preferred mode.

5. ISOMERISM IN $_{85}At^{212}$

W. Barclay Jones
(Ph.D. Thesis)

(From UCRL-11238)

Experiments are reported on the study of $Bi^{209}(\alpha, n)At^{212}$ for alpha energies from 15 to 26 MeV. Isomers of At^{212} were found with half-lives of 0.118 sec and 0.305 sec decaying to Bi^{208} by alpha emission with alpha energies of (7.66, 7.60 MeV) and (7.88, 7.82 MeV). The energy-level assignments and the half-life schematics are discussed in terms of the shell model. The excitation functions were measured and are correlated to compound-nuclear theory.

6. STUDIES IN THE LIQUID-DROP THEORY OF NUCLEAR FISSION

James Rayford Nix
(Ph.D. Thesis)

(From UCRL-11338)

In connection with nuclear fission we study the division of an idealized charged drop, using a simplified version of the liquid-drop model. The degrees of freedom essential to a discussion of the division of a charged drop and the separation of the fragments to infinity are taken into account: a fragment-separation coordinate, a mass-asymmetry coordinate, a deformation coordinage for each fragment, and rotational coordinates for each fragment. To specify fragment deformation, the fragments are represented by spheroids; a nucleus prior to division is represented by two overlapping spheroids. The Hamiltonian for the idealized system consists of a sum of surface, Coulomb, and kinetic energies. A study of the saddle-point energies and shapes calculated in this two-spheroid approximation indicates that the approximation is most useful for discussing the fission of elements lighter than about radium. On the basis of this model, we calculate probability distributions for certain observable characteristics of fission fragments at infinity—their total translational kinetic energy, mass, individual excitation energies, and individual angular momenta. This is done by applying standard static, dynamical, and statistical methods to the Hamiltonian for the system. The present treatment, for the most part, is classical; quantum mechanics is considered only in the statistical-mechanics discussion of the behavior of the system near the saddle point.

The predictions of the model are compared with existing experimental data for distribu- in fragment mass and total translational kinetic energy, for nuclei lighter than radium. The comparisons are made without the use of any adjustable parameters. The theory is capable of accounting for the magnitudes of the most probable values and widths of the experimental distributions, as well as some, but not all, finer details of the distributions. The dependence of the experimental distributions upon nuclear temperature, and the dependence of the experimental most probable kinetic energies upon fissionability parameter are also approximately reproduced by the calculations.

7. FORMATION OF Be^7 IN He^3-INDUCED NUCLEAR REACTIONS

Arthur J. Pape
(Ph.D. Thesis)

(From UCRL-11598)

This work was begun to determine the importance of the direct interaction mechanism $_2He^3 + {}_2He^4$ (cluster) $= {}_4Be^7$ for the "alpha-cluster" nucleus C^{12} and for the Al^{27} nucleus.

The results of the investigation indicate that of a $C^{12}(He^3, Be^7)$ cross section of 57 mb at a He^3 bombarding energy of 31.2 MeV, the direct interaction process has a cross section of approximately one millibarn. The remainder of the Be^7 is formed by compound-nucleus-type processes of which the $C^{12}(He^3;\alpha_1\alpha_2)Be^7$ mechanism is the most important. Recoil data at lower He^3 bombarding energies were fitted assuming only compound-nucleus processes.

The results of the $Al^{27}(He^3, Be^7)$ thick-target recoil experiments indicate that at He^3 bombarding energies up to 30 MeV, Be^7 evaporation accounts for approximately 90 percent of the Be^7 production cross section. The other 10 percent is attributed to direct interaction processes. The magnitudes of the direct interaction cross sections for (He^3, Be^7) and (He^4, Be^7) reactions on aluminum are consistent with the idea that alpha clustering is favored over He^3 clustering in the nuclear surface.

8. PURIFICATION METHODS USED FOR THE MASS-SPECTROMETRIC STUDY OF FISSION OF U-235 AND U-238 AT MODERATE ENERGIES

Roger C. Pettersen
(M. S. Thesis)

(From UCRL-11074)

The sources of natural rare-earth contamination in U_3O_8 pressed-powder targets for cyclotron bombardments have been investigated further and studied more systematically. Mass-spectrometric analysis with an enriched Nd^{144} spiking solution is employed to follow the successive steps of target preparation, and to check the purity of the reagents and handling materials. Target purity is at the level of 2 parts per billion (ppb) for Nd^{144} when it is ready for cyclotron bombardment.

A solvent-extraction method for Ce(IV) is modified to remove cerium-fission products quickly and quantitatively from a bombarded target. We hoped to determine yields for cerium and praseodymium isotopes, but natural contamination in the extraction procedure prevented accurate measurements.

A previously known technique was used to determine independent fractional-chain yields for the mass-135 chain for fission of U^{238} and Th^{232} with 60-MeV helium ions. The independent fractional yields were found to fit a smooth Gaussian curve that was somewhat broader than that for lower-energy bombardments reported elsewhere. Relative independent yields for some of the cesium isotopes and relative cumulative yields for some cerium isotopes are also reported.

9. ENERGY-MASS DISTRIBUTIONS AND ANGULAR MOMENTUM EFFECTS IN HEAVY-ION-INDUCED FISSION

Franz Plasil
(Ph.D. Thesis)

(From UCRL-11193)

This work involves measurements of the energy and mass distributions of fission fragments produced by the bombardment of a number of relatively light elements with heavy ions. The results have been interpreted in terms of an approximate version of the liquid drop model which applies to this region of elements. The energies of both fission fragments from every event considered have been measured with solid-state detectors, and recorded in a correlated manner. The energy data has been transformed to give mass-total kinetic energy density-of-events distributions. The reactions studied were (a) $Er^{170} + O^{16} = Os^{186}$, (b) $Yb^{174} + C^{12} = Os^{186}$, and (c) $W^{182} + O^{16} = Pb^{198}$. Data at several bombarding energies in each case have been obtained. Comparisons with quantitative liquid-drop calculations were made and good agreement was found in the gross features of the distributions, and in the nuclear temperature dependence of the widths. Fission cross sections have been calculated by evaluating fission widths, and fitted to measured cross section data. From the parameters used in these fits, average values for the nuclear temperature of the fissioning nuclei have been obtained. The fission barriers needed for these calculations have been obtained from calculated energies of deformation of rotating charged-liquid drops in their equilibrium configurations.

10. INVESTIGATION OF HIGHLY POPULATED LEVELS OF THE $(d_{5/2})_5^2$ AND $(f_{7/2})_7^2$ CONFIGURATIONS BY THE (α, d) REACTION

Ernest Jean-Marie Rivet
(Ph.D. Thesis)

(From UCRL-11341)

The (α, d) reaction was observed on C^{12}, N^{14}, N^{15}, O^{16}, Ne^{20}, Mg^{24}, S^{32}, Ar^{40} and Ca^{40}. This reaction was induced by the 48-MeV α-particle beam of the William H. Crocker Radiation Laboratory's 60-inch cyclotron, and by the 45- and 50-MeV beams of the new 88-inch variable-energy cyclotron. All the deuteron-energy spectra obtained were dominated by one or more highly populated states called the "gross structure" levels. Evidence that these levels have a common configuration is obtained from (a) the remarkable similarity of their angular distributions, and (b) the relationship between their Q values of formation and the atomic-mass number of the recoil nuclei.

In the assumption of a direct interaction, it is proposed that the levels preferentially populated are of the $[J_T + (J_p J_n)_{J'}]_J$ configuration, where the proton and the neutron couple their spin to J', which in turn couples with the angular momentum of the target to give the final state J. It is also shown that the proton-neutron pair is captured in the $d_{5/2}$ or $f_{7/2}$ shell of the recoil nucleus investigated, and that the maximum final spin (5 or 7) is favored.

The (He^3, p) reaction was observed on C^{12} and O^{16}, and, as expected, the levels highly populated in the (α, d) reactions were once again preferentially populated. The scattering of α particles from N^{14} and O^{16} was also investigated to confirm the two-nucleon nature of the highly populated levels formed by two-nucleon transfer reactions.

The monotonically decreasing pattern of the angular distributions of these gross-structure levels is explained in terms of increasing momentum mismatch.

11. SOME OBSERVATIONS ON LIQUID-LIQUID SETTLING

Wilbur F. Sweeney
(M. S. Thesis)

(From UCRL-11182)

The separation of water from Aroclor 1248 in a gravity settler was investigated with and without induced coalescence. The extent of mixing of the dispersion entering the settling chamber was determined by a light-intensity measuring device. At low flow rates and extents of mixing these two variables appear to control the water concentration of the effluent Aroclor. However, at higher flow rates the water concentration of the effluent Aroclor was affected by many factors, including the flow rate, the extent of mixing, the dispersion zone present between the Aroclor and water phases, and the short circuiting of the Aroclor layer in the settling chamber. The short-circuiting effect was reduced by increasing the Aroclor layer's flow rate. The short circuiting is well illustrated by drawings of the various Aroclor flow patterns produced by varying the operating conditions.

A 1-inch-thick Fiberglas pad mounted in the settling chamber to induce coalescence effectively separated the two phases within the first foot of the settling chamber for all conditions investigated.

12. OPTIMUM PROPORTIONAL CONTROL OF A BLENDING PROCESS USING IMPRECISE FEEDBACK INFORMATION

Carl N. Taylor
(M. S. Thesis)

(From UCRL-11295)

This experimental study verifies the applicability of Acrivos's analysis of linear processes to a randomly disturbed continuous liquid blender which blends water and a salt solution. The process is controlled by a simple proportional controller which is fed imprecise feedback information. Evaluation of process performance is based on the time-averaged value of the square of the concentration fluctuations of the blended stream. Calculation of the mean-square-concentration fluctuations by Acrivos' method shows the mean-square deviations to be a function of loop gain, the relative magnitude of the measurement error and the effluent concentration fluctuations at zero control, the relative-frequency content of the measurement error and the input disturbance signals, and natural damping-frequency characteristics of the blending process.

The predictions of process performance calculated by this method are verified by the experimental results, which show that the mean-square deviations cannot be reduced to zero, but rather a minimum value is obtained as the amount of control action is varied. This minimum results from the counteraction of the favorable effect of feedback of the concentration measurement and the undesirable effect of measurement error.

In general, use of proportional control in this type of problem would greatly improve process performance when measurement error is either small or high-frequency in nature. When the measurement error is large, proportional control is ineffective and other types of control action are recommended.

13. POLARIZATION OF SILVER NUCLEI IN FERROMAGNETS AND THE INTERNAL MAGNETIC FIELD

Gene A. Westenbarger
(Ph. D. Thesis)

(From UCRL-11143)

The signs and magnitudes of the hyperfine-structure constants of two silver isotopes dissolved in the ferromagnetic metals iron and nickel have been determined. The silver nuclei were

polarized by application of a small magnetic field to alloys that had been cooled to near 0.01° K. Thermometry was performed by measurement of the polarization of Co^{60} in the alloy. Spatial anisotropies of both beta and gamma rays from Ag^{104} and Ag^{110m} were measured. Parity was shown not to be conserved in the allowed beta decay of these isotopes. Spin assignments were made or confirmed for several excited states in Cd^{110}. The M1-E2 mixing ratios were determined for the 1384-keV and 1504-keV γ rays following the decay of polarized Ag^{110m}. The products of the nuclear magnetic moment of Ag^{110m} and the internal magnetic fields at the nuclei of silver dissolved in iron and nickel were found to be negative and equal to $-(9.0 \pm 0.5) \times 10^5$ nm gauss for Ag^{110m} in iron and $-(3.5 \pm 0.3) \times 10^5$ nm gauss in nickel. The role of conduction-electron polarization in the production of internal magnetic fields in ferromagnetic metals is discussed.

14. NUCLEAR AND MAGNETIC RESONANCE STUDIES IN S-STATE IONS

H. Hollis Wickman
(Ph.D. Thesis)

(From UCRL-11538)

The S-state ions Fe^{3+} $^6S_{5/2}$, Eu^{2+} $^8S_{7/2}$, and Cm^{3+} $^8S_{7/2}$ have been investigated by means of Mössbauer or electron-spin resonance experiments, or both. Nuclear resonance of Eu^{151} was employed to study the isomer shifts and internal fields in the ferromagnetic insulators EuO and EuS. These results, and isomer shifts for several other europium compounds, are correlated on the basis of core polarization. The temperature dependence of the internal field of EuO was obtained and compared with spin-wave and Weiss-field theories. Iron-57 was studied in the metallo-organics ferrichrome and ferrichrome A. In these paramagnetic compounds the long electronic relaxation time allows a nonvanishing hyperfine field to be observed by Mössbauer resonance. Electron spin resonance measurements with these compounds are also described. A crystal field model is developed which correlates the Mössbauer and electron spin resonance results. In addition, a simple theory for the effect of electronic relaxation on Mössbauer spectra is described and applied to the ferrichrome A results. The paramagnetic resonance of Cm^{3+} has been observed in trichloride and ethylsulfate crystals. The large deviation of Cm^{3+} from S-state behavior was evidenced by the anisotropic g values found for this ion in the above crystals. Experiments with Cm^{3+} in the double nitrate lattice are also described.

H. AUTHOR INDEX

1. PAPERS PUBLISHED AND UCRL REPORTS ISSUED, 1964

BOWMAN, H. R. (See Watson, R. L., UCRL-11848)

BREIVOGEL, F. W., Jr., A. Hebert, and K. Street, Jr.
The Radio-Frequency and Microwave Spectra of Li^6I^{127} by the Molecular-Beam Electric Resonance Method
UCRL-11404, July 1964

J. Chem. Phys.

BREIVOGEL, Francis William, Jr.
The Radio-Frequency and Microwave Spectra of LiBr and LiI
UCRL-11665, September 18, 1964

Ph.D. Thesis

BREIVOGEL, F. W., Jr. (See Hebert, A. J., UCRL-11012)

BUCHER, J. J., and R. M. Diamond
The Extraction of $HClO_4$ by Trilauryl Amine. I. Aromatic Diluents
UCRL-11616, September 1964

J. Phys. Chem.

BUDICK, Burton, Isaac Maleh, and Richard Marrus
Atomic-Beam Studies of Nuclear Properties of Some Rare-Earth Isotopes
UCRL-11345, March 25, 1964

Phys. Rev. 135, B1281 (1964)

BURGER, R. N. (See Conzett, H. E., UCRL-11492)

BURNETT, John L., and B. B. Cunningham
Heats of Formation of $Eu^{+3}(aq)$, $Au^{+2}(aq)$, and $EuO_{1.02}$
UCRL-11126, February 1964

For the Fourth Rare Earth Research Conference, Arizona State University, Tempe, Arizona, April 22-25, 1964)

BURNETT, John L.
The Thermochemistry of Di- and Tri-Valent Europium
UCRL-11850, December 18, 1964

Ph.D. Thesis

BURNETT, D. S. (See Plasil, F., UCRL-11377)

BUSSIERE, André, Norman K. Glendenning, Bernard G. Harvey, Jeannette Mahoney, John R. Meriwether, and Daniel J. Horen
Octupole States in N^{15} and O^{16}
UCRL-11633, August 1964

Phys. Letters

BUSSIERE de NERCY, A. (See Harvey, B. G., UCRL-11378)

BUSSIERE de NERCY, A. (See Meriwether, J. R., UCRL-11484)

CERNY, Joseph, and Richard H. Pehl
The (p, t), (p, He^3), and (p, α) Reactions on O^{16} Induced by 43.7 MeV Protons
UCRL-11223, January 1964

Abstract for the Conference on Nuclear Spectroscopy with Direct Reactions (Argonne National Laboratory, Report No. 6848) Chicago, Illinois, March 9-11, 1964

CERNY, Joseph, and Richard H. Pehl
A Comparison of the O^{16}(p, t) and (p, He^3) Reactions Populating Analog Final States In O^{14} and N^{14}
UCRL-11394, April 1964

Phys. Rev. Letters 12, 619 (1964)

CERNY, J., R. H. Pehl, and G. T. Garvey
T = 2 States in the T_Z = 0 Nuclei O^{16}-Ne^{20} and the T_Z = 1 Nuclei N^{16}-F^{20}
UCRL-11593, July 1964

Phys. Letters

CERNY, J., R. H. Pehl, D. G. Fleming, and C. C. Maples
Observation of T = 3/2 States in C^{13} and N^{15} Via (p, He^3) and (p, t) Reactions
UCRL-11714, October 12, 1964

Abstract for the Winter Meeting of the American Physical Society, Berkeley, California, December 21-23, 1964

CERNY, Joseph, Richard H. Pehl, Fred S. Goulding, and Donald A. Landis
Completion of the Mass 9 Isobaric Quartet Via the Three-Neutron Pickup Reaction $C^{12}(He^3, He^6)C^9$
UCRL-11772, November 1964

Phys. Rev. Letters

CERNY, Joseph (See Garvey, Gerald T.)

CERNY, J. (See Harvey, B. G., UCRL-11231)

CERNY, Joseph III (See Goulding, Fred S., UCRL-11245)

CERNY, Joseph (See Pehl, Richard H., UCRL-11498)

CERNY, J. (See Garvey, G. T., UCRL-11680)

CERNY, Joseph (See Pehl, Richard H., UCRL-11829)

CLEM, Ray G., and E. H. Huffman
Azide Complexes of Palladium (II)
UCRL-11350 Rev., June 1964

J. Inorg. Nucl. Chem.

CLEM, Ray G., and E. H. Huffman
Spectrophotometric Determination of Palladium with Azide
UCRL-11604, August 1964

Anal. Chem.

CLEM, Ray G., and E. H. Huffman
Determination of Azide Ion by Hydrogen Ion Titration After Oxidation with Nitrite
UCRL-11777, November 1964

Anal. Chem.

CONOCCHIOLI, T., M. I. Tocher, and R. M. Diamond
The Extraction of Acids by Basic Organic Solvents. V. Trioctyl Phosphine Oxide-$HClO_4$ and Trioctyl Phosphine Oxide-$HReO_4$
UCRL-11422, May 1964

J. Phys. Chem.

CONWAY, John G.
Energy Levels of 4+ Actinide
UCRL-11332, March 16, 1964

J. Chem. Phys. 41, 904 (1964)

CONWAY, J. G., and B. R. Judd
A Missing Band in the Spectrum of the Tripositive Americium Ion
UCRL-11401, April 1964

J. Chem. Phys. 41, 1526 (1964)

CONZETT, H. E., G. Igo, and W. J. Knox
Polarization in the Elastic Scattering of 22-MeV Protons from Deuterons
UCRL-10586, January 1964

Phys. Rev. Letters 12, B523 (1964)

CONZETT, H. E., R. J. Slobodrian, S. Yamabe, and E. Shield
Elastic Alpha-Alpha Scattering Near 40 MeV
UCRL-11382, April 1964

For the International Conference on Nuclear Physics, July 2-8, 1964, Paris

CONZETT, H. E., H. S. Goldberg, E. Shield, R. J. Slobodrian, and S. Yamabe
The Polarization of 40-MeV Protons Elastically Scattered from Deuterons
UCRL-11415, May 1964

Phys. Letters 11, 68 (1964)

CONZETT, H. E., L. B. Robinson, and R. N. Burger
Semi-Conductor Probe for Investigating Accelerator Beam Pulses
UCRL-11492, June 1964

Nucl. Instr. Methods

CONZETT, H. E., E. Shield, R. J. Slobodrian, and S. Yamabe
Final State Interactions in the $He^3(d, t)2p$ Reaction at 24.7 and 33.4 MeV
UCRL-11689, October 1964

Phys. Rev. Letters 13, 625 (1964)

CONZETT, H. E., P. Darriulat, H. G. Pugh, E. Shield, and R. J. Slobodrian
Excitation Functions for α-He^4 Scattering
UCRL-11715, October 1964

Abstract for the Winter Meeting of the American Physical Society, Berkeley, California, December 21-23, 1964

CONZETT, H. E., E. Shield, R. J. Slobodrian, and S. Yamabe
Complex Phase Shift Analysis of the Elastic α-α Scattering Near 40 MeV
UCRL-11716, October 13, 1964

Abstract for the Winter Meeting of the American Physical Society, Berkeley, California, December 21-23, 1964

COOPER, John A., Raymond C. Gatti, John O. Rasmussen, and Stanley G. Thompson
Gamma-Ray Spectrum of Sb^{131}
UCRL-11255, February 4, 1964

J. Inorg. Nucl. Chem.

CROFT, Paul D.
Recoil Studies of Nuclear Reactions of Ir, Bi, and Pb^{208} with O^{16}
UCRL-11563, July 20, 1964

Ph.D. Thesis

CUNNINGHAM, B. B.
Chemistry of the Actinide Elements
UCRL-11389, April 1964

"Annual Review of Nuclear Science," Vol. 14 (Annual Reviews, Inc., Palo Alto, California, 1964) p. 323

CUNNINGHAM, B. B. (See Burnett, John L., UCRL-11126)

CUNNINGHAM, B. B. (See Fuger, J., UCRL-11596)

DARRIULAT, P., G. Igo, H. G. Pugh, and H. D. Holmgren
Elastic Alpha-Helium Scattering up to 120 MeV
UCRL-11455, May 1964

Phys. Rev. Letters 11, 326 (1964)

DARRIULAT, P., G. Igo, H. G. Pugh, and H. D. Holmgren
The Elastic Scattering of Alpha Particles by Helium between 53 MeV and 120 MeV
UCRL-11603, August 1964

Phys. Rev.

DARRIULAT, P. (See Pugh, H. G., UCRL-11289 Abstract)

DARRIULAT, P. (See Conzett, H. E., UCRL-11715 Abstract)

DAVIDSON, J. P., and M. G. Davidson
Effect of Deformation Vibrations on E2 Branching Ratios in Deformed Even-Even Nuclei
UCRL-11600, August 1964

Phys. Rev.

DAVIDSON, M. G. (See Davidson, J. P., UCRL-11600)

DAVIES, D. W., and J. M. Hollander
Observation of a Second K = 1/2 Band in $_{94}Pu^{239}$
UCRL-11707, October 1964

Nucl. Phys.

DAVIS, Robert M.
Measurement of the Velocity of a Gas in a Field of Variable Composition and Temperature
UCRL-11552, August 11, 1964

M. S. Thesis

DESHPANDE, R. Y.
The Effect of Ambients on the Charge Density and Carrier Mobility in a Silicon–Silicon Dioxide Interface
UCRL-11419, May 8, 1964

Solid-State Electronics

DESHPANDE, R. Y.
Calculations of Surface Potential for Oxide-Passivated High-Resistivity Silicon
UCRL-11508, June 22, 1964

DIAMOND, R. M., F. S. Stephens, and W. J. Swiatecki
Centrifugal Stretching of Nuclei
UCRL-11421, May 1964

Phys. Letters 11, 315 (1964)

DIAMOND, R. M. (See Whitney, D. C., UCRL-10935)

DIAMOND, R. M. (See Stephens, F. S., UCRL-11248)

DIAMOND, Richard (See Stephens, Frank, UCRL-11402)

DIAMOND, R. M. (See Conocchioli, T., UCRL-11422)

DIAMOND, R. M. (See Bucher, J. J., UCRL-11616)

DIETRICH, Klaus
On the Connection of the Independent-Pair Model with a Variational Principle
UCRL-11123, November 11, 1963

Z. Physik 178, 335 (1964)

DIETRICH, K., H.-J. Mang, and J. Pradal
Nuclear Structure Calculations for Deformed Nuclei
UCRL-11376, April 1964

For the International Conference on Nuclear Physics, July 2-8, 1964, Paris

EASLEY, W., J. Huntzicker, E. Matthias, S. S. Rosenblum, and D. A. Shirley
Nuclear Zeeman Effect in Ir^{193}
UCRL-11264, February 1964

Abstract for the Meeting of the American Physical Society, Washington, D. C., April 27-30, 1964

EASTERDAY, H. T., A. J. Haverfield, and J. M. Hollander
An Internal Conversion Coefficient Spectrometer Utilizing Semi-Conductor Detectors
UCRL-11524, July 1964

Nucl. Instr. Methods

EASTERDAY, H. T. (See Haverfield, A. J., UCRL-11607)

FLEISCHER, R. L., P. B. Price, R. M. Walker, and E. L. Hubbard
Track Registration in Various Solid-State Nuclear Track Detectors

Phys. Rev. 133, A1443 (1964)

FLEMING, D. G. (See Cerny, J., UCRL-11714 Abstract)

FORRESTER, J. D., Allan Zalkin, and David H. Templeton
The Crystal and Molecular Structure of Di-(Tetra-n-Butyl Ammonium) Cobalt (II) Bis-(Maleonitrile Dithiolate) and the Geometry of the Divalent Cobalt (II) Bis-(Maleonitrile Dithiolate) Ion
UCRL-11497

Inorg. Chem. 3, 1500 (1964)

FORRESTER, J. D., Allan Zalkin, and David H. Templeton
The Crystal and Molecular Structure of Tetra-N-Butyl Ammonium Copper (III) Bis-(Maleonitrile Dithiolate) and the Geometry of the Monovalent Copper (III)
UCRL-11506, June 1964

Inorg. Chem. 3, 1507 (1964)

FORRESTER, J. D. (See Zalkin, Allan, UCRL-11461)

FORRESTER, J. D. (See Zalkin, Allan, UCRL-11478)

FORRESTER, J. D. (See Zalkin, Allan, UCRL-11514)

FRAENKEL, Z., and S. G. Thompson
Properties of the Alpha Particles Emitted in the Spontaneous Fission of Cf^{252}
UCRL-11655, September 1964

Phys. Rev. Letters

FRANKEL, R. B., D. A. Shirley, and N. J. Stone
The Angular Distributions of Conversion Electrons from Oriented Ce^{137m} Nuclei
UCRL-11462, June 1964

Phys. Rev. 136, B577 (1964)

FRANKEL, R. B. (See Stone, N. J., UCRL-11262 Abstract)

FRANKEL, R. B. (See Huntzicker, J. J., UCRL-11722 Abstract)

FRANKEL, R. B. (See Stone, N. J., UCRL-11734 Abstract)

FUGER, J., and B. B. Cunningham
Microcalorimetric Determination of the Enthaipy of Formation of the Complex Ions of Trivalent Plutonium, Americium and Lanthanum with EDTA
UCRL-11596, February 1964

J. Inorg. Nucl. Chem.

GARRISON, Warren M., Michael E. Jayko, and Winifred Bennet-Corniea
Radiation-Chemical Evidence for Excited Electronic States of the Peptide Bond
UCRL-11381, April 1964

Science 146, 250 (1964)

GARRISON, Warren M., Michael E. Jayko, and Winifred Bennett-Corniea
Production of Excited Electronic States of the Peptide Bond in the Radiolysis of Polyamino Acids and Polypeptides in the Solid State
UCRL-11453, May 1964

For the Twelfth Annual Meeting of the Radiation Research Society, May 18-22, 1964, Miami, Florida

GARRISON, Warren M. (See Sokol, Harvey A., UCRL-11311 Abstract)

GARRISON, Warren M. (See Weeks, Boyd M., UCRL-11314 Abstract)

GARRISON, Warren M. (See Willix, Rodney L. S., UCRL-11467 Abstract)

GARRISON, Warren M. (See Kland-English, Mathilde, UCRL-11469 Abstract)

GARRISON, Warren M. (See Kamal, Ahmad, UCRL-11561)

GARRISON, Warren M. (See Willix, Rodney L. S., UCRL-11728)

GARRISON, Warren M. (See Sokol, Harvey A., UCRL-11733)

GARVEY, Gerald T., Joseph Cerny, and Richard H. Pehl
T = 2 States in Mg^{24}, Ti^{44}, and Fe^{52}

Phys. Rev. Letters 12, 726 (1964)

GARVEY, G. T., J. Cerny, and R. H. Pehl
Energies of Isobaric Multiplets in A = 16 and 20
UCRL-11680, September 1964

Phys. Rev. Letters

GARVEY, G. T. (See Cerny, J., UCRL-11593)

GATTI, Raymond C. (See Cooper, John A., UCRL-11255)

GETZINGER, R. W., and C. R. Wilke
An Experimental Study of Non-Equimolal Diffusion in Ternary Gas Mixtures
UCRL-9987 Rev. 2

A. I. Ch. E.

GILAT, Jacob, and John M. Alexander
Stopping of Dysprosium Ions in Gases and Aluminum
UCRL-11055, December 11, 1963

Phys. Rev.

GILAT, J.
Nuclear Reactions Induced by 50–120-MeV He^4 and 60–140-MeV N^{14} Ions in the Rare Earth Region
UCRL-11283, February 1964

Abstract for the Meeting of the American Physical Society, Washington, D. C., April 27-30, 1964

GILAT, Jacob (See Alexander, John M., UCRL-11187)

GLENDENNING, Norman K.
Nuclear Stripping Reactions

"Annual Review of Nuclear Science," Vol. 13 (Annual Reviews, Inc., Stanford, California, 1963) p. 191

GLENDENNING, Norman K.
Analysis of Two-Nucleon Stripping Reactions
UCRL-11206, January 1964

For the Conference on Nuclear Spectroscopy with Direct Reactions (Argonne National Laboratory, Report No. 6848) Chicago, Illinois, March 9-11, 1964

GLENDENNING, Norman K.
Nuclear Spectroscopy with Two-Nucleon Transfer Reactions
UCRL-11353, May 21, 1964

Phys. Rev.

GLENDENNING, Norman K., and Kichinosuke Harada
Shell Model Calculation of Po^{212}
UCRL-11361, April 1964

Abstract for the Meeting of the American Physical Society, Denver, Colo., June 25-27, 1964

GLENDENNING, Norman K. and Marcel Vénéroni
A Microscopic Description of Inelastic Scattering. Application to Nickel Isotopes
UCRL-11726, October 1964

Phys. Rev. Letters

GLENDENNING, Norman K. (See Bussière, André, UCRL-11633)

GOLDBERG, H. S. (See Conzett, H. E., UCRL-11415)

GOULDING, Fred S., Donald A. Landis, Joseph Cerny, III, and Richard H. Pehl
A New Particle Identifier Technique for Z = 1 and Z = 2 Particles in the Energy Range > 10 MeV
UCRL-11245, February 3, 1964

For the Proceedings of the 9th Scintillation and Semi-Conductors Symposium, Washington, D. C., February 26-28, 1964

GOULDING, Fred S. (See Cerny, Joseph, UCRL-11772)

GRAEFFE, G. (See Siivola, A., UCRL-11559)

GRAHAM, R. L. (See Horen, D. J., UCRL-10943)

GRAHAM, R. L. (See Hollander, J. M., UCRL-11486)

HAAG, J. (See Harvey, B. G., UCRL-11231)

HANSEN, William L., and Blair V. Jarrett
Techniques for the Fabrication of Lithium-Drifted Germanium Gamma Detectors
UCRL-11589, August 7, 1964

Nucl. Instr. Methods

HARADA, Kichinosuke
Note on the Y_{40} Deformation in Heavy Nuclei
UCRL-11234, January 31, 1964

Phys. Letters 10, 80 (1964)

HARADA, Kichinosuke (See Glendenning, Norman K., UCRL-11361 Abstract)

HARVEY, B. G., E. Rivet, J. Cerny, R. H. Pehl, and J. Haag
The Formation of Strongly Populated Levels of $(d_{5/2})^2_5$ and $(f_{7/2})^2_7$
UCRL-11231, January 1964

For the Conference on Nuclear Spectroscopy with Direct Reactions (Argonne National Laboratory, Report No. 6848) Chicago, Illinois, March 9-11, 1964

HARVEY, B. G., J. R. Meriwether, A. Bussière de Nercy, and D. J. Horen
Search for Core-Excited States in N^{15}
UCRL-11378, April 1964

For the International Conference on Nuclear Physics, July 2-8, 1964, Paris

HARVEY, B. G. (See Meriwether, J. R., UCRL-11484)

HARVEY, Bernard G. (See Pehl, Richard H., UCRL-11498)

HARVEY, Bernard G. (See Bussière, André, UCRL-11633)

HARVEY, B. G. (See Springer, A., UCRL-11708)

HAVERFIELD, A. J., H. T. Easterday, and J. M. Hollander
Note on the Pt and Hg Mass-197 Isomers
UCRL-11607, August 1964

Nucl. Phys.

HAVERFIELD, A. J. (See Easterday, H. T., UCRL-11524)

HEBERT, A. J., F. W. Breivogel, Jr., and K. Street, Jr.
The Radiofrequency and Microwave Spectra of LiBr by the Molecular Beam Electric Resonance Method
UCRL-11012, April 1964

J. Chem. Phys. 41, 2368 (1964)

HEBERT, A. J., C. D. Hollowell, and K. Street, Jr.
The Radiofrequency Spectra of LiF by the Molecular Beam Electric Resonance Method
UCRL-11026, October 1964

J. Chem. Phys.

HEBERT, A. J. (See Hollowell, C. D., UCRL-11087)

HEBERT, A. (See Breivogel, F. W., Jr., UCRL-11404)

HEINZELMANN, Fred J., Darshanlal Wasan, and Charles R. Wilke
Concentration and Velocity Profiles in A Stefan Diffusion Tube
UCRL-10421 Rev. 2, July 1964

Ind. Eng. Chem., Fundamentals

HENNICO, Alphonse (See Jacques, Gabriel L., UCRL-10696 Rev. Pt. II)

HEUSS, Jon M.
Mass Transfer in Cocurrent-Gas Liquid Flow
UCRL-11570, August 17, 1964

M.S. Thesis

HOLLANDER, J. M., M. D. Holtz, T. Novakov, and R. L. Graham
Determination of the Atomic Electron Binding Energies in Element 97
UCRL-11486, June 1964

Arkiv Fysik

IGO, G. (See Darriulat, P., UCRL-11455)

IGO, G. (See Darriulat, P., UCRL-11603)

JACQUES, Gabriel L., Alphonse Hennico, Joon Sang Moon, and Theodore Vermeulen
Longitudinal Dispersion in Single-Phase Liquid Flow Through Ordered and Random Packings
UCRL-10696 Rev. Pt. II, November 16, 1964

Chem. Eng. Sci.

JARRETT, Blair (See Hansen, William L., UCRL-11589)

JAYKO, Michael E. (See Garrison, Warren M., UCRL-11381)

JAYKO, Michael E. (See Garrison, Warren M., UCRL-11453)

JOHANSSON, Sven A. E.
Gamma Deexcitation of Fission Fragments. I. Prompt Radiation
UCRL-11739, October 1964

Nucl. Phys.

JOHANSSON, Sven A. E.
Gamma De-Excitation of Fission Fragments. II. Delayed Radiation
UCRL-11740, October 1964

Nucl. Phys.

JONES, W. Barclay
Isomerism in $_{85}At^{212}$
UCRL-11238, February 3, 1964

Ph.D. Thesis

JUDD, B. R. (See Conway, J. G., UCRL-11401)

JUDD, B. R. (See Bordarier, Y., UCRL-11745)

KAMAL, Ahmad, and Warren M. Garrison
Radiolytic Degradation of Aqueous Cytosine: Enhancement by a Second Organic Solute
UCRL-11561, July 1964

Nature

KIM, Yeong E., and J. O. Rasmussen
Energy Levels of Tl^{208} and Bi^{208}
UCRL-11597

Phys. Rev. 135, B44 (1964)

KING, C. Judson
Mass Transfer During Short Surface Exposures in Counter-Current Flow
UCRL-11196, January 1964

KLAND-ENGLISH, Mathilde, and Warren M. Garrison
Dehydropeptide Production in the Radiolysis of Solid Peptides. II
UCRL-11469, May 1964

Abstract for The National Meeting of the American Chemical Society, August 30–September 4, 1964, Chicago, Illinois

KLAPISCH, M. (See Bordarier, Y., UCRL-11745)

KLEIN, Melvin P. (See Wickman, H. Hollis, UCRL-11685)

KNOX, W. J. (See Conzett, H. E., UCRL-10586)

KOCH, Charles W. (See Zalkin, Allan, UCRL-11514)

KORTELING, Ralph G., and Earl K. Hyde
Interaction of High Energy Protons and Helium Ions with Niobium
UCRL-11391, April 1964

Phys. Rev. 136, B425 (1964)

KRAFT, Mary, Nolan Mangleson, and George Rogers
Distribution in Energy Lost by Charged Particles in Passing Through Thin Absorbers
UCRL-11602, August 1964

LANDIS, Donald A. (See Goulding, Fred S., UCRL-11245)

LANDIS, Donald A. (See Cerny, Joseph, UCRL-11772)

LARK, N. (See Stephens, F. S., UCRL-11248)

LARK, N. (See Stephens, Frank, UCRL-11402)

LEVY, Richard M.
Perturbed Angular Correlation Measurements on Ce^{140} and Pr^{143}
UCRL-11663, September 18, 1964

Ph.D. Thesis

MACFARLANE, R. D., and D. W. Seegmiller
Alpha Decay Properties of Some Terbium and Dysprosium Isotopes Near the 82-Neutron Closed Shell
UCRL-11145

Nucl. Phys. 53, 449 (1964)

MACFARLANE, R. D., and A. Siivola
Isobaric Spin Non-Conservation in the Delayed Alpha Decay of Na^{20}
UCRL-11348, July 1964

Nucl. Phys.

MACFARLANE, R. D., J. O. Rasmussen, and M. Rho
Theoretical Calculations of Properties of Rare-Earth Alpha Emitters
UCRL-11416, March 1964

Phys. Rev. 134, B1196 (1964)

MACFARLANE, R. D.
Alpha Decay Properties of Some Thulium and Ytterbium Isotopes Near the 82-Neutron Closed Shell
UCRL-11641, August 1964

Phys. Rev.

MACFARLANE, R. D.
Alpha Decay Properties of Some Lutetium and Hafnium Isotopes Near the 82-Neutron Closed Shell
UCRL-11652, December 1964

Phys. Rev.

MACFARLANE, R. D., and A. Siivola
A New Region of Alpha Radioactivity
UCRL-11765, December 1964

Phys. Rev. Letters

MAHONEY, Jeannette (See Bussière, André, UCRL-11633)

MALEH, Isaac (See Budick, Burton, UCRL-11345)

MANG, H. J., J. K. Poggenburg, and J. O. Rasmussen
Nuclear Structure and Pairing Correlations for the Heavy Elements
UCRL-10939, June 1964

Nucl. Phys.

MANG, H. J.
Alpha Decay
UCRL-11326, February 4, 1964

"Annual Review of Nuclear Science," Vol. 14 (Annual Reviews, Inc., Stanford, California, 1964)

MANG, H.-J. (See Dietrich, K., UCRL-11376)

MANGELSON, Nolan (See Kraft, Mary, UCRL-11602)

MAPLES, C. C. (See Cerny, J., UCRL-11714 Abstract)

MARRUS, Richard (See Budick, Burton, UCRL-11345)

MATTHIAS, E., S. Rosenblum, and D. A. Shirley
G-Factor of the 90-keV Level in Ru^{99} and the Internal Magnetic Field of Ru Dissolved in Ni
UCRL-11719, October 13, 1964

Abstract for the Winter Meeting of the American Physical Society, Berkeley, California, December 21-23, 1964)

MATTHIAS, E., and D. A. Shirley
Perturbation of an Angular Correlation by a Randomly Oriented Magnetic Field
UCRL-11767, November 1964

Abstract for the Annual Meeting of the American Physical Society, New York, January 27-30, 1965

MATTHIAS, E., S. S. Rosenblum, and D. A. Shirley
The Influence of a Randomly Oriented Magnetic Field on Angular Correlations
UCRL-11820, December 1964

Phys. Rev. Letters

MATTHIAS, E. (See Easley, W., UCRL-11264 Abstract)

McLAUGHLIN, Ralph
The Absorption Spectrum of Astatine
UCRL-11233, February 1964

J. Opt. Soc. Am. 54, 965 (1964)

MERIWETHER, J. R., A. Bussière de Nercy, B. G. Harvey, and D. J. Horen
Energy Variation of the Phase Rule in Alpha Particle Scattering
UCRL-11484, June 1964

Phys. Letters

MERIWETHER, J. R. (See Harvey, B. G., UCRL-11378)

MERIWETHER, John R. (See Bussière, André, UCRL-11633)

MICHEL, M. C. (See Asaro, F., UCRL-11379)

MOON, Joon Sang (See Jacques, Gabriel L., UCRL-10696 Rev. Pt. II)

NEWTON, Amos S. (See Olmsted, John, III, UCRL-11631 Abstract)

NEWTON, Amos S. (See Olmsted, John, III, UCRL-11631)

NIX, James Rayford
Studies in the Liquid-Drop Theory of Nuclear Fission.
UCRL-11338, April 1, 1964

Ph.D. Thesis

NOVAKOV, T., and J. M. Hollander
L-Subshell Conversion Ratios in Mixed M1-E2 Transitions
UCRL-11284, February 1964

For the Meeting of the American Physical Society, Washington, D. C., April 27-30, 1964

NOVAKOV, T., and J. M. Hollander
Anomalous L-Subshell Ratios in Mixed M1-E2 Transitions
UCRL-11400, May 1, 1964

Nucl. Phys.

NOVAKOV, T., and J. M. Hollander
Effect of an External Electric Field on Inner Electron Shells in Uranium Observed by Means of Internal Conversion
UCRL-11673, October 12, 1964

Abstract for the Winter Meeting of the American Physical Society, Berkeley, California, December 21-23, 1964

NOVAKOV, T. (See Hollander, J. M., UCRL-11486)

OLMSTED, John, III, Amos S. Newton, and K. Street, Jr.
Determination of the Excitation Functions for Formation of Metastable States of the Rare Gases and Some Diatomic Molecules by Electron Impact
UCRL-11631, September 1964

Abstract for the XXth International Congress on Pure and Applied Chemistry, Moscow, July 12-18, 1965

OLMSTED, John, III, Amos S. Newton, and K. Street, Jr.
Determination of the Excitation Functions for Metastable States of the Rare Gases and Diatomic Molecules by Electron Impact
UCRL-11631, August 1964

J. Chem. Phys.

PAPE, Arthur J.
Formation of Be^7 in He^3-Induced Nuclear Reactions
UCRL-11598, August 4, 1964

Ph.D. Thesis

PEHL, Richard H., Ernest Rivet, Joseph Cerny, and Bernard G. Harvey
The $C^{12}(\alpha, d)N^{14}$ Reaction
UCRL-11498, June 1964

Phys. Rev.

PEHL, Richard H., and Joseph Cerny
Corrected Na^{20} Mass and Levels in Na^{20} and F^{16} Using the (He^3, t) Reaction
UCRL-11839, December 1964

Phys. Letters

PEHL, Richard (See Garvey, Gerald T.)

PEHL, Richard H. (See Cerny, Joseph, UCRL-11223 Abstract)

PEHL, R. H. (See Harvey, B. G., UCRL-11231)

PEHL, Richard H. (See Goulding, Fred S., UCRL-11245)

PEHL, Richard H. (See Cerny, Joseph, UCRL-11394)

PEHL, R. H. (See Cerny, J., UCRL-11593)

PEHL, R. H. (See Garvey, G. T., UCRL-11680)

PEHL, R. H. (See Cerny, J., UCRL-11714 Abstract)

PEHL, Richard H. (See Cerny, Joseph, UCRL-11772)

PERLMAN, I. (See Asaro, F., UCRL-11379)

PLASIL, Franz
Energy-Mass Distributions and Angular Momentum Effects in Heavy-Ion-Induced Fission
UCRL-11193, December 31, 1963

Ph.D. Thesis

PLASIL, F., D. S. Burnett, and S. G. Thompson
Energy Mass Distributions in Induced Fission
UCRL-11377, April 1964

For the International Conference on Nuclear Physics, July 2-8, 1964, Paris

POGGENBURG, J. K. (See Mang, H. J., UCRL-10939)

PRADAL, J. (See Dietrich, K., UCRL-11376)

PRICE, P. B. (See Fleischer, R. L.)

PUGH, H. G., P. Darriulat, and G. Igo
Scattering of 63.7-MeV α Particles from Ni^{64} and Zn^{64}
UCRL-11289, February 1964

Abstract for the Meeting of the Am. Phys. Soc., Washington, D. C., April 27-30, 1964

PUGH, H. G.
Report on the Gatlinburg Conference on "Correlations of Particles Emitted in Nuclear Reactions," October 15-17, 1964
UCRL-11758, November 1964

Science

PUGH, H. G. (See Darriulat, P., UCRL-11455)

PUGH, H. G. (See Darriulat, P., UCRL-11603)

PUGH, H. G. (See Conzett, H. E., UCRL-11715 Abstract)

RAJNAK, K., and B. G. Wybourne
Configuration Interaction in Crystal Field Theory

J. Chem. Phys. 41, 565 (1964)

RAJNAK, K., and B. G. Wybourne
Electrostatically Correlated Spin-Orbit Interactions in ^{N}-Type Configurations
UCRL-11175, December 1963

Phys. Rev. 134, A596 (1964)

RAJNAK, K.
Configuration Interaction in the $4f^3$ Configuration of Pr III
UCRL-11523, July 1964
J. Opt. Soc. Am.

RASMUSSEN, J. O. (See Mang, H. J., UCRL-10939)

RASMUSSEN, John O. (See Bowman, Harry R., UCRL-11203)

RASMUSSEN, J. O. (See Rho, M., UCRL-11224)

RASMUSSEN, John O. (See Cooper, John A., UCRL-11255)

RASMUSSEN, John O. (See Vergnes, Michel N., UCRL-11393)

RASMUSSEN, J. O. (See Macfarlane, R. D., UCRL-11416)

RASMUSSEN, J. O. (See Kim, Yeong E., UCRL-11597)

RASMUSSEN, J. O. (See Watson, R. L., UCRL-11848)

REDLICH, Martin G. (See Baer, Robert M., UCRL-11447)

RHO, M., and J. O. Rasmussen
Comparisons of BCS Nuclear Wave Functions with Exact Solutions
UCRL-11224, March 1964
Phys. Rev. 135, B1295 (1964)

RHO, Mannque
Quasi-Particle Interactions in Even-Even Nuclei
UCRL-11225, January 27, 1964
Nucl. Phys.

RHO, M.
A Contribution to the Quasi-Particle Description of Spherical Nuclei
UCRL-11373, April 1964
For the International Conference on Nuclear Physics, July 2-8, 1964, Paris

RHO, M. (See Macfarlane, R. D., UCRL-11416)

RIVET, Ernest Jean-Marie
Investigation of Highly Populated Levels of the $(d_{5/2})^2_5$ and $(f_{7/2})^2_7$ Configurations by the (a, d) Reaction
UCRL-11341, March 24, 1964
Ph.D. Thesis

RIVET, E. (See Harvey, B. G., UCRL-11231)

RIVET, Ernest (See Pehl, Richard H., UCRL-11498)

ROBINSON, L. B. (See Conzett, H. E., UCRL-11492)

ROGERS, George (See Kraft, Mary, UCRL-11602)

ROSENBLUM, S. S. (See Shirley, D. A., UCRL-11263 Abstract)

ROSENBLUM, S. S. (See Easley, W., UCRL-11264 Abstract)

ROSENBLUM, S. (See Matthias, E., UCRL-11719 Abstract)

ROSENBLUM, S. S. (See Matthias, E., UCRL-11820)

SEEGMILLER, D. W. (See Macfarlane, R. D., UCRL-11145)

SHIELD, E. (See Conzett, H. E., UCRL-11382)

SHIELD, E. (See Conzett, H. E., UCRL-11415)

SHIELD, E. (See Conzett, H. E., UCRL-11689)

SHIELD, E. (See Conzett, H. E., UCRL-11715 Abstract)

SHIELD, E. (See Conzett, H. E., UCRL-11716 Abstract)

SHIRLEY, D. A., and S. S. Rosenblum
High-Resolution Gamma Ray Spectroscopy of Ho^{166m}
UCRL-11263, February 1964

Abstract for the Meeting of the Am. Phys. Soc., Washington, D. C., April 27-30, 1964

SHIRLEY, D. A., and G. A. Westenbarger
Systematics of Hyperfine Fields in an Iron Lattice
UCRL-11664, July 1964

Phys. Rev.

SHIRLEY, D. A. (See Stone, N. J., UCRL-11262 Abstract)

SHIRLEY, D. A. (See Easley, W., UCRL-11264 Abstract)

SHIRLEY, D. A. (See Frankel, R. B., UCRL-11462)

SHIRLEY, D. A. (See Westenbarger, G. A., UCRL-11505)

SHIRLEY, D. A. (See Blok, J., UCRL-11644 Rev.)

SHIRLEY, D. A. (See Wickman, H. Hollis, UCRL-11685)

SHIRLEY, D. A. (See Matthias, E., UCRL-11719 Abstract)

SHIRLEY, D. A. (See Huntzicker, J. J., UCRL-11722 Abstract)

SHIRLEY, D. A. (See Stone, N. J., UCRL-11734 Abstract)

SHIRLEY, D. A. (See Matthias, E., UCRL-11767 Abstract)

SHIRLEY, D. A. (See Matthias, E., UCRL-11820)

SIIVOLA, A., and G. Graeffe
The Alpha Decay of Gd^{151} and Gd^{149}
UCRL-11559, July 8, 1964

Nucl. Phys.

SIIVOLA, Antti
Delayed Protons in the Decay of Te^{108}
UCRL-11834, December 11, 1964

Phys. Rev. Letters

SIIVOLA, A. (See Macfarlane, R. D., UCRL-11348)

SIIVOLA, A. (See Macfarlane, R. D., UCRL-11765)

SIKKELAND, Torbjørn
Fission Excitation Functions in Interactions of C^{12}, O^{16}, and Ne^{22} with Various Targets
UCRL-11242, January 31, 1964

Phys. Rev. 135, B669 (1964)

SISSON, David H. (See Alexander, John M., UCRL-11187)

SLOBODRIAN, R. J. (See Conzett, H. E., UCRL-11382)

SLOBODRIAN, R. J. (See Conzett, H. E., UCRL-11415)

SLOBODRIAN, R. J. (See Conzett, H. E., UCRL-11689)

SLOBODRIAN, R. J. (See Conzett, H. E., UCRL-11715 Abstract)

SLOBODRIAN, R. J. (See Conzett, H. E., UCRL-11716 Abstract)

SOKOL, Harvey A., Winifred Bennett, and Warren M. Garrison
Radiation Chemistry of Peptides: γ-Ray-Induced Oxidation of Poly-L-Glutamic Acid in Aqueous Solution
UCRL-11311, February 1964

Abstract for the Twelfth Annual Meeting of the Radiation Research Society, Miami Beach, Florida, May 18-20, 1964

SOKOL, Harvey A., Winifred Bennett-Corniea, and Warren M. Garrison
A Marked Effect of Conformation in the Radiolysis of Poly-α-L-Glutamic Acid in Aqueous Solution
UCRL-11733, October 1964

J. Chem. Phys.

SPRINGER, A., and B. G. Harvey
Inelastic Scattering of 50.9-MeV Alpha Particles from Calcium-40
UCRL-11708, October 1964

Phys. Letters

STEPHENS, F. S., N. Lark, and R. M. Diamond
Properties of High-Spin Rotational States in Nuclei
UCRL-11248, January 1964

Phys. Rev. Letters 12, C525 (1964)

STEPHENS, Frank, Richard Diamond, and N. Lark
Rotational States Produced in Heavy-Ion Nuclear Reactions
UCRL-11402, May 1964

Nucl. Phys.

STEPHENS, F. S. (See Diamond, R. M., UCRL-11421)

STONE, N. J., R. B. Frankel, and D. A. Shirley
Gamma Ray Spectroscopy Using Ge(Li) Counters
UCRL-11262, February 1964

Abstract for the Meeting of the American Physical Society, Washington, D. C., April 27-30, 1964

STONE, N. J., R. B. Frankel, J. J. Huntzicker, and D. A. Shirley
Nuclear Polarisation of Sb^{125} Using Ge(Li) γ-Ray Detectors
UCRL-11734, October 1964

Abstract for the Winter Meeting of the American Physical Society, Berkeley, California, December 21-23, 1964

STONE, N. J. (See Frankel, R. B., UCRL-11462)

STONE, N. J. (See Huntzicker, J. J., UCRL-11722 Abstract)

STREET, K., Jr. (See Hebert, A. J., UCRL-11012)

STREET, K., Jr. (See Hebert, A. J., UCRL-11026)

STREET, K., Jr. (See Hollowell, C. D., UCRL-11087)

STREET, K., Jr. (See Breivogel, F. W., Jr., UCRL-11404)

STREET, K., Jr. (See Olmsted, John, III, UCRL-11631 Abstract)

STREET, K., Jr. (See Olmsted, John, III, UCRL-11631)

SWEENEY, Wilbur F.
Some Observations on Liquid-Liquid Settling
UCRL-11182, March 12, 1964

M.S. Thesis

SWIATECKI, W. J. (See Diamond, R. M., UCRL-11421)

TAYLOR, Carl N.
Optimum Proportional Control of a Blending Process Using M-Imprecise Feedback Information
UCRL-11295, February 17, 1964

M. S. Thesis

TEMPLETON, David H. (See Ueki, Tatzuo, UCRL-11449)

TEMPLETON, David H. (See Zalkin, Allan, UCRL-11461)

TEMPLETON, D. H. (See Zalkin, Allan, UCRL-11478)

TEMPLETON, David H. (See Forrester, J. D., UCRL-11497)

TEMPLETON, David H. (See Forrester, J. D., UCRL-11506)

TEMPLETON, David H. (See Zalkin, Allan, UCRL-11514)

THOMPSON, S. G.
Fission Barriers of Nuclei Lighter Than Radium
UCRL-11692, September 1964

Abstract for the IAEA Symposium on the Physics and Chemistry of Fission, Salzburg, Austria, March 22-26, 1965

THOMPSON, Stanley G. (See Bowman, Harry R., UCRL-11203)

THOMPSON, Stanley G. (See Cooper, John A., UCRL-11255)

THOMPSON, S. G. (See Plasil, F., UCRL-11377)

THOMPSON, S. G. (See Asaro, F., UCRL-11379)

THOMPSON, S. G. (See Fraenkel, Z., UCRL-11655)

THOMPSON, S. G. (See Watson, R. L., UCRL-11848)

TOCHER, M. I. (See Conocchioli, T., UCRL-11422)

UEKI, Tatzuo, Allan Zalkin, and David H. Templeton
The Crystal Structure of Osmium Tetroxide
UCRL-11449, May 1964

Acta Cryst.

VENERONI, Marcel (See Glendenning, Norman K., UCRL-11726)

VERGNES, Michel N. and John O. Rasmussen
Influence of Pairing Correlations on E1 Transition Probabilities in Odd-A, Deformed, Rare-Earth Nuclei
UCRL-11393, April 1964

Nucl. Phys.

VERMEULEN, Theodore
Longitudinal Dispersion in Process Equipment
UCRL-11157

For the Meeting of Institution Medland Section, Birmingham, England, March 11, 1964

VERMEULEN, Theodore (See Jacques, Gabriel L., UCRL-10696 Rev. Pt. II)

WALKER, R. M. (See Fleischer, R. L.)

WALLMAN, J. C.
A Structural Transformation of Curium

J. Inorg. Nucl. Chem. 26, 2053 (1964)

WASAN, D. T.
Note on a Three-Point Extrapolation Formula
UCRL-11306, February 1964

Chem. Engr. Sci.

WASAN, D. T. and C. R. Wilke
A Diffusion-Convection Analysis of Gas-Phase Mass Transfer in Turbulent Flow
UCRL-11557, July 1964

Abstract for the A. I. Ch. E. Annual Meeting, Symposium of Fundamentals of Heat and Mass Transfer, Boston, December 6, 1964

WASAN, Darshanlal T.
Analysis of Gas-Phase Mass Transfer in Turbulent Flows
UCRL-11629, September 1964

Ph.D. Thesis

WASAN, Darshanlal (See Heinzelmann, Fred J., UCRL-10421 Rev. 2)

WASAN, D. T. (See Wilke, C. R., UCRL-11629)

WATSON, R. L., H. R. Bowman, S. G. Thompson, and J. O. Rasmussen
Prompt Electron Spectra from Cf^{252} Fission Fragments
UCRL-11848, December 1964

Phys. Rev. Letters

WATSON, Rand (See Bowman, Harry R., UCRL-11693 Abstract)

WEEKS, Boyd M., and Warren M. Garrison
Reactions of the Hydrated Electron with Amino Acids
UCRL-11314, February 1964

Abstract for the Twelfth Annual Meeting of the Radiation Research Society, Miami Beach, Florida, May 18-20, 1964

WESTENBARGER, G. A., and D. A. Shirley
Polarization of Silver Nuclei in Metallic Iron and Nickel
UCRL-11505, June 1964

Phys. Rev.

WESTENBARGER, G. A. (See Shirley, D. A., UCRL-11664)

WHITNEY, D. C., and R. M. Diamond
Ion Exchange Studies in Concentrated Solutions. IV. The Nature of the Resin Sulfonate-Cation Bond in Strong Acid Solutions
UCRL-10935, December 1963

J. Phys. Chem. 68, 886 (1964)

WICKMAN, H. Hollis
Nuclear and Magnetic Resonance Studies in S-State Ions
UCRL-11538, September 1964

Ph. D. Thesis

WICKMAN, H. Hollis, Melvin P. Klein, and D. A. Shirley
Paramagnetic Resonance of Fe^{3+} in Polycrystalline Ferrichrome A
UCRL-11685, September 1964

J. Chem. Phys.

WILKE, C. R., and D. T. Wasan
A New Correlation for the Psychrometric Ratio
UCRL-11629, September 1964

For the Joint A. I. Ch. E. and British Institute of Chemical Engineers Transport Phenomena Symposium, June 13-19, 1965

WILKE, C. R. (See Getzinger, R. W., UCRL-9987 Rev. 2)

WILKE, Charles R. (See Heinzelmann, Fred J., UCRL-10421 Rev. 2)

WILKE, C. R. (See Wasan, D. T., UCRL-11557 Abstract)

WILLIAMSON, Stanley M. (See Zalkin, Allan, UCRL-11514)

WILLIX, Rodney L. S., and Warren M. Garrison
Radiation Chemistry of the Aqueous Glycine–Cupric Sulfate System
UCRL-11467, May 1964

Abstract for the National Meeting of the American Chemical Society, August 30-September 4, 1964, Chicago, Illinois

WILLIX, Rodney L. S., and Warren M. Garrison
The Effect of Cupric Ion on the Radiation Chemistry of Aqueous Glycine
UCRL-11728, October 1964

J. Phys. Chem.

WINSBERG, Lester
Recoil Studies of Nuclear Reactions Induced by High-Energy Particles. I. The Production of Tb^{149}

Phys. Rev. 135, B1105 (1964)

WYBOURNE, B. G. (See Rajnak, K.)

WYBOURNE, B. G. (See Rajnak, K., UCRL-11175)

YAMABE, S. (See Conzett, H. E., UCRL-11382)

YAMABE, S. (See Conzett, H. E., UCRL-11415)

YAMABE, S. (See Conzett, H. E., UCRL-11689)

YAMABE, S. (See Conzett, H. E., UCRL-11716 Abstract)

ZALKIN, Allan, J. D. Forrester, and David H. Templeton
Crystal and Molecular Structure of Ferrichrome A
UCRL-11461, May 1964

Science 146, 261 (1964)

ZALKIN, Allan, J. D. Forrester, and D. H. Templeton
The Crystal Structure of Sodium Perxenate Hexahydrate
UCRL-11478, June 1964

Inorg. Chem. 3, 1417 (1964)

ZALKIN, Allan, J. D. Forrester, David H. Templeton, Stanley M. Williamson, and Charles Koch
Potassium Perxenate Nonahydrate
UCRL-11514, June 1964

J. Am. Chem. Soc. 86, 3569 (1964)

ZALKIN, Allan (See Ueki, Tatzuo, UCRL-11449)

ZALKIN, Allan (See Forrester, J. D., UCRL-11497)

ZALKIN, Allan (See Forrester, J. D., UCRL-11506)

2. CONTRIBUTIONS TO THIS REPORT

ADAMSON, M.
D.6

ALMARAZ, H. A.
E.15,16

ASARO, F.
A.24

BAER, R. M.
A.5

BENNETT-CORNIEA, W.
D.18,20

BLOK, J.
A.20

BORDARIER, Y.
D.3

BOWMAN, H. R.
B.8,11

BREIVOGEL, F. W.
D.26

BRITT, H. C.
B.6,9

BURGER, R. N.
E.10

BURNETT, D. S.
B.4

BUSSIERE, A.
C.12,13

CERNY, J.
C.8,9,10,11

CLARK, D. J.
E.18

CLARKSON, J. E.
B.2

CLEM, R. G.
D.12,13,14

CLOSE, E.
E.18

COHEN, S.
B.3

CONOCCHIOLI, T. J.
D.25

CONWAY, J. G.
D.1,2,11

CONZETT, H. E.
C.1,3,14
E.10

COOPER, J. A.
A.25

DARRIULAT, P.
C.5

DAVIES, D. W.
A.12

DAVIS, R. M.
F.3

DESHPANDE, R. Y.
E.3

DIAMOND, R. M.
A.16,17
D.23,24,25

EASTERDAY, H. T.
A.2,3

FORRESTER, J. D.
D.4,5,7,8,9

FRAENKEL, Z.
B.7

FRANKEL, R. B.
A.23
D.28

GARRISON, W. M.
D.18,19,20,21

GARVEY, G. T.
C.9

GATTI, R. C.
B.4,5

GLENDENNING, N. K.
C.2,4,12

GOLDBERG, H. S.
C.3

GOLDSWORTHY, W. W.
E.13

GOULDING, F. S.
C.11
E.2,7

GRAEFFE, G.
A.8

GRAHAM, R. L.
A.15

GRUNDER, H. A.
E.18

GUTMACHER, R. G.
D.2

HANSEN, W. L.
E.4

HARRIS, J. A.
D.27

HARVEY, B. G.
C.6,7,10,12,13

HAVERFIELD, A. J.
A.2,3

HEBERT, A. J.
D.26

HEUSS, J. M.
F.5

HOLLANDER, J. M.
A.2,3,7,12,13,14,15,25
D.27

HOLLOWELL, C. D.
D.26

HOLMGREN, H. D.
C.5

HOLTZ, M. D.
A.15

HOPKINS, T. E.
D.6

HOREN, D. J.
C.12,13